Master's thesis

NTNU
Norwegian University of Science and Technology
Faculty of Engineering
Department of Geoscience and Petroleum

Gaute Moe Fløan

# Caledonian structural, metamorphic and magmatic evolution of the Rödingsfjället Nappe Complex

Master's thesis in Geology
Supervisor: Bjørn Eske Sørensen
Co-supervisor: Trond Slagstad & Kerstin Saalmann
May 2022

NTNU
Norwegian University of
Science and Technology

Gaute Moe Fløan

# Caledonian structural, metamorphic and magmatic evolution of the Rödingsfjället Nappe Complex

Master's thesis in Geology
Supervisor: Bjørn Eske Sørensen
Co-supervisor: Trond Slagstad & Kerstin Saalmann
May 2022

Norwegian University of Science and Technology
Faculty of Engineering
Department of Geoscience and Petroleum

NTNU
Norwegian University of
Science and Technology

# Abstract

The Rödingsfjället Nappe Complex and the Helgeland Nappe Complex are the two major components of the Uppermost Allochthon and are believed to contain rocks with both oceanic and continental affinity representing the outer margin of peri-Laurentia and unknown microcontinents. The metasediments in the Kjerringfjell Group hosting the 578 Ma Umbukta gabbro within the Rödingsfjället Nappe Complex has shown signs of regional partial melting and migmatization at 624 Ma. The Umbukta gabbro is geochemically similar to the Seiland Igneous Province located within the Kalak Nappe Complex in Finnmark, which records an extensive Neoproterozoic tectonothermal history. A correlation between the Rödingsfjället Nappe Complex and the Kalak Nappe Complex has been suggested based on an apparently similar metamorphic and magmatic history.

In order to test the correlation with the Kalak Nappe Complex and the Seiland Igenous Province, the shores along the western part of Kallvatnet in the Kjerringfjell Group have been carefully mapped and sampled for petrographic, whole-rock geochemical and U-Pb geochronological analyses. The analyses were used to increase the understanding of the geological evolution of the Rödingsfjället Nappe Complex, and to constrain the timing of Neoproterozoic through Silurian metamorphic and magmatic events.

The geochemical data, field observations and petrography indicate that the Kjerringfjell Group has not undergone regional partial melting. The "leucosomes" observed at Kallvatnet are instead felsic veins that have altered their immediate host rock forming reaction rims. The felsic veins did not yield a good crystallization age, but structural considerations suggest they are likely to be Neoproterozoic in age.

A Neoproterozoic metamorphic event at 560 Ma was dated at Kallvatnet and Sauvasshytta which is located near the Umbukta gabbro, dated at 614 Ma in this study, which cross-cuts open folds. The lack of an extensive Neoproterozoic metamorphic evolution in the Kjerringfjell Group weakens the correlation between the Rödingsfjället Nappe Complex and the Kalak Nappe Complex. The geochemical data show that the mafic rocks from Kallvatnet, Umbukta and Mofjell differ, which strengthens the hypothesis that an undiscovered tectonic contact exists between Umbukta and Kallvatnet, i.e., internally in the Kjerringfjell Group. It is suggested that the 624 Ma high-grade event is related to contact metamorphism related to the Umbukta gabbro.

Metamorphic events dated at 450 Ma and, 484 Ma and tonalitic magmatism at 466 Ma and the activation of the 475 Ma Langfjell Shear Zone in the Kjerringfjell Group overlap with tectonothermal events in the Taconian orogeny and in the Helgeland Nappe Complex, confirming the affinity between the Rödingsfjället Nappe Complex and the Helgeland Nappe Complex. The geochemical data show that there are at least two generations of mafic rocks at Kallvatnet. Concordant mafic sheets with reaction rims intruded either during the late Ordovician in association with an island-arc system associated with the Helgeland Nappe Complex or during the Neoproterozoic in association with a pre-Taconian island-arc. Discordant mafic sheets at Kallvatnet have likely intruded in a back-arc basin behind an island-arc related to the Helgeland Nappe Complex during the late Ordovician. Dating of monazites and zircons in combination of structural mapping suggests that the Kjerringfjell Group underwent a tectonothermal event at 437 Ma under epidote amphibolite facies representing the Scandian collision forming isoclinal F1 and N-S/NE-SW plunging F2 folds.

# Sammendrag

Rödingsfjälldekkekomplekset og Helgelanddekkekomplekset utgjør de to store komponentene i øverste allokton og består av bergarter med både oseanisk og kontinental affinitet som representerer den ytterste marginen av peri-Laurentia og ukjente mikrokontinent. Metasedimentene i Kjerringfjellgruppen som er vertskap for den 578 Ma Umbuktagabbroen i Rödingsfjälldekkekomplekset har vist spor av regional oppsmelting og migmatisering ved 624 Ma. Umbuktagabbroen har lik geokjemisk signatur som Seiland Magmatiske Provins lokalisert innad i Kalakdekkekomplekeset i Finnmark, som har en dokumentert omfattende neoproterosoisk geologisk utvikling. En korrelasjon mellom Rödingsfjälldekkekomplekset og Kalakdekkekomplekset har blitt foreslått basert tilsynelatende lik metamorf og magmatisk historie.

For å teste korrelasjonen med Kalakdekkekomplekset og Seiland Magmatiske provins, områder langs de godt eksponerte blotningene på den vestlige delen av Kallvatnet har blitt grundig kartlagt og prøvetatt for petrografiske, geokjemiske og U-Pb geokronologiske analyser. Analysene ble brukt til å øke forståelsen av den geologiske utviklingen av Rödingsfjälldekkekomplekset og for å undersøke den metamorfe og magmatiske utviklingen fra neoproterosoikum til silur.

Geokjemiskeanalyser, feltobservasjoner og petrografi indikerer at Kjerringfjellgruppen ikke har gjennomgått regional delvis oppsmelting. «Leukosomene» observert på Kallvatnet viser seg å være felsiske årer som har omdannet vertsbergarten og dannet reaksjonshaloer. De felsiske årene ga ingen god krystallisasjonsalder, men strukturelle betraktninger indikerer at de er neoproterosoiske.

En neoproterosoisk 560 Ma metamorf hendelse ble datert på Kallvatnet og Sauvasshytta som er lokalisert nær Umbuktagabbroen. Gabbroen har blitt datert til 614 Ma i denne studien og kutter åpne folder. Mangelen på dokumentasjon av en omfattende neoproterosoisk geologisk utvikling av Kjerringfjellgruppen svekker korrelasjonen mellom Rödingsfjälldekkekomplekset og Kalakdekkekomplekset. Geokjemidataen viser at de mafiske bergartene fra Kallvatnet, Umbukta og Mofjell stammer fra ulike kilder. Dette styrker hypotesen som omhandler en uoppdaget tektoniskgrense mellom Umbukta og Kallvatnet, f.eks., internt i Kjerringfjellgruppen. Det er foreslått at den 624 Ma høygrads metamorfosen kan være relatert til kontaktmetamorfose relatert til intrusjonen av Umbuktagabbroen.

Metamorfe hendelser i Kjerringfjellgruppen har også blitt datert; 450, 484 Ma og tonalittisk magmatisme ved 466 Ma, samt aktivering av den 475 Ma Langfjellskjærsonen. Disse hendelsene overlapper med den Takoniske orogenesen og tektonotermale hendelser i Helgelanddekkekomplekset, som indikerer affinitet mellom Rödingsfjälldekkekomplekset og Helgelanddekkekomplekset. Den geokjemiske dataen indikerer at det finnes minst to generasjoner av mafiske bergarter på Kallvatnet. De konkordante mafiske lag med reaksjonshaloer intruderte enten i løpet av sen-ordovisium i et øybuesystem assosiert med Helgelanddekkekomplekset eller i løpet av neoproterosoikum assosiert med en pre-Takonsk øybue. De diskordante mafiske lagene ved Kallvatnet har mest sannsynlig intrudert i et rift-basseng bak en øybue relatert til Helgelanddekkekomplekset i løpet av sen-ordovisium. Dateringer av monasitter og zirkoner i kombinasjon av strukturell kartlegging og petrografi indikerer at Kjerringfjellgruppen gjennomgikk en 437 Ma tektonotermal hendelse under epidot-amfibolitt-facies som representerer den Skandiske-kollisjonen som dannet F1 og N-S/NØ-SW stupende F2 folder.

# Acknowledgement

This project was carried out with the guidance of Dr. Bjørn Eske Sørensen as the internal supervisor from the Norwegian University of Science and Technology (NTNU), Dr. Trond Slagstad, and Dr. Kerstin Saalmann from the Geological Survey of Norway (NGU) as external supervisors.

This project has been inspiring and challenging. To get the opportunity to spend twenty days in the field in the beautiful Rana County has been highly educational and has made me a much better field geologist. I really appreciate that I got the opportunity to discuss with highly experienced and competent geologists from NTNU and NGU.

I would like to thank my supervisors, Dr. Bjørn Eske Sørensen, Dr. Trond Slagstad and Dr. Kerstin Saalmann for all the support and guidance throughout the project. Bjørn you have always been available, spread joy, given me support and good educational discussions, and helped in the microscopy lab. Trond, you have been highly dedicated, friendly, and given me much more help than I could ever expect with geochronology, geochemistry, lab work and field work. We have had many interesting discussions during the last year, I have learned a lot, and I have really appreciated your support and guidance. Kerstin, thanks for the help with structural geology, both in the field and in the office and for the help with difficult questions throughout the project.

I would like to thank the friendly people at NGU that have given me guidance at the lab with mineral separation, LA-ICP-MS, and good discussions at lunchtime. I want to thank Dr. Stefanie Lode, who has helped me in the SEM-lab at NTNU, with coating, to take CL- and BSE-images and generate EDS-maps. Thanks to Ingrid Moe Dahl for reading my thesis and for the feedback. Thanks to Kjetil Eriksen and Jostein Røstad at the thin section lab at NTNU.

In the end I would like to thank med fellow students at NTNU, you have given me joy, and incredible many good memories throughout my time as a student. I would like to give a special thanks to Kristoffer and Sindre (Fniffene), Johanne, Ingeborg, Johanne, Lisa, Sofie, Anders, Sander and Brage. You have made all those long days/nights at school feel like a party!

Finally, I would like to thank my parents for unlimited support and help throughout all my years as a student. You have always been available, and I am forever grateful for that.

Gaute Moe Fløan
Trondheim, May 2022

# Table of Contents

# Figures

# Tables



# Abbreviations and symbols

| | | |
|---|---|---|
| alm | - | almandine |
| an | - | anorthite |
| ap | - | apatite |
| BAB | - | Back-Arc Basin basalt |
| BSE | - | Backscattered Electron |
| bt | - | biotite |
| cal | - | calcite |
| chl | - | chlorite |
| CL | - | Cathodoluminescence |
| COOR | | Coordinates |
| czo | - | clinozoisite |
| EDS | - | Energy-Dispersive X-ray Spectroscopy |
| E-MORB | - | Enriched-Mid-Ocean-Ridge Basalt |
| EPMA | - | Electrone Probe Micro-Analyzer |
| fs | - | feldspar |
| Ga | - | One billion years (giga annum) |
| GBM | | Grain Boundary Migration |
| grt | - | garnet |
| hbl | - | hornblende |
| HFSE | - | High Field Strength Elements |
| HNC | - | Helgeland Nappe Complex |
| HREE | - | Heavy Rare Earth Elements |

| | | |
|---|---|---|
| ICP-AES | - | Inductively Coupled Plasma Atomic Emission Spectroscopy |
| ID-TIMS | - | Thermal Ionization Mass Spectrometry Isotopic Dilution |
| Ill-smc | - | Ilmenite-smectite |
| Ilm | - | Ilmenite |
| IP | - | Ionic Potential |
| KD | - | Partition coefficient |
| KFMASH | - | $K_2O$-FeO-MgO-$Al_2O_3$-$SiO_2$-$H_2O$ |
| LA-ICP-MS | - | Laser Ablation Inductively Coupled Plasma Mass Spectrometry |
| LILE | - | Large Ion Lithophile Elements |
| LREE | - | Light Rare Earth Elements |
| LSZ | - | Langfjell Shear Zone |
| Ma | - | One million years (mega annum) |
| mnz | - | monazite |
| MORB | - | Mid-Ocean-Ridge Basalt |
| ms | - | muscovite |
| MSWD | - | Mean Square of Weighted Deviates |
| myr | - | Millions of Years |
| $N_n$ | - | Concentration of isotope |
| NGU | - | Norges Geologiske Undersøkelse |
| N-MORB | - | Normal-Mid-Ocean-Ridge Basalt |
| NTNU | - | Norwegian University of Science and Technology |
| OIB | - | Ocean Island Basalt |
| Pbc | - | Common lead |
| Plag | - | plagioclase |
| PPL | - | Plane Polarized Light |
| ppm | - | Parts Per Million |
| P-T | - | Pressure-Temperature |
| Q | - | Energy released during decay |
| qz | - | quartz |
| REE | - | Rare Earth Elements |

| | | |
|---|---|---|
| RNC | - | Rödingsfjället Nappe Complex |
| rt | - | rutile |
| SEM | - | Secondary Electron Microscopy |
| SHRIMP | - | Sensitive High-Resolution Ion MicroProbe |
| SIMS | - | Secondary Ion Mass Spectrometry |
| SIP | - | Seiland Igneous Province |
| SPO | - | Shape Preffered Orientation |
| S-T | - | Sauren-Torghatten |
| SZ | | Subduction Zone |
| t | - | Time |
| ttn | - | titanite |
| TW | - | Tera Wasserburg |
| UHP | - | Ultra-High-Pressure |
| VAB | - | Volcanic-Arc Basalt |
| WP Alk | - | Within-Plate Alkali basalt |
| WP Th | - | Within-Plate Tholeiites |
| wt. % | - | Weigth percent |
| Z | - | Ionic charge |
| zo | - | zoisite |
| zr | - | zircon |
| Å | - | Ionic radius |
| α | - | Alpha particle |
| β | - | Beta particle |
| λ | - | Decay constant |
| σ | - | Standard deviation |

# 1 Introduction

## 1.1 Background and aim of study

The Scandinavian Caledonides has traditionally been divided into allochthons including, in tectonostratigraphic order, the Lower, Middle, Upper and Uppermost Allochthon, where the Lower and the Middle allochthons are believed to have originated on the Baltican margin, whereas the Upper and Uppermost allochthons represent rock formed within the Iapetus ocean and near Laurentian margin, respectively (Gee et al., 1985). Recent studies have shown that this simple view of the structure of the Scandinavian Caledonides is simplified (Corfu et al., 2014) and a number of recent studies have suggested deviations from the traditional view.

The Rödingsfjället Nappe Complex and the Helgeland Nappe Complex are the two major units in the Uppermost Allochthon in the Scandinavian Caledonides, and share several similarities, e.g. Ordovician shear zone activity which has been correlated with the Taconian orogeny on the Laurentian margin (Yoshinobu et al., 2002, Roberts et al., 2007, Slagstad et al., 2021) The geological evolution of the Helgeland Nappe Complex has been widely studied, in contrast the Rödingsfjället Nappe Complex is relatively poorly studied.

Slagstad et al. (2021) found evidence of a Neoproterozoic (ca. 624 Ma) high-grade metamorphic event in the Kjerringfjell Group within the Rödingsfjället Nappe Complex, located in the Rana area. The 578 Ma Umbukta gabbro is also located in the Kjerringfjell Group and is believed to have originated in a within-plate setting (Høyen, 2016, Slagstad et al., 2021). The Umbukta gabbro has a similar chemical signature as the Seiland Igneous Province located within the Kalak Nappe Complex in Finnmark, which is known to have undergone an extensive Neoproterozoic tectonothermal evolution (Slagstad et al., 2021). A link between the Rödingsfjället Nappe Complex and the Kalak Nappe Complex has been suggested by Slagstad et al. (2021) based on at least partly similar Neoproterozoic metamorphic evolution and similar and coeval within-plate intrusions. This correlation implies that the Kalak Nappe Complex and other nappe complexes in the Middle Allochton are exotic to Baltica rather than indigenous.

The aim of this study is to develop a better understanding of the structural, metamorphic, and magmatic evolution of the Kjerringfjell Group in the Rödingsfjället Nappe Complex. The validity of the hypothesis proposed by Slagstad et al. (2021), the relation between the rocks at Kallvatnet and Umbukta, and similarities between the Rödingsfjället Nappe Complex and Helgeland Nappe Complex will be investigated. In addition, differences between the Kjerringfjell Group and the Mofjell Group within the Rödingsfjället Nappe Complex will be examined. An improved understanding will help to clarify the origin and evolution of the Rödingsfjället Nappe Complex and increase the knowledge of the structure and origin of different components in the Scandinavian Caledonides.

## 1.2 Study area description

This study is based on field observations, U-Pb zircon and monazite isotope and whole-rock geochemical analyses. The main study area is located at Kallvatnet in the Rana area southeast of Mo i Rana in Nordland County (*Figure 1)*. The lake is dammed up, so the rocks have excellent exposure along the shores. Approximately 20 square km (including the lake) was carefully mapped, including areas along the shores of Kallvatnet and at Damtjønnfjellet. A geological map is presented in *Figure 41*. The map includes structural measurements and lithology differentiation. Areas indicated on the map have been described in detail in *5.1.* Some field work was also done at Gammelgardsfjellet and at Sauvasshytta near Umbukta. Most of the samples were collected at Kallvatnet, a complete sample map is shown in *Figure 33.*

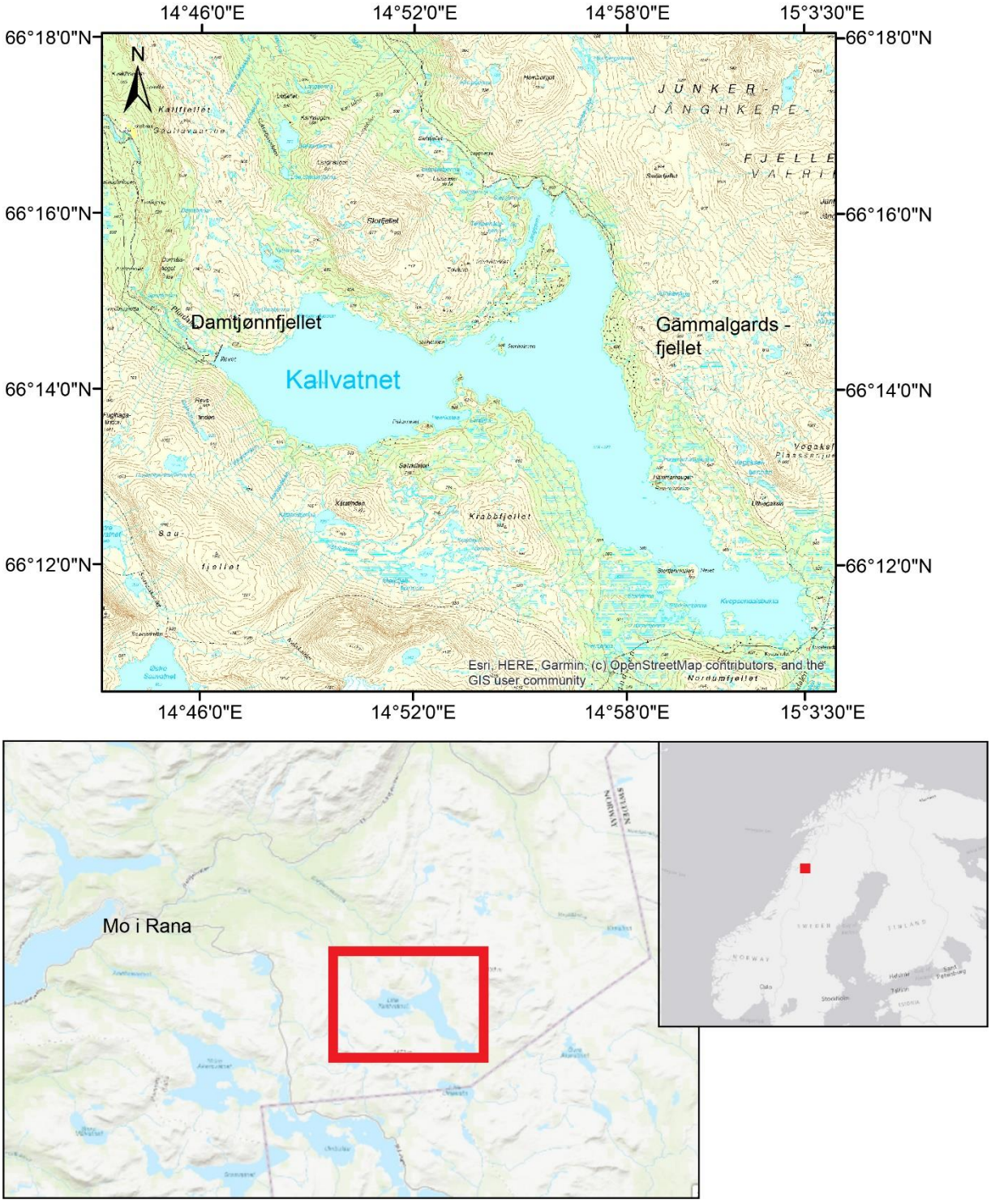


***Figure 1**: Study area. Coordinate System: WGS 1984 UTM Zone 33N.*

# 2 Regional geology

## 2.1 A tectonic summary of Laurentia and Baltica

In the Archean, Laurentia and peri-Baltica may have been assembled in a Neoarchean supercontinent called Kenorland (Lubnina and Slabunov, 2011). The existence of the supercontinent Kenorland has been heavily debated e.g., by Bleeker (2003) and is still questionable (Evans and Mitchell, 2011). In the Proterozoic it is believed that two supercontinents existed, Nuna and Rodinia. The supercontinent Nuna formed at ca. 1.9-1.8 Ma (Hawkesworth et al., 2009). The global reconstruction of Nuna shows Laurentia located in the northern hemisphere and Baltica (Fennoscandia) at approximately 30 degrees north (Zhang et al., 2012). The assembly of Rodinia occurred through worldwide orogenic events between 1300 and 900 Ma (Li et al., 2008). The Grenville, Sveconorwegian and the Sunsans orogens are typically used as the proof of the collision between Laurentia, Baltica and Amazonia forming a central part of Rodinia in a triple-junction configuration (Hoffmann, 1991, Li et al., 2008). The first major break-up event occurred at the western margin of Laurentia around 750 Ma (Li et al., 2008). It is thought that Laurentia was the center of both the assembly and the break-up, because the continent is flanked by Neoproterozoic passive margins (Hoffmann, 1991).

The common interpretation is that Laurentia and Baltica were assembled and shared a common clockwise rotation from equatorial position towards the south from 750 to 600 Ma (Torsvik et al., 1996). In Ediacaran times, at latitudes of 30 degrees south, the break-up of between Laurentia and Baltica (the final break-up of Rodinia) began, and marked the opening of the Iapetus ocean with asymmetric rifting and relative rotations of the two continents resulting in several dyke complexes (Torsvik et al., 1996). Rift-related magmatism between 615 and 550 Ma at the south east coast of Laurentia indicates separation from Amazonia (e.g., Miller and Barr, 2004, Torsvik et al., 1996).

After the Iapetus opening, Laurentia and Amazonia drifted and rotated separately. Baltica drifted anticlockwise northwards from 60 to 30 degrees on southern latitudes and collided with Avalonia at 445 Ma and finally with Laurentia resulting in the closure of the Iapetus ocean, formation of the Scandinavian Caledonides and the new supercontinent called Laurasia at equatorial latitudes at 430 Ma (Torsvik et al., 1996, Cocks and Torsvik, 2002, Cocks and Torsvik, 2005). The exact drifting history of Baltica towards the equator is uncertain. Cambrian through Silurian reconstructions, e.g., *Figure 2* from Corfu et al. (2014), suggest that Baltica was proximal to Siberia and peri-Gondwanan terranes and that the positions of Siberia, Gondwana and Baltica were uncertain. This could indicate the possibility of Siberian or Gondwanan terranes in the different nappe complexes in the Scandinavian Caledonides.

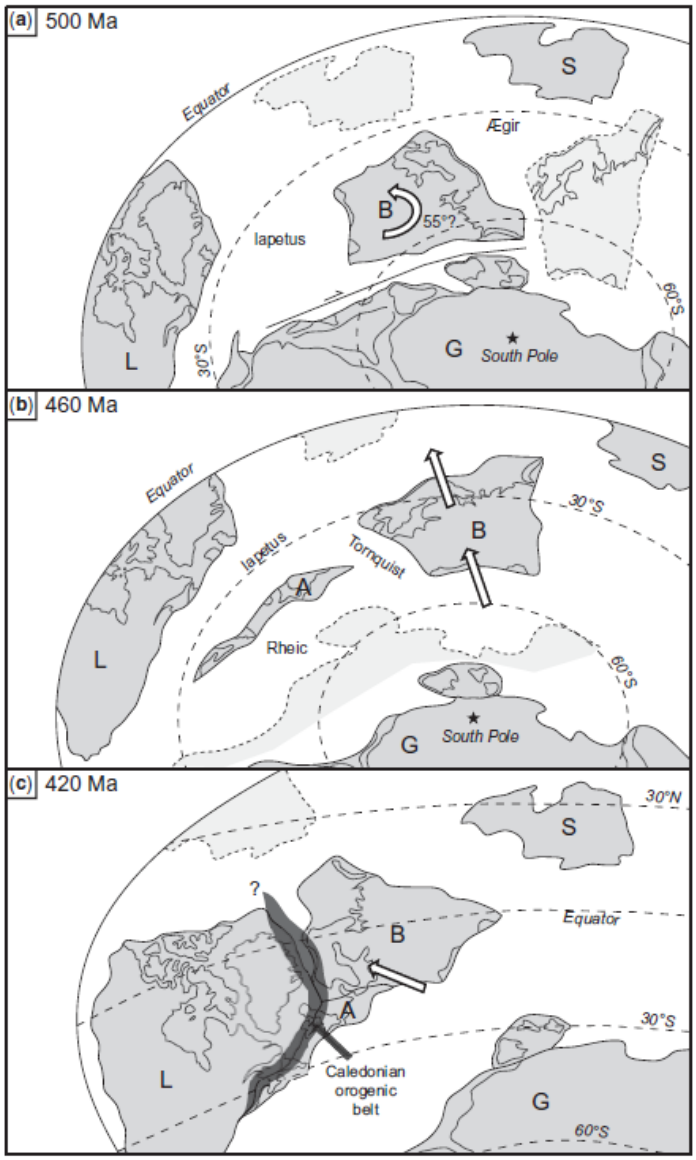


***Figure 2**: Possible Cambrian through Silurian palaeogeographical positions of Baltica (B), Laurentia (L), Siberia (S), Gondwana (G) and Avalonia. Alternative positions for the different continents are shaded grey. Figure from (Corfu et al., 2014).*

The youngest known supercontinent, Pangea, formed in the Carboniferous (at 300 Ma) when Gondwana collided with Laurasia, and lasted until the end of the Triassic (Stampfli et al., 2013). During the break-up of Pangea, rifting between Baltica and Laurentia resulted in the formation of the North Atlantic Ocean and the drifting of Baltica and Laurentia towards their current positions. Baltica at the northwestern part of Eurasia and Laurentia at the eastern part of the North American continent (Irving, 1983).

The common reconstruction of Rodinia is that Baltica and Laurentia were in direct contact or in near proximity to each other during and after the assembly of Rodinia. However Slagstad et al. (2019) argue that the Grenville and the Sveconorwegian orogens are highly unlikely to be correlative and that Laurentia and Baltica were separated during peak orogenesis and probably before and after the existence of the supercontinent Rodinia. If

confirmed, this new theory will have implications for the classical drift history for Laurentia and Baltica and the creation of the Iapetus ocean.

## 2.2 The Break-up of Rodinia and opening of the Iapetus Ocean – Late Neoproterozoic tectonic activity

The break-up of Rodinia is believed to have started at ca. 750-725 Ma at a rift margin between East Gondwana (Australia and Antarctica) and at the western margin of Laurentia prior to the 600-550 Ma large asymmetric rifting between Laurentia (anticlockwise) and Baltica (clockwise) (*Figure 3*) (Torsvik et al., 1996). The NW-SE trending 650 Ma age Egersund plume-derived dyke swarm in South western Norway, the coeval Varangerian tilites in Northern Norway and the tholeiitic Ottafjall dikes in the Sarve nappe in southcentral Sweden are some of the existing evidence at Baltica for initial rifting between Baltica and Laurentia (Torsvik et al., 1996). In addition, the 560-520 Ma Seiland Igneous Province (SIP) within the Middle Allochthon is believed to have intruded during intracontinental rifting (Roberts, 2007, Kirkland et al., 2007b, Root and Corfu, 2012, Gasser et al., 2015). In the Uppermost Allochthon the within-plate gabbroic intrusion, the Umbukta gabbro have been dated to 578 Ma indicating a intracontinental rifting which is uncommon for the Uppermost Allochton (Høyen, 2016, Slagstad et al., 2021).

Evidence for initial opening of the Iapetus Ocean is also present at Laurentia, e.g.; rift related 615 Ma Long Range dikes of southern Labrador and the 600-580 Ma Catoctin basalts with associated mafic dikes at Virginia. These ages are younger and indicate that the rifting accumulated from north to south (Torsvik et al., 1996). *Figure 3* shows a schematic model from Torsvik et al. (1996) for the final break-up of Rodina which illustrate how the continents could have been torn apart from each other with velocities up to 20 cm/year. This model is based on supercontinental insulation (hot spot) and or prolonged subduction towards cold spots.

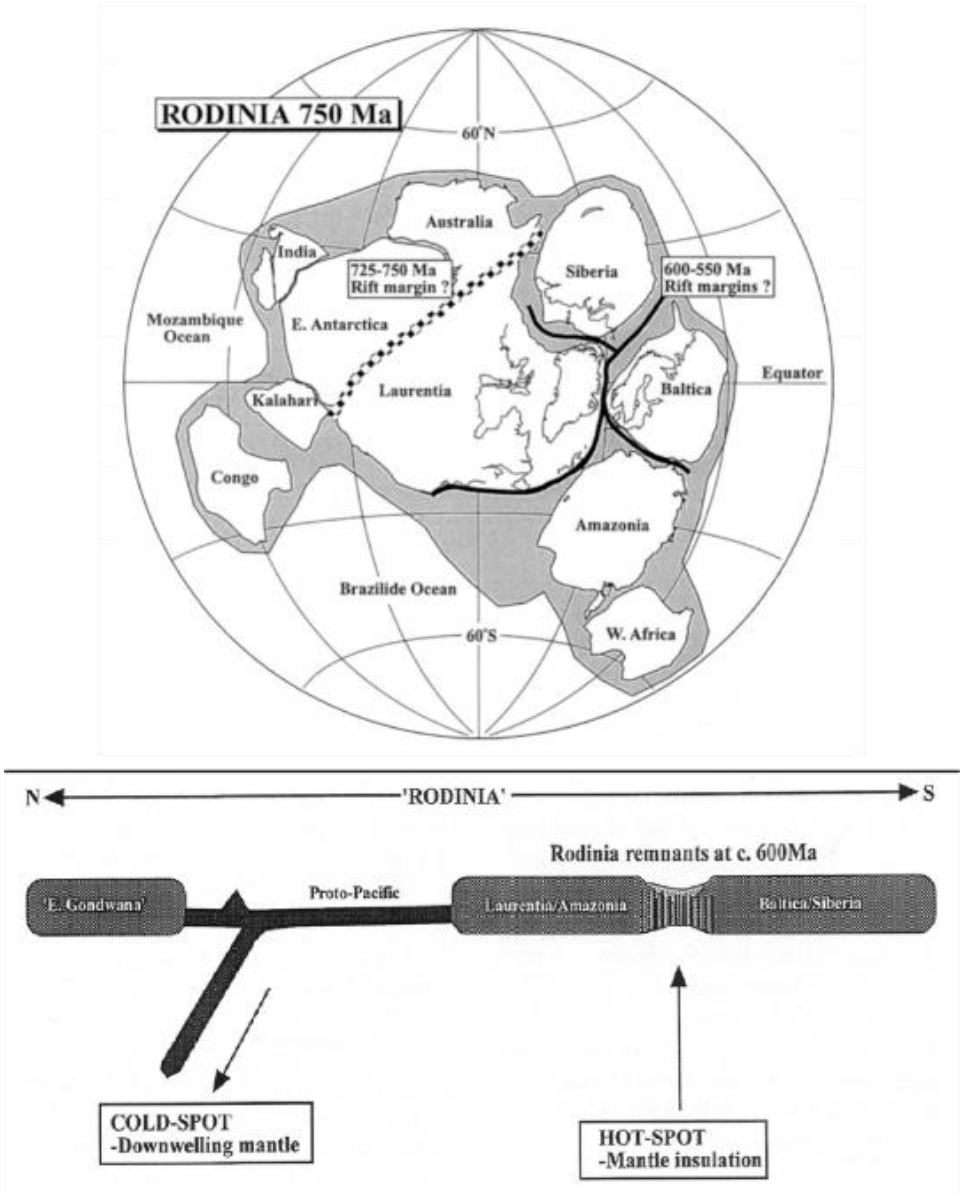


***Figure 3**: The apparent geographical position of the continents during the rifting of the supercontinent Rodinia with associated schematic cross section showing the mechanism of the supercontinent rifting. Figure from Torsvik et al. (1996).*

## 2.3 The Caledonian Orogeny

The Caledonian orogeny is a term used regarding tectonic events restricted within and on the borders of the Iapetus Ocean and can be divided into several orogenic phases and could involve arc-arc, arc-continent and continent-continent collisions. (McKerrow et al., 2000, Roberts, 2003). In the Meso-Cenozoic before the rifting and opening of the North Atlantic Ocean the orogen is believed to have been at least 700-800 km wide. The Paleozoic areas of Scandinavia, the British Isles, the adjacent areas of Svalbard, Greenland, Ireland and the northern Appalachians were exposed to several orogenic events during the closure of the Iapetus Ocean and are therefore traditionally included in the Caledonian Orogen, see *Figure 4* (McKerrow et al., 2000).

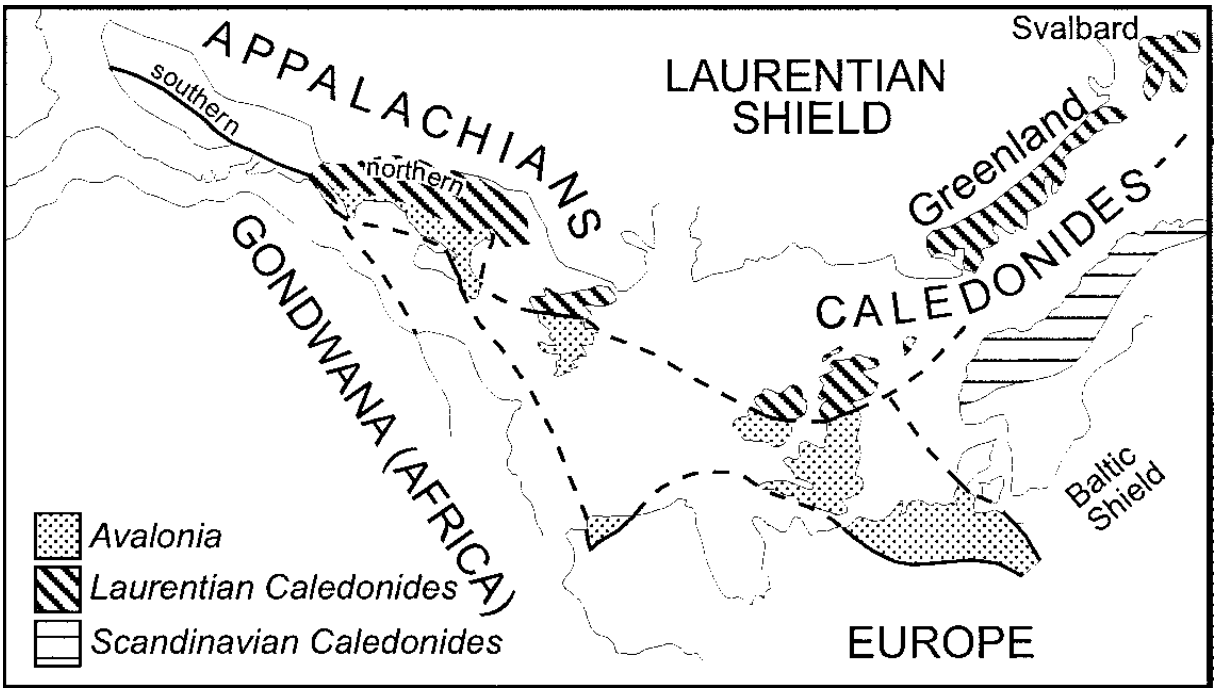


***Figure 4:*** *Schematic map showing the location and extent of the rocks associated with the Caledonides, collision between Laurentia, Baltica and Avalonia from McKerrow et al. (2000).*

## 2.4 The Scandinavian Caledonides

The Scandinavian Caledonides are approximately 1500 km long and range from the Stavanger region in southern Norway to the Barents Sea region in northern Norway (Corfu et al., 2014). The Scandinavian Caledonides comprises several different rock sheets with different metamorphic grade and origin which were developed during different tectonic events before the final oblique collision between Baltica and Laurentia during the Silurian to Early Devon (Roberts, 2003). This collision involved subduction of the Baltica margin beneath the Laurentian margin which led to the accretion of exotic, oceanic and arc terranes associated with the Iapetus Ocean onto Baltica (Fennoscandian shield) (Stephens and Gee, 1985, Roberts, 2003).

Several tectonic events have been recorded in the Scandinavian Caledonides these include the Finnmarkian event, Trondheim event, Taconian event, Scandian event and Late- to post Scandian events (Roberts, 2003).

The Finnmarkian event was thought to be a tecthonotermal event in Late Cambrian-earliest Ordovician involving a west-ward subduction of Baltica beneath a magmatic arc or a microcontinental block which have earlier rifted away from Baltica. This event resulted in high-pressure rocks in the Seve and Kalak Nappe Complex (Roberts, 2003). Newer research has shown that the concept of the Finnmarkian orogeny is no longer valid, the ages used to define the orogen were not relevant for the structures observed (Corfu et al., 2014). In addition the high pressure rocks in Seve Igneous Province was formed later (Early Ordovician, 482 Ma (Root and Corfu, 2012)) than previous concluded.

The Trondheim event is known to be a orogenic event, exposed in the Køli Nappe (Upper Allochthon) occurring at ca. 480-475 Ma characterized by tonalitic magmatism, blue-schist

metamorphic paragenesis and ophiolitic obduction, marking the incipient stages for the closure of the Iapetus Ocean (Roberts (2003) and references therein).

The term Taconian events is the equivalent to tectonothermal events which occurred at the Laurentian margin in Mid to Late Ordovician (470-450 Ma) prior to the closure of the Iapeus Ocean. Laurentian margin subducted beneath an island-arc which resulted in the formation of high-pressure metamorphism and ophiolite obduction along the continental margin of Laurentia (Roberts, 2003). Structurally evidence indicating Taconian events are abundant in the Upper Allochthon and is characterized by NW-verging folds and SE-dipping shear zones. Taconian deformation is also characteristic for the eastern margin of North America (Yoshinobu et al., 2002, Roberts, 2003, Roberts et al., 2007).

Following the Taconian orogeny the Scandian main collision between Laurentia and Baltica culminated in early to mid-Silurian (ca. 430-390 Ma) (Gee et al., 2008). Baltica margin subducted beneath Laurentia which resulted in the formation of UHP (ultra-high-pressure) rocks locally with coesite and microdiamonds formed at depth down to ca. 125 km, today exposed in the Western Gneiss Region (Roberts, 2003, Gee et al., 2008).

In addition to the orogenic events, Devonian post-orogenic extension events occurred (Osmundsen and Andersen, 2001, Gee et al., 2008, Corfu et al., 2014). These post orogenic events consisting of major W to NW extensional faults resulted in rapid exhumation of high-grade metamorphic complexes and deep erosion. These processes strongly influenced the sedimentation and created tectonic controlled basins where the Old Red Sandstones were deposited (Gee et al., 1994).

Over the last decades, the Scandinavian Caledonides have been subdivided into different allochthons; Gee et al. (1985), see *Figure 5*. These allochthons were assembled by in-sequence thrusting onto Baltica. The Lower Allochthon is interpreted to be derived from Baltica, hence the shortest transport distance (Stephens et al., 1985). The Middle Allochthon is interpreted to be derived from the continental margin of Baltica and was exposed to high-pressure metamorphism caused by deep subduction (Stephens et al., 1985). The Upper Allochthon is interpreted to be derived from different marginal basins in the Iapetus Ocean producing ophiolites and arc related rocks (Stephens, 1988, Gee et al., 2014), and the Uppermost Allochthon, which has been thrusted the longest distance, is interpreted to be exotic to Baltica and was derived from the peri-Laurentian margin (Roberts et al., 2007). This model is based on in-sequence thrusting where the nappes deformation gets younger towards the foreland, in this case towards Baltica (Gee et al., 2008).

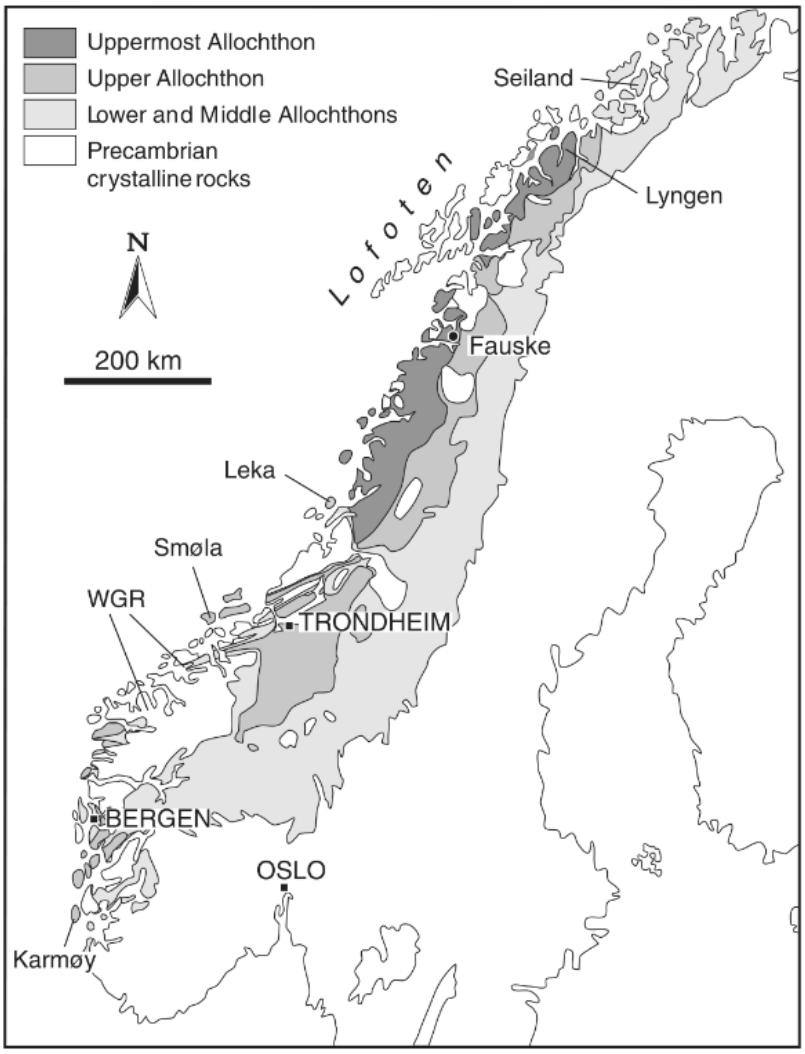


***Figure 5**: Simplified geological map with the traditional subdivision of allochthons which have been translated several 100 km (Roberts and Gee, 1985).*

In recent years, this model has been viewed as too simplistic and have been challenged by e.g., Corfu et al. (2014), who pointed out several arguments against this model: 1) The Jotun and Lindås nappes have been correlated with the Middle Allochthon but structurally overlie a mélange unit with peridotites which is interpreted to have affinity form the Iapetus Ocean. 2) Neoproterozoic tectono-thermal events have been identified in the Kalak Nappe Complex which have traditionally been assigned to the Middle Allochthon. Neoproterozoic tectono-thermal events are atypical for the Middle Allochthon. 3) The difficulty to separate Iapetus-derived nappes and the peri-Laurentian margin-derived nappes. This problem can be seen in the case of the Leka ophiolite (oceanic affinity, typical for Upper Allochthon) which is located within the Helgeland Nappe Complex (Uppermost Allochthon). The ophiolite is both overlain and underlain by units of continental affinity. This interleaving between possibly Laurentian continental derived nappes with nappes with oceanic affinity unites increase the complexity of the nappe stacking.

Other examples of current research that contradicts this in-sequence thrusting model used for the Scandinavian Caledonides are found in the Seve Igneous Province and Rödingsfjället Nappe Complexes. Bender et al. (2018) present an out-of-sequence thrust model which

generated the metamorphic zonation in the Seve Igneous Province (Middle Allochthon). This model included coeval westward intra-Iapetus subduction of Baltica and westward subduction of Iapetus under Laurentia. This resulted in accretion of Laurentia onto Iapetus and Iapetus accretion onto Baltica. When the Iapetus Ocean finally closed, Baltica was subducted under Laurentia and an already earlier accreted orogenic wedge at the Baltica margin was thrusted eastward, resulting in the out-of-sequence thrusting and a downward-decreasing metamorphism gradient in the Seve Igneous Province. The Umbukta gabbro, which is located within the Rödingsfjället Nappe Complex (Uppermost Allochthon) has been correlated trough U-Pb zircon age and geochemical signature with the Seiland Igneous Province (Middle Allochthon) (Høyen, 2016). This suggests correlation between the Uppermost Allochthon and the Middle Allochthon. The mentioned research above indicates several weaknesses to the traditionally simplified in sequence thrusting cake model.

## 2.5 Exotic components in the Scandinavian Caledonides

Slagstad et al. (2021) discuss the possibility of exotic components in the Scandinavian Caledonides and presents a model which illustrate the Early Paleozoic evolution of Laurentia, Baltica and Gondwana before and during the main collision between Laurentia and Baltica in the Silurian.

Baltica's margin inferred to have been relatively passive during its anticlockwise rotation before the main collision in the Silurian, except for the northern part of Baltica which seemed to have an short orogenic event named the Timanide orogeny in the late Neoproterozoic (Roberts and Olovyanishnikov, 2004). The relatively passive behavior of the margin of Baltica is justified by sparse evidence for tectonomagmatic and tectonometamorphic evidence at the Baltican margin during the Early Paleozoic and late Neoproterozoic. In contrast to the Laurentian and Gondwanan margins which seem to have much more complex tectonometamorphic and teconomagmatic history during, and after the Neoproterozoic (Corfu et al., 2007, Kirkland et al., 2007a, Kirkland et al., 2007b, Corfu et al., 2011). The model presented in *Figure 6* (from Slagstad et al. (2021)) suggests several exotic nappe complexes to Baltica located today in the Scandinavian Caledonides including Kalak, Helgeland and the Rödingsfjället Nappe Complexes and the Seve Igneous Province.

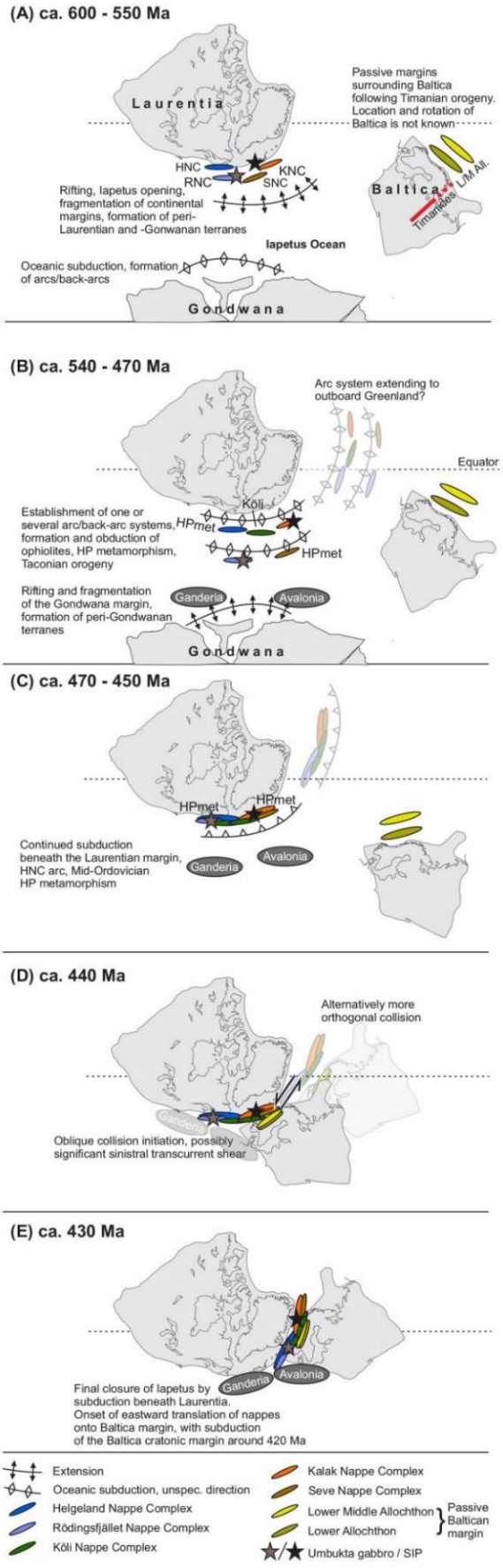


***Figure 6**: Neoproterozoic to Silurian temporal and spacial evolution for nappes currently located in the Scandinavian Caledonides. Figure from Slagstad et al. (2021).*

Evidence for exotic affinity for the Kalak Nappe Complex (originally interpreted to be a part of the Middle Allochthon) include the presence of complex Neoproterozoic activity which formed orogenic rocks that can be correlated with terranes developed on the Neoproterozoic eastern Laurentian and Gondwana margin (Corfu et al., 2007). In the Kalak Nappe Complex at least two high-grade events are recorded, with Scandian collision at 440-430 Ma and a pre-Scandian event at 800-600 Ma (Gasser et al., 2015). In addition Grenvillian age granites and the 570 to 560 Ma SIP do not show any similarities in terms of age with the autochthonous Baltic basement, indicating that these rocks are atypical for Baltica and proves that the Kalak Nappe Complex most likely did not form at the margin of Baltica (Corfu et al., 2007).

The Seve Igneous Province is traditionally believed to be a part of the outermost Baltican margin and structurally underlies the Køli Nappe Complex (Gee et al., 1985). In the Seiland Igneous Province, Neoproterozoic sedimentary and volcanic rocks with subordinate Archean components have been dated (Corfu et al 2014). Overall top-to-the-ESE thrusting have been mapped through the nappe and Ordovician eclogites have been dated at 482 and 446 Ma in Norbotten and Jämtland, respectively, and indicate an Ordovician high-pressure event (Root and Corfu, 2012, Bender et al., 2018). These eclogites formed during subduction of continental supracrustal sequences in an uncertain tectonic setting (Root and Corfu, 2012). Several models have been proposed for these high-pressure events: Ordovician westward subduction of the Baltican margin (Barnes et al., 2019), subduction of Baltica under a microcontinent and later Iapetan arc subduction explaining the different ages of the Norbotten and Jamtland eclogites (Brueckner and van Roermund, 2007). Later research have revealed a Neoproterozoic poly-orogenic evolution suggesting a Laurentian and or peri-Gondwana affinity (Corfu et al., 2007).

The Helgeland Nappe Complex is typically interpreted to be derived from the Laurentian margin (Uppermost Allochthon) (Gee et al., 1985). The main evidence for the exotic derivation are extensive Neoproterozoic and Ordovician top-towards-NW (Taconian according to Roberts et al. (2002)) deformation, sedimentary, metamorphic, and magmatic events with detrital zircons similar to the zircons in the Dalradian sedimentary rocks in Scotland, which is thought to have an SE Greenland sedimentary source (Barnes et al., 2007, McArthur et al., 2014). Subduction activity resulted in the formation of suprasubduction-zones (ophiolites, e.g., Leka), coarse to fine grained siliciclastic and carbonate successions and nappe thrusting during the early Paleozoic prior to the Scandian collision (Barnes et al., 2007, McArthur et al., 2014).

Helgeland overlies the Rödingsfjället Nappe Complex, which has also been interpreted as exotic to Baltica (Slagstad et al., 2021). Neoproterozoic sedimentation, high-grade metamorphism and Taconian-age thrusting and emplacement of mafic intrusions correlative with the SIP have currently been presented and strongly suggests an exotic affinity (Slagstad et al., 2021). The pre-Scandian thrusting could possibly be Taconian and related to Helgeland Nappe Complex but the thrust direction is not yet mapped. The mafic intrusion (Umbukta gabbro) in the Rödingsfjället Nappe Complex has been suggested to be correlated with the SIP (Høyen, 2016, Slagstad et al., 2021). The main argument for the correlation is the signs of extensive Neoproterozoic metamorphic activity in the Rödingsfjället Nappe Complex and the Kalak Nappe Compelx which both are hosts for geochemically similar mafic intrusions, the Umbukta gabbro and the Seiland Igneous Province. The Neoproterozoic activity recorded, are coeval with the tectonothermal activity in the northern Appalachians (Slagstad et al., 2021).

## 2.6 The Uppermost Allochthon

The Uppermost Allochthon is today exposed over a strike length of more than 700 km in Troms, Nordland and in the northern parts of Trøndelag. It can also be observed in Sweden, SE of Mo i Rana (Roberts et al., 2007). Following the tectonostratigraphic division in Roberts and Gee (1985): The Uppermost Allochthon is divided in: Tromsø Nappe Complex in northern Norway, Helgeland, Beiarn and Rödingsfjället Nappe Complexes in north-central Norway/Sweden. Helgeland Nappe Complex also extend down to the south-central Norway/Sweden. The Uppermost Allochthon consist of abundant partly migmatitic gneisses, large volumes of schist and psammites, conglomerates, dolomites, marbles subordinate sedimentary iron deposits, amphibolites, greenstones and serpentinites (Roberts and Gee, 1985, Roberts et al., 2007). The presence of these oceanic and continental rocks which did not occur in the adjacent nappes led researchers in the 1980's to suggest derivation from exotic components such as Laurentia or other microcontinents (Roberts and Gee, 1985). The nappe complex was accreted onto Baltica during the Scandian phase in Silurian against the sub-adjacent Köli Nappe Complex. The Basal contact of Uppermost Allochthon is characterized by a thick zone of imbricated slices of mylonites, blastmyllonites and phyllonites with post-Scandian extensional faults present (Osmundsen et al., 2003).

### 2.6.1 Rödingsfjället and Helgeland Nappe Complexes

The Uppermost Allochthon consist mainly of Rödingsfjället and the structurally overlain Helgeland Nappe Complex (Roberts et al., 2007). Rödingsfjället Nappe Complex is located in north central Norway/Sweden as mentioned earlier, more specific the nappe extends geographically from Narvik to a few 10ns of km south of Mo i Rana, the Nappe is best exposed around the Mo i Rana region (See *Figure 7*). The Helgeland Nappe Complex is dominantly located in northern Norway south for Mo i Rana but can be observed in Bodø and southward all the way to Trøndelag County.

The geology in Rödingsfjället and Helgeland Nappe Compelex is characterized by abundant gneisses, localized migmatitic, psammites, pelites and calcareous schists with associated amphibolites (Barnes et al., 2007, Roberts et al., 2007, Slagstad et al., 2021). Sedimentary iron deposits in dolomite and calcite marbles are also typical for these nappes, in some areas the marbles are conglomeratic (Stephens and Gee, 1985). Several authors (Barnes et al., 2007, Roberts et al., 2007, Slagstad et al., 2021) suggest that Rödingsfjället and Helgeland Nappe Complex have undergone Neoproterozoic-Silurian sedimentary, tectonic, metamorphic, and magmatic events, and that the complexes a have undergone several deformation events both pre-Caledonian and Caledonian events.

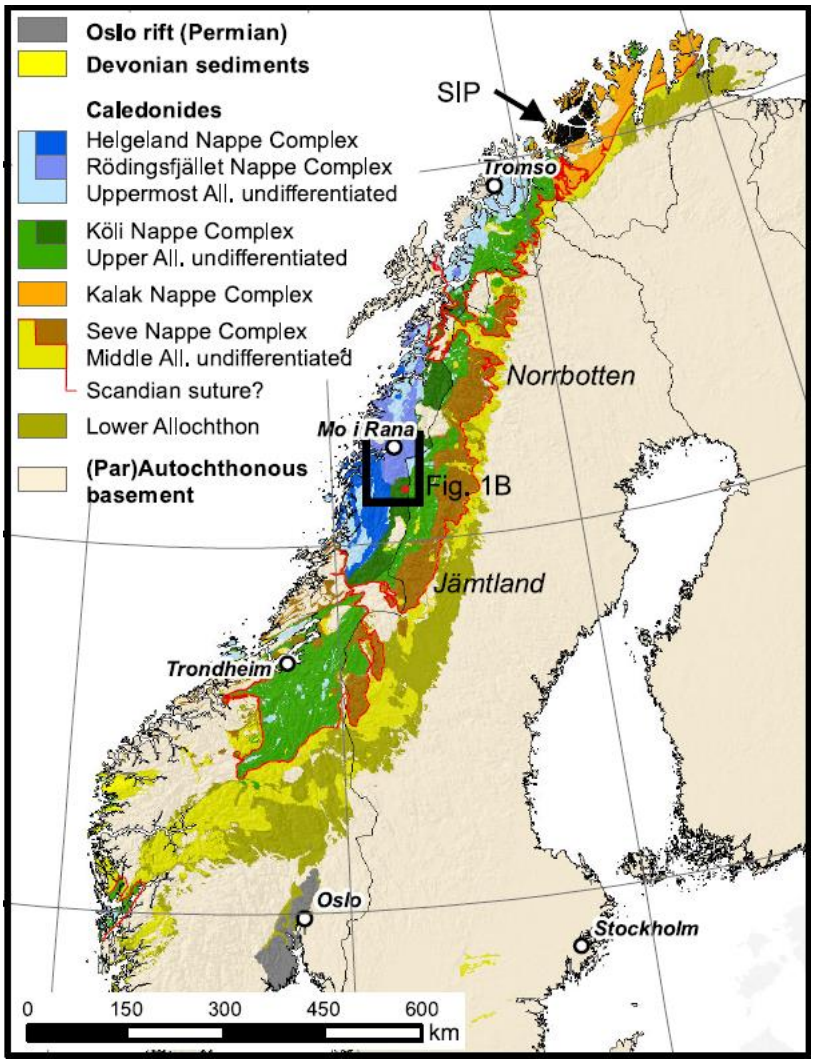


***Figure 7**: Simplified map of the Scandinavian Caledonides. Figure from Slagstad et al. (2021).*

### 2.6.2 Helgeland Nappe Complex

The Helgeland Nappe Complex is divided in four main disparate east dipping nappes with west-vergent shear zones with reactivation, in structurally ascending order (See *Figure 8* Sauren-Torghatten, Lower, Middle and the Upper Nappes. Two additional nappe units may also be considered a part of the Helgeland Nappe Complex, The Leka ophiolite and the Horta Nappe (Yoshinobu et al. (2002), Barnes et al. (2007) and references therein).

Parts of the Horta and the Lower Nappe consist of Neoproterozoic carbonates, gneisses and sandstones which are believed to have been deposited in a continental shelf environment at the Laurentian side of Iapetus (Barnes et al., 2007). The detrital zircons in the Neoproterozoic metasediments in the Lower Nappe have similarities with the zircons found in the Dalradian sedimentary rocks in Scotland (Barnes et al., 2007).

At 497 Ma these Neoproterozoic continental shelf sediments were exposed to rifting and mafic magmatism resulted in several ophiolitic basement rocks ranging from peridotite to gabbro and metavolcanic rocks (Yoshinobu et al., 2002, Barnes et al., 2007). The complete ophiolitic sequence, the Leka ophiolite in the Sauren-Torghatten Nappe and other

associated serpentinized and ophilitic rocks in the Middle Nappe were formed. Such (500-475 Ma) suprasubduction-zone ophiolitic rocks are typical for the Norwegian- and the Appalachia-Caledonian orogen (Dunning, 1987).

The Cambrian ophiolitic floored basins were filled with Ordovician clastic and carbonate sediments which developed the Skei Group, Sauren Torghatten Nappe, Middle Nappe and the stratigraphically highest part of the Horta nappe and probably the Upper Nappe (Barnes et al., 2007). Detrital zircons indicate that the deposition of these nappes ended after 481 Ma, depositional basement in the Lower and Upper Nappe is lacking (Barnes et al., 2007).

All the Paleozoic units underwent high-grade metamorphism within 5 and 10 myr. after the end of deposition. The Horta Nappe was overturned by ca. 478 Ma and was exposed to regional migmatization producing S-type magma (Yoshinobu et al., 2002, Barnes et al., 2007). All of the nappes were imbricated by 475 Ma after the Lower and Upper Nappe underwent migmatization at ca. 480 Ma (Yoshinobu et al., 2002, Barnes et al., 2007). The Sauren Torghatten and Middle Nappe were exposed to amphibolite facies conditions (Yoshinobu et al., 2002).

Following the amalgamation of the nappes in Helgeland Nappe Complex the Bindal Batholite began to form (Barnes et al., 2007). Minor mafic subrasubduction magmatism occurred including the Hortavær igneous complex and the Svarthopen pluton intruded at 466 and 465 Ma respectively. Further magmatism related to exhumation occurred between 450 and 444 Ma where Troholmen pluton, Andalshatten pluton, smaller plutons and tonalitic intrusions in the Upper Nappe were emplaced. At 439 Ma the Heilhornet pluton was emplaced. Mafic, intermediate, and felsic magmas were continuously emplaced until 424 Ma (Barnes et al., 2007). The magmatic activity ranged from granite and gabbro and chemical and isotopic evidence indicate mixed crust and mantle sources. (Yoshinobu et al., 2002).

Yoshinobu et al. (2002) presents several arguments for the Helgeland Nappe Complex to not be a part of an early phase of Scandian orogeny: 1) West-vergence compressional deformation. 2) Scandian extension exhumation related structures are Silurian or younger. 3) Lithologies show that the Upper Allochthon is exotic to the paleo-Baltican margin. As mentioned earlier the zircons found in the Lower Nappe is nearly identical to the Dalradian Supergroup of Scotland which indicate that the Lower Nappe had a depositional source proximal to the Laurentian margin, north of the Grenville-Sveconorwegian front (Barnes et al., 2007). In addition, the formation of ophiolite complexes is also common in the Caledonian-Appalachian mountain belt (Dunning, 1987).

*Figure 9* shows a tectonic model of the Ordovician evolution of the Uppermost Allochthon and the Helgeland Nappe Complex, proposed by (Yoshinobu et al., 2002). *Figure 9a and b* illustrates two continental slivers between Laurentian and Baltica with an eastward-dipping subduction zone where the Leka ophiolite were formed and preserved during the collision of the continental fragments. Early peraluminous magma (e.g., Vega pluton) intruded. After the collision (*Figure 9c - d*), the nappes collided with Laurentia and were exposed to high-grade-metamorphism and later metamorphic overprint indicating exhumation of the Helgeland Nappe Complex at ca. 447 Ma.

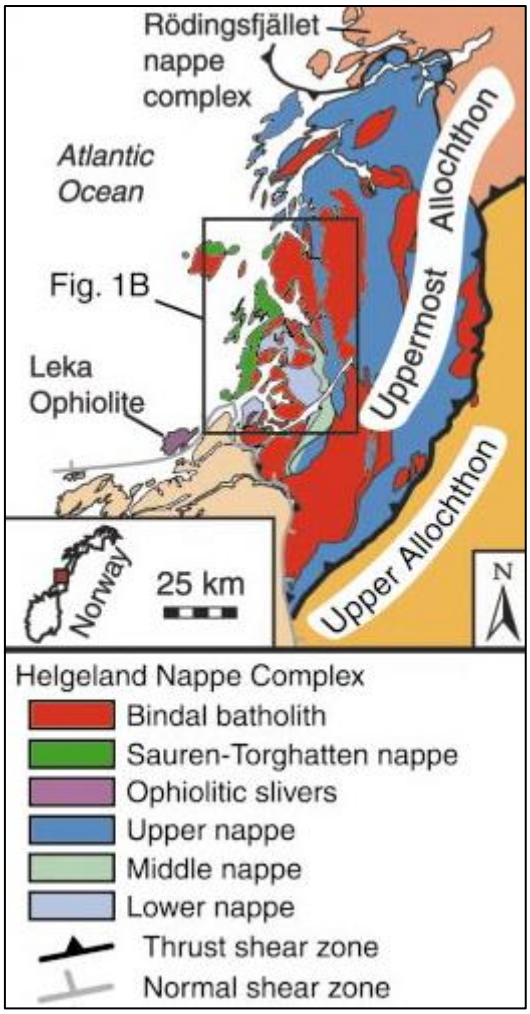


***Figure 8**: Tectonic map of the Upper and Uppermost Allochthon in the northern Norway. The different units in Helgeland Nappe Complex: Bindal batholith, Sauren Torghatten Nappe, ophiolitic slivers, Upper Nappe, Middle Nappe and the Lower Nappe. Figure from Yoshinobu et al. (2002).*

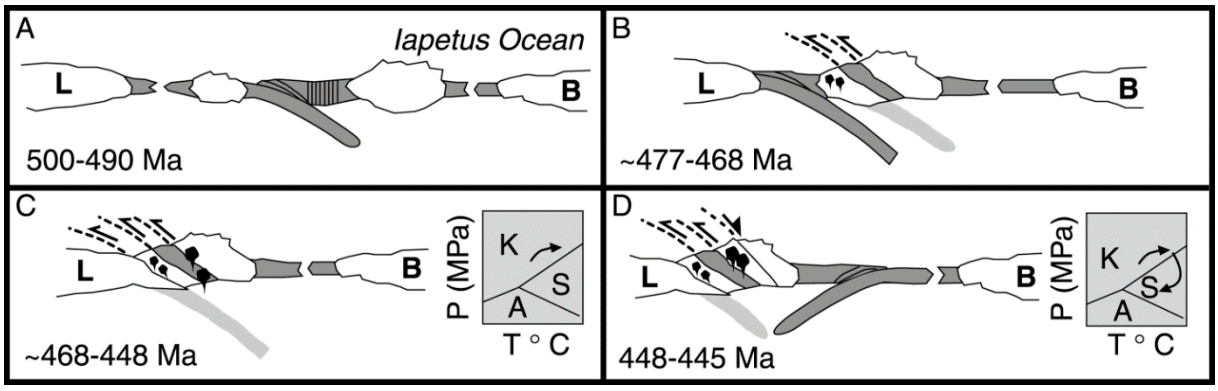


***Figure 9**: The Ordovician evolution of Helgeland Nappe Complex and the Uppermost Allochthon. A) Locations of continental slivers between Laurentia and Baltica. Suprasubduction-zone where the Leka ophiolite were formed above the east-dipping subducting slab. B) The Preservation of the Leka ophiolite by collision between the two continental slivers. Early peraluminous volcanism. C) Continental collision between the amalgamated continental slivers and Laurentia resulting in high-grade metamorphism in Helgeland Nappe Complex (loading of the nappe is shown in the P-T diagram). D) Exhumation of the Helgeland Nappe Complex at ca. 447 Ma, before the closure of the Iapetus Ocean. Figure is taken from (Yoshinobu et al., 2002).*

### 2.6.3 Rödingsfjället Nappe Complex

The Rödingsfjället Nappe Complex in the Mo i Rana region is divided into three main nappes with metasedimentary and metaigneous rock suites from structurally lowest to highest, Ravnålia Nappe, Plura Nappe and the Slagfjellet Nappe (*Figure 10*) (Slagstad et al. (2021) and references therein).

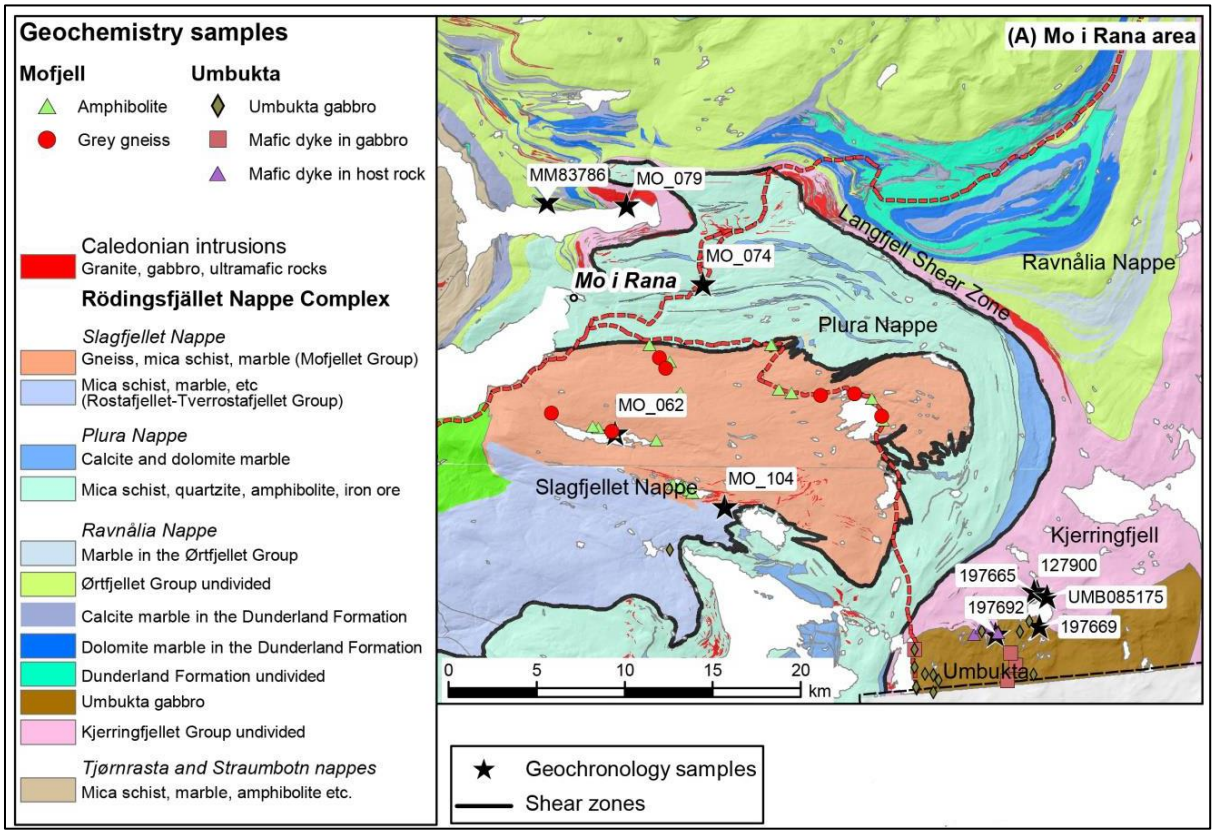


***Figure 10**: Simplified geological map of the Rödingsfjället Nappe Complex area near Mo i Rana. The figure and samples shown on the map are from Slagstad et al. (2021).*

The Ravnålia Nappe is divided into three groups/formations. The Kjerringfjell Group, Ørtfjell Group and Dunderland Formation. The Kjerringfjell Group is currently (before this study) believed to consist primarily of high-grade metamorphosed, migmatitic garnet-biotite gneisses, quartzites and garnet bearing amphibolite layers which have been intruded by pegmatite sheets (Slagstad et al., 2021). In addition the genisses are cut by the medium-coarse grained and massive Umbukta gabbro (Høyen, 2016). Detrital zircons from the host rock in Kjerringfjell indicated a maximum depositional age of 1030 Ma (Slagstad et al., 2021). The Umbukta gabbro have a within-plate chemical signature and intruded at 578 Ma, and the high-grade metamorphism (migmatization) in Kjerringfjell was dated to 623 Ma (Slagstad et al., 2021). Older extensive deformed mafic dikes are also present, indicating pre-metamorphic magmatism (Slagstad et al., 2021).

The Ørtfjell Group and the Dunderland Formation is characterized by amphibolite-facies dolomite and calcite marble associated with iron formations, several types of mica schists, glacial diamictite and a minor tonalitic body (Melezhik et al., 2015). Dating of the marbles

in the Ørtfjell Group and in the Dunderland Formation by Melezhik et al. (2015) gave depositional ages of 660 Ma and 800-730 Ma respectively. The minor tonalitic body intruded at 541 Ma (Slagstad et al., 2021). The iron formations are believed to be exotic to Baltica and deposited on a glacially influenced carbonate-siliciclastic shelf on a margin of an unknown microcontinent (Melezhik et al., 2015).

The Ravnålia and the Plura Nappe are separated by the Langfjell Shear Zone. Highly deformed schists and gneisses locally intruded by pegmatite sheets characterize the shear zone. A syntectonic pegmatite was dated at 475 Ma indicating active deformation in the shear zone at that time, possibly pre-Scandian/Taconian deformation (Slagstad et al., 2021).

The Plura Nappe is characterized by amphibolite-facies mica schists and gneisses, apparently volcanic grey gneisses, quartzites, amphibolites, dolomites and calcite marbles and associated minor iron ores (Slagstad et al. (2021) and references therein). The age of deposition in the Plura Nappe is somewhat ambiguous. Melezhik et al. (2015) published C-Sr isotope chemostratigrapy of the marbles yielding deposition age of 700-670 Ma while detrital zircon dating of the garnet-mica schist in Slagstad and Kirkland (2017) indicate a depositional age between 1.8 and 1.0 Ga. The grey gneisses of possibly volcanic origin have been dated to have intruded at ca. 510 Ma (Slagstad et al., 2021).

The Slagfjell Nappe consists of the Rostafjellet-Tverrostafjellet Group and The Mofjell Group. The Rostafjellet-Tverrostafjellet Group consists mainly of mica schists and marbles, assumed to have a late Proterozoic to Cambro-Ordovician age (Marker et al., 2012, Slagstad et al., 2021). The Mofjell Group is characterized by folded fine- to medium-grained grey gneisses by possibly igneous origin (Slagstad et al., 2021). The grey gneisses have an island arc-related geochemical signature and is believed to have intruded at 501 Ma (Gundersen, 2020, Slagstad et al., 2021). At the Røssvatnet area further south in the Rödingsfjället Nappe Complex a 515 Ma syn-tectonic pegmatite in the host rock indicate a Cambrian tectonic event (Slagstad et al., 2021). Such early Cambrian tectonic event in the Scandinavian Caledonides has not previous been dated and can possibly be correlated with the 510 Ma grey gneisses in the Plura Nappe and the 501 Ma grey gneisses in the Slagfjell Nappe (Slagstad et al., 2021). This type of early Cambrian deformation indicates that the Iapetus convergence started earlier than previously thought, and could mark the pre-Caledonian orogenic development or mark the starting stage of Taconian orogenic development (Slagstad et al., 2021). The closest tectonic event in the Scandinavian Caledondies is the 497 Ma Leka supra subduction zone (Pedersen et al., 1988). A granite dike with an age of ca. 480 Ma (coeval with the deformation in Langfjell Shear Zone) cross cuts the 515 Ma foliation which proves evidence for a polyphase tectonothermal evolution of the host rock near the Røssvatnet area (Slagstad et al., 2021).

# 3 Theory

## 3.1 U-Th-Pb Geochronology

Zircon and monazite U-Th-Pb geochronology has been an important tool to collect geological data to this thesis. Laser Ablation Inductively Coupled Plasma Mass Spectrometry (LA-ICP-MS) have been used to date rock samples in the Kjerringfjell Group. This chapter will briefly introduce the most important aspects of U-Th-Pb geochronology.

### 3.1.1 U-Th-Pb decay chains

U-Th-Pb geochronology is one of the most important isotopic dating methods in geology and can be utilized to date rocks from approximately 4.57 Ga into the Pleistocene. The main principle of U-Th-Pb geochronology involves decay of three different parent isotopes: $^{238}U$, $^{235}U$, and $^{232}Th$ to their respective stable daughter isotopes $^{206}Pb$, $^{207}Pb$, and $^{208}Pb$ (Schoene, 2014). Each of the parent isotopes decays to several intermediate daughter isotopes by following a sequence of alpha and beta decays before finally decaying to the stable Pb isotope (Bateman, 1910). The three different decay chains are shown in *Figure 11*. The decay time depends on the decay constant, λ, for the isotopes where λ for the intermediate daughter is much smaller than for the parent. The elapsed time can be known by looking at the relationship between the parent and the daughter isotopes when the half-life of the isotopes is known.

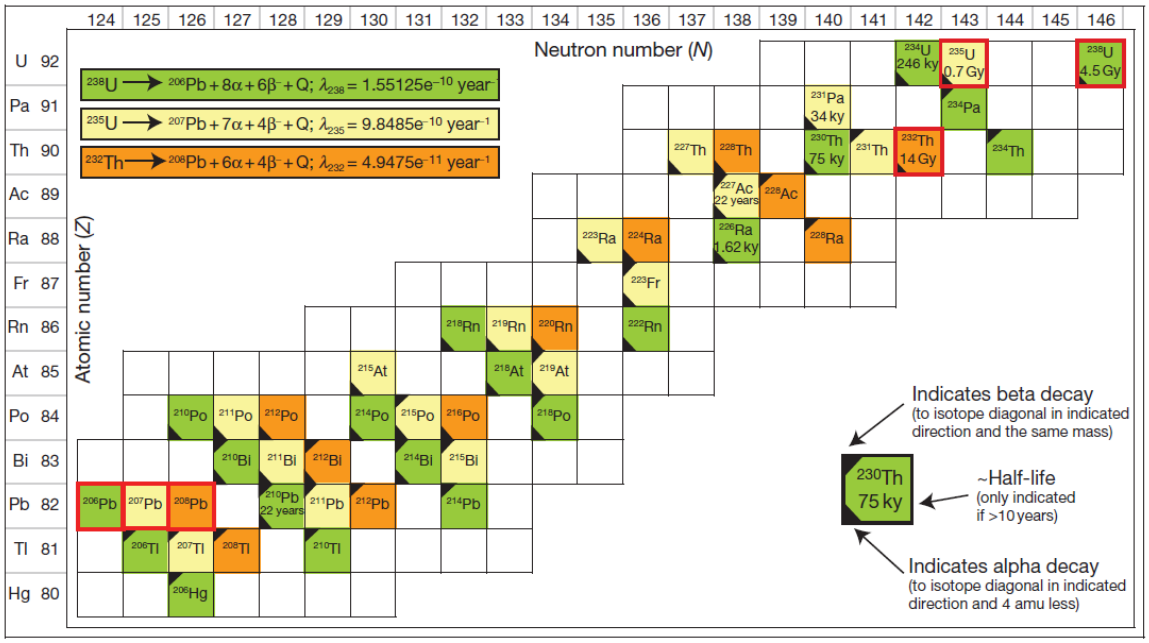


***Figure 11**: U-Th-Pb decay chains. The three different chains are marked with different colors. The red outlined isotopes highlight the parent isotopes and the stable daughter Pb isotopes. α = alpha particle. β= beta particle. Q = energy released during decay. Box symbols is explained in the inset. Figure from Schoene (2014).*

One very important concept in geochronology is secular equilibrium. When a decay chain is in secular equilibrium, the product of the concentration of the isotope and the corresponding decay constant is equal among all isotopes in the decay chain:

$$N_1\lambda_1 = N_2\lambda_2 = N_3\lambda_3 = \ldots \quad (1)$$

Where $N_1$ is the concentration of isotope 1 in moles and $\lambda_1$ is the decay constant.

Secular equilibrium in a system can be disturbed if one or more daughter isotopes is fractionated out during the decay process. For instance, this fractionation can occur in a magmatic system during chemical partitioning or during chemical weathering by low-temperature fractionation (Schoene, 2014).

The reaction equations for the three parent isotopes to the daughter isotopes in the U-Th-Pb system is given below:

$$^{238}U \rightarrow {}^{206}\mathrm{Pb} + 8\alpha + 6\beta + \mathrm{Q};\ \lambda_{238} = 1.55125 \times 10^{-10}\ \mathrm{years}^{-1} \quad (2)$$

$$^{235}U \rightarrow {}^{207}\mathrm{Pb} + 7\alpha + 4\beta + \mathrm{Q};\ \lambda_{235} = 9.8485 \times 10^{-10}\ \mathrm{years}^{-1} \quad (3)$$

$$^{232}Th \rightarrow {}^{208}\mathrm{Pb} + 6\alpha + 4\beta + \mathrm{Q};\ \lambda_{232} = 4.9475 \times 10^{-11}\ \mathrm{years}^{-1} \quad (4)$$

Where $^{238}$U, $^{235}$U, and $^{232}$Th are the parent isotopes, $^{206}$Pb, $^{207}$Pb and $^{208}$Pb are the stable daughter isotopes, respectively, and $\lambda_{238}$, $\lambda_{235}$, and $\lambda_{232}$ are the decay constants. α is an alpha particle, β is a beta particle, and Q is the energy released during the decay.

To make this dating system applicable, it is obvious that it is necessary to collect rock samples which contain minerals with "high" concentrations of uranium. Zircon is the most utilized mineral for U-Pb dating (Hanchar and Hoskin, 2003), monazite, apatite, and titanite are also common minerals used in U-Th-Pb dating (Corfu, 1988). The minerals investigated in this thesis, zircon and monazite will be discussed further in chapter 3.1.4 and 3.1.5.

### 3.1.2 Visualizations of U-Pb data

If one assumes independence between the three decay chains, no initial lead and secular equilibrium at the time of system closure, three different isochron equations can be derived:

$$\frac{^{206}Pb}{^{238}U} = \left(e^{\lambda_{238}\mathrm{t}} - 1\right) \quad (5)$$

$$\frac{^{207}Pb}{^{235}U} = \left(e^{\lambda_{235}t} - 1\right) \quad (6)$$

$$\frac{^{208}Pb}{^{232}Th} = \left(e^{\lambda_{232}t} - 1\right) \quad (7)$$

These equations can be used to plot diagrams that show graphical representations of e.g., U-Pb evolution. The two most common diagrams are the Wetherill concordia diagram and the Tera-Wasserburg diagram.

The Wetherill concordia diagram, use *equation 5* and *6* to plot $^{206}Pb/^{238}U$ against $^{207}Pb/^{235}U$ (Wetherill, 1956). *Figure 12* illustrates how the Wetherill concordia diagram works.

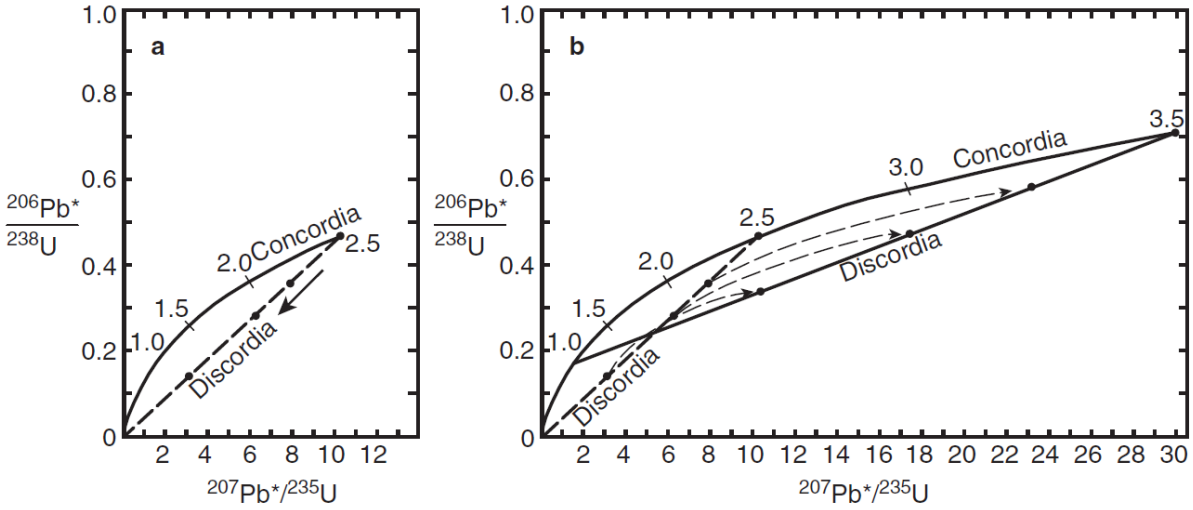


***Figure 12**: Wetherill concordia diagrams showing the development of uranium and lead in a 3.5 Ga rock which has been exposed to one episode of lead loss. A) Radiogenic $^{206}Pb$ and $^{207}Pb$ were being created simultaneously at different rates for 2.5 billion years, when a lead-loss event occurred. The amount of lead-loss (resetting) varied for the different zircons. B) The same system keeps evolving for another 1 billion years. The fully reset zircons follow the concordia and the partially reset zircons follow other evolutionary curves (dashed lines) parallel to the concordia. A discordia line can now be drawn through these different zircons. The discordia intersects the concordia-curve at two places. An upper intercept giving the age of the protolith, 3.5 Ga, and a lower intercept at 1 Ga marking the timing of lead loss. Diagrams from Winter (2014).*

The samples which have remained a closed system since the formation of the mineral will plot on the concordia curve. The concordia curve has a curved shape because the decay constants of the two U-Pb systems differ. Samples which experienced open-system behavior will not be plotted on the concordia but rather on a discordia line. The two concordia diagrams in *Figure 12* shows the development of a 3.5 Ga rock which underwent a lead-loss 2.5 Ga years after the formation of the rock (1 Ga years ago). At 2.5 Ga the different zircons experienced a variable amount of lead-loss. After the lead-loss event, the

system is closed again, and accumulation of lead continues. The variably reset zircon grains evolve along paths parallel to the concordia, defining a straight line – the discordia – that intercepts the concordia at two points. The upper intercept corresponds to the protolith age of the rock, and the lower intercept corresponds to the time of lead-loss.

The Tera-Wasserburg concordia diagram, see *Figure 13*, plots $^{207}Pb/^{206}Pb$ against $^{238}U/^{206}Pb$ (Tera and Wasserburg, 1972). It is necessary to combine *equation 5* and *6* to create a fourth isochrone for the following equation:

$$\frac{\left(\frac{^{207}Pb}{^{204}Pb}\right)-\left(\frac{^{207}Pb}{^{204}Pb}\right)_0}{\left(\frac{^{206}Pb}{^{204}Pb}\right)-\left(\frac{^{206}Pb}{^{204}Pb}\right)_0}=\left(\frac{^{235}U}{^{238}U}\right)\frac{(e^{\lambda_{235}t}-1)}{(e^{\lambda_{238}t}-1)}=\frac{^{207}Pb}{^{206}Pb} \quad (8)$$

The advantages for the fourth isochrone equation are: $^{235}U/^{238}U$ is a known constant, one does not need to consider the concentration of lead and one can directly calculate a date by using $^{207}Pb/^{206}Pb$ if initial lead is negligible. The same interpretation as for the Wetherill diagram of concordant and discordant samples apply for this diagram. The big advantage with the TW diagram is that if several cogenetic samples fall of the concordia solely from variable common lead one could draw a line through these samples. The point of intercept with the concordia show the true age, while the intercept with the $^{204}Pb/^{207}Pb$ axis will show the composition of the common lead. One could also add an axis with $^{204}Pb/^{206}Pb$ to construct a 3D diagram, then it is possible to find the $^{204}Pb/^{206}Pb$ composition of the $Pb_c$ ($^{238}U/^{206}Pb$ = 0).

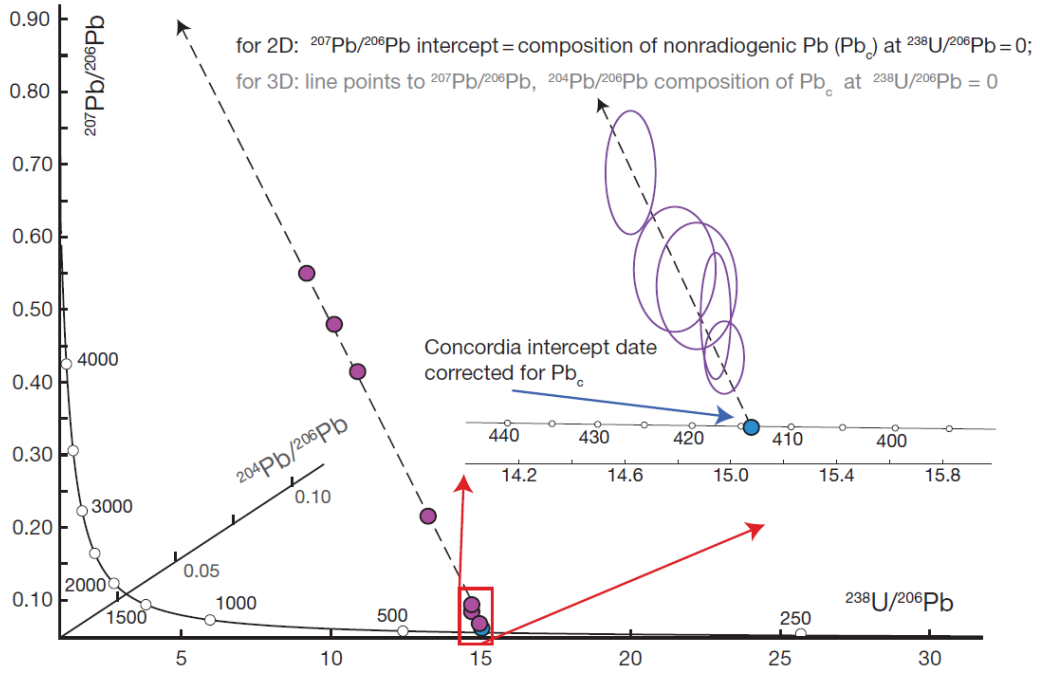


***Figure 13**: Tera-Wasserburg diagram in 2D and 3D. From Schoene (2014).*

### 3.1.3 Causes of discordance and visualization in a TW diagram

The main causes of discordance/open system behavior of the U-Th-Pb system are; 1) age domain mixing, 2) Pb loss, 3) secular disequilibrium, and 4) initial Pb (Schoene, 2014).

**Age domain mixing and Pb loss**

Zircon grains often consist of several growth phases formed at different times (Schoene, 2014). A typical internal texture is a core-rim texture where the core is older than the rim, but the grains can have complicated textures with several age domains. If the dating method used, does not have good enough spatial resolution to analyze one age domain at a time, the analysis will consist of a mix between these two ages (Schoene, 2014). Such mixing will cause analyses to lay on a discordia exemplified in *Figure 14*. Varying Pb loss caused by, e.g., a metamorphic event will also cause analyses to be spread the same way as mixing (Winter, 2014). Another type of Pb loss is recent Pb loss which is also marked with an arrow on *Figure 14. (Andersen et al., 2019)*. This discordia has a lower intercept of close to present-day, suggesting Pb loss in recent time. Grains that have undergone recent Pb loss often have a high degree of metamictization (high degree of crystal damage) due to high alpha particle dose (Sliwinski et al., 2017). By looking at varying trends in the alpha dose in the analyzes, one can get an indication if recent Pb loss could have been the cause of discordance.

**Secular disequilibrium**

If open system behavior occurs, such that intermediate daughter products is fractionated from the parent isotope (uranium), secular equilibrium is not achieved (Schoene, 2014). This open system behavior can occur during partial melting and crystallization (Schoene, 2014). If an intermediate daughter product is incorporated into the zircon crystal, the calculated age will increase. On the other hand, if the intermediate daughter product prefers the melt, the age will be too young.

**Common Pb ($Pb_c$)**

Radiogenic Pb ($^{206}Pb$, $^{207}Pb$ and $^{208}Pb$) and non-radiogenic $^{204}Pb$ can occur as common Pb. Common Pb consists of both contamination in the preparation work at the lab and the initial Pb incorporated in the crystal (Schoene, 2014). In this study very small monazite grains as inclusions in feldspar have been dated. If the spatial resolution of the laser is not good enough, one will hit the feldspar which contains a lot of Pb, resulting in an analysis with high values of $Pb_c$. In a TW plot, analyses with initial Pb will plot on a discordia towards and initial Pb composition, as shown in *Figure 14* and *Figure 101 (Schoene, 2014).* It is important to note that in Paleoproterozoic and Archean samples, it can be hard to distinguish between the incorporation of initial Pb or mixing/Pb loss, because of the similarities of the angles of the discordias.

In this study, no correction of the initial or common Pb was done, only the visualization in the TW plot (Tera Wasserburg plot) has been used to interpret the incorporation of initial Pb. Andersen et al. (2019) present these four methods for $Pb_c$ correction.

1) The traditional $^{204}Pb$ correction: The $^{206}Pb/^{204}Pb$ ratio is measured in the zircon. Assumed values of $^{206}Pb/^{204}Pb$, $^{207}Pb/^{204}Pb$, and $^{208}Pb/^{204}Pb$ are chosen based on the average crustal lead isotopic evolution, e.g., Stacey and Kramers (1975). Then the $^{206}Pb$, $^{207}Pb$, and $^{208}Pb$ are subtracted based on the measured $^{206}Pb/^{204}Pb$ ratio.

2) The $^{207}Pb$ and $^{208}Pb$ correction: One assumes that the Pb composition only consists of radiogenic lead and $Pb_c$ , no lead loss after crystallization. The correction methods involve projecting the observed value back to the concordia along a mixing line with a slope given by the $^{206}Pb/^{207}Pb$ ratio of common lead. For $^{208}Pb$ the same is done with the assumption that the zircon is concordant in $^{208}Pb/^{232}Th$ and $^{206}Pb/^{238}U$. These assumptions are highly unlikely and not a common method.
3) Modeling of 3D discordance pattern without a known $^{204}Pb$: This method can be useful when using LA-ICP-MS where isobaric interference by $^{204}Hg$ is a problem. The age of a lead loss event needs to be known or estimated, and one needs accurate measurements of $^{206}Pb/^{238}U$, $^{207}Pb/^{235}U$, $^{208}Pb/^{232}Th$, and $^{232}Th/^{238}U$. In addition, the composition of the $Pb_c$ must be known. See Andersen (2002) for further explanation of this method.
4) The TW concordia diagram: Similar method as 2) but the correction is done in a TW-plot. Radiogenic Pb and common Pb with a constant composition define a mixing line. The mixing line intercepts an age on the concordia curve and a $^{207}Pb/^{206}Pb$ initial ratio on the y-axis. The analyses will be projected along the line down to the concordia, as shown in *Figure 14*.

**Fractionation**

During the ablation of the sample with LA-ICP-MS, the laser will hit the sample deeper with increasing time at the same spot. This will cause fractionation of Pb and U (Schoene, 2014), due to differences in chemical behavior; the ratio of these elements will change during the ablation process. Increasing fractionation will cause the analyses to be scattered the way shown in *Figure 14*. Pb and U are different elements, hence they fractionate differently. In contrast, two isotopes of Pb behave similar chemically, hence also fractionate similarly, that is why the $^{207}Pb/^{206}Pb$ age does not change significantly.

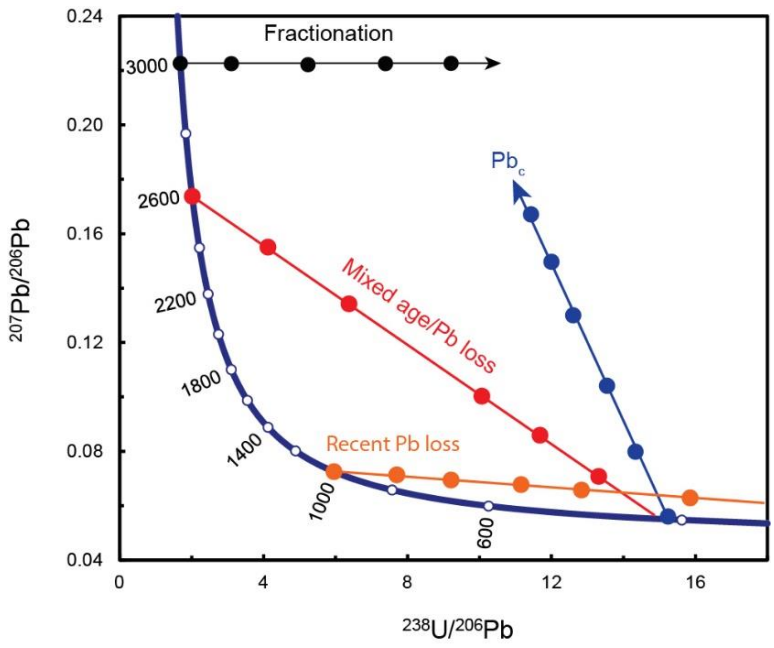


***Figure 14**: Different textbook patterns of discordance in a TW plot caused by mixing of different age domains/Pb loss, incorporation of $Pb_c$*, recent Pb loss and fractionation. Inspired by Andersen et al. (2019).

### 3.1.4 Zircon

Zircon is a common orthosilicate mineral in most igneous and metamorphic rocks, with zirconium (Zr) as an essential structural component ($ZrSiO_4$). Significant U, Th, Hf, and REE fractions often occur in the crystal lattice. (Hoskin and Schaltegger, 2003). Zircon is relatively insoluble in crustal melts and fluids and is highly resistant to chemical and physical breakdown. These properties make it possible to retain several generations of geochemical information (Cherniak and Watson, 2003, Morner, 2014). The element diffusion in zircon is slow, allowing the possibility of using zircon as a geochronometer (Cherniak and Watson, 2003).

The external and internal morphology of zircon varies greatly. By looking at the morphology of a zircon grain and minerals like monazite and titanite, one can study features that reflect different geological events such as magmatic and metamorphic crystallization and recrystallization, chemical alteration, and metamictization (Corfu et al., 2003). Morphology can be studied by, e.g., transmitted and reflected microcopy, binocular microscope, cathodoluminescence (CL), backscattered electron (BSE), and secondary electron microscopy (SEM). The best internal textures can be imaged using cathodoluminescence, while fractures and inclusions are best seen with backscattered electron microscopy (Corfu et al., 2003).

The crystal structure of zircon is typically tetragonal and commonly grows as doubly terminated prismatic crystals with length-to-width ratios ranging from 1 to 5 based on the crystallization rate. Hence, needle-shaped and acicular crystals are common in porphyritic, sub-volcanic intrusions, high-level granites, and gabbros. Slower crystallization results in stubby and equant forms, common in deep-seated intrusions. Subrounded and highly resorbed shapes characterize metamorphic zircon crystals, but euhedral shapes are also possible in fluid-rich environments, e.g., amphibolite-facies, mica schists, and migmatites. One typical feature of magmatic zircon is the presence of distinct growth zonation, which reflects the variation in the concentrations of Hf, P, Y, REE (Rare Earth Elements), Th, and U (Corfu et al., 2003). Euhedral, oscillatory, and sector zoning is typical in zircons from igneous rocks, while anhedral zoning, weak/no zoning rounded cores, and rims are typical in zircons from metamorphic rocks (Hanchar and Miller, 1993, Wu and Zheng, 2004). In addition, the Th/U ratio has been used to distinguish between magmatic and metamorphic zircon (Rubatto, 2002, Schoene, 2014). A zircon with a $Th/U < 0.1$ most likely has a metamorphic origin, whereas a $Th/U > 0.1$ is typically interpreted to reflect a magmatic origin (Hoskin and Schaltegger, 2003). Xenocrystic zircon is often observed in igneous rocks and high-grade metamorphic rocks. Xenocrystic zircon has cores mantled by newly grown magmatic zircon. They can also occur as unmantled subrounded anhedral crystals entrained in a magma during late-stage crystallization (Corfu et al., 2003).

### 3.1.5 Monazite

Monazite is a monoclinic light-rare-earth element phosphate [$(Ce, La, Nd, Th)PO_4$], which contains significant amounts of uranium and thorium and is a helpful accessory mineral for constraining the timing of metamorphic events in high-grade rocks. (Košler and Sylvester, 2003, Clavier et al., 2011). Typically all Pb in monazite is radiogenic, and the closure temperature is high, up to 900°C (Morner, 2014). Monazite typically occurs as a minor

accessory mineral in medium- to high-grade metamorphic rocks derived from clay-rich sediments. It also occurs in magmatic rocks with a composition ranging from diorite to muscovite granite, and it is associated with pegmatite, greisen, and quartz veins (Overstreet, 1967). Monazite is commonly zoned with respect to age and composition, preserving several zones with different compositions and ages, which makes monazite well suited to in situ spot analysis. Monazite is especially suited to help study the evolution from igneous processes to hydrothermal alteration, which is crucial in ore formation (Townsend et al., 2001). Compared to zircon, monazite has a higher resistance to radiation damage, lower diffusion rates, and crystalizes easier. (Morner, 2014).

### 3.1.6 U-Th-Pb dating methods

Thermal ionization mass spectrometry isotopic dilution (ID-TIMS), secondary ion mass spectrometry (SIMS), and laser ablation inductively coupled plasma mass spectrometry (LA-ICP-MS) are the three main principal methods used for U-Th-Pb geochronology (Schoene, 2014). A brief introduction to these analytic methods will be given below.

**Thermal Ionization Mass Spectrometry Isotopic Dilution (ID-TIMS)**

First, the U and Pb are separated from the other elements in selected minerals using ion-exchange chemistry (Schoene, 2014). This is done by spiking the selected samples with a tracer solution dissolved in Teflon vessels in HF or HCl. The separation can increase the thermal ionization quality, remove the potential for elements to impede ionization of Pb and U in the filament, and remove isobaric interference (Schoene, 2014).

Further, samples are placed in the TIMS instrument, see *Figure 15*. The instrument consists of three main components (Mueller and Vervoort, 2022). 1) Source house. The samples are placed in the source house and are slowly heated until the atoms are converted to ions. 2) Magnet separator. After the thermal ionization, the ions are accelerated into a magnetic separator and separated by mass/charge ratio. 3) Multi collector housing. Further, the ions are detected in the multi-collector housing, and isotope ratios can be calculated. The whole ID-TIMS procedure is summarized in *Figure 16*.

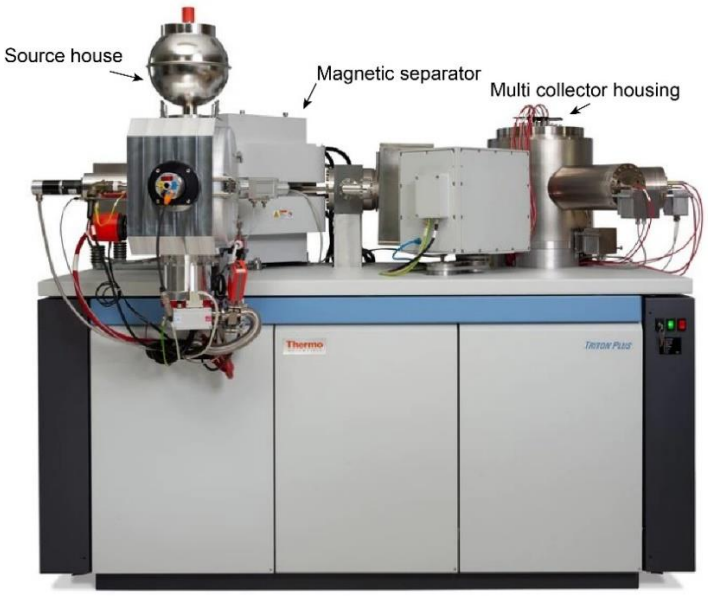


***Figure 15**: Thermal ionization mass spectrometry instrument. The three main components. Source house, magnetic separator and multi collector housing. Photo from Thermo-Fisher (2022).*

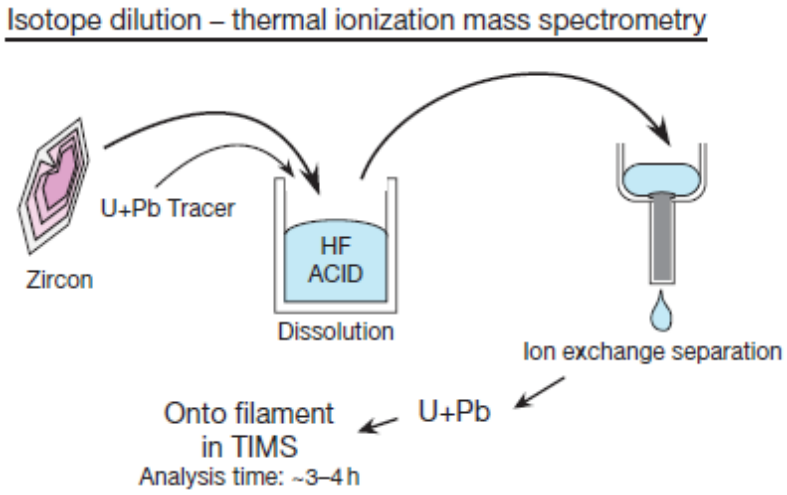


***Figure 16**: ID-TIMS procedure summarized. Figure from Schoene (2014).*

### Secondary ion mass spectrometry (SIMS)

SIMS utilizes a process called sputtering to measure the isotopic composition and elemental abundances on a small area on a rock/mineral (Schoene, 2014). In short, a high-energy ion beam produced by a microprobe, often $O^-$ or $O_2^-$ hits the sample and ablates material that is ionized to produce secondary ions, the ions are further accelerated into a mass spectrometer (Schoene, 2014). The method is illustrated in *Figure 17*. The method can be used to investigate spots as small as 10-40 µm with pit depth smaller than 4 µm with a mass resolution as high as 10 0000 (Schoene, 2014). The first ion microprobe constructed

for isotopic analysis was the SHRIMP (Sensitive High-Resolution Ion MicroProbe) and was specially made for zircons (Ireland and Williams, 2003). During the analysis, varying beam intensity, elemental fractionation combined with compositional changes in the targeted mineral can prevent the desired precision (Schoene, 2014). Advantages using SIMS are precise ages, high spatial resolution (especially in-depth profiling), and low damage of the sample during analysis (Košler and Sylvester, 2003). Compared to TIMS which uses isotope dilution to calculate the Pb/U, SIMS utilizes reference samples with known U/Pb in rotation with the unknown samples to obtain the Pb/U, (Schoene, 2014). Hence it is important to use high quality standards to obtain high-quality data.

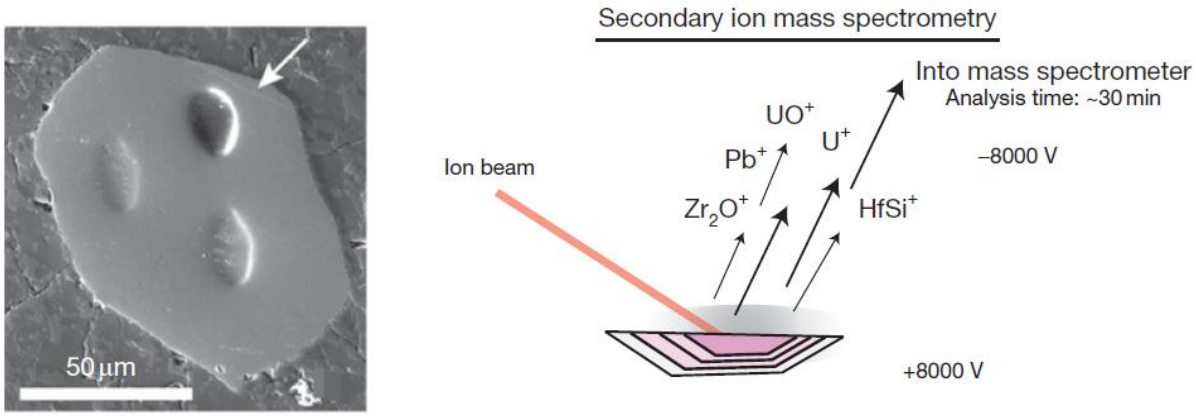


***Figure 17**: Secondary ion mass spectrometry (SIMS). Figure from Schoene (2014).*

**LA-ICP-MS**

The LA-ICP-MS instrument consists of two main parts, the laser ablation system, and the ICP-MS system (*Figure 19*) (Schoene, 2014). The main principle of LA-ICP-MS involves that a mineral surface is ablated by a laser beam, an aerosol that is further transported by a carrier gas of He and mixed with an Ar gas into an ICP to be ionized (Schoene, 2014). The Ar gas makes the ionization process of the aerosols easier (Schoene, 2014). The mass spectrometer system then separates the ions by mass-to-charge ratio, and the ions are measured by a detector (Liu et al., 2013). The schematic drawing of the method and a photo of an ablated zircon grain are illustrated in *Figure 18*.

Several factors influence the accuracy of an analysis, such as wavelength, the pulse width of the laser, pulse duration, laser repetition rate, energy per pulse, the composition of ambient gas, sensitivity and mass resolution of the ICP-MS, and the type and standard of calibration (Košler and Sylvester, 2003, Liu et al., 2013). Advantages of the LA-ICP-MS are its high spatial resolution, fast analysis time, broader availability in the geological community and low cost compared with SIMS (Košler and Sylvester, 2003, Schoene, 2014). With LA-ICP-MS, it is possible to collect a lot of U-Pb data, which is ideal for detrital zircon analyses (Fedo et al., 2003). Detrital zircon analyses can, e.g., provide information about the provenance of sediments, correlation of sediment units, and maximum depositional ages (Gehrels, 2011). It is also easy to collect information about internal zoning by combining the polarizing microscope, an integrated part of the ablation system, with pre-prepared BSE, CL, and EPMA (electrone probe micro-analyzer) X-ray elemental

maps (McFarlane and Luo, 2012). The main analytical problem regarding LA-ICP-MS and SIMS is the calibration step. A known reference standard is used to achieve quantitative results, which should correlate with the signal obtained. Often The preparation of these standards is difficult and time-consuming, and the quality of the reference standard is crucial for accurate elemental analysis (Miliszkiewicz et al., 2015).

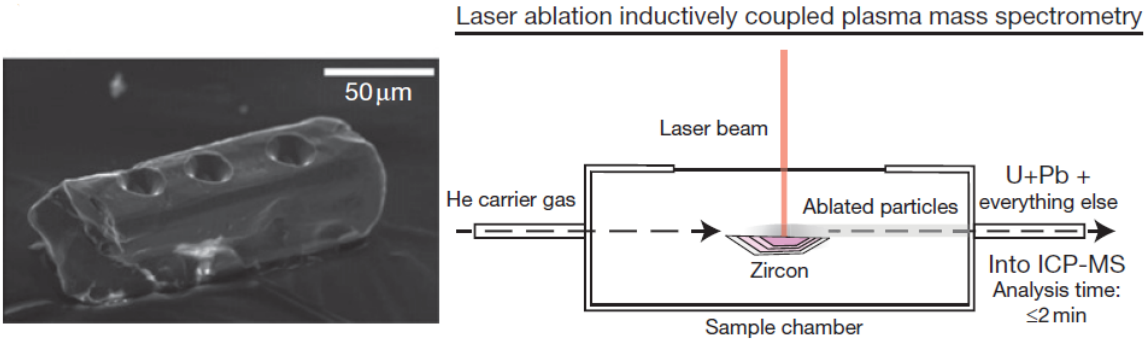


***Figure 18**: Ablated zircon grain and the LA-ICP-MS method. The figure is from (Schoene, 2014).*

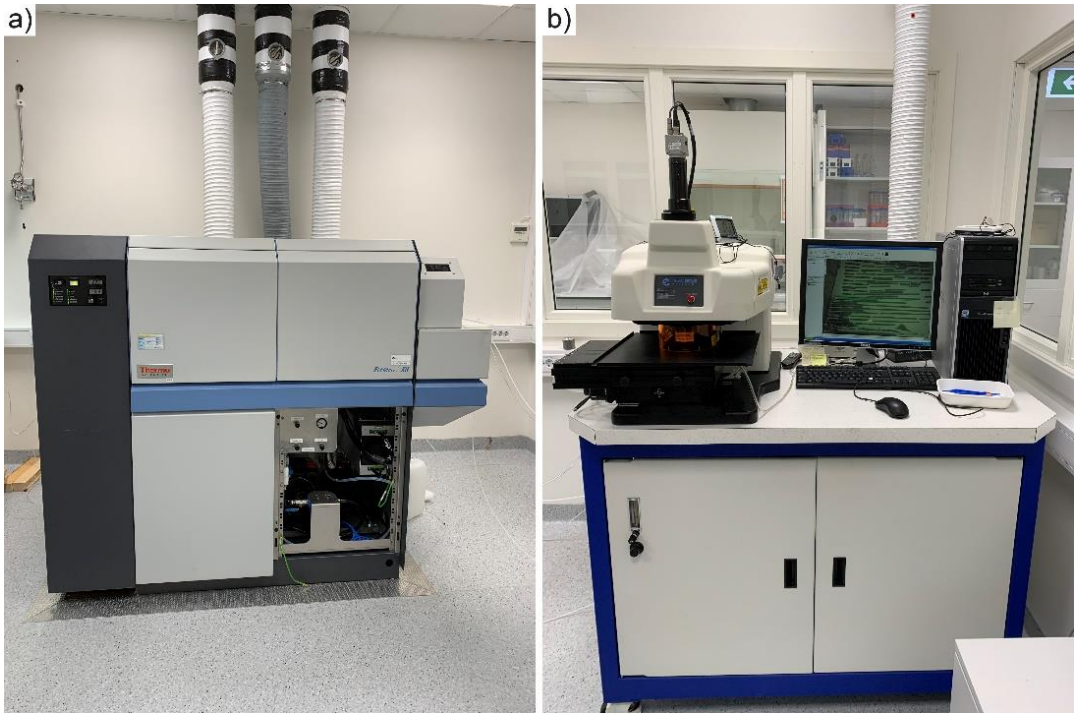


***Figure 19**: Laser ablation inductively coupled mass spectrometer instrument at NGU. A) Laser ablation system with the navigation screen. B) ICP-MS instrument.*

## 3.2 Geochemistry

Geochemistry can be used as a tool to investigate geological processes by linking the behavior and mobility of elements to various igneous, metamorphic, and hydrothermal processes. Thus, geochemistry can help test a specific hypothesis based on geological data.

### 3.2.1 Major and minor elements

Elements in a rock with concentrations greater than 1.0 wt. % are known as major elements and are the main building blocks in a rock (Winter, 2014). They are typically expressed as oxides in geochemical data sets. According Ronov and Yaroshevsky (1976) and Poldervaart (1955), the most abundant major elements in the crust are: O, Si, Al, Fe, Ca, Mg, Na, and K, where O and Si are the two dominant elements with 59.3 and 15.3% respectively.

The oxides which make up 0.1 to 1.0 wt. % are labeled minor elements and typically substitute for the major elements in a mineral. Typical minor elements are, e.g., Mn and Ti. If sufficient minor elements are present in a system, they can form accessory minerals such as titanite ($CaTiSiO_5$), rutile ($TiO_2$), and ilmenite ($FeTiO_3$).

The major and minor elements behave differently, such that the chemical analysis can be used to get insight into igneous processes, crystallization, and melting processes, and classify rocks (Winter, 2014). It is common to plot the chemical analysis in normalized diagrams, which may give useful information about the geological system. Some of these diagrams will be discussed below.

### 3.2.2 Harker diagram

Systematic geochemical variations can be found by using bivariate plots such as the Harker diagram, first used by (Iddings, 1892). This diagram plots wt. % $SiO_2$ on the y-axis against any other major element on the x-axis. In *Figure 20*, Winter (2014) explains how one can use these diagrams. *Figure 20* shows Harker diagrams for 310 analyzed rocks from Crater Lake. The linear trends in the diagrams indicate a relation between the samples, suggesting they formed from a magma that underwent chemical differentiation.

It is important to note that every element not incorporated in the crystallizing assemblage will have an increasing trend with increasing $SiO_2$ in the Harker diagram (Winter, 2014). This does not mean that it is an increase in an absolute sense, only relative in the system because the analyses must have a total of 100%. This effect is shown in *Figure 20*. The alkalis (Na and Ca) increase because they are not incorporated in the crystallizing minerals. Nevertheless, it is possible to add alkalis to the system, e.g., by assimilation or mixing processes (Winter, 2014). Fe and Mg-rich phases such as olivine and pyroxene will crystalize first, making the magma relatively richer in $SiO_2$ during the removal of Fe and Mg. In a Harker diagram this process reflects as negative trends for Mg and Fe (*Figure 20*).

When using the Harker diagram, one needs to be aware of which assumption one uses when interpreting. The explanation above assumes that the relative increase in $SiO_2$ is

proportional to the increase in evolving magma, only using one process, crystal fractionation. This simplification does not always work, so caution should be made when utilizing the Harker diagram.

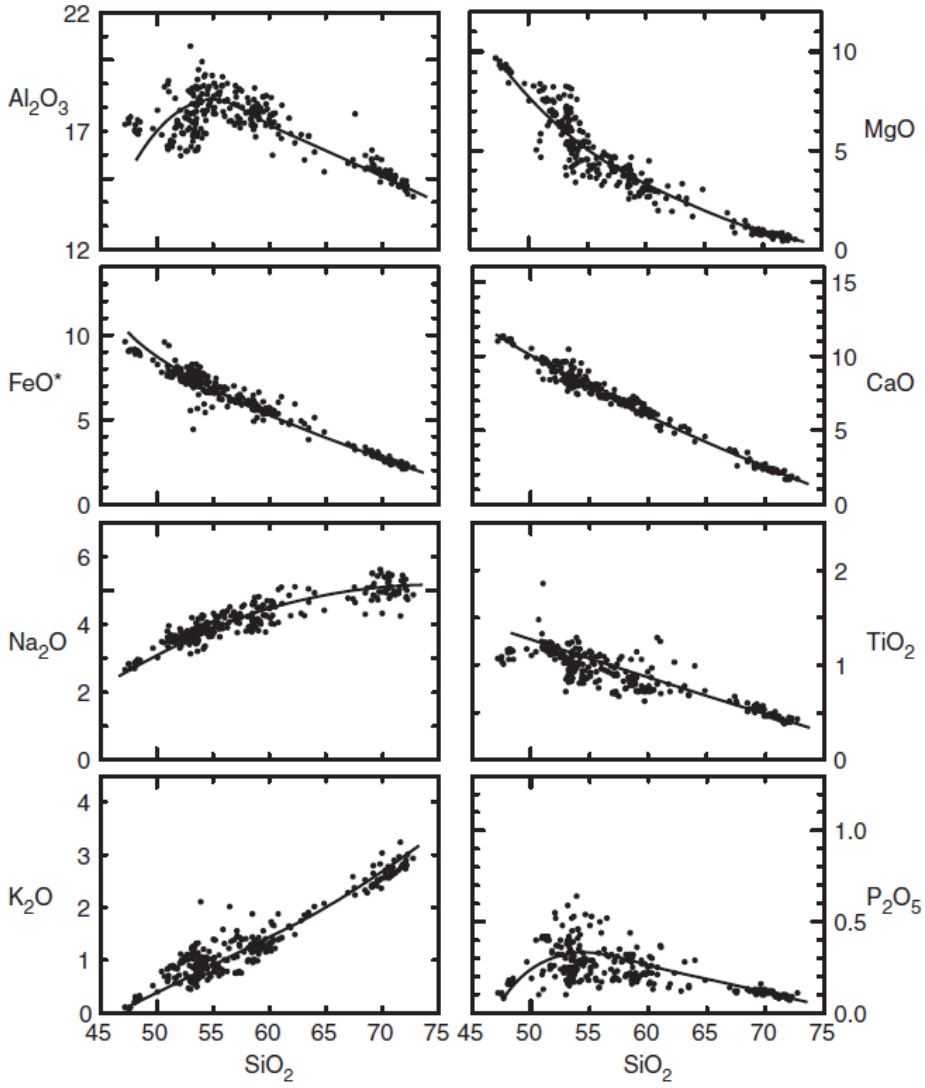


***Figure 20**: Major element data for 310 volcanic rocks from Crater Lake plotted in Harker diagrams to illustrate chemical trends between the rocks. Figure from Winter (2014).*

### 3.2.3 Trace elements

Trace elements constitute less than 0.1 wt. % of a rock and their concentrations are usually expressed in parts per million (ppm), unlike the minor and major elements that are expressed as wt. % oxides (Winter, 2014). The most helpful trace elements are the REE (Rare Earth Elements), transition metals, especially Sc, Ti, V, Cr, Mn, Co, Ni, Cu and Zn, and Rb, Sr, Y, Zr, Nb, Cs, Ba, Hf, Ta, Pb, Th, and U (Winter, 2014).

The fractional crystallization process which has produced the evolved magma can be studied much better by looking at the trace element content compared to the major

elements (Best, 2003). During progressive crystallization, different trace elements fractionate into the solid, depending on the chemical behavior of the trace elements (Best, 2003, Winter, 2014). Goldschmidt (1937) proposed three rules which can be used to qualitatively predict the affinity of a trace element based on the valence and the ionic radius:

1. If two ions have the same valence and ionic radius, the concentration of ions in the solid is proportional to their concentration.

2. If two ions have a different ionic radius and the same valence, the ion with the smaller ionic radius is preferably incorporated into the solid.

3. If two elements have the same radius but different valence. The ion with the higher charge is preferably incorporated into the solid over the liquid.

Later, these rules have been deemed too simplistic because other factors than valence and ionic radius also influence the substitution of trace elements into minerals. These factors include; electronegativity, crystal field effects, and valence electron shell configurations (Winter, 2014).

During melting or crystallization, trace elements behave differently (Rollinson, 1993, Best, 2003, Winter, 2014). Incompatible elements are those that prefer to remain in the liquid or melt, while the compatible elements prefer to enter the solid phases. A partition coefficient (KD) (*equation 9*) is used to formalize how compatible or incompatible an element is. If KD > 1, it is defined as a compatible element and incompatible if KD < 1.

$$K_D = \frac{C_s}{C_L} \tag{9}$$

Where:

$C_s$ = Concentration of a trace element in the solid phase (ppm or wt. %)

$C_L$= Concentration of a trace element in the liquid phase (ppm or wt. %)

The incompatible elements are usually divided into two groups based on the ionic radius and the valence (Rollinson, 1993, Winter, 2014): 1) High field strength elements (HFSE), are highly charged small cations and include the REE, Sc, Y, Th, U, Ce, Pb, Zr, Hf, Ti, Nb, and Ta. 2) Large ion lithophile elements (LILE) are, large cations with small charge including K, Rb, Cs, Ba, $Pb^{2+}$, Sr, and $Eu^{+2}$. The LILE are more mobile than the HFSE, especially when a fluid phase is present (Winter, 2014). Typical compatible elements during mantle melting include Ni, Cr, Cu, W, Ru, Rh, Pd, Os, Ir, Pt, and Au (Winter, 2014). However, the compatibility of elements in a system is dependent on the minerals present in the magma, e.g., in a felsic magma where zircon is crystallizing, uranium (HFSE) will prefer to be incorporated into the solid zircon because of $U^{4+}$ substitutes for $Zr^{4+}$ (Best, 2003).

### 3.2.4 Rare earth elements

The rare earth elements (REE) are a series of elements with atomic number from 57 to 71. They include (from lowest to highest atomic number): La, Ce, Pr, Nd, Pm, Sm, Eu, Gd, Tb, Dy, Ho, Er, Tm, Yb, and Lu (Rollinson, 1993, Voncken, 2016). All these elements have an oxidation state of +3 except Eu, which occurs as $Eu^{2+}$ in low oxygen fugacity environments, and Ce can occur as $Ce^{4+}$ under oxidizing conditions. In addition, the ionic radius decreases evenly with increasing atomic number, making the elements a coherent series, making the heavy rare earth elements (HREE) slightly more compatible than the light rare earth elements (LREE). The elements are relatively insoluble in aqueous fluids, making it possible to analyze the originally rare earth elements in altered and weathered rocks (Rollinson, 1993). By studying the concentrations of these elements in rocks, one can help test different petrogenetic hypotheses due to their atomic structure (Rollinson, 1993, Best, 2003, Winter, 2014).

**REE diagrams**

REE diagrams are used to study the concentration variations and trends in the REE content in a rock that can be used to interpret its igneous petrogenesis (Rollinson, 1993). An REE diagram is generated by plotting the concentrations of the REE on the y-axis and the atomic number on the x-axis. If one plot the concentrations directly in the diagram, one will get a sawtooth pattern, the Oddo-Harkins effect (Winter, 2014). This effect occurs because of a higher natural abundance of elements with even numbers in the universe compared to odd ones. This effect is removed by normalizing the concentrations to REE concentrations from chondritic meteorites which are believed to be the approximate chemical composition of the early Earth. *Figure 21* from Best (2003) shows a REE diagram with three different analyses. The Lunar basalt has a distinct negative Eu anomaly, which means that the rock crystallized from an Eu-depleted magma. The Eu depletion is possibly caused by the crystallization of plagioclase, later separated from the melt (Winter, 2014). N-MORB (normal-mid-ocean ridge basalt) represents a mid-ocean ridge tholeiitic basalt. This rock shows depletion of the LREE, indicating that the source has undergone extensive partial melting and depletion prior to formation of the MORB (i.e., depleted mantle). Adakite is a type of dacite formed deep in a subduction zones (Best, 2003). New research indicates that Adakites is not slab derived but formed by high-pressure mantle fractionation or as hybridized mantle melts (Ribeiro et al., 2016). The steep negative slope can be explained by partial melting of a rock under high pressure where garnet is stable. The heavy rare earth elements are strongly compatible in garnet and will be retained in the source.

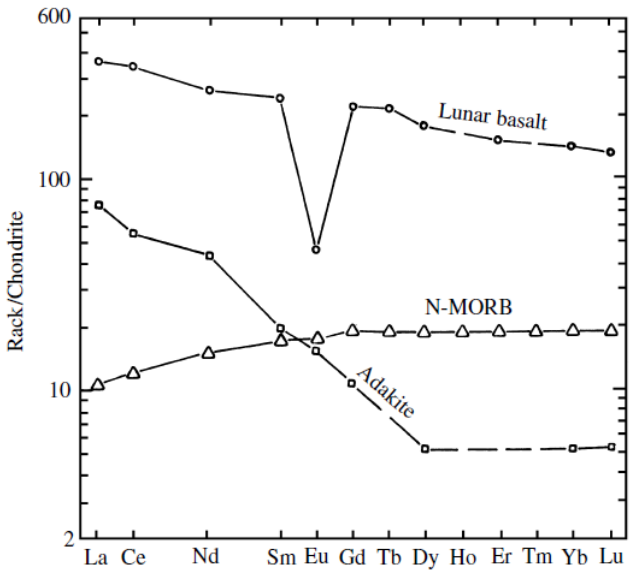


***Figure 21**: Three different REE patterns from three rocks. See text for interpretation. From (Best, 2003).*

### 3.2.5 Spider diagrams

Spider diagrams are similar to the normalized REE diagram and based on the same principles (Winter, 2014). The two main differences between these REE and other spider diagrams are (Winter, 2014): 1) The spider diagrams utilize not only the REE but incorporate other trace elements as well. 2) Several normalization schemes, e.g., the hypothetical primordial mantle, MORB, chondrite meteorite and others, can be used. This makes the spider diagrams more flexible than the REE diagrams and they may reveal other types of information. *Figure 22* shows an example of a spider diagram of an average ocean island basalt (OIB) normalized to an average mid-ocean ridge basalt where the trace elements used are the LILE and the HFSE (These elements are further discussed in *3.2.8*). This type of setup makes it possible to directly compare the concentrations of HFSE and LILE in an OIB to a MORB. One can see that the OIB is more enriched in the LILE, most likely caused by higher crustal contamination compared to the MORB. LILE is often extracted from the mantle and concentrated in the crustal component of the Earth (Winter, 2014).

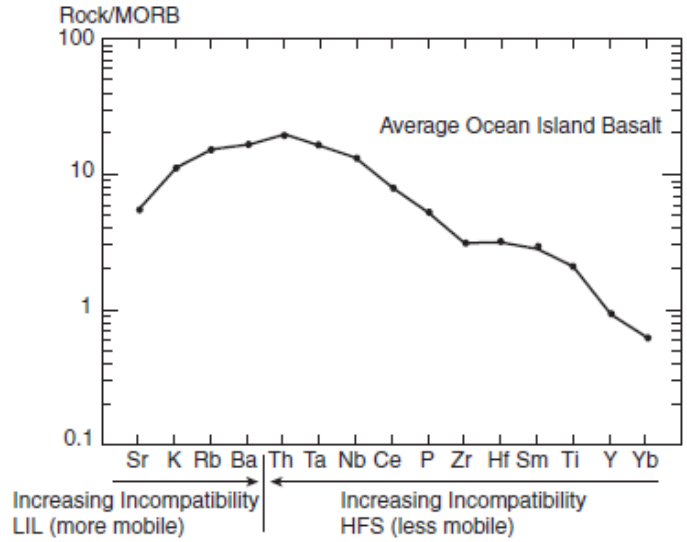


***Figure 22**: Spider diagram, average ocean island basalt normalized to an average mid ocean basalt. From Winter (2014).*

### 3.2.6 AFM diagram

The subalkaline series can be split into two sub-series, the calc-alkaline and tholeiitic magma series (Winter, 2014). The AFM diagram can be used to differentiate between these two magma series. In the AFM diagram the A represents the alkalis ($Na_2O$ + $K_2O$), F is iron (FeO and $Fe_2O_3$), and M is magnesium (MgO), usually expressed in wt. % (Rollinson, 1993, Winter, 2014). *Figure 23* shows an example of an AFM diagram with samples from the Skaergård intrusion and Crater Lake plotted. These two rock suites follow two distinct evolutionary paths from primitive to more evolved magma. The Skaergård rocks are tholeiitic and show Fe enrichment in the early stages of evolution, while the Crater Lake rocks follow a calc-alkaline path with no iron enrichment.

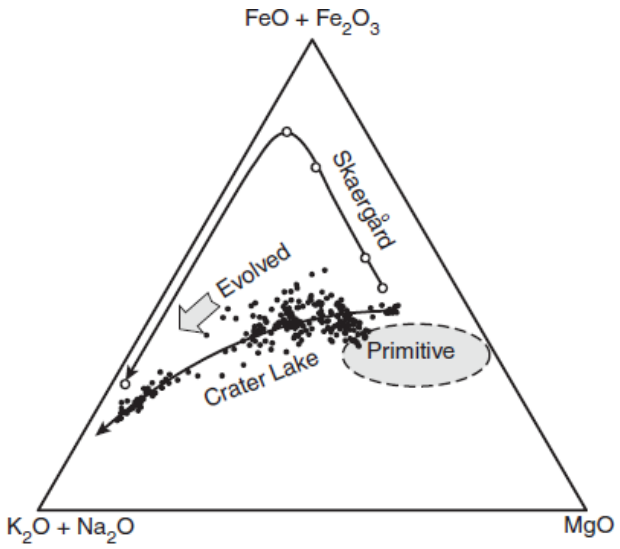


***Figure 23:** AFM diagram. Plotted analyses are from Crater Lake and the Skaergård intrusion. Figure from Winter (2014).*

### 3.2.7 Tectonic discrimination diagrams

Chemical characteristics of igneous rocks can be used to empirically relate a suite of rocks to a particular tectonic setting (Rollinson, 1993). This practice is mostly used by plotting trace elements for samples in discrimination diagrams with predefined groups belonging to different tectonic settings (Rollinson, 1993). This technique has been developed by studying the chemical composition of rocks in known tectonic environments; hence this analysis assumes a direct correlation between the amount of trace elements and the tectonic setting (Rollinson, 1993). Many variables can influence the chemical composition of the source rock, such as; partial melting, fractional crystallization, magma mixing, assimilation, and metamorphism (Winter, 2014). To mitigate the effect of metamorphism, one should use discrimination diagrams with immobile elements such as the HFSE (e.g., Nb, Y, Zr, and Ti). These elements are relatively immobile in aqueous fluids, unless the fluid has high fluorine concentrations (Rollinson, 1993, Winter, 2014). Minimizing the effects of fractional crystallization, mixing and assimilation can be done by only plotting mafic volcanic rocks (Winter, 2014). Using discriminations diagrams, one can recognize tectonic environments such as ocean ridges, back-arcs, fore-arc basins, volcanic-arcs, collisional settings, and intraplate settings. See *Figure 24* for a very simplified schematic overview of the different tectonic settings.

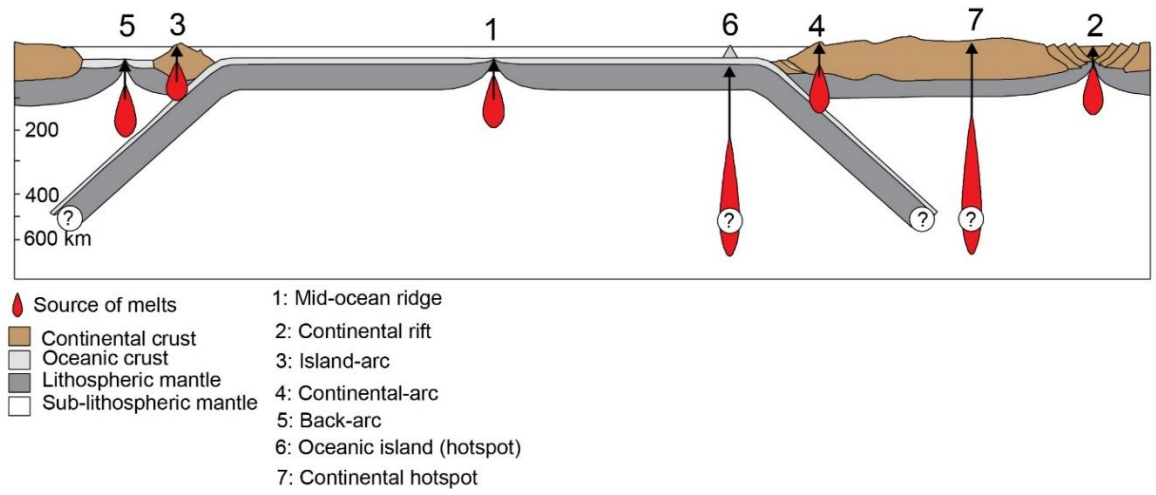


***Figure 24**: Simplified generalized schematic cross section of tectonic settings. Modified from Winter (2014).*

In this study, four different tectonic discrimination diagrams were used, and each one will be described briefly below.

**The Ti-Zr-Y diagram (Pearce and Cann, 1973)**

The Ti-Zr-Y tectonic discrimination diagram after Pearce and Cann (1973) can most effectively discriminate between within-plate basalts and other types of basalts (Rollinson, 1993). The elements are plotted in ppm, and the diagram (*Figure 25*) is split up into four fields: A, Island-arc, B, ocean-floor, calc-alkali or island-arc, C, calc-alkali, and D, within-plate. The diagram is applicable to tholeiitic basalts with a compositional range 20 wt. %

> CaO + MgO > 12 wt. %, rocks with high cumulate content and Ti-bearing phases should be avoided (Rollinson, 1993).

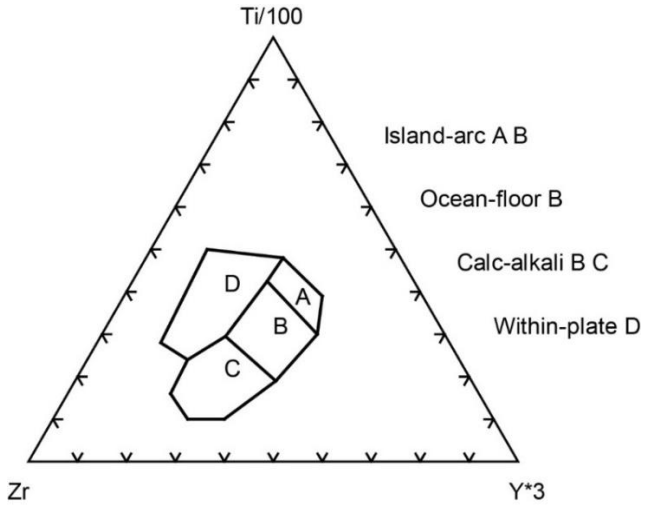


***Figure 25**: Ti-Zr-Y tectonic discrimination diagram after Pearce and Cann (1973). A: Island-arc. B: Island-arc, ocean-floor, and calc-alkali. C: Calc-alkali. D: Within-plate.*

### The Zr/Y-Zr diagram (Pearce and Norry, 1979)

The Zr/Y-Zr diagram by Pearce and Norry (1979) utilizes the ratio Zr/Y (both are high-field strength elements) plotted against the fractionation index Zr to discriminate between island-arc, MORB and within-plate basalts. The diagram (*Figure 26*) is split up into four main fields: Volcanic-arc, MORB, and within-plate basalts. The volcanic-arc and MORB fields overlap, so does the MORB and within-plate fields (field E).

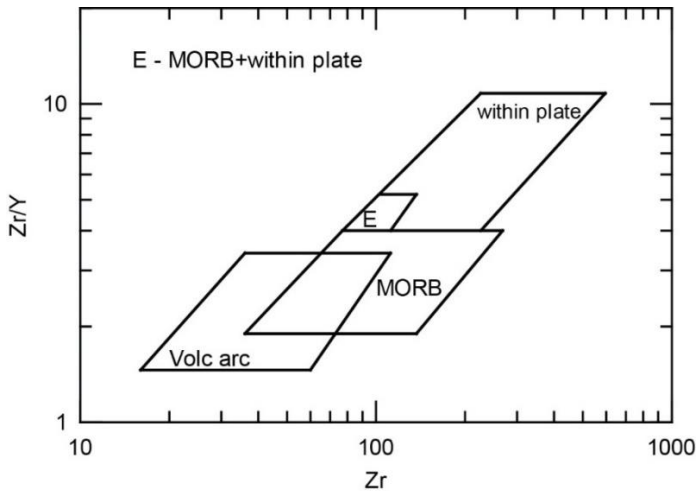


***Figure 26**: Zr/Y-Zr tectonic discrimination diagram by Pearce and Norry (1979). Three main fields: Volcanic-arc, MORB and within-plate basalts. E: Both MORB and within-plate basalts. The volcanic and MORB fields also overlap.*

### The Zr-Nb-Y diagram (Meschede, 1986)

The Zr-Nb-Y diagram by Meschede (1986) plots Zr/4, Y, and Nb*2 at each corner in the triangular plot (*Figure 27*). This was the first diagram to show that it was possible to discriminate between different types of MORB/ocean basalts. The concentration of Nb can be used to distinguish between a depleted MORB often associated with mid-ocean ridges (N-MORB) and an enriched MORB (E-MORB) associated with plume-influenced regions, e.g., Iceland (Meschede, 1986). The diagram is split into five fields: AI, within-plate alkali basalts (WP Alk); AII, Within-plate alkalis and within-plates tholeiites (WP th); B, E-MORB; C, Within-plates tholeiites and volcanic-arc basalts (VAB); D, N-MORB, and volcanic-arc basalts. The several overlaps make them somewhat ambiguous. The E-MORB and within-plate alkali basalts can be identified without any ambiguity.

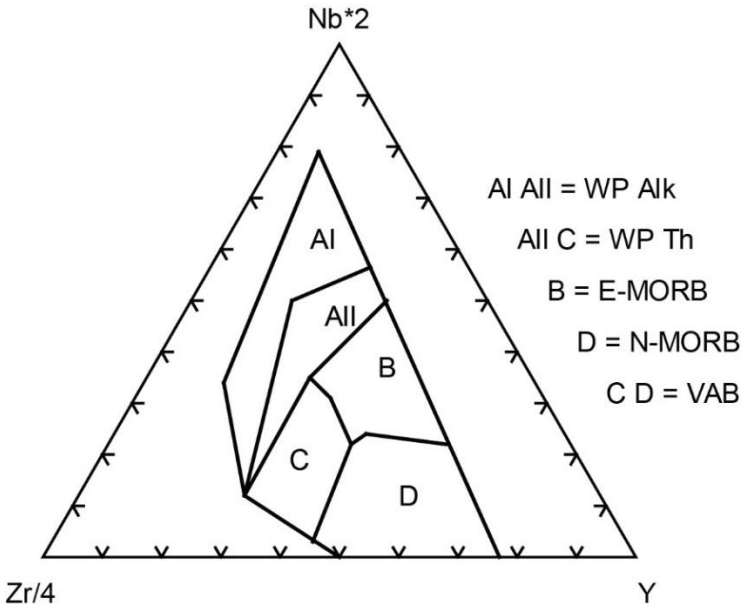


***Figure 27**: Zr-Y-Nb tectonic discrimination diagram. AI: Whitin plate alkali basalts (WP Alk). AII: Whitin plate alkalis and within plate tholeiites (WP Th). B: E-MORB. C: Within plates tholeiites and volcanic-arc basalts (VAB). D: N-MORB and volcanic-arc basalts. After Meschede (1986).*

### The La-Y-Nb diagram (Cabanis and Lecolle, 1989)

This triangular diagram plots La, Y, and Nb concentrations to discriminate between volcanic-arc basalts (field 1), continental basalts (field 2), and oceanic basalts (field 3). The elements are expressed inn ppm and plotted as La/10, Y/15, and Nb/8, see *Figure 28*. The volcanic-arc field is subdivided into three fields: Calc-alkali basalts (1A), island-arc tholeiites (1C), and mixes between these two (1B). The continental basalts plots in 2A and the back-arc basin basalts in 2B. The oceanic field is subdivided into three fields: Alkali basalts (3A), E-type MORB (3B), and N-MORB (3C). An advantage with this diagram is that it can separate between different types of MORB, a disadvantage is that La can be mobile during hydrothermal conditions (Rollinson, 1993).

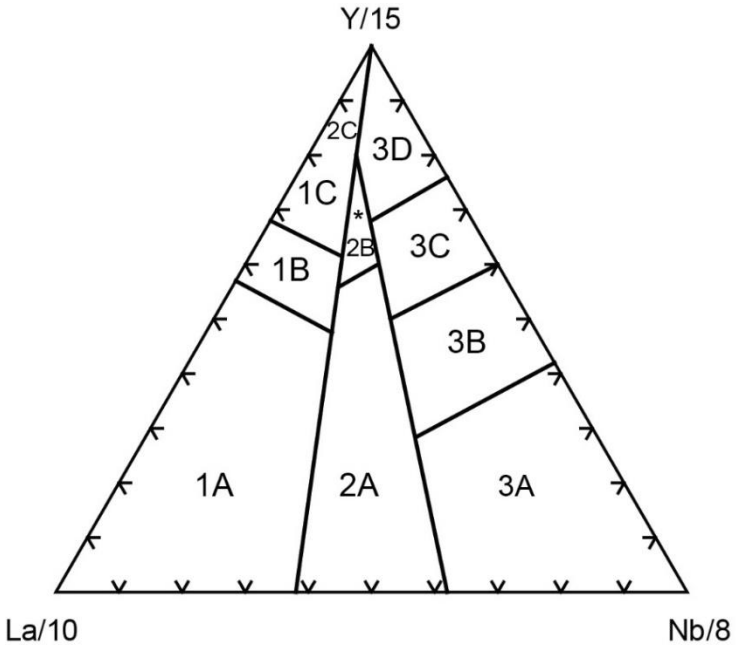


***Figure 28**: La-Nb-Y tectonic discrimination diagram. 1: Volcanic-arc basalts. Calc-alkali basalts (1A), island-arc tholeiites (1C) and mixed between these two (1B). 2: Continental basalts. Back-arc basin basalts (2B). 3: Oceanic basalts. Alkali basalts (3A), E-type MORB (3B and 3C) and N-MORB (3D). After Cabanis and Lecolle (1989).*

### 3.2.8 Element mobility

During metamorphism or hydrothermal activity, element mobility can create apparent trends in variation diagrams (Rollinson, 1993, Jung et al., 1999, Zack and John, 2007, Winter, 2014). Scattered plotting in variation diagrams can indicate element mobility, and it is essential to notice that element mobility can create systematic changes that will generate trends similar to fractional crystallization (Winter, 2014). These apparent trends are generated by the removal or addition of specific elements in a rock. Element mobility controlled by fluid interaction is dependent on three main factors (Rollinson, 1993): 1. The composition and stability of the protolith. 2. The composition and stability of the altered rock. 3. The temperature, composition, and volume of the fluid phase. Table 1 shows an overview of major element mobility in common rocks under different hydrothermal conditions.

As a general rule, the LILE are mobile, HFSE immobile, the transition metals Mn, Zn, and Cu mobile (especially in high-temperature environments), and Co, Ni, V, and Cr tend to be immobile (Rollinson (1993) and references therein). *Figure 29* from Orvik (2019) shows the discrimination of the LILE and HFSE based on the ionic potential (IP) (ionic radius (Å) divided on the ionic charge (Z)). The elements with similar IP easily substitute for each other, and the compatibility of elements increases with the IP whereof elements with smaller radius and higher charge are preferred in the solid (Best, 2003, Winter, 2014). Hence the HREE is preferred incorporated into the solid compared to the LREE.

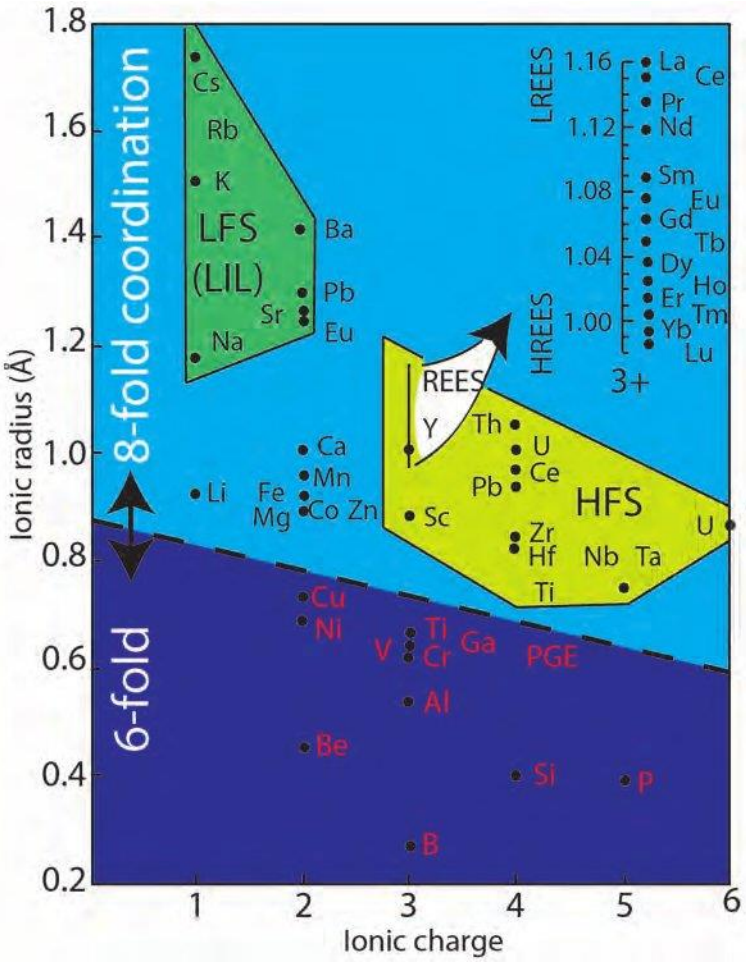


***Figure 29**: Distinction between LILE and HFSE based on ionic potential. Figure from Orvik (2019).*

Element mobility can be the basis on some interpretations e.g., when investigating migmatites (Jung et al., 1999). One expects the leucosome to be enriched in the incompatible elements and the melanosome to be depleted by those elements. The chemical composition of the partial melted rock (migmatite source) should be equal to the addition of the leucosome and melanosome (Jung et al., 1999). Another example where the mobility of elements lay the foundation for the interpretations are in investigating subduction components in mafic rocks. Ba which are mobile in most fluids can for example be used as a proxy for fluid incorporation when be combined with Th or the LREE (Hochstaedter et al., 2001, Pearce and Stern, 2006). For example a high Ba/Nb indicates that the system has a significant component of slab-derived hydrous fluids (Hochstaedter et al., 2001, Pearce and Stern, 2006). In a case where immobility of elements is desired can be in the association with tectonic discrimination diagrams. For example in the Ti-Zr-Sr diagram after Pearce and Cann (1973). Only fresh samples can be analyzed because of the high mobility of Sr. Any alteration involving hydrothermal fluids will increase the uncertainty when using the diagram (Rollinson, 1993).

***Table 1**: Major element mobility in common rocks under different hydrothermal conditions. Green: Element enriched. Red: Element depleted. Yellow: Element mobile. Different sources are used when several rows of the same rock and process are present. Modified from Rollinson (1993).*

| Rock type | Si | Ti | Al | Fe | Mn | Mg | Ca | Na | K | P |
|---|---|---|---|---|---|---|---|---|---|---|
| Komatiite (Hydrothermal alteration) | | | | | | | | | | |
| | | | | | | | | | | |
| Basalt (Hydrothermal alteration) | | | | | | | | | | |
| Basalt (Hydrothermal alteration) | | | | | | | | | | |
| | | | | | | | | | | |
| Basalt (Submarine weathering) | | | | | | | | | | |
| Basalt (Weathering) | | | | | | | | | | |
| Basalt (Green schist metamorphism) | | | | | | | | | | |
| | | | | | | | | | | |
| Basalt (Amphibolite metamorphism) | | | | | | | | | | |
| | | | | | | | | | | |
| Granite (Weathering) | | | | | | | | | | |
| | | | | | | | | | | |
| Granite (Contact metamorphism) | | | | | | | | | | |
| | | | | | | | | | | |
| Granite (Granulite facies metamorphism) | | | | | | | | | | |
| | | | | | | | | | | |
| Calcareous sediment (Medium grade metamorphism) | | | | | | | | | | |
| | | | | | | | | | | |
| Calcareous sediment (Contact metamorphism) | | | | | | | | | | |
| | | | | | | | | | | |
| Sandstone-clay (Diagenesis) | | | | | | | | | | |

## 3.3 Metamorphism

### 3.3.1 Metamorphic facies and reactions

Metamorphism is associated with changes in a rock due to external factors such as pressure and temperature changes. Bucher and Grapes (2011) highlight the effects metamorphism can have on a rock: 1) Formation of new minerals and mineral assemblages, which grows at the expense of the old ones. 2) Minerals may systematically change their composition, e.g., The Fe content of garnet and cordierite can increase simultaneously during metamorphism. 3) Minerals may be oriented in a preferred way, changing the rock structure. 4) The bulk rock composition may be changed due to the removal or adding of components. Components are commonly removed/added by dissolution or precipitation processes associated with fluid phases.

Eskola (1915) was the first geologist who proposed that the mineral assemblages, rock composition, and metamorphic grade were correlated. Today one can estimate the pressure and temperature conditions for the formation of specific mineral assemblages by using various techniques (e.g., geothermobarometry), only dependent on the bulk composition of the rock (Bucher and Grapes, 2011).

### 3.3.2 Petrogenetic grid

Petrogenetic grids are experimentally P-T diagrams consisting of different fields representing different metamorphic conditions (Bucher and Grapes, 2011, Winter, 2014). The fields are divided by univariant mineral reactions, which must be fully completed before the temperature can change. It means that a unique stable mineral assemblage characterizes every field in the grid; hence, by interpreting mineral assemblages, one can estimate a rock's pressure and temperature during formation by using a petrogenetic grid. Figure 30 shows a simplified petrogenetic grid for metamorphosed mafic rocks in the CaO-MgO-$Al_2O_3$-$SiO_2$-$H_2O$-($Na_2O$) system.

Spear and Cheney (1989) introduced the AFM compatibility diagrams and the KFMASH ($K_2O$-FeO-MgO-$Al_2O_3$-$SiO_2$-$H_2O$) petrogenetic grid for pelitic rocks. The AFM compatibility diagrams can be combined with the KFMASH petrogenetic grid to estimate pressure and temperature during the formation of pelitic mineral assemblages. When using these diagrams, the assumption of $H_2O$ and quartz saturation in the rocks is needed. In addition, to plot mineral assemblages in the AFM diagrams, the pelites need to contain either K-feldspar or muscovite. An example of one of the AFM compatibility diagrams and the petrogenetic grid is shown in *Figure 31*. A pelitic rock with the mineral assemblage grt + chl + bt + ms (assuming $H_2O$ and quartz saturation) will, e.g., plot in AFM diagram J and the belonging field in the petrogenetic grid. It is important to mention that the one mineral assemblage can plot in several AFM diagrams and fields in the KFMASH petrogenetic grid. The presence of the aluminum silicates kyanite, sillimanite and andalusite or the use of a geothermal gradient can further discriminate the fields in the petrogenetic grid.

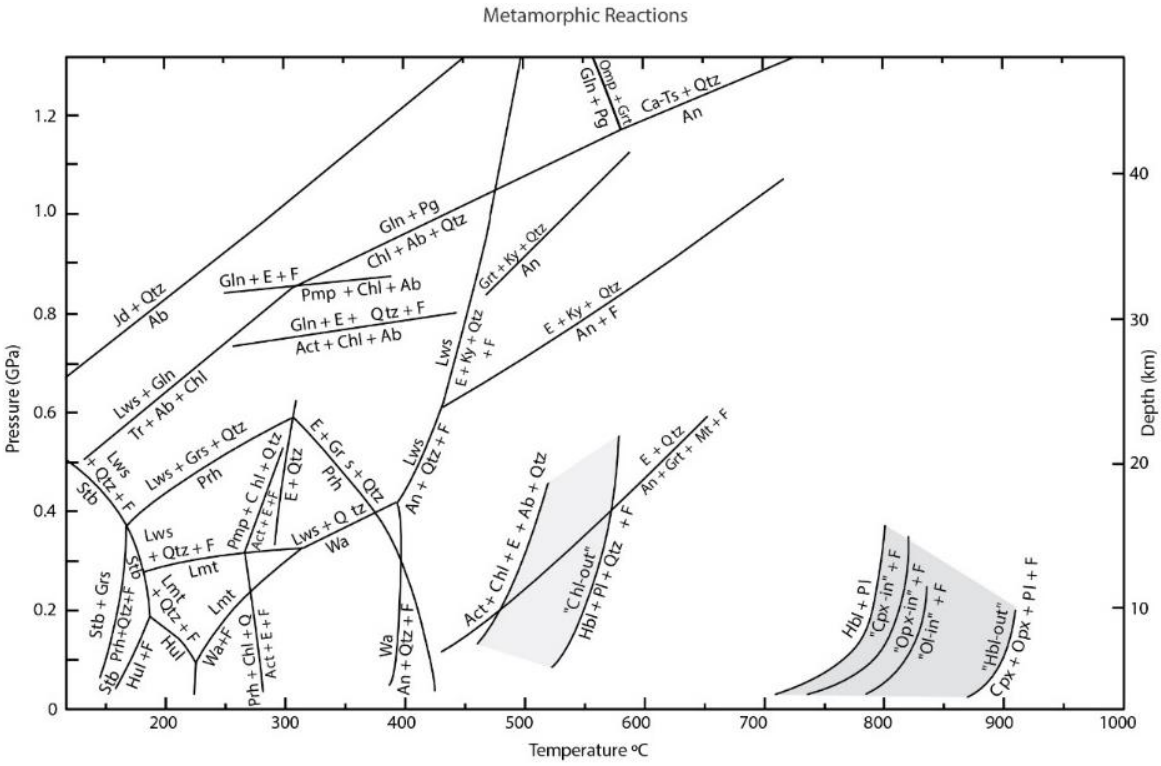


***Figure 30**: Petrogenetic grid for metamorphosed mafic rocks in the CaO-MgO-$Al_2O_3$-$SiO_2$-$H_2O$-($Na_2O$) system, from Winter (2014) and references therein.*

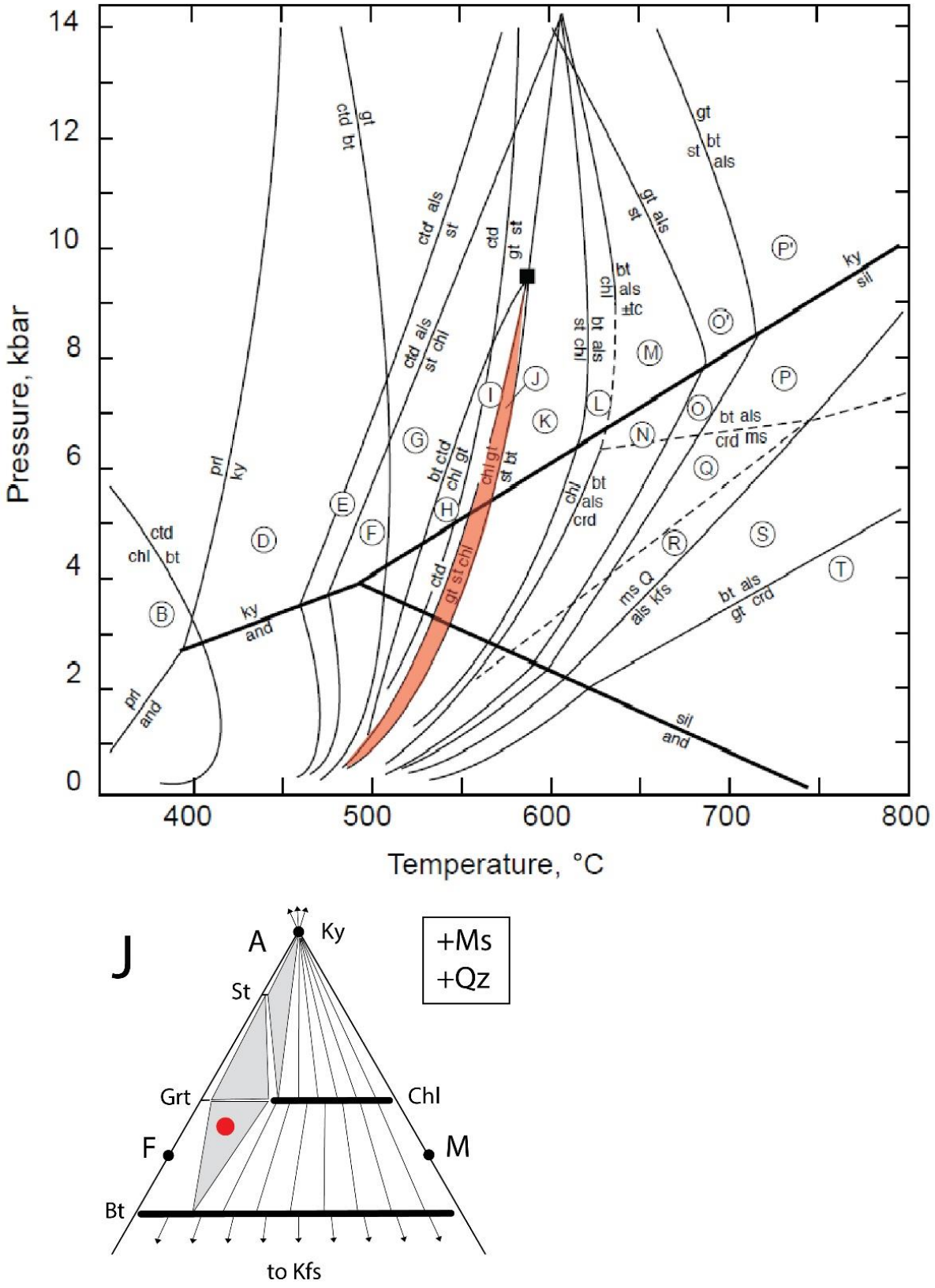


***Figure 31**: KFMASH petrogenetic grid and an AFM diagram. A mineral assemblage grt + chl + bt + ms (assuming qz and $H_2O$ saturation) (red dot) can e.g., plot in compatibility diagram J and belonging field in the KFMASH petrogenetic grid (red field). Figures modified from Spear and Cheney (1989).*

# 4 Methods

## 4.1 Field work

Two field seasons were completed. Two weeks in the summer of 2020 and two weeks in the summer of 2021.

The main study area is located along the shores of Kallvatnet (*Figure 1*). The lake is located in Nordland County, southeast in Rana between the Gammelgardsfjellet and Melkfjellet. Kallvatnet is dammed, resulting in excellent exposed rock surfaces when the water is lowered during the summer months. The western part of Kallvatnet, approximately 20 square km (including the lake) around the lake and areas at Damtjønnfjellet, has been carefully mapped. Some fieldwork and sampling were also done at Gammelgardsfjellet and adjacent to the eastern part of Østre Sauvatnet.

The mapping was carried out using digital and non-digital aids. A geological compass was used to measure geometrical characteristics such as planes and lines. The Dip/dip direction and plunge/azimuth were noted for planes and lines, respectively. Observations and measurements were noted in a waterproof field book. During the mapping of summer 2020 a tablet with a software called Arcpad was used. All the observations and measurements were linked to the tablet and the software such that every geological locality was assigned to coordinates. During the second field season in the summer of 2021, technical issues meant that the tablet and the arcpad software could not be used any more. Instead, an application named "Norgeskart friluftsliv" was used to assign GPS coordinates to the different geological localities. Mapping was also carried out using 1:10 000 map and colored pencils. Different colors were chosen for each lithology and plotted on the map while walking in the field. A geological hammer and a rock saw were used to take rock samples and to expose fresh rock surfaces in the field. One field day, a motorized boat was used, making accessibility to the main study area significantly easier. An iPhone XR was used to take field photos and a north arrow, pencil or the geological hammer were used for scale and to indicate the spatial orientation.

## 4.2 Sampling

*Figure 32* shows a flow chart illustrating an overview of the numbers of samples collected and the numbers chosen for thin section production, geochronological and geochemical analysis. Altogether, sixty-four rock samples were collected during two field seasons (summer 2020 and 2021), (Sample map is shown in *Figure 33*). Thin sections were produced for twenty-eight of these samples whereof four were chosen for monazite geochronological analysis. Three of these samples were successfully dated and the data are presented in *5.2.1.* Thirty-seven samples for geochemistry. Twelve samples plus one additional sample collected by Kerstin Saalmann, four samples from Bergliot Kulsrud Storruste's thesis (Storruste, 2017), and three samples from Anne Bruland Høyen's thesis (Høyen, 2016) were chosen for zircon geochronological analysis. From the total of twenty samples, seven were successfully dated and are presented in *5.2.1*. Thin sections were produced, and geochemical data obtained for all geochronology samples collected during field season 2020 or 2021. A complete table of all the samples with description, coordinates, and utilized method is given in Appendix A.

A more detailed description of the thin section preparation, zircon and monazite geochronology, and geochemistry are given in chapters: *4.5*, *4.3.1*, *4.3.2*, and *4.4*.

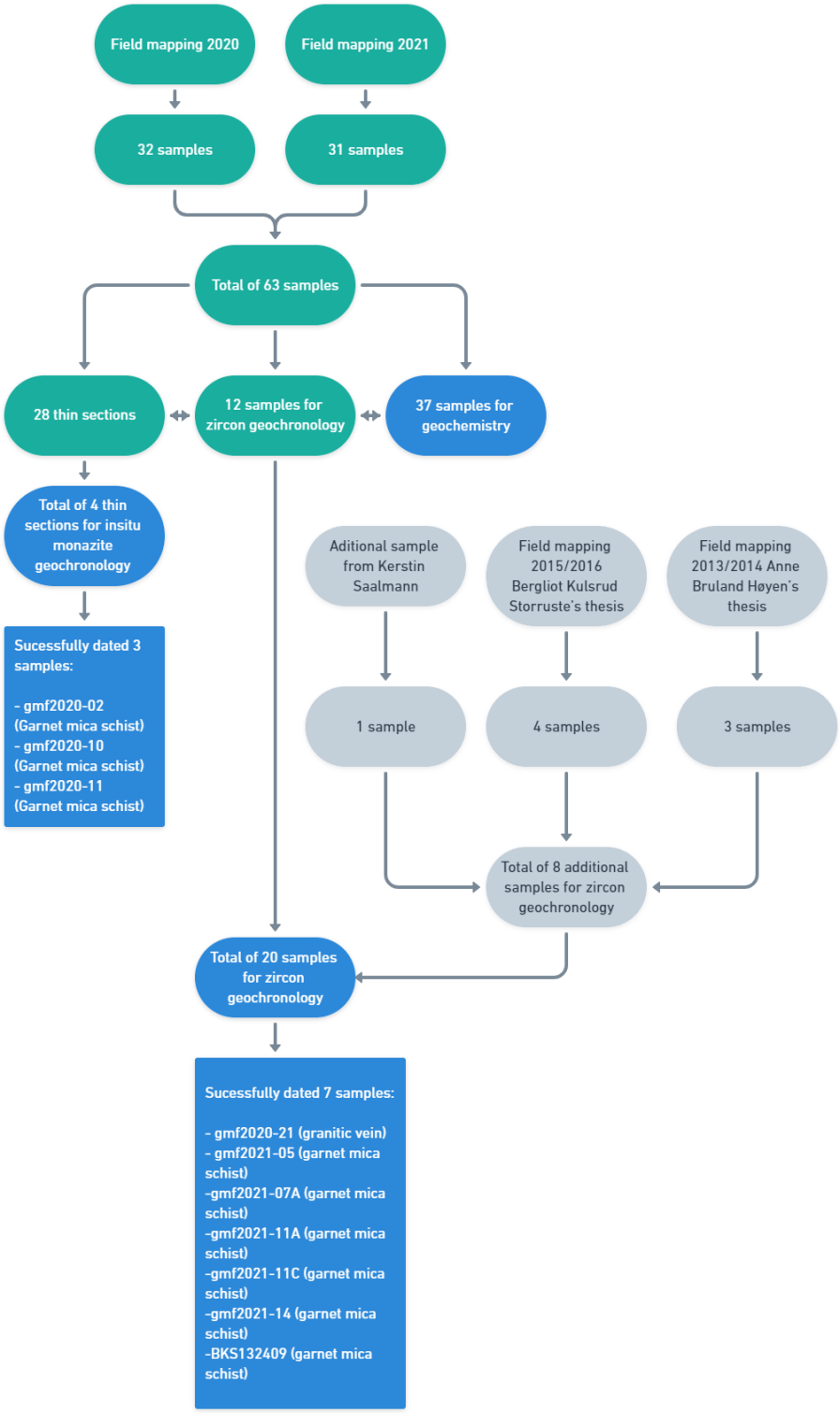


***Figure 32**: Flow chart illustrating an overview of numbers of samples collected and the numbers of samples chosen for production of thin section, geochronological and geochemistry analysis.*

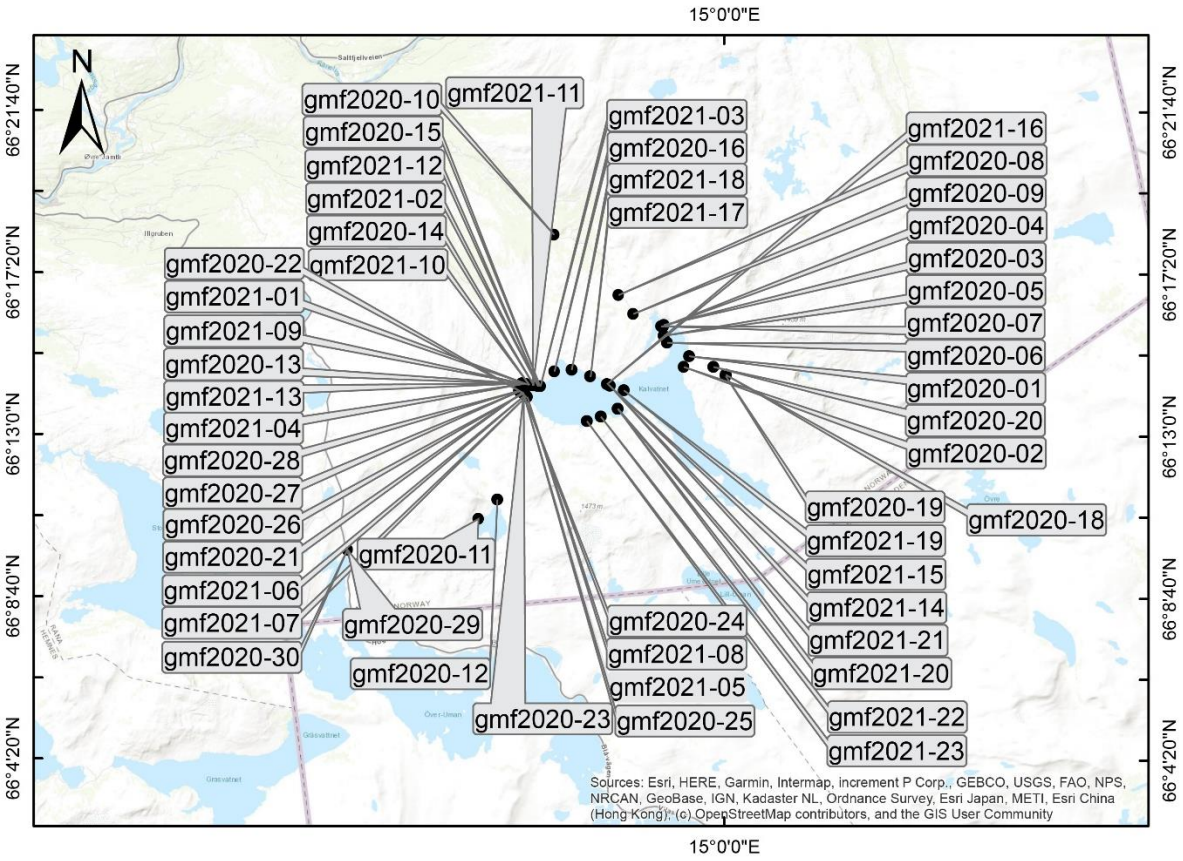


***Figure 33**: Sample map (this thesis).*

## 4.3 Geochronology

### 4.3.1 Zircon geochronology

The workflow from taking the sample in the field to obtaining an age consists of eight main stages: 1) preparation and logistics, 2) crushing, 3) splitting, 4) mineral separation, 5) imaging, 6) LA-ICP-MS analysis, 7) data reduction, 8) interpretation of data. *Figure 34* shows the main stages of the workflow. The stages are described in detail below.

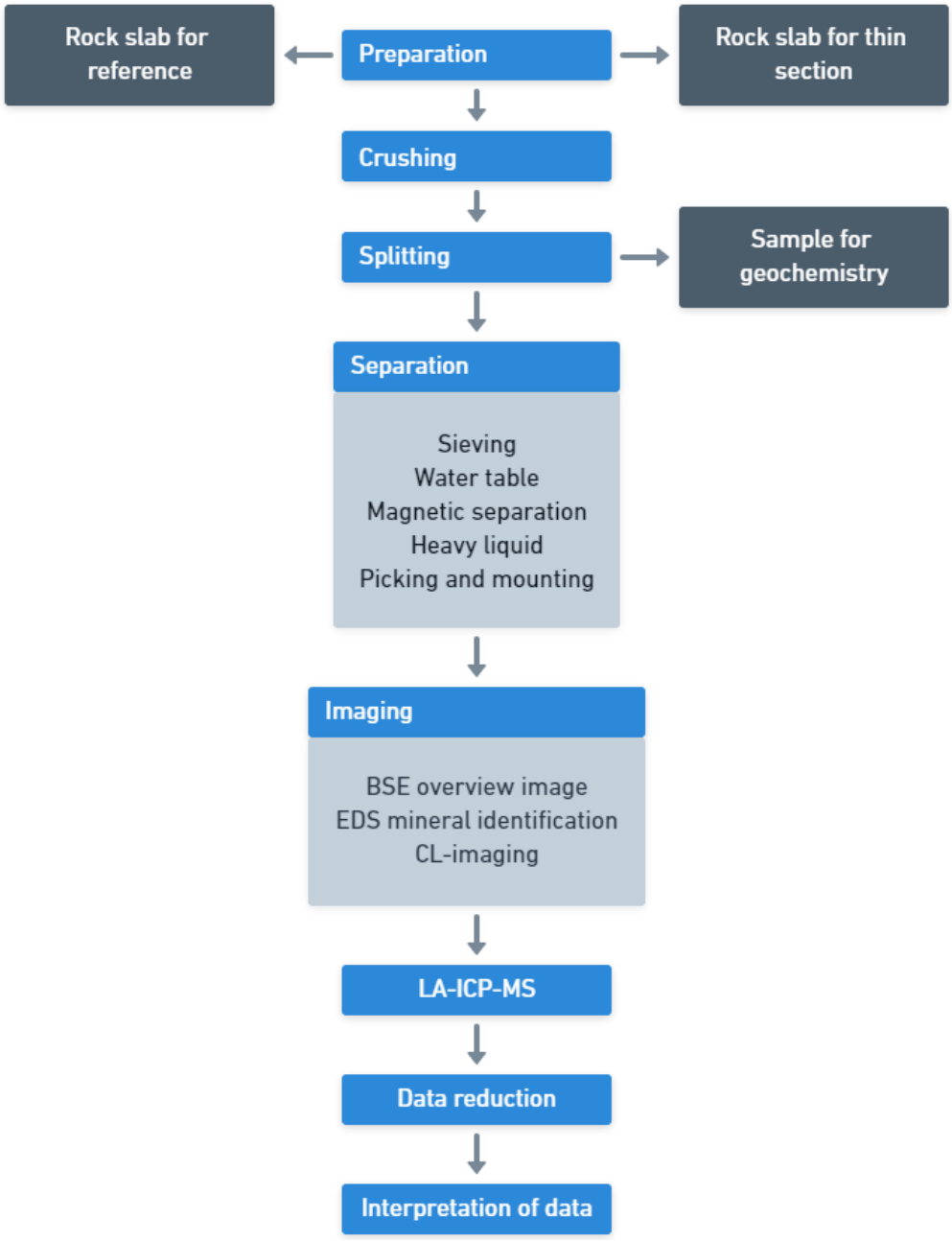


***Figure 34**: Workflow for the main stages during geochronological analysis.*

### *Preparation*

A list of rock samples collected in the fields where obtained. Samples were chosen for further geochronological analysis based on the lithological and structural characteristics observed in the fields. The primary purpose of geochronological analysis was to obtain ages for metamorphisms, felsic vein formation, and mafic volcanism, which could help constrain the timing of the geological history of the Kjerringfjell Group. For every sample chosen for zircon geochronology, a slab was cut for thin section, and a reference slab was stored.

### *Crushing*

#### Jaw crusher

The first step in the sample preparation is to crush the rock samples into smaller fractions using a jaw crusher. NGU's jaw crusher of the type Pulverisette 1, model II was used to crush the samples, see *Figure 35a*. The Jaw crusher crushes the samples between to steel plates, one mobile plate applies mechanical power against a stationary steel plate. The samples were carefully fed down in the jaw crusher, crushed, and collected in a box at the bottom of the jaw crusher. To be sufficiently crushed, the samples were sent through the crushers at least twice. Sometimes, it was necessary to send the samples through the crusher three times, especially if they were small. After crushing each sample, the two crushing plates were disassembled and washed thoroughly using dust suction, iron brush, alcohol, and high-pressure air.

### *Splitting*

After the crushing of the samples, they were split. The splitting was carried out to obtain a representative sample for geochemical analysis. The splitting was done at NGU's lab using splitters of stainless steel. This process was repeated several times to obtain an appropriate amount that was later sent to geochemical analysis (approximately 100 grams to geochemical analysis).

### *Separation*

#### Sieving

The crushed material was sieved to separate the < 250 µm fraction. If the sample was relatively big, a 400 µm sieve was set on top of the 250 µm meter sift to increase the efficiency of the sieving process. The fraction larger than 250 µm was saved in case of the future need for new analysis. The fraction less than 250 µm went on the next step in the separation procedure. The splitting and sieving equipment was thoroughly cleaned by vacuuming, alcohol, and high-pressure air. The sieves were placed in an ultrasonic bath to release the small grains that had become stuck in the mesh, then the mesh was dried with high-pressure air and then a final inspection with a light table.

#### Water table

The < 250 µm fraction for each sample was then processed on a Wilfley water table. This process was done to separate the heaviest minerals from the lighter minerals. *Figure 35b* shows a picture of the water table used. The water table is slightly tilted both sideways and forward and consists of a water system that distributes water on the table and a motor that allows the table to shake horizontally. The table has longitudinal grooves, which impede the water from flowing unhindered straight down the table. The washing was carried out by pouring small amounts of the sample at the top of the washing table. The lightest minerals will flow faster than the heaviest minerals. Two different containers were used to collect the material at the end of the water table. One container for the material

which flowed fastest off the table and one for the slower, heavy fraction. The lightest fraction was then dried and stored, while the heaviest fraction was stored in small plastic bowls with alcohol, ready for heavy liquid separation. The water table was cleaned with water between samples to avoid any contamination.

### Magnetic separation

Before the heavy liquid separation, a hand magnet stick was used to remove some of the magnetic minerals. In addition, some samples were dried and sent through a vertical Franz. A vertical Franz is a magnetic separator that consists of two magnets, the one used is shown in *Figure 35c*. A clean sheet of paper was rolled to create a vertical paper tube, that was taped onto the vertical Franz, as shown in the figure. The material was dropped through this paper tube while the vertical Franz induced a magnetic field (1.5 A). The minerals with the highest magnetic susceptibility stuck to the paper, while the non-magnetic minerals ended up in a container. The magnetic minerals were collected in a different container and stored. The paper tube was changed between each sample, and the vertical Franz was cleaned.

### Heavy liquid separation

All samples selected for geochronology went through heavy liquid separation. This process was done at the mineral separation lab at NGU under supervision in safe conditions in a fume hood when handling the heavy liquid. Figure 36 shows the heavy liquid separation process step for step.

The following equipment was used: two beakers, three funnels, three filters, one separation funnel, acetone, alcohol, heavy liquid with a density of 3.33 g/cm$^{3,}$ and water. All the equipment was checked if it was completely dry and clean before use. The setup is shown in *Figure 35*d.

A) The chosen sample was dried while the equipment was set up as shown in Figure 36*a.* First the burette was filled with heavy liquid. The heavy liquid was filtered to remove the risk of contamination from earlier use.

B) The funnel and filter that the liquid had gone through was then removed and washed with acetone. The dried sample was then dropped into the heavy liquid, and the separation funnel was carefully shaken to mix the material and speed up the sinking process.

C) After the heaviest mineral grains had settled at the bottom, the separation funnel was opened and quickly closed to ensure that the only the material to end up in the filter was the material which has sunk to the bottom in the heavy liquid, see Figure 36c. Care was taken not to let out too much material and heavy liquid to avoid light minerals mixed with the heavier ones.

D) The filter with the heavy minerals (> 3.33 g/cm$^3$) was then switched with a clean filter, and the filter with heavy minerals was cleaned with acetone and dried before transfer to a petri dish for hand picking.

E) Further, the separation funnel was opened, and all the heavy liquid and the light minerals went through the separation funnel.

F) At this stage, the beaker used was only filled with heavy liquid. This beaker was switched with a clean beaker, and the heavy liquid in the first beaker was returned to the heavy liquid bottle for reuse. Then the equipment was washed with acetone. The filter with the light minerals was then dried and transferred to a plastic bag. All the equipment used was cleaned with acetone, and the filters were placed in a fume hood.

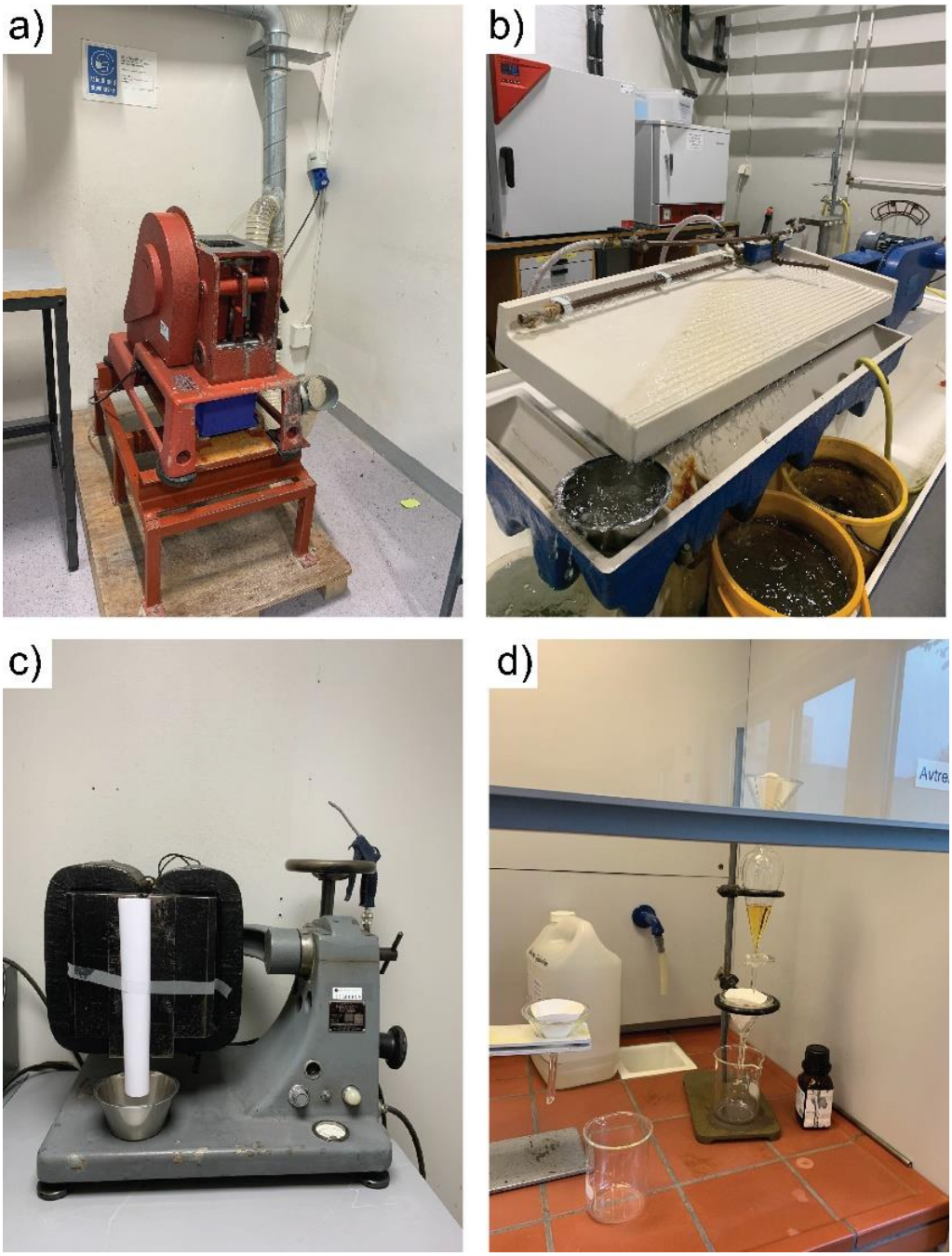


***Figure 35**: A) Jaw crusher of the type Pulverisiette 1, model II. B) Wilfey water table C) The vertical Franz.*

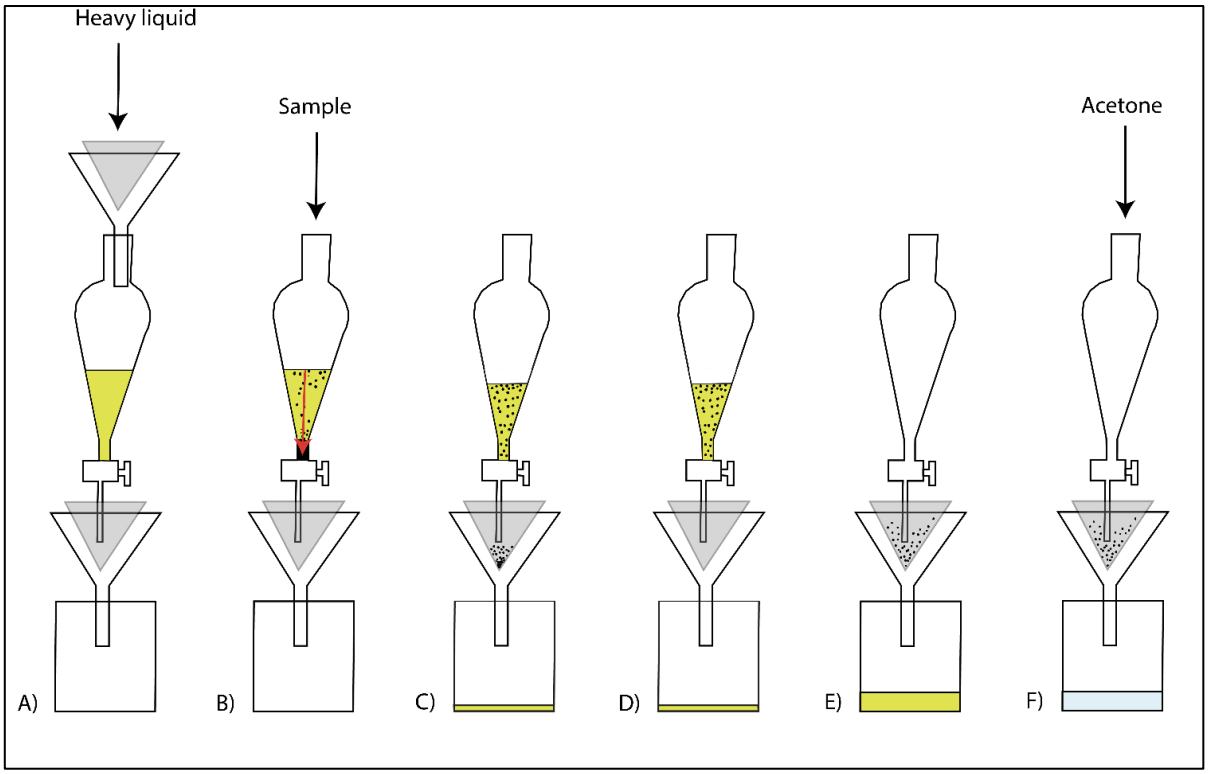


***Figure 36**: A) Heavy liquid with density 3.33 g/cm$^3$ was filtered and poured in the separation funnel. B) The sample was put in the heavy liquid, minerals heavier than 3.3 g/cm$^3$ sunk. C) The separation funnel was open and quickly closed to let the sunken minerals down in the filter. D) The filter with the heavy minerals was dried and stored and switched with a new filter. E) The separation funnel was open so that the light minerals were let down in the filter. F) The beaker used from A) to E) (filled with only heavy liquid) was switched with a new clean beaker and the heavy liquid was poured back in the heavy liquid bottle for reuse.*

**Picking and mounting**

The process of picking minerals for geochronological analysis began with cleaning of a binocular microscope and the surrounding workspace with alcohol. Then the workspace was covered with clean paper sheets. Alcohol was then poured carefully into the sample to make the picking easier; a grain-free area was cleared in the center of the sample where the picked grains would be placed temporarily. Zircon was then picked with tweezers. Approximately 40 grains for each mineral were picked if possible. After the minerals were collected in the grain-free area, a photograph of the grains was taken and the sample was set to dry, a pipette was used to remove as much alcohol as possible. Then the collected grains were moved with tweezers onto a double-sided tape taped on a glass plate. A cover paper with a small rectangular hole, large enough to contain a sample was put carefully on the tape to prevent grains from getting stuck in unwanted places or among previously picked samples, see *Figure 37a and b* for set up. All 12 samples were mounted on the same tape, and photographs of the tape-mounted samples were taken. The cleaning process was repeated for every sample. Then, the epoxy mold was put on the tape, filled with a small amount of epoxy, and set to dry. The next day the mold was completely filled.

The mount was set to drying in three days before it was polished. The mount was carefully polished by hand with a rotating polisher. The polisher was equipped with micro-diamond grains, and a microscope with reflected light was used to investigate the visibility of the grains during the polishing (see Figure 37*c and d*).

During the polishing, some grains were lost. Probably because of bad quality of epoxy or that the tape reacted in some way with the epoxy so that the grains did not get adequately attached. Another explanation could be that the polishing was done in a skewed way or that the zircons had too big of a size difference, so the biggest grains were polished out of the epoxy before the small one even appeared.

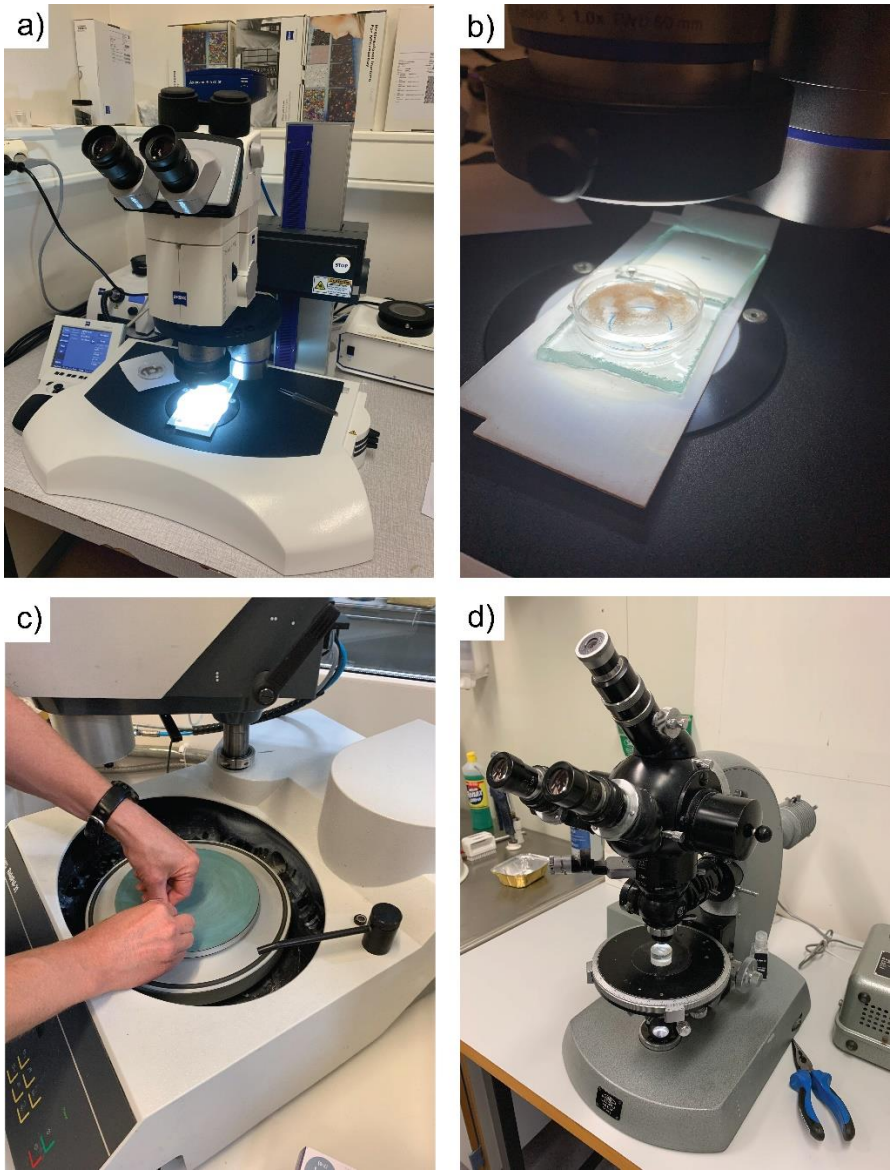


***Figure 37**: A) Microscope used to pick zircon. B) Setup when transporting picked grains from the sample to the double-sided tape. The sample was transported on the small, squared cavity on the paper where the tape is exposed. The sample is placed on a glass board to make the sample and the tape on approximately on the same elevation to simplify the focusing when moving between the tape and sample. C) Manually polishing the mount by hand with a rotating polisher with sandpaper (with diamond grains). D) Microscope used to check the visibility of the zircon grains. If the visibility was not sufficient, more polishing was necessary.*

### *Imaging*

#### SEM

An electron microscope (from ZEISS) at NTNU was used to confirm which minerals that had been picked, acquire an overview backscatter electron image map of the mount with zircons, and take Cathodoluminescence imaging (CL) of the zircon grains. This procedure was conducted with help by Stefanie Lode.

The purpose of the generated backscatter map was to reveal cracks and inclusions in the zircon grains and make navigation with the laser-ablation system easier when doing geochronological analyses. The backscatter map was generated by using backscatter which detected particles, which was then classified using effective energy-dispersive X-ray spectroscopy (EDS) in a software called MINERALOGIC. The mount was coated with carbon before it was put in the electron microscope.

CL was also conducted with the same electron microscope, but only of the zircon grains. The primary purpose of the imaging was to obtain information on the internal structure of the zircon grains. When doing geochronological spot and line analyses with the LA-ICP-MS of a zoned zircon crystal, the age can vary significantly depending on what area of the zircon grain is ablated and analyzed. For example, core analyses usually yield older ages than rim analyses on the same grain, consistent with the latter typically representing metamorphic growth, discussed further below. If an analysis is placed in two different zones, e.g., in both core and the rim, the analysis will result in a mixed-age. An electron high tension voltage of 15 kV and a beam current of 100 microampere were used when doing CL- mapping. The cathodoluminescence emission from the zircon grains varies too much to conduct an automatic mapping, so it was done manually.

### *LA-ICP-MS*

The samples were cleaned in acid (2% $HNO_3$) and then placed in the LA-ICP-MS at NGU. A laser spot size of 15 µm with a repetition rate of 10 Hz and a energy corresponding to a fluence of 2-3 J/cm$^2$ were used. Line analyses with a length of 60 µm were conducted. The ablation was done in a direction away from the suction to avoid contamination from other grains. The standards used were GJ-1 (608.5 ± 1.5 Ma) (Jackson et al., 2004), 91500 (1065.4 ± 0.3 Ma) (Wiedenbeck et al., 1995), OS-99-14 (1797 ± 3 Ma) (Skår, 2002), and Z-6412 (1160 ± 2 Ma) (unpublished, GSC Ottawa).

### *Data reduction*

The data reduction was done by Trond Slagstad using the Glitter software at NGU. When reducing the data, corrections are applied, isotope ratios and uncertainties are calculated (Horstwood, 2008). Less data reduction is preferred because the uncertainty of the data usually go up with increasing amount of reduction (Horstwood, 2008). Data reduction should be done in a non-biased way.

### *Interpretation of data*

A Microsoft Excel add-in in called Isoplot (version 4.15.11.10.15) was used to plot the data in TW diagrams and to calculate ages. In addition to the columns with data and the analysis number in the spreadsheet, columns were assigned to give information about which sample and grain the analysis was conducted on and rock type, see *Figure 38*. A column was also labled "comment" which would store the given interpretation, e.g if the analysis is interpreted as detrital, magmatic, or metamorphic. Specific font colors were given to the analysis based on interpretations. This made interpreting easier, the color of the error ellipses in the TW-diagrams could be changed based on the specific font colors. The interpretations were made by studying the shape and internal structures of the zircons by using CL-images in addition to Th/U ratio.

| 2 | | | | | |
|---|---|---|---|---|---|
| 3 | **Analysis_#** | **Grain nr.** | **Sample** | **Comment** | **Rock** |
| 4 | zircon_001 | 1 | gmf2020-21 | Rim (Cl and Th/U --> metamorphic) | Vein |
| 5 | zircon_002 | 2 | | Core (CL and Th/U --> detrital) | |
| 6 | zircon_003 | 3 | | Core (CL and Th/U --> detrital) | |
| 7 | zircon_004 | 4 | | Rim (CL --> metamorphic) | |
| 8 | zircon_005 | 5 | | Core (CL and Th/U --> detrital) | |
| 9 | zircon_006 | 6 | | Rim (CL and Th/U --> metamorphic) | |
| 10 | zircon_007 | 7 | | Mixed core and rim (Th/U --> metamorphic rim) | Mixed analysis |
| 11 | | | | | |

***Figure 38**: Screen shot of a part the spreadsheet containing the zircon geochronological data. Columns as grain nr., sample, comment, and rock were used to organize the data to make the interpretation of the data easier.*

## 4.3.2 Monazite geochronology

Six main stages were conducted during the methodology process in the monazite geochronology: 1) preparation, 2) imaging, 3) LA-ICP-MS analysis, 4) data reduction, 5) Interpretation of data. *Figure 39* shows the main stages of the workflow. The stages are described in detail below.

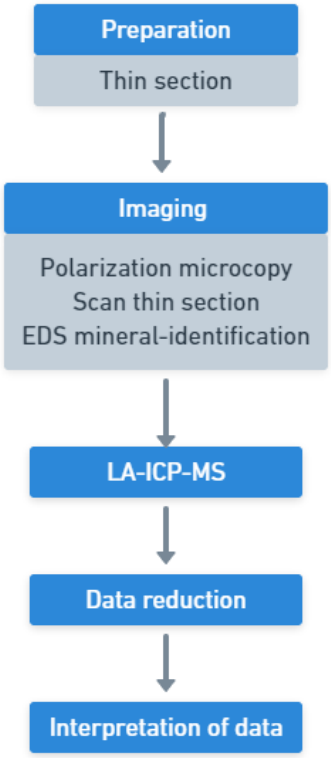


***Figure 39**: Workflow diagram for the five main stages in the monazite geochronology.*

### *Preparation*

In the field, samples that could possibly contain monazite where chosen. Typically, monazite occurs in medium- to high-grade metamorphic rocks derived from clay-rich sediments (*3.1.5*). In the preparation stage the selected samples collected in the field was chosen for thin section preparation. In addition, a reference slab was stored.

### *Imaging*

The main goal during the imaging stage was to identify the monazites and to prepare for navigation with the LA-ICP-MS. A quick mineral identification was done in all the prepared thin sections using optical microscopy, and high-resolution plane-polarized thin-section scans were taken using the Olympia scanner at NTNU. The thin section scans were further used to make the navigation with the electron microscope and the LA-ICP-MS easier. Thin sections that apparently had monazite, were marked for further investigation with electron microscope, and they were coated with graphite. The electron microscope was used to identify monazites using BSE and EDS. The identified monazites were marked on the high-resolution plane-polarized thin section scans. The thin sections were systematically investigated with the electron microscope to identify as many monazites as possible. In BSE, monazite is one of the brightest minerals, so the brightness was turned down making it easy to identify them.

### *LA-ICP-MS*

The thin sections were placed directly in the LA-ICP-MS at NGU. A laser spot size of 10 µm with a repetition rate of 10 Hz and an energy corresponding to a fluence of 2-3 J/cm$^2$ were used. Line analyses with a length of 20-40 µm were conducted depending on the size of the analyzed grain. The standards used were BB-0109 (1137 ± 1 Ma) (Bingen et al., 2008), Moacair (504.4 ± 0.2 Ma) (Gasquet et al., 2010), BB-0030 (1092 ± 1) (Bingen et al., 2008), A-276 (1915 ± 4 Ma) (Salli, 1983), and BB-9952 (403 ± 5 Ma) (Bingen, unpublished).

### *Data reduction*

The data reduction was done in the same procedure as in the zircon geochronology, see *4.3.1*.

### *Interpretation of data*

The same interpretation procedure as described in the zircon geochronology (*4.3.1*) was used. All monazites were interpreted as metamorphic, but it was important to distinguish whether the monazites were in the matrix or as inclusions inside garnet.

## 4.4 Geochemistry

In the fall of 2021, 37 samples were sent to the ALS Chemex geochemistry lab in Sweden (Hammarvegen 22 SE-943 36 Ojebyn Piteå Norrbotten) to obtain major, minor, trace, and rare earth elements.

REE, trace element and whole rock chemical data were obtained by ALS with lithium borate fusion prior to acid dissolution, ICP-MS and ICP-AES (Inductively coupled plasma atomic emission spectroscopy) analyses on the same fusion, code "ME-MS81d". Twenty-three of the samples that had not been crushed during preparation for geochronological analyses had to be crushed by ALS and were marked with the code "PREP-31". Further, the crushed samples were then total up to 250 g to 85% passing 75 µm, code "PUL-31".

## 4.5 Thin section and petrography

Twenty-eight samples were sawn and marked with the desired thin section position on the slab. In addition, the slabs were scanned with a standard paper scanner. Further, the slabs were sent to the thin section lab at NTNU (14 in 2020 and 14 in 2021). The samples were polished down to a 25 µm thickness with an area of 28 x 48 mm. All the thin sections were produced so it could be utilized in a scanning electron microscope.

A brief petrographic description was done for every thin section (see *Appendix D*) using a LEICA DM2500 P polarization microscope with an attached camera connected to a computer

with ProgRes CapturePro (version: 2.10.0.1) software installed (*Figure 40*). Thin section scans of all the thin sections were also generated with the Olympus BX51 thin section scanner at the IGP – Microscopy Laboratory at NTNU. Overveiw and detailed EDS-scans were also conducted on several thin section. The scanning was done using SEM and MINERALOGIC at NTNU with the help by Stefanie Lode which set up the scanning and did the data reduction. The petrographic descriptions, slab-scans, thin section and overview EDS scans are given in *Appendix D*.

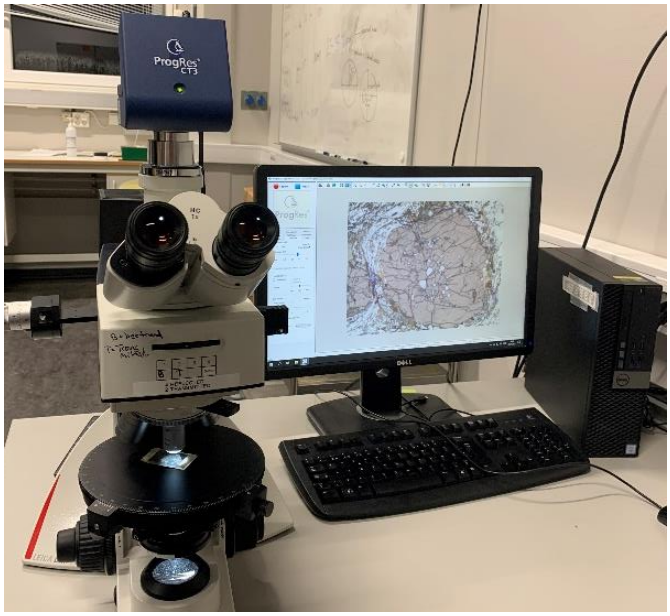


***Figure 40**: Petrographic description setup. LEICA DM2500 P microscope with an attached camera connected to a computer with ProgRes CapturePro software.*

## 4.6 Sources of error

In this thesis four main methods have been conducted: 1) Field work, 2) Geochronology, 3) Geochemistry, 4) Thin section and petrography. Errors and miss interpretations can occur during all these stages and potentially influence the results and conclusions. This section will briefly discuss some of these errors.

**Fieldwork**

During field work, several sources of error can occur. The main source for errors during the field work is wrong interpretation based on the observed geology. Observing and interpreting the geology in an area could be challenging, especially if one does not have a lot of experience. Wrong interpretations and missing critical data could influence the later interpretations done at campus, hence preparation before fieldwork is essential. To make good notes, drawings and navigating effectively in the field are critical and can affect the quality of later interpretations. In addition, taking high-quality photos and connecting the notes, photos, and sample locations to a coordinate system is essential. The GPS should be accurate enough so that further geologists can seek out the locations for further studies. The accuracy of the geology compass and appropriate maps should be investigated before going out in the field. Organizing the obtained field data in a good way by using location number, sample numbers, and coordinates is crucial. A summarized field report should be

written during and/or after the fieldwork. The weather, current mood and motivation should be sufficient so that human error can be reduced as much as possible. To bring and ingest enough water and food is also important so that the fieldworker can collect as much high-quality data as possible.

**Geochronology**

For the U-Th-Pb methodology, the sources for error can be associated with e.g., contamination, the chosen sample, instrumental errors, reference samples, data reduction, and the interpretation of the data.

It is essential to have a clean workspace during the preparation stage and clean the chosen sample. Contamination during lab work can result in $Pb_c$, which will cause discordance in the TW plot. Other causes for discordance are linked to age domain mixing, Pb loss, lack of secular equilibrium, and fractionation (*3.1.3*). These natural causes for discordance could be reduced by sufficient imaging of the chosen mineral by BSE and CL. For example, zircons can consist of several age domains and growth phases which could cause a variation in Pb concentrations in a single zircon grain. By mapping these zones, one could further analyze those specific zones one by one. One could also exclude damaged and metamict minerals by studying them in an optical and electron microscope. Fractionation can be corrected by doing several analyses and using correction constants or using elements that do not significantly fractionate, e.g., isotopes from the same element.

When doing geochronological analyses, one separate between, random uncertainties and systematic uncertainties. The accuracy represents the ability to obtain the correct age for a dated sample, while precision represents the ability to recreate an experiment. The accuracy may be hard to measure because the exact age of a rock is normally unknown when doing geochronology, while precision can be measured by doing the same analysis several times. Random uncertainties are random effects that occur during an analysis and can be improved by doing several analyses, e.g., the analytical uncertainties in isotope ratio mass spectrometry (Schoene, 2014). Systematic uncertainties are associated with systematic errors that cannot be fixed solely by doing several analyses. Example of systematic uncertainties associated with LA-ICP-MS are decay constants, age standards, amount of gas and laser output (Schoene, 2014). It is also important to mention that the data reduction should be conducted non-biased so that noise could be removed without affecting the actual real date. After the data reduction one have a data set that can be plotted in a e.g., TW plot using software. It is essential to have an interpreter who has knowledge about the software, experience with geochronology, and knows the potential causes for discordance.

**Geochemistry**

The geochemical analysis was done by an external laboratory, so the potentially analytically errors will not be discussed. Relevant errors are mainly linked to the interpretations of the geochemical data. The combinations of lack of knowledge, bad software, not specific enough hypothesis, and few samples can make it hard to discover systematic trends when interpreting geochemical data.

**Thin section and petrography**

It is important to mention that a thin section is only a small piece of a huge rock mass and only a 2D representation of a 3D rock. Thus, it is unlikely that one thin section can represent the large-scale regional geology and structures can be missed or look different in 2D compared with 3D. The interpretations of thin sections are highly subjective and is based on the knowledge and experience on the interpreter, hence this is a huge source for error during petrographic studies.

# 5 Results

## 5.1 Rock description and structural features

The study area shown in *Figure 41* was mapped carefully during two field seasons in 2020 and 2021. This chapter will first present the main lithologies present in the mapped area followed by an area-by-area description, including structural observations. From east to west, the study area has been split up into four subareas (subareas marked in *Figure 41*): 1) Area 1, layered quartz-rich schist as the main lithology with an abundance of concordant and discordant mafic sheets (yellow). 2) Area 2, Transition area. An increase in phyllosilicate minerals in the lithologies. Alternation between layered quartz-rich schists, psammitic schists, garnet mica schists, and garnet amphibolites (green). 3) Area 3, garnet mica schist with abundant felsic veins with reaction rim symmetry. Concordant mafic sheets and semi-concordant mafic sheets (sills) are also present. 4) Area 4, garnet mica schist with fewer felsic veins and reaction rim symmetry compared to area 3.

### 5.1.1 Rock descriptions

The studied area consists of a cm to meter-scale alternation of different lithologies, which is hard to illustrate using a 10:000 map. Systematic lithology variations are present; hence the mapped lithological units are composed of 7 main lithologies: Layered quartz-rich schist, garnet mica schist, garnet amphibolite, reaction rim, felsic vein, calcsilicate, and pegmatite. The lithology varies a bit throughout the study area, but the most representative rocks in the whole study area will be described.

Throughout the study area crenulation folding is often observed. When using the term "crenulation cleavage" it does not refer to a distinct crenulation cleavage showing the crenulation plane with new minerals. Rather the term crenulation cleavage refers a foliation defined by crests of crenulation folds. Only the garnet mica schists show indications of a real crenulation cleavage.

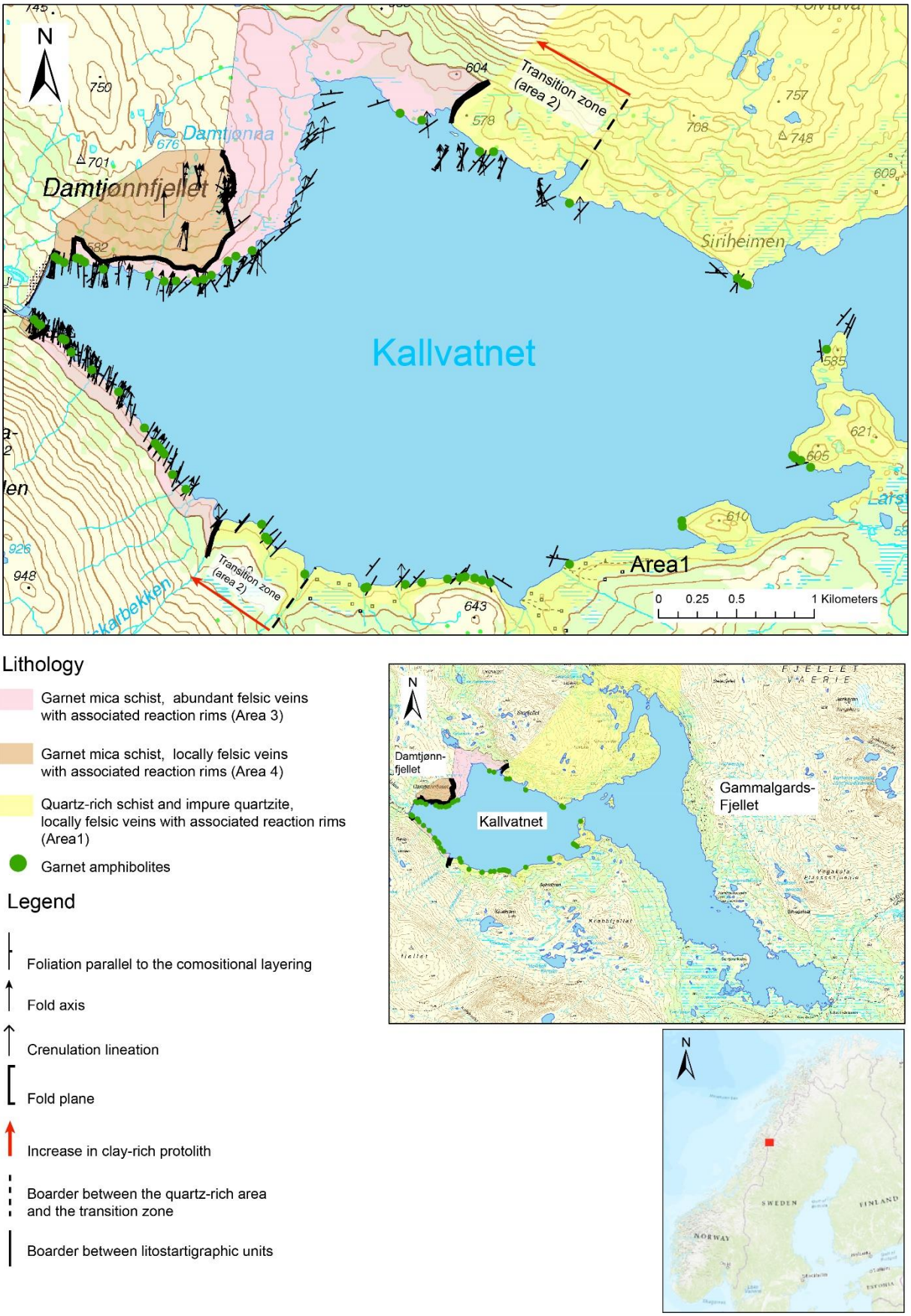


***Figure 41**: Field map of the main study area. Structural measurements and mapped lithologies. Coordinate system: WGS 1984 UTM Zone 33N.*

**Layered quartz-rich schist**

The layered quartz-rich schist is light grey and consists of approximately 65% grey to blue quartz, 20% black biotite, 10% white to yellow plagioclase, 5% white muscovite, 1% titanite, and 1% apatite. Accessory minerals like zoisite, zircon, rutile, and opaques are also present. The biotite content strongly controls the color of the quartzite. In most places biotite is present and makes the layered quartz-rich schist darker grey compared to a purer quartzite which appears lighter in color, see *Figure 42*. The rock is strongly folded foliated and concordant parallel to the compositional layering. The quartz-rich schist is finely laminated with mm to cm schist and silt layers, see *Figure 42*. Felsic veins were also observed in the quartz-rich area, but only locally.

In thin section (*Figure 43*) the rock is fine to medium-grained, hypidioblastic, equigranular and have a continuous cleavage parallel to the compositional layering. The cleavage is defined by the fine-grained subhedral to euhedral prismatic to tabular biotite. The fine to medium-grained, equant to more elongated, subhedral quartz-feldspar layers show a weakly developed shape preferred-orientation (SPO) parallel to the compositional layering. Undulatory extinction and polysynthetic twins are present in quartz and plagioclase, respectively. Saussuriterization in the plagioclase is visible.

***Figure 42**: Layered quartz-rich schist. To the left: Layered quartz-rich schist with mm to cm layering of a more schistose rock. Finger for scale. COOR: 66.23762° N, 014.89005° E. To the right: A purer quartzite adjacent to a garnet amphibolite layer. The north arrow is 10 cm. COOR: 66.22290° N, 014.83873° E.*

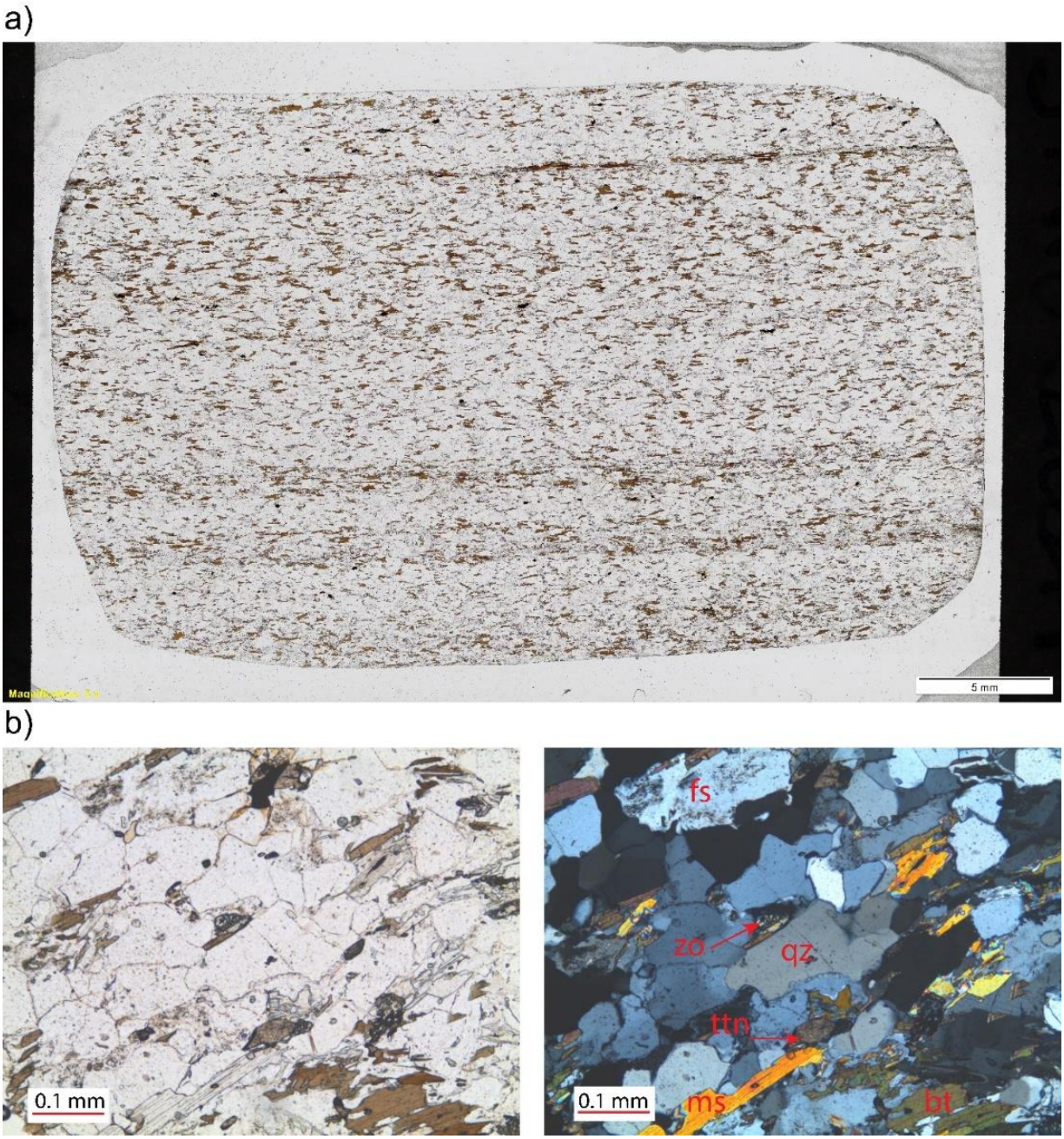


***Figure 43**: Thin section scan of a quartz-rich schist. A): Thin section scan in PPL (plane polarized light) showing the continuous E-W cleavage. B): Microphotographs of the same thin section in both PPL (left) and XPL (cross polarized light) (right).*

**Garnet mica schist**

The rock is medium grey, heterogeneous, dominantly equigranular, medium-grained with locally foliated pegmatite veins and, due to folding of the layering, -shows mostly a distinct crenulation cleavage. It contains approximately 40% grey to white quartz, 40% white muscovite, 5-10% red to pink garnet, 5-10% white to grey plagioclase, and some black biotite.

The white and grey quartz and white and yellow plagioclase form mm-thick veins and laminae in the schist. The light silver to greenish muscovite defines the distinct crenulation cleavage, which is especially visible in the mm to cm wide yellow to white pegmatite veins,

see *Figure 44.* The thin (generally < 1 mm) layering is defined by grey muscovite layers alternating with quartz and plagioclase layers. The black biotite appears as flakes, not as continuous foliae as the muscovite. The garnet is dark to purple and has approximately the same grain size as the rest of the minerals. The rock can also be coarse-grained with garnet up to 1 cm.

In thin section (*Figure 45*) the majority of the garnet mica schists shows one distinct crenulation cleavage (S2) and one spaced cleavage parallel to the compositional layering (S1). The spaced anastomosing to parallel folded cleavage (S1) consist of 30-60% volume percentage of cleavage domains with gradational transition between the cleavage domains and the microlithons. The spaced cleavage is defined by the preferred orientation of mica such as subhedral-euhedral prismatic biotite, muscovite and chlorite in the same direction as the compositional layering. Mica minerals also define the crenulation cleavage, they have a preferred orientation towards the axial planes. Plagioclase and quartz define the microlithons that show SPO for both the spaced- (S1) and crenulation cleavage (S2).

***Figure 44**: Garnet mica schist adjacent to the parking and dam. COOR: 66.23760° N, 014.77335° E. The north arrow is 10 cm long.*

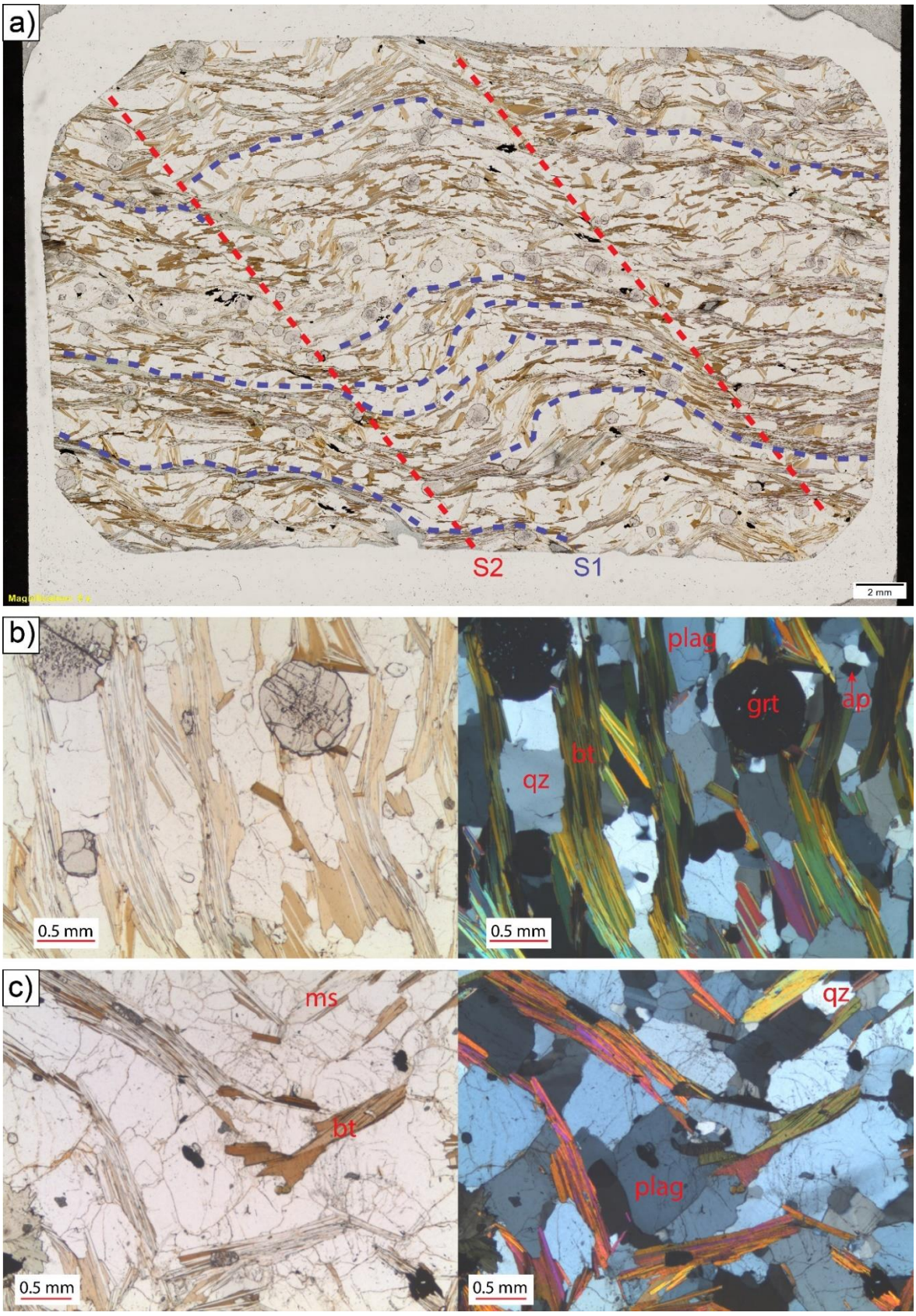


***Figure 45**: Thin section of a garnet mica schist (gmf2021-11C). A) Thin section scan of the garnet mica schist in PPL., grey to brown garnet, brown biotite, green chlorite and white plagioclase, quartz and muscovite. S1 cleavage (blue), S2 cleavage (red). B) Microphotograph of the same thin section as shown in "A)". PPL to the left and XPL to the right. C) Microphotograph of the distinct crenulation cleavage in the garnet mica schist. From thin section gmf2020-13.*

**Garnet amphibolite**

The rock is dark, with red to brown spots of garnet. The majority of the garnet amphibolite sheets in the study area have a mineral assemblage consisting of approximately 65-80% of green to weak blue hornblende, 0-5% brown biotite, 15-25% white plagioclase and 0-10% red to brown garnet. Accessory minerals like titanite, zoisite, chlorite, and zircon are present. The amphibolites are between few mm's up to approximately 25 m thick. The black amphibole is dominantly fine-grained but can become coarser crystalline, especially in more massive garnet amphibolite sheets that are more gabbroic and consist of a higher concentration of plagioclase. The white to yellow plagioclase occurs as fine-grained crenulated laminae in strongly foliated layers (see *Figure 46a*) and as coarser grains with prismatic shape in massive and weakly foliated layers. The garnet varies from red to brown, euhedral to anhedral, mm to up to 2 cm in diameter throughout the study area. The amount of garnet in the amphibolites varies greatly and seems to be particularly high at the contact with the host rock or pegmatite veins. The black to green biotite is fine to coarse-grained. In the more biotite-rich garnet amphibolite sheets, the biotite (in addition to the hbl) clearly defines the foliation. Throughout the study area, two layers were often observed between the garnet amphibolite and the garnet mica schist (see *Figure 46b*). The first layer consists of a concentration of coarse green biotite and garnet, and the second layer of a light grey rim (reaction rim, see *page 70*). Both concordant folded mafic sheets *Figure 46c* and discordant mafic sheets *Figure 46d* were observed at Kallvatent and had similar mineralogy. The discordant mafic sheets cross-cuts folds and foliations in the host rock and were not associated with reaction rims.

In thin section, the garnet amphibolites are fine to medium-grained, equigranular (porphyroblastic when garnet appears) and hypidioblastic to xenoblastic. One amphibolite shows rough anastomosing spaced cleavage parallel to the compositional layering with 60% cleavage domains. The spaced cleavage seems to represent relicts of isoclinal to tight F1 folds (*Figure 47*). The spaced cleavage domain is defined by oriented fine-grained, subhedral-euhedral, prismatic to diamond shaped hornblende. The fined-grained, anhedral-subhedral, tabular-elongated plagioclase (microlithon) show a SPO in the same direction. The weak crenulation cleavage is defined by preferred orientation of hornblende, parallel to the axial planes of the crenulation folds (F2) of the compositional layers. Another amphibolite shows a continuous cleavage parallel to the compositional layering and another one shows no visible foliation. The continuous cleavage is defined by the preferred orientation of fine to medium-grained, subhedral-euhedral, prismatic to diamond shaped hornblende and fine-grained, anhedral-subhedral tabular to elongated plagioclase. The plagioclase shows polysynthetic twins, and locally, saussuritization and chloriterization are present.

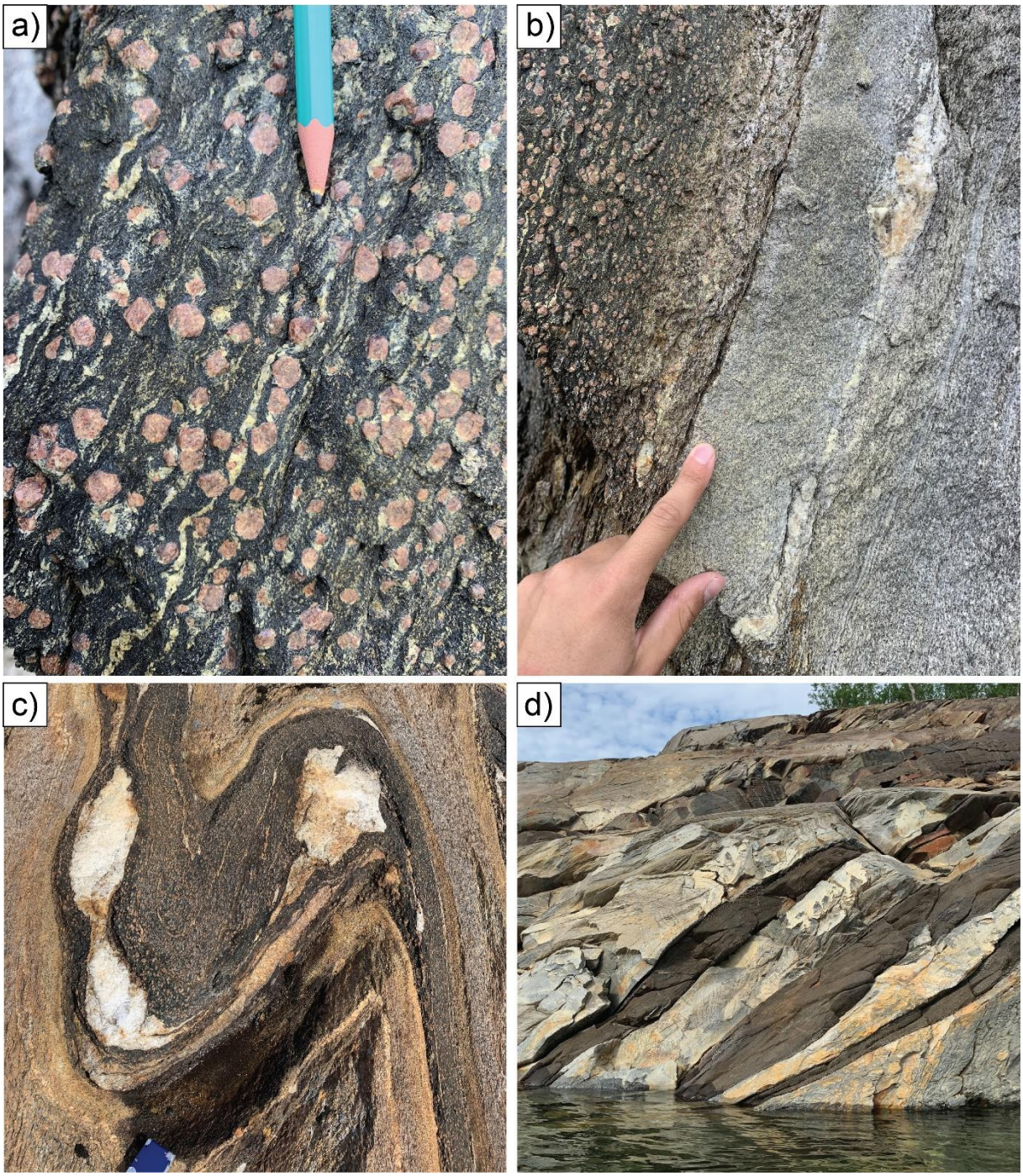


***Figure 46**: A) Garnet amphibolite with distinct crenulation folding visible in the plagioclase. B) Reaction rim (10 cm thick) layer and a concentration of green biotite between the garnet amphibolite layer and the host rock, garnet mica schist. COOR: 66.23755° N, 014.77368° E. C) Folded concordant mafic sheet. COOR: 66.24115° N 14.78002° E D) Discordant mafic sheets which cross cuts folds and foliation. COOR: 66.22969° N, 014.88120° E.*

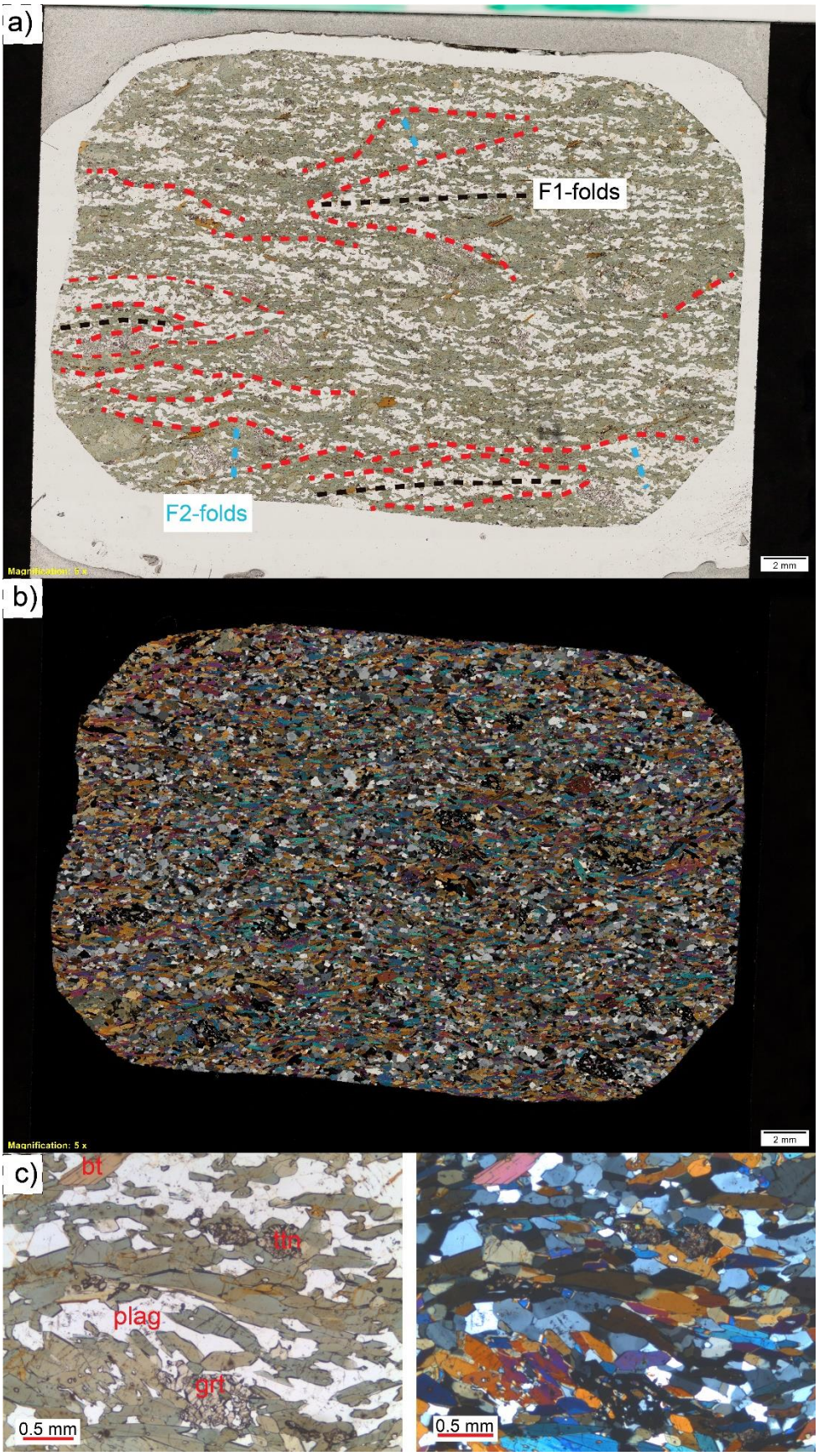


***Figure 47**: Thin section scan of a garnet amphibolite. A) Thin section scan of a garnet amphibolite (gmf2021-03) in PPL. Green hornblende, grey to brown garnet, brown biotite and white plagioclase. F1 fold axial traces (black), F2 fold axial traces (blue). B) Thin section scan of the same thin section in XPL. C) Microphotograph of the thin section. PPL to the left and XPL to the right.*

**Felsic veins with fine-grained, light grey rims**

One interesting feature in the study area is that felsic veins exclusively lay in the middle of fine-grained, light grey rims. *Figure 48a and b* illustrate typical field relationships. The fine-grained, light grey rims occur symmetrically on both sides of the veins with a sharp contact to the host garnet mica schist. The felsic veins in the center of the fine-grained, light grey rims also occur without a light vein within, but if one followed the rim layer for some distance, one could again find the associated vein in the middle, terminating prior to the end of the rim. The thickness of the fine-grained, light grey rims varies according to the thickness of the felsic veins. The thickness of 51 random veins were measured and compared with the thickness of the rims, *Figure 50* shows a regression analysis between the measured vein width and the total width of the vein and the rim symmetry. This analysis resulted in an $R^2$ of 0.7821, indicating statistically significant relationship between the vein and the rim thickness. These fine-grained, light grey rims are hereinafter described as reaction rims.

The felsic veins are leucocratic and occur as mm to dm thick layers, locally as lenses with corona texture and have a tonalitic composition (*Figure 49*). The mineral assemblage varies, but generally, the rock has a white, yellow to brown greenish, fine to a medium-grained matrix consisting of 15-55% white to grey quartz and 15-60% yellow to white plagioclase. Locally the matrix appears afinitic. The matrix often consists of 0-25% hornblende, 0-30% biotite (no biotite is present where hornblende is present), 0-1% chlorite, 0-1% zircon and 0-1% titanite, 3-40% garnet, and 0-20% zoisite/clinozoisite porphyroblasts. Accessory minerals like muscovite, rutile, ilmenite, apatite and calcite were also present. The porphyroblasts include black coarse to fine hornblende with lath and tabular shapes, brown fine to medium-grained biotite with prismatic to tabular shapes, pink to brown coarse to fine-grained garnet, and white coarse to medium-grained needle-shaped zoisite, see *Figure 49c*.

The different concentrations and characteristics of the hornblende, biotite, garnet, and matrix make up a zonation pattern which is very common in these veins. Figure 49a show a typically folded vein with this zonation pattern. The hornblende clearly shows foliation, and the abundance of the hornblende varies significantly across the folded vein. The pink to brown garnet has a more even abundance than the hornblende which can be completely absent in some layers. The hornblende content seems to be higher at the edges. The thicker the veins are, the less amount and smaller the grain size of the porphyroblasts appear to be. *Figure 49b* shows one of the thicker veins observed in the study area.

The reaction rims are light to grey, have an equigranular character and are fine to medium-grained (*Figure 51*). The reaction rim layering often occurs in cm to dm scale and shows no distinct crenulation folding in the field. They contain weakly oriented, 20-35% black biotite, 5-35% purple to pink garnets, and 25-45% light minerals like white to grey quartz, 15-45% white to yellowish plagioclase, 0-10% muscovite, 0-5% green chlorite, and 0-1% black ilmenite. Accessory minerals like zoisite, rutile, apatite, and titanite can be present. Garnet-rich reaction rims contain hornblende and not biotite. Compared to the surrounding garnet mica schist, the reaction rims are more resistant to weathering, resulting in more prominent layers that stick out, shown in *Figure 51c*.

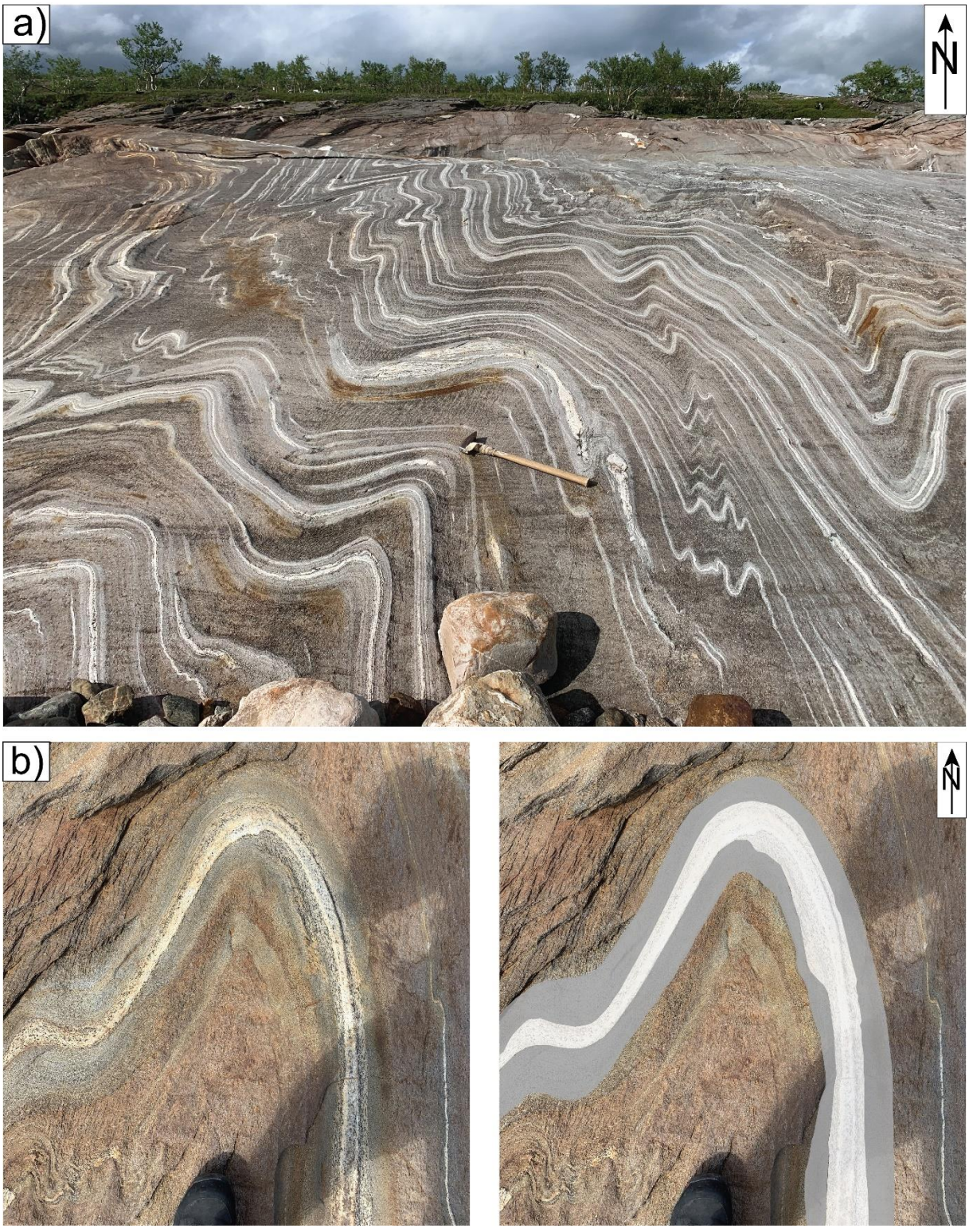


***Figure 48**: A) Field photo of an area with a high concentration of felsic veins with associated reaction rims. COOR: 66.23964° N, 014.79445° E. B) Close up picture of a felsic vein with reaction rims in the garnet mica schist. Adjacent to the marked vein one can see reaction rim with no vein, but if one follows the reaction rim one will eventually encounter a felsic vein. COOR: 66.24028° N, 014.78579° E.*

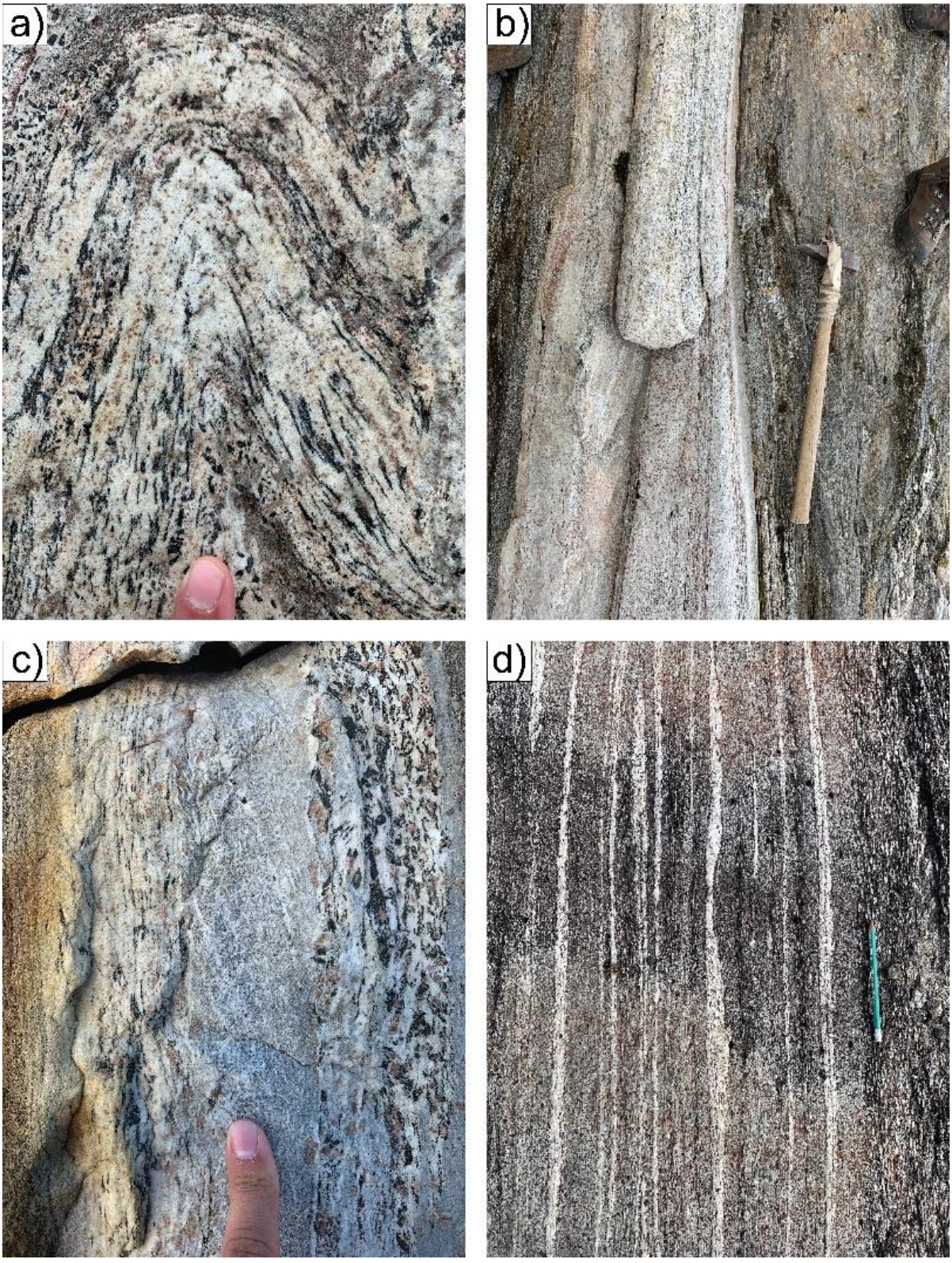


***Figure 49**: Different types of felsic veins. A) Felsic vein with several zones with different concentration of garnet and hornblende. COOR: 66.23543° N, 014.78159° E. B) A thicker felsic vein observed (sample gmf2021-6AB). COOR: 66.235791° N, 014.78038° E. C) Zoisite rich core in a felsic vein. COOR: 66.240261° N, 014.78773° E. D) Several typical felsic veins with reaction rims in between them. The garnet mica schist is visible to the right in the photo. COOR: 66.23696° N, 14.77882° E.*

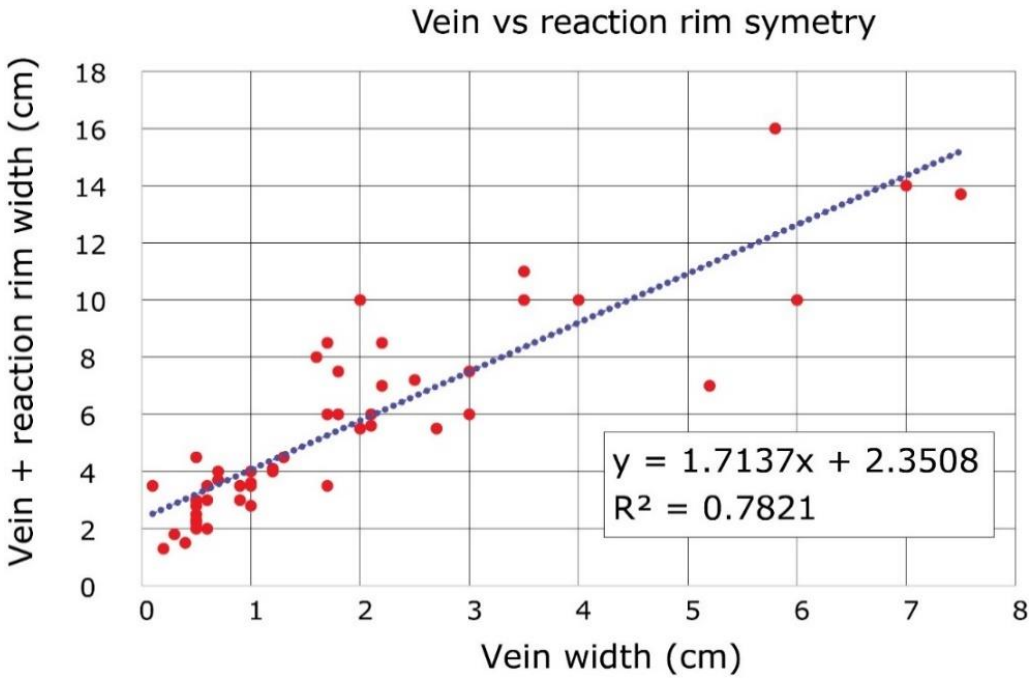


***Figure 50**: Regression analysis of the measured vein width and the total width (both vein and reaction rim symmetry).*


***Figure 51**: A) and B) Hand specimen of the reaction rim C) More resistant reaction rims, resulting in more prominent layers that sticks out more than the adjacent garnet mica schist. COOR: 66.23687° N, 14.7777° E. D) Reaction rim associated with a garnet amphibolite. COOR: 66.237519° N, 14.77426° E.*

The variation in mineralogy described above for the felsic veins, reaction rims and garnet mica schists have been studied in several thin section and is presented in *Figure 52* and by quantitative analyses using SEM and the Mineralogic software *(Figure 55).*

In thin section, the felsic veins are fine to medium-grained (only coarse hornblende has been identified), zoned, hypidioblastic and can have subhedral to euhedral garnet, zoisite, biotite and hornblende porphyroblasts. Foliations parallel to the compositional layering (S1) and hints of crenulation cleavage (S2) is present.

The thinnest veins have a spaced smooth, rough to wriggly spaced cleavage parallel to the compositional layering defined by oriented biotite, hornblende, zoisite and chlorite grains. The cleavage domains are parallel to anastomosing and make up 2-40% of the volume percentage. The transition from the cleavage domain to the microlithons (quartz and plagioclase) is gradational and the quartz and plagioclase show grain boundary migration (*Figure 54a*), some thin sections show preferred elongation of the microlithons. Locally, crenulation folding is present and is defined by the buckling of the foliation parallel to the compositional layering. The minerals in the crest of the crenulation folds define the weak crenulation cleavage (S2). (*Figure 53a*).

The thicker felsic veins have less distinct foliation. The central part of such a thick vein, show no foliation, but the garnet seems to have grown in preferred planes parallel to the compositional layering. Grain boundary migration is shown in the quartz and plagioclase, and the minerals are elongated in the same direction as the garnet preferred growth. The outer part of the thicker felsic vein shows wriggly parallel spaced cleavage and is defined by subhedral-euhedral, prismatic to tabular zoisite, garnet and biotite grains (ca. 3% of the thin section consist of cleavage domains). The microlithons, quartz and plagioclase show grain boundary migration and interlocking magmatic texture (*Figure 54b*), in addition myrmecitic texture is also present (*Figure 54*g and h).

In thin section, the reaction rims are fine to medium-grained, hypidioblastic, show a distinct foliation parallel to the compositional layering and weak crenulation cleavage. The reaction rims can have subhedral to euhedral garnet, biotite and hornblende porphyroblasts.

The majority of the reaction rims show a folded, parallel to anastomosing spaced cleavage and a hint of cross-cutting crenulation cleavage related to folding of the layering. The spaced cleavage is parallel to the compositional layering and is defined by subhedral to euhedral muscovite, biotite and chlorite. These rocks are composed of ca. 25-40% cleavage domains, quartz and plagioclase, the microlithons show SPO parallel to the compositional layering (*Figure 54*c and d). The weak crenulation cleavage is defined by mica minerals which have obtained a preferred orientation parallel to the fold axial planes of the crenulation folds (*Figure 53a*). Other reaction rims show a continues cleavage parallel to the compositional layering, defined by subhedral to euhedral biotite, chlorite and elongated quartz and plagioclase (*Figure 53b*). One of the reaction rims show a wavy, anastomosing spaced cleavage parallel to the compositional layering. The spaced cleavage is defined by subhedral to euhedral hornblende and the microlithons, quartz and plagioclase show grain boundary migration (*Figure 54e* and *f*).

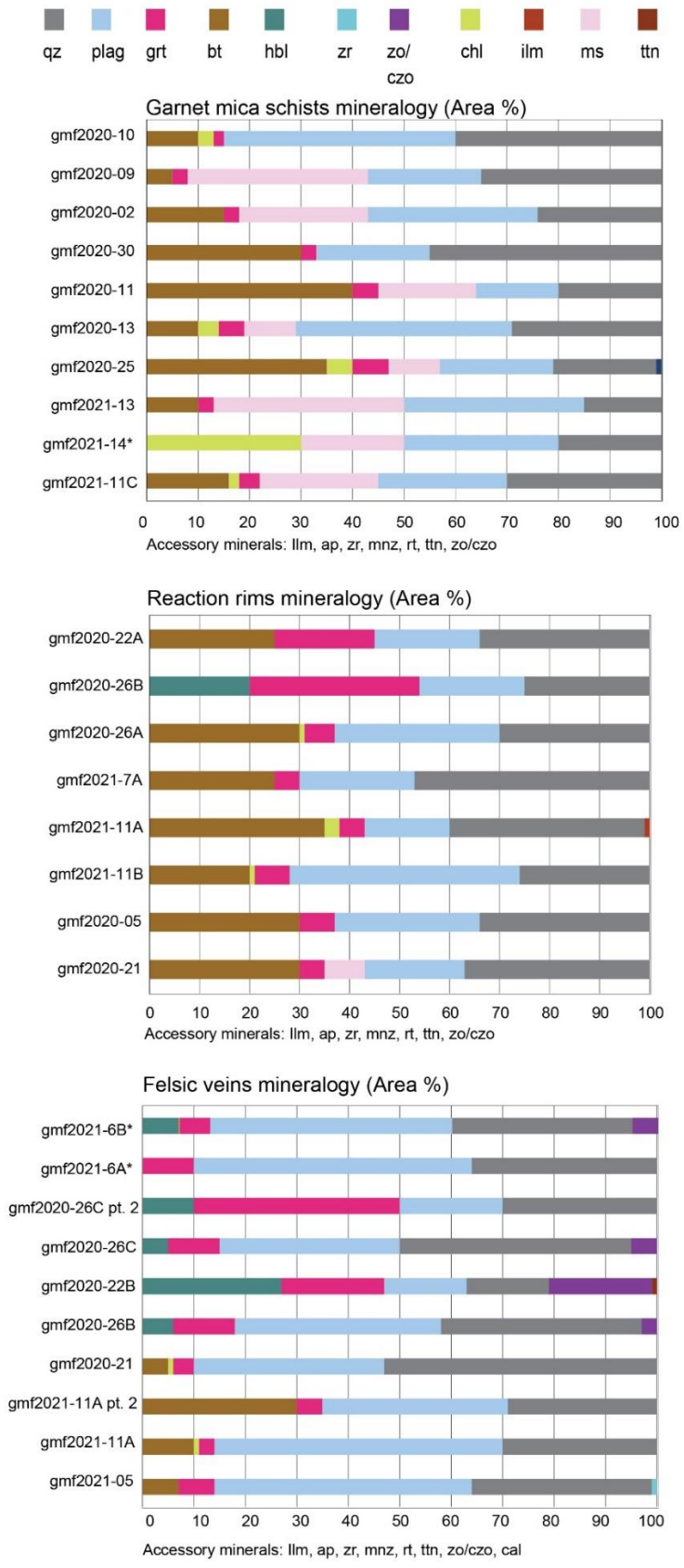


***Figure 52**: Optical estimated modal mineralogy diagram for the garnet mica schists, reaction rims and felsic veins. The main phases are presented in the diagram and normalized to 100%. Two of the thin sections have been split into two parts because of the zonation. *Thicker veins. **no garnet mica schist.*

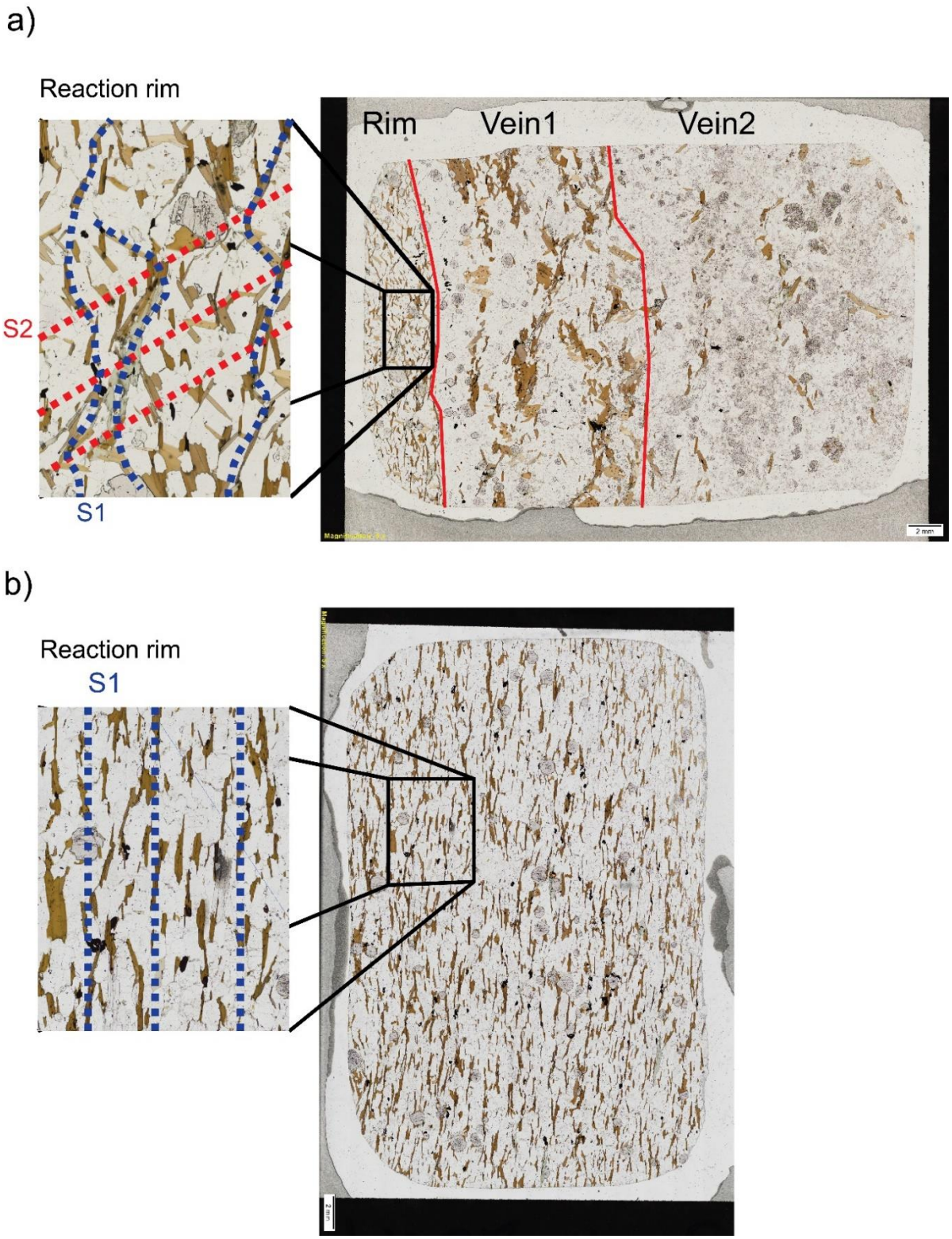


***Figure 53**: A) Thin section scan (PPL) across a vein with reaction rim. The weak crenulation cleavage (S2) is visible in the reaction rim, some crenulation is shown in the mica-rich zone (vein1) in the felsic vein. B) Thin section scan of a reaction rim showing continuous cleavage.*

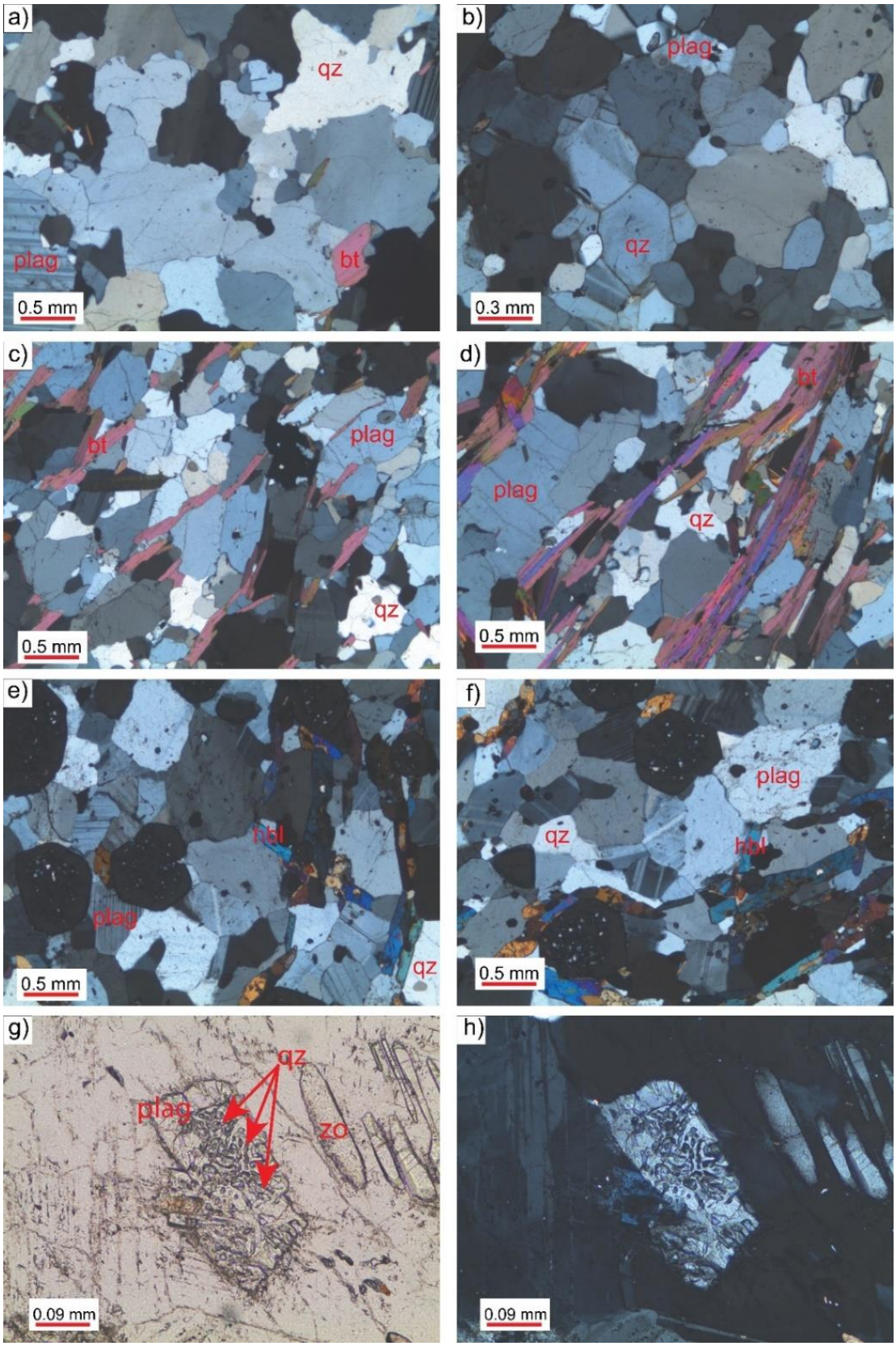


***Figure 54**: Microphotograph of felsic veins and reaction rims. A) Grain boundary migration in the typical thin vein (gmf2020-21). B) Grain boundary migration in a thicker felsic vein (gmf2021-06B). C) and D) Developed SPO in the microlithons (plag and qz) in a typical reaction rim with foliated biotite (gmf2020-21). E) and F) Reaction rim with hornblende showing grain boundary migration texture in the quartz and plagioclase (gmf2020-26C). G) and H) Myrmekitic texture in a felsic vein (gmf2021-6A).*

Automated quantitative mineralogy was conducted using effective energy-dispersive X-ray spectroscopy (EDS) analysis with a scanning electron microscope (SEM). The software Zeiss Mineralogic was used to process and classify the data. The automated quantitative mineralogy was used to confirm the optical mineralogy and to investigate systematic chemical variations such as zonation in garnet.

The quantitative mineralogical analysis was done for several thin sections (see *Appendix D*). It confirms the optical mineralogy estimation (*Figure 55*). The main differences between the reaction rims and the garnet mica schists are the lack of muscovite in the reaction rims. Instead, the reaction rims have a higher concentration of plagioclase.

In addition, three detailed EDS maps of garnets were done to detect possible compositional zoning in garnets. *Figure 56* shows two garnets, one in a garnet mica schist (gmf2021-11C,) and one in a reaction rim (gmf2021-11B). Figure 56*a* and *c* show the EDS-maps and *Figure 56b* and *d* show the belonging BSE-Images. The garnet mica schist (*Figure 56a*) shows a garnet in which the Mn component decreases from the center towards the rim, with a simultaneous increase in Ca component towards the rim which consist of almost pure almandine (Fe-component). The garnet in the reaction rim (*Figure 56b*) show a homogenous concentration of Mn, Ca and Fe until the rim which has a higher concentration of Fe (almandine).

*Figure 57* shows a detailed EDS-map of a garnet from another garnet mica schist (gmf2020-25). This garnet shows weak oscillatory zonation with mainly three different zones. 1) The innermost zone is dominantly consisting of Mn and Fe. 2) The second zone consist of ca. the same Fe component, but Mn has been replaced by Ca. 3) The outermost zone, have a higher concentration of Ca compared with zone 2, some place pure Ca. Mica wraps around garnet indicating that the porphyroblast has grown before or synchronous with the deformation.

*Figure 58* shows a thin section scan of a reaction rim (gmf2021-11B) and a belonging EDS map. The reaction rim shows a fracture filled with discordant albite, muscovite and chlorite, indicating a retrogression event accompanied by fluid propagation.

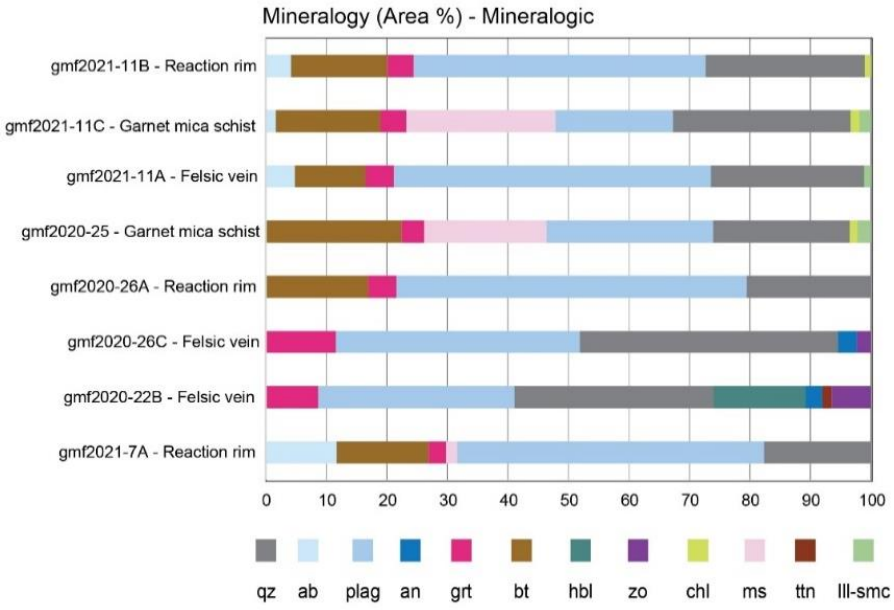


***Figure 55**: Quantitative estimates of the mineralogy using Mineralogic. Minerals > 1% (Area) are normalized and plotted in the diagram.*

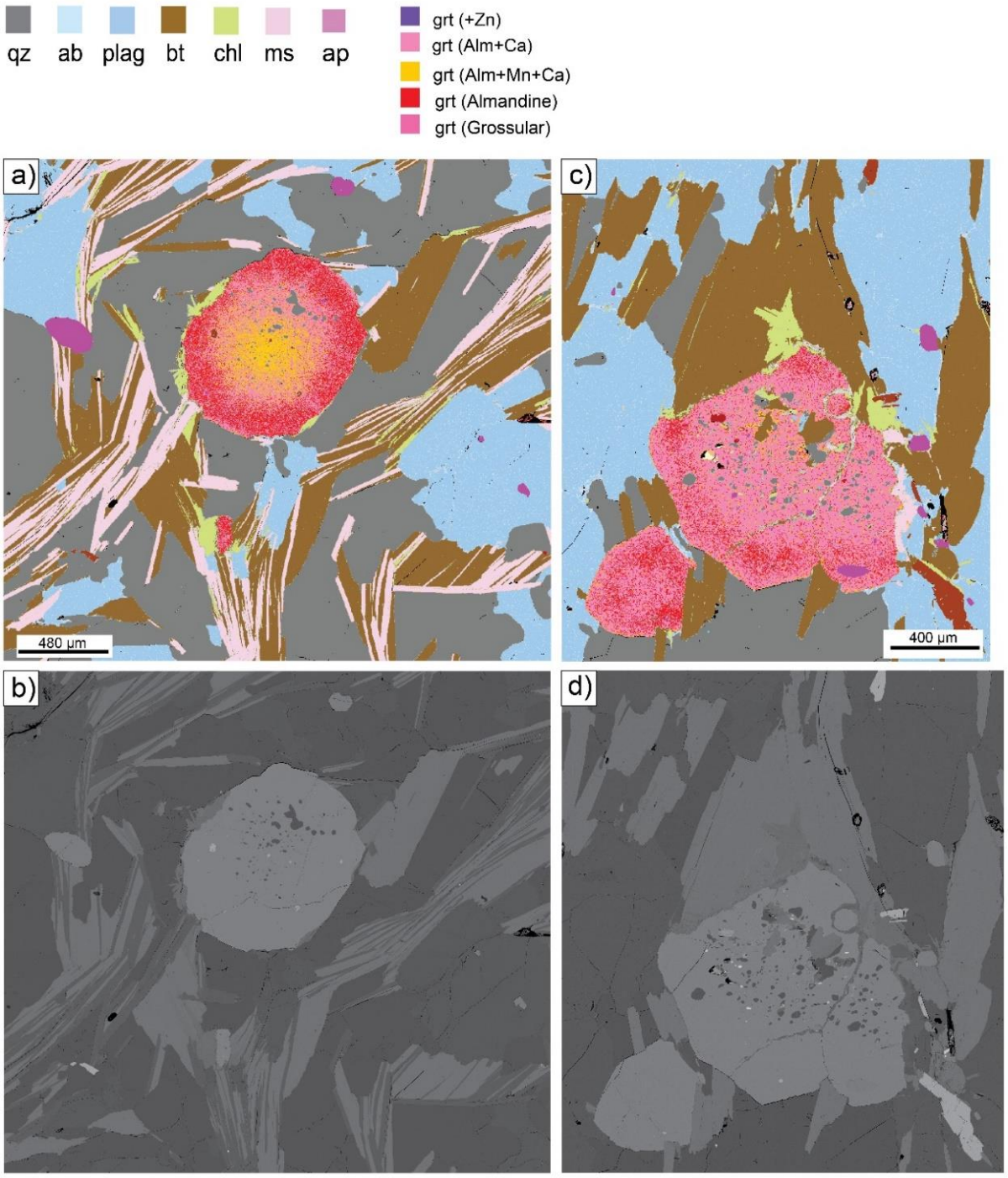


***Figure 56**: Detailed EDS-scan of garnets in a garnet mica schist and a reaction rim. A) Detailed EDS-scan of a zoned garnet in a garnet mica schist (gmf2021-11C). B) BSE-image of the same scan shown in A). C) Detailed EDS-scan of a zoned garnet in a reaction rim (gmf2021-11B). D) BSE-image of the same scan shown in C).*

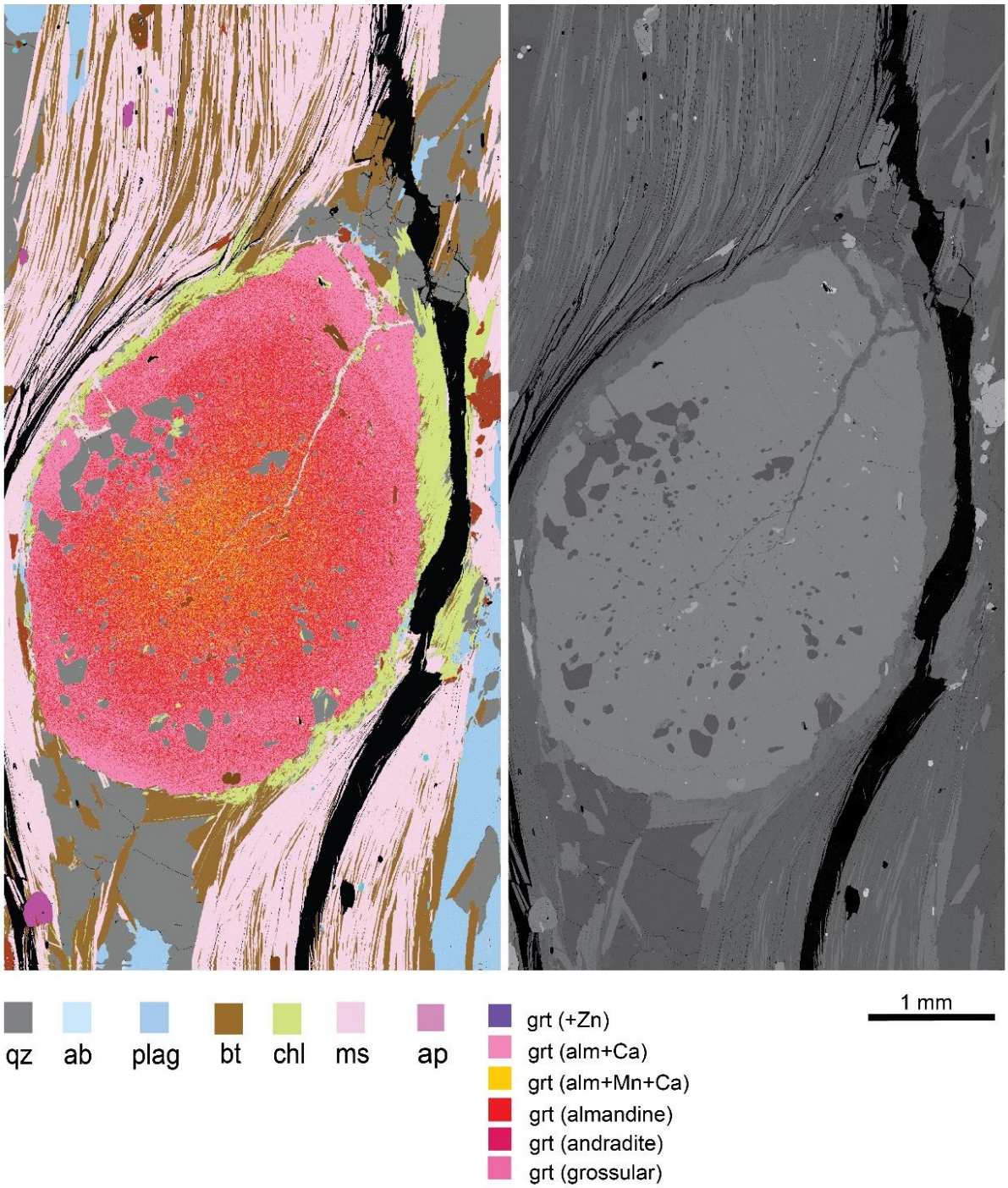


***Figure 57**: Detailed EDS-scan and BSE-image of garnet in a garnet mica schist (sample gmf2020-25).*

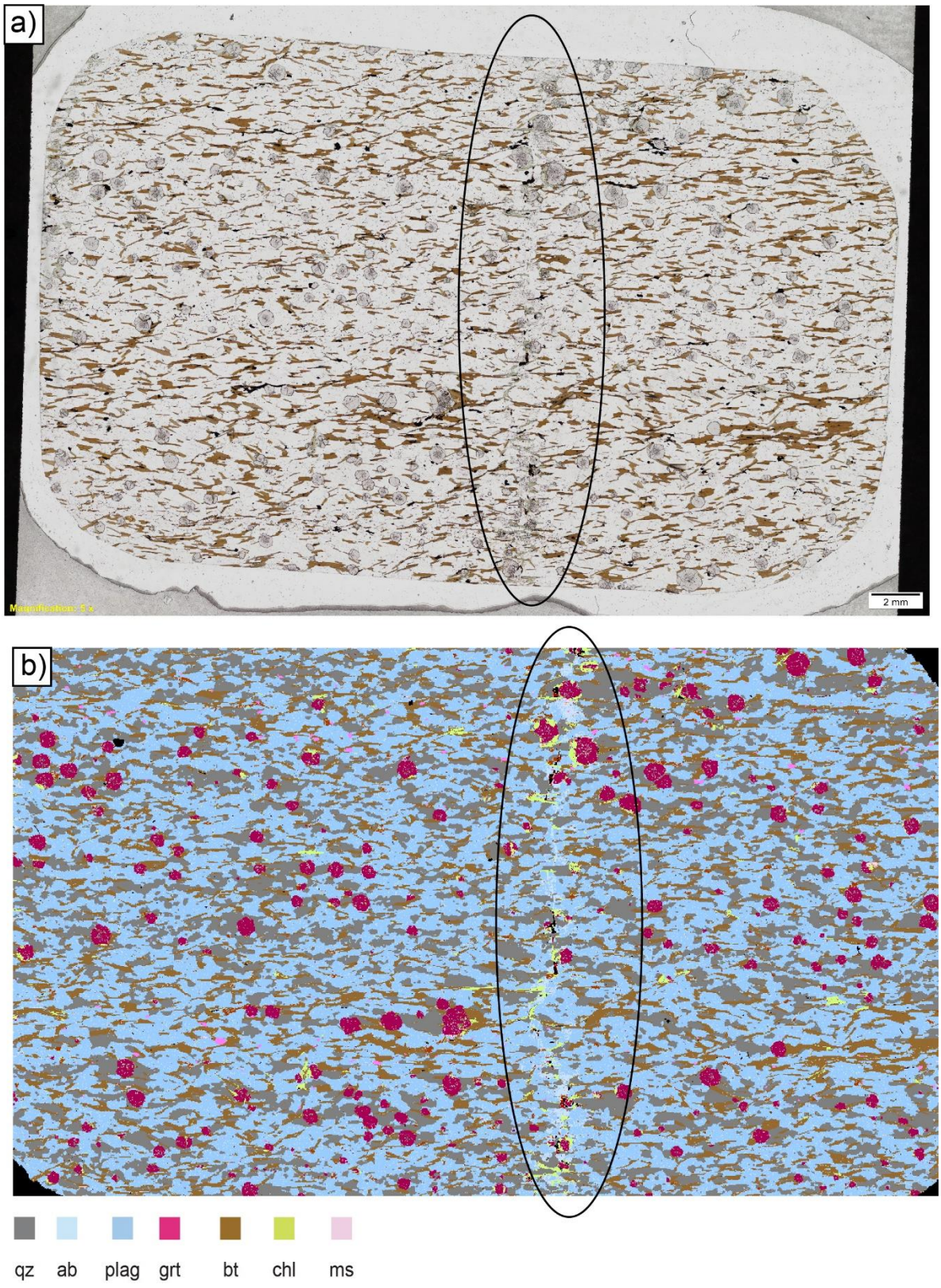


***Figure 58**: A) Thin section scan of a reaction rim (gmf2021-11B) (PPL). B) EDS scan of the thin section. A fracture filled with discordant muscovite, albite and chlorite is marked.*

**Calcsilicate layers**

Calcsilicate layers with green and brown matrix were observed in the study area, and they were often hard to differentiate from the felsic veins in the field. Weathering holes were observed in these layers. The calcsilicates are typically zoned, but the main mineral assemblage is zoisite (30-55%), quartz (35-50%) and hornblende (0-10%). The zonation is mainly controlled by the concentration of porphyroblastic hornblende in the quartz and zoisite-rich matrix. The accessory minerals are zircon, skeletal titanite, and chlorite. *Figure 59* shows a lens-shaped vein with a green calcsilicate-rich core with a cm thick black hornblende band in the middle. Further out from the green core, the layers become richer in quartz and feldspar and consist of the typical zonation pattern with garnet and amphibole. Other associated white (plagioclase and quartz-rich) veins seem to cut and surround the calcsilicate vein.

In thin section (*Figure 60),* the fine-grained calcsilicate has three distinct zones in which the concentrations of quartz, zoisite and amphibole varies. The rock is fine-grained, porphyroblastic to equigranular and-, hypidioblastic. The hornblende-rich zone (outermost zone) shows continuous cleavage parallel to the compositional layering defined by oriented subhedral prismatic to tabular hornblende porphyroblastst, with developed SPO in the quartz and zoisite (*Figure 60*a1 and b). The hornblende-free areas show grain boundary migration texture in the equigranular quartz and zoisite matrix. Quartz layers parallel to the compositional layering are present (*Figure 60*a2 and c). The last innermost zone is similar to the latter sone, but have some oriented anhedral skeletal hornblende porphyroblasts, parallel to the compositional layering (*Figure 60*a1 and d).

***Figure 59****: Calcsilicate layers with zonation pattern. COOR: 66.24079° N, 014.80384° E.*

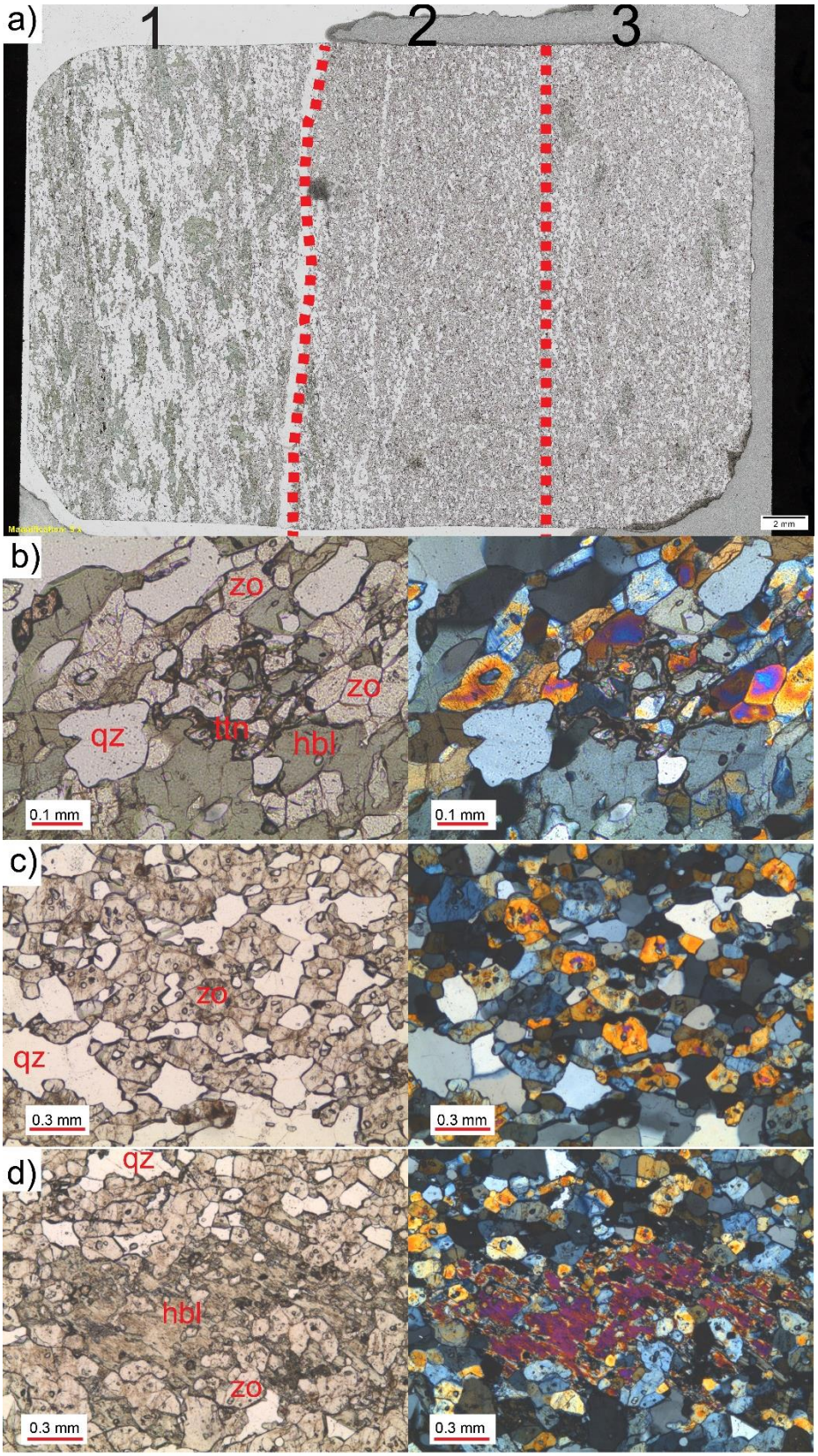


***Figure 60**: Thin section of a calcsilicate (gmf2021-02). A) Thin section scan of a zoned calcsilicate (PPL). Green hbl, grey zo and white qz. B) Microphotograph zone 1 (innermost zone), PPL and XPL (see scan in A). Hbl-rich zone with zo and skeletal ttn. C) Microphotograph zone 2 (middle zone), PPL and XPL. No hbl, only qz and zo. D) Microphotograph zone 3 (innermost zone) PPL and XPL. Mainly qz and zo, some skeletal hbl porphyroblasts.*

**Pegmatites and aplites**

Pegmatites and aplite dikes and veins are widespread in the study area. Their thickness varies from mm to cm veins to m thick dikes in outcrops. Some are concordant with the layer-parallel foliation (*Figure 61a*, b, and c), others cut the foliation (*Figure 61c*), and have been folded together with the layering. Generally, the pegmatite/aplite consists of white to grey quartz, white to yellow feldspar, and black to green biotite.

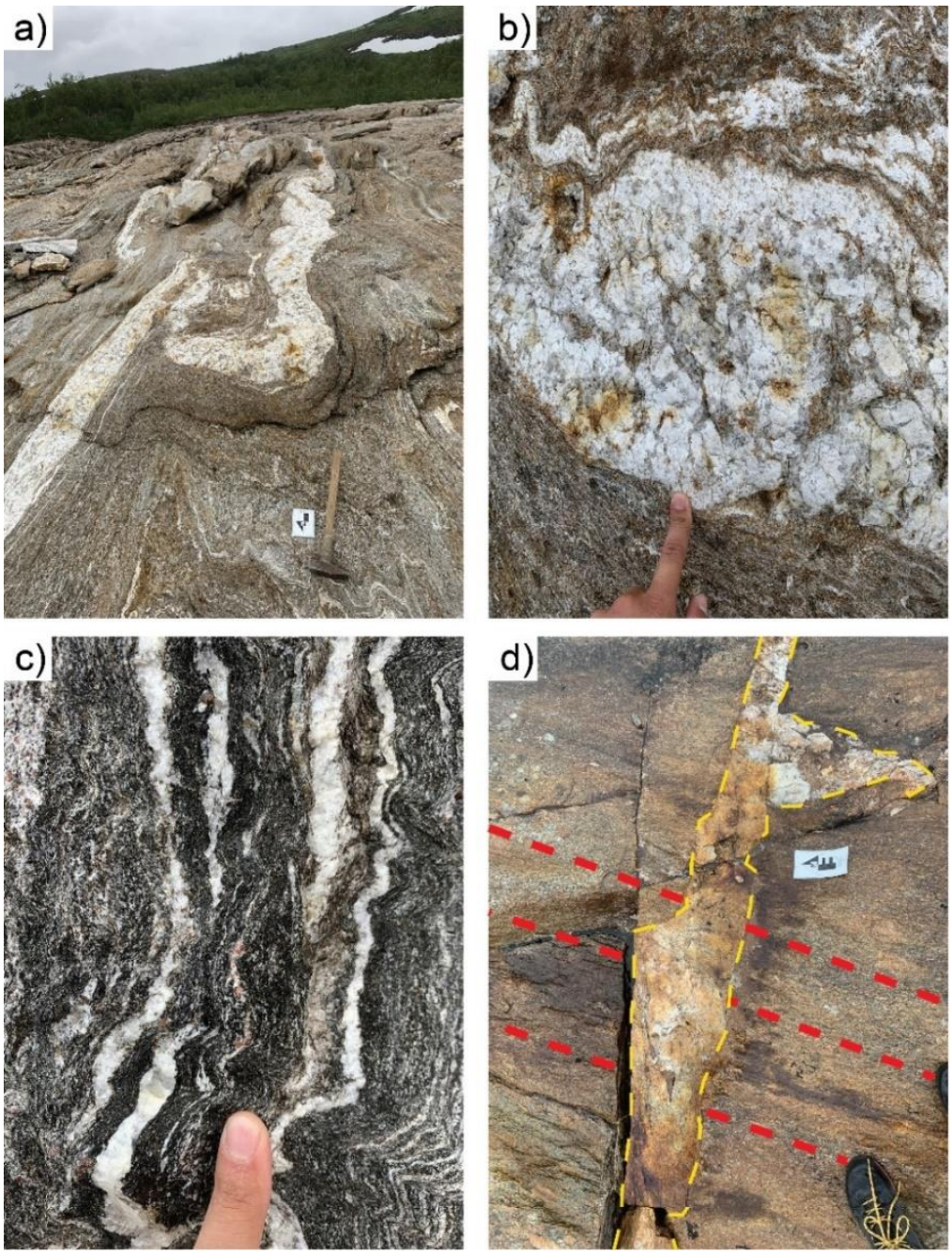


***Figure 61**: A) 30 cm thick folded pegmatite layer in garnet mica schist. COOR: 66.23574° N, 014.78214° E. B) Close picture of the same pegmatite layer shown in A. Yellow and white feldspar and white to grey quartz, crenulation folding is visible. COOR: 66.23574° N, 014.78214° E. C) mm to cm thick crenulated aplite layers in a deformed garnet amphibolite layer. COOR: 66.23735° N, 014.77510° E. D) Discordant dm-scale pegmatite layer. The red dashed lines illustrate the foliation in the garnet mica schist, which the pegmatite layers cut. COOR: 66.23467° N, 014.78312° E.*

### 5.1.2 Area 1 – quartz-rich area with concordant and discordant mafic sheets

**Rock variation description**

The main rocks in the eastern part of the study area are layered quartz-rich schist with discordant and concordant garnet amphibolite sheets. Some parts with pure massive quartzite and felsic veins are locally present.

The quartz-rich rocks are strongly foliated with mm to cm mica and garnet mica schist laminae. The northeastern part of the quartzite area is characterized by an approximately 30-meter-wide garnet amphibolite dike that cuts the quartz-rich schist. This massive dike has less garnet compared to the other garnet amphibolites in the area, and it contains xenoliths of quartzite (*Figure 62a and b)*. One another possible interpretation is that the quartz-rich schist is located above the erosional surface to the garnet amphibolite, so that it looks like a xenolith. Either way the garnet amphibolite cut the quartz-rich schist.

Along the strike towards south, an alternation between layered quartz-rich schist and discordant garnet amphibolite sheets was observed. *Figure 62c* shows a field photograph of this alternation of cm to meter-thick discordant mafic sheets and strongly folded and foliated quartzite.

The northern side of the quartz-rich area is characterized by the presence of impure layered quartzite, layered quartz-rich schist, foliated cm to m thick concordant garnet amphibolite sheets, and some felsic veins. One unique observation in this area is the concentration of felsic veins in a concordant garnet amphibolite. *Figure 62d* and *e* show the abundance of veins with porphyroblasts of garnet and hornblende. The veins have locally intruded the garnet amphibolite sheet (see *Appendic D* for thin section description of the post mafic vein).

The southern part of the quartz-rich area is characterized by the presence of layered and highly strained impure quartzites and garnet amphibolites that occurs as both layer-parallel and discordant sheets. Locally some more massive and purer quartzites are present (*Figure 63a*).

Westward, some parts with garnet mica schists and more psammitic schists are present, but overall, the quartz-rich schist is the dominant rock. Several 10-25 cm thick garnet mica schist layers are exposed when walking even more westward. The garnet amphibolite sheets are highly deformed (*Figure 63*b), and the layered quartz-rich schist has distinct benching (*Figure 63c and d*).

**Structural features**

**Tectonic foliations**

Fifteen measurements of the tectonic foliation parallel to the compositional layering were obtained in the quartz-rich area. The foliation planes in the eastern part of the area dip towards the northwest with a dip angle between 65° and 36° (*Figure 64*a). The dip direction varies slightly to more easterly and northerly directions, but the variation is minor.

**Folds and lineations**

Several folds of open to close folds (F2) were observed in the quartz-rich area. Since it was not easy to measure the geometrical data, hence only one fold axis was measured. (*Figure 64b*). *Figure 64c* shows a field photo of the fold type observed in the highly strained impure quartzite. These folds are open to close, asymmetrical, and moderately plunging. Overall, the fold axes seem to be plunging towards the north, but the one fold axis measured plunged towards the northwest (high uncertainty because of few measurements). The crenulation lineations plunged towards the north, the same direction as the F2 fold axes.

**Cross-cutting relations**

Several garnet amphibolite sheets cut the folds of the compositional layering in the quartz-rich area. *Figure 65a* and *b* show the highly strained and folded impure quartzite being cut by the discordant garnet amphibolite dikes. The discordant garnet amphibolite sheets were only observed in the eastern and southern part of the quartzite-rich area. Internal foliation in the discordant mafic sheets is visible in the field and in thin section (*Figure 66*).

**Kinematic indicators**

Few kinematic indicators were observed in this area. A small sinistral shear zone associated with a garnet amphibolite layer and a sinistral asymmetric aplitic lens (*Figure 67*) in a quartz-rich schist were observed.

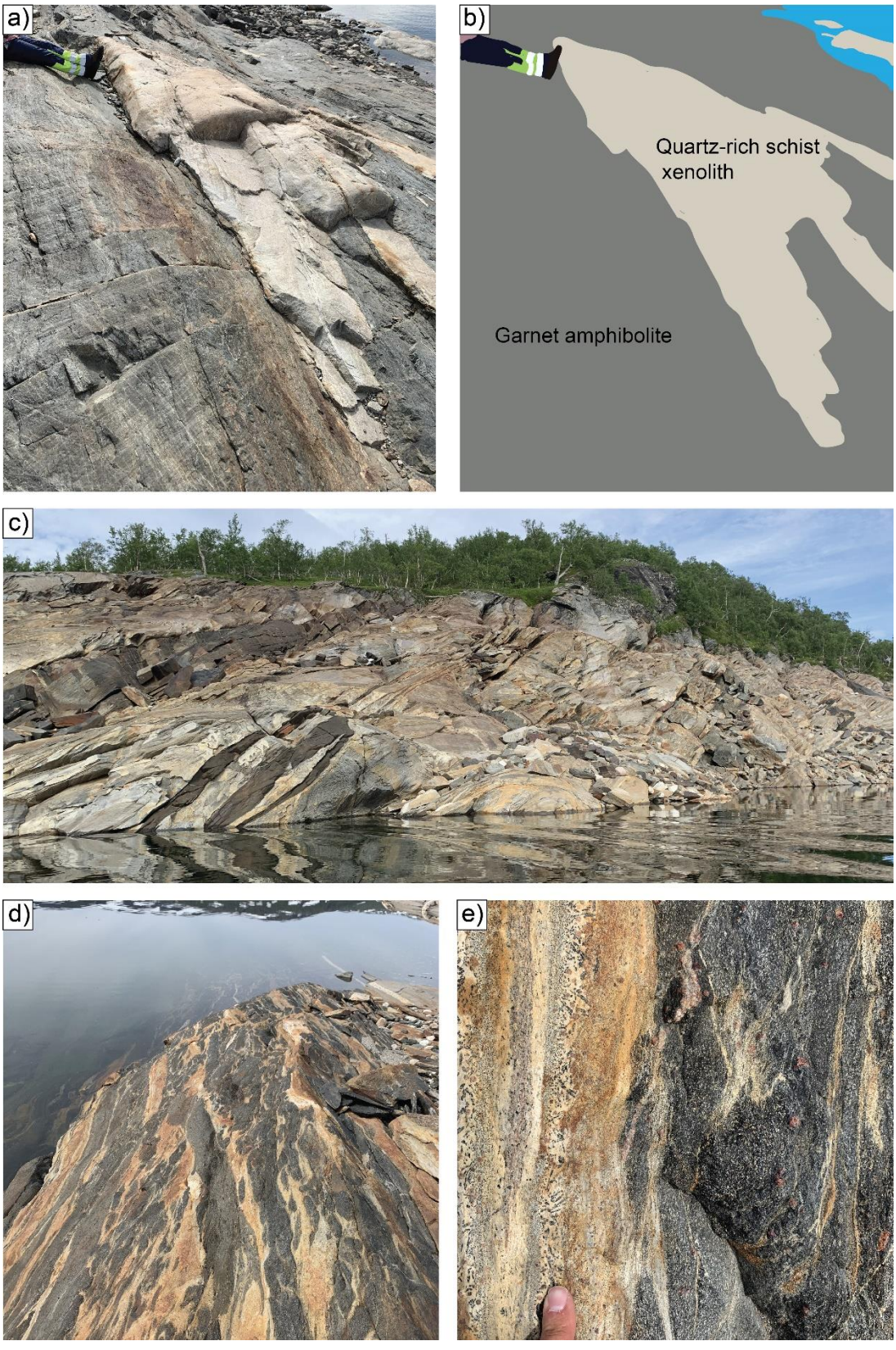


***Figure 62**: A) and B) Apparent quartzite xenolith in a 30 m massive discordant garnet amphibolite dike in the northeast part of the quartz-rich area. COOR: 66.23813° N, 014.99931° E. C) Characteristic alternation of discordant dark mafic sheets and white to yellow quartz-rich schist along the strike at the east part of the quartz-rich area. COOR: 66.22969° N, 014.88120° E. D and E) Locally concentrated garnet and amphibole-rich felsic veins in a foliated garnet amphibolite layer. COOR: 66.24406° N, 014.85232° E.*


***Figure 63**: A) Purer and more massive quartzite and a quartz dike. COOR: 66.22290° N, 014.83873° E. B) Deformed concordant garnet amphibolite layer in the quartz-rich schist COOR: 66.22290° N, 014.83873° E. C) and D) Alternation of concordant garnet amphibolite sheets and highly strained and layered quartz-rich schist with distinct benching. COOR: 66.22296° N, 014.83016° E.*

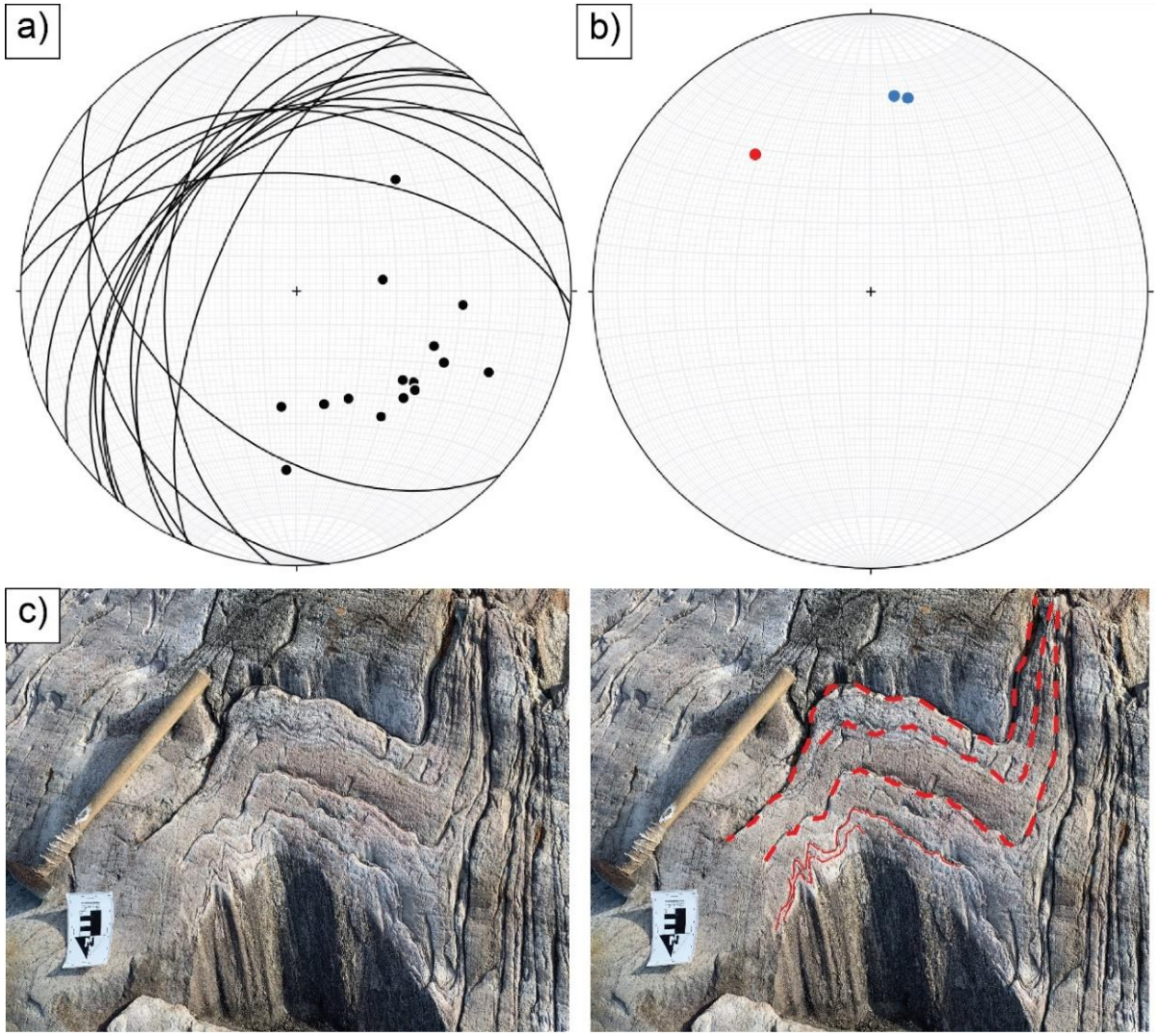


***Figure 64**: Foliation, folds and crenulation lineations measurements from the quartz-rich area. A) Tectonic foliation parallel to the compositional layering B) Fold axis (red dot) and crenulation lineation (blue dots) measurements from the quartz-rich area, plotted in a steronet C) Folds observed in the quartz-rich area. Open to closed, asymmetric, moderately plunging, and crenulated. COOR: 66.22290° N, 014.83873° E.*

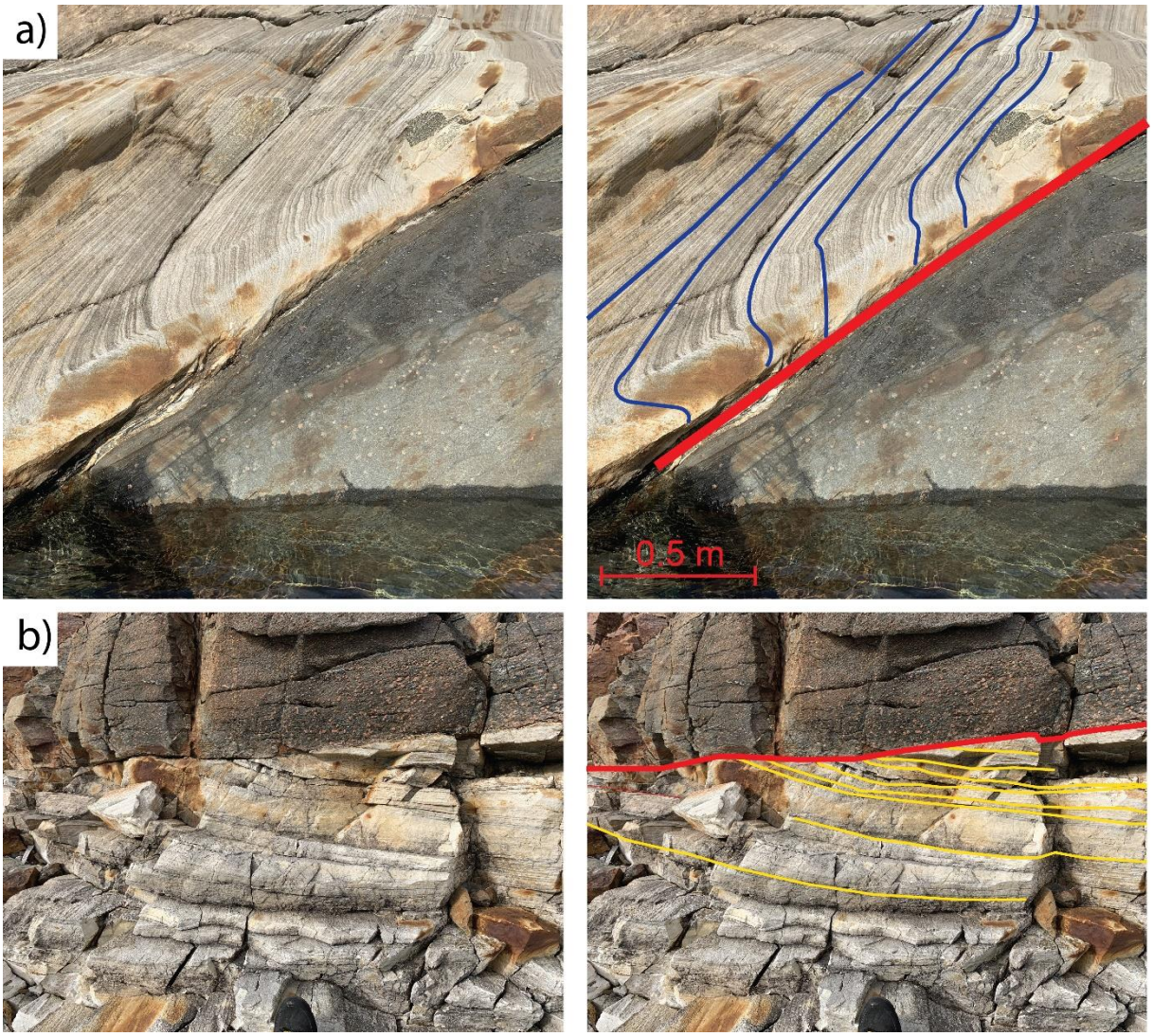


***Figure 65**: A) Garnet amphibolite layer cuts the fold flanks and the main foliation in the eastern part of quartz-rich area. COOR: 66.22962° N, 014.88271° E. B) Deformed garnet amphibolite cuts the main foliation in the southern part of the quartzite-rich area. COOR: 66.22412° N, 014.84873° E.*

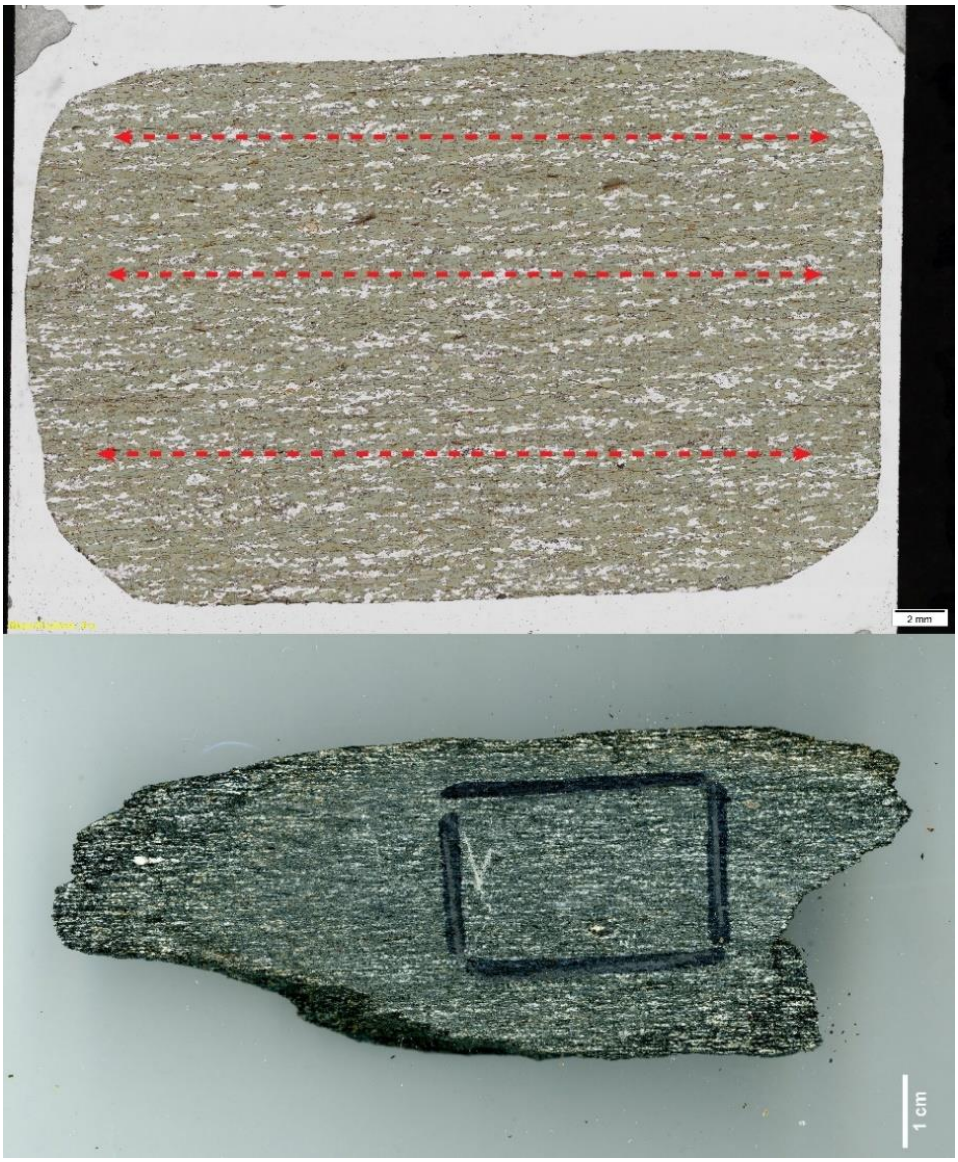


***Figure 66**: Thin section and the belonging rock slab of a discordant garnet amphibolite (garnet seen in field) which cuts the foliation and folds at Kallvatnet. Sample gmf2021-21. The discordant garnet amphibolite shows a distinct foliation both in the thin section and in the field.*

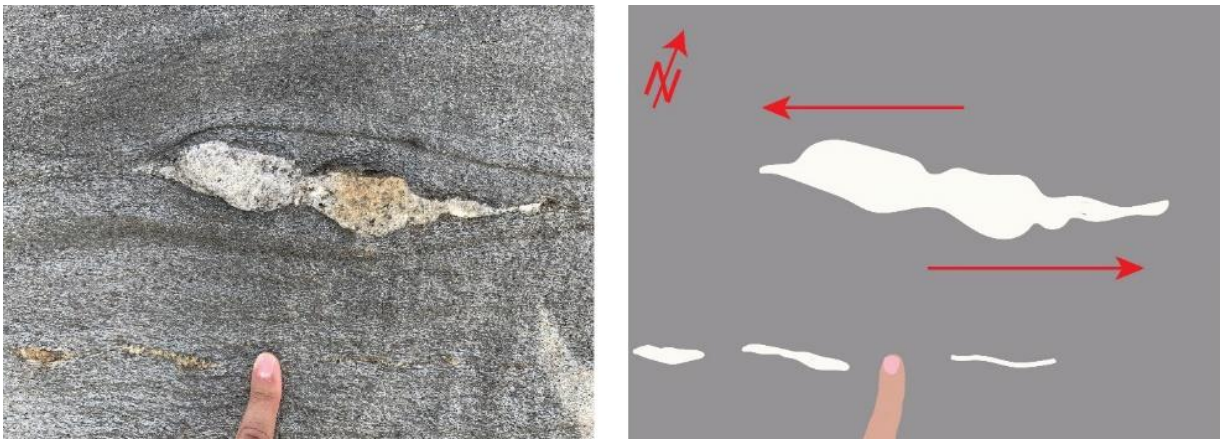


***Figure 67**: Sinistral felsic lens in a quartz-rich schist. COOR: 66.24412° N, 014.85180° E.*

### 5.1.3 Area 2 – Transition area

**Rock variation descriptions**

The transition area from proximal to more distal metasediments is characterized by more phyllosilicate-rich lithologies. The northern part of the transition area was mainly studied by boat with several stops on land to make field descriptions. The southern area was studied on foot with limited rock exposures. *Figure 68* shows the typical lithologies observed in the transition area with an alternation of quartzite/quartz-rich schist, psammitic schist, garnet mica schist, and concordant garnet amphibolite sheets.

The immediate change walking from the quartz-rich area into the transition area was the presence of more mica-rich metasediments with distinct cm-scale benching seen on *Figure 69a.* The rock is a feldspar-rich schist with red and pink garnet with sizes up to 1 cm. Some felsic veins and garnet amphibolite sheets concordant with the foliation parallel to the compositional layering were also present.

Further west, the characteristic alternation between the quartzite/quartz-rich schist, psammitic schist, garnet mica schist and garnet amphibolite layers begin (*Figure 68)*. Figure 69c shows an alternation sequence of a sandy to silt-rich psammitic schist and a coarse to medium-grained garnet mica schist. The different layers are cm-scale thick, discontinuous, and folded, and can represent the original bedding. Parts with impure layered quartzite are intercalated in the more mica-rich areas (*Figure 69b)*.

Parts with thicker garnet mica schists are observed further west. Several concordant garnet amphibolite sheets with distinct reaction rims are present (*Figure 70*), as well as some felsic veins. The succession is folded. The westernmost part of the transition area is characterized by a higher concentration of felsic veins with reaction rim symmetry and concordant garnet amphibolite sheets within in the garnet mica schist. Some alternation of schist and more psammitic/silty layers are still present.

**Structural features:**

**Foliations**

Fifteen measurements of foliation planes parallel to the compositional layering were taken (*Figure 71a*). The foliation is dipping with approximately 40° towards the northwest. The trend is similar as observed in the quartz-rich area, but with less variation.

**Folds and lineations**

Five fold axes and three fold axial planes were measured in the transition area (*Figure 71b*). The fold axes plunge between 15 and 39° towards the north. The fold axial planes have an approximately N-S strike with a dip between 65 and 79°. The single lineation measurement has approximately the same trend and plunge as the fold axis. The folds in this area are the same type as observed in the quartz-rich area, open to close, asymmetric, and moderately plunging. They are related to a crenulation folding. *Figure 71c* and *d* show folded layers of felsic veins, reaction rims and garnet mica schist. The crenulation folds is most evident in the garnet mica schist, the red rusty part.

***Figure 68**: Field photo of an outcrop in the transition area. Alternation of quartzite/quartz-rich schist (lightest colors), psammitic schist, garnet mica schist, and concordant garnet amphibolite sheets (darkest colors). COOR: 66.24607° N, 014.84253° E.*

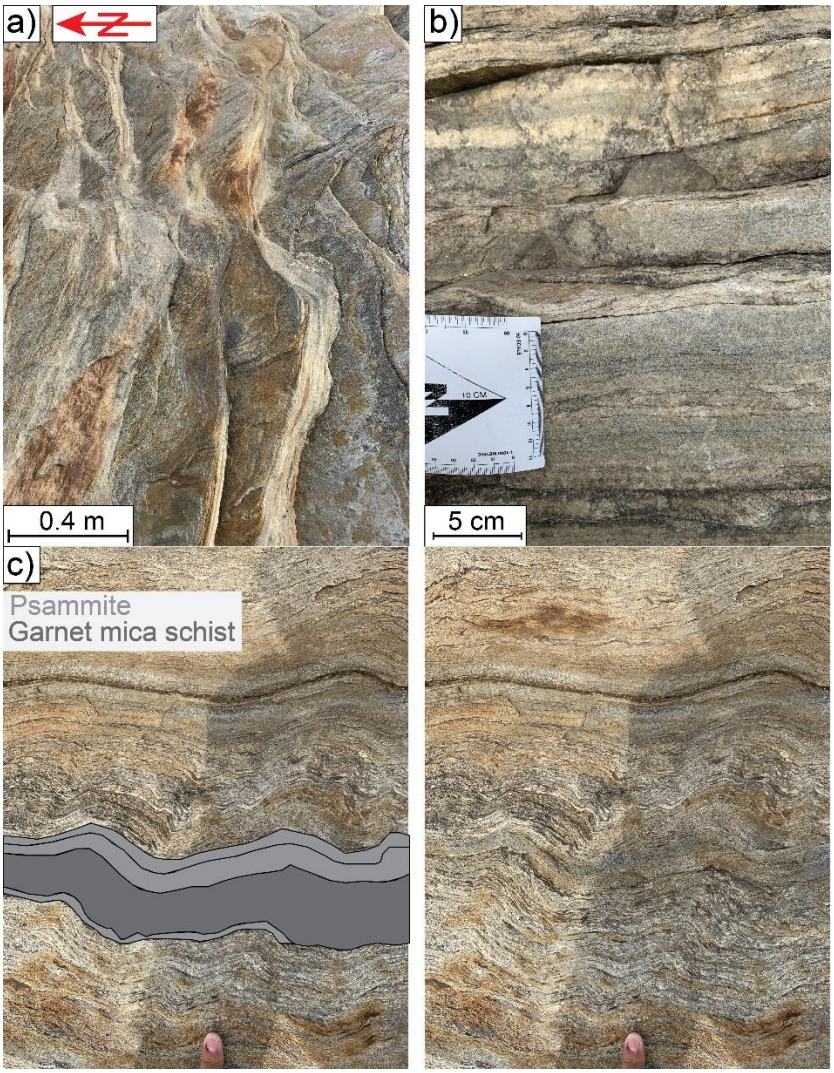


***Figure 69**: A) plag-rich garnet schist, garnet up to 1 cm. Distinct cm-scale benching. COOR: 66.24471° N, 014.84679° E. B) Impure quartzite layers in the transition zone. COOR: 66.24515° N, 014.84642° E. C) Alternation sequence of psammitic/mica layers and coarse and darker garnet mica schist, indicating original bedding. COOR: 66.24515° N, 014.84642° E.*

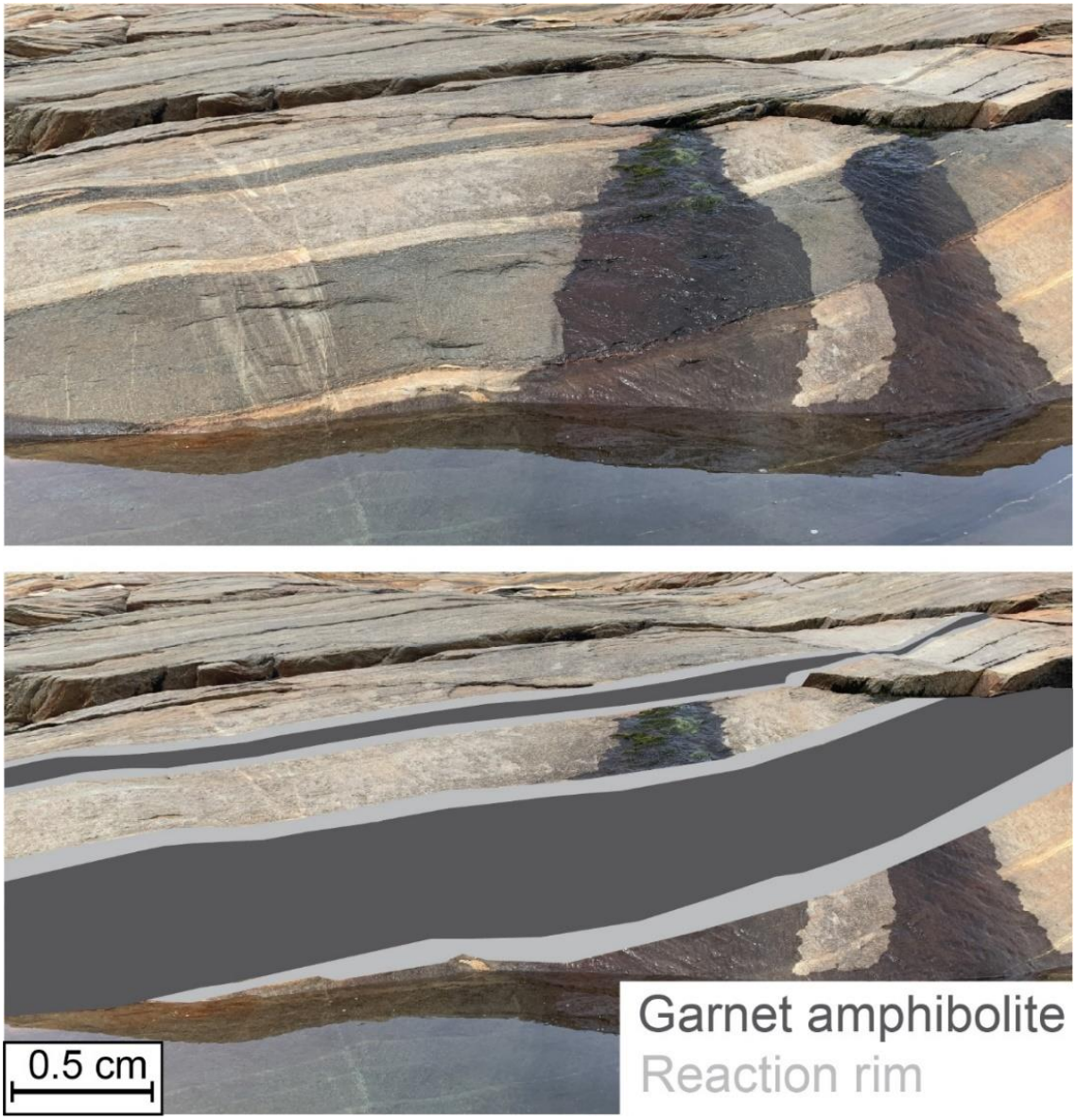


***Figure 70**: Reaction rim symmetry associated with concordant garnet amphibolite sheets in the transition zone. COOR:66.24647° N, 014.83995° E.*

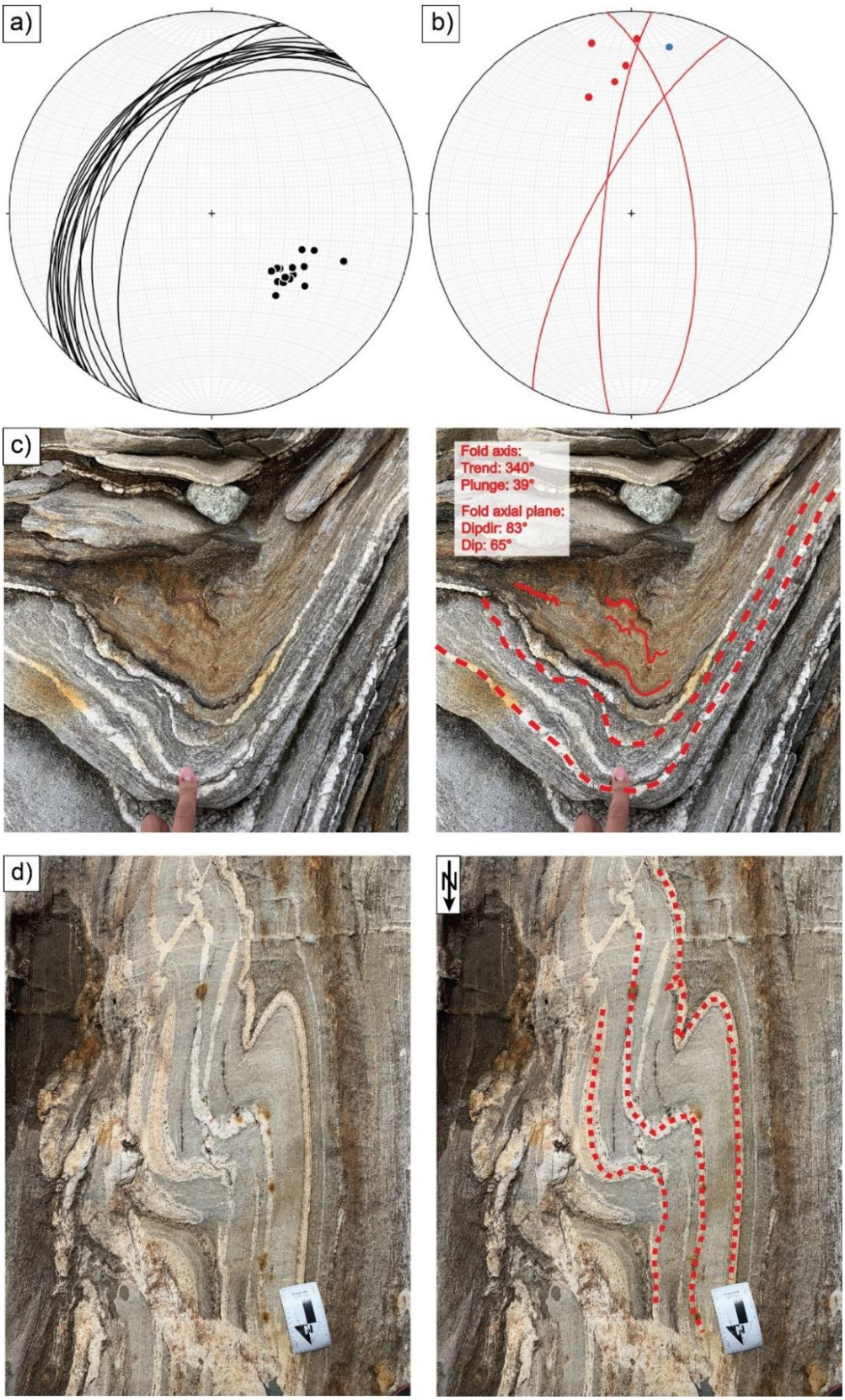


***Figure 71**: A) Foliation measurements from the transition area, in steronet. B) Fold axis (red dots), fold axial planes (red half circles) and lineations (blue dots), in steronet. C) Folding of felsic veins, reaction rims and garnet mica schists from the transition zone. The fold axis has a trend towards 340° with a plunge of 39°. The fold axial plane has a dip direction towards 083° with a dip of 65 °. COOR: 66.24515° N, 014.84642° E. D) Folding of layers with felsic veins, reaction rims and garnet mica schist from the transition zone.*

### 5.1.4 Area 3 – Garnet mica schist with abundance veins with reaction rim symmetry

**Rock variation description**

Walking westwards into area 3, the main changes from the transition area are the decreasing amounts of single layers of mica and sand, and an increase in the concentration of felsic veins, and the presence of calcsilicate layers in a garnet mica schist. The whole area is dominated by a thick package of garnet mica schist with an abundance of felsic veins surrounded by reaction rims. (*Figure 72*).

**Structural features:**

**Tectonic foliations**

One hundred and two measurements of the foliation parallel to the compositional layering from area 3 are plotted in *Figure 73a*. The foliation varies a bit more than in both the transition and the quartz-rich area. Most foliation planes dip with 20 to 60° towards NW or are subvertical with steep dips towards east or west.

**Folds and lineations**

Folding in this area is abundant and is especially visible in the more competent layers, such as the concordant garnet amphibolite sheets, pegmatites, felsic veins, and the reaction rims. The amplitude of the folds is typically mm to dm thick and the folds are asymmetric, and open to close. Crenulation folding is best exposed in the garnet mica schists or in strongly deformed plagioclase layers in concordant garnet amphibolite sheets. Pegmatite veins are also associated with the veins and can be both concordant and discordant to the layer-parallel foliation.

*Figure 73b* shows the fold axis, fold axial plane, and lineation measurements from area 3 plotted in a stereonet. Overall, the fold axis plunges gently towards the north or south. The fold axial planes strike approximately N-S to NNE-SW with a c. 70° dip towards the west. Most of the lineations plunge slightly towards the north, the same directions as the fold axes. *Figure 73c* and *d* shows the same trend and fold axial surface orientation as observed in area 1 (quartz-rich area), area 2 (transition area), and area 3 (vein-rich area).

*Figure 74* shows several field photos of folded felsic veins and reaction rims in the garnet mica schist. In addition to the open to close folds (F2) earlier described, isoclinal folds with axial traces parallel to the foliation parallel to the compositional layering have been observed (F1). These isoclinal folds have been refolded by F2, indicating two folding phases at Kallvatnet. Similar F1 folds were also observed in thin section in a garnet amphibolite sampled from the same area (*Figure 47)*.

Penetrative F2 folding of the layering is also visible in this domain. The M-/W-symmetry of the parasitic folds (*Figure 75*) suggests that this area is located in the hinge region of a larger fold structure, with transition to a synformal structure to the east as indicated by S-shaped parasitic folds (*Figure 72*).

### Boudins

Several boudins and pinch-and-swell structures were observed in concordant garnet amphibolite sheets in this area. *Figure 76a* shows an extended concordant garnet amphibolite with pinch-and-swell structures in a less competent garnet mica schist. Shear fractures associated with boudins were also common. *Figure 76b* shows a mafic asymmetrical boudin with a shear fracture in the NW-SW direction.

### Cross-cutting relations

The garnet amphibolite sheets are concordant with the compositional layering in area 3 (vein-rich area). One semi-discordant several-meter thick garnet amphibolite layer is partially more gabbroic and deflect the S1 foliation in the host garnet mica schist (*Figure 77*). The small angle between the foliation and the garnet amphibolite layer indicate that the layer has intruded sub-parallel with the host rock layering, only partially cutting the foliation.

### Kinematic indicators

In area 3 (vein-rich area), several kinematic indicators were observed. Two local sinistral shear zones associated with garnet amphibolite boudins (*Figure 78a and Figure 76b*) and two sinistral asymmetric felsic veins, see *Figure 78b* and *c*. The orientations of the shear zones associated with the boudins are towards NW-SE.

***Figure 72**: Folded felsic veins with associated reaction rims. The felsic veins and the reaction rims are folded in a z-folding pattern. COOR: 66.23964° N, 014.79445° E.*

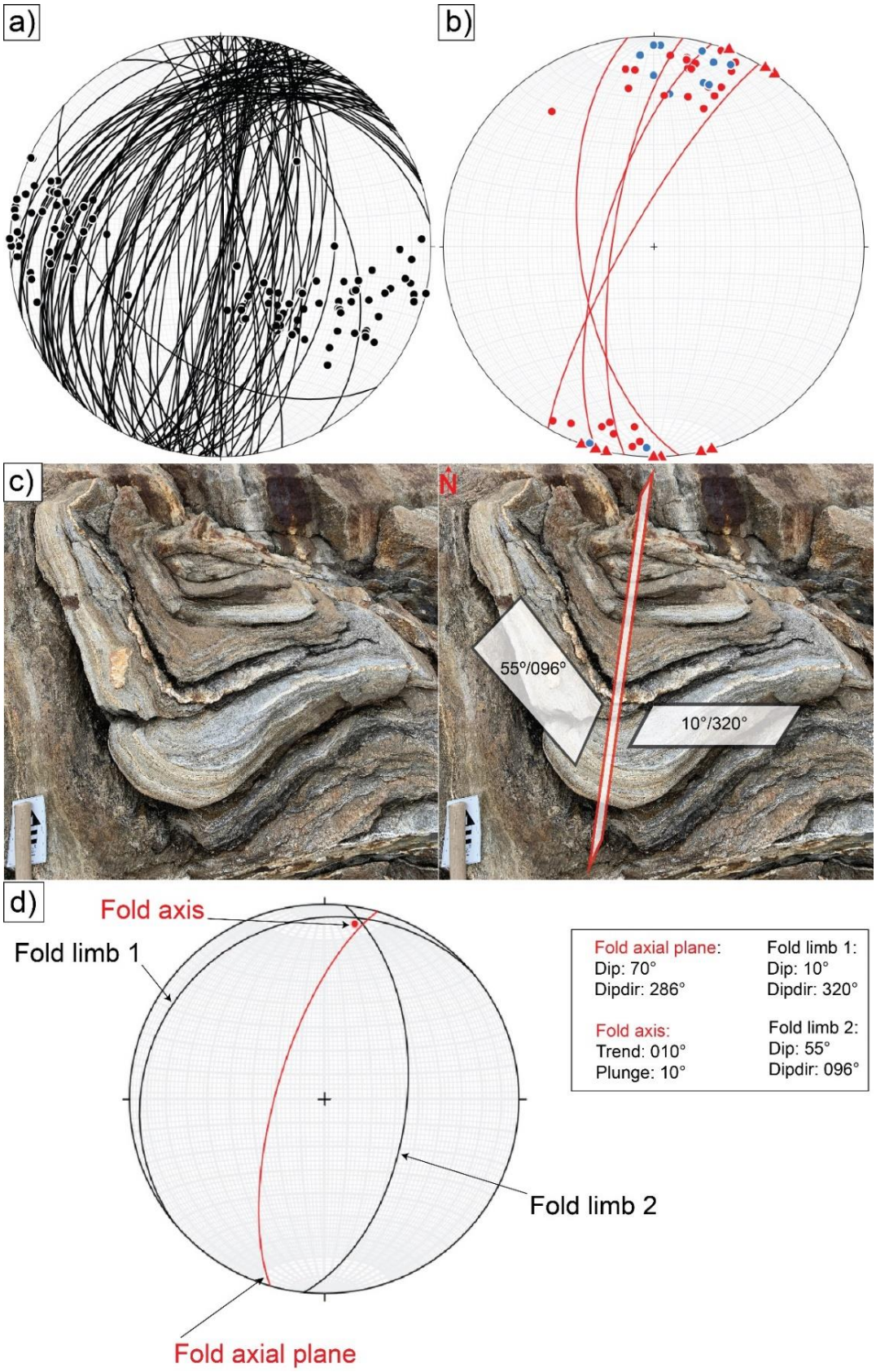


***Figure 73**: A) Foliation and the belonging poles from area 3 in stereonet B) Fold axis (red dots), fold axial plane (red half circles), trend of fold axial planes (red triangles) and lineation (blue dots) C) and D) Fold in the vein-rich area. Open fold with illustrated fold axial plane and fold limbs with belonging measurements in stereonet. COOR: 66.24037° N, 14.78241° E.*

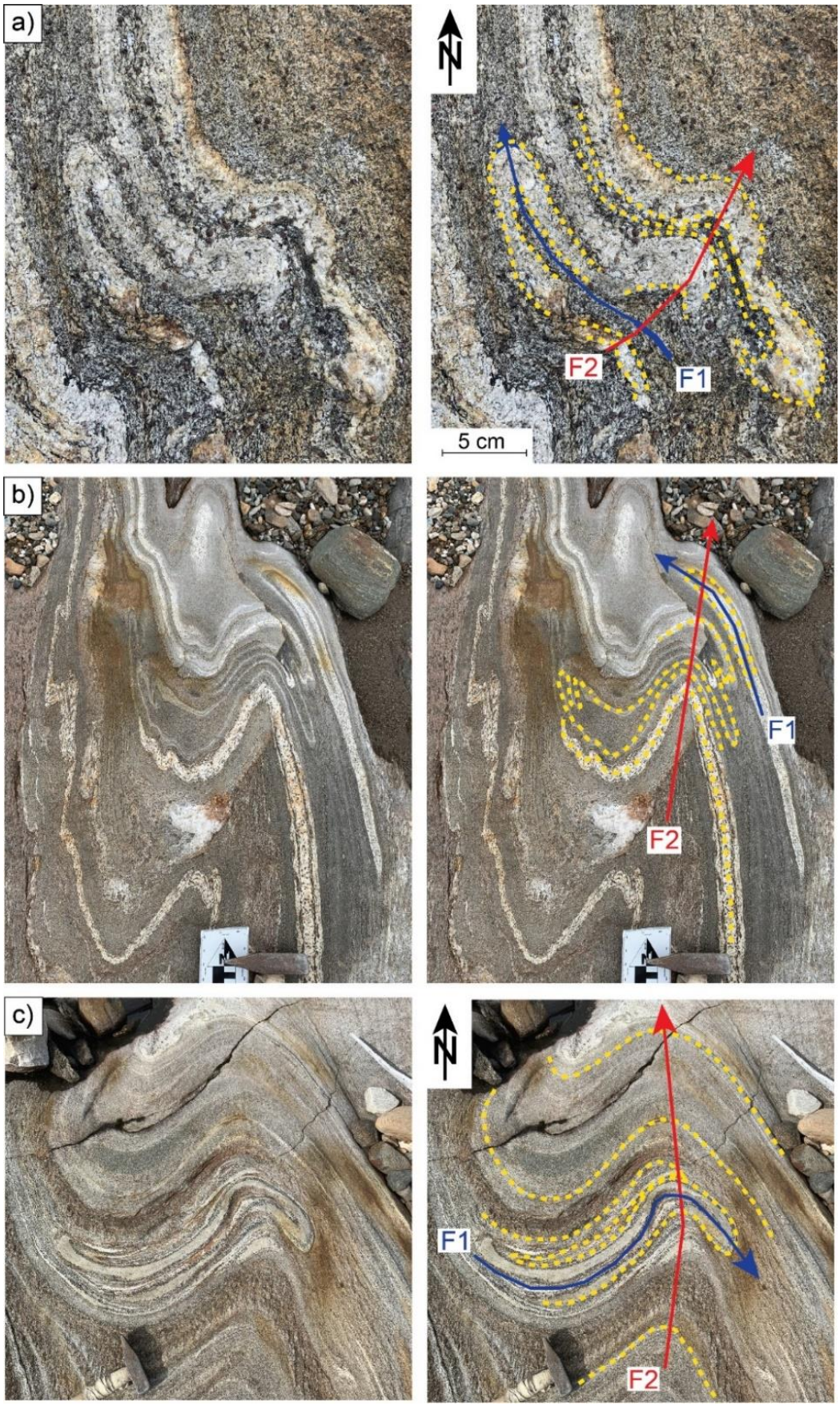


***Figure 74**: Isoclinal F1 folds with axial trace parallel with foliation and open abundant typical open F2 folds. A) COOR: 66.24081° N, 14.77895° E. B) COOR: 66.23990° N, 14.79231° E. C) COOR: 66.23948° N, 014.79591° E.*

***Figure 75**: Distinct w/m-folding of a garnet amphibolite layer located in area 3. COOR: 66.24062° N, 014.77860° E.*

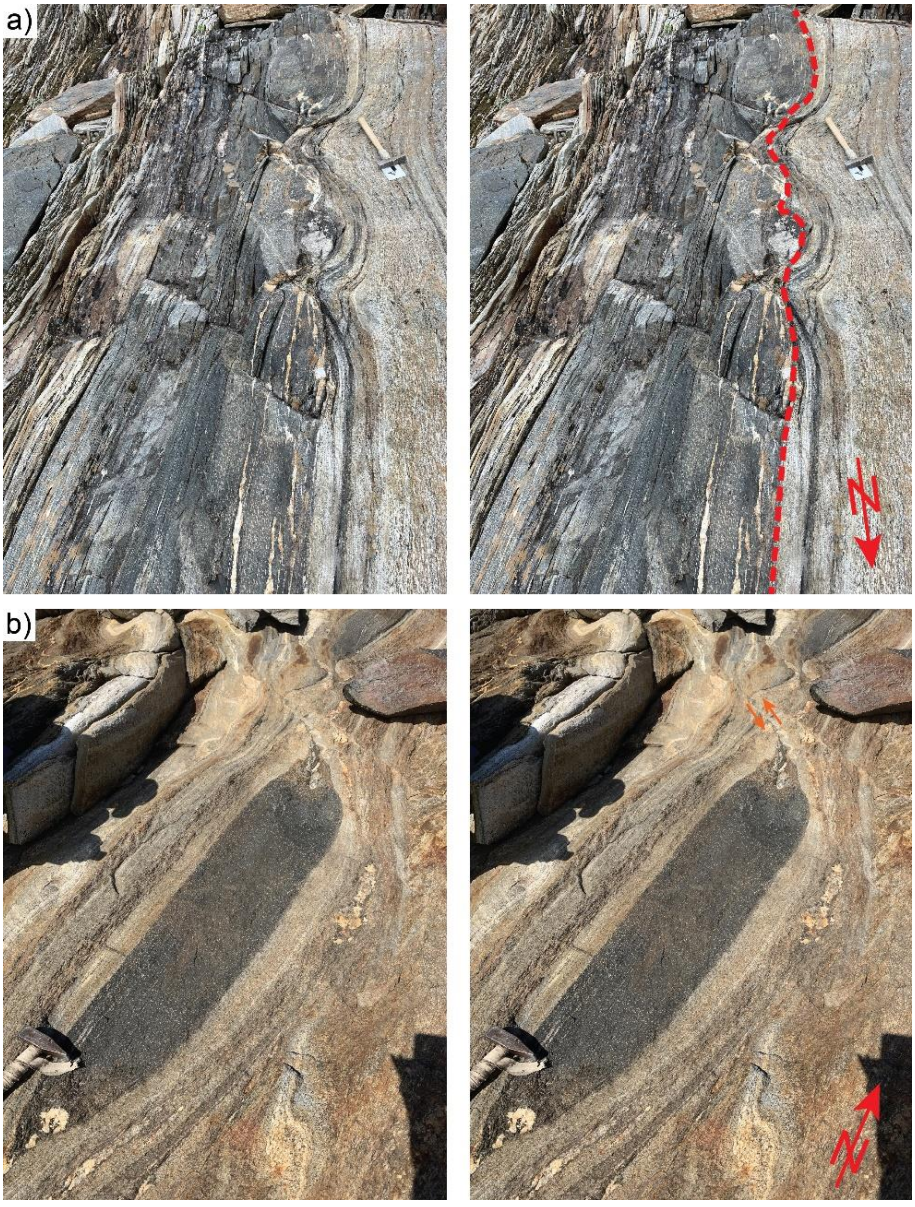


***Figure 76**: Pinch-and-swell structures and asymmetrical boudin in garnet amphibolites A) Pinch-and-swell structures in a garnet amphibolite. COOR: 66.23650° N, 014.77884° E. B) Asymmetric garnet amphibolite boudin. COOR: 66.24043° N, 014.78033° E.*

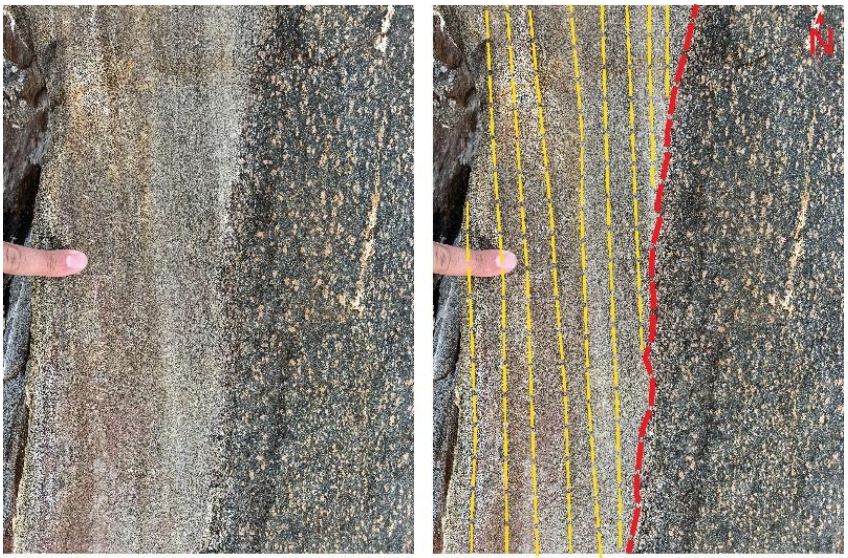


***Figure 77**: Garnet amphibolite layer deflects the foliation in the vein-rich area. (sample: gmf2020-03) COOR: 66.23975° N, 014.79714° E.*

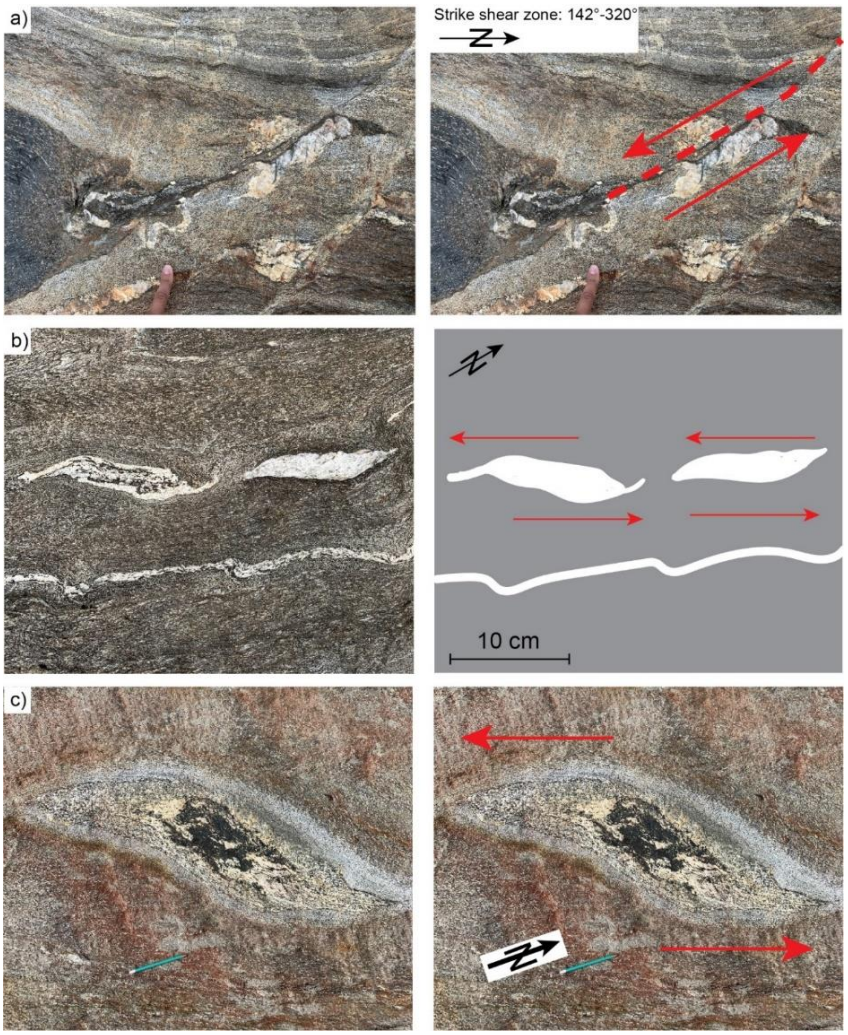


***Figure 78**: A) Sinistral shear zone associated with a boudined garnet amphibolite layer. COOR: 66.24081° N, 14.77895° E. B) Sinistral kinematic in felsic veins. COOR: 66.24031° N, 014.80065° E. C) Sinistral kinematic in a felsic lens. COOR: 66.24011° N, 14.79939° E.*

### 5.1.5 Area 4 – Garnet mica schist, with fewer veins

**Rock variation description**

This area is composed of garnet mica schist with layers of pegmatite, concordant garnet amphibolite sheets and felsic veins with associated reaction rims, similar to area 3 (vein-rich area). The main difference between this area and area 3 is that it has a significant lower concentration of felsic veins. The abundance of garnet mica schist makes the crenulation cleavage especially distinct in the area (*Figure 79a* and b). The crenulation folding is distinct in the concordant garnet amphibolite sheets (*Figure 79b*).

**Structural features:**

**Tectonic foliations**

Thirteen measurements of foliation planes parallel to the compositional layering (S1) were conducted in the area, see *Figure 80a.* The majority of the measured foliation planes have a vertical to 50° dip towards the east. Still several S1 planes also dip towards west as seen on the western limbs of the folds (*Figure 80c* and d).

**Folds and lineations**

The open to close folds (F2) and related crenulation folds observed in the previous areas also occur here. Fold axis, fold axial plane, and lineation measurements are presented in *Figure 80b,* the measurements are similar to the measurements in the other areas. *Figure 80c* shows the distinct crenulation folding in garnet mica schist and the pegmatite layers. *Figure 81b* shows several z-folds in the garnet mica schist, indicating the presence of an antiform to the west. A pre- or inter-tectonic garnet shows an internal foliation (Si) which is different from S1 and S2 (*Figure 81a*). This observation indicates that the garnet porphyroblast growth occurred before the formation of the S1 and S2. The garnet either overprinted an earlier secondary foliation (tectonic foliation) or primary foliation (sedimentary bedding). In the case of an inter-tectonic porphyroblast, a third deformation event has occurred in the Kjerringfjell Group.

Some parts of Damtjønnfjellet were also mapped and is included in area 4. *Figure 82* shows M-folds in the garnet mica schist observed on Damtjønnfjellet (see map in *Figure 41*).

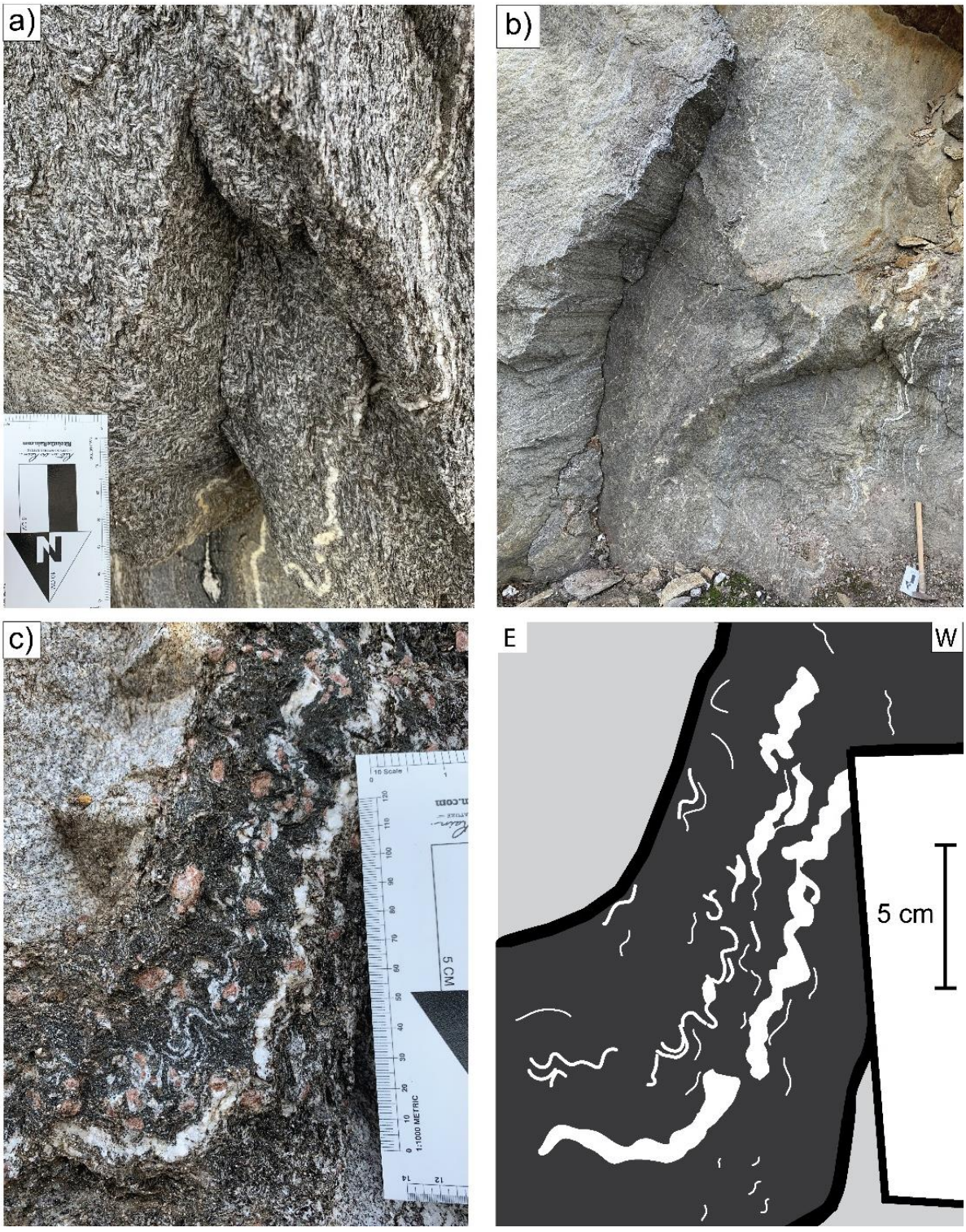


***Figure 79**: Garnet mica schist with pegmatite and a concordant garnet amphibolite sheet. A) Distinct crenulation folding is visible at the outcrop. COOR: 16.23812° N, 014.77339° E. B) Garnet mica shist with layers of pegmatite. Crenulation lineation and cleavage is visible. C) Distinct crenulation folding in a garnet amphibolite sheet. The crenulation folding is especially distinct in the plagioclase layer. COOR: 66.23706° N, 014.77643° E.*

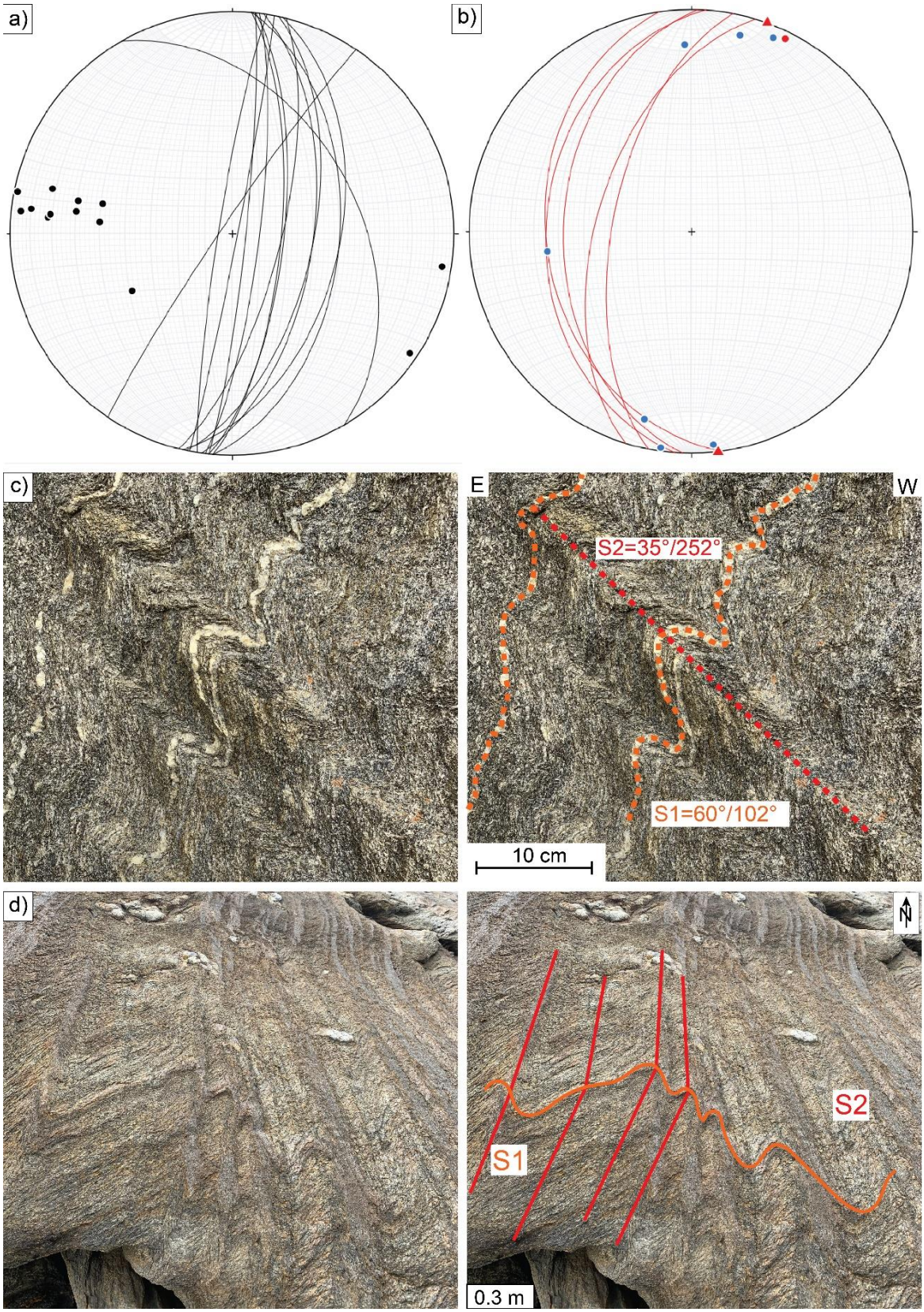


***Figure 80**: Structural measurements and field photo, area 4. A) Foliation planes parallel to the compositional layering (black half circles) and poles to belonging planes (black dots). B) Fold axis (F2) (red dot), fold axial planes (F2) (red half circles), lineation (blue dots) and direction for the strike to fold axial planes (red triangle). C) Typical crenulation folding in the garnet mica schist. COOR: 66.23760°, N, 014.77335° E. D) The S1 foliation and S2 crenulation cleavage are distinct in the garnet mica schist.*

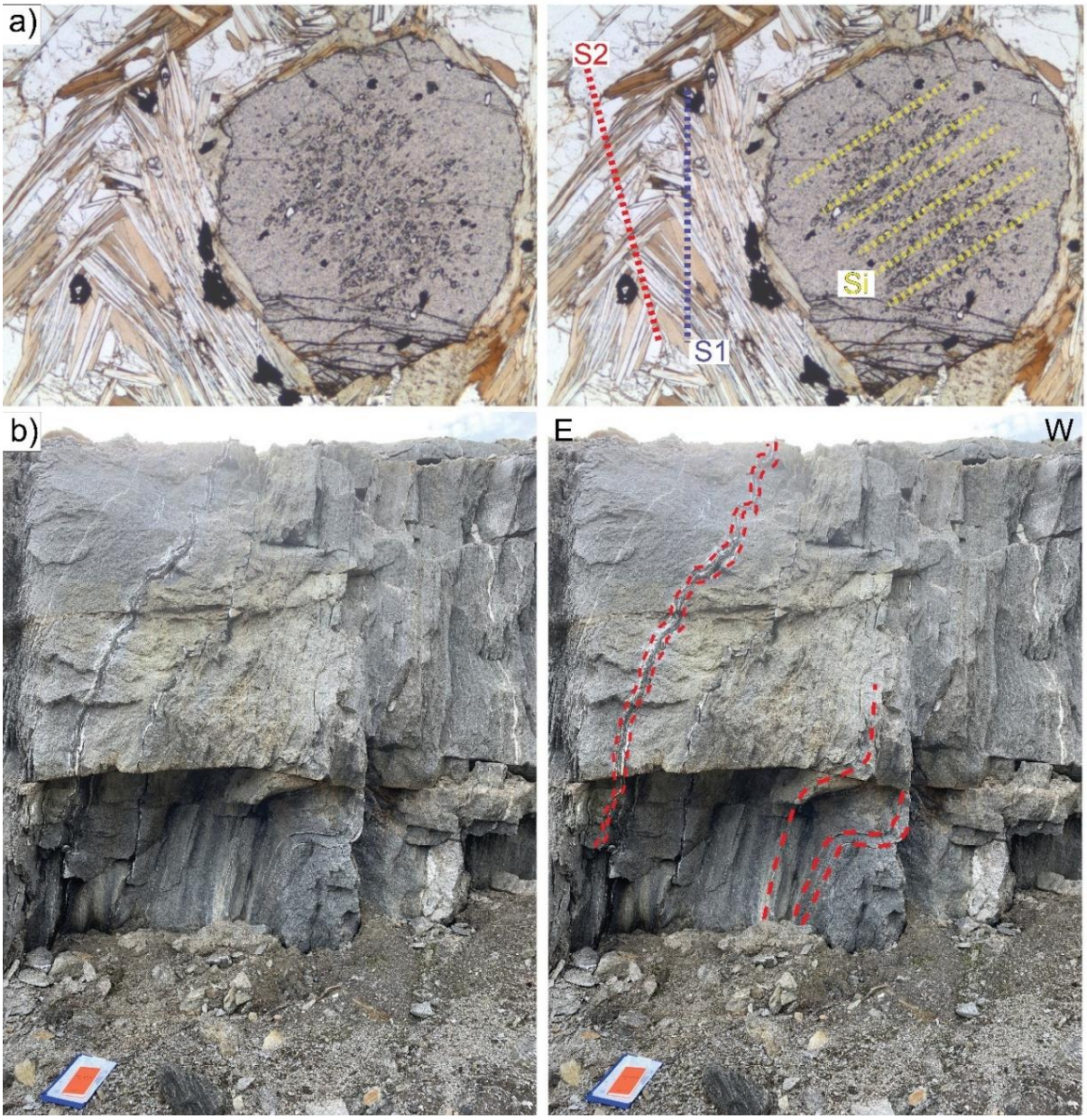


***Figure 81**: Pre-tectonic garnet and dm thick z-folds in the garnet mica schist with distinct crenulation folding. A) Pre/inter-tectonic garnet in a garnet mica schist (gmf2020-13). B) Z-folds in the garnet mica schist. COOR: 66.23722° N, 014.77545° E.*


***Figure 82**: M-folds in garnet mica schist on Damtjønnfjellet. COOR: 66.24590° N, 014.80038° E.*

### 5.1.6 Structural Summary

Structural measurements from the four areas described above are summarized in *Figure 83.*

The foliation parallel to the compositional layering (S1) has two main pole concentrations (*Figure 83*a and b). 1: Planes dipping towards NW. 2: Planes dipping steeply towards E-SE. Most of the fold axis plunges gently towards N, and fold axial planes dip steeply towards W-NW *Figure 83c*.

A generalized fold axial plane and a fold axis were calculated based on the poles to the S1 foliation measurements (*Figure 83d)*. The trend and plunge of the fold axis were calculated to be 007° and 20°, respectively. The interlimb angle was calculated to be 66°, and the axial plane dipping 64° towards 288°.

As described in the text, the tectonic foliation (S1) is folded, hence the dip and dip-direction vary a lot throughout the study area. Generally, the E-dipping planes are steeper than the W-dipping planes and the W-NW dipping fold axial planes indicate an overall east-vergence of the area-scale folding. The open to close F2 folds in the area corresponds well to the area-scale calculated fold and overall E-vergence. In addition, isoclinal F1 folds have been observed in thin section and in the field, and an internal foliation is preserved in inclusions in garnet.

In short, two fold-generations have been observed, isoclinal F1 folds and open to close F2 folds gently plunging towards N. A dominant compositional parallel S1 foliation, a weak crenulation cleavage (S2) (defined by the crests of crenulation folds) and an internal foliation (Si) preserved in garnet inclusions have been observed. Overall, the F2 folds and the area-scale S1 foliation indicate an overall E-vergence.

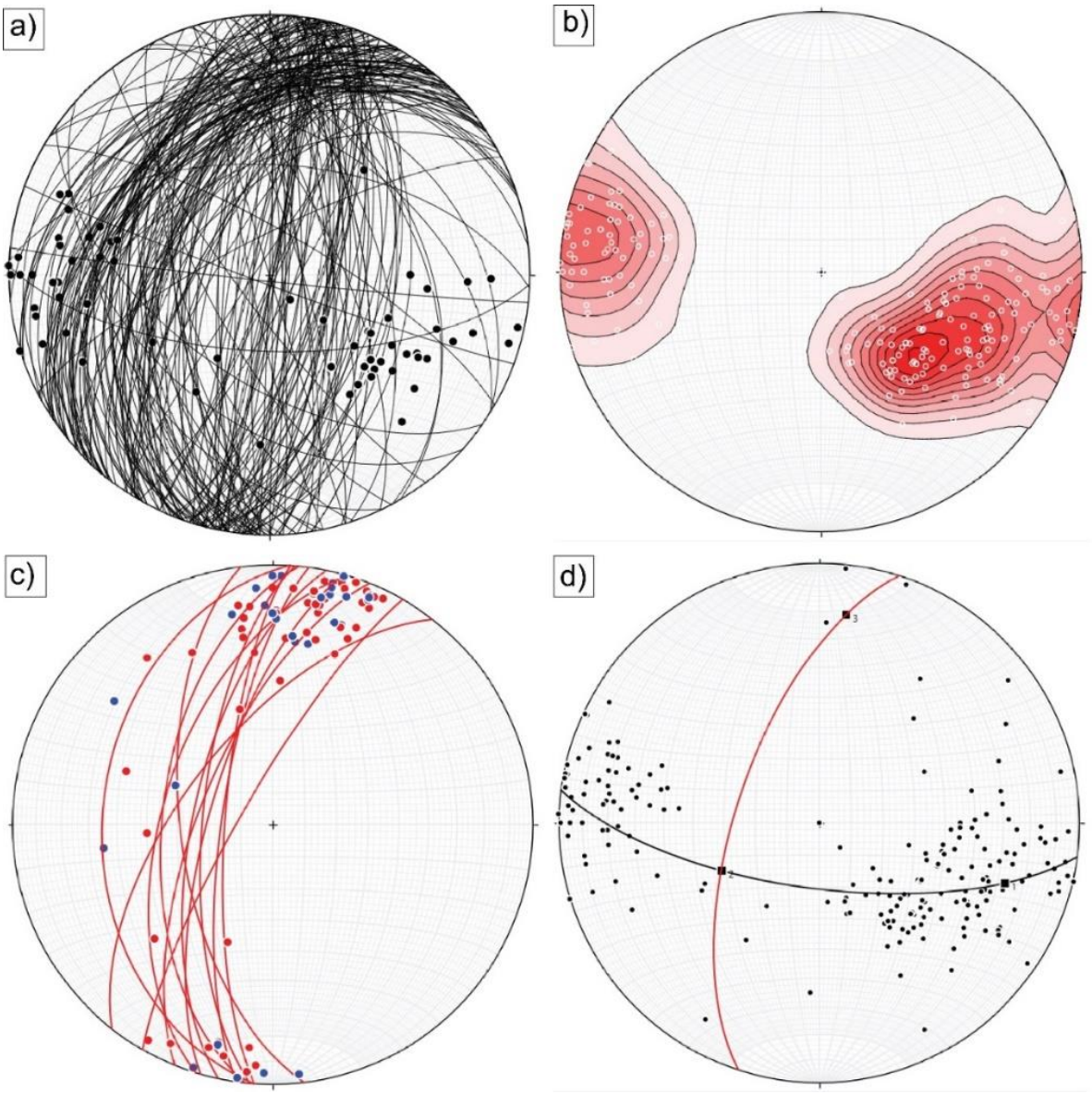


***Figure 83**: All structural measurements plotted in stereonets. A) S1 foliation and it's belonging poles (black dots) plotted in a steronet. The foliation is parallel to the compositional layering. B) Calculated Komb contours based on the poles to the same foliation planes shown in A). C) All fold axis (red dots), fold axial planes (red half circle) and lineations (blue dots) plotted in a steronet. D) A fold axial plane (red half circle) was calculated based on poles (black dots) to the S1 foliation.*

## 5.2 Geochronological data

This chapter will present the geochronological results obtained from the Kjerringfjell Group. 1) Metamorphic zircon and monazite geochronology from Kallvatnet and Sauvasshytta (near Umbukta). 2) Igneous zircon geochronological data from the Umbukta gabbro and a tonalite located northeast in the Kjerringfjell group. Data sets from the Umbukta and tonalite samples are from Trond Slagstad (unpublished).

### 5.2.1 Metamorphic geochronology

This chapter will present the metamorphic geochronological data obtained in this study. Both zircon and monazite were dated using LA-ICP-MS in an attempt to obtain data to constrain the timing of high-grade metamorphism in the Kjerringfjell Group. The location of the metamorphic zircon and monazite samples are shown in *Figure 84.* The data are in TW-plots diagrams with 2σ data point error ellipses and box plots with 2σ data point error symbols. The calculated ages are also presented with a Mean Square of Weighted Deviates (MSWD), which is a measure for how the predicted uncertainties fit the observed data. If MSWD = 1, the age fits a univariate normal distribution. If MSWD < 1, the observed scatter is less than the analytical uncertainties predicted, indicating an overestimation of the analytical uncertainties. In the case of an MSWD > 1, the observed scatter is higher than predicted by the analytical uncertainties, the data is said to be "overdispersed."

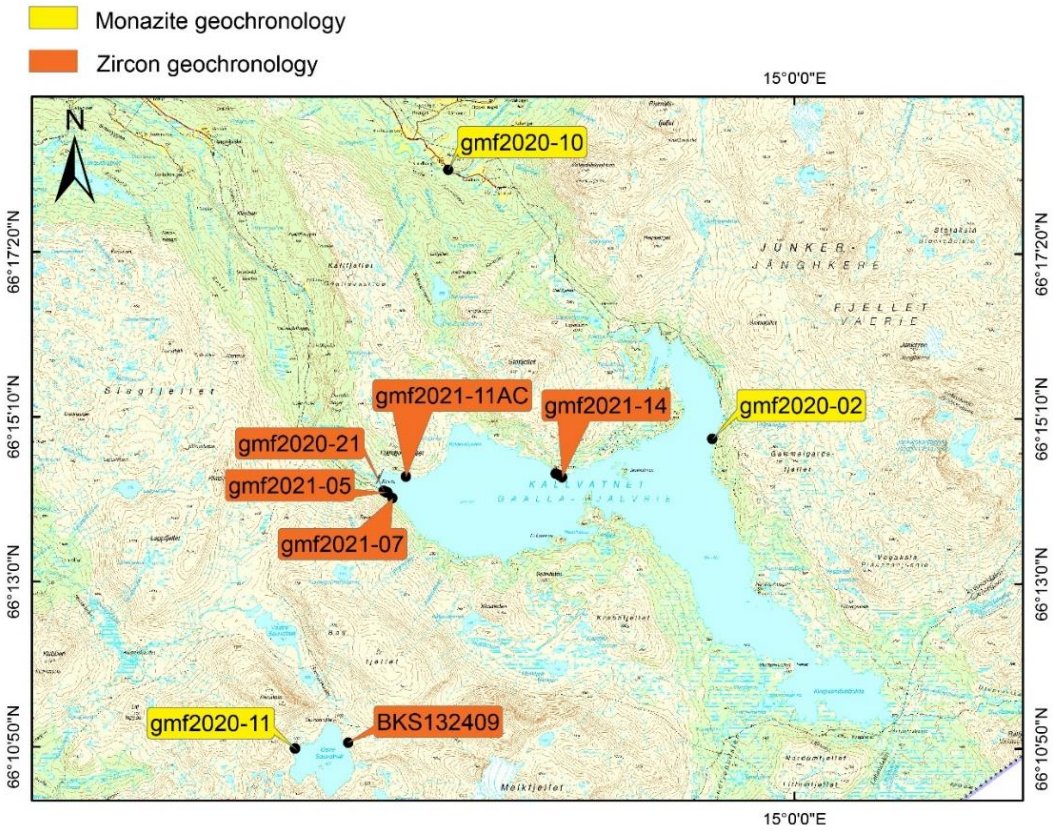


***Figure 84**: Sample locations for the metamorphic geochronology, dated zircons and monazites in this study.*

## Zircon geochronology

A total of twelve samples were collected in the field for metamorphic zircon geochronology. The location for the dated samples is shown in *Figure 84*. Due to lack of zircon in many samples, only six of the twelve samples could be dated. The zircons are described and their geological significance interpreted based on petrography, BSE images, Cl-images, and the Th-U ratio measured by the LA-ICP-MS. A complete table with the zircon U-Pb data, BSE and CL-images are presented in *Appendix E*.

The zircons dated in this study were collected from metasediments, felsic veins, and reaction rims, thus it was expected to find detrital zircon populations in several samples. Most of the oldest zircons are interpreted as detrital, while the majority of the Paleozoic zircons are interpreted as metamorphic. None of the zircons in this study have been interpreted as magmatic zircons related to the crystallization of the felsic veins.

In addition to the samples collected in the study area around Kallvatnet, a sample (BKS132409) near the Umbukta gabbro collected by Bergliot Kulsrud Storruste was dated (Storruste, 2017). Unfortunately, only detrital zircons were analyzed from this sample.

### Sample gmf2020-21 – vein

In this sample, seven analyses on five zircon grains were done. Generally, the zircons are round to sub-angular and vary in size from 50 to 100 µm with core-rim textures. Several grains have complex internal structures in CL, showing several zones with different uranium concentrations. Some grains show weak oscillatory zoning, especially the cores. The sector zoning is irregular, at some places rounder. The cores and the outermost rims are generally darker than the rims closest to the core in CL, indicating uranium-rich areas (*Figure 85*).

*Figure 86* Shows a TW plot with two main groups of analyses: 1: Three Paleozoic analyses, two rim analyses, and one mixed analysis. The two rim analyses are interpreted as metamorphic mainly based on the textural appearance in the CL-image, while the low Th/U content in the mixed analysis indicates that the laser mainly hit the metamorphic rim. 2: Three concordant core analyses plot around 1400-1550 Ma and are interpreted as inherited. In addition to the two main groups, one concordant rim analysis is Mesoproterozoic and interpreted as an inherited metamorphic rim.

A $^{238}U/^{206}Pb$ age of the youngest and most concordant Paleozoic rim analyses was calculated to be 434 ± 5 Ma and is interpreted as the timing of a metamorphic event.

A discordia was also constructed through the two youngest rims and one mixed analysis, yielding a lower intercept age of 429 ± 17 Ma and an upper intercept age of 2083 ± 880 Ma. All these metamorphic grains have a Th/U = 0.00. Two of these line analyses were conducted on rims, while the mixed one was conducted on an oscillatory-zoned core and rim.

One discordia was also constructed through a rim and a core analysis in grain number 1 (see tables in *Appendix E*). The core analysis is 99.4% concordant and is the oldest detrital zircon in the sample. The rim analysis is 66.9% concordant and is the oldest of the three Paleozoic metamorphic analyses. The discordia yielded a lower intercept age of 413 ± 89 Ma and an upper intercept age of 1575 ± 60 Ma. The discordance of the oldest rim may be

caused by some mixing with the core analysis as the analysis partially hit the core (see *Appendix E*).

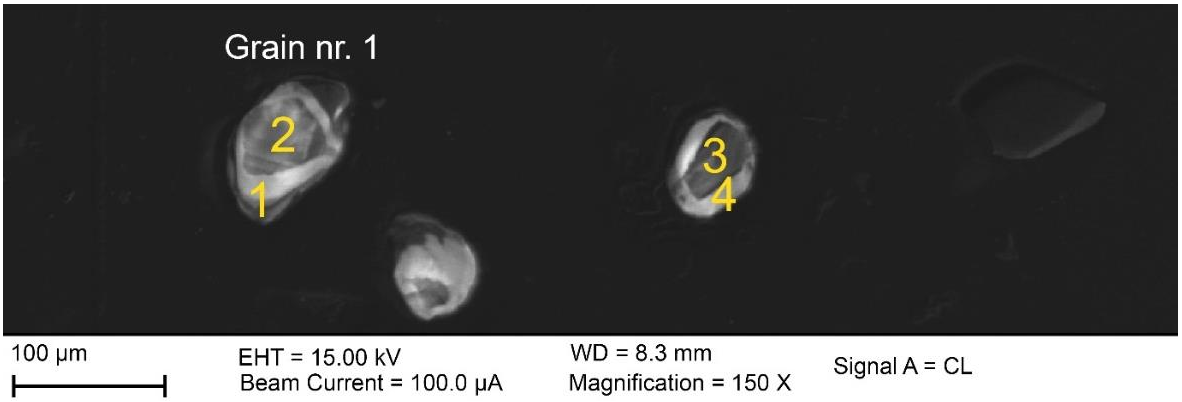


***Figure 85**: CL-image of two of the analyzed zircons from sample gmf2020-21.*

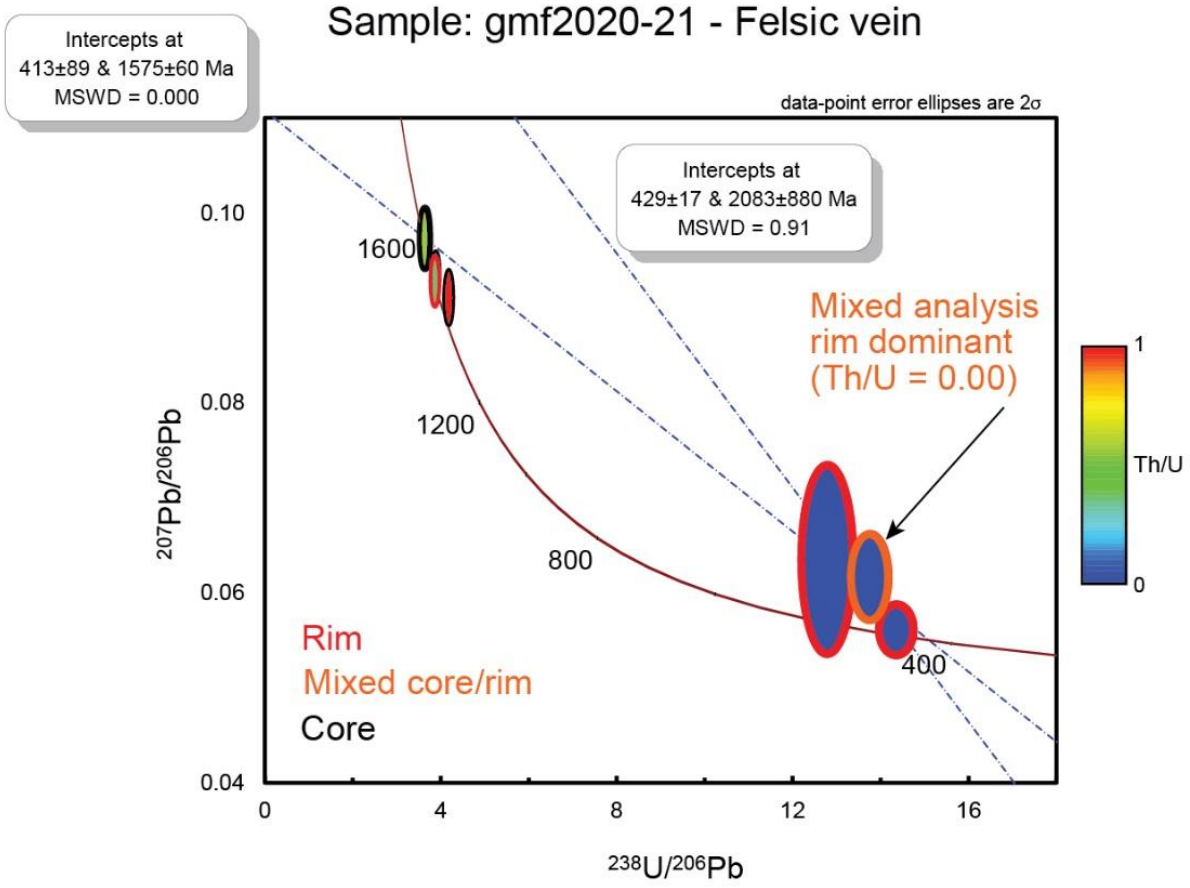


***Figure 86**: TW plot of the seven analyses from sample gmf2020-21. The color-filling of the ellipses indicates the Th/U content in each analysis. Red ellipses show rim analyses, black ellipses show core analyses.*

The number of analyses conducted on this sample is low thus, none of these calculated ages are reliable and just an indication. One can see in the TW plot (*Figure 86*) that the

uncertainty of the $^{207}Pb/^{206}Pb$ age of the rim analyses is high. This uncertainty is most likely caused by the small concentration of U in the rim. Small concentrations of U will lead to smaller radiogenic $^{207}Pb$ being formed in the rim, inhibiting precise measurements.

The 429 ± 17 Ma age is based on the assumption of a relationship between all the Paleozoic rim analyses. In addition to having incorporation of $Pb_c$ leading to a 2083 Ma age of the upper intercept. One can see that the inherited zircons have a concordance > 90% and are scattered between c. 1400 and 1550 Ma, indicating these zircons were derived from different sources. The discordance for the Paleoproterozoic analyses is assumed to have occurred due to mixed analyses or common Pb.

The 434 ± 5 Ma**,** the concordant $^{238}U/^{206}Pb$ age derived from one analysis is assumed to be the best indication of the timing of a metamorphic event in this sample.

**Summary key points:**

- Indication of a metamorphic event at 434 ± 5 Ma.

**Sample gmf2021-05 – Felsic vein**

Thirty-two analyses were distributed on twenty-three zircon grains (see table in *Appendix E*). The grains are dominantly sub-prismatic, anhedral to euhedral, have distinct core-rim internal structure, and are approximately 100 µm in size (*Figure 87*). Most of the cores are dark in CL, have weak to distinct oscillatory zonation, and are occasionally truncated or cracked. These are interpreted as magmatic zircons. The rims are light in CL, mostly homogenous with some weak sector zoning, and these are interpreted as metamorphic rims.

*Figure 88a* shows a TW plot with all the thirty-two analyses plotted. The yellow ellipses are the rim-analysis, while the black ones are the core analyses. One can see that the rim analyses have Paleozoic and Proterozoic ages, while the core analyses only have Proterozoic ages. Only one of thirty-two analyses have a concordance of less than 85%, and almost every analysis has a Th/U higher than 0.1; this indicates that the Th/U alone cannot be fully trusted to decide the origin of the zircons.

The scattered Proterozoic rim and core analyses in *Figure 88a* are believed to represent metamorphic and magmatic inherited ages. The four Paleozoic rim analyses are suggested to represent ages for a metamorphic event at Kallvatent.

A $^{206}Pb/^{238}U$ weighted average of the three overlapping Paleozoic analyses yielded an age of 437.4 ± 6.4 Ma (MSWD = 0.78) and a probability of 46% (*Figure 88b* and *Figure 88c*). This age is interpreted as the time of a metamorphic event.

**Summary key points:**

- Indication of a metamorphic event at 437.4 ± 6.4 Ma.

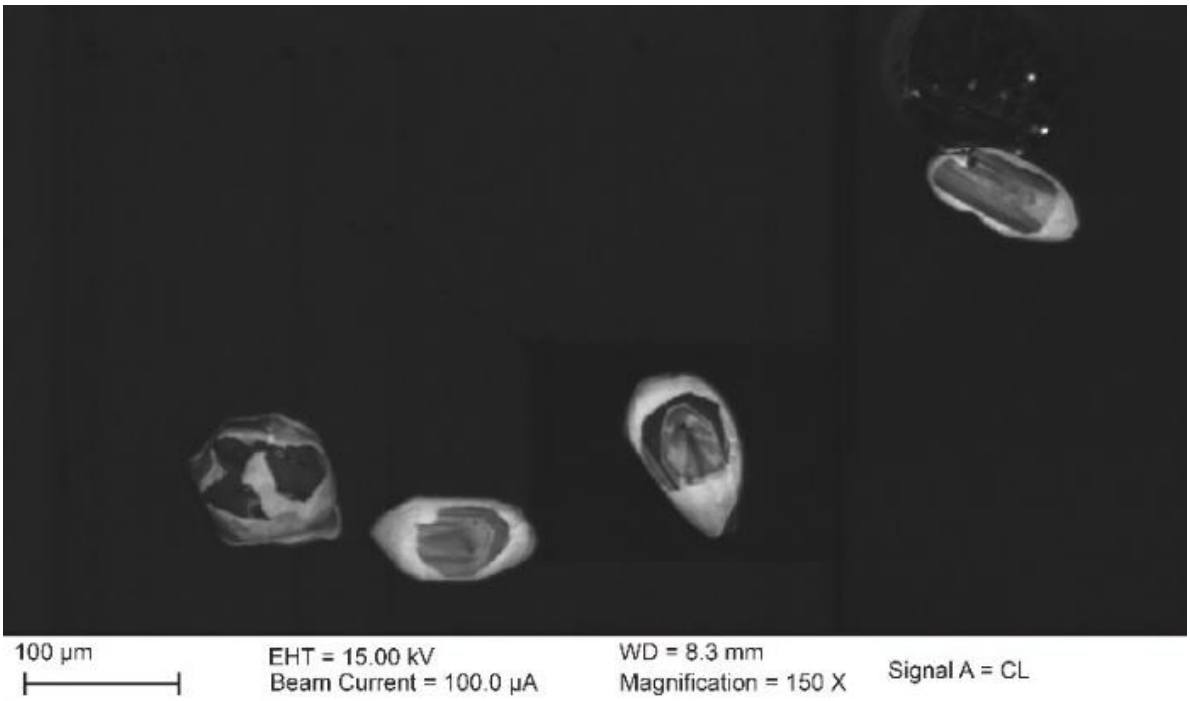


***Figure 87**: CL-image of characteristic zircon grains in sample gmf2021-05 with distinct core-rim internal structure.*

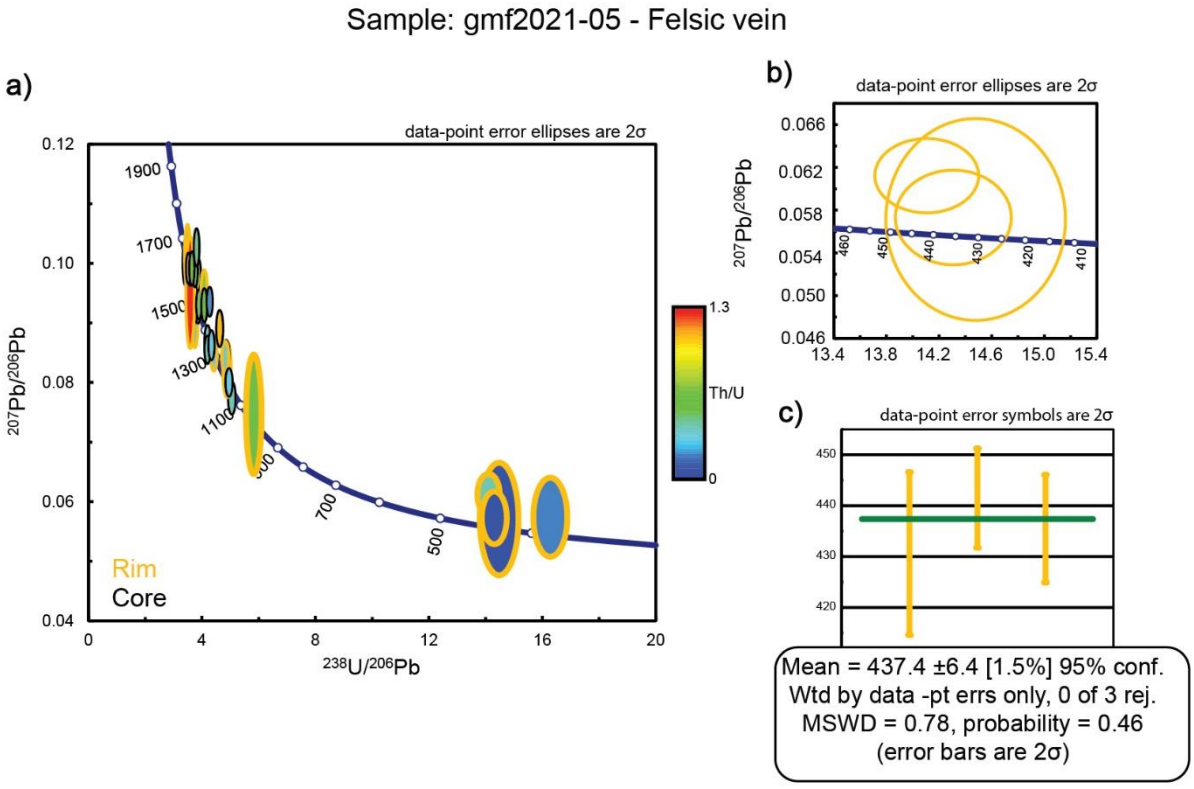


***Figure 88**: A) TW plot of the zircon data obtained from sample gmf2021-05. Yellow ellipses are the rim analyses which are interpreted to have a metamorphic origin. The core analyses have black ellipses and are interpreted as magmatic. B) TW plot of the three most concordant analyses. C) $^{238}U/^{206}Pb$ weighted mean of the three concordant analyses.*

**Sample gmf2021-07A – Reaction rim**

The sample was taken from a reaction rim in the metasedimentary wall rock around a felsic vein. In total ten analyses were conducted on sample gmf2021-07A containing seven zircon grains (see table in *Appendix E*). The sample contains two main types of zircons: 1) In CL, dark sub-angular grains with weak to clear oscillatory zonation, interpreted as magmatic detrital zircons. 2) Core-rim zircons with light cores and dark rims. Most of the cores have distinct oscillatory zoning, and the rims are homogenous, with no apparent zonation. The rims are interpreted as metamorphic and the cores as magmatic. The zircons in the sample varies in size from 50 to 120 µm.

*Figure 89* shows the analyses plotted in a TW-diagram. The cores, interpreted as detrital zircon, plot around 1200 and 1600 Ma with concordance > 85% and a Th/U > 0.1. The rim analysis consists of two concordant analyses around 450 Ma and two discordant analyses around 500-600 Ma and 1000 Ma that are interpreted as metamorphic ages. The Th/U for the metamorphic analysis plot between 0.01 and 0.32. The higher discordance of the two rim analyses are likely caused by mixing of the core and the rim domains in the grain.

A discordia was constructed through all the metamorphic analyses yielding a lower intercept age of 446 ± 11 Ma and an upper intercept of 1631 ± 62 Ma (MSWD = 0.44). The lower intercept is interpreted as the age of a Paleozoic metamorphic event, while the age of the upper intercept is interpreted as the crystallization of the detrital zircons.

In addition, a concordia age of the two concordant metamorphic analyses was calculated to be 449 ± 6 Ma (MSWD = 0.074), with a probability of concordance of 79%. This age is similar to the metamorphic event indicated by the lower intercept of the discordia.

Both ages discussed above, indicate a Paleozoic metamorphic event occurring around 445 or 450 Ma. The scatter of the detrital zircons indicates several sources. *Figure 90* shows a TW plot with three pairs of core-rim analyses with three discordias constructed for each of the core-rim pairs. The lower intercepts yielded three ages: 446, 448, and 466 Ma. The 466 age is the most uncertain thus, we conclude that the two youngest ages are the most reliable ages. These two ages agree well with the concordia age shown in *Figure 89*, 449 ± 6 Ma, which is the preferred chosen age of a metamorphic event from this sample.

**Summary key points:**

- Indicating a metamorphic event at 449 ± 6 Ma

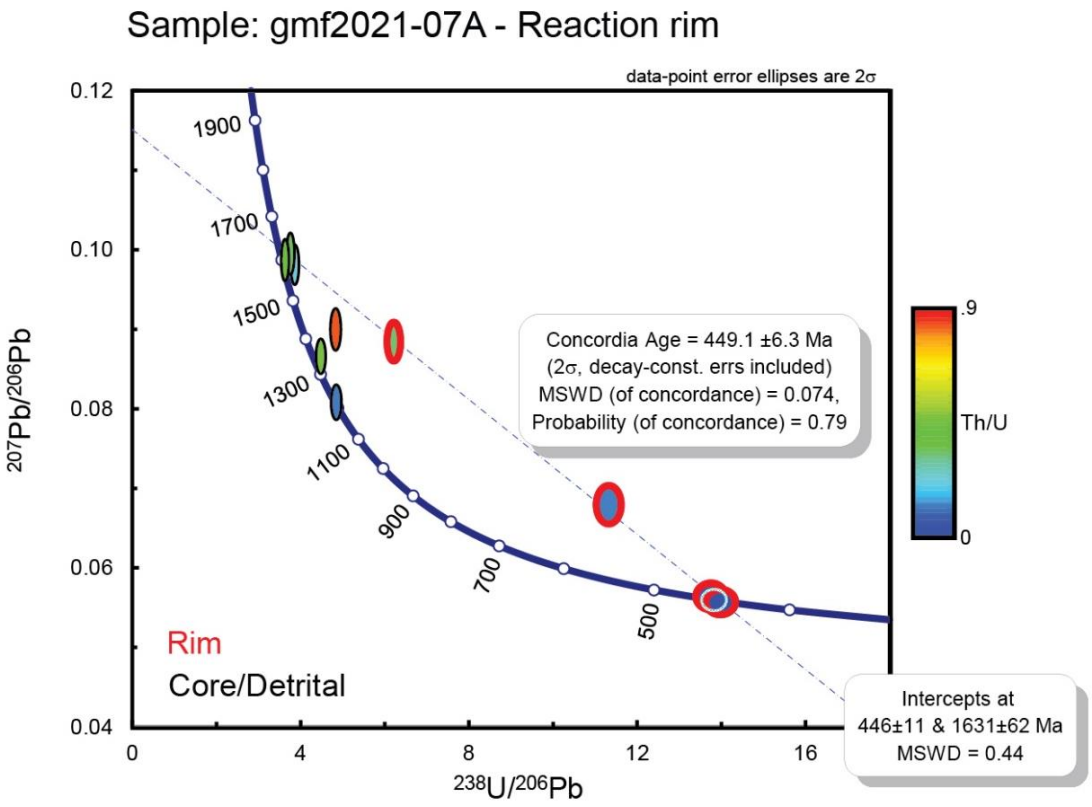


***Figure 89**: TW plot with analyses from sample gmf2021-07A (reaction rim). Analyses with red ellipses (rims) are interpreted as metamorphic zircons, black (cores) indicated as inherited.*

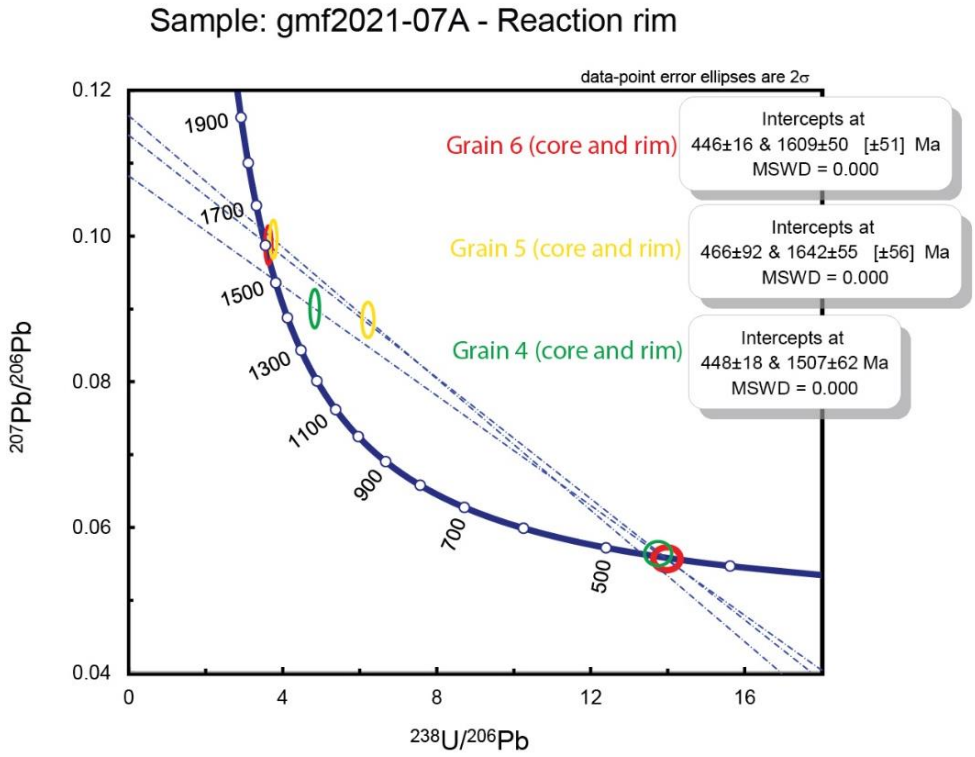


***Figure 90**: TW-plot with three pairs of core-rim analyses of grain 4, 5 and 6 from sample gmf2021-07A (reaction rim).*

**Sample gmf2021-11A – Felsic vein**

Together seven analyses were conducted on three zircons in this sample, (see table in *Appendix E*). The first grain is prismatic, approximately 150 µm, subhedral with core double-rim internal structure in CL. Oscillatory zonation is visible in the truncated core. The light rim has patchy zonation, the dark one has weak patchy zonation. The second grain is approximately 70 µm, euhedral, equant with a core-rim internal structure. Truncation, oscillatory zonation, and light patchy zonation are apparent structures in the core. The rim is light with straight angles. The third grain is tabular, approximately 150 µm, and subhedral with a core-mantle structure. The core has no visible zonation, and the mantle is light with patchy zonation. Closer to the core, it gets gradually lighter. The rims are interpreted as metamorphic, while the cores are interpreted as magmatic detrital.

The seven analyses were plotted in a TW-diagram, shown in *Figure 91*. The core analyses interpreted as detrital zircon lay around 1400-1500 Ma and have a concordance > 90% with a Th/U > 0.17. The metamorphic analyses are scattered in the TW-diagram, with two discordant analyses and one almost concordant. One mixed analysis is present, interpreted as mainly inherited due to a high Th/U ratio.

Despite few analyses, a possible explanation for the discordant analyses is indicated in the TW-diagram (*Figure 91*). The causes of discordance can be several factors, as discussed in *3.1.3*. If one assumes that the metamorphic analysis represents the same metamorphic event obtained from the other samples (around 430 Ma), a possible explanation for the most discordant metamorphic analysis can be the incorporation of $Pb_c$. A discordia was constructed through the concordant metamorphic and the detrital zircons analyses yielding a lower intercept of 414 ± 8.6 Ma and an upper intercept of 5112 ± 590 Ma (MSWD = 0.000). The lower intercept is interpreted as a metamorphic event, while the upper intercept age is interpreted as the crystallization of the detrital zircon plus the additional years due to the incorporation of $Pb_c$.

A discordia was also constructed through analyses 1 and 2, which are the core and the rim of grain 1 (see table in *Appendix E*). The lower intercepts yielded an age of 399 ± 20 Ma, interpreted as the age of a metamorphic event. The upper intercept yielded an age of 1509 ± 54 Ma, interpreted as the crystallization of the detrital zircons.

An explanation for the second most discordant analysis can be a combination of age mixing (and or Pb loss) and the incorporation of $Pb_c$. Age mixing between the metamorphic and inherited ages and or Pb loss will cause the analyses to be located on a discordia between these two zircon populations. In this case, the analysis does not lay directly on the discordia, which could possibly be explained by the incorporation of $Pb_c$ as shown with an arrow in the TW plot.

Due to only few and a lack of concordant analyses it is not possible to calculate a reasonable age for the Paleozoic metamorphism. Regardless, one can see an indication of a metamorphic event at ca 400 Ma.

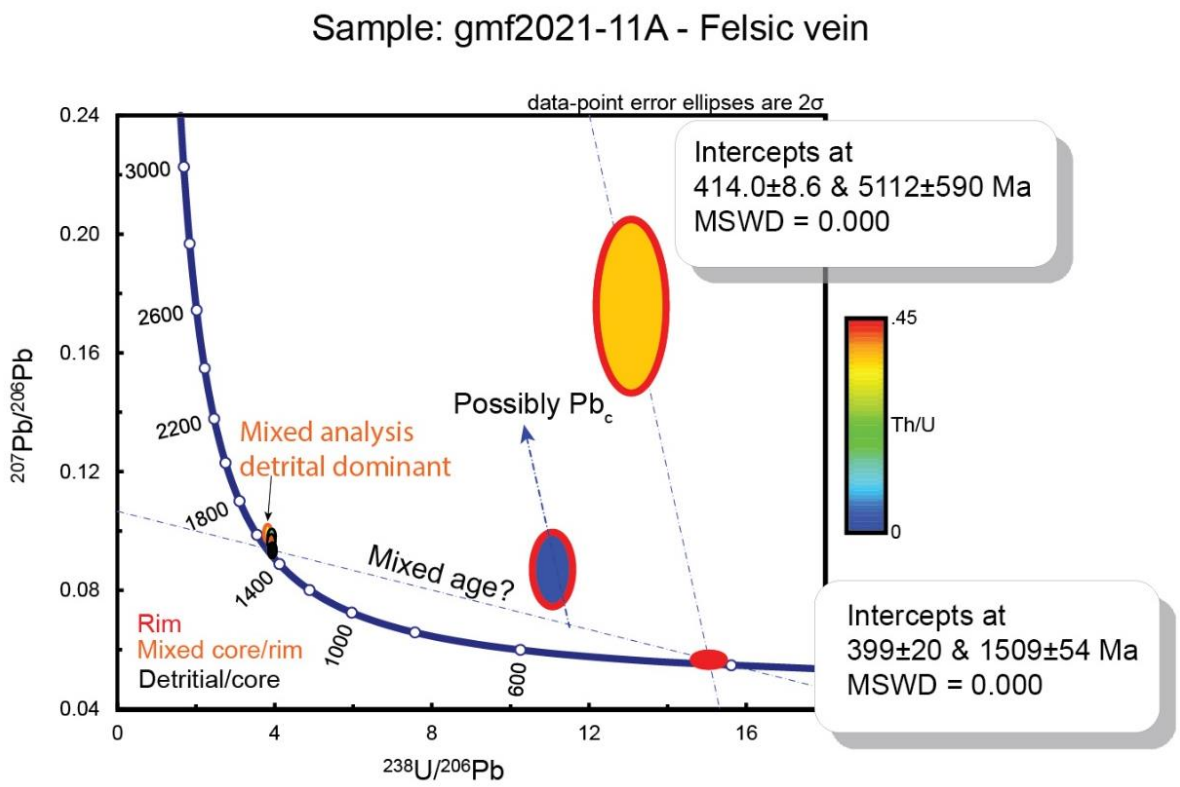


***Figure 91**: TW plot of the geochronological analyses from sample gmf2021-11A (felsic vein). Red ellipses are interpreted as zircons with a metamorphic origin, the black, magmatic origin.*

**Sample gmf2021-11C - Garnet mica schist**

Twenty-three analyses were done on twenty-two zircon grains in this sample (see table in *Appendix E*). The grains vary between 50 and 100 µm and have subhedral and prismatic to a rounded/tabular shape. Three main different internal structures are visible in CL. 1) Tabular to prismatic dark grains with no zonation, interpreted to have a metamorphic origin. 2) Tabular to prismatic grains with mantle core structure. Light cores and dark mantles. The mantles are dark with no visible zonation, interpreted as metamorphic. Some of the lighter cores show oscillatory zonation and are interpreted to be magmatic detrital zircons. 3) Dark grains with round to prismatic shapes and weak to distinct oscillatory zonation, are interpreted to be magmatic detrital zircons.

The twenty-three analyses were plotted in a TW-diagram, see *Figure 92*. The ellipses with a green rim (rim analyses) are interpreted as metamorphic, mainly based on internal structures revealed on CL images. The black ellipses are analyses conducted on cores (detrital) or whole grains (detrital or metamorphic). The Paleozoic whole grains analyses are interpreted as providing metamorphic ages based on the low Th/U content and the metamorphic texture revealed in CL. The cores and detrital whole grains have Proterozoic ages with concordance > 85%. The red ellipses are mixed core-rim analyses based on low Th/U these analyses are interpreted as metamorphic. The correlation between the Th/U content and the origin of the zircon is apparent in this diagram. The detrital grains and detrital cores have higher Th/U content than the Paleozoic metamorphic zircons, which matches the theory discussed in *3.1.4*.

Three different ages were calculated from sample gmf2021-11C:

Constructing a discordia through the Paleozoic metamorphic analysis with concordance > 88%, anchoring in 1 Ma, yielded an upper intercept age of 471 ± 17 Ma (MSWD = 0.64) (*Figure 92b*). This age is interpreted as the timing of a metamorphic event, assuming that a recent Pb loss has occurred.

A discordia was also constructed through all the Paleozoic analyses (*Figure 92c*). A lower intercept age of 439 ± 11 Ma and an upper intercept age of 1958 ± 680 Ma (MSWD = 4.7). This discordia calculation assumes that all the metamorphic analyses are related and that the more discordant analyses occur due to varying Pb loss. The 439 ± 11 Ma age is interpreted as the timing of a metamorphic event, while the 1958 ± 680 Ma age is interpreted as the timing of crystallization of the belonging detrital zircons.

One way to test the hypothesis about recent Pb loss occurring is to look at variation patterns in the alpha dose value (*3.1.3*). *Figure 92d* shows a TW plot with the Paleozoic metamorphic analyses with concordance > 88% (same analyses as in *Figure 92b*). The filling color in the ellipses illustrates the alpha content in each analysis calculated using the Th and U content. The hypothesis is that the youngest discordance analysis has undergone a recent Pb loss and thus abandoned the concordia from the hypothetical age, which was set to 450 Ma. If actual recent lead loss had occurred, one would expect the alpha dose to the analyses to increase gradually away from ca. 450 Ma towards the youngest and most discordant analyses (as discussed in 3.1.3). One can see in this diagram that this is not the case, thus it is hard to argue in favor of a recent Pb loss and that the age calculated by anchoring in 1 Ma (471 ± 17 Ma, *Figure 92b*) is reliable.

The 439 ± 11 Ma age calculated by constructing a discordia through all the Paleozoic analyses does not seem likely because of the high MSWD (MSWD = 4.4). The scatter of the zircons indicates that the analyses plot on several discordias, not just one, as assumed in this calculation. One explanation for the high MSWD could be the presence of several metamorphic events between 480 and 420 Ma.

As discussed above, recent Pb loss does not seem like the cause for the scattering of the analyses, so it is assumed that the actual metamorphic event or events happened in one place between the youngest and the oldest Paleozoic metamorphic analysis. It is not possible to separate these events based on this diagram so the preferred age for a metamorphic event for sample gmf2021-11C is 439 ± 11 Ma.

**Summary key points:**

- Indication of a metamorphic event at 439 ± 11 Ma.
- Indication of several metamorphic events between 480 and 420 Ma

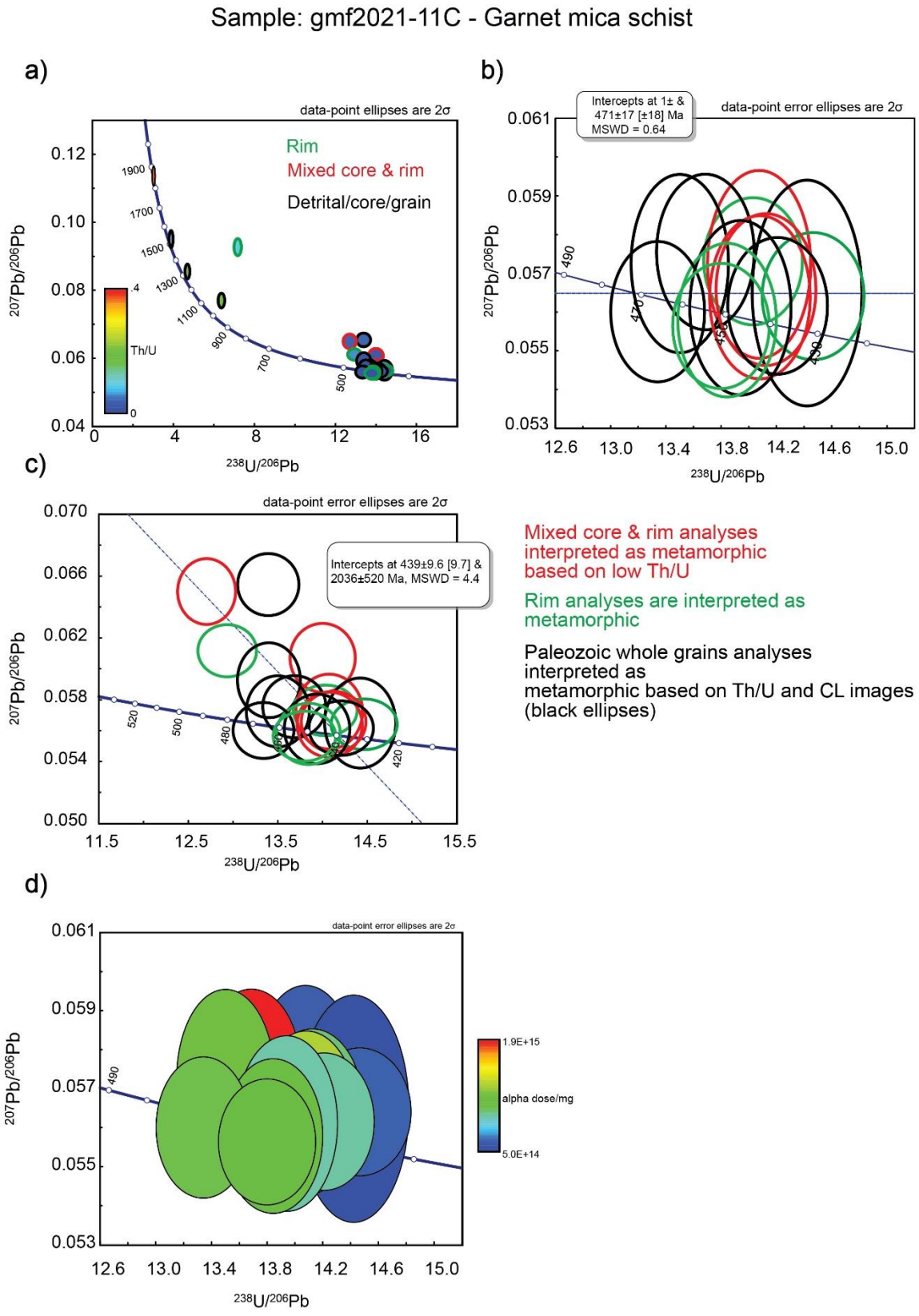


***Figure 92**: A) TW plot of the line analyses from sample gmf2021-11C. The filling color of ellipses indicates the Th/U content. B) Discordia through the Paleozoic metamorphic analysis with concordance > 88% with anchoring in 1 Ma. C) Discordia constructed through all the Paleozoic analyses. D) TW plot of the Paleozoic metamorphic analyses with concordance > 88%. The filling color display the variation in alpha dose/mg.*

**Sample gmf2021-14 - Garnet mica schist**

In sample gmf2021-14, eighteen analyses on eighteen different zircon grains were conducted (see table in *Appendix E*). The zircons vary in size from 40 to 100 µm. They are prismatic to rounded and have euhedral to anhedral shapes; the majority are subhedral and tabular in shape. In CL, the rounded to subrounded dark grains with oscillatory zonation and light cores are interpreted to be of magmatic origin. Dark homogenous rims and grains with no visible zonation are interpreted as metamorphic. Th/U was also used as an additional indicator of whether the grains had a magmatic or metamorphic origin.

*Figure 93a* shows a TW plot with the eighteen analyses plotted. The red ellipses show the analyses conducted on rims, while the black ellipses were conducted on cores (detrital) or whole grains (detrital or metamorphic). The Paleozoic whole grains are interpreted as metamorphic based on the low Th/U ratio. One mixed rim/core analysis is plotted in the diagram (orange ellipse). Two metamorphic analyses are present, one rim and one whole grain, possibly associated with Pb loss.

Two ages were calculated in an attempt to obtain an indication of the timing of a Paleozoic metamorphic event. 1) One concordia age of the four Paleozoic most concordant analyses was calculated to 449.6 ± 5 Ma (MSWD = 3.0, probability of concordance = 0.083) (*Figure 93b*). 2) A $^{206}Pb/^{238}U$ weighted average age of the same four Paleozoic analyses was calculated to be 449.1 ± 5 Ma (MSWD = 1, probability = 0.39) *(Figure 93c*).

Both ages are similar, making 449 Ma the most likely age for a metamorphic event. Two analyses stand out in the TW plot. The youngest ($^{238}U/^{206}Pb$ age) Paleozoic analysis could possibly have been exposed to recent lead loss, so that the analysis could initially plot on one of many discordias between the Proterozoic and Paleozoic analyses. The incorporation of $Pb_c$ could explain the most discordant analysis.

**Summary key point:**

- Indication of a metamorphic event around 449 Ma

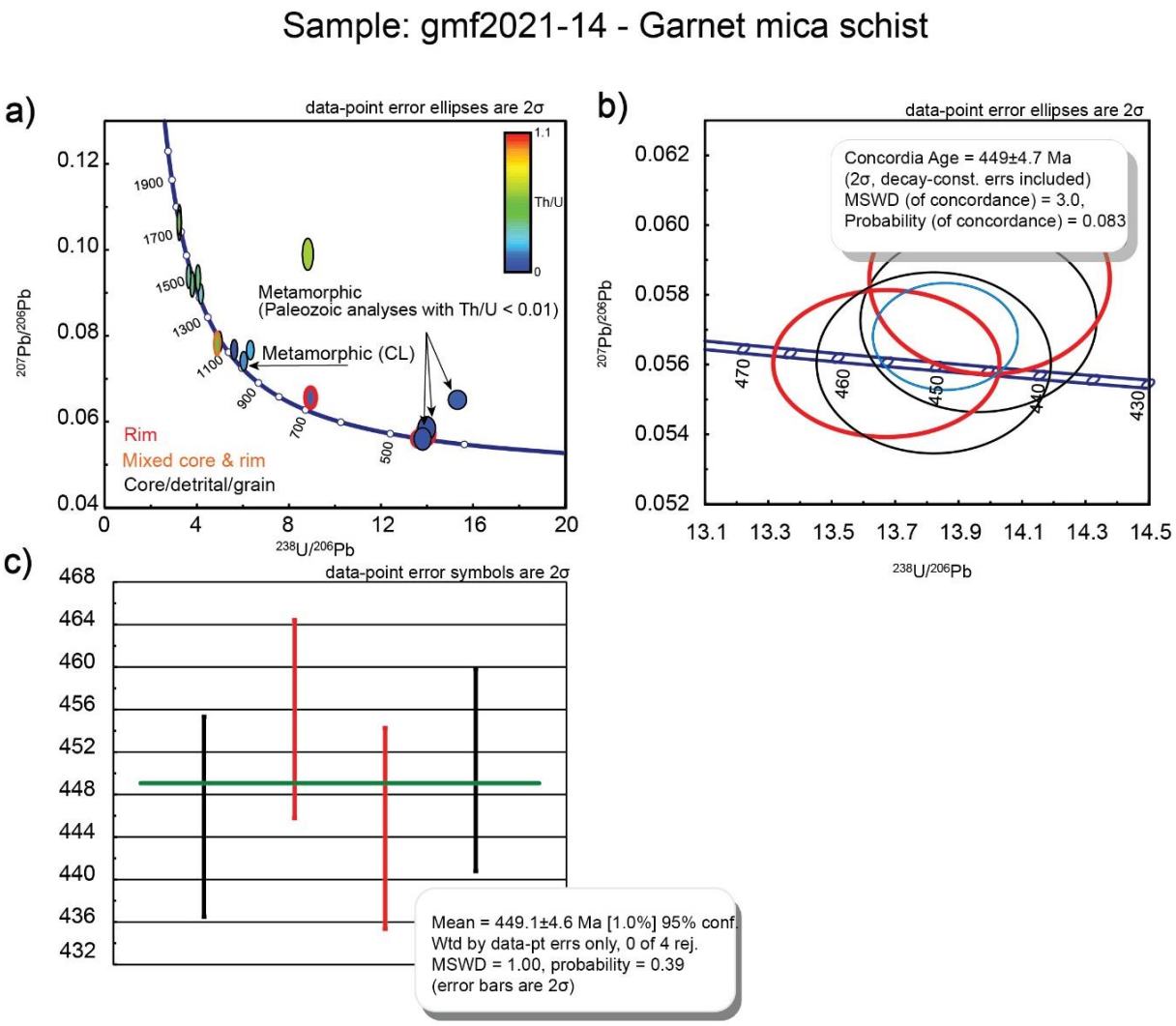


***Figure 93**: A) TW plot of analyses from sample gmf2021-14. The ellipses with red rims are interpreted as metamorphic analysis, while the black ellipses, magmatic. The filling color of ellipses indicates the Th/U content.*

### Sample BKS132409 – Garnet mica schist

Twenty-eight analyses were conducted on nineteen different grains in sample BKS132409 (sample from Storruste (2017), data in *Appendix E*). The zircon varies in size from approximately 50 to 100 µm, anhedral to euhedral, have subrounded, tabular and prismatic shapes. In CL-imaging, most of the zircons have complex internal structures with several generations of cores and rims. The rims are interpreted as metamorphic zircon, while the homogenous and oscillatory zoned cores and the whole grains are interpreted as magmatic.

*Figure 94* shows a TW plot with the twenty-eight plotted analyses. The red ellipses show the rim analyses, and the black ellipses show the core and whole grain analyses. The analyses are mainly scattered around three areas on the concordia, 1600-1700 Ma, 1400-1500 Ma, and 1000 Ma, looking at $Pb^{207}/Pb^{206}$ ages. The high Th/U value for all the analyses and the old ages indicate strongly that the zircon analyzed are inherited.

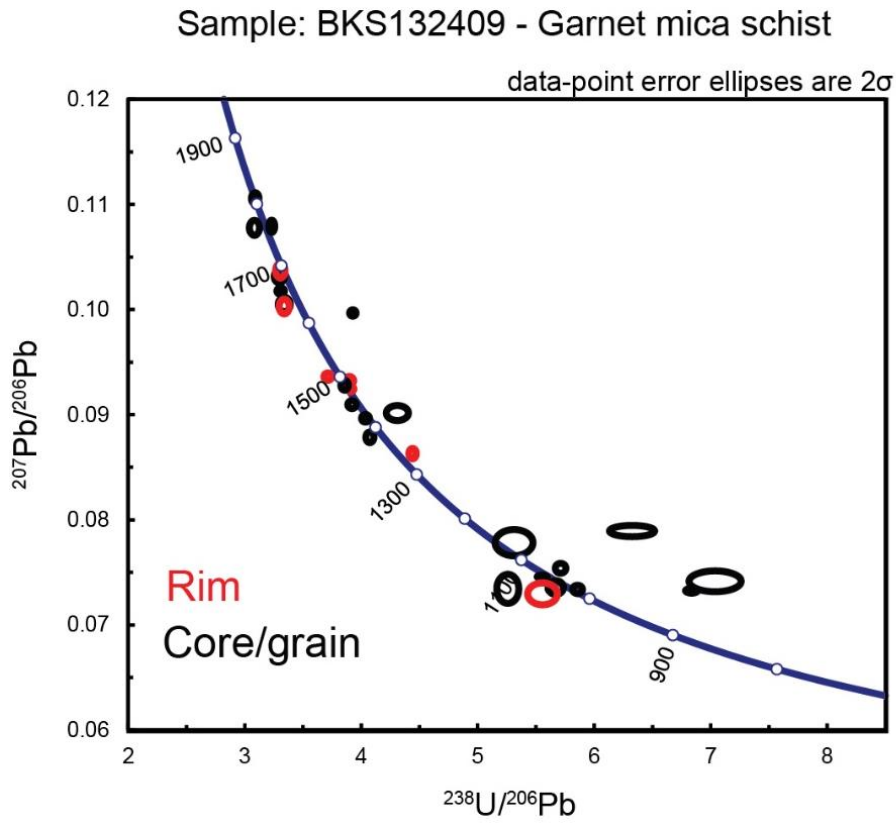


***Figure 94**: TW plot of the analyses from sample BKS132409.*

### Summary of the metamorphic zircon ages

An overview of the metamorphic ages obtained from this study is shown in *Table 2*. The data mainly suggests metamorphic events around 437 Ma and 450 Ma.

***Table 2**: Summary of U-Pb dating of metamorphic zircon.*

| Sample | UTM E | UTM N | Rock description | Age (Ma) | Comment |
|---|---|---|---|---|---|
| gmf2020-21 | 66.23696 | 14.77714 | Felsic vein | 434 ± 5 | Metamorphic event |
| gmf2021-05 | 66.23661 | 14.77872 | Felsic vein | 437.4 ± 6 | Metamorphic event |
| gmf2021-07A | 66.23534 | 14.78177 | Reaction rim | 449 ± 6 | Metamorphic event |
| gmf2021-11C | 66.24006 | 14.78904 | Garnet mica schist | 439 ± 11<br>480-420 | Metamorphic event/events |
| gmf2021-14 | 66.24005 | 14.87401 | Garnet mica schist | 449.6 ± 5<br>449.1 ± 5 | Metamorphic event |

### Summary of detrital zircon ages

*Figure 95* shows a relative probability density plot of all the detrital zircons with concordance > 90% in this study. The data are based on the $^{207}Pb/^{206}Pb$ ages and their standard derivations.

The plots illustrate two main peak ages, around 1480 and 1620 Ma. Otherwise, smaller peaks occur at around 980, 1040, 1080, 1140, 1180, 1340, 1380, 1420, 1440, 1660, 1680, 1760 and 1820 Ma.

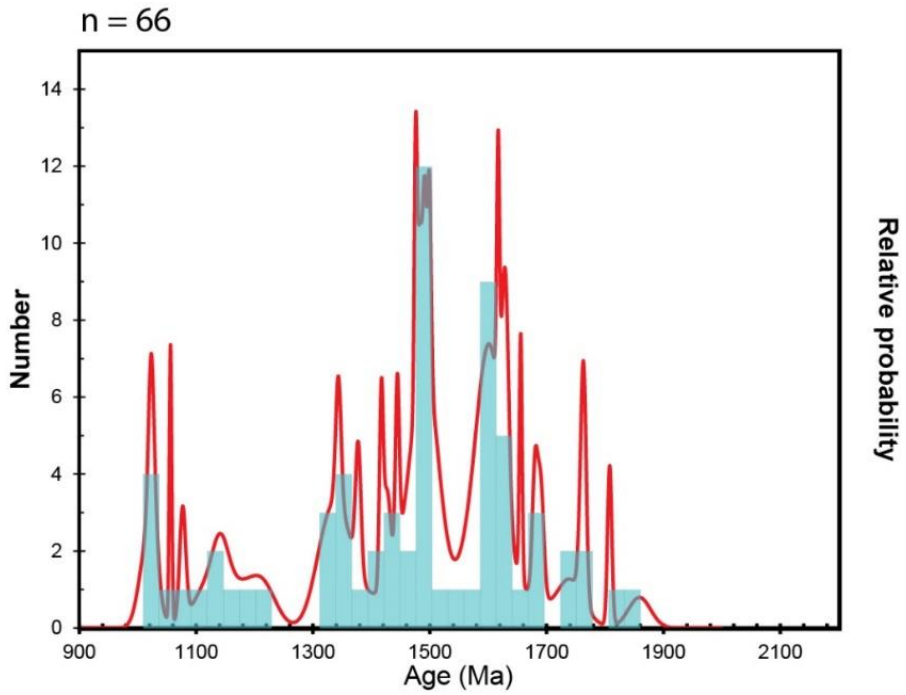


***Figure 95**: Relative probability plot and histogram of the detrital zircons dated in this study. The vertical axis shows numbers of zircons, and the horizontal shows the dated ages.*

## Monazite geochronology

This section will present the geochronological data obtained by dating monazite in thin section with LA-ICP-MS. Thin sections collected were examined by polarization microscope and SEM to check if the samples contained monazite. Four thin sections with monazite were analyzed. The monazite data from sample gmf2020-02, gmf2020-10, and gmf2020-11 are shown in *Appendix E* (see *Figure 84* for sample locations). Sample gmf2020-09 was excluded because of inadequate data. In most samples, the monazite grains were too small to be analyzed with the laser, so the amount of data initially desired was not fulfilled.

### Sample gmf2020-02 – garnet mica schist

In sample gmf2020-02, eight different analyses were done. The monazite grains vary in size from 25 to 50 µm, six monazites located in garnet (1 analysis excluded due to high age uncertainty), and two monazites in the matrix (*Appendix E* and *Figure 96*).

*Figure 97* shows the analyses plotted in a TW diagram. The monazites occurring as inclusions in garnet are marked with red ellipses, while the ellipses belonging to the monazites in the matrix have black ellipses. One immediate observation between the monazites in the garnet and the matrix is that the monazite in the garnet has both Paleozoic and Neoproterozoic ages. Older ages could be explained by the garnet behaving like a shield around the monazite and protecting the monazites from Pb loss. The analyses plotted have a concordance > 85% except for two analyses, one in garnet and one in the matrix.

Despite limited data, two different ages were calculated:

A concordia age of two concordant analyses was calculated to be 484.1 ± 6 Ma (MSWD = 2.5, probability of concordance = 0.12) and one $^{238}U/^{206}Pb$ age of the youngest monazite was calculated to 458.6 ± 4 Ma.

In addition, by studying the TW-plot one can observe that there are two Neoproterozoic analyses around 560 and 600 Ma indicating one or several Neoproterozoic events. The two most discordant analyses could be explained by the incorporation of common Pb and could possibly plot on a discordia intercepting any of the concordant monazite analyses.

**Summary key points:**

- Indication of a metamorphic event at 484.1 ± 6 Ma
- Indication of a metamorphic around 458 Ma
- Indication of Neoproterozoic metamorphism (around 560 and 600 Ma)

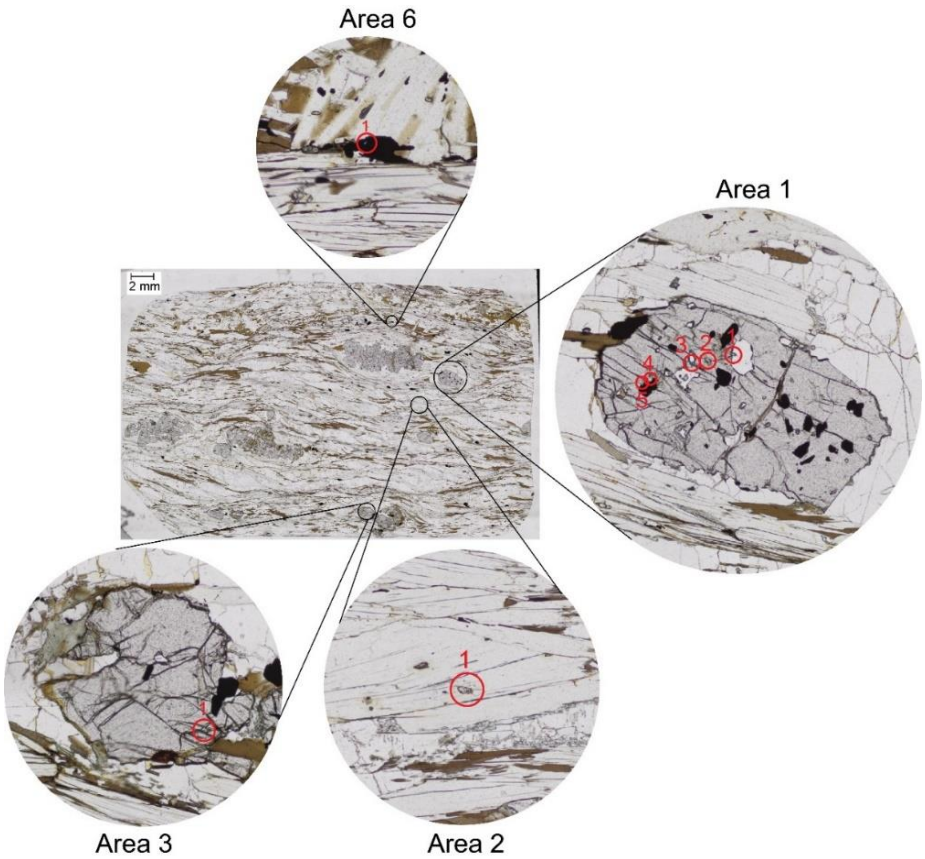


***Figure 96****: Scan of a thin section from sample gmf2020-02 with enlarged images of the areas where the monazites analyzed are located. The monazites are marked with red circles and numbers. The area and numbers match the information given in Appendix E.*

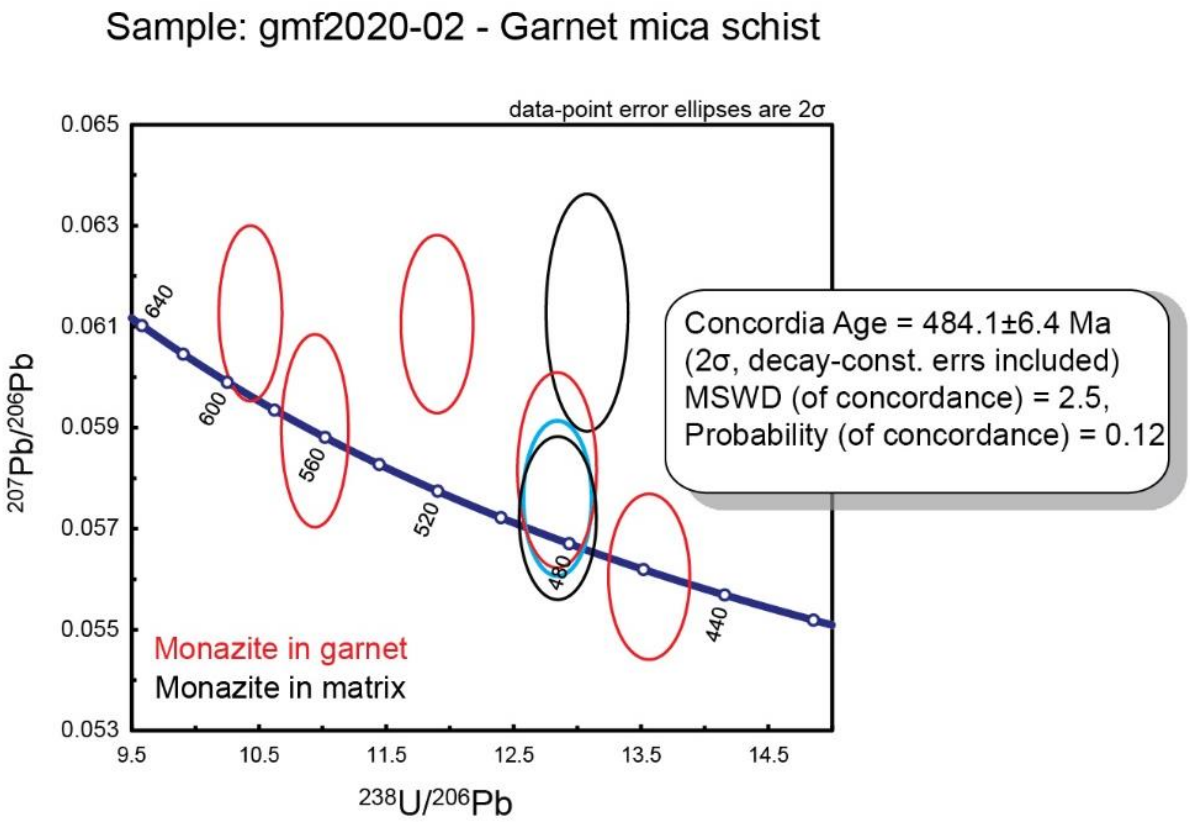


***Figure 97**: TW plot of monazite analyses from sample gmf2020-02. Analyses of monazite as inclusions in garnet have red ellipses, the monazites located in the matrix have black ellipses.*

**Sample gmf2020-10 – garnet mica schist**

Four analyses were conducted on four different monazite grains in sample gmf2020-10 (see *Appendix E*). The grain sizes vary between 30 and 50 µm. One of the analyzed grains is located in a garnet, the rest in the matrix (*Figure 98*).

*Figure 99* shows a TW diagram with the four analyses plotted. Two of the analysis are highly discordant, while two are more concordant. The concordant Paleozoic analyses located inside a garnet have a $^{238}U/^{206}Pb$ age of 366 ± 19 Ma, and the monazite within the matrix has an age of 412.7 ± 6 Ma.

**Summary key points:**

- Indication of a Paleozoic metamorphic event around 412 and or 360 Ma

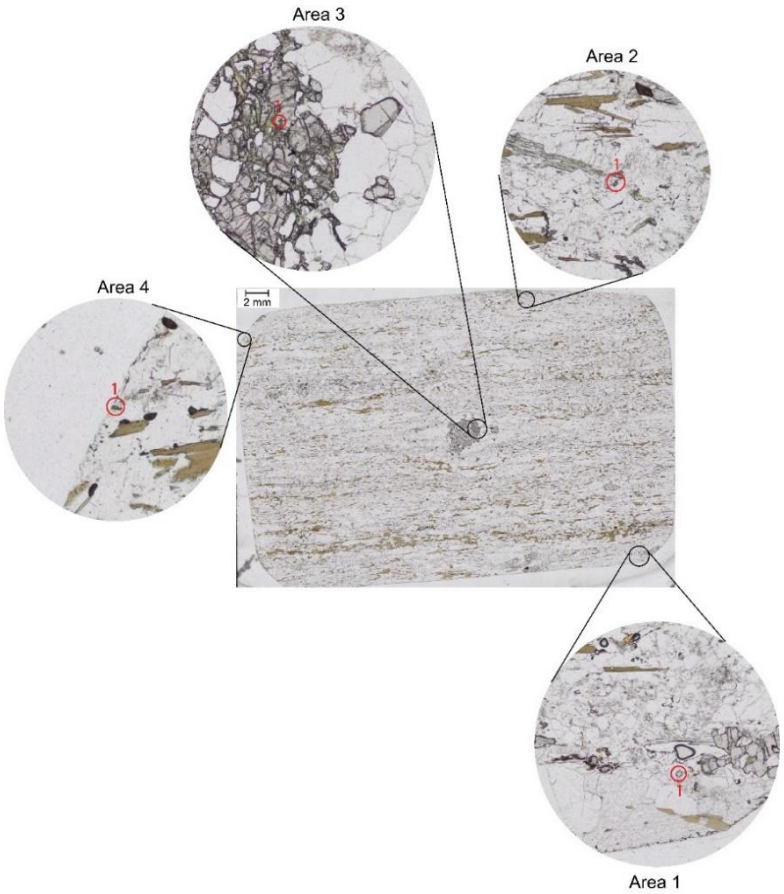


***Figure 98**: Scan of a thin section from sample gmf2020-10, enlarged images of the areas where the monazites analyzed are located. Monazites are marked with red circles and numbers. The areas and numbers match the information given in Appendix E.*

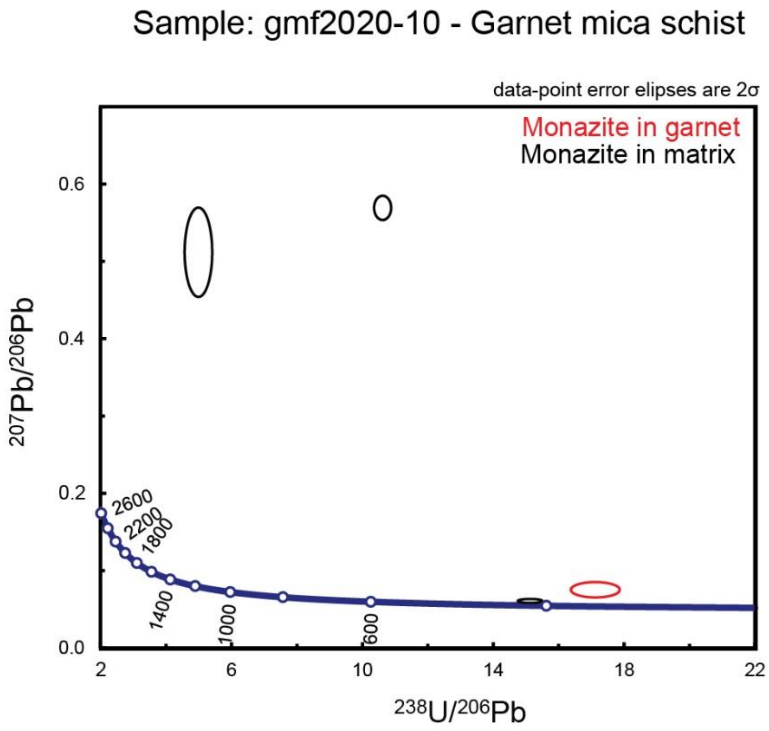


***Figure 99**: TW plot of monazite analyses from gmf2020-10. The red ellipse marks the analysis conducted of a monazite as inclusion in a garnet.*

**Sample gmf2020-11 – garnet mica schist**

This sample was taken at sauvasshytta (near Umbukta). In sample gmf2020-11, six monazite grains were dated (see table in *Appendix E*). The monazites are located in the matrix and vary in size from 20 to 40 µm (*Figure 100*).

*Figure 101* shows the analyses plotted in a TW diagram. The six analyses lay on an apparent line showing a gradual increase in $^{207}Pb/^{206}Pb$ and a decrease in $^{238}U/^{206}Pb$ towards the older analyses. The main cause for this discordance is probably by the incorporation of $Pb_c$.

A discordia was constructed through all the monazite analyses. The upper intercept age, 4233 ± 190 Ma, is interpreted as elevated due to $Pb_c$ in the discordant analysis. A lower intercept age was calculated to be 559.9 ± 8 Ma (MSWD = 2.3), interpreted to be the age of a Neoproterozoic metamorphic event.

**Summary key points:**

- Indication of a metamorphic event at 559.9 ± 8 Ma.
- Clear illustration of variable incorporation of $Pb_c$ in the analyses.

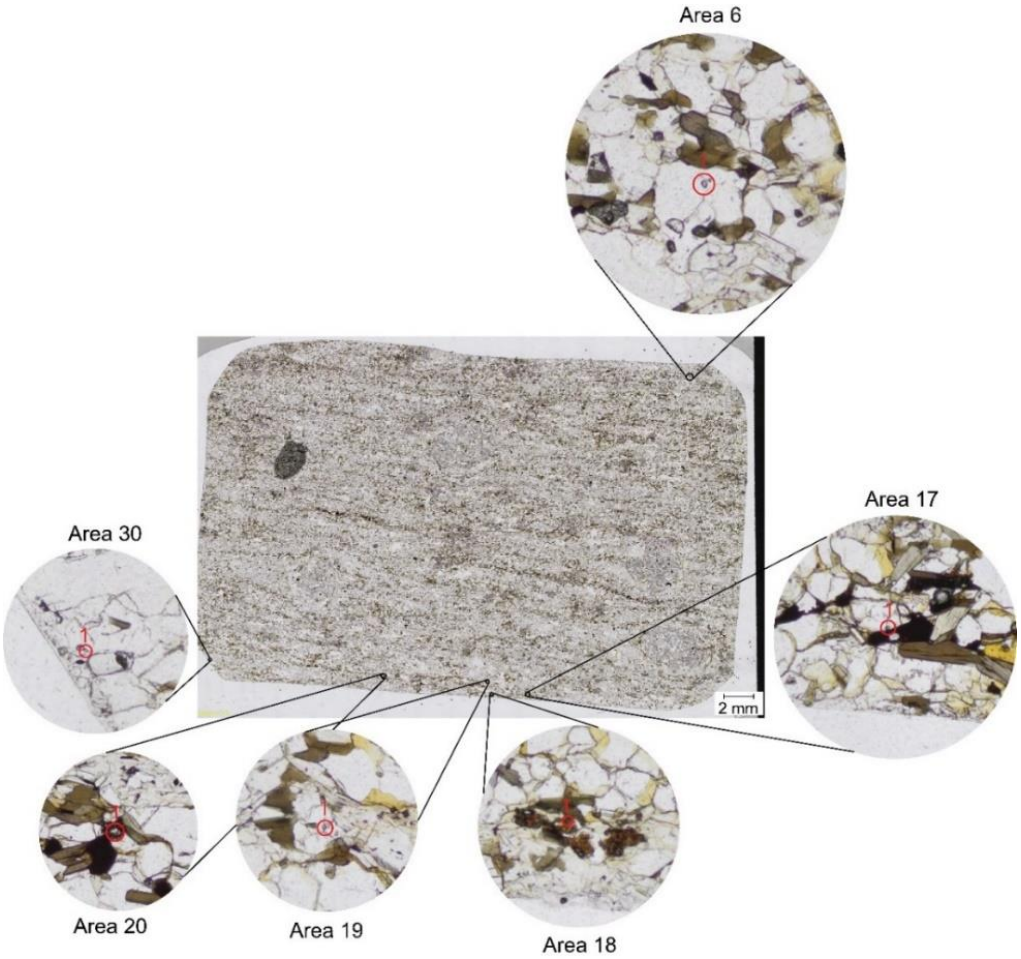


***Figure 100**: Scan of a thin section gmf2020-11 with enlarged images of the areas where the monazites analyzed are located. The monazites are marked with red circles and numbers. The area and numbers match the information given in Appendix E.*

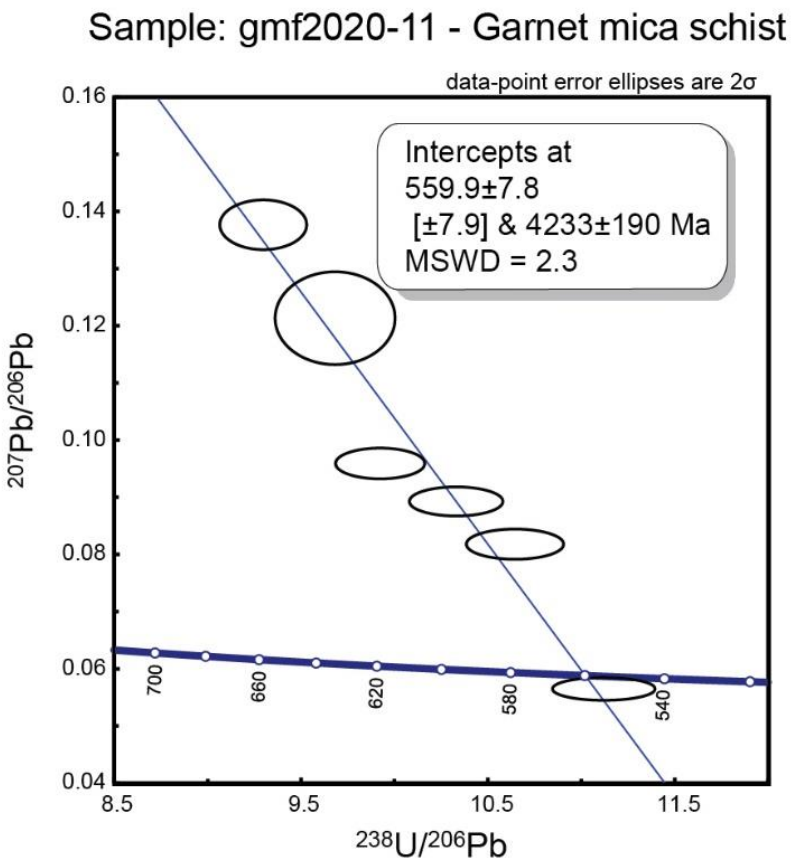


***Figure 101**: TW plot of monazite analyses from gmf2020-11. All these monazites were located in the matrix.*

### Summary of metamorphic monazite ages

Despite not a lot of data, the analyses indicate metamorphic events around 360-412, 458, 484, 560 and 600 Ma (*Table 3*).

***Table 3**: Summary of the U-Pb monazite data.*

| Sample | UTM E | UTM N | Rock description | Age (Ma) | Comment |
|---|---|---|---|---|---|
| gmf2020-02 | 66.24847 | 14.95553 | Garnet mica schist | 484.1 ± 6<br>458.6 ± 4<br>600-560 Ma | Metamorphic events |
| gmf2020-10 | 66.30726 | 14.81168 | Garnet mica schist | c. 412 and 360 | Metamorphic event (based on two analyses) |
| gmf2020-11 | 66.18046 | 14.72946 | Garnet mica schist | 559.9 ± 8 | Metamorphic event |

### 5.2.2 Igneous geochronology

This section will showcase igneous geochronology from the Kjerringfjell Group. Three additional data sets, field descriptions and field photographs were added to this thesis, collected from Trond Slagstad (unpublished data) and is presented below. Full U-Pb data sets are given in *Appendix E*.

**Sample MO_028781 – Tonalite – NE in Kjerringfjell**

The tonalite is located in the Kjerringfjell Group a few km northeast of Kallvatnet. The tonalite is medium to coarse, weakly foliated and locally pegmatitic. The main mafic mineral biotite is dispersed but locally forming rounded lumps in sizes of 3-4 cm.

*Figure 102* show a TW-plot presenting a concordia-age of 466 ± 2 Ma (MSWD = 2.1) for a tonalite (sample MO_028781) in the northeastern part of Kjerringfjell. The age is interpreted as the crystallization age of the tonalitic body. The light grey ellipses in the TW-plot were not included in the concordia-age calculation.

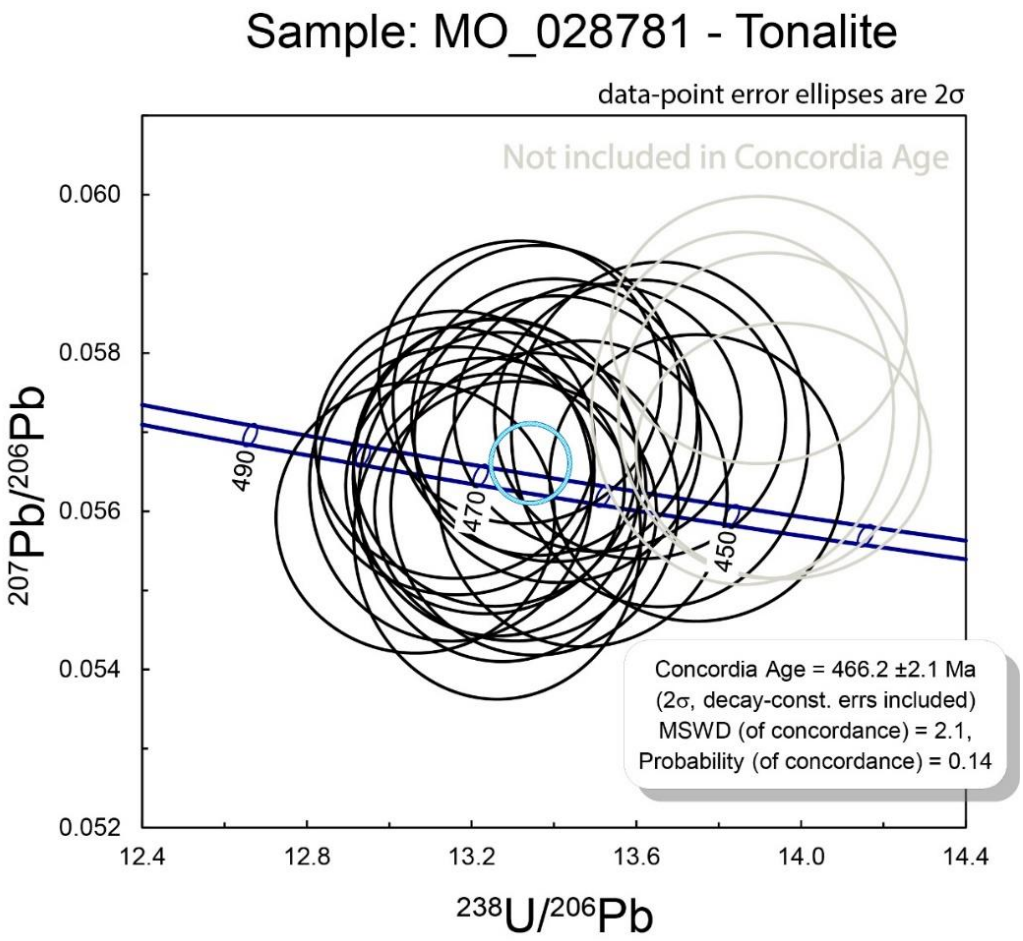


***Figure 102**: Concordia age for the tonalite in the Kjerringfjell Group. Sample MO_028781. The grey ellipses were not included in the age calculation. Data set from Trond Slagstad (unpublished).*

**Sample 200037 and 200038 – Umbukta**

Two data sets from the Umbukta gabbro were also added and is presented below (data from Trond Slagstad (unpublished).

Sample 200037 is a feldspar-porphyroblastic gneiss consisting of 1-2 cm stubby white plagioclase porphyroblasts that are irregular distributed and surrounded by high-strain mafic matrix. In one low-strain boudin the rock has 1-2 cm dark purple plagioclase phenocrysts along the margin. (*Figure 103*).

Sample 200038 is a sample from a mafic dike that is fine to medium-grained cutting deformed porphyroblastic-rich mafic gneiss. Younger dikes also cut the mafic gneiss and the sampled dike. Both generations of dikes are strongly folded (*Figure 103*).

The first Umbukta sample (200037) (*Figure 104*a) show a TW-plot that show an upper intercept age of 614±13 Ma (MSWD = 0.76) representing the crystallization age of the gabbro. The lower intercept age is interpreted as the timing of recent lead loss. In the second sample (200038) (*Figure 104*b) a concordia age of 593 ± 3 Ma was calculated and is interpreted as the crystallization age of the dike that cuts the gabbro. The two different crystallization ages indicate several intrusion ages of the Umbukta gabbro.


***Figure 103**: Field photographs of sample 200037 and 200038 from the Umbukta gabbro. Photos from Trond Slagstad (unpublished).*

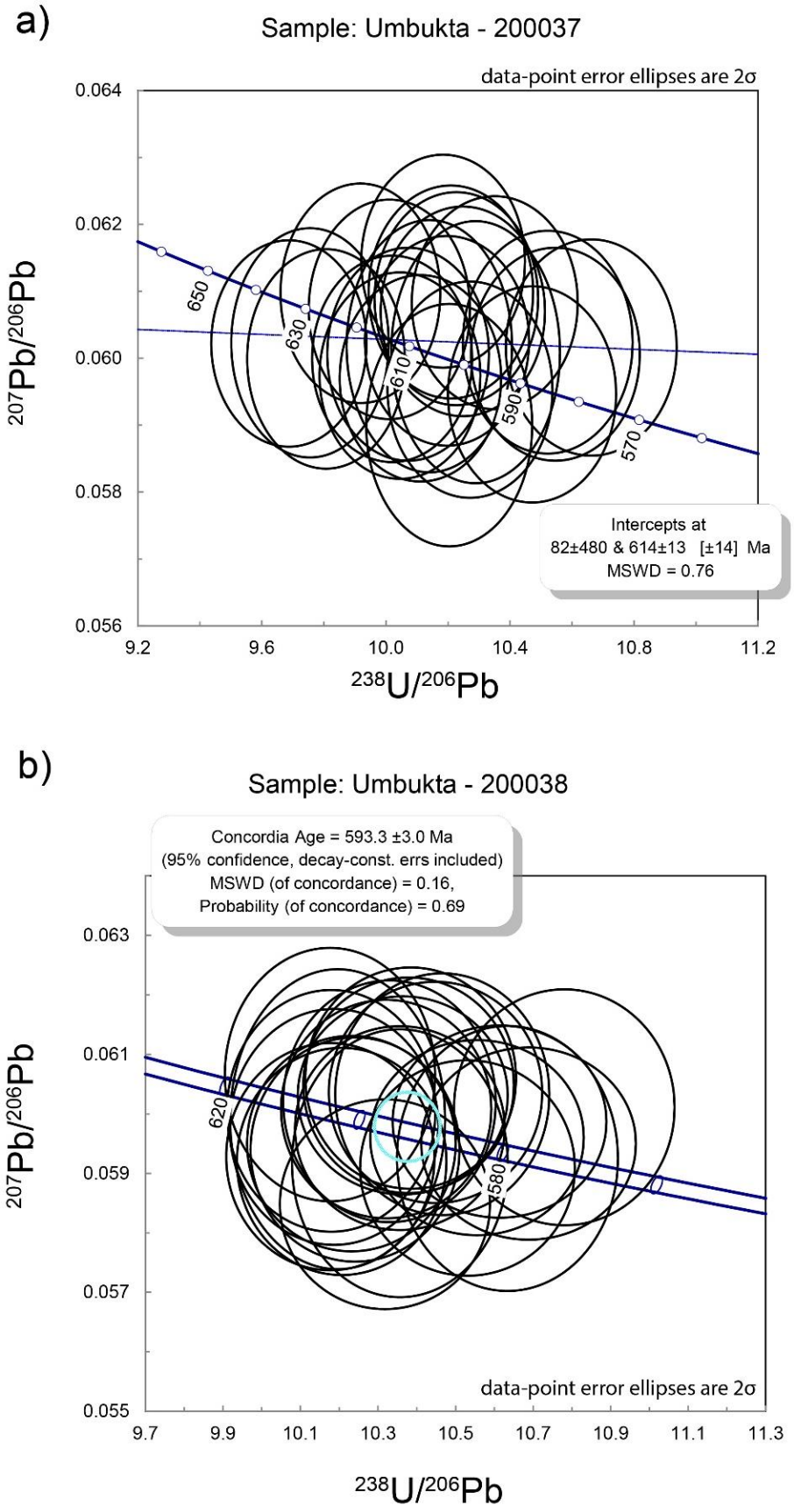


***Figure 104**: TW plot of igneous zircon ages from the Umbukta gabbro. Data set from Trond Slagstad (unpublished). A) TW plot of the analyzed gabbro. B) TW plot of a dike cutting the gabbro.*

## 5.3 Geochemistry

Geochemical data obtained from this study will be presented in this chapter. The data will be given in two main sections:

1) The concordant and discordant mafic sheets sampled at Kallvatnet and from Gammelgardsfjellet (from this study) will be compared with geochemical data from Høyen (2016); the Umbukta gabbro, mafic dikes cutting the gabbro and dikes cutting the host rock (Kjerringfjell Group). The Umbukta gabbro is located a few km south in relation to Kallvatnet. In addition, amphibolites from the Mofjellet Group (data from Slagstad et al. (2021)) located a few km west of Kallvatnet will be compared.

2) Major, minor and trace elements from the felsic veins, reaction rims, and garnet mica schists from this study will be presented and compared. Reaction rims surrounding felsic veins and garnet amphibolites are included. All the samples were gathered in the Kallvatnet area.

In total, thirty-seven samples were chosen for geochemical analyses in this study. See *Figure 105* for sample locations, subsection *4.4* for analytical methods, and *Appendix C* for the complete geochemical data set. Other datasets were also added for comparison in this study; twenty-three samples from Høyen (2016) and twenty-two samples from Slagstad et al. (2021).

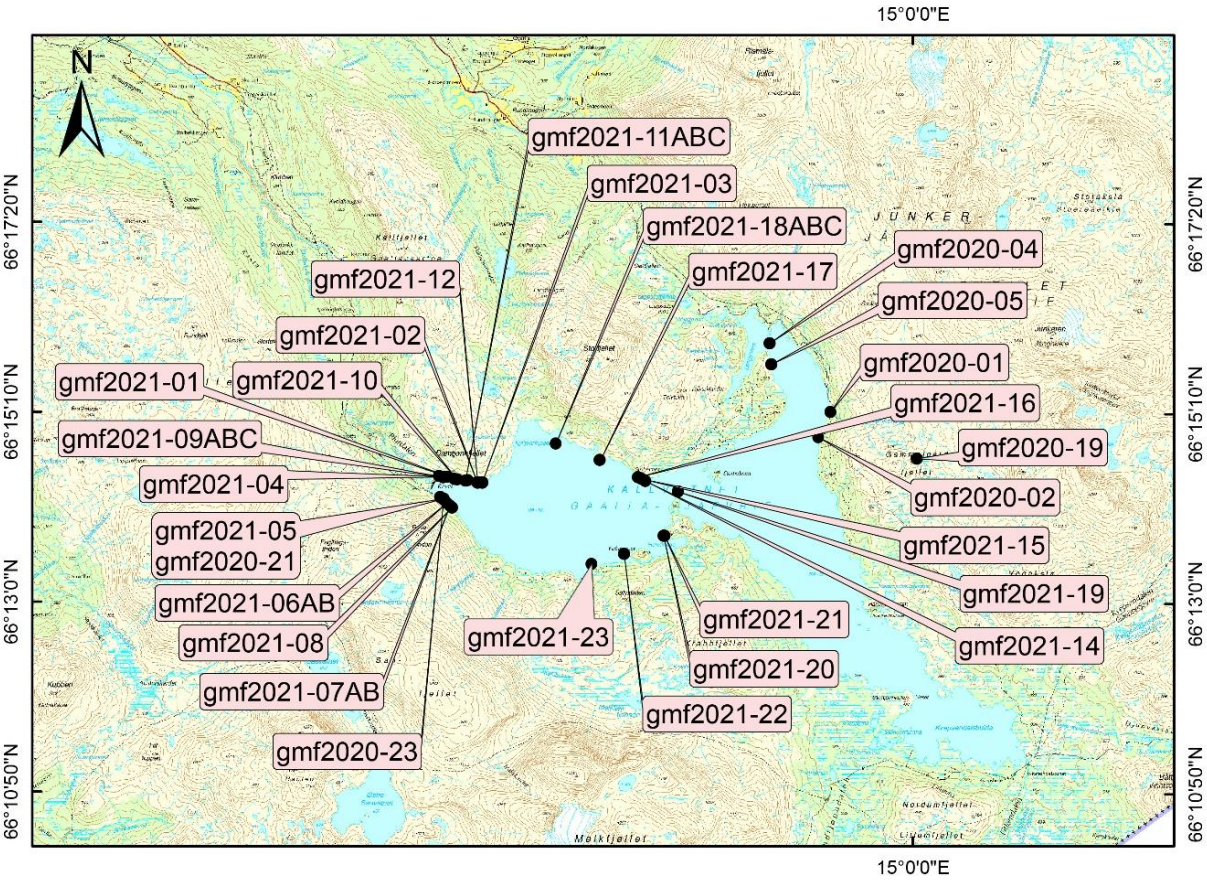


***Figure 105**: Sample map showing locations for collected samples for geochemical analyses.*

### 5.3.1 Mafic rocks – Kallvatnet compared to Umbukta and Mofjell

*Figure 106* shows the AFM diagram after Irvine and Baragar (1971). The mafic rock samples from this study and the rocks from Umbukta (from Høyen (2016)), except for one sample plot on the tholeiitic path. The amphibolites from Mofjell (from Slagstad et al. (2021)) plot on both the tholeiitic and the calc-alkaline fields in the diagram.

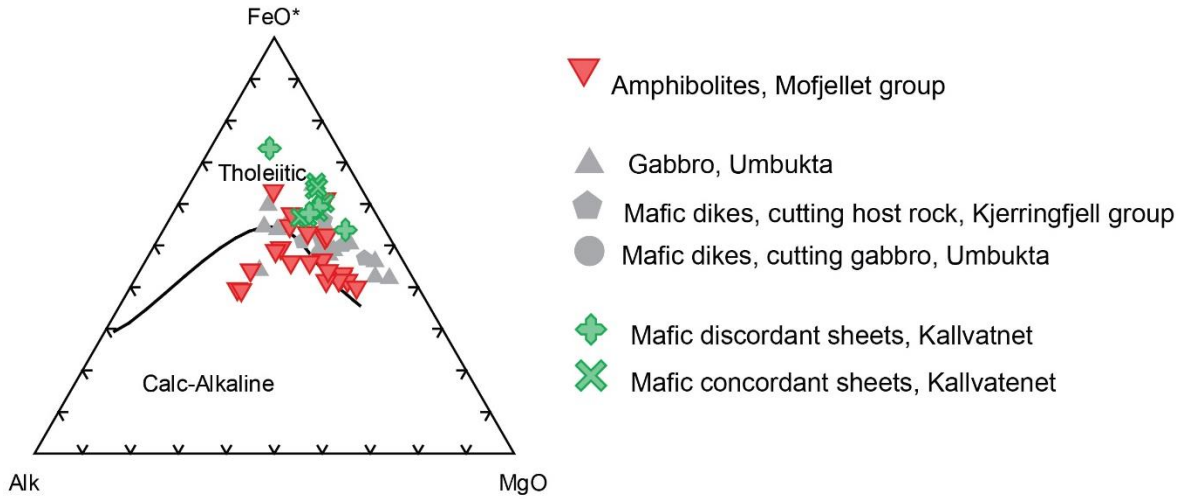


***Figure 106**: AFM diagram from Irvine and Baragar (1971). Rocks from this study (green) and Umbukta (grey) (data from Høyen (2016)) plots in the tholeiitic field. The amphibolites from Mofjell (red) (data from Slagstad et al. (2021)) plot in both the tholeiitic and the calc-alkaline fields.*

**Major elements**

*Figure 107* shows Harker diagrams displaying major elements expressed in oxides. Mafic samples from Kallvatnet/Gammelgardsfjellet (this study), Umbukta (from Høyen (2016), and Mofjell (from Slagstad et al. (2021)).

The mafic rocks sampled in this study plot mainly in linear trends with some expected scattering, the samples do not show any significant systematic differences in composition with respect to the sample locations. Hence the rocks seem to be genetically related with small variations in melt composition. The $SiO_2$ composition varies from 45,7 to 54.3 wt. %. The major elements show a negative trend for CaO, $Fe_2O_3$, MnO, and MgO, with increasing $SiO_2$ slightly positive scattered trends for $Na_2O$, $Al_2O_3$, $P_2O_5$, and $K_2O$. The diagram with $TiO_2$ is scattered, making it hard to identify trends.

The fractional crystallization of olivine can explain the negative trends for $Fe_2O_3$, MnO, and MgO, the slightly positive trend for $Al_2O_3$, and the negative trend for CaO can be explained by fractional crystallization of clinopyroxene. The slightly positive trends for $Na_2O$, $Al_2O$, $P_2O$, and $K_2O$ can be explained by the increase in the relative concentrations of feldspar and apatite in the melt during fractional crystallization of mafic minerals during the liquid line of descent. One can speculate that the scattering in $TiO_2$ has been caused by varying degrees of hydrothermal alteration, which causes depletion of Ti in basalts (see theory in *3.2.8*). Overall, the composition is relatively homogenous, the trends discussed above are not distinct, and the $SiO_2$ range is narrow, indicating a small degree of fractional crystallization.

The mafic rocks at Umbukta, on the other hand, have a higher range of $SiO_2$ concentration (42.32 to 58.4 wt. %), and have generally a higher spread in the Harker diagrams (higher degree of heterogeneity). In addition, negative and positive trends are much more distinct. The Mofjell amphibolites have a range of $SiO_2$ composition between 45.98 and 56.62 wt. %. The homogenous signature is similar to the mafic rocks at Kallvatnet, the most significant difference is the higher concentration of $Na_2O$, $Al_2O_3$ and lower concentration of $Fe_2O_3$.

**Trace elements**

Harker diagrams of trace elements from the same samples are plotted in *Figure 108* and *Figure 109*. Overall, the trace elements content has low variation, but some weak trends are observable. Nb, Ta, and Th show weakly positive trends, Y and Yb have very weak negative trends while the rest of the trace elements have flat or no clear trends. Nb and Ta tend to be incorporated into Ti-rich phases such as titanite and Ti-amphibole. Thus, the positive trend indicates that Ti-rich phases were not fractionated out of the melt during the line of descent. The increasing concentration of Th can be explained by increased feldspar content or/and continental assimilation. The negative trends for Y and Yb indicate crystal fractionation of garnet.

As with the major elements, the trace elements for Umbukta show a higher degree of fractionation. This is especially apparent in the increasing trend for Rb, which usually acts as a substitute for K in K-feldspar and mica. In addition, the Umbukta samples have a higher content of Sr, Ba, Ta, Nb, Ce, Zr, Sm and lower content of Y and Yb compared with the samples from Kallvatnet. The Mofjell samples also show a higher degree of fractionation. The most significant differences are the higher content of Sr and the lower content of Nb, Ce, Zr, Hf, Y, and Yb.

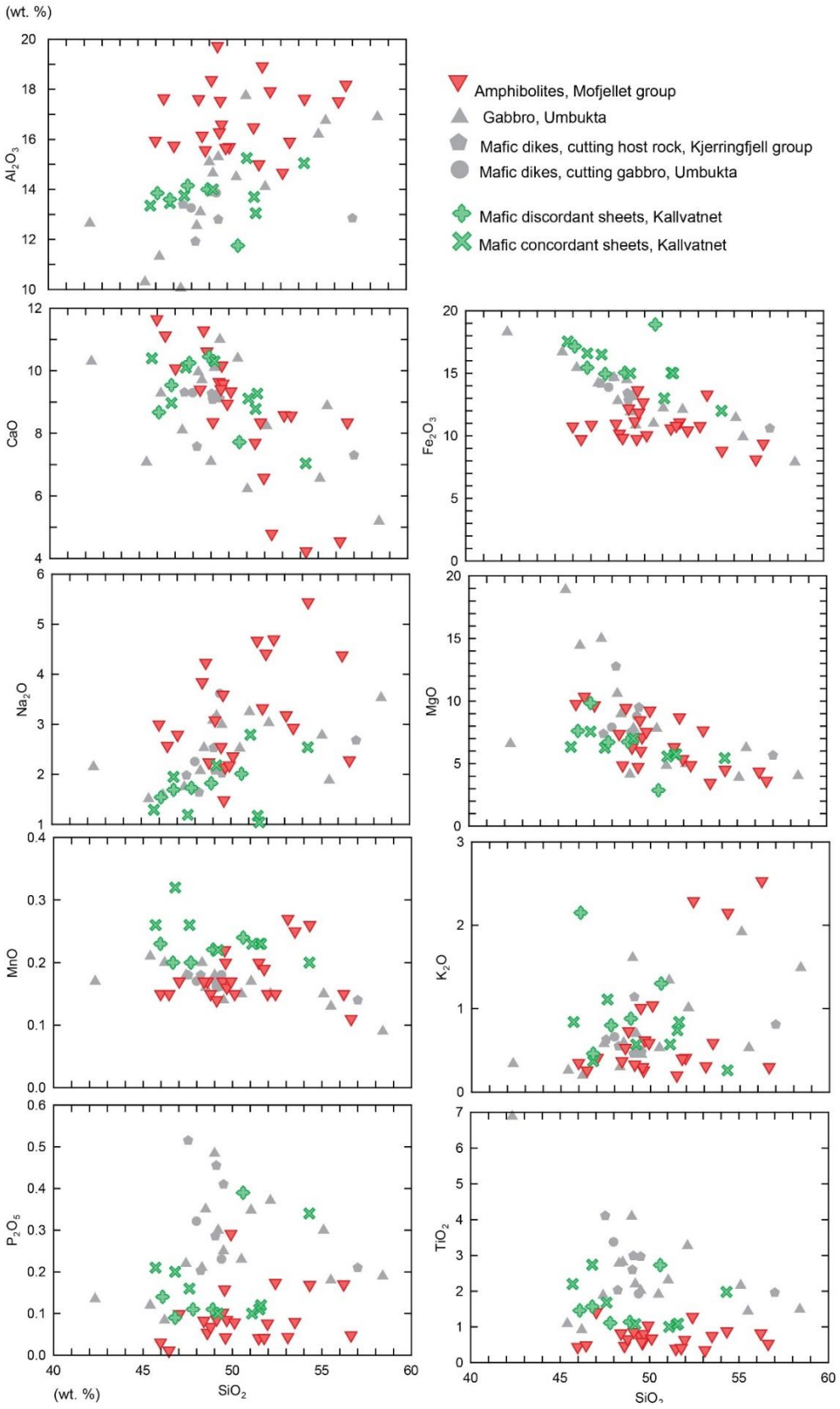


***Figure 107**: Harker diagrams with major elements from mafic rocks from Kallvatnet (green), discordant mafic sheets at Kallvatnet cutting host rock (cross), mafic concordant sheets Kallvatnet (x). Mafic rocks from Umbukta (grey), gabbro (grey triangle), Umbukta dikes cutting host rock in Kjerringfjell (grey pentagon), Umbukta dikes cutting the gabbro (grey circle). Mafic rocks from Mofjell (red).*

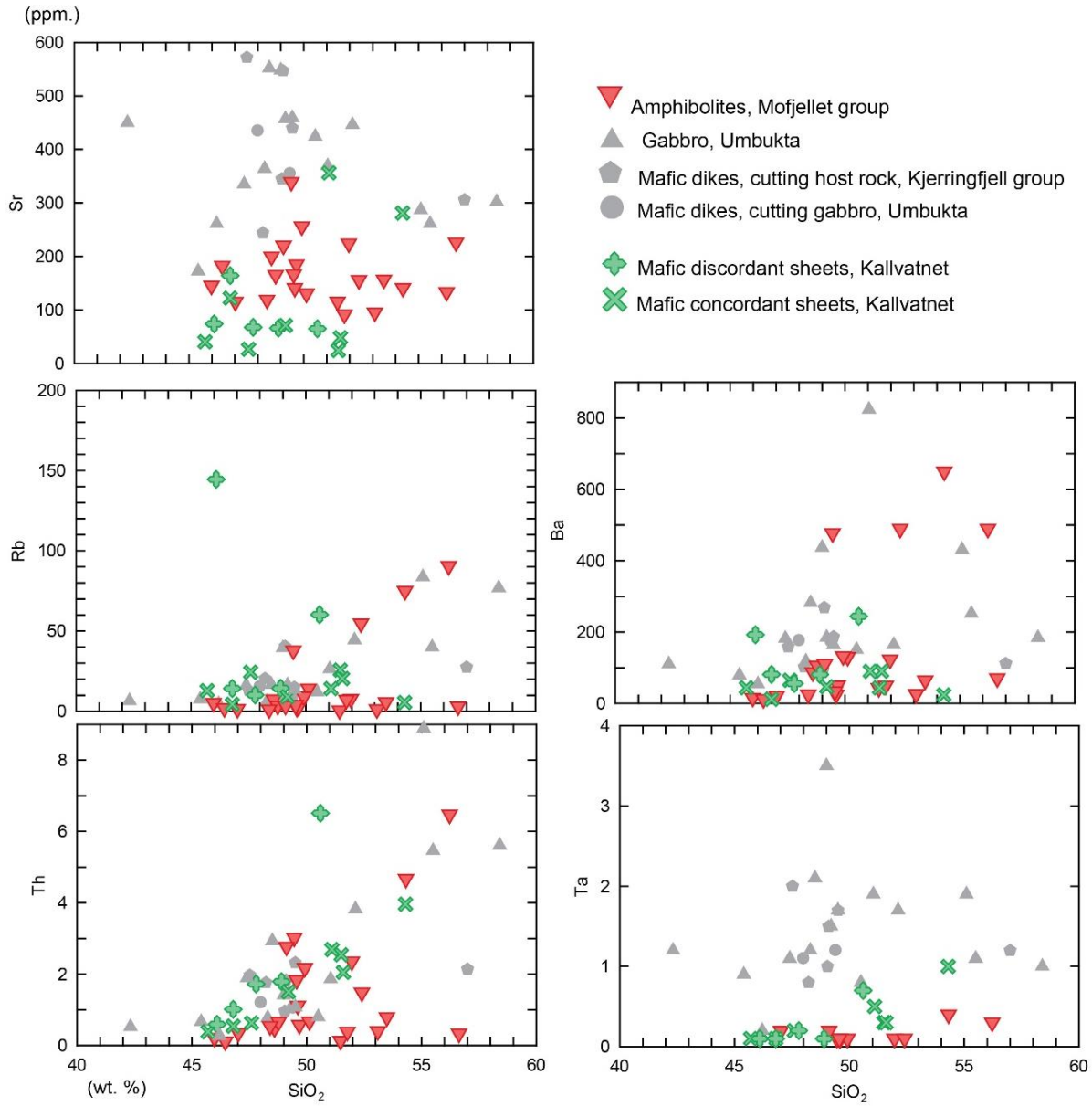


***Figure 108**: Harker diagrams with trace elements from mafic rocks from Kallvatnet (green), Umbukta (grey) and Mofjell (red).*

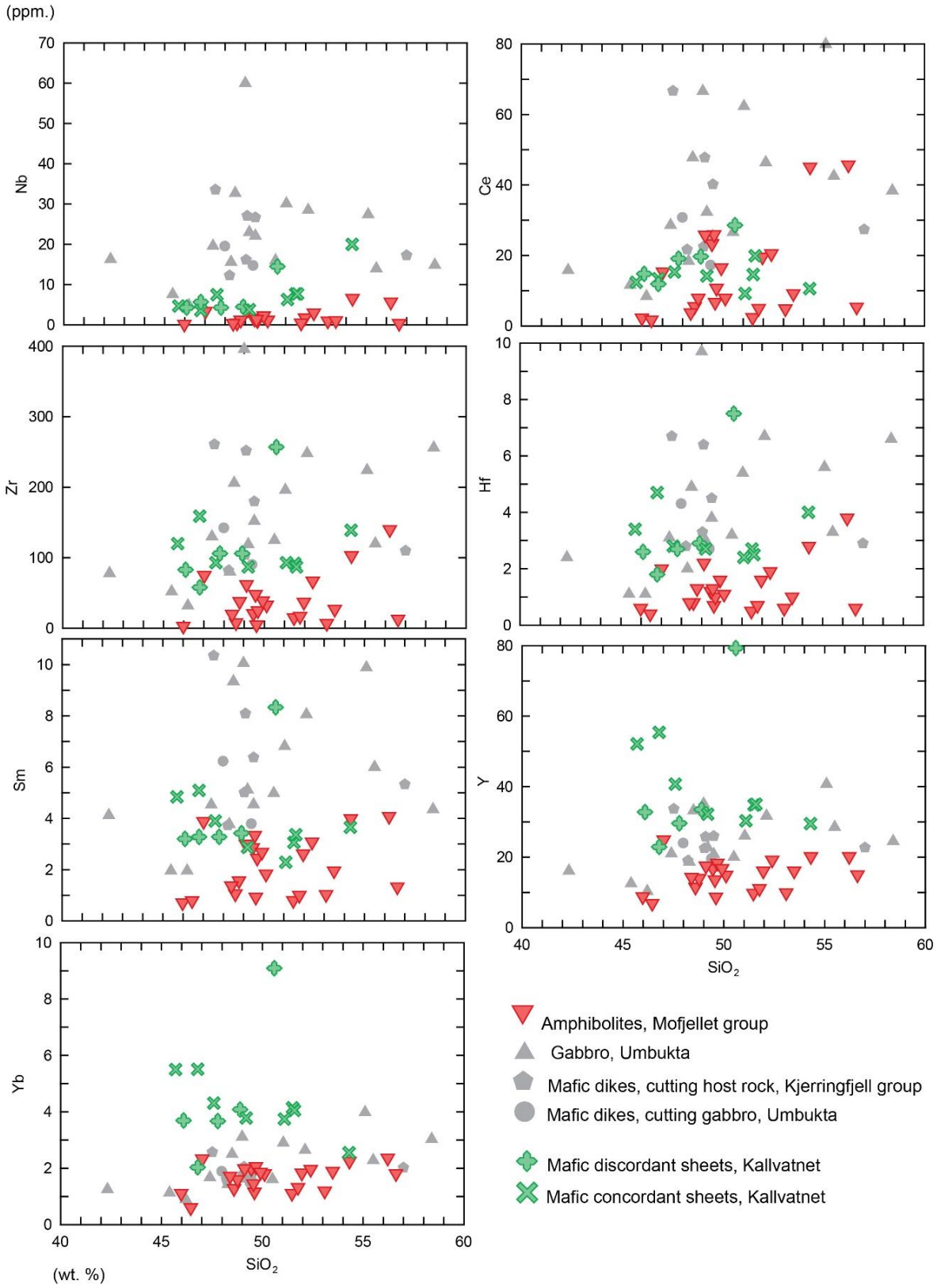


***Figure 109**: Harker diagrams with trace elements from mafic rocks from Kallvatnet (green), Umbukta (grey) and Mofjell (red).*

**Spider diagrams**

The trace elements from Kallvatnet/Gammelgardsfjellet, Umbukta, and Mofjell are presented in spider diagrams, normalized to chondrite and primitive mantle after Sun and McDonough (1989) (*Figure 110a* and *Figure 110b*) and to MORB after Pearce (1983) (*Figure 110c*).

The samples from this study (green symbols) have a flat REE signature, indicating a depletion of the LREE. The rock/chondrites values (*Figure 110a*) range from approximately 15 to 60%. The $(La/Yb)_N$ varying from 0.6 to 1.6 shows a relatively flat trend from La to Yb, showing that the difference between the incompatible and compatible elements is low (The elements get more compatible from left to right). Most samples have a negative Eu anomaly, which can be explained by the fractional crystallization of plagioclase. Overall, the REE pattern seems to plot between E- and N-MORB signatures.

The primitive mantle normalized spider diagram (*Figure 110b*) shows several anomalies, positive for K, U, Th and negative for Ba, Ta and Sr emphasizing that the chemical compositions between the samples and the primitive mantle differ. The MORB normalized spider diagrams (*Figure 110c*) shows an overall enrichment of the LREE compared with the typical MORB composition. Negative anomalies in Nb and Ta indicate that rocks could have a subduction-related source (Winter, 2014). The LREE are enriched compared to the HREE. A positive K and Rb anomaly indicate some crustal contamination. The negative Sr and Ba anomaly indicates either fractional crystallization of feldspar or a magma source with no felsic component (Winter, 2014).

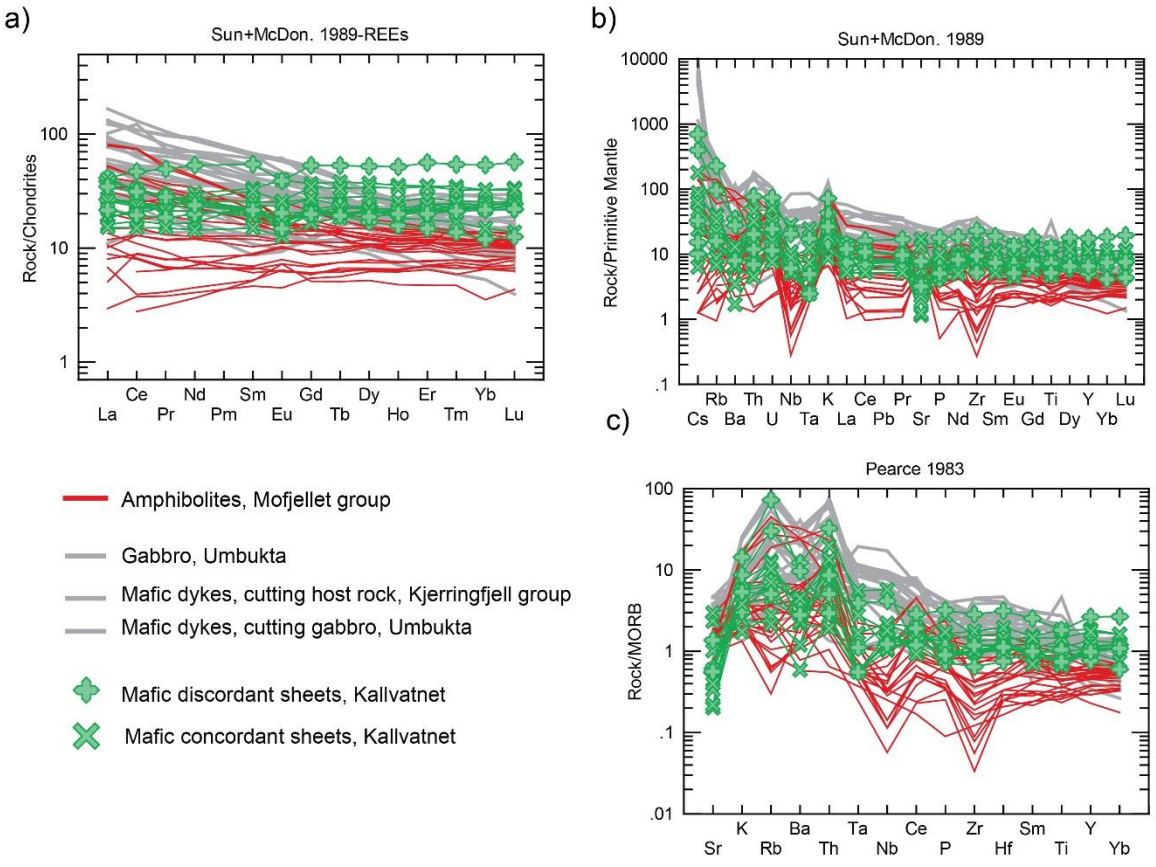


***Figure 110**: Spider diagrams with trace elements from Kallvatnet, Umbukta and Mofjell. A) and B) Chondrite and primitive mantle normalized spider diagram from Sun and McDonough (1989). C) MORB normalized spider diagram from Pearce (1983).*

**Tectonic discrimination diagrams**

Samples from Kallvatnet/Gammelgardsfjellet, Umbukta and Mofjell are plotted in tectonic discrimination diagrams. Samples from Kallvatnet/Gammelgardsfjellet (this study) plot in the ocean-floor/calc-alkali and field in the Ti-Zr-Y diagram (*Figure 111a*), MORB or MORB/Volcanic-arc field in the Z/Y-Zr diagram (*Figure 111b*), N-MORB field in the Zr-Y-Nb diagram (*Figure 111c*), and the field between E- and N-MORB in the La-Y-Nb diagram (*Figure 111d)*. The samples from Kallvatnet/Gammelgardsfjellet plot in different fields in the tectonic discrimination diagrams compared to Umbukta and Mofjell. Samples from Umbukta mainly plot in within-plate settings, while the Mofjell samples in the volcanic-arc settings.

Samples from Mofjell and Kallvatent were plotted in Ba/Nb and Ba/Th diagrams in an attempt to better illustrate the differences between these two areas (*Figure 112)*. The Ba/Nb plot (*Figure 112a)* shows that samples from Kallvatnet plot between the MORB array and the island-arc rocks from Mofjell, showing that the discordant mafic sheets from Kallvatnet have a higher subduction component compared to the concordant ones (but not as high as the rocks from Mofjell). In addition, the Ba/Th diagram (*Figure 112b)* shows that the discordant rocks from Kallvatent have a higher Ba/Nb and Th/Nb indicating higher components of the deep subduction component. These trends indicates that the discordant and concordant mafic rocks from Kallvatnet originate from two different sources.

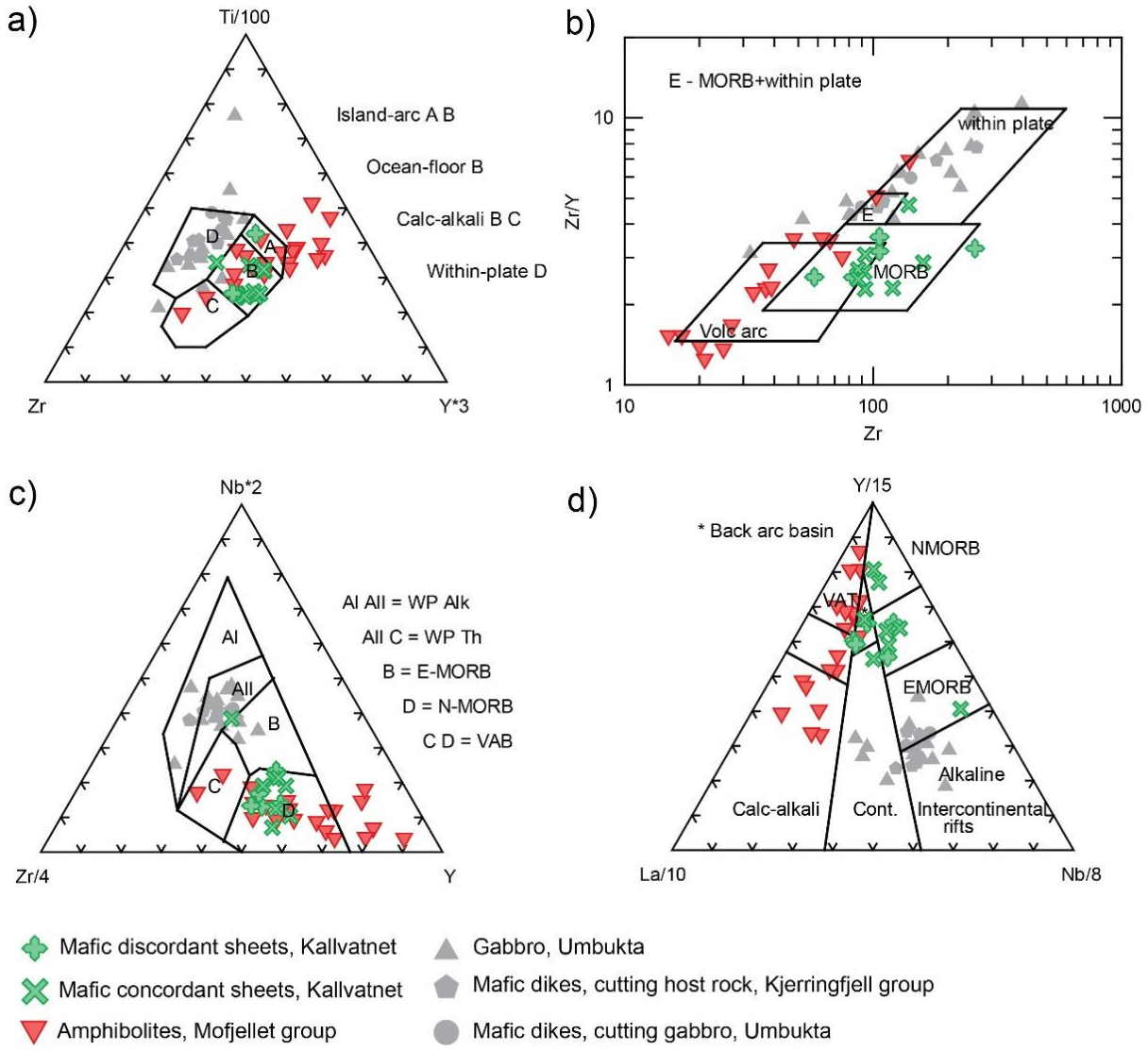


***Figure 111**: Tectonic discrimination diagrams with mafic rocks from Kallvatnet/Gammelgardsfjellet (green symbols), Umbukta (grey symbols) and Mofjell (red symbols). A) Tectonic discrimination diagram after Pearce and Cann (1973), plotting Zr, Y and Ti. Samples from this study mostly plot inside the Ocean-floor field. B) Zr/Y-Zr tectonic discrimination diagram after Pearce and Norry (1979). Most samples from this study, plot in the MORB field. C) Tectonic discrimination diagram after Meschede (1986), plotting Zr, Y and Nb. All except 1 sample plots inside the N-MORB field. D) Tectonic discrimination diagram after Cabanis (1989), using La, Nb and Y. Most samples from this study plot in the field MORB or Back arc basin basalts.*

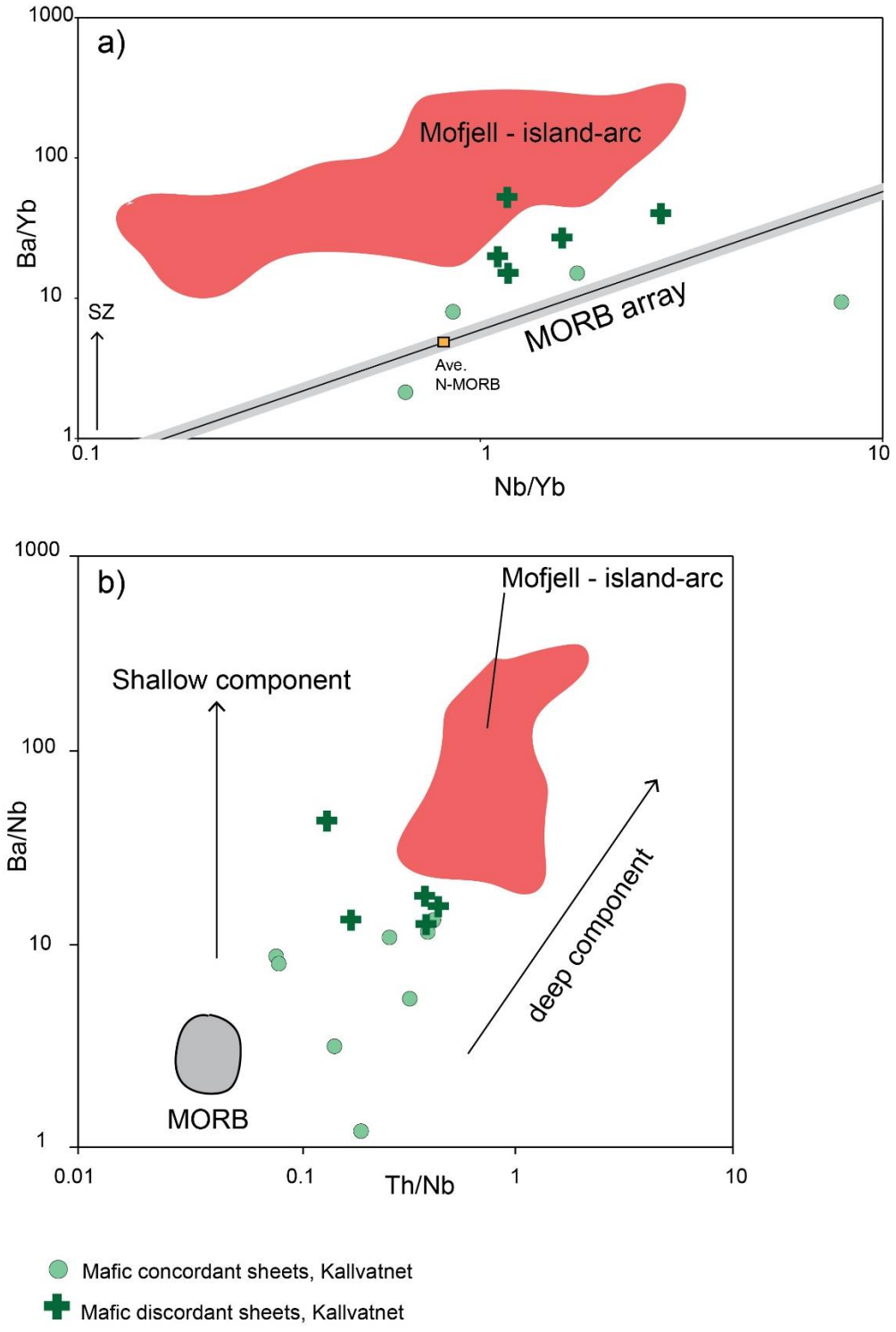


***Figure 112**: Ba/Nb and Ba/Th plot with mafic rocks from Kallvatnet plotted. A) Ba/Yb – Nb/Yb diagram with plotted mafic rocks from Kallvatnet. mafic rocks from Mofjell, average N-MORB and MORB array indicated in the diagram. B) Ba/Nb – Th/Nb diagram with plotted mafic rocks from Kallvatnet, mafic rocks from Mofjell and typical MORB indicated. Figures and MORB data from Pearce and Stern (2006).*

### 5.3.2 Felsic veins, reaction rims and garnet mica schists

Geochemical data for the felsic veins, reaction rims associated with both felsic veins and garnet amphibolites, and garnet mica schists have been plotted in Harker diagrams and spider diagrams. These samples are obtained from the Kallvatnet area.

**Major elements**

The silica content for the felsic rocks varies from 54.4 to 75.4% and shows some trends in the Harker diagrams (*Figure 113*). Negative trends for $Al_2O_3$, CaO, $Na_2O$ and $P_2O_5$ and a very weak positive trend for $K_2O$. The negative trends for $Al_2O_3$, CaO, $NaO_2$ and $P_2O_5$ can be explained by the crystal fractionation of plagioclase and apatite. The positive trends for $K_2O$, can be explained by the lack of potassium feldspar fractionating with the increasing maturing of the felsic magma.

Compared with the garnet mica schists, the reaction rims have similar major elements concentrations, except for $NaO_2$, $K_2O$ and CaO. The reaction rims have a higher content of $Na_2O$ and CaO, while the garnet mica schists have a higher $K_2O$. The garnet mica schists have a higher content of muscovite which can explain the higher content of K, while the reaction rims have a higher content of Na-Ca plagioclase.

The similar geochemistry indicates that the reaction rims and the garnet mica schists have the same protolith hence some chemical reactions involving fluids have most likely reacted with the common protolith and mobilized the K, Ca and Na.

**Trace elements**

*Figure 114* and *Figure 115* show Harker diagrams with a selection of mobile and immobile trace elements for the felsic veins, reaction rims, and garnet mica schists.

The Harker diagrams for the felsic veins show negative trends for Sm, Y, and Yb and positive for Rb, Ba, and Zr.

The weak negative trend for Sm can be explained by the crystal fractionation of Ca-rich plagioclase (Winter, 2014). The elements Rb and Ba are expected to be high in felsic melts due to their highly incompatible behavior. They prefer to be in the melt and will eventually crystallize to K-feldspar, micas, or hornblende, where they substitute for K (Winter, 2014). The negative trends for Y and Yb can be explained by the crystal fractionation of garnet (Winter, 2014). The positive trend for Zr can indicate that the felsic rocks have an enriched source or have undergone extensive liquid evolution (Winter, 2014).

The trace elements also show the similarity between the reaction rims and the garnet mica schists. The garnet mica schists and the reaction rims plot on top of each other for all elements except for Sr, Rb and Ba which have systematic differences. The reaction rims have higher concentrations of Sr and lower concentrations of Ba and Rb. Sr is typically a substitute for Ca in plagioclase, reflecting the higher plagioclase concentration in the reaction rims. As discussed earlier, Ba and Rb have are highly mobile elements and usually substitute for potassium.

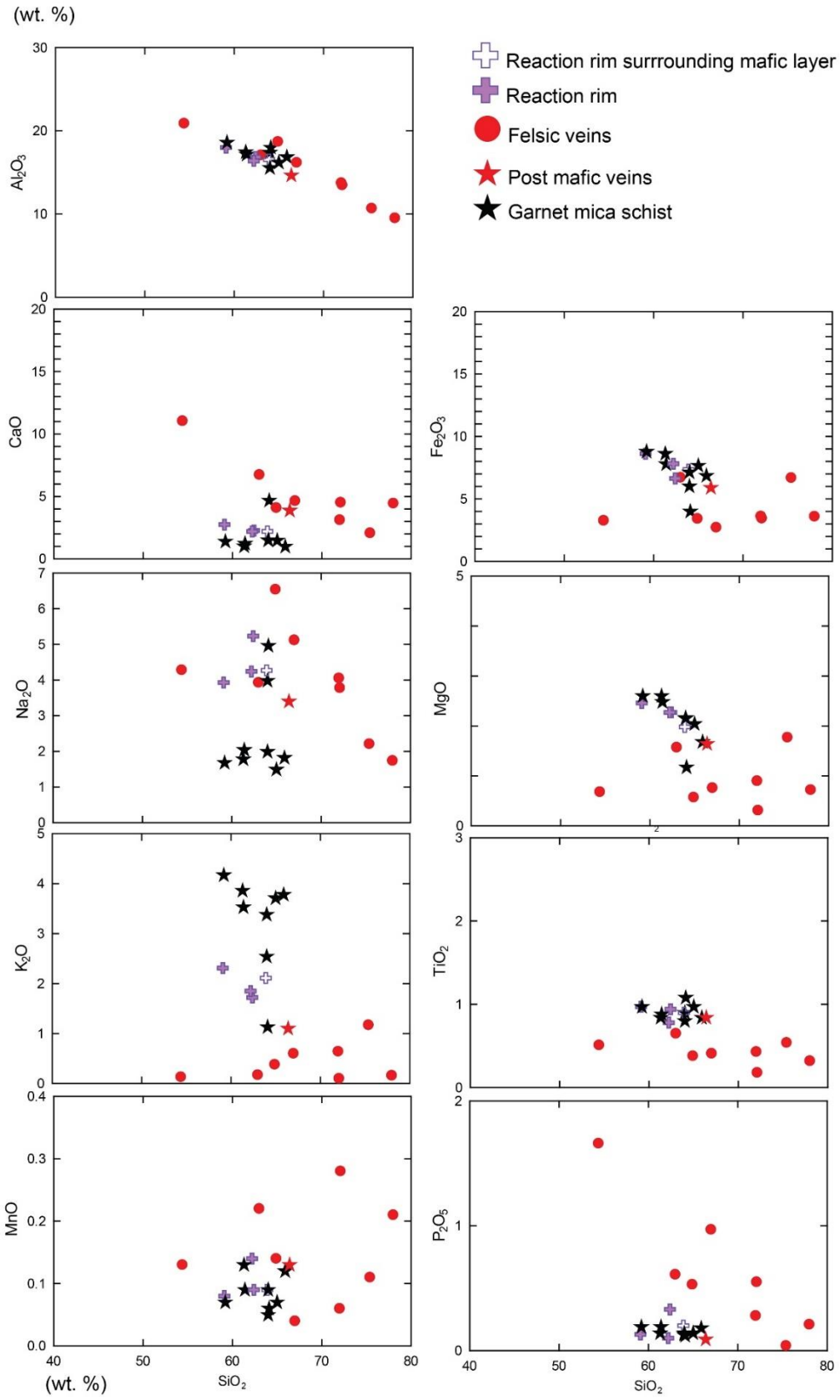


***Figure 113**: Harker diagrams with major elements from felsic veins (filled red circle), post mafic vein (filled red star), reaction rims associated with felsic veins (filled purple cross), reaction rims associated with garnet amphibolite (open purple cross). The data is gathered at the Kallvatnet area (this study).*

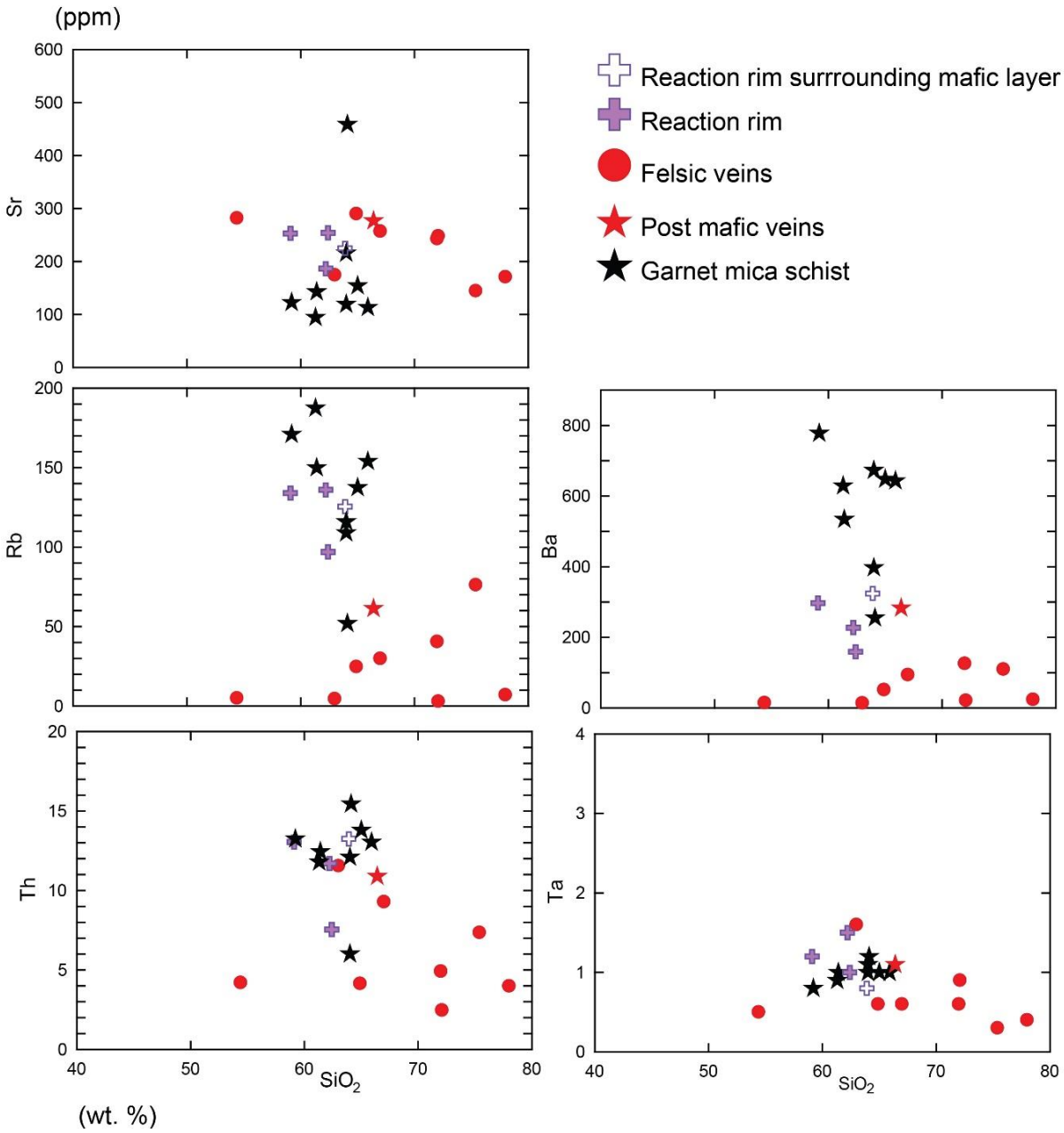


***Figure 114**: Harker diagrams with trace elements from garnet mica schists (black stars), reaction rims associated with felsic veins (filled purple cross), reaction rims associated with mafic rocks (open purple cross), felsic veins (filled red circle), and post mafic vein (filled red star). Elements plotted are Sr, Rb, Ba, Th and Ta (ppm).*

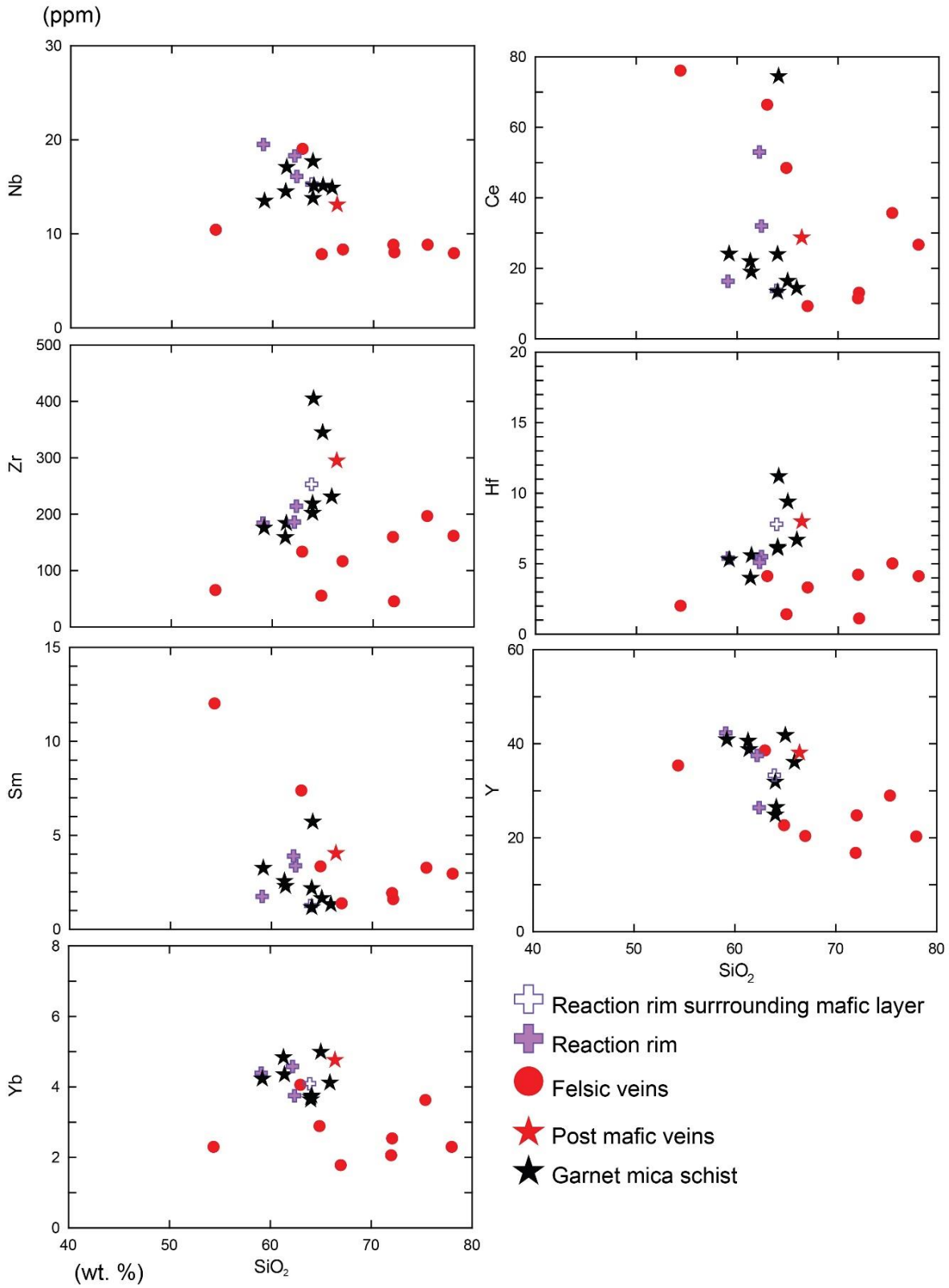


***Figure 115**: Harker diagrams with trace elements from garnet mica schists (black stars), reaction rims associated with felsic veins (filled purple cross), reaction rims associated with mafic rocks (open purple cross), felsic veins (filled red circle). Elements plotted are Nb, Ce, Zr, Hf, Sm, Y and Yb (ppm).*

**Spider diagrams**

Samples of felsic veins, reaction rims, and garnet mica schists were taken to investigate the relations between these rocks. *Figure 116c* shows a field photograph of sample gmf2021-11A (felsic vein), gmf2021-11B (reaction rim) and gmf2021-11C (garnet mica schist). *Figure 116a* and *Figure 116b* show the geochemistry from these data plotted in spider diagrams. The data emphasize that the reaction rims have less concentration of incompatible and mobile elements such as K, Rb, and Ba than the garnet mica schist. A similar figure has been constructed for samples gmf2021-18A, gmf2021-18B, and gmf2021-18C (*Figure 117*) and spider diagrams with all reaction rims and garnet mica schists are shown in *Figure 118*.

To really illustrate the difference between the garnet mica schists and the reaction rims, an average garnet mica schist composition was calculated and compared with the reaction rims. *Figure 119* shows a spider diagram with reaction rims plotted against the average garnet mica schist composition. The diagram illustrates systematic negative anomalies for $K_2O$, Rb and Ba. Systematic positive anomalies are apparent for Sr. For the less mobile trace elements (Th, Ta, Nb, Ce, P2O, Zr, Hf, Sm, TiO2, Y, and Yb), no systematic negative or positive anomaly is apparent.

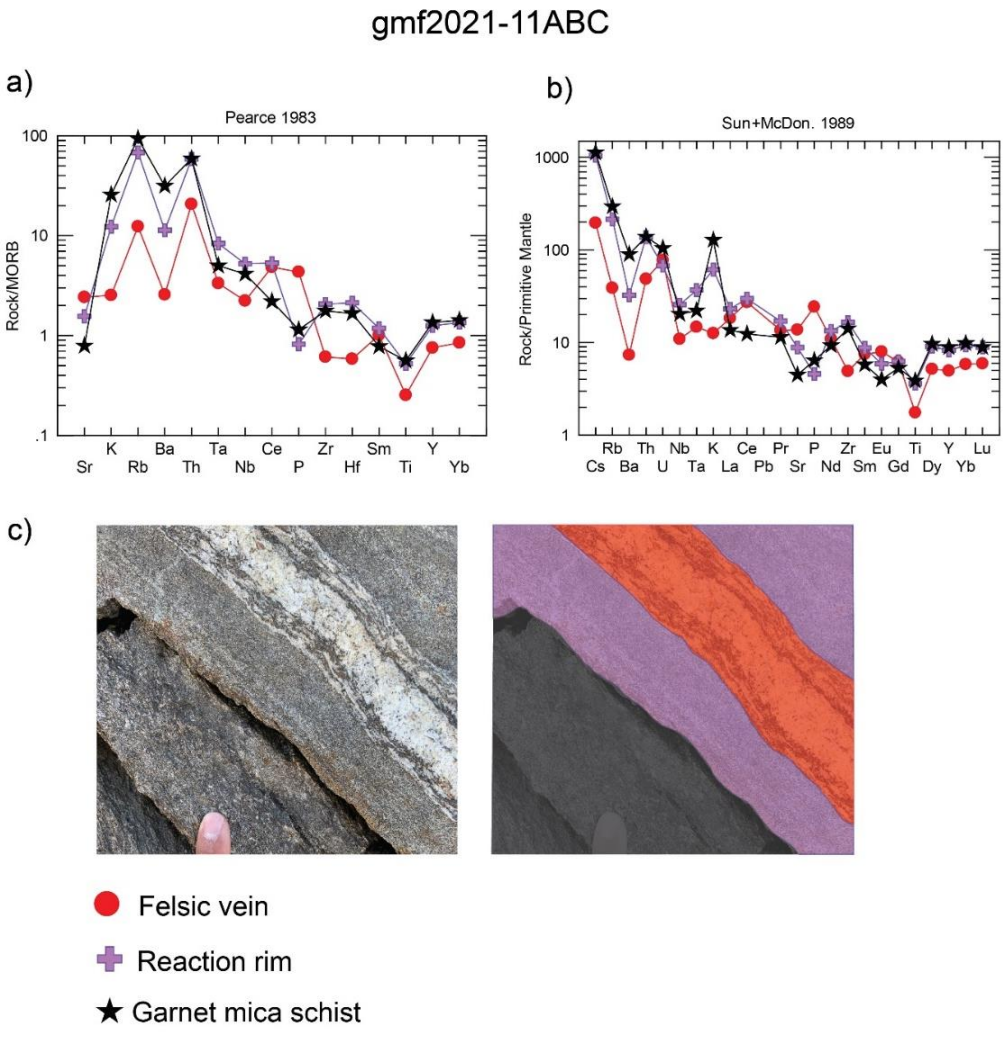


***Figure 116**: Spider diagrams and field photo for felsic vein, reaction rim and garnet mica schist (gmf2021-11ABC).*

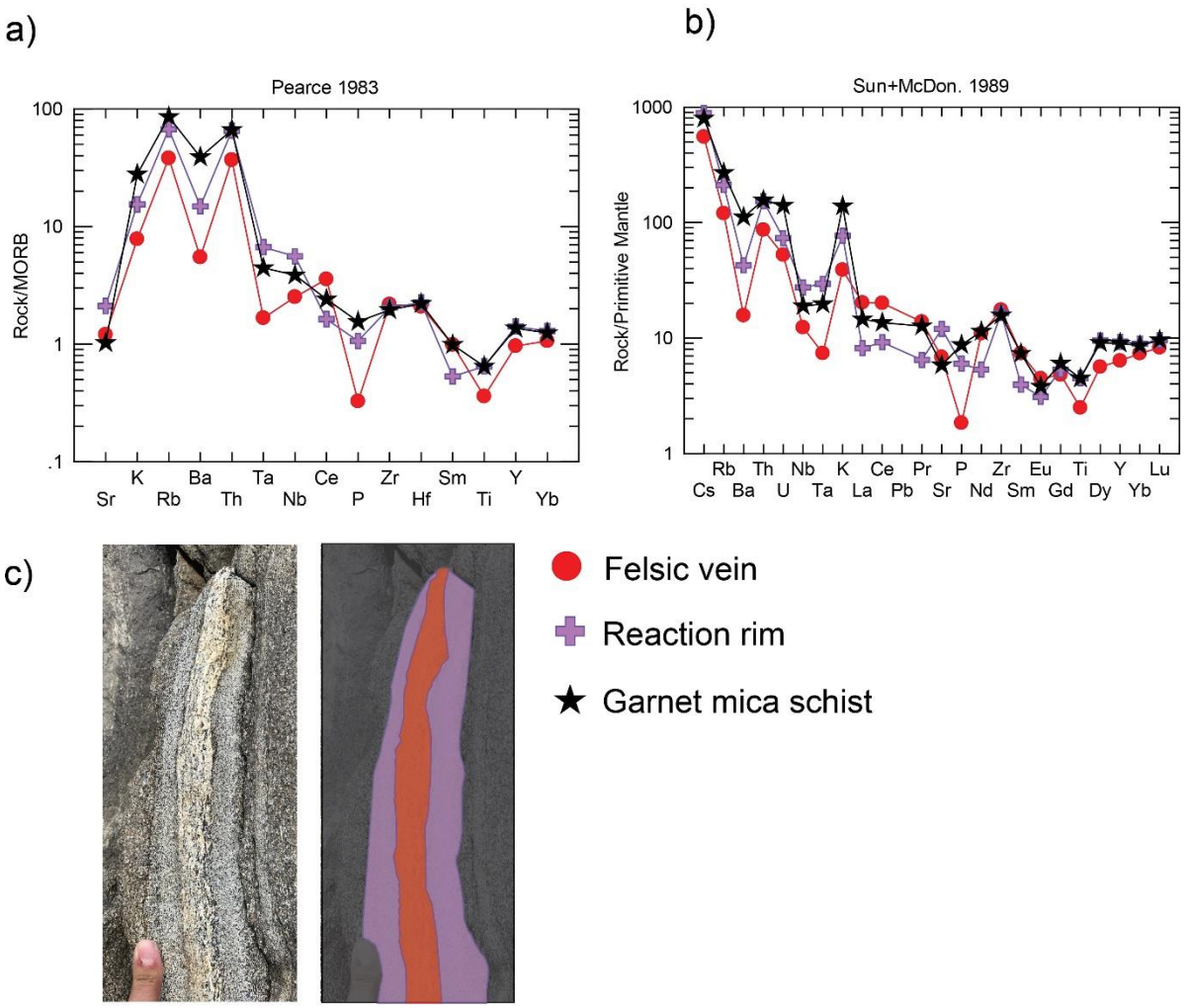


***Figure 117**: Spider diagrams and field photo for felsic vein, reaction rim and garnet mica schist (gmf2021-18ABC).*

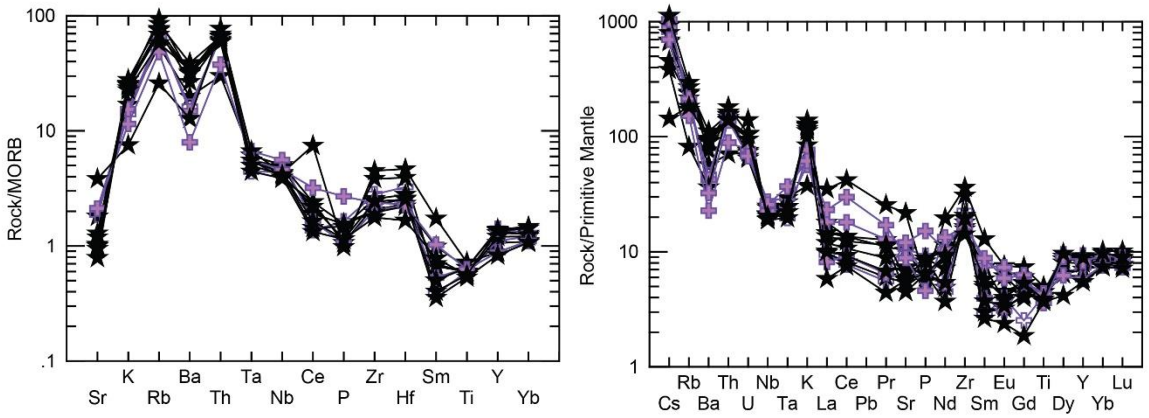


***Figure 118**: Spider diagrams with all reaction rims and garnet mica schists plotted. The diagram to the left after Pearce (1983) and to the right after Sun and McDonough (1989).*

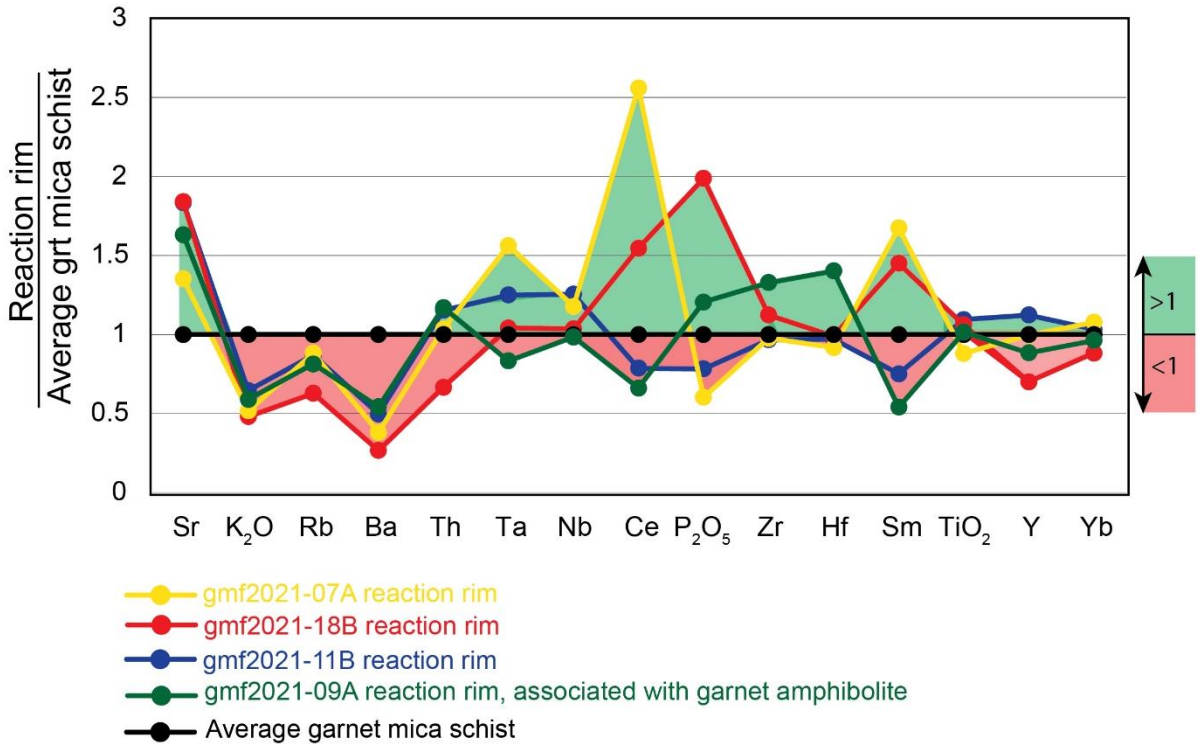


***Figure 119**: Spider diagram plotting reaction rims normalized on an average garnet mica schist composition.*

### 5.3.3 Summary of geochemical data

**Mafic rocks:**

Mafic rocks at Kallvatnet and Gammelgardsfjellet (this study) show a apparent similar geochemistry, except for the higher Ba/Yb, Ba/Nb and Th/Nb content for the discordant mafic sheets than for the concordant mafic sheets. Overall, the mafic rocks from Kallvatnet have a low degree of fractionation, and have different major and trace element chemistry compared to the mafic rocks from Umbukta and Mofjell. The rocks from Kallvatnet/Gammelgardsfjellet have a flat signature in the spider diagrams normalized to chondrite, and plot in MORB and volcanic-arc fields in tectonic discrimination diagrams, which is distinctly different from the mafic rocks from Umbukta. The mafic rocks from Mofjell have a similar island-arc affinity, but the rocks at Kallvatnet do not show as strong volcanic-arc signature as the rocks at Mofjell.

**Felsic veins, reaction rims and garnet mica schists**

The reaction rims and garnet mica schists have similar major and trace elements indicating the same protolith. The reaction rims are depleted in mobile elements such as K, Rb and Ba and enriched in Sr, Ca and Na compared to the garnet mica schists. The depletion indicates that fluids and heat from the felsic veins have reacted with the garnet mica schist and formed reaction rims.

# 6 Discussion

The following chapter will discuss the findings presented in this study to better understand the Kjerringfjell Group's geological history located within the Rödingsfjället Nappe Complex. The results will be interpreted and compared with previous relevant literature. In addition, the results will be put in context of the large-scale geological history of Norway.

The discussion is split up into three main sections. 1) Geological evolution of the Kjerringfjell Group. This part summarizes and interprets the field observations, petrography, geochemical data, and geochronological data. 2) Correlation with surrounding tectonic units. The geological history of Kallvatnet, will be compared to surrounding tectonic units such as the Mofjell Group and the Helgeland Nappe Complex. In addition, this section will discuss the differences between the rocks at Kallvatnet and Umbukta which both have been assigned to the Kjerringfjell Group. 3) Implication on the tectonostratigraphy. This part discusses how the new findings from this study will affect the current understanding of the tectonostratigraphy in the Scandinavian Caledonides.

## 6.1 Geological evolution of the Kjerringfjell Group

### 6.1.1 Depositional environment

The mapped area shows a gradual change of main lithology from quartz and feldspar-rich rocks such as quartz-rich schist, psammites, and quartzites in the eastern part, to garnet-mica-schists with high contents of phyllosilicate minerals like muscovite and biotite in the western-part. This gradual change is most likely caused by the change from a proximal to a more distal depositional environment, e.g., from a coastal to an offshore environment (Nichols, 2009), which is typical in the Uppermost Allochthon (Roberts et al., 2007). The lack of an abrupt transition from quartz-rich lithologies to phyllosilicate-rich lithologies suggests the absence of a tectonic contact, a hiatus, or significant transgression or regression events (Nichols, 2009). Philpotts and Ague (2009) emphasized the difficulty of identifying sedimentary layering in high-grade rocks because the mm to cm-scale layering, which resembles sedimentary bedding can be developed during metamorphism. The isoclinal folds (F1) with fold axial planes parallel to S1 and the internal foliation in garnet (Si) suggest that the original bedding ($S_0$) has been folded and transposed (S1 and S0 are sub- parallel, *Figure 120)* (Passchier and Trouw, 2005). Several zircon and monazite ages indicate more than one metamorphic event in the Kjerringfjell Group, which likely were accompanied by deformation.

### 6.1.2 Felsic veins and reaction rims

The Kjerringfjell Group has been considered to have undergone migmatization and extensive regional Neoproterozoic high-grade metamorphism (Slagstad et al., 2021). The geochemical data deny the hypothesis about regional partial melting. The felsic veins ("leucosomes") at Kallvatnet do not have an enrichment of the LREE compared to the garnet mica schist ("migmatite source"). In addition, it is expected that the garnet mica schist should fall on a straight line between the felsic veins and the light gray rims

("melanosome") in the Harker diagrams (Figure 113), which is not the case (Jung et al., 1999).

Field observations, geochemical and geochronological data from this study indicate that the "leucosomes" are instead injected felsic veins surrounded by reaction rims.

The light grey rims (reaction rims) symmetrically surround the felsic veins (*Figure 48*), with a clear correlation in thickness between the two layers (*Figure 50*) (similar to that shown in Engvik et al. (2005)). Such abrupt color change with symmetrical features indicates the presence of alteration halos (Engvik et al., 2005). Such alteration halos indicate that a volatile-rich felsic melt has intruded and reacted with the pelite. The volatiles that did not incorporate into minerals in the felsic vein were liberated as a fluid phase, penetrated the surrounding wall rock, and altered the mineralogy (Burnham, 2015). The thicker the veins, the more fluids were transported into the wall rock. The geochemical data (5.3.2) confirm the presence of element mobility. The mobile elements K, Rb, and Ba, are systematically depleted in the reaction rims with respect to the element concentrations in the garnet mica schists, while the immobile elements do not show any systematic changes. The element depletion indicates that the fluid has "flushed out" the elements from the pelite and further transported them into the felsic vein or into the surrounding pelite.

The reaction rims mainly consist of biotite, garnet, plagioclase, and quartz (*Figure 52, Figure 55*). The garnet mica schist has the same minerals, except that the schist has a higher muscovite and lower plagioclase content, hence higher $H_2O$ content. In addition, the grain size in the reaction rims is generally smaller than in the garnet mica schists. The generally smaller grain size and lack of muscovite in the reaction rims indicate that the reaction rims have a different bulk composition and are more dehydrated, suppressing the crystallization of muscovite during metamorphism.

A hypothesis is that the fluid infiltration has "cooked" the wall rock, metasomatized, and dehydrated the reaction rims with heat and a Na-rich fluid, preventing mica growth. The lack of muscovite in the reaction rims agrees well with the depletion of K, Ba and Rb which substitutes for K in muscovite (Sorensen et al., 1997). This study suggests that a metasomatic reaction occurred during the intrusion of the felsic veins. The Na-rich felsic veins enriched the pelite with Na and depleted them of K, Rb, and Ba. The K-feldspar in the garnet mica schist protolith may have been replaced by plagioclase during the metasomatism, including a cation exchange reaction including a Na-rich fluid (Orville, 1962):

$$KAlSi_3O_8 + Na^+ \leftrightarrow NaAlSi_3O_8 + K^+$$

K-rich feldspar  plagioclase

The generated K-rich fluid is less dense and less viscous than the surrounding rock, hence the K-rich fluid was transported away from the system, probably by migration towards the earth's surface through the felsic veins or in cracks in the pelite. Later during albite-epidote facies the following reaction may have occurred (Best, 2003):

$$\text{chlorite} + \text{K-feldspar} = \text{biotite} + \text{muscovite} + \text{quartz} + H_2O$$

Replacing the K-feldspar in the schist by biotite, muscovite, quartz, and releasing $H_2O$. The lower $H_2O$ content and the depletion of K, Rb, and Ba suppressed muscovite crystallization in the reaction rims compared to the garnet mica schists.

The local presence of calc-silicate lenses associated with the felsic veins can be related to a $CO_2$-rich fluid which could possibly has been derived from underlying or surrounding carbonate rocks (typical lithology in the Uppermost Allochthon (Roberts et al., 2007)), which later locally precipitated calcsilicates. It is also possible that felsic veins intruded by coincidence at the same place as the calcsilicate minerals. The dehydrated reaction rims indicate that dehydration occurred during the intrusion of the felsic veins. The $H_2O$ may have been transported out of the system as suggested above, or the dehydration may also be related to the input of $CO_2$-rich fluids.

The concordant mafic sheets also have similar reaction rims (*Figure 70*). Fluids associated with mafic rocks are usually higher in Ca (Bucher and Stober, 2010). This is caused by a reaction between the Ca-rich plagioclase with dissolved NaCl to albitize the plagioclase and producing a $CaCl_2$ fluid (Bucher and Stober, 2010). The reaction rims associated with mafic rocks have not been studied in thin section, so the exact mineralogy is unknown nevertheless, a cation exchange reaction including a Ca-rich fluid is suggested (Orville, 1962):

$$KAlSi_3O_8 + Ca^{2+} \leftrightarrow CaAlSi_3O_8 + K^+$$

K-rich feldspar  Ca-plagioclase

Replacing the K-feldspar with Ca-rich plagioclase generates K-rich fluids. The reaction rims associated with the felsic veins are enriched in Ca and Sr (Sr usually substitutes for Ca (Winter, 2014)) compared to the garnet mica schist, suggesting the same reaction may have occurred in association with the intrusion of the felsic veins.

The thickness of the mafic-associated reaction rims did not seem to correlate with the thickness of the mafic sheets in the same way as with the felsic veins, indicating that the fluid concentration in the intruding mafic sheets were lower than in the felsic veins. Higher temperatures are needed to melt mafic rocks compared to felsic rocks (Winter, 2014), indicating that the temperature was not the main controlling factor regarding the radius of the reaction halos.

The felsic veins show some myrmekitic texture (*Figure 54g* and *h*), indicating subsolidus ionic reactions between the feldspar and a fluid (Winter, 2014). Micro-cracks in the plagioclase sealed by albite and muscovite in the reaction rim (*Figure 58*) indicate fluid infiltration in a permeable rock (Engvik et al., 2005). These micro-cracks and indication of fluid infiltrations are most likely not related to the intrusions of the felsic veins. The felsic veins have undergone at least one deformation event that has removed the proof for permeability at the time of intrusion. The micro-cracks discussed above are likely related to a post-Caledonian retrogression event.

### 6.1.3 Tectonic significance of mafic magmatism

At Kallvatnet both mafic concordant and discordant sheets are present. This chapter will discuss the geochemical data from Kallvatnet and compare them with the mafic rocks at Umbukta and and Mofjell.

The geochemical data for the mafic rocks (*5.3.1*) are used to get insight into their petrogenesis. The data strongly indicate that the mafic rocks at Umbukta, Kallvatnet, and Mofjell are not genetically related. The mafic rocks from Umbukta are suggested to have formed in an intracontinental rift (Høyen, 2016, Slagstad et al., 2021), and the Mofjell rocks in a volcanic-arc environment (Marker, 1983, Bjerkgård et al., 2013, Slagstad et al., 2021) (See *Figure 111*).

The AFM diagram from Irvine and Baragar (1971) was used to investigate whether the mafic rocks from Kallvatnet are tholeiitic or calc-alkaline in composition. The mafic rocks clearly show a small variation in silica and have a stronger enrichment in Fe relative to Mg hence they plot on the tholeiitic path in the AFM diagram (*Figure 106*). Tholeiitic rocks are mainly associated with zones of crustal extension and are the most abundant rock in mid-ocean ridges, but can also be found in large oceanic islands, (Philpotts and Ague, 2009, Winter, 2014) and subduction zones (Best, 2003). The mafic rocks from Umbukta plot in the tholeiitic field, and so do the Mofjell rocks, with some exceptions.

The Harker diagrams (*Figure 107*, *Figure 108,* and *Figure 109*) with plotted major and trace elements were mainly used to investigate if the mafic rocks from Kallvatnet were genetically related. In addition, the mafic geochemical data from Umbukta and Mofjell were plotted to observe any potential relations between the mafic rocks from Kjerringfjell and Umbukta/Mofjell. The garnet amphibolites from Kallvatnet show an overall smooth linear trends with some expected scatter, indicating that the rocks are genetically related (Winter, 2014). The Harker diagrams with plotted trace elements show systematically compositional differences between the rocks at Kallvatnet and Umbukta/Mofjell, including lower concentrations of Sr and higher concentrations of Yb.

The REE-spider diagrams (*Figure 110*) show three distinct signatures for the rocks at Kallvatnet, Umbukta, and Mofjell. The rocks at Kallvatnet have a flat signature with slightly positive slopes for the LREE in the chondrite normalized spider-diagram (after Sun and McDonough (1989)) (*Figure 110a*) with negative Eu-anomaly (one sample shows positive Eu-anomaly and some have no Eu-anomaly). The flat, weakly positive LREE pattern with an Eu-anomaly indicates a depletion of the LREE and fractional crystallization of plagioclase (Winter, 2014). A weak positive LREE-slope signature is typical for N-MORB magmas, which are believed to have been generated during the partial melting of an already depleted source (Best, 2003). The weak negative LREE slope indicates a less depleted source, reflecting some compositional variation in the source; overall, the rocks lay within the MORB range (Winter, 2014). It is possible that the weak LREE-enrichment was produced from partial melting of a slightly depleted source or by the mixture of a depleted and a more enriched magma (Saunders et al., 1988, Winter, 2014).

The MORB normalized spider diagram (*Figure 110c*) after Pearce (1983) shows weak negative Ta and Nb anomalies indicating that the magma could have been modified by slab-derived fluids. (Winter, 2014). Compared to the MORB composition, the rocks are enriched in LREE and have positive K and Rb anomalies indicating crustal contamination and/or fluid infiltration during metasomatism (Winter, 2014). The Rb concentration is variable, mostly positive compared with the MORB composition. Rb substitutes for K in mica and K-feldspar, indicating that Rb has been incorporated into the source, likely by fluid infiltration or crustal contamination (Best, 2003). The HFSE seems to lay

approximately at 1, indicating that the source did not crystallize garnet (Winter, 2014). The primitive mantle normalized spider diagram after Sun and McDonough (1989) also shows irregular enrichment in the LREE compared to the HREE (*Figure 110b)*. The negative Ta anomaly compared and the irregular pattern is typical for volcanic-arcs (Jenner and Wyman, 1996). The negative Ta and Nb anomalies are not as distinct as shown in the samples from the Mofjell Group, and the LREE enrichment is much higher for the Umbukta samples.

Many tectonic discrimination diagrams utilize the concentrations of immobile trace elements (such as the HFSE: Ti, Zr, Y, Nb, and P), which are relatively stable during metamorphism and hydrothermal alteration to distinguish between tectonic environments (Rollinson, 1993). To investigate and constrain the tectonic environment the mafic rocks at Kallvatnet were formed in, four tectonic discrimination diagrams were used (see *Figure 111*). The Ti-Zr-Y tectonic discrimination diagram (*Figure 111a*) (from Pearce and Cann (1973)) plots the mafic rocks from Kallvatnet in the ocean-floor/calc-alkali basalt field (MORB, island-arc tholeiites, and calc-alkali basalt field). The Zr/Y-Zr diagram (*Figure 111b*) from Pearce and Norry (1979) plot the samples in the MORB and the MORB/volcanic-arc field, indicating MORB or island-arc affinity. The Zr-Y-Nb tectonic discrimination diagram (*Figure 111c*) from Meschede (1986) shows a unanimous plotting, all expect from one sample plot in the N-MORB/volcanic-arc field. The Nb concentrations are too low for the rocks to be classified as E-MORB (Rollinson, 1993). The fourth tectonic discrimination diagram, the La-Y-Nb diagram (*Figure 111d*) from Cabanis (1989) plots the majority of the samples in the field between N-MORB and E-MORB, slightly enriched MORB. Two samples plot in the N-MORB field, one in the E-MORB field, four in the back-arc basin field, and one in the continental basalt field.

The rocks at Kallvatnet are tholeiitic in composition and enriched in the LREE compared with an N-MORB, with both positive and negative slopes for the LREE, indicating some source variation. The magma source seems to have been contaminated by fluids and or crustal contamination, and the discrimination diagrams used indicate MORB or island-arc, affinity.

Basalts with transitional composition between MORB and island-arc typically occur in back-arc basins (Pearce and Stern, 2006). The main geochemical characteristics for back-arc basin basalts are the enrichment of subduction-mobile elements (e.g., Rb, Ba, Sr, K, Th, U, LREE ) and the depletion of subduction-immobile elements (e.g., Ta and Nb) (Pearce and Stern, 2006, Zheng, 2019). The subduction component in the rocks at Kallvatnet is present, but not as distinct as in the mafic rocks in the Mofjell Group which are believed to have island-arc affinity. Rocks with a significant subduction component, but not as large as in island-arc basalts are typical for back-arc-basin basalts (Pearce and Stern, 2006).

The subduction proxy Ba/Nb which is independent of mantle source, partial melting, or fractional crystallization can be used to measure the total subduction input (Pearce and Stern, 2006). The mafic rocks from Kallvatnet have been plotted in a Ba/Nb Yb-normalized diagram (*Figure 112a).* Most of the samples from Kallvatnet plot between the MORB array and the island-arc rocks from Mofjell, some plot in the MORB array (see *Figure 112a)*. This pattern is typical for basalts formed in a back-arc basin (Pearce and Stern (2006) and references therein). The discordant mafic sheets from Kallvatnet have systematically higher subduction content than the concordant mafic sheets, indicating that the mafic rocks from Kallvatent are derived from two difference sources (Pearce and Stern, 2006). The Ba/Th Nb-normalized diagram shown in *Figure 112b*, can be used to investigate the relative influence of the shallow and deep subduction components in a back-arc basin. The figure shows that the discordant mafic sheets from Kallvatnet have a higher component of deep subduction compared with the mafic concordant sheets.

Summarized, the rocks from Kallvatnet are distinctly different compared to the mafic rocks at Umbukta and Mofjell which are believed to have an intracontinental-rift and volcanic-arc sources, respectively. This study suggests that there are two generations of mafic rocks at Kallvatnet:

1: The first generation of mafic sheets is concordant, have locally reaction rims and has a MORB or back-arc basin source.

2: The second generation is discordant, appear to have no reaction rims and have originated from a back arc-basin source.

### 6.1.4 Deformation, metamorphism, and magmatism

This chapter will discuss deformation, metamorphic and magmatic events occurring at Kallvatnet. The chapter is split into the following three sub-sections:

1) Deformation. The formation of F1 and F2 folds, S1 (compositional parallel), S2 (crenulation cleavage), and Si (internal foliation) will be discussed. 2) Metamorphism. The petrographic analyses, the metamorphic zircon and monazite geochronological analyses and the deformation history will be discussed to obtain information about metamorphic events in the Kjerringfjell Group. 3) Magmatism. The time of intrusion of the mafic sheets and the felsic veins from Kallvatnet will be discussed. To date the time of intrusion of these rocks from Kallvatnet was not attainable, hence the field relations and geochemical data will be used to constrain the timing of intrusion. In addition, the new crystallization ages for the Umbukta gabbro will be discussed.

**Deformation**

Several generations of folding are a common feature in regionally metamorphosed rocks. the different generations are easiest recorded in low to medium-grade rocks, while in high-grade rocks, the structures can be obscured (Means and Williams, 1976). When interpreting the geological history of an area, it is important to emphasize the importance of studying the whole area to obtain the full picture and not just base conclusions on just one or two outcrops (Williams, 1985). For example, the first generation of folds and the crenulation cleavage were only observed in area 4 (garnet mica schist-rich) and 3 (felsic vein-rich). The lack of crenulation cleavage in area 1 (quartz-rich) and 2 (transition) can be explained by crenulation cleavage being restricted to rocks with a certain minimum amount of mica minerals (Fossen, 2016).

Crenulation cleavage is known to form normal, or at an obtuse angle to the principal compression (Cosgrove, 1972). In this case, it will be in an E-W direction with some obliquity due to the asymmetrical character. Such crenulation cleavage that overprints the spaced cleavage is common in slaty belts (Means and Williams, 1976). The similarities between the crenulation folding (which is related to the crenulation cleavage) and the bigger F2 folds indicate that the crenulation cleavage is formed by microfolding, and not during shearing, followed by extensional crenulation cleavage (microfaulting), (Cosgrove, 1972, Fossen, 2016)

The isoclinal F1 folds with fold axial traces parallel to the S1 foliation and the F2 folds with associated crenulation cleavage indicate that the Kjerringfjell Group has undergone at least 2 deformation phases (Passchier and Trouw, 2005). The geochronological data presented in this study suggest several tectonothermal events, but this sub-chapter will only discuss

the indicators for deformation and metamorphism obtained from the observations in the field and in thin section.

*Figure 120* shows a schematic presentation of a possible two-phase deformation sequence in a schist (from Passchier and Trouw (2005)). In the first deformation phase (D1), a continuous or spaced cleavage is developed with a varying angle than the apparent bedding (S0). The bedding is folded asymmetric (F1). In the long limbs, the angle between S1 and S0 may be so small that they are indistinguishable in the field and in thin section. In the second deformation-phase (D2), the crenulation cleavage and the open folds are developed and refolds the F1 folds. It is possible that the continuous/spaced cleavage (S1), the tight F1 folds, crenulation cleavage (S2) and the open F2 folds were generated during one deformation phase. It can occur if the stress orientation changes during the progressive deformation (Fossen, 2016).

The structural mapping of the S1 foliation and the F2 folds indicates that the asymmetric folds in the study area have likely been developed during large-scale folding (Ramberg, 1963) (*Figure 121*). The figure shows a schematic possible large-scale evolution of D2 (F1 folds are not illustrated) forming asymmetric F2 folds of felsic veins and reaction rims within layers of garnet mica schist and quartz-rich schist. The thinnest competent layers (felsic veins and reaction rims) start folding symmetrically during the start of compression (*Figure 121b*). The thickest competent layers (quartz-rich schist) begin to fold with continued shorting (*Figure 121c)*. During shorting, the felsic veins, and reaction rims start folding asymmetrically due to the larger layer parallel shear strain in the internal incompetent layers (garnet mica schist) at the flanks of the slowly growing major fold. This regional-scale synclinal fold is most likely a part of the known large synformal structure in the Uppermost Allochthon located between culminated antiformal Precambrian crystalline rocks (Brattli, 1996).

Asymmetrical boudines are common in deformed metamorphic rocks and can indicate non-coaxial strain under high temperatures (Cosgrove, 1972, Fossen, 2016). Boudins can also occur in a pure strain environment if the orientation of the layers have oblique orientation respect to the shortening axis (Fossen, 2016). The viscosity contrast between the competent garnet amphibolites and the less competent garnet mica schist in addition to the high strain rate, has formed several shear fractures associated with the boudines (Goscombe and Passchier, 2003, Fossen, 2016). The majority of the kinematic indicators, including shear fractures associated with amphibolite boudins, asymmetrical veins, and pegmatites, show sinistral N-S strike-slip movement. The lineations mapped in this area were crenulation lineations, which may not indicate a specific transport direction, making it hard to conclude the particular transport direction (Fossen, 2016).

The Scandinavian Caledonides is characterized by SE-directed thrusting structures reflecting the continent-continent collision followed by orogen collapse generating parallel extensional structures (Gee et al., 1985, Braathen et al., 2002). Extensive deformation and folding are also recognizable in the Kjerringfjell Group. The deformation is dominated by an overall E-vergence, the S1 foliation (*Figure 83*a and b) (composition parallel) and the open F2-folds (*Figure 83*c) with fold axes trending N-S/NE-SW associated with a bigger synclinal (*Figure 83*d). These structures correspond to the well-known structures caused by the collision between Laurentia and Baltica in Siluro-Devonian time (Gee et al., 1985, Braathen et al., 2002).

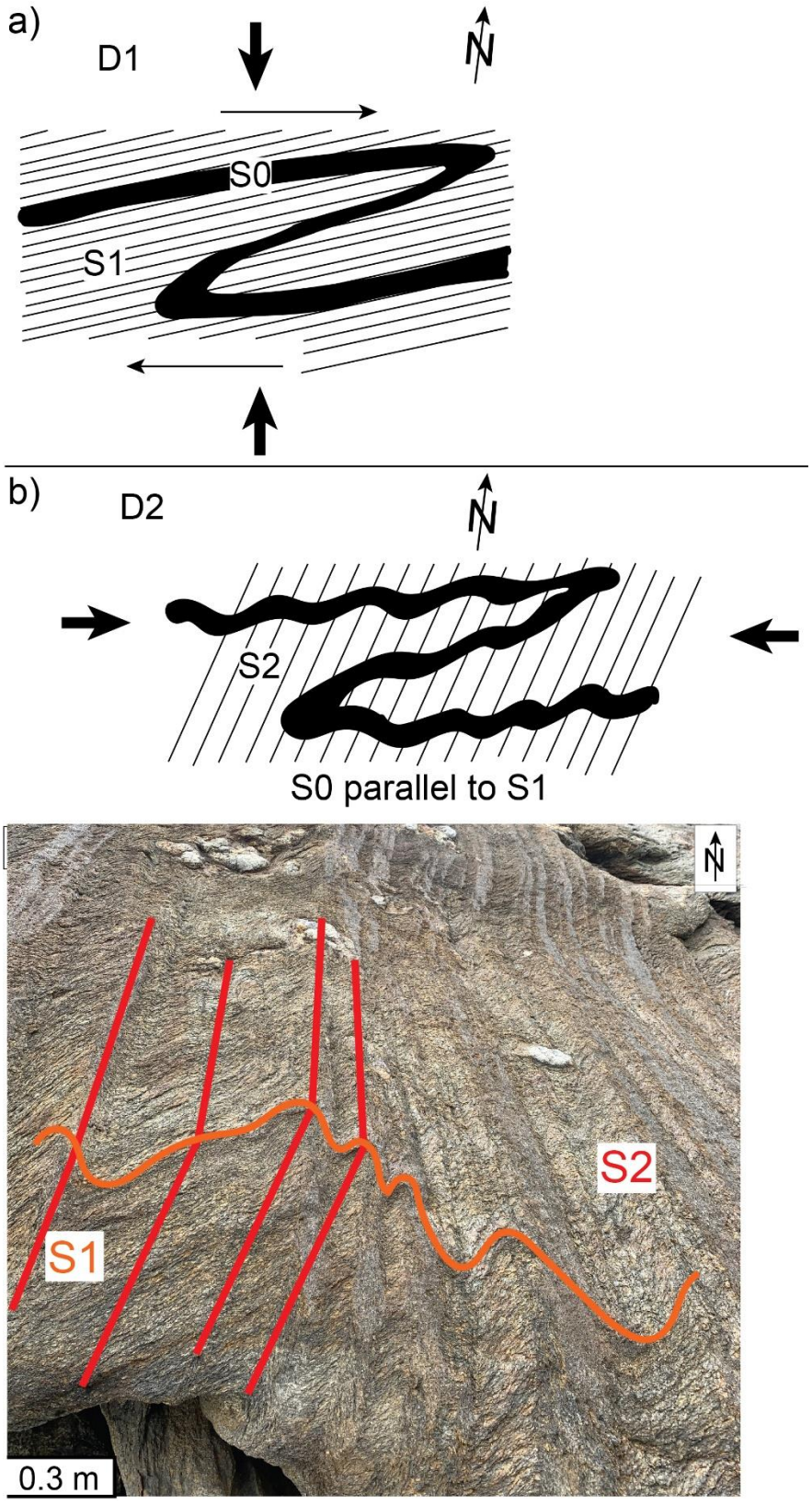


***Figure 120**: Schematic model of the foliation development during two deformation phases. Typical development in schist belts. A) Deformation phase 1. Development of a spaced cleavage (S1) and the belonging F1 folds (sub simple shear). B) Deformation phase 2. Development of a crenulation cleavage (S2) and F2 folds, folding the F1 folds during simple shear or sub-simple shear. C) Field photograph of the crenulation cleavage (S2) in the garnet mica schist. The folding in the garnet mica schist shows the S1 cleavage, which can be parallel to S0. Figure modified from Passchier and Trouw (2005).*

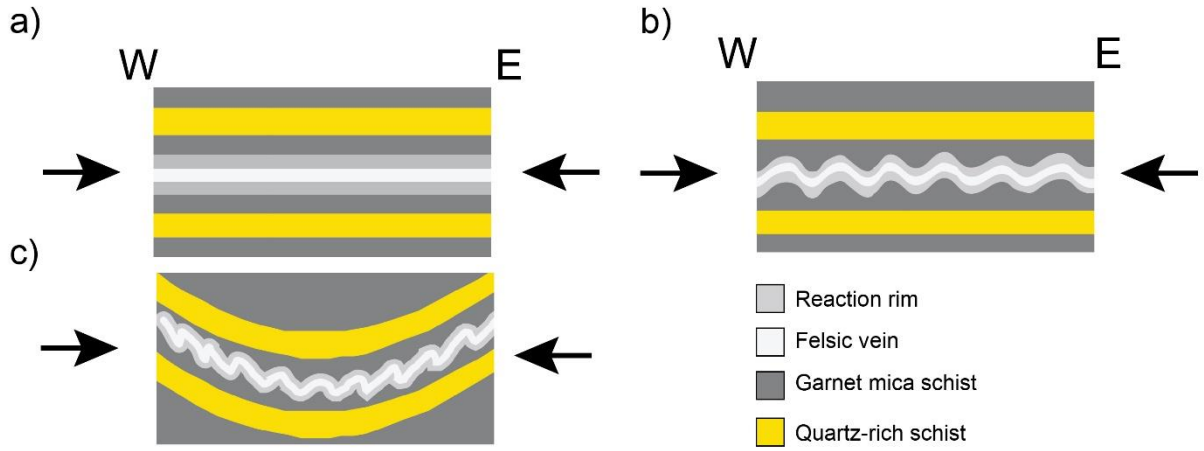


***Figure 121**: A schematic model of the formation of asymmetric folds (F2) observed in the field. The reaction rims, felsic veins and garnet mica schists has different competencies making them buckle at different times. Chronological order from A to C. Modified from Ramberg (1963).*

**Metamorphism**

The mineralogy and structural textures have been studied in thin section in an attempt to obtain information about the metamorphic history for the rocks at Kallvatnet. Both S1 and S2 seem to be associated with the same mineral assemblage, indicating that the S1 and S2 were formed under similar metamorphic conditions. Some discordant muscovite and chloritization indicates the addition of fluids resulting in retrograde metamorphic reactions (Best, 2003, Winter, 2014).

The garnets at Kallvatnet that have been studied in thin sections are interpreted as pre/intra tectonic (see *Figure 81a*) due to the external foliation which buckles around the garnet showing an internal foliation (Si). The straight internal foliation differs from S1 and S2, meaning that the garnet probably crystallized before the formation of F1 and F2. This indicates that the peak mineral assemblage conditions were achieved before the formation of F1 and F2.

Garnets show compositional zoning with distributions of inclusions, which have shown to be related to metamorphic reactions involving other minerals in the rock (Thompson et al., 1977). The concentric compositional zoning observed reflects progressive growth of the garnet crystal as the availability of chemical components changes in response to metamorphic reactions (Tobisch, 2005). The garnets analyzed in the garnet mica schist (*Figure 56a*) and the reaction rim (*Figure 56c*) have a typical core-and-margin zonation (Tobisch, 2005), which is typical in high-grade pelites (Ikeda, 1993). The Mn concentrations are highest in the core and lower towards the rim, reflecting the preferred incorporation of Mn in the garnet, which is later depleted in the matrix (Ikeda, 1993). One garnet shows weakly oscillatory zonation (Mn-Fe core, Fe-Ca rim, Ca rim, zonation) (*Figure 57*) which is typical for open system growth with changes in the fluid composition (Jamtveit and Andersen, 1992). Some local changes in the fluid composition could have caused this type of zonation (Tobisch, 2005). Overall, all three garnets show normal zonation (i.e., decrease in the Mn component from core to rim), indicating that the garnet did not undergo any important pressure and temperature changes after the crystallization of the garnet (Passchier and Trouw, 2005).

The mafic layers (optically estimated) consist of garnet + amphibole (hornblende) + plagioclase + quartz + titanite ± biotite ± chlorite ± zoisite. This assemblage corresponds well to the amphibolite facies (Bucher and Grapes, 2011). The presence of epidote and the

green to weak blue hornblende indicate that the minerals formed within the lower temperature field in the amphibolite facies (epidote amphibolite, see *Figure 122b* and *c* (Binns, 1965, Bucher and Grapes, 2011, Winter, 2014) with PT-conditions of ca. 450-600°C and ca 7-10 kbar. No pyroxene is present, and the hornblende is not brown, which are expected in the granulite facies (Binns, 1965, Bucher and Grapes, 2011). Care should be taken when distinguishing between the amphibolite and granulite facies using metabasic rocks. Metabasic rocks lack truly unique mineral assemblages for the granulite facies, hence felsic rocks are preferred for this purpose (Bucher and Grapes, 2011).

No staurolite, kyanite, and partial-melting have been observed in the Kjerringfjell Group as suggested by Slagstad et al. (2021). The dominant garnet mica schist assemblages consist of garnet + biotite + plagioclase + albite ± chlorite ± muscovite. Plotting the assumed mineral assemblage in the facies diagram (*Figure 122a* from Bebout et al. (1999)) indicates epidote amphibolite facies. The AFM diagrams from Spear and Cheney (1989) yield fields H, I, and J in the KFMASH-grid (red field in *Figure 123a*). Assuming a typical geothermal gradient ((Brown and Mussett, 1993)), the pressure-temperature conditions in the petrogenetic grid are approximately 7-8 kbar and 550-600°C (yellow field). The KFMASH diagrams estimated a higher temperature and lower pressures compared to the estimation with the mafic rocks. These differences can be explained by high Mn and Ca-components in the system. As shown in *Figure 123b* the garnet-chlorite stability fields will shift towards lower temperatures and higher pressures with increasing Mn and Ca component in the garnet. The detailed EDS-maps of garnet (*Figure 56a* and *c* and *Figure 57*) show that the Mn and Ca components are significant and have likely influenced the stability of chlorite and garnet in the pelite samples. P-T conditions of ca. 450-600°C and ca 7-10 kbar are preferred.

This is only a rough estimation, further geothermobarometry is needed to constrain the metamorphic conditions.

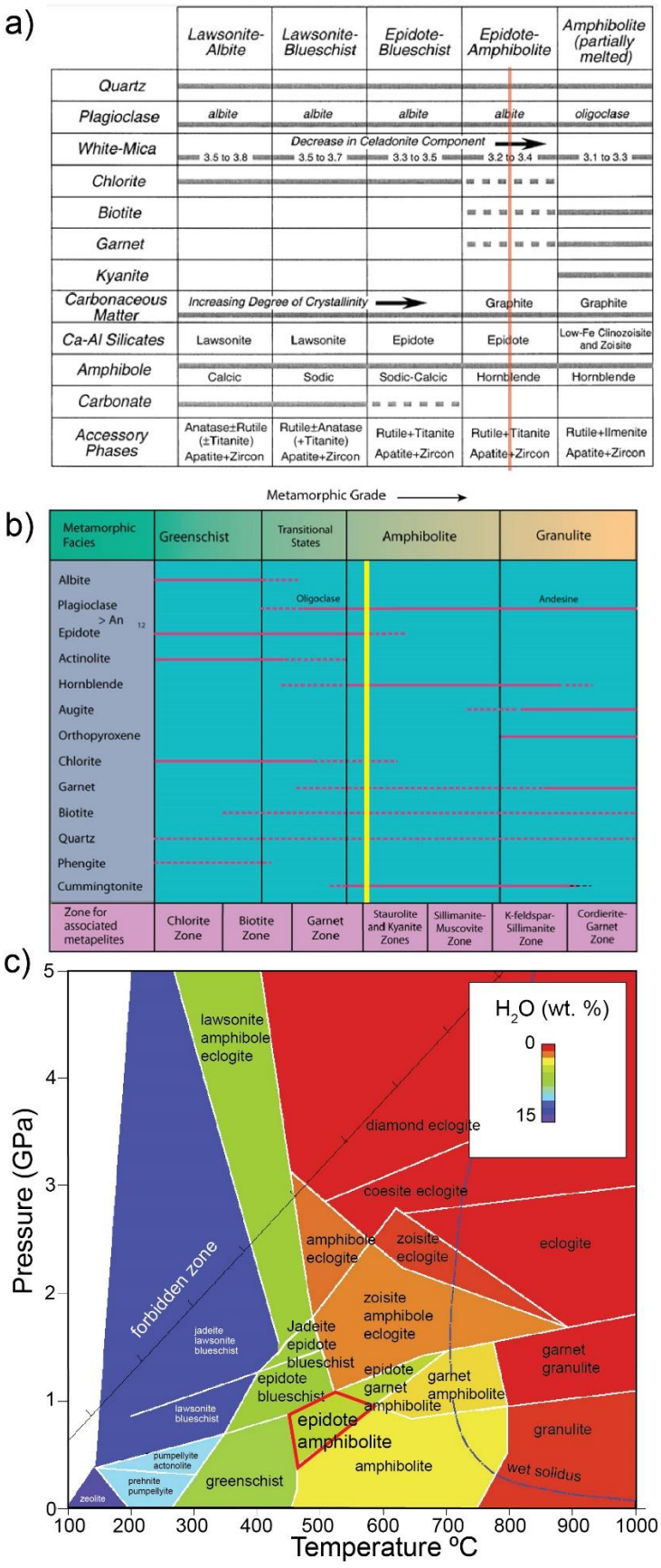


***Figure 122**: A) Metamorphic facies diagram for metasedimentary rocks from Bebout et al. (1999). B) Metamorphic facies diagram for mafic rocks during progressive metamorphism in the medium P/T series, from Winter (2014). C) Facies diagram for mafic rocks. From (Hacker, 2022).*

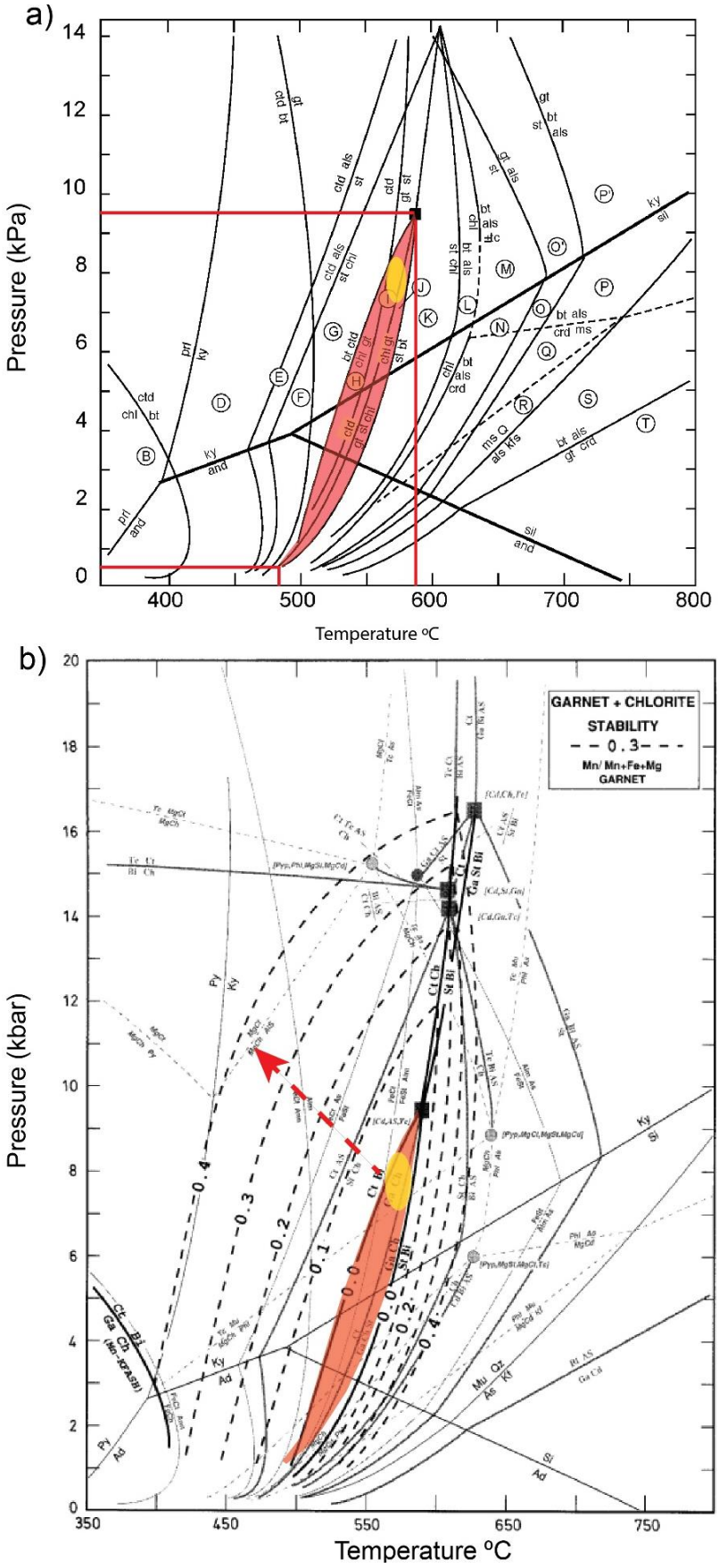


***Figure 123***:. *A) KFMASH-Petrogenetic grid from Spear and Cheney (1989). B) The dashed arrow indicates the influence of Mn and Ca component in garnet on the stability of garnet + chlorite in the grid. From Spear and Cheney (1989).*

The ages obtained from the metamorphic geochronology are summarized in *Table 4.* Two garnet mica schist samples (gmf2020-02 and gmf2020-11) show signs of Neoproterozoic monazite crystallization. Sample gmf2020-02 was sampled at Kallvatnet and has one concordant monazite at 560 Ma and one discordant at ca. 600 Ma (*Figure 97*). Sample gmf2020-11 was sampled near Sauvasshytta (near Umbukta). This sample shows a classical $Pb_c$ discordia consisting of six monazite grains (*Figure 101*). The lower intercept of the discordia yields an age of 559 ± 7.8 Ma. The systematic increase in $Pb_c$ can be explained by the size of the analyzed monazites. Several of the monazites were very small, making it likely that the laser hit the surrounding feldspar which has a high content of lead. The 600 Ma analysis in gmf2020-02 is discordant, possibly affected by $Pb_c$ and not considered a reliable age, hence the 560 Ma age is the preferred age for the Neoproterozoic metamorphic event in the Kjerringfjell Group.

One concordia age based on two monazites from sample gmf2020-02 was calculated to be 484.1 ± 6 Ma (*Figure 97*). This age is only based on two monazites but indicates a metamorphic event at ca. 484 Ma in the Kjerringfjell Group.

A reaction rim and one garnet mica schist (gmf2021-07A (*Figure 89*) and gmf2021-14 (*Figure 93*)) at Kallvatnet contain metamorphic zircons crystallized at 449 ± 6 and 449 ± 5 Ma. In addition, one $^{238}U/^{206}Pb$ age of a monazite in sample gmf2020-02 was calculated to be 458.6 ± 4 Ma (*Figure 97*). These ages overlap and are interpreted as the timing of an Ordovician metamorphic event at in the Kjerringfjell Group.

Four dated samples from Kallvatnet (gmf2020-21 (*Figure 86*), gmf2021-05 (*Figure 88*), gmf2021-11C (*Figure 92*) and gmf2020-10 (*Figure 99*)) contain metamorphic zircons or monazites crystallized at 434 ± 5, 437 ± 6, 439 ± 11, 412.7 ± 6 and 366 ± 19 Ma respectively. The three first ages overlap and are interpreted to represent the same metamorphic event. The youngest ages 412.7 ± 6 and 366 ± 19 are based on only two monazites, hence they are highly uncertain. The youngest monazite may have undergone recent lead loss during a retrogression event and the high uncertainty can be explained by the incorporation of $Pb_c$. The 412 Ma age may indicate a retrogression event, but this is only speculation and is only based on one monazite grain. The metamorphic event occurring at ca. 437 Ma is interpreted to represent the Scandian-Collision between Laurentia and Baltica (Gee et al., 1985, Roberts and Gee, 1985). As mentioned earlier the deformation structures in the Kjerringfjell Group have a typical Scandian signature, hence it is preferable to link the deformation event/events to the 437 Ma metamorphic event.

The internal foliation observed in the garnet (*Figure 81a*) is most likely a tectonic foliation formed either during the Neoproterozoic (560 Ma), Early Ordovician (484 Ma), or Ordovician (450) metamorphic event. Further petrography, geochronological, and isotope studies are needed to connect the pre-Scandian deformation with an age.

Summarized, the mineral assemblages from the mafic rocks and pelites from Kallvatnet indicate the peak mineral assemblage formed during epidote amphibolite facies representing pressure temperature conditions of 7-10 kbar and 450-600°C. Internal foliation in the garnet indicates that the peak mineral assemblage was probably formed before the main deformation event forming isoclinal F1, open to close F2, and crenulation folds during the Scandian-Collision at ca. 437 Ma. The internal foliation likely represents an earlier metamorphic event in the Kjerringfjell Group either during a Neoproterozoic (560 Ma), Early Ordovician (484) or Ordovician event (450 Ma).

***Table 4:*** *Summarizes the dated metamorphic zircons and monazites in this study. The number of zircons/monazites the ages are based on is given in column "#Mineral".*

| Metamorphic zircon and monazite | | | | | |
|---|---|---|---|---|---|
| Sample | UTM E | UTM N | Rock | Age (Ma) | #Mineral |
| gmf2020-21 | 66.23696 | 14.77714 | Felsic vein | 434 ± 5 | 1 x zr |
| gmf2021-05 | 6623661 | 14.77872 | Felsic vein | 437.4 ± 6 | 3 x zr |
| gmf2021-07A | 66.23534 | 14.78177 | Reaction rim | 449 ± 6 | 2 x zr |
| gmf2021-11C | 66.24006 | 14.78904 | Garnet mica schist | 439 ± 11 (480-420) | 18 x zr |
| gmf2021-14 | 66.24005 | 14.87401 | Garnet mica schist | 449.6 ± 5<br>449.1 ± 5 | 4 xzr |
| gmf2020-02 | 66.24847 | 14.95553 | Garnet mica schist | 484.1 ± 6<br>458.6 ± 4<br>560<br>600 | 2 x mz<br>1 x mz<br>1 x mz<br>1 x mz |
| gmf2020-10 | 66.30726 | 14.81168 | Garnet mica schist | 412 and 360 | 1 x mz<br>1 x mz |
| gmf2020-11 | 66.18046 | 14.72946 | Garnet mica schist | 559 ± 8 | 6 x mz |

**Magmatism**

The Umbukta gabbro was previously dated to 578 ± 6 Ma (Slagstad et al., 2021). This study presents two new crystallization ages, 614 ± 13 (*Figure 104a*) and 593 ± 3 Ma (*Figure 104b*) which are significantly older than the published age. The contact zone between the Umbukta gabbro and the garnet biotite gneiss (host rock) has shown mingling between the mafic and the felsic magma, gabbro cutting folds in the host rock and mafic dikes cutting both the gabbro and the host rock (Høyen, 2016). This range of crystallization ages and structural observations indicates that the gabbro intrusion had several active intrusion periods. The interval between 614 and 578 Ma is significantly long, so it is unlikely that the intrusion of the Umbukta gabbro occurred during such a long period. Coincidences and lead loss may have been factors which resulted in the youngest 578 ± 6 Ma age. The older 614 ± 13 Ma age of the gabbro and the 593 ± 3 Ma age of a dike related to the gabbro indicates that the gabbro intruded at 614 Ma and have several intrusion periods e.g., at 593 Ma.

The geochemical signature indicates that the concordant and discordant mafic sheets intruded the metasediments at Kallvatnet during two different magmatic events (*5.3.1*). The concordant and discordant mafic sheets have a mineral assemblage and a developed foliation which dictates that the mafic rocks were exposed to the Scandian Collision at 437 Ma.

The claim above means that the discordant mafic sheets managed to resist extensive folding during the Scandian event at 437 Ma. One can speculate if this can occur because of favorable intrusion direction/angles relative to the present stress field. The lack of observed discordant mafic sheets in the garnet mica schist indicates that the amount of deformation is lithology dependent.

Sills are common within shale formations, and several factors can explain why no discordant mafic sheets were observed in the garnet mica schist area

Gressier et al. (2010) presented a model which suggested that pore fluid pressure resulting from the maturation of organic matter may control sill initiation. In this case, fluid migration in the shales generates significant vertical fluid pressure gradients, resulting in vertical seepage forces that significantly reduce the effective vertical stress. The reduction of the effective vertical stress is so significant that it becomes smaller than the horizontal effective stress, resulting in favorable stress conditions for horizontal fracturing.

While organic-rich lithologies may control the initiation of sills, the lack of graphite in the garnet mica schist argues against this hypothesis.

The preferred hypothesis for the lack of discordant mafic sheets in the garnet mica schist concerns the rheology difference between the garnet mica schist and the quartz-rich lithologies (Galland et al., 2018). Schofield et al. (2012) and Spacapan et al. (2017) suggested that inelastic deformation behavior such as brittle shear and ductile deformation in shales controls the initiation of sills to a large degree. The pelites are weaker than the quartz-rich lithologies (Suppe, 1985), hence during deformation a more pervasive foliation developed in the mafic sheets located in the less competent pelite.

The discordant mafic sheets may have developed at a larger angle to the S1 foliation because the more competent host absorbed more of the stress. More competent layers are expected to fold in a larger scale than less competent rocks, making it hard to observe the folds in the field (Fossen, 2016) (same principle as shown in *Figure 121*). Further studies of the discordant mafic sheets and associated field relations need to be studied to conclude further.

The time of intrusion of the deformed concordant mafic sheets is believed to have occurred at approximately the same time as the intrusion of the felsic veins. The concordant mafic sheets and the felsic veins are both concordant with S1, folded by F1, F2 and have associated reaction rims. It is very important to mentioned that one cannot exclude the presence of two generations of mafic sheets in the garnet mica schist, especially if the deformation is rheology dependent. It is possible that the concordant mafic sheets with a relative high subduction component belongs to the second generation of mafic magmatism (*Figure 112*).

The time of intrusion of the felsic veins and the concordant mafic sheets (1. generation) is highly uncertain, this study will discuss two alternatives:

A) The intrusion of the felsic veins and the concordant mafic sheets with associated reaction rims intruded before or during the low-grade stages of the first metamorphic event in the Kjerringfjell Group, i.e., in the Neoproterozoic (*6.2.1 Neoproterozoic evolution*).

B) The intrusion of the felsic veins and the concordant mafic sheets with associated reaction rims occurred before the youngest recorded metamorphic event but after the Neoproterozoic, and Ordovician events (*6.2.2 Cambrian to Ordovician evolution*).

The timing of the intrusion is dependent on how the regional metamorphism affected the reactive properties of the garnet mica schist. If the Neoproterozoic metamorphic event did not suppress the reactive properties significantly one cannot exclude that the concordant mafic sheets and the felsic veins with associated reaction rims intruded post-Neoproterozoic.

Concerning the discordant mafic sheets (2. generation), this study argues that their intrusion at Kallvatnet occurred before the main metamorphic and deformation event at 437 Ma. The hypothesis depends on whether the discordant mafic sheets managed to resist the extensive 437 Ma deformation. The exact timing of the intrusion events for the concordant and the discordant mafic sheets in the Kjerringfjell Group are highly uncertain.

## 6.2 Correlation with surrounding tectonic units

A schematic time-space diagram including rocks at Kallvatnet, Umbukta, Mofjell, and Helgeland Nappe Complex is shown in *Figure 124*. The figure summarizes the interpreted geological data from Kallvatnet and compares it with the geological history of Umbukta (including the gabbro and the host rock), Mofjell Group, and Helgeland Nappe Complex.

### 6.2.1 Neoproterozoic evolution

The Neoproterozoic evolution of the Kjerringfjell Group will be discussed in this sub-section. Two main issues will be discussed. 1) The relations between the rocks at Kallvatnet and Umbukta, both areas are located within the Kjerringfjell Group. 2) Neoproterozoic felsic veins and mafic magmatism. The possibility of the intrusion of the concordant mafic sheets and felsic veins with reaction rims will be discussed (Alternative A).

**Kallvatnet vs Umbukta**

The metasediments just south of the Umbukta gabbro have yielded a 1030 Ma maximum age of deposition with dominant ages of detrital zircons between 1.9 and 1.0 Ga (Slagstad et al., 2021). The few data of detrital zircons (*Figure 95*) in this study indicate that the metasediments at Kallvatnet have approximately the same detrital zircon signature, indicating a similar sediment source for the rocks at Kallvatnet and Umbukta.

Slagstad et al. (2021) presented a crystallization age of a leucosome from a migmatitic psammite cut by a mafic dike related to the Umbukta gabbro (*Figure 125*b) to be 624 ± 6 Ma., interpreted as the timing of a regional high-grade metamorphic event in the Kjerringfjell Group. It is earlier argued (in this study) against the regional high-grade metamorphism and partial melting in the Kjerringfjell Group. The Umbukta gabbro intruded at 614 ± 13 Ma cross-cutting folds and fabric in the host rock at Sauvasshytta (*Figure 125a*). The observations dictate pre-614 Ma deformation, which generated open folds, looking similar to the open F2 folds observed at Kallvatnet. A sample (gmf2020-11 (*Figure 101*)) taken at Sauvasshytta close to the Umbukta gabbro indicates a metamorphic event at 560 Ma, so did a sample at Kallvatnet (gmf2020-02 (*Figure 97*)).

The attempt to date the 624 Ma metamorphic event at Kallvatnet was not successfully, indicating that the metamorphic event is exclusively related to the rocks close to the Umbukta gabbro. The monazites from the sample at Sauvasshytta (near Umbukta) (sample gmf2020-11 (*Figure 101*)) only show indication of a metamorphic event at 560 Ma, not 624 Ma. The 624 Ma crystallization age of the migmatite could be related to a contact metamorphic event related to the intrusion of the 614 Ma Umbukta gabbro.

It is important to emphasize that the spread in different ages for the Umbukta gabbro indicates the high uncertainty for the timing of the intrusion. Further isotope studies on the gabbro and the host rock are needed to constrain the intrusion history

(Høyen, 2016) presented a hypothesis that the rocks at Kallvatnet/Plurdal and Saufjellet may be separated from the rocks at Østre Sauvatnet and Umbukta. This hypothesis was derived from the differences in the lithology, appearances, and the presence of cross-cutting amphibolites at Østre Sauvatnet, which were not documented at Kallvatnet at that time. This study documents discordant amphibolites at Kallvatnet (*Figure 46d* and *Figure 65*), showing cross-cutting amphibolites also exist at Kallvatnet and Østre

Sauvatnet/Umbukta, seemingly weakens the hypothesis. On the other hand, the geochemical data from this study (*5.3.1*), comparing the rocks at Umbukta and Kallvatnet, emphasizes the genetic differences between the rocks. The new findings still strengthen the hypothesis that the rocks at Kallvatnet/Plurdal and Saufjellet/Umbukta are separated by an undiscovered tectonic contact, as suggested by Høyen (2016).

In the case of a tectonic contact, the regional 560 Ma metamorphic event dated at Sauvasshytta (Near Umbukta) and at Kallvatnet indicate that the rocks at both Kallvatnet and Umbukta were juxtaposed at that time.

The pre-614 Ma deformation event generating open folds recorded at Umbukta was not recorded at Kallvatnet. The extensive deformation generating open to close F2 folds at Kallvatnet has not been dated, but as earlier stated it is suggested that they are related to the latest Scandian collision at ca. 437 Ma. If the F2 folds at Kallvatnet are not pre-614 Ma, it is reasonable to believe that an unknown distance separated the metasediments at Kallvatent and Umbukta during the time of pre-614 deformation at Umbukta.

This is only speculation, further detailed fieldwork, geochemical, and geochronological analyses need to be done in the area between Umbukta and Kallvatnet.

**Neoproterozoic Metamorphism and Magmatism**

Despite the failed attempt to date the intrusion of the felsic veins and the concordant mafic sheets with associated reaction rims at Kallvatnet. Possible intrusion timing will be discussed.

*Alternative A) Neoproterozoic mafic magmatism and intrusion of felsic veins* (see *page 162*).

This alternative suggests that the felsic veins and mafic sheets intruded before the first metamorphic event. This means they intruded after 1030 Ma and before the Neoproterozoic metamorphic event at 560 Ma. The lack of felsic veins and garnet amphibolites with associated reaction rims near Umbukta could indicate that the intrusion occurred before Kallvatnet and Umbukta were juxtaposed (assuming a tectonic contact).

The concordant mafic sheets at Kallvatnet are believed to have originated from a MORB or back-arc basin source. No coeval magmatism is recorded in the Helgeland Nappe Complex, nor in the rest of the Rödingsfjället Nappe Complex. Tectonothermal events in this time interval have, e.g., been recorded in the Kalak Nappe Complex hosting the plume-related 560 to 520 Ma Seiland Igneous Province, which have been correlated to represent the Iapetus formation during the rifting of the super continent Rodinia (Kirkland et al., 2007b, Root and Corfu, 2012, Gasser et al., 2015).

High-grade metamorphism, as early as 560 Ma has not been recorded in other nappe complexes, which are believed to have been derived from the Laurentian margin. To the contrary, the Gondwana margin is believed to have been characterized by the formation of island-arc and back-arc systems (Murphy et al., 2013, Slagstad et al., 2021). So, one can speculate whether the 560 Ma metamorphic event and the intrusion of the concordant mafic sheets (MORB/back-arc basin) and felsic veins are associated with the arc-formation at the Gondwana margin or related to the rifting of the Laurentian margin. A third and the most likely alternative is that the intrusions are related to island-arc formation at the Laurentian margin, pre-Taconian orogenic development.

### 6.2.2 Cambrian to Ordovician evolution

This subsection will discuss the Cambrian to Ordovician geological evolution. Two main issues will be discussed: 1) Taconian signs in the Kjerringfjell Group 2) Late Ordovician magmatism, including the possibility of the intrusion of the concordant mafic sheets and felsic veins with reaction rims, will be discussed (Alternative B).

**Taconian signs in the Kjerringfjell Group?**

The Mofjell Group and the Kjerringfjell Group are separated by the Ørtfjell Group, the Dunderland formation, the Langfjell Shear Zone, and the Plura Nappe (Slagstad et al. (2021) and references therein). A 475 Ma pegmatite sheet in the shear zone was dated by Slagstad et al. (2021) and is interpreted to be syn-tectonic, dating the activation of the Langfjell Shear Zone. The vergence of the shear zone is unknown but the shear zone activation age is coeval with the well-known Taconian orogeny (Yoshinobu et al., 2002, Slagstad et al., 2021). The Mofjell group has been constrained to be formed at ca. 500 Ma (Gundersen, 2020, Slagstad et al., 2021), and the geochemistry confirms that the mafic rocks at Mofjell do not relate to the garnet amphibolites at Kallvatnet. The Mofjell group was most likely formed in an island-arc setting at the margin of a continent with some unknown distance from the Kjerringfjell Group (Gundersen, 2020). A syn-tectonic boudinaged granite pegmatite at northern Røssvatnet (further southwest in Rödingsfjället Nappe Complex) has been dated to be 515 Ma (Slagstad et al., 2021), which is coeval with both the vulcanism at Mofjell and the formation of the 497 Ma suprasubduction-zone-related Leka ophiolite in the Helgeland Nappe Complex (Dunning and Pedersen, 1988). These ages have been interpreted as the start of convergence in the Iapetus system either as the start of the Taconian or the Caledonian orogeny.

At Kallvatnet a 484 Ma monazite concordia-age based on two analyses was conducted and indicates a metamorphic event. This age is coeval with the 484 Ma cross-cutting granite dike at Røsssvatnet, which is the minimum age of deformation of the host rock (mica gneiss) in that area. Røssvatnet is located approximately 70 km southwest for Kallvatnet, the area between Røssvatnet and Kallvatnet has not yet been studied in detail. The 484 Ma age dated at Kallvatent is highly uncertain but correlates well with the intrusion age of the granitic dike at Røssvatnet.

To the west, The Helgeland Nappe Complex structurally overlies the Rödingsfjället Nappe Complex (Roberts et al., 2007). Both nappes show several similarities, such as Neoproterozoic-Early Silurian supracrustal successions containing voluminous marbles, iron formations, and pelitic schists deposited in a shelf-slope environment (Roberts et al., 2007) and Ordovician to early Silurian granitoid plutonism and batoliths (Nordgulen et al., 1993a, Barnes et al., 2007). The 484 Ma age from Kallvatnet and Røssvatnet overlap with the start of the imbrication of the Upper and Lower Nappes within the Helgeland Nappe Complex (Barnes et al., 2007). The Lower and Upper Nappes underwent high-grade metamorphism, crustal melting, and imbrication at ca 482 Ma (Barnes et al., 2007). The Middle, Sauren-Torghatten, and Horta Nappe underwent metamorphism at 475 Ma, marking the end of amalgamation of the nappes within the Helgeland Nappe Complex. The coeval 484 Ma ages from Kallvatnet and Røssvatnet and 475 Ma syn-tectonic age in the Langfjell shear zone indicate signs of Taconian orogeny in the Rödingsfjället Nappe Complex. Several folding phases at Mofjell have been described by Gundersen (2020). The F1 and F2 folds have been formed between 500 and 465 Ma, while the subsequent F3 folding have been dated and suggested to have formed at 465 ± 21 Ma, which is coeval with the Taconian events in the Helgeland Nappe Complex discussed above. Several

metamorphic zircons and one monazite indicate that a later metamorphic event occurred at 450 Ma at Kallvatnet. This age is coeval with the 453 Ma age from a migmatitic amphibole-biotite gneiss from the Helgeland Nappe Complex (Kirkland et al., 2018).

**Late Ordovician magmatism**

Helgeland Nappe Complex is characterized by post-amalgamation magmatic activity, with the incipient stages marked by the emplacement of the mafic Svarthopen pluton and the Hortavær igneous complex at 465 Ma (Barnes et al., 2007). Most of the Bindal Batholith was intruded during the emplacement of the 447 Ma Troholmen and Andalshatten pluton (Nordgulen et al., 1993b). The Velfjord pluton was emplaced in the interval 445-448 Ma (Yoshinobu et al., 2002), and smaller magmatic bodies such as the 447 Ma tonalitic intrusion (Yoshinobu et al., 2005), and the Kalvøya pluton were emplaced at 444 Ma (Barnes et al., 2007). The Heilhornet pluton was emplaced at 439 Ma followed by mafic, intermediate and felsic plutonism until 424 Ma. (Nordgulen and Sundvoll, 1992, Nissen et al., 2006).

Late Ordovician magmatism has also been recognized in the Kjerringfjell Group. A tonalitic body in the northeastern part in the Kjerringfjell Group has been dated to have intruded at 466 Ma, see *Figure 102*.

Alternative B) *Late Ordovician mafic magmatism and intrusion of felsic veins (see page 162):*

The felsic veins and the concordant mafic sheets with associated reaction rims (1. generations of mafic sheets) may have intruded during the Late-Ordovician. This alternative assumes that the reactive properties in the garnet mica schist were significant enough to generate the reaction rims. This means that the metasediments at Kallvatnet were exposed to two generations of mafic magmatism derived from two different sources during the Ordovician, one with more subduction component than the other.

It is possible that the intrusion of the two generations occurred in two periods during the progressive formation of an Ordovician island-arc related to the Taconian orogeny (*Figure 126*). The first generation of mafic magmatism occurred in the earlier stages of the formation of the arc, farther away from the subduction zone in a MORB environment. The second generation occurred later in the development of the arc-producing mafic magmatism with a higher subduction component, back-arc-magmatism.

The main arguments for alternative B) are: 1) The intrusion of the felsic veins would be coeval with 466 Ma emplacement of the tonalitic body in Kjerringfjell, which could have been the main magmatic source for the felsic veins. 2) The magmatic interlocking and GMB texture in the felsic veins indicate that the felsic veins have not undergone extensive metamorphic events. 3) The coeval frequent magmatism of both tonalitic and mafic magmatism in the Helgeland Nappe Complex.

Whether alternative *A)* "Neoproterozoic intrusion of the concordant mafic sheets and felsic veins with associated reaction rims" or alternative *B)* "Late Ordovician intrusion of the concordant mafic sheets and felsic veins with associated reaction rims" are correct are highly uncertain.

This study suggests that alternative "A)" is the best alternative. The main argument for Neoproterozoic intrusion is the presence of the distinctive reaction rims even in association with mm to cm thin felsic veins. The Neoproterozoic metamorphic event would likely suppress the reactive properties, making it harder for felsic intrusions to generate such distinct reaction rims.

This is mainly speculations so further studies of the Neoproterozoic metamorphic evolution of the Kjerringfjell Group are needed. It is important to investigate the formation of the reaction rims and how the Neoproterozoic metamorphism would have influenced the reactive properties in the metasediments. If the reaction properties were not significantly suppressed, it would be possible to form reaction rims after the Neoproterozoic metamorphism. Further attempts to date the Neoproterozoic metamorphic event and the concordant mafic sheets and the felsic veins are also needed.

As earlier stated, the discordant mafic sheets (2. generation) observed in the Kjerringfjell Group have not yet been dated. However, this study suggests that the back-arc basin derived discordant mafic sheets (2. generation) intruded before the Scandian-Collision, most likely behind an arc system associated with the Helgeland Nappe Complex (Figure 126). The five main arguments for this interpretation are: 1) Post-Scandian-Collision back-arc basin derived mafic sheets are not known to have occurred elsewhere in the Scandinavian Caledonides. 2) The Kjerringfjell Group has coeval tonalitic magmatism with the Helgeland Nappe Complex. 3) A 484 Ma metamorphic event recorded at Kallvatnet is coeval with the beginning of the nappe amalgamation in the Helgeland Nappe Complex. 5) The recorded thrusting in the Langfjell Shear Zone is coeval with the thrusting recorded in the Helgeland Nappe Complex. It is important to mention that this is highly uncertain, further isotopic studies are needed to strengthen this hypothesis.

### 6.2.3 Silurian evolution

**The Scandian-Collision**

A metamorphic event at 437 Ma and the formation of isoclinal F1 and F2 folds at Kallvatnet have been interpreted to have occurred during the Scandian collision. Slagstad et al. (2021) dated a 429 Ma syn-tectonic granite sheet at Mofjell, and Barnes et al. (2007) recorded a 430 Ma high-grade metamorphic event in the Helgeland Nappe Complex. All these Mid-Silurian events are interpreted to be associated with the collision between Laurentia and Baltica during the Scandian-thrusting. No Scandian event has yet been dated at Umbukta, but the gabbro and the host rock is garnet-bearing, indicating a high-grade event (Slagstad et al., 2021).

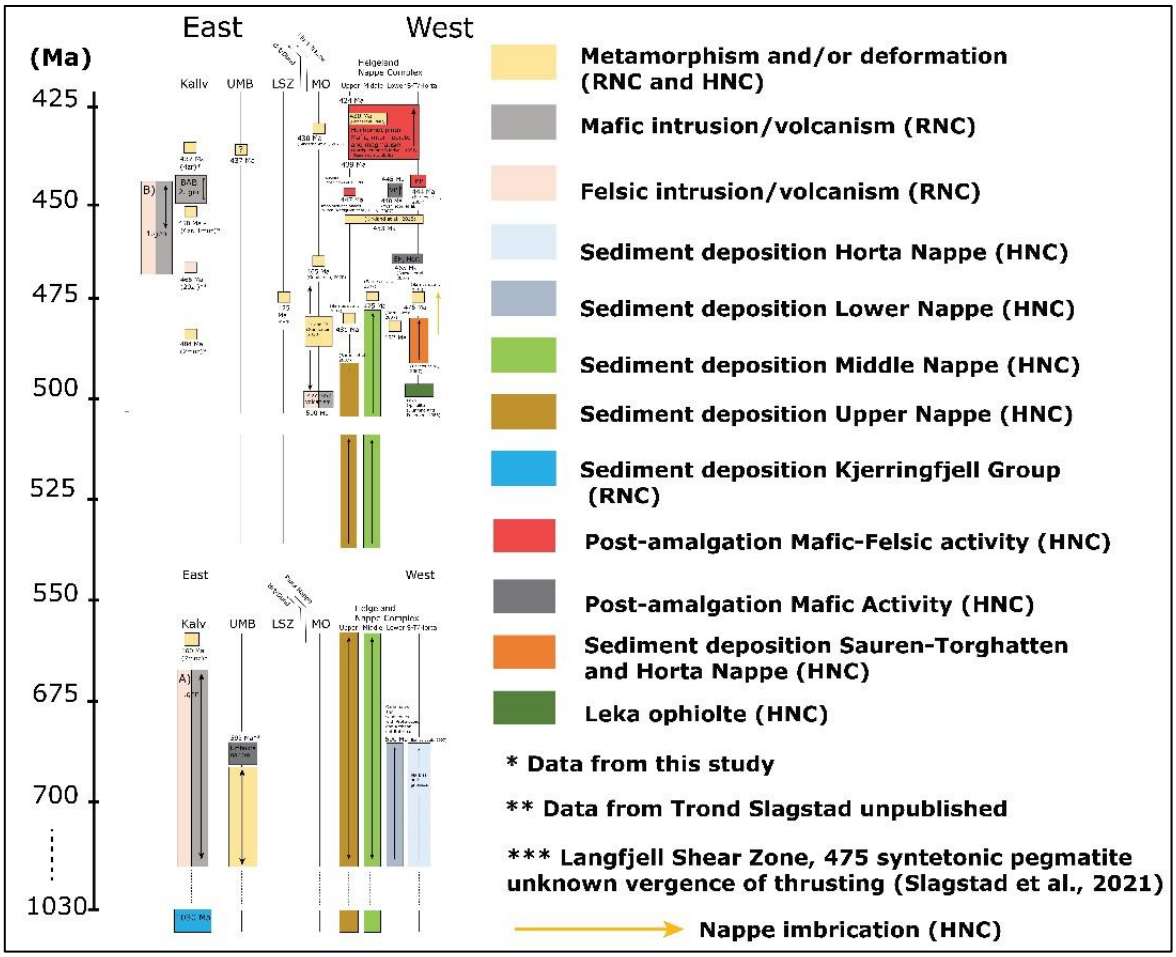
East
West
(Ma)
425
450
475
500
525
550
675
700
1030
Kallv
UMB
LSZ
MO
Helgeland Nappe Complex
East
West
Kalv
UMB
LSZ
MO
Helgeland Nappe Complex
Metamorphism and/or deformation (RNC and HNC)
Mafic intrusion/volcanism (RNC)
Felsic intrusion/volcanism (RNC)
Sediment deposition Horta Nappe (HNC)
Sediment deposition Lower Nappe (HNC)
Sediment deposition Middle Nappe (HNC)
Sediment deposition Upper Nappe (HNC)
Sediment deposition Kjerringfjell Group (RNC)
Post-amalgation Mafic-Felsic activity (HNC)
Post-amalgation Mafic Activity (HNC)
Sediment deposition Sauren-Torghatten and Horta Nappe (HNC)
Leka ophiolte (HNC)
* Data from this study
** Data from Trond Slagstad unpublished
*** Langfjell Shear Zone, 475 syntetonic pegmatite unknown vergence of thrusting (Slagstad et al., 2021)
Nappe imbrication (HNC)

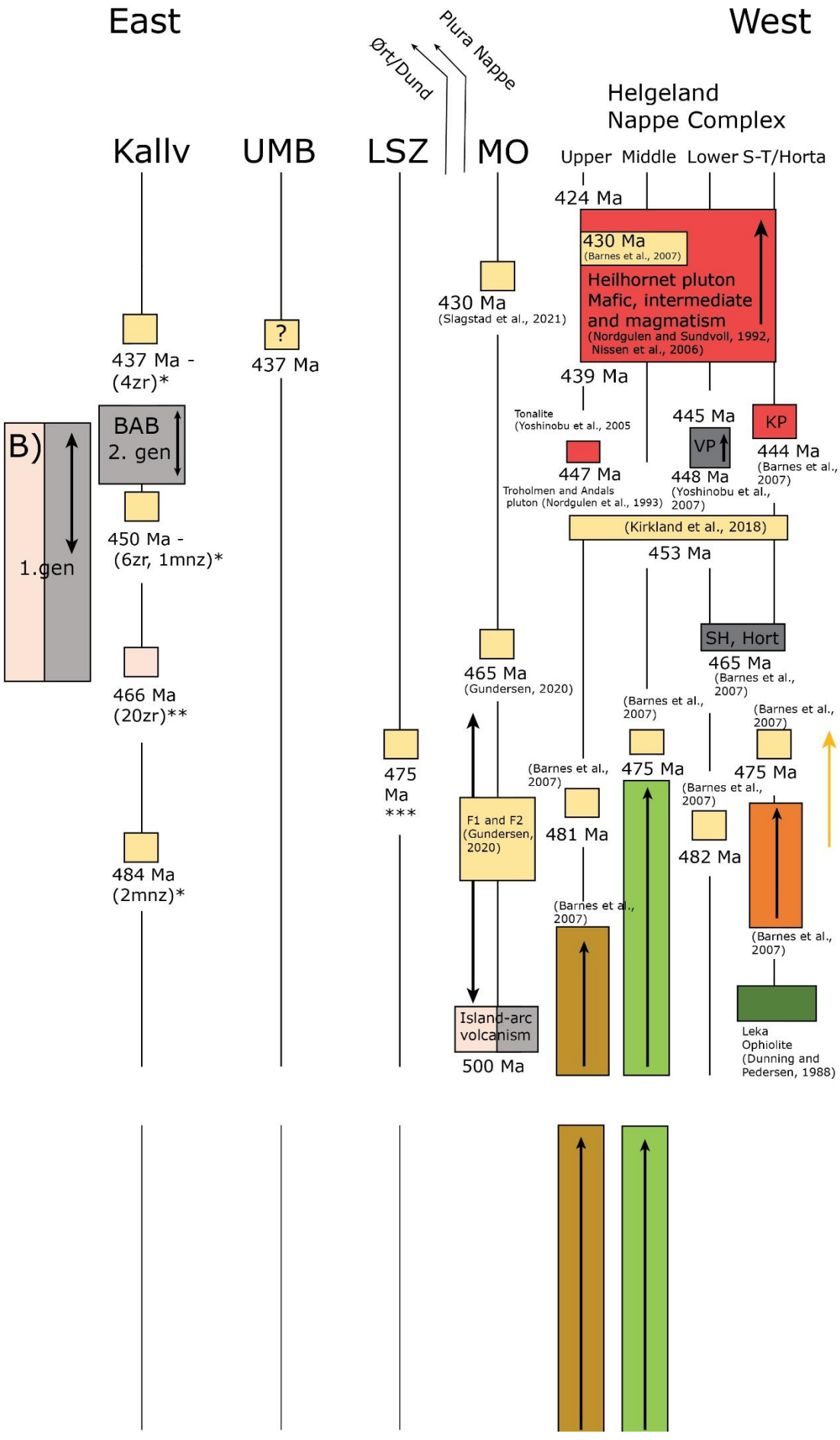
East
West
Ørt/Dund
Plura Nappe
Helgeland
Nappe Complex
Kallv
UMB
LSZ
MO
Upper
Middle
Lower
S-T/Horta
424 Ma
430 Ma
(Barnes et al., 2007)
Heilhornet pluton
Mafic, intermediate
and magmatism
(Nordgulen and Sundvoll, 1992,
Nissen et al., 2006)
430 Ma
(Slagstad et al., 2021)
439 Ma
Tonalite
(Yoshinobu et al., 2005
445 Ma
KP
444 Ma
(Barnes et al.,
2007)
VP
448 Ma
(Yoshinobu et al.,
2007)
447 Ma
Troholmen and Andals
pluton (Nordgulen et al., 1993)
(Kirkland et al., 2018)
453 Ma
SH, Hort
465 Ma
(Barnes et al.,
2007)
465 Ma
(Gundersen, 2020)
(Barnes et al.,
2007)
(Barnes et al.,
2007)
(Barnes et al.,
2007)
475 Ma
475 Ma
475
Ma
***
(Barnes et al.,
2007)
481 Ma
(Barnes et al.,
2007)
482 Ma
F1 and F2
(Gundersen,
2020)
(Barnes et al.,
2007)
(Barnes et al.,
2007)
Island-arc
volcanism
500 Ma
Leka
Ophiolite
(Dunning and
Pedersen, 1988)
437 Ma -
(4zr)*
?
437 Ma
B)
BAB
2. gen
1.gen
450 Ma -
(6zr, 1mnz)*
466 Ma
(20zr)**
484 Ma
(2mnz)*

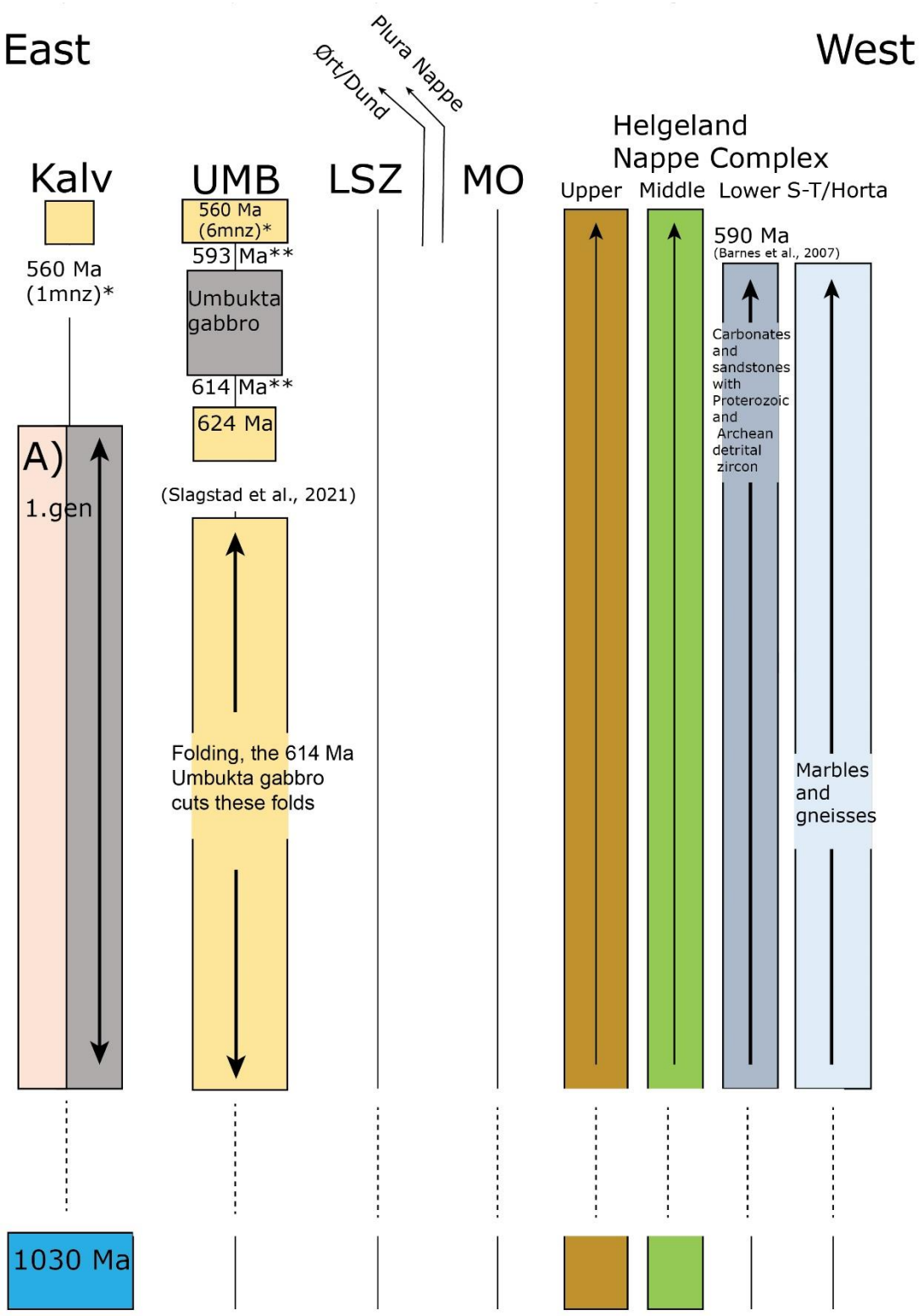


***Figure 124**: Schematic time-space diagram including rocks at Kallvatnet (Kalv), Umbukta (UMB), Mofjell (MO), Rödingsfjället Nappe Complex (RNC) and Helgeland Nappe Complex (HNC). Summarize the interpreted geological data from Kallvatnet and comparing it with the geological history of Umbukta, Mofjell Group and Helgeland Nappe Complex. Abbrevetions: Dunderland Formation (DUND), Ørtfejll Group (Ørt), Langfjell Shear Zone (LSZ), Sauren-Torghatten (ST), Svarthopen pluton (SH), Velfjord pluton (VP), Kalvøya pluton (KP). Data from: Slagstad et al. (2021), Barnes et al. (2007), Nordgulen and Sundvoll (1992), Nissen et al. (2006), Yoshinobu et al. (2005), Nordgulen et al. (1993a), Yoshinobu et al. (2002), Kirkland et al. (2018), Gundersen (2020), Dunning and Pedersen (1988), Inspired from Barnes et al. (2007) and (Slagstad et al., 2021).*

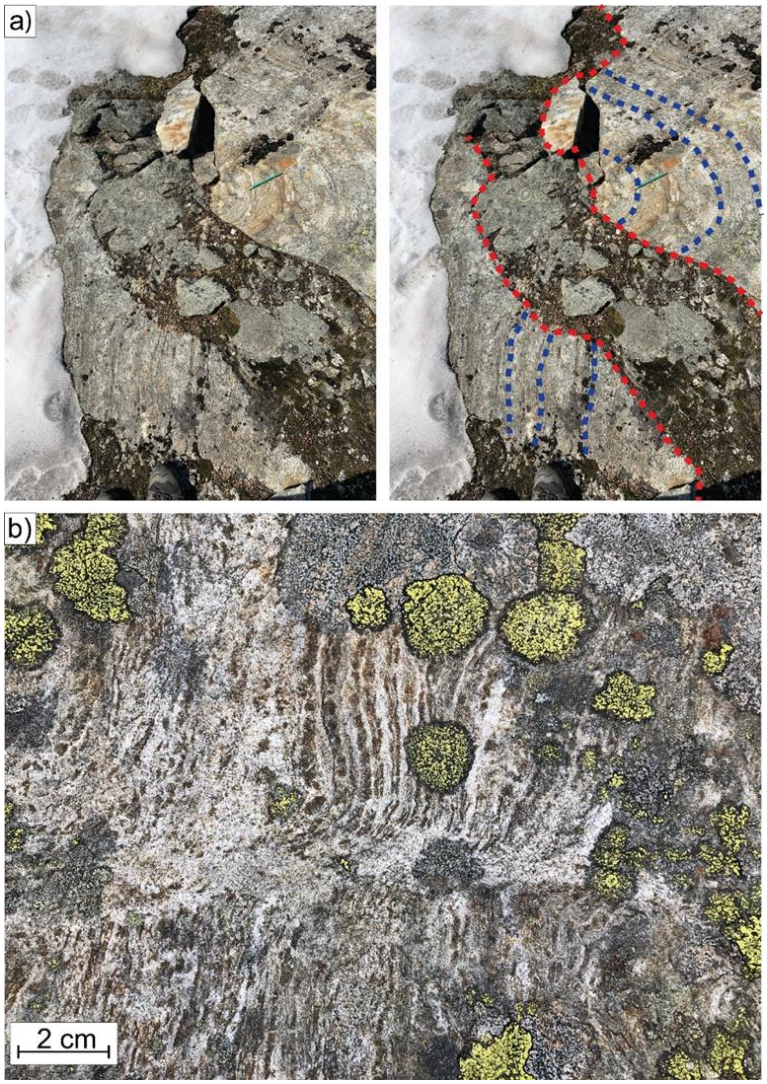


***Figure 125**: Mafic dike from the Umbukta gabbro cutting fold in the host rock at Sauvasshytta and migmatite in the contact zone. A) Mafic dike cuts both fold flanks at Sauvasshytta. The open folds the Umbukta dikes cut dictates a pre-614 Ma deformation event. It is suggested that these open folds are not the same as the open to close F2 folds at Kallvatnet B) A leucosome in the contact zone adjacent to the Umbukta gabbro.*

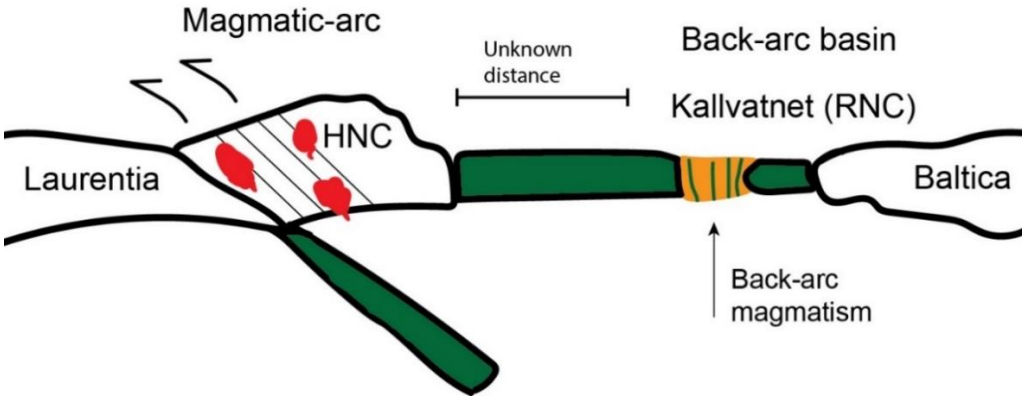


***Figure 126**: Schematic cross-section of the Taconian orogenesis with HNC and the position of Kallvatnet indicated. The rocks at Kallvatnet are position in a back-arc environment generating the apparent discordant mafic sheets. The distance between the HNC and RNC are unknown. Figure modified from Yoshinobu et al. (2002).*

## 6.3 Implication on the tectonostratigraphy

The Scandinavian Caledonides have traditionally been divided into a series of allochthons in tectonostratigraphic order, Lower, Middle, Upper, and the Uppermost Allochthon, which have been trusted on top of each other during the final Scandian collision during Silurian to late Devonian time (e.g., Gee et al. (1985), Roberts and Gee (1985)). The low- to high-grade metasedimentary rocks in the Lower and Middle Allochthons are interpreted to have been deposited at the western margin of Baltica in between the Baltican crystalline basement (Stephens et al., 1985). Arc-complexes, metasedimentary rocks and dismembered ophiolites in the Upper Allochthon represent the continent-ocean transition zone and the structurally overlain Iapetus terranes (Gee et al., 2014). The Uppermost Allochthon is believed to contain rocks with both oceanic and continental affinity representing the outer margin of Laurentia and unknown microcontinents (Roberts et al., 2007).

The Rödingsfjället Nappe Complex and the Helgeland Nappe Complex are known to be the two major units in the Uppermost Allochthon (Roberts et al., 2007). The structurally lowest part of the Ravnålia Nappe in the Rödingsfjället Nappe Complex; The Kjerringfjell Group have been studied in this thesis. Metamorphism overlapping with the Taconian orogeny, Ordovician tonalitic magmatism and 450 Ma metamorphism have been recorded in the Kjerringfjell Group, indicating affiliation to the Helgeland Nappe Complex. These observations confirm the current view on the coherence and similarities between the Kjerringfjell Group, belonging to the Rödingsfjället Nappe Complex, and the Helgeland Nappe Complex.

Several authors have been critical to the traditionally nappe stacking model, e.g., Corfu et al. (2014), suggesting that units of different origins have been juxtaposed with each other in a complex fashion. One argument for this complexity that Corfu et al. (2014) points at is the origin of the Kalak Nappe Complex. The nappe has traditionally been assigned to the Middle Allochthon, representing the outer part of the Baltican margin. Research (e.g., Gasser et al. (2015)) has shown extensive Neoproterozoic tectonothermal activity in the nappe which is atypical for the Baltican margin at that time, indicating the Kalak Nappe Complex to be exotic to Baltica.

As mentioned earlier, Slagstad et al. (2021) suggested that the Kjerringfjell Group underwent high-grade metamorphism with partial melting at 624 Ma prior to the intrusion of the Umbukta. A link between the Kalak Nappe Complex and the Rödingsfjället Nappe Complex was suggested based on the similar Neoproterozoic high-grade rocks and hosting of similar plume related rocks, the Seiland Igneous Province and the Umbukta gabbro respectively. The Neoproterozoic high-grade tectonothermal events in the Kalak Nappe Complex have been correlated with the Grenville and Porsanger Orogeny (Kirkland et al., 2007b). This correlation would assign the Kalak Nappe Complex and the Seiland Igneous Province to be exotic to Baltica. The assignation of peri-Laurentian affinity to the Kalak nappe Complex results in the correlative Seve Igneous Province also being exotic to Baltica (Slagstad et al., 2021).

The similiar complex and extensive Neoproterozoic tectonothermal history recorded in the Kalak Nappe Complex has not been recorded in the Rödingsfjället Nappe Complex. The partial melting (migmatization) in the Umbukta gabbro host rock seems to be locally and not representative to a regionally partial melting in the Kjerringfjell Group as suggested by Slagstad et al. (2021). It is suggested that the partial melting is associated with contact metamorphism locally in the contact zone related to the intrusion of the Umbukta gabbro.

Despite no dating of extensive complex Neoproterozoic metamorphism, a 560 Ma metamorphic event in the Rödingsfjället has been presented in this study, possibly related to a pre-Taconian event. It is also suggested in this study that the intruded felsic veins and the concordant deformed mafic layers with associated reactions rims are related to rift magmatism and metamorphism post-dating 1030 and pre-dating 560 Ma.

The few signs of Neoproterozoic tectonothermal events in the Rödingsfjället Nappe Complex weakens the hypothesis suggested (by Høyen (2016), Slagstad et al. (2021)): To correlate the Seiland Igneous Province and the Umbukta gabbro based on similar extensive and complex Neoproterozoic tectonothermal events in the host rocks are no longer as evident. This weakens the hypothesis about the correlation between the Rödingsfjället Nappe Complex and the Kalak Nappe Complex, which has resulted in a possible Baltica-exotic affinity to the Seven Igneous Province.

# 7 Conclusions

The Kjerringfjell Group in the Rödingsfjället Nappe Complex has been carefully mapped and samples collected for geochemical, geochronological, and petrographic analyses. The main findings from this study are presented below.

- Field observations and geochemistry indicate that the apparent "leucosomes" observed in the Kjerringfjell Group are felsic intrusions that caused alteration of the immediate host rock (reaction rims) and are not associated with regional partial melting as proposed by Slagstad et al. (2021).

- The lack of an extensive Neoproterozoic metamorphic history in the Kjerringfjell Group weakens the previously proposed correlation between the Rödingsfjället Nappe Complex and the Kalak Nappe Complex which has been used to argue for a non-possible Baltican affinity for the Seve Igneous Province.

- Geochemical, geochronological, petrography and structural analyses indicate that the rocks in the Kjerringfjell Group underwent metamorphism at ca. 437 Ma during the Scandian-collision between Laurentia and Baltica under epidote amphibolite facies conditions.

- Ordovician metamorphic and tonalitic magmatic events, and the 475 Ma Langfjell shear zone in the Kjerringfjell Group indicate affiliation with the Helgeland Nappe Complex and the Taconian orogeny.

- The geochemical data from the mafic rocks indicate that there are at least two generations of mafic rocks at Kallvatnet. It is suggested that the second generation is associated with back-arc basin formation behind an island-arc belonging to the Helgeland Nappe Complex. The first generation appears to be associated with late Neoproterozoic tectonothermal events.

- New zircon ages indicate that the Umbukta gabbro intruded at 614 Ma with several intrusion periods e.g., at 593 Ma. The spread in geochronological data (578-614 Ma) from the Umbukta gabbro makes the timing of the intrusion of the gabbro uncertain.

- A 624 Ma high-grade metamorphic event in the Kjerringfjell Group presented by Slagstad et al. (2021) is likely related to a contact metamorphic event generated by the intrusion of the Umbukta gabbro. The gabbro cuts open folds which dictates pre-614 Ma deformation.

- The mafic rocks at Kallvatnet are geochemically distinctly different from the mafic rocks at Mofjell and Umbukta.

- The 560 Ma metamorphic event recorded at both Kallvatnet and Umbukta indicate that the Kjerringfjell Group underwent a regional metamorphic event at that time.

- Geochemical data strengthen the hypothesis suggested by Høyen (2016) about the presence of a tectonic contact between the rocks at Kallvatnet and Umbukta; however, no direct evidence of such a contact has been found.

# Further work

- Structural field mapping, petrographic, geochemical, and geochronological analyses in the area between Kallvatnet and Umbukta. This is needed to investigate a possible tectonic contact and relations between the mafic rocks at Kallvatnet and Umbukta. In addition to examine the Neoproterozoic metamorphic evolution and the pre-614 deformation event near Umbukta.

- Do further geochronological analyses on the Umbukta gabbro to increase the certainty of the intrusion timing.

- Investigate the apparent discordant mafic rocks at Kallvatnet and its internal foliation and its relation to the external foliation in the host rock in more detail.

- Use other isotopic dating techniques to attempt to date the timing of the intrusion of the felsic veins and the mafic magmatism at Kallvatnet.

- Structural mapping and petrographic analyses of the Langfjell shear zone to investigate the vergence direction of the shear zone.

- Conduct geochemical analyses of the tonalite in the Kjerringfjell Group to investigate possible similarities between the tonalite and the felsic veins.

- Continue the mapping, geochemical and geochronological analyses further east at Kallvatnet.

# References


ANDERSEN, T. 2002. Correction of common lead in U-Pb analyses that do not report $^{204}$Pb. *Chemical Geology,* 192**,** 59-79.

ANDERSEN, T., ELBURG, M. A. & MAGWAZA, B. N. 2019. Sources of bias in detrital zircon geochronology: Discordance, concealed lead loss and common lead correction. *Earth-Science Reviews,* 197**,** 102899.

BARNES, C., MAJKA, J., SCHNEIDER, D., WALCZAK, K., BUKAŁA, M., KOŚMIŃSKA, K., TOKARSKI, T. & KARLSSON, A. 2019. High-spatial resolution dating of monazite and zircon reveals the timing of subduction–exhumation of the Vaimok Lens in the Seve Nappe Complex (Scandinavian Caledonides). *Contributions to Mineralogy and Petrology,* 174**,** 5.

BARNES, C. G., FROST, C. D., YOSHINOBU, A. S., MCARTHUR, K., BARNES, M. A., ALLEN , C. M., NORDGULEN, Ø. & PRESTVIK, T. 2007. Timing of sedimentation, metamorphism, and plutonism in the Helgeland Nappe Complex, north-central Norwegian Caledonides. *Geosphere,* 3**,** 683-703.

BATEMAN, H. 1910. Solution of a system of differential equations occuring in the theory of radioactive transformations. *Proceedings of the Cambridge Pilosophical Society,* 15**,** 423-427.

BEBOUT, G. E., RYAN, J. G., LEEMAN, W. P. & BEBOUT, A. E. 1999. Fractionation of trace elements by subduction-zone metamorphism—effect of convergent-margin thermal evolution. *Earth and Planetary Science Letters,* 171**,** 63-81.

BENDER, H., RING, U., ALMQVIST, B. S. G., GRASEMANN, B. & STEPHENS, M. B. 2018. Metamorphic Zonation by Out-of-Sequence Thrusting at Back-Stepping Subduction Zones: Sequential Accretion of the Caledonian Internides, Central Sweden. *Tectonics,* 37**,** 3545-3576.

BEST, M. G. 2003. *Igneous and metamorphic petrology second edition*, Blackwell Science Ltd.

BINGEN, B., DAVIS, W. J., HAMILTON, M. A., ENGVIK, A. K., STEIN, H. J., SKÅR, Ø. & NORDGULEN, Ø. 2008. Geochronology of high-grade metamorphism in the Sveconorwegian belt, S. Norway: U-Pb, Th-Pb and Re-Os data. *Norwegian Journal of Geology/Norsk Geologisk Forening,* 88.

BINNS, R. 1965. The mineralogy of metamorphosed basic rocks from the Willyama complex, Broken Hill district, New South Wales. Part I. Hornblendes. *Mineralogical magazine and journal of the Mineralogical Society,* 35**,** 306-326.

BJERKGÅRD, T., MARKER, M., SLAGSTAD, T. & SOLLI, A. 2013. The Mofjell Project: Summary and conclusions. *Geological Survey of Norway Report.* Trondheim: Geological Survey of Norway

BLEEKER, W. 2003. The late Archean record: a puzzle in ca. 35 pieces. *Lithos,* 71**,** 99-134.

BRATTLI, B. 1996. Structures and metamorphism at Brygfjell-Simafjell within the Rødingsfjellet Nappe Complex, Nordland, Norway.

BROWN, G. C. & MUSSETT, A. E. 1993. The Inaccessible Earth: An Integrated View of its Structure and Composition, 276 pp. Chapman and Hall, London.

BRUECKNER, H. K. & VAN ROERMUND, H. L. M. 2007. Concurrent HP metamorphism on both margins of Iapetus: Ordovician ages for eclogites and garnet pyroxenites from the Seve Nappe Complex, Swedish Caledonides. *Journal of the Geological Society,* 164**,** 117-128.

BRAATHEN, A., OSMUNDSEN, P. T., NORDGULEN, Ø., ROBERTS, D. & MEYER, G. B. 2002. Orogen-parallel extension of the Caledonides in northern Central Norway: an overview. *Norwegian Journal of Geology/Norsk Geologisk Forening,* 82.

BUCHER, K. & GRAPES, R. 2011. *Petrogenesis of metamorphic rocks*, Springer Science & Business Media.

BUCHER, K. & STOBER, I. 2010. Fluids in the upper continental crust. *Geofluids,* 10**,** 241-253.

BURNHAM, C. W. 2015. Chapter 16. THE IMPORTANCE OF VOLATILE CONSTITUENTS. *Evolution of the Igneous Rocks.* Princeton University Press.

CABANIS, B. 1989. The La/10-Y/15-Nb/8 diagram-A tool for discriminating volcanic series and evidencing continental-crust magmatic mixtures and/or contamination. *Comptes Rendus de l'Acaddmie des Sciences, ser. 2,* 309**,** 2023-2029.

CABANIS, B. & LECOLLE, M. 1989. Le diagramme La/10 – Y/15 – Nb/8: Un outil pour la discrimination des series volcaniques et en evidence des mélange et/ot de vontamination crustale. *Comptes Rendus de l'Académie des Sciences,* 2**,** 2023-2029.

CHERNIAK, D. J. & WATSON, E. B. 2003. Diffusion in zircon. *In:* HANCHAR, J. M. & HOSKIN, P. W. O. (eds.) *Zircon. Reviews in Mineralogy and Geochemistry.*

CLAVIER, N., PODOR, R. & DACHEUC, N. 2011. Crystal chemistry of the monazite structure. *Journal of the European Ceramic,* 31**,** 941-976.

COCKS, L. R. & TORSVIK, T. H. 2002. Earth geography from 500 to 400 million years ago: a faunal and palaeomagnetic reveiw. *Journal of the Geological Society of London,* 159**,** 631-644.

COCKS, L. R. & TORSVIK, T. H. 2005. Baltica from the late Precambrian to mid-Palaeozoic times: The gain and loss of a terrane's identity. *Earth-Science Reviews,* 72**,** 39-66.

CORFU, F. 1988. Differential response of U-Pb systems in coexisting accessory minerals, Winnipeg River Subprovince, Canadien Shield: implications for Archean crustal growth and stabilization. *Contributions to Mineralogy and Petrology,* 98**,** 312-325.

CORFU, F., ANDERSEN, T. B. & GASSER, D. 2014. The Scandinavian Caledonides: main features, conceptual advances and critical questions. *Geological Society, London, Special Publications,* 390**,** 9-43.

CORFU, F., GERBER, M., ANDERSEN, T. B., TORSVIK, T. H. & ASHWAL, L. D. 2011. Age and significance of Grenvillian and Silurian orogenic events in the Finnmarkian Caledonides, northern NorwayThis article is one of a series of papers published in this Special Issue on the theme of Geochronology in honour of Tom Krogh. *Canadian Journal of Earth Sciences,* 48**,** 419-440.

CORFU, F., HANCHAR, J. M., HOSKIN, P. W. O. & KINNY, P. D. 2003. Atlas of zircon textures. *In:* HANCHAR, J. M. & HOSKIN, P. W. O. (eds.) *Zircon.*

CORFU, F., ROBERTS, R. J., TORSVIK, T. H., ASHWAL, L. D. & RAMSAY, D. M. 2007. Peri-Gondwanan elements in the Caledonian nappes of Finnmark, northern Norway: implications for the paleogeographic framework of the Scandinavian Caledonides. *American Journal of Science,* 307**,** 434-458.

COSGROVE, J. W. 1972. The development and interrelationship of microfolds and crenulation cleavage.

DUNNING, G. 1987. U/Pb zircon ages of Caledonian ophiolites and arc sequences: Implications for tectonic setting. *European Union of Geosciences IV Strasbourg***,** 179.

DUNNING, G. & PEDERSEN, R.-B. 1988. U/Pb ages of ophiolites and arc-related plutons of the Norwegian Caledonides: Implications for the development of Iapetus. *Contributions to Mineralogy and Petrology,* 98**,** 13-23.

ENGVIK, A. K., BERTRAM, A., KALTHOFF, J. F., STÖCKHERT, B., AUSTRHEIM, H. & ELVEVOLD, S. 2005. Magma-driven hydraulic fracturing and infiltration of fluids into the damaged host rock, an example from Dronning Maud Land, Antarctica. *Journal of Structural Geology,* 27**,** 839-854.

ESKOLA, P. 1915. On the relations between the chemical and mineralogical composition in the metamorphic rocks of Orijarvi region. *Bull. comm. géol. Finlande,* 44.

EVANS, D. A. D. & MITCHELL, R. N. 2011. Assembly and breakup of the core of Paleoproterozoic-Mesoproterozoic supercontinent Nuna. *Geology,* 39**,** 443-446.

FEDO, C. M., SIRCOMBE, K. N. & RAINBIRD, R. H. 2003. Detrital Zircon Analysis of the Sedimentary Record. *Reviews in Mineralogy and Geochemistry,* 53**,** 277-303.

FOSSEN, H. 2016. *Structural geology*, Cambridge university press.

GALLAND, O., BERTELSEN, H., EIDE, C., GULDSTRAND, F., HAUG, Ø., LEANZA, H. A., MAIR, K., PALMA, O., PLANKE, S. & RABBEL, O. 2018. Storage and transport of magma in the layered crust—Formation of sills and related flat-lying intrusions. *Volcanic and igneous plumbing systems.* Elsevier.

GASQUET, D., BERTRAND, J.-M., PAQUETTE, J.-L., LEHMANN, J., RATZOV, G., DE ASCENCAO GUEDES, R., TIEPOLO, M., BOULLIER, A.-M., SCAILLET, S. & NOMADE, S. 2010. Miocene to Messinian deformation and hydrothermal activity in a pre-Alpine basement massif of the French

western Alps: new U-Th-Pb and argon ages from the Lauzière massif. *Bulletin de la Société Géologique de France,* 181**,** 227-241.
GASSER, D., JEŘÁBEK, P., FABER, C., STÜNITZ, H., MENEGON, L., CORFU, F., ERAMBERT, M. & WHITEHOUSE, M. J. 2015. Behaviour of geochronometers and timing of metamorphic reactions during deformation at lower crustal conditions: phase equilibrium modelling and U–Pb dating of zircon, monazite, rutile and titanite from the Kalak Nappe Complex, northern Norway. *Journal of Metamorphic Geology,* 33**,** 513-534.
GEE, D. G., FOSSEN, H., HENRIKSEN, N. & HIGGINS, A. K. 2008. From the Early Paleozoic Platforms of Baltica and Laurentia to the Caledonide Orogen of Scandinavia and Greenland. *Episodes,* 31**,** 44-51.
GEE, D. G., KUMPULAINEN, R. A., ROBERTS, D., STEPHENS, M. B., THON, A. & ZACHRISSON, E. 1985. *Scandinavian Caledonides tectonostratigraphic map*, 1:2,000,000. Sveriges Geologiska Undersökning, Ser. Ba NR 35.
GEE, D. G., LADENBERGER, A., DAHLQVIST, P., MAJKA, J., BE'ERI-SHLEVIN, Y., FREI, D. & THOMSEN, T. 2014. The Baltoscandian margin detrital zircon signatures of the central Scandes. *Geological Society, London, Special Publications,* 390**,** 131-155.
GEE, D. G., LOBKOWICZ, M. & SINGH, S. 1994. Late Caledonian extension in the Scandinavian Caledonides—the Røragen detachment revisited. *Tectonophysics,* 231**,** 139-155.
GEHRELS, G. 2011. Detrital zircon U-Pb geochronology: Current methods and new opportunities. *Tectonics of sedimentary basins: Recent advances***,** 45-62.
GOLDSCHMIDT, V. M. 1937. The principles of distribution of chemical elements in minerals and rocks. The seventh Hugo Müller Lecture, delivered before the Chemical Society on March 17th, 1937. *Journal of the Chemical Society (Resumed)***,** 655-673.
GOSCOMBE, B. D. & PASSCHIER, C. W. 2003. Asymmetric boudins as shear sense indicators—an assessment from field data. *Journal of Structural Geology,* 25**,** 575-589.
GRESSIER, J.-B., MOURGUES, R., BODET, L., MATTHIEU, J.-Y., GALLAND, O. & COBBOLD, P. 2010. Control of pore fluid pressure on depth of emplacement of magmatic sills: An experimental approach. *Tectonophysics,* 489**,** 1-13.
GUNDERSEN, S. F. 2020. *Structural controls on selected sulphide deposits in the Mofjellet Group.* NTNU.
HACKER, B. 2022. *Part 6. Mafic rocks* [Online]. Available: https://hacker.faculty.geol.ucsb.edu/geo102C/lectures/part6.html [Accessed 05.05.2022 2022].
HANCHAR, J. & HOSKIN, P. 2003. Zircon. Reviews in Mineralogy and Geochemistry. *The Mineralogical Society of America,* 153.
HANCHAR, J. M. & MILLER, C. F. 1993. Zircon zonation patterns as revealed by cathodoluminescence and backscattered electron images: Implications for interpretation of complex crustal histories. *Chemical Geology,* 110**,** 1-13.
HAWKESWORTH, C., CAWOOD, P., KEMP, T., STOREY, C. & DHUIME, B. 2009. A Matter of Preservation. *Science,* 323**,** 49-50.
HOCHSTAEDTER, A., GILL, J., PETERS, R., BROUGHTON, P., HOLDEN, P. & TAYLOR, B. 2001. Across-arc geochemical trends in the Izu-Bonin arc: Contributions from the subducting slab. *Geochemistry, Geophysics, Geosystems,* 2.
HOFFMANN, P. F. 1991. Did the break-out of Laurentia turn Gondwana inside-out? *Science,* 252**,** 1409-1412.
HORSTWOOD, M. 2008. *Data reduction strategies, uncertainty assessment and resolution of LA-(MC-) ICP-MS isotope data*, Mineralogical Association of Canada.
HOSKIN, P. W. & SCHALTEGGER, U. 2003. The composition of zircon and igneous and metamorphic petrogenesis. *Reviews in mineralogy and geochemistry,* 53**,** 27-62.
HØYEN, A. B. 2016. *Within-plate gabbroic intrusion at 565 Ma in the Uppermost Allochthon.* MSc, Norwegian University of Science and Technology.

IDDINGS, J. P. 1892. The mineral composition and geological occurrence of certain igneous rocks in the Yellowstone National Park.
IKEDA, T. 1993. Compositional zoning patterns of garnet during prograde metamorphism from the Yanai district, Ryoke metamorphic belt, southwest Japan. *Lithos,* 30**,** 109-121.
IRELAND, T. R. & WILLIAMS, I. S. 2003. Considerations in zircon geochronology by SIMS. *Reviews in mineralogy and geochemistry,* 53**,** 215-241.
IRVINE, T. N. & BARAGAR, W. R. A. 1971. A guide to the chemical classification of the common volcanic rocks. *Canadian Journal of Earth Sciences,* 8**,** 523-548.
IRVING, E. 1983. Fragmentation and assembly of the continents, mid-Carboniferous to present. *Geophysical surveys,* 5**,** 299-333.
JACKSON, S. E., PEARSON, N. J., GRIFFIN, W. L. & BELOUSOVA, E. A. 2004. The application of laser ablation-inductively coupled plasma-mass spectrometry to in situ U–Pb zircon geochronology. *Chemical geology,* 211**,** 47-69.
JAMTVEIT, B. & ANDERSEN, T. B. 1992. Morphological instabilities during rapid growth of metamorphic garnets. *Physics and Chemistry of Minerals,* 19**,** 176-184.
JENNER, G. A. & WYMAN, D. 1996. Trace element geochemistry of igneous rocks: geochemical nomenclature and analytical geochemistry. *Trace element geochemistry of volcanic rocks: applications for massive sulfide exploration. Edited by DA Wyman. Geological Association of Canada, Short Course Notes,* 12**,** 51-77.
JUNG, S., HOERNES, S., MASBERG, P. & HOFFER, E. 1999. The petrogenesis of some migmatites and granites (Central Damara Orogen, Namibia): evidence for disequilibrium melting, wall-rock contamination and crystal fractionation. *Journal of Petrology,* 40**,** 1241-1269.
KIRKLAND, C. L., DALY, J. S., EIDE, E. A. & WHITEHOUSE, M. J. 2007a. Tectonic evolution of the Arctic Norwegian Caledonides from texturally- and structurally-constrained multi-isotopic (Ar-Ar, Rb-Sr, Sm-Nd, U-Pb) study. *American Journal of Science,* 307**,** 459-526.
KIRKLAND, C. L., DALY, J. S. & WHITEHOUSE, M. J. 2007b. Provenance and terrane evolution of the Kalak Nappe Complex, Norwegian Caledonides: Implications for Neoproterozoic Paleogeography and tectonics. *Journal of Geology,* 115**,** 21-41.
KIRKLAND, C. L., SLAGSTAD, T. & JOHNSON, T. E. 2018. Zircon as a metamorphic timekeeper: A case study from the Caledonides of central Norway. *Gondwana Research,* 61**,** 63-72.
KOŠLER, J. & SYLVESTER, P. J. 2003. Present trends and the future of zircon in geochronology: laser ablation ICPMS. *In:* HANCHAR, J. M. & HOSKIN, P. W. O. (eds.) *Zircon.*
LI, Z. X., BOGDANOVA, S. V., COLLINS, A. S., DAVIDSON, A., DE WAELE, B., ERNST, R. E., FITZSIMONS, I. C. W., FUCK, R. A., GLADKOCHUB, D. P., JACOBS, J., KARLSTROM, K. E., LU, S., NATAPOV, L. M., PEASE, V., PISAREVSKY, S. A., THRANE, K. & VERNIKOVSKY, V. 2008. Assembly, configuration, and break-up history of Rodinia: A synthesis. *Precambrian Research,* 160**,** 179-210.
LIU, Y., HU, Z., LI, M. & GAO, S. 2013. Applications of LA-ICP-MS in the elemental analyses of geological samples. *Chinese Science Bulletin,* 58**,** 3863-3878.
LUBNINA, N. & SLABUNOV, A. 2011. Reconstruction of the Kenorland supercontinent in the Neoarchean based on paleomagnetic and geological data. *Moscow University Geology Bulletin,* 66**,** 242-249.
MARKER, M. 1983. *Caledonian and Pre-Caledonian geology of the Mofjell area, Nordland, Norway.* PhD, University of Copenhagen.
MARKER, M., BJERKGÅRD, T., SLAGSTAD, T. & SOLLI, A. 2012. *Storakersvatnet 2027 III, bedrock geological map*, 1:50,000. Geological Survey of Norway.
MCARTHUR, K. L., FROST, C. D., BARNES, C. G., PRESTVIK, T. & NORDGULEN, Ø. 2014. Tectonic reconstruction and sediment provenance of a far-travelled oceanic nappe, Helgeland Nappe Complex, west-central Norway. *Geological Society, London, Special Publications,* 390**,** 583-602.

MCFARLANE, C. R. M. & LUO, Y. 2012. U-Pb geochronology using 193 nm Excimer LA-ICP-MS optimized for in-Situ accessory mineral dating in thin sections. *Geoscience Canada,* 39**,** 158-172.
MCKERROW, W. S., MAC NIOCAILL, C. & DEWEY, J. F. 2000. The Caledonian Orogeny redefined. *Journal of the Geological Society of London,* 157**,** 1149-1154.
MEANS, W. D. & WILLIAMS, P. F. 1976. *An outline of structural geology*, John Wiley.
MELEZHIK, V. A., IHLEN, P. M., KUZNETSOV, A. B., GJELLE, S., SOLLI, A., GOROKHOV, I. M., FALLICK, A. E., SANDSTAD, J. S. & BJERKGÅRD, T. 2015. Pre-Sturtian (800–730 Ma) depositional age of carbonates in sedimentary sequences hosting stratiform iron ores in the Uppermost Allochthon of the Norwegian Caledonides: A chemostratigraphic approach. *Precambrian Research,* 261**,** 272-299.
MESCHEDE, M. 1986. A method of discriminating between different types of mid-ocean ridge basalts and continental tholeiites with the Nb-Zr-Y diagram. *Chemical Geology,* 56**,** 207-218.
MILISZKIEWICZ, N., WALAS, S. & TOBIASZ, A. 2015. Current approaches to calibration of LA-ICP-MS analysis. *Journal of Analytical Atomic Spectrometry,* 30**,** 327-338.
MORNER, N.-A. 2014. *Geochronology: Methods and Case Studies*, BoD–Books on Demand.
MUELLER, P. & VERVOORT, J. 2022. *Thermal Ionization Mass Spectrometry (TIMS)* [Online]. SERC. Available: https://serc.carleton.edu/msu_nanotech/methods/TIMS.html [Accessed 22.04.2022 2022].
MURPHY, J. B., PISAREVSKY, S. & NANCE, R. D. 2013. Potential geodynamic relationships between the development of peripheral orogens along the northern margin of Gondwana and the amalgamation of West Gondwana. *Mineralogy and Petrology,* 107**,** 635-650.
NICHOLS, G. 2009. *Sedimentology and stratigraphy*, John Wiley & Sons.
NISSEN, A. L., ROBERTS, D. & GROMET, L. P. 2006. U-Pb zircon ages of a tonalite and a granodiorite dyke from the southeastern part of the Bindal Batholith, central Norwegian Caledonides. *Norges geologiske undersøkelse Bulletin,* 446**,** 5-9.
NORDGULEN, Ø., BICKFORD, M., NISSEN, A. & WORTMAN, G. 1993a. U-Pb zircon ages from the Bindal Batholith, and the tectonic history of the Helgeland Nappe Complex, Scandinavian Caledonides. *Journal of the Geological Society,* 150**,** 771-783.
NORDGULEN, Ø., BICKFORD, M. E., NISSEN, A. L. & WORTMAN, G. L. 1993b. U-Pb zircon ages from the Bindal batholith, and the tectonic history of the Helgeland Nappe Complex, Scandinavian Caledonides. *Journal of the Geological Society of London,* 150**,** 771-783.
NORDGULEN, Ø. & SUNDVOLL, B. 1992. Strontium isotope composition of the Bindal Batholith, central Norwegian Caledonides.
ORVIK, A. 2019. *The dyke swarm in the Reinfjord Ultramafic Complex: A window into the terminal stages forming the Seiland Igneous Province.* Msc, Norwegian University of Science and Technology.
ORVILLE, P. M. 1962. Alkali metasomatism and feldspars. *Norsk Geologisk Tidsskrift,* 42**,** e316.
OSMUNDSEN, P., BRAATHEN, A., NORDGULEN, Ø., ROBERTS, D., MEYER, G. & EIDE, E. 2003. The Devonian Nesna shear zone and adjacent gneiss-cored culminations, North–Central Norwegian Caledonides. *Journal of the Geological Society,* 160**,** 137-150.
OSMUNDSEN, P. T. & ANDERSEN, T. B. 2001. The middle Devonian basins of western Norway: Sedimentary response to large-scale transtensional tectonics? *Tectonophysics,* 332**,** 51-68.
OVERSTREET, W. C. 1967. The geologic occurrence of monazite. [US Geological Survey; for sale by the Supt. of Docs.] US Govt. Print. Off.
PASSCHIER, C. W. & TROUW, R. A. 2005. *Microtectonics*, Springer Science & Business Media.
PEARCE, J. A. 1983. Role of the Sub-continental Lithosphere in Magma Genesis at Active Continental Margins. *In:* HAWKESWORTH, C. J. & NORRY, M. J. (eds.) *Continental Basalts and Mantle Xenoliths.*
PEARCE, J. A. & CANN, J. R. 1973. Tectonic setting of basic volcanic rocks determined using trace element analyses. *Earth and Planetary Science Letters,* 19**,** 290-300.

PEARCE, J. A. & NORRY, M. J. 1979. Petrogenetic Implications of Ti, Zr, Y, and Nb Variations in Volcanic Rocks. *Contributions to Mineralogy and Petrology,* 69**,** 33-47.
PEARCE, J. A. & STERN, R. J. 2006. Origin of back-arc basin magmas: trace element and isotope perspectives. *Geophysical Monograph-American Geophysical Union,* 166**,** 63.
PEDERSEN, R.-B., FURNES, H. & DUNNING, G. 1988. Some Norwegian ophiolite complexes reconsidered. *Norges geologiske undersøkelse Special Publication,* 3**,** 80-85.
PHILPOTTS, A. & AGUE, J. 2009. *Principles of Igneous and Metamorphic Petrology*, Cambridge University Press.
POLDERVAART, A. 1955. Chemistry of the earth's crust. *Crust of the Earth.* Geol. Soc. of Amer. Special Paper.
RAMBERG, H. 1963. Evolution of drag folds. *Geological Magazine,* 100**,** 97-106.
RIBEIRO, J. M., MAURY, R. C. & GRÉGOIRE, M. 2016. Are adakites slab melts or high-pressure fractionated mantle melts? *Journal of Petrology,* 57**,** 839-862.
ROBERTS, D. 2003. The Scandinavian Caledonides: Event chronology, palaeographic settings and likely modern analogues. *Tectonophysics,* 365**,** 283-299.
ROBERTS, D. & GEE, D. G. 1985. An introduction to the structure of the Scandinavian Caledonides. *In:* GEE, D. G. & STURT, B. A. (eds.) *The Caledonide Orogen - Scandinavia and Related Areas.* Chichester: John Wiley & Sons.
ROBERTS, D., MELEZHIK, V. A. & HELDAL, T. 2002. Carbonate formations and early NW-directed thrusting in the highest allochthons of the Norwegian Caledonides: Evidence of a Laurentian ancestry. *Journal of the Geological Society of London,* 159**,** 117-120.
ROBERTS, D., NORDGULEN, Ø. & MELEZHIK, V. A. 2007. The Uppermost Allochthon in the Scandinavian Caledonides: From a Laurentian ancenstry through Taconian orogeny to Scandian crustal growth on Baltica. *In:* HATCHER JR., R. D., CARLSON, M. P., MCBRIBDE, J. H. & MARTÍNEZ CATALÁN, J. R. (eds.) *4-D Framework of Continental Crust.*
ROBERTS, D. & OLOVYANISHNIKOV, V. 2004. Structural and tectonic development of the Timanide orogen. *Geological Society, London, Memoirs,* 30**,** 47-57.
ROBERTS, R. J. 2007. *The Seiland Igneous Province, Northern Norway: Age, Provenance, and Tectonic Significance.* PhD PhD, University of Witwatersrand.
ROLLINSON, H. R. 1993. *Using geochemical data: Evaluation, presentation, interpretation,* Essex, Longman.
RONOV, A. & YAROSHEVSKY, A. 1976. A new model of chemical composition of the Earth crust. *Geokhimiya,* 12**,** 1763.
ROOT, D. & CORFU, F. 2012. U–Pb geochronology of two discrete Ordovician high-pressure metamorphic events in the Seve Nappe Complex, Scandinavian Caledonides. *Contributions to Mineralogy and Petrology,* 163**,** 769-788.
RUBATTO, D. 2002. Zircon trace element geochemistry: partitioning with garnet and the link between U–Pb ages and metamorphism. *Chemical geology,* 184**,** 123-138.
SALLI, I. 1983. Pielaveden kartta-alueen kalliopera. *Kallioperan selitykset,* 3314**,** 1-31.
SAUNDERS, A., NORRY, M. & TARNEY, J. 1988. Origin of MORB and chemically-depleted mantle reservoirs: trace element constraints. *Journal of Petrology***,** 415-445.
SCHOENE, B. 2014. 4-10 - U-Th-Pb Geochronology. *In:* HOLLAND, K. T. H. (ed.) *Treatise on Geochemistry 2nd Edition.* Oxford: Elsevier Scinece.
SCHOFIELD, N. J., BROWN, D. J., MAGEE, C. & STEVENSON, C. T. 2012. Sill morphology and comparison of brittle and non-brittle emplacement mechanisms. *Journal of the Geological Society,* 169**,** 127-141.
SKÅR, Ø. 2002. U–Pb geochronology and geochemistry of early Proterozoic rocks of the tectonic basement windows in central Nordland, Caledonides of north-central Norway. *Precambrian Research,* 116**,** 265-283.
SLAGSTAD, T. & KIRKLAND, C. L. 2017. The use of detrital zircon data in terrane analysis: A nonunique answer to provenance and tectonostratigraphic position in the Scandinavian Caledonides. *Lithosphere,* 9**,** 1002-1011.

SLAGSTAD, T., KULAKOV, E., KIRKLAND, C. L., ROBERTS, N. M. & GANERØD, M. 2019. Breaking the Grenville–Sveconorwegian link in Rodinia reconstructions. *Terra Nova,* 31**,** 430-437.
SLAGSTAD, T., SAALMANN, K., KIRKLAND, C. L., HØYEN, A. B., STORRUSTE, B. K., COINT, N., PIN, C., MARKER, M., BJERKGÅRD, T., KRILL, A., SOLLI, A., BOYD, R., ANGVIK, T. L. & LARSEN, R. B. 2021. Late Neoproterozoic–Silurian tectonic evolution of the Rödingsfjället Nappe Complex, orogen-scale correlations and implications for the Scandian suture. *Geological Society, London, Special Publications,* 503**,** 279-304.
SLIWINSKI, J. T., GUILLONG, M., LIEBSKE, C., DUNKL, I., VON QUADT, A. & BACHMANN, O. 2017. Improved accuracy of LA-ICP-MS U-Pb ages of Cenozoic zircons by alpha dose correction. *Chemical Geology,* 472**,** 8-21.
SORENSEN, S. S., GROSSMAN, J. N. & PERFIT, M. R. 1997. Phengite-hosted LILE enrichment in eclogite and related rocks: implications for fluid-mediated mass transfer in subduction zones and arc magma genesis. *Journal of Petrology,* 38**,** 3-34.
SPACAPAN, J. B., GALLAND, O., LEANZA, H. A. & PLANKE, S. 2017. Igneous sill and finger emplacement mechanism in shale-dominated formations: a field study at Cuesta del Chihuido, Neuquén Basin, Argentina. *Journal of the Geological Society,* 174**,** 422-433.
SPEAR, F. S. & CHENEY, J. T. 1989. A petrogenetic grid for pelitic schists in the system SiO2-Al2O3-FeO-MgO-K2O-H2O. *Contributions to Mineralogy and Petrology,* 101**,** 149-164.
STACEY, J. S. & KRAMERS, J. D. 1975. Approximation of terrestrial lead isotope evolution by a two-stage model. *Earth and Planetary Science Letters,* 26**,** 207-221.
STAMPFLI, G. M., HOCHARD, C., VÉRARD, C., WILHEM, C. & VONRAUMER, J. 2013. The formation of Pangea. *Tectonophysics,* 593**,** 1-19.
STEPHENS, M. & GEE, D. 1985. A tectonic model for the evolution of the eugeoclinal terranes in the central Scandinavian Caledonides. *The Caledonide Orogen: Scandinavia and Related Areas. Wiley, Chichester,* 953**,** 978.
STEPHENS, M., GUSTAVSON, M., RAMBERG, I. & ZACHRISSON, E. 1985. The Caledonides of central-north Scandinavia–a tectonostratigraphic overview. *The Caledonide orogen–Scandinavia and related areas***,** 135-162.
STEPHENS, M. B. 1988. The Scandinavian Caledonides: a complexity of collisions. *Geology Today,* 4**,** 20-26.
STORRUSTE, B. K. 2017. *Deciphering magmatic processes in the 565 Ma Umbukta gabbro, Rødingsfjellet Nappe Complex, Northern Norway.* MSc, Norwegian University of Science and Technology.
SUN, S.-S. & MCDONOUGH, W. F. 1989. Chemical and isotopic systematics of oceanic basalts: Implications for mantle composition and processes. *In:* SAUNDERS, A. D. & NORRY, M. J. (eds.) *Magmatism in the Ocean Basins: Geological Society of London Special Publication.*
SUPPE, J. 1985. *Principles of structural geology*, Prentice Hall.
TERA, F. & WASSERBURG, G. J. 1972. U-Th-Pb systematics in lunar highland samples from the Luna 20 and Apollo 16 missions. *Earth and Planetary Science Letters,* 17**,** 36-51.
THERMO-FISHER. 2022. *Triton Series Multicollector Thermal Ionization Mass Spectrometer* [Online]. Available: https://www.thermofisher.com/order/catalog/product/IQLAAEGAASFAFYMAMV [Accessed 22.4.2022 2022].
THOMPSON, A. B., TRACY, R. J., LYTTLE, P. T. & THOMPSON, J. 1977. Prograde reaction histories deduced from compositional zonation and mineral inclusions in garnet from the Gassetts schist, Vermont. *American Journal of Science,* 277**,** 1152-1167.
TOBISCH, O. 2005. A PRACTICAL GUIDE TO ROCK MICROSTRUCTURE: by Ron H. Vernon. Cambridge, 2004. 594 pp. Hardbound 130,softbound 70. Mineralogical Society of America.
TORSVIK, T., SMETHURST, M., MEERT, J. G., VAN DER VOO, R., MCKERROW, W., BRASIER, M., STURT, B. & WALDERHAUG, H. 1996. Continental break-up and collision in the Neoproterozoic and Palaeozoic—a tale of Baltica and Laurentia. *Earth-Science Reviews,* 40**,** 229-258.

TOWNSEND, K., MILLER, C., D'ANDREA, J., AYERS, J., HARRISON, T. & COATH, C. 2001. Low temperature replacement of monazite in the Ireteba granite, Southern Nevada: geochronological implications. *Chemical geology,* 172**,** 95-112.
VONCKEN, J. H. L. 2016. *The rare earth elements: an introduction*, Springer.
WETHERILL, G. W. 1956. Discordant U-Pb ages. *Transactions of the American Geophysical Union,* 37**,** 320-326.
WIEDENBECK, M., ALLE, P., CORFU, F., GRIFFIN, W., MEIER, M., OBERLI, F. V., QUADT, A. V., RODDICK, J. & SPIEGEL, W. 1995. Three natural zircon standards for U-Th-Pb, Lu-Hf, trace element and REE analyses. *Geostandards newsletter,* 19**,** 1-23.
WILLIAMS, P. F. 1985. Multiply deformed terrains—problems of correlation. *Journal of Structural Geology,* 7**,** 269-280.
WINTER, J. D. 2014. *Principles of igneous and metamorphic petrology*, Pearson education Harlow, UK.
WU, Y. & ZHENG, Y. 2004. Genesis of zircon and its constraints on interpretation of U-Pb age. *Chinese Science Bulletin,* 49**,** 1554-1569.
YOSHINOBU, A., REID, K., BARNES, C. & ALLEN, C. Crustal melting in the Helgeland Nappe Complex, central Norway. AGU Fall Meeting Abstracts, 2005. V13E-0598.
YOSHINOBU, A. S., BARNES, C. G., NORDGULEN, Ø., PRESTVIK, T., FANNING, M. & PEDERSEN, R.-B. 2002. Ordovician magmatism, deformation, and exhumation in the Caledonides of central Norway: An orphan of the Taconic orogeny? *Geology,* 30**,** 883-886.
ZACK, T. & JOHN, T. 2007. An evaluation of reactive fluid flow and trace element mobility in subducting slabs. *Chemical Geology,* 239**,** 199-216.
ZHANG, S., LI, Z.-X., EVANS, D. A., WU, H., LI, H. & DONG, J. 2012. Pre-Rodinia supercontinent Nuna shaping up: A global synthesis with new paleomagnetic results from North China. *Earth and Planetary Science Letters,* 353**,** 145-155.
ZHENG, Y.-F. 2019. Subduction zone geochemistry. *Geoscience Frontiers,* 10**,** 1223-1254.

# Appendix

**Appendix A** – Overview of samples and methods applied

**Appendix B** - Field map

**Appendix C** – Geochemical data

**C1**: Whole-rock major elements

**C2**: Whole-rock trace elements

**Appendix D** – Petrography

**D1**: Thin section description

**D2**: Mineralogic - Area% data

**Appendix E** Geochronology

**E1**: BS-images and zircon on tape (Kallvatnet)

**E2**: CL-images with laser traces (Kallvatnet)

**E3**: CL-images with laser traces (Umbukta)

**E4**: Metamorphic zircon U-Pb data (Kallvatnet)

**E5**: Zircon U-Pb data (Sample from Storruste (2017)) (Umbukta)

**E6**: Igneous zircon U-Pb data (Umbukta from Trond Slagstad (unpublished))

**E7**: Igneous zircon U-Pb data (Tonalite from Trond Slagstad (unpublished))

**E8**: Monazite U-Pb data (Kallvatnet)

# Appendix A – Overview of samples and methods applied

**X:** No datable material was applied, or the data was not good enough

(**x**): Thin section produced in another project or thesis

| Sample | Rock type | thin section | geochron. (mz.) | geochron (zr.) | geochem. | Comment | Coordinates (4326 WGS 84) | |
|---|---|---|---|---|---|---|---|---|
| gmf2020-01 | Garnet mica schist | | | | **x** | | 66.25324 N | 14.96124 E |
| gmf2020-02 | Garnet mica schist | **x** | **x** | | **x** | | 66.24846 N | 14.95552 E |
| gmf2020-03 | Pegmatite | | | | | | 66.26708 N | 14.93308 E |
| gmf2020-04 | Garnet amphibolite | | | | **x** | | 66.26625 N | 14.93247 E |
| gmf2020-05 | Garnet amphibolite | | | | **x** | | 66.26225 N | 14.93331 E |
| gmf2020-06 | Garnet amphibolite | | | | | | 66.25926 N | 14.93700 E |
| gmf2020-07 | Pegmatite | | | | | | 66.26645 N | 14.93055 E |
| gmf2020-08 | garnet mica psammite | | | | | | 66.28048 N | 14.88313 E |
| gmf2020-09 | garnet mica psammite | **x** | **x** | | | | 66.27204 N | 14.89950 E |
| gmf2020-10 | Garnet mica schist | **x** | **x** | | | | 66.30725 N | 14.81167 E |
| gmf2020-11 | Garnet mica schist | **x** | **x** | | | | 66.18045 N | 14.72946 E |
| gmf2020-12 | Granitic contact rock | | | | | Mingling contact | 66.18918 N | 14.75009 E |
| gmf2020-13 | Garnet mica schist | **x** | | | | | 66.24076 N | 14.78038 E |
| gmf2020-14 | Garnet mica schist | | | | | | 66.24010 N | 14.79012 E |
| gmf202-15 | Garnet mica schist | | | | | | 66.23964 N | 14.79703 E |
| gmf2020-16 | Gabbroic rock | | | | | | 66.24624 N | 14.81279 E |
| gmf2020-18 | Gabbroic mafic lense | | | | | | 66.24494 N | 15.00190 E |
| gmf2020-19 | Amphibolite | | | | **x** | | 66.24438 N | 15.00196 E |
| gmf2020-20 | Reaction rim | | | | | | 66.24851 N | 14.98832 E |
| gmf2020-21 | Felsic vein | **x** | | **x** | | | 66.23696 N | 14.77714 E |
| gmf2020-22A | Felsic vein | **x** | | | | | 66.22623 N | 14.77882 E |
| gmf2020-22B | Reaction rim | **x** | | | | | 66.22623 N | 14.77882 E |
| gmf2020-23 | Garnet amphibolite | **x** | | | **x** | | 66.23658 N | 14.77882 E |
| gmf2020-24 | Felsic vein | | | | | | 66.23661 N | 14.77846 E |
| gmf2020-25 | Garnet mica schist | **x** | | | | | 66.23661 N | 14.77846 E |
| gmf2020-26A | Reaction rim | **x** | | | | | 66.23664 N | 14.77850 E |
| gmf2020-26B | Felsic vein & reaction rim | **x** | | | | | 66.23664 N | 14.77850 E |
| gmf2020-26C | Felsic vein & reaction rim | **x** | | | | | 66.23664 N | 14.77850 E |

| | | | | | | | | |
|---|---|---|---|---|---|---|---|---|
| gmf2020-27 | Garnet amphibolite | | | | | | 66.23743 N | 14.77419 E |
| gmf2020-28 | Garnet mica schist | | | | | | 66.23761 N | 14.77366 E |
| gmf2020-29 | Amphibolite | | | | | | 66.16645 N | 14.58547 E |
| gmf2020-30 | Garnet mica schist | x | | | | | 66.16645 N | 14.58547 E |
| gmf2021-01 | Felsic vein | | | | x | | 66.24038 N | 14.78386 E |
| gmf2021-02 | Calc silicate | x | | | x | | 66.23973 N | 14.79465 E |
| gmf2021-03 | Garnet amphibolite | x | | x | x | | 66.23975 N | 14.79714 E |
| gmf2021-04 | Garnet mica schist | | | | x | | 66.24078 N | 14.77887 E |
| gmf2021-05 | Felsic vein | x | | x | x | | 66.23661 N | 14.77871 E |
| gmf2021-06A | Felsic layer | x | | x | x | | 66.23579 N | 14.78038 E |
| gmf2021-06B | Felsic layer | x | | x | x | | 66.23579 N | 14.78038 E |
| gmf2021-07A | Reaction rim | x | | x | x | | 66.23534 N | 14.78177 E |
| gmf2021-07B | Garnet mica schist | | | | x | | 66.23534 N | 14.78177 E |
| gmf2021-08 | Garnet amphibolite | | | | x | | 66.23496 N | 14.78286 E |
| gmf2021-09A | felsic vein | | | | x | | 66.24072 N | 14.77853 E |
| gmf2021-09B | Garnet amphibolite | | | | x | | 66.24072 N | 14.77853 E |
| gmf2021-09C | Garnet mica schist | | | | | | 66.24072 N | 14.77853 E |
| gmf2021-10 | Felsic vein | | | | x | | 66.24031 N | 14.78522 E |
| gmf2021-11A | Felsic vein | x | | x | x | | 66.24005 N | 14.78903 E |
| gmf2021-11B | Reaction rim | x | | x | x | | 66.24005 N | 14.78903 E |
| gmf2021-11C | Garnet mica schist | x | | x | x | | 66.24005 N | 14.78903 E |
| gmf2021-12 | Calc silicate | | | | x | | 66.23968 N | 14.79485 E |
| gmf2021-13 | Garnet mica schist | | | | | | 66.24092 N | 14.77668 E |
| gmf2021-14 | Garnet mica schist | x | | x | x | | 66.24005 N | 14.87401 E |
| gmf2021-15 | Garnet amphibolite | | | | x | | 66.24049 N | 14.87218 E |
| gmf2021-16 | layered impure quartzite | x | | | x | | 66.24076 N | 14.87050 E |
| gmf2021-17 | Felsic vein | x | | x | x | post mafic | 66.24406 N | 14.85232 E |
| gmf2021-18A | Felsic vein | | | | x | | 66.24711 N | 14.83179 E |
| gmf2021-18B | Reaction rim | | | | x | | 66.24711 N | 14.83179 E |
| gmf2021-18C | Garnet mica schist | | | | x | | 66.24711 N | 14.83179 E |
| gmf2021-19 | Garnet amphibolite | | | | x | | 66.23806 N | 14.88932 E |
| gmf2021-20 | Garnet amphibolite | | | | x | | 66.22967 N | 14.88256 E |
| gmf2021-21 | Garnet amphibolite | x | | x | x | | 66.22966 N | 14.88297 E |
| gmf2021-22 | Garnet amphibolite | | | | x | | 66.22623 N | 14.86401 E |
| gmf2021-23 | Garnet amphibolite | | | | x | | 66.22430 N | 14.84868 E |

| | | | | | | | | |
|---|---|---|---|---|---|---|---|---|
| BKS132409 | Garnet mica schist | | | **x** | | | 66.17865 N | 14.76185 E |
| BKS132410 | Granitoid | **(x)** | | **x** | | | 66.17292 N | 14.76388 E |
| BKS132411 | Granitoid | **(x)** | | **x** | | | 14.76173 N | 14.76173 E |
| BKS132414 | Granitoid | **(x)** | | **x** | | | 66.17109 N | 14.74402 E |
| MO28771 | | | | **x** | | | | |
| P8.2 | Garnet biotite gneiss | **(x)** | | **x** | | | 66.18633 N | 14.74679 E |
| P8.3 | Garnet mica schist | | | **x** | | | 66.18574 N | 14.74474 E |
| P8.4 | Garnet biotite gneiss | **(x)** | | **x** | | | 66.17357 N | 14.72582 E |
| P9.1 | Garnet biotite gneiss | | | **x** | | | 66.17621 N | 14.76192 E |
| | | | | | | | 66.17621 N | 14.76192 E |

# Appendix B – Field map


## Lithology

- Garnet mica schist, abundant felsic veins with associated reaction rim (Area 3)
- Garnet mica schist, locally felsic veins with associated reaction rims (Area 4)
- Quartz-rich schist and impure quartzite, locally felsic veins with associated reaction rim (Area1)
- Garnet amphibolites

## Legend

- Foliation parallel to the comositional layering
- Fold axis
- Crenulation lineation
- Fold plane
- Increase in clay-rich protolith
- Boarder between the quartz-rich area and the transition zone
- Boarder between litostartigraphic units

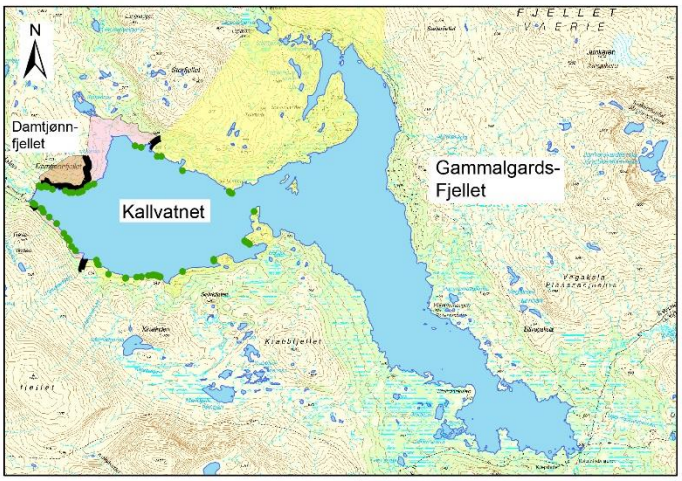


# Appendix C – Geochemical data

## C1: Whole-rock major elements

| Sample | SiO2 | Al2O3 | Fe2O3 | CaO | MgO | Na2O | K2O | Cr2O3 | TiO2 | MnO | P2O5 | SrO | BaO | LOI | Total |
|---|---|---|---|---|---|---|---|---|---|---|---|---|---|---|---|
| | % | % | % | % | % | % | % | % | % | % | % | % | % | % | % |
| gmf2021-01 | 63 | 17.1 | 6.71 | 6.74 | 1.57 | 3.93 | 0.17 | 0.009 | 0.65 | 0.22 | 0.61 | 0.01 | <0.01 | 0.22 | 100.94 |
| gmf2021-02 | 60 | 15.7 | 5.98 | 13.75 | 1.1 | 0.11 | 0.04 | 0.008 | 0.55 | 0.2 | 0.38 | 0.03 | <0.01 | 1.35 | 99.2 |
| gmf2021-04 | 61.4 | 17.15 | 7.78 | 1.22 | 2.48 | 2.04 | 3.53 | 0.013 | 0.88 | 0.09 | 0.19 | 0.01 | 0.06 | 1.95 | 98.79 |
| gmf2021-07B | 64 | 17.4 | 6.01 | 1.48 | 2.15 | 3.98 | 2.54 | 0.013 | 0.9 | 0.05 | 0.13 | 0.01 | 0.04 | 1.3 | 100 |
| gmf2021-08 | 54.3 | 15.05 | 12 | 7.04 | 5.44 | 2.54 | 0.26 | 0.019 | 1.98 | 0.2 | 0.34 | 0.02 | <0.01 | 0.48 | 99.67 |
| gmf2021-09A | 63.9 | 16.55 | 7.35 | 2.2 | 1.98 | 4.27 | 2.11 | 0.013 | 0.9 | 0.09 | 0.2 | 0.01 | 0.04 | 1.12 | 100.73 |
| gmf2021-9B | 51.5 | 13.7 | 15.05 | 8.78 | 5.74 | 1.17 | 0.74 | 0.009 | 1.06 | 0.23 | 0.11 | <0.01 | <0.01 | 0.42 | 98.51 |
| gmf2021-9C | 65.9 | 16.85 | 6.85 | 0.98 | 1.68 | 1.82 | 3.78 | 0.012 | 0.84 | 0.12 | 0.18 | <0.01 | 0.07 | 1.97 | 101.05 |
| gmf2021-10 | 54.4 | 20.9 | 3.27 | 11.05 | 0.68 | 4.28 | 0.13 | 0.005 | 0.51 | 0.13 | 1.66 | 0.02 | <0.01 | 1.14 | 98.18 |
| gmf2021-12 | 66.5 | 12.4 | 6.11 | 9.33 | 1.24 | 0.79 | 0.11 | 0.008 | 0.51 | 0.16 | 0.32 | 0.02 | <0.01 | 0.71 | 98.21 |
| gmf2021-15 | 46.8 | 13.45 | 16.6 | 8.97 | 7.56 | 1.95 | 0.37 | 0.028 | 2.74 | 0.32 | 0.2 | <0.01 | <0.01 | 0.25 | 99.24 |
| gmf2021-16 | 72 | 13.5 | 4.31 | 2.05 | 1.27 | 3.04 | 2.48 | 0.011 | 0.82 | 0.07 | 0.16 | 0.01 | 0.06 | 1.14 | 100.92 |
| gmf2021-18A | 75.4 | 10.7 | 6.69 | 2.07 | 1.77 | 2.21 | 1.17 | 0.01 | 0.54 | 0.11 | 0.04 | <0.01 | 0.01 | 0.53 | 101.25 |
| gmf2021-18B | 59.1 | 18 | 8.62 | 2.74 | 2.46 | 3.93 | 2.31 | 0.013 | 0.97 | 0.08 | 0.13 | 0.02 | 0.03 | 0.85 | 99.25 |
| gmf2021-18C | 59.2 | 18.6 | 8.78 | 1.38 | 2.6 | 1.68 | 4.17 | 0.014 | 0.97 | 0.07 | 0.19 | <0.01 | 0.09 | 2.04 | 99.78 |
| gmf2021-19 | 48.9 | 14 | 15.05 | 10.45 | 6.74 | 1.82 | 0.88 | 0.018 | 1.14 | 0.22 | 0.11 | <0.01 | 0.01 | 0.73 | 100.07 |
| gmf2021-20 | 47.6 | 13.75 | 16.5 | 10.1 | 6.26 | 1.19 | 1.11 | 0.025 | 1.68 | 0.26 | 0.16 | <0.01 | 0.01 | 0.93 | 99.58 |
| gmf2021-22 | 45.7 | 13.35 | 17.55 | 10.4 | 6.33 | 1.29 | 0.84 | 0.015 | 2.2 | 0.26 | 0.21 | <0.01 | <0.01 | 0.99 | 99.14 |
| gmf2021-23 | 50.6 | 11.75 | 18.9 | 7.72 | 2.87 | 2.01 | 1.3 | 0.005 | 2.73 | 0.24 | 0.39 | <0.01 | 0.03 | 0.42 | 98.97 |
| gmf2020-01 | 64.1 | 18 | 3.99 | 4.67 | 1.17 | 4.96 | 1.13 | 0.013 | 1.08 | 0.06 | 0.12 | 0.04 | 0.03 | 0.81 | 100.17 |
| gmf2020-02 | 65 | 16.2 | 7.66 | 1.47 | 2.04 | 1.49 | 3.71 | 0.014 | 0.97 | 0.07 | 0.14 | 0.01 | 0.07 | 1.74 | 100.58 |
| gmf2020-04 | 46.1 | 13.85 | 17.15 | 8.67 | 7.61 | 1.54 | 2.15 | 0.012 | 1.46 | 0.23 | 0.14 | <0.01 | 0.02 | 1.01 | 99.94 |
| gmf2020-05 | 49.2 | 14 | 15 | 10.3 | 7.01 | 2.18 | 0.57 | 0.019 | 1.08 | 0.22 | 0.1 | <0.01 | 0.01 | 0.7 | 100.39 |
| gmf2020-19 | 46.8 | 13.6 | 15.45 | 9.54 | 9.83 | 1.69 | 0.46 | 0.052 | 1.57 | 0.2 | 0.09 | 0.01 | 0.01 | 1.68 | 100.98 |
| gmf2020-23 | 51.6 | 13.05 | 15 | 9.27 | 5.74 | 1.04 | 0.84 | 0.008 | 1.09 | 0.23 | 0.12 | <0.01 | 0.01 | 0.78 | 98.78 |

C2: Whole-rock Minor elements

| Sample | Ba | Ce | Cr | Cs | Dy | Er | Eu | Ga | Gd | Hf | Ho | La | Lu | Nb | Nd |
|---|---|---|---|---|---|---|---|---|---|---|---|---|---|---|---|
| | ppm | ppm | ppm | ppm | ppm | ppm | ppm | ppm | ppm | ppm | ppm | ppm | ppm | ppm | ppm |
| gmf2021-01 | 13.8 | 66.3 | 50 | 0.28 | 5.99 | 4.04 | 1.75 | 23.3 | 6.38 | 4.1 | 1.37 | 32.5 | 0.62 | 19 | 32.1 |
| gmf2021-02 | 4 | 76 | 50 | 0.06 | 6 | 3.48 | 1.57 | 34.7 | 7.03 | 5.1 | 1.18 | 40.6 | 0.55 | 9.7 | 38.3 |
| gmf2021-04 | 534 | 19 | 80 | 7.29 | 6.36 | 4.13 | 0.76 | 26.6 | 3.2 | 5.6 | 1.43 | 8.2 | 0.62 | 17.1 | 9.7 |
| gmf2021-07B | 397 | 24 | 80 | 5.27 | 4.72 | 3.49 | 1.03 | 23.4 | 2.56 | 6.2 | 1.11 | 12.3 | 0.57 | 17.7 | 12.2 |
| gmf2021-08 | 24 | 10.6 | 130 | 0.37 | 5.59 | 2.95 | 1.34 | 21.6 | 5.54 | 4 | 1.03 | 3.8 | 0.35 | 20 | 7.8 |
| gmf2021-09A | 324 | 13.7 | 80 | 6.47 | 4.85 | 3.62 | 0.67 | 22.5 | 1.51 | 7.8 | 1.16 | 6.5 | 0.63 | 15.3 | 6.1 |
| gmf2021-9B | 43.6 | 14.6 | 50 | 1.41 | 5.5 | 4.03 | 1.04 | 22.7 | 4.18 | 2.7 | 1.24 | 6.5 | 0.61 | 7.7 | 9.7 |
| gmf2021-9C | 643 | 14.4 | 80 | 5.42 | 5.96 | 4.14 | 0.54 | 25.5 | 2.53 | 6.7 | 1.25 | 6.7 | 0.64 | 14.9 | 6.6 |
| gmf2021-10 | 14.2 | 76 | 20 | 0.08 | 7.63 | 3.04 | 3.36 | 43.8 | 12.55 | 2 | 1.24 | 41.4 | 0.32 | 10.4 | 46.5 |
| gmf2021-12 | 6.7 | 73.1 | 40 | 0.09 | 6.48 | 4.03 | 1.35 | 28.6 | 7 | 4.5 | 1.2 | 38.2 | 0.54 | 19.8 | 37.6 |
| gmf2021-15 | 11.8 | 13.4 | 210 | 0.1 | 9.41 | 5.8 | 2.29 | 22.9 | 7.54 | 4.7 | 2.01 | 4.3 | 0.85 | 3.6 | 14.2 |
| gmf2021-16 | 529 | 73.9 | 60 | 1.76 | 6.35 | 4.28 | 1.41 | 18.8 | 6.5 | 10.5 | 1.42 | 33.9 | 0.71 | 13.2 | 34.1 |
| gmf2021-18A | 109.5 | 35.6 | 50 | 4.37 | 4.14 | 3.11 | 0.75 | 11.4 | 2.86 | 5 | 0.94 | 13.9 | 0.61 | 8.8 | 14.8 |
| gmf2021-18B | 297 | 16.3 | 80 | 7 | 7 | 4.44 | 0.52 | 21 | 3.17 | 5.4 | 1.57 | 5.6 | 0.71 | 19.5 | 7.2 |
| gmf2021-18C | 778 | 24.1 | 80 | 6.31 | 6.69 | 4.64 | 0.64 | 31.8 | 3.6 | 5.3 | 1.55 | 10 | 0.71 | 13.5 | 15.4 |
| gmf2021-19 | 80.7 | 19.7 | 120 | 0.08 | 5.32 | 3.86 | 1.02 | 17.9 | 4.62 | 2.9 | 1.19 | 9.1 | 0.62 | 4.5 | 12 |
| gmf2021-20 | 64.9 | 15.3 | 170 | 0.57 | 7.18 | 4.54 | 1.45 | 21.7 | 5.6 | 2.8 | 1.45 | 6.5 | 0.65 | 7.5 | 12 |
| gmf2021-22 | 44 | 12.4 | 90 | 0.19 | 8.69 | 5.72 | 1.49 | 21.3 | 7.08 | 3.4 | 1.9 | 4.5 | 0.82 | 4.7 | 12.6 |
| gmf2021-23 | 244 | 28.6 | 20 | 3.12 | 13.25 | 9.29 | 2.25 | 21.9 | 10.9 | 7.5 | 2.92 | 9.8 | 1.44 | 14.5 | 24.8 |
| gmf2020-01 | 255 | 74.5 | 80 | 3.02 | 4.74 | 3.27 | 1.27 | 21.8 | 4.38 | 11.2 | 1 | 24.1 | 0.56 | 15.1 | 26.5 |
| gmf2020-02 | 648 | 16.4 | 90 | 3.61 | 6.36 | 4.99 | 0.57 | 24.7 | 2.37 | 9.4 | 1.58 | 6.9 | 0.75 | 15.1 | 7.3 |
| gmf2020-04 | 192.5 | 14.8 | 70 | 5.5 | 5.82 | 3.67 | 0.95 | 21.1 | 4.49 | 2.6 | 1.17 | 6.3 | 0.55 | 4.3 | 10.9 |
| gmf2020-05 | 46.8 | 14.2 | 130 | 0.05 | 5.12 | 3.47 | 0.86 | 18.5 | 4.23 | 2.7 | 1.16 | 6.1 | 0.61 | 3.8 | 10 |
| gmf2020-19 | 81.1 | 11.9 | 380 | 0.26 | 4.3 | 2.46 | 1.18 | 20 | 4.26 | 1.8 | 0.89 | 5.1 | 0.32 | 5.7 | 9.3 |
| gmf2020-23 | 90.3 | 19.9 | 40 | 0.69 | 5.59 | 3.98 | 0.96 | 21.1 | 4.2 | 2.5 | 1.25 | 9.5 | 0.64 | 7.7 | 11.6 |

| Sample | Pr | Rb | Sm | Sn | Sr | Ta | Tb | Th | Tm | U | V | W | Y | Yb | Zr |
|---|---|---|---|---|---|---|---|---|---|---|---|---|---|---|---|
| | ppm | ppm | ppm | ppm | ppm | ppm | ppm | ppm | ppm | ppm | ppm | ppm | ppm | ppm | |
| gmf2021-01 | 8.28 | 4.5 | 7.37 | 4 | 174.5 | 1.6 | 1.01 | 11.55 | 0.62 | 3.34 | 93 | <1 | 38.5 | 4.05 | 133 |
| gmf2021-02 | 9.43 | 0.9 | 7.25 | 5 | 354 | 0.6 | 0.98 | 7.1 | 0.51 | 2.38 | 159 | 1 | 35.9 | 3.51 | 188 |
| gmf2021-04 | 2.44 | 150 | 2.3 | 4 | 143 | 1 | 0.82 | 12.45 | 0.64 | 1.41 | 117 | 2 | 38.8 | 4.35 | 184 |
| gmf2021-07B | 3.06 | 109 | 2.19 | 3 | 216 | 1.1 | 0.58 | 6.01 | 0.54 | 1.54 | 111 | 1 | 31.9 | 3.71 | 202 |
| gmf2021-08 | 1.54 | 5.5 | 3.65 | 4 | 281 | 1 | 0.9 | 3.96 | 0.43 | 1 | 169 | 2 | 29.5 | 2.55 | 139 |
| gmf2021-09A | 1.53 | 125.5 | 1.26 | 1 | 225 | 0.8 | 0.48 | 13.25 | 0.66 | 1.55 | 114 | <1 | 33.3 | 4.09 | 253 |
| gmf2021-9B | 2.04 | 25.6 | 3.06 | 5 | 24.2 | 0.3 | 0.74 | 2.54 | 0.57 | 1.07 | 380 | <1 | 34.8 | 4.14 | 92 |
| gmf2021-9C | 1.66 | 154 | 1.33 | 4 | 113.5 | 1 | 0.69 | 13.05 | 0.58 | 1.59 | 100 | 1 | 36.1 | 4.12 | 231 |
| gmf2021-10 | 11.1 | 4.9 | 12 | 11 | 282 | 0.5 | 1.57 | 4.2 | 0.38 | 4.19 | 139 | <1 | 35.3 | 2.29 | 65 |
| gmf2021-12 | 9.16 | 2.1 | 7.47 | 7 | 261 | 1 | 1.05 | 7.14 | 0.48 | 6.97 | 147 | 3 | 41.4 | 3.89 | 156 |
| gmf2021-15 | 2.35 | 4.3 | 5.09 | 4 | 122 | 0.1 | 1.42 | 0.54 | 0.88 | 0.23 | 502 | <1 | 55.4 | 5.51 | 159 |
| gmf2021-16 | 9.07 | 97.6 | 7.1 | 2 | 196.5 | 0.8 | 1.09 | 10.55 | 0.64 | 1.7 | 81 | <1 | 37.5 | 4.36 | 375 |
| gmf2021-18A | 3.81 | 76.2 | 3.26 | 1 | 144.5 | 0.3 | 0.57 | 7.35 | 0.49 | 1.1 | 75 | <1 | 28.9 | 3.62 | 196 |
| gmf2021-18B | 1.78 | 134 | 1.75 | 2 | 253 | 1.2 | 0.87 | 13.05 | 0.69 | 1.54 | 109 | <1 | 42.3 | 4.39 | 184 |
| gmf2021-18C | 3.5 | 171 | 3.26 | 4 | 123 | 0.8 | 0.88 | 13.25 | 0.69 | 2.94 | 166 | 1 | 40.9 | 4.23 | 176 |
| gmf2021-19 | 2.76 | 14.3 | 3.42 | 1 | 65.8 | 0.1 | 0.74 | 1.79 | 0.53 | 0.42 | 345 | <1 | 33.5 | 4.08 | 106 |
| gmf2021-20 | 2.24 | 24.3 | 3.9 | 3 | 26.4 | 0.2 | 1.04 | 0.63 | 0.66 | 0.17 | 473 | 1 | 40.7 | 4.31 | 93 |
| gmf2021-22 | 2.18 | 12.8 | 4.84 | 2 | 40.3 | 0.1 | 1.24 | 0.38 | 0.83 | 0.16 | 531 | <1 | 52.1 | 5.5 | 120 |
| gmf2021-23 | 4.69 | 60.2 | 8.33 | 3 | 64.8 | 0.7 | 1.98 | 6.51 | 1.38 | 1.55 | 292 | <1 | 79.3 | 9.09 | 257 |
| gmf2020-01 | 7.03 | 52 | 5.72 | 1 | 459 | 1.2 | 0.74 | 15.45 | 0.54 | 2.23 | 112 | <1 | 26.5 | 3.75 | 405 |
| gmf2020-02 | 1.87 | 137.5 | 1.66 | 3 | 154.5 | 1 | 0.62 | 13.8 | 0.74 | 1.36 | 106 | 1 | 41.8 | 4.99 | 345 |
| gmf2020-04 | 2.17 | 144.5 | 3.2 | <1 | 73.8 | 0.1 | 0.88 | 0.59 | 0.59 | 0.32 | 419 | <1 | 32.8 | 3.69 | 83 |
| gmf2020-05 | 2 | 9 | 2.87 | <1 | 70.8 | <0.1 | 0.76 | 1.5 | 0.57 | 0.34 | 345 | <1 | 32.2 | 3.78 | 87 |
| gmf2020-19 | 1.75 | 14.2 | 3.28 | 1 | 164 | 0.1 | 0.73 | 1.01 | 0.35 | 0.24 | 268 | <1 | 22.9 | 2.03 | 58 |
| gmf2020-23 | 2.66 | 20.4 | 3.36 | 3 | 47.8 | 0.3 | 0.84 | 2.05 | 0.63 | 0.7 | 375 | <1 | 35 | 4.05 | 87 |

# Appendic D – Petrography

D1: Thin section description

**gmf2020-02**

**Coordinates:** 66.24846° N, 14.95552° E

**Rock:** Garnet mica schist

**Minerals:**

- Quartz: 24% (fine to medium-grained, 0.06-1.8 mm, average: 0.6 mm, mode: 0.5 mm) anhedral to subhedral, equant to elongated.
- Biotite: 15% (fine to medium-grained, 0.14-1.3 mm, average: 0.5 mm, mode: 0.5 mm), subhedral to euhedral, prismatic to tabular.
- Plagioclase: 33% (fine to medium grained, 0.26-1.2 mm, average: 0.64, mode: 0.5 mm), anhedral to subhedral, tabular.
- Muscovite: 25% (fine to medium-grained, 0.38-1.25 mm, average: 0.76 mm mode: 0.6 mm), subhedral to euhedral.
- Garnet: 3% (medium-grained, 1-3 mm, average: 2, mode: 3), anhedral to subhedral, equant.
- Ilmenite: < 1%
- Rutile: < 1%
- Zoisite: < 1%
- Apatite: < 1%
- Zircon: <1%
- Monazite < 1%

**Textures:**

The rock is fine to medium-grained, porphyroblastic, hypidioblastic, showing crenulation cleavage. The crenulation cleavage is defined by the orientation of fined to medium-grained subhedral to euhedral muscovite and biotite parallel to the fold axial plane to the folded compositional layering. The microlithons, fined-grained quartz and plagioclase show developed SPO parallel to the compositional layering.

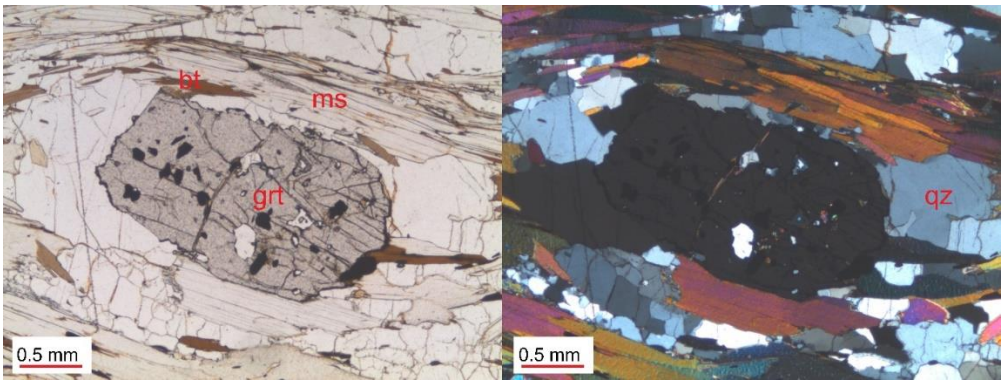


Thin section images of the garnet mica schist (gmf2020-02). PPL left, XPL right.

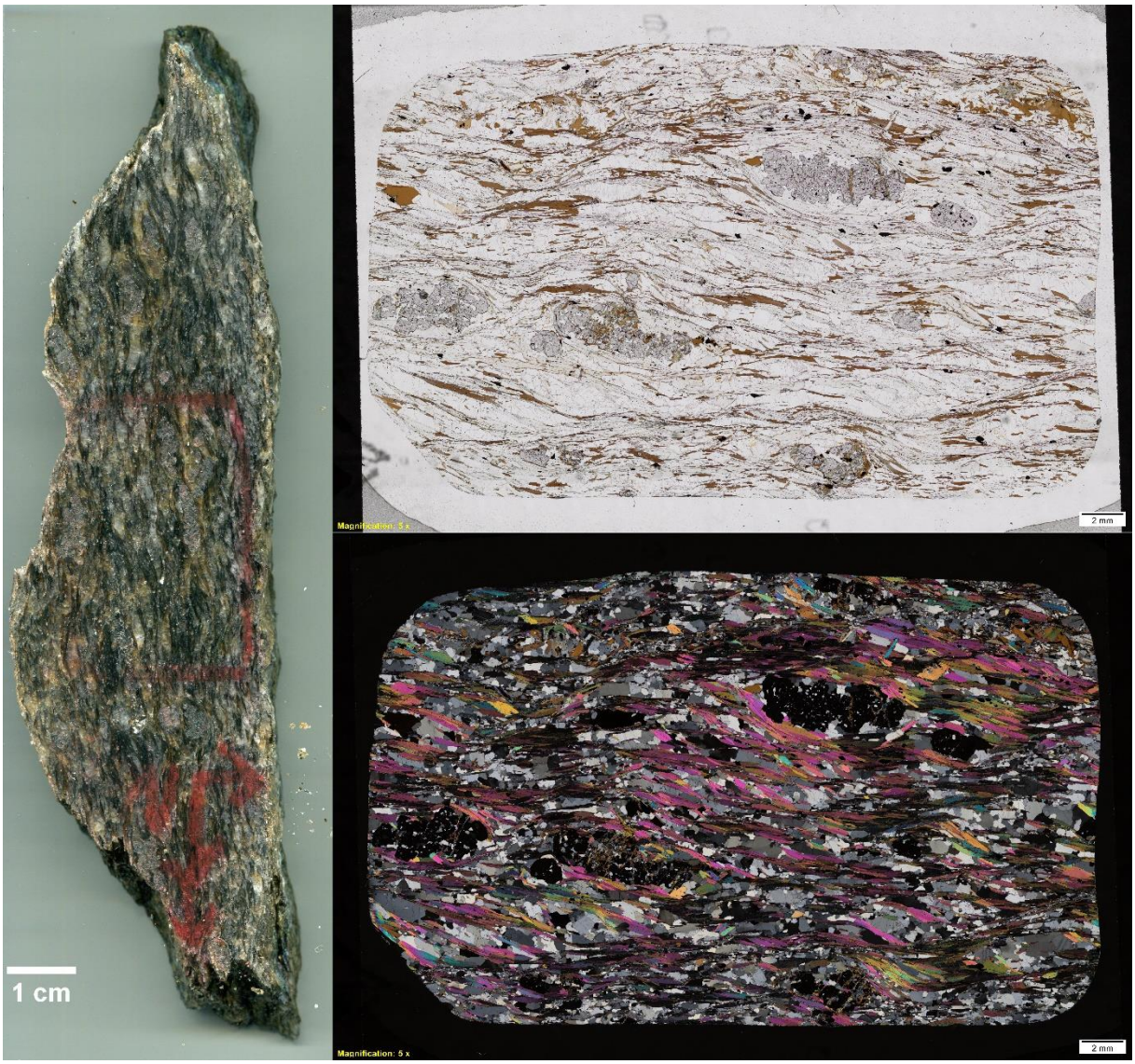


Rock slab, and thin section scans of gmf2020-02. PPL top, XPL bottom.

**gmf2020-09**

**Coordinates:** 66.27204° N, 14.89950° E

**Rock:** Garnet mica schist

**Minerals:**

- Quartz: 35% (fine-grained, 0.02-0.87 mm, average: 0.38 mm, mode: 0.3 mm), anhedral to subhedral, elongated.
- Biotite: 5% (fine-grained, 0.11-0.59 mm, average: 0.25 mm, mode: 0.2 mm) subhedral, prismatic.
- Plagioclase: 20% (fine to medium-grained, 0.19-1 mm, average: 0.6 mm, mode: 0.4 mm), subhedral, tabular to elongated.
- Muscovite: 35% (fine to medium-grained, 0.16-1.52 mm, average: 0.6 mm, mode: 0.5 mm), subhedral to euhedral, prismatic to needle shape.
- Garnet: 3 % (medium to coarse-grained, 1.4-5 mm), anhedral, equant.
- Ilmenite: < 1%
- Apatite: < 1%
- Zircon: < 1%
- Monazite: < 1%

**Textures:**

The rock is fine to coarse-grained, porphyroblastic, hypidioblastic, showing crenulation cleavage. The crenulation cleavage is defined by the orientation of fined to medium-grained subhedral to euhedral muscovite and biotite parallel to the fold axial plane to the folded compositional layering. The microlithons, fined-grained quartz and plagioclase show developed SPO parallel to the compositional layering.

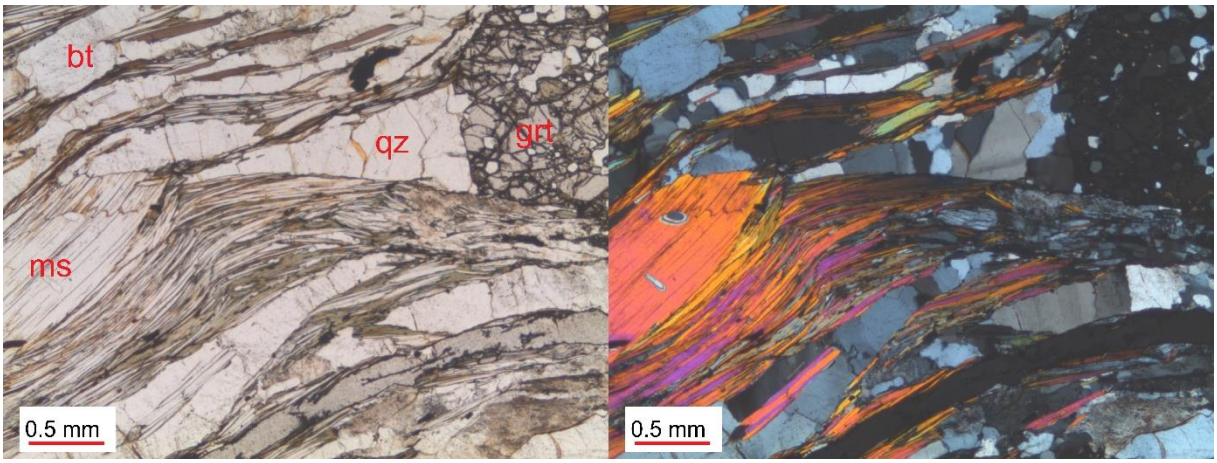


Thin section images of the garnet mica schist (gmf2020-09). PPL left, XPL right.

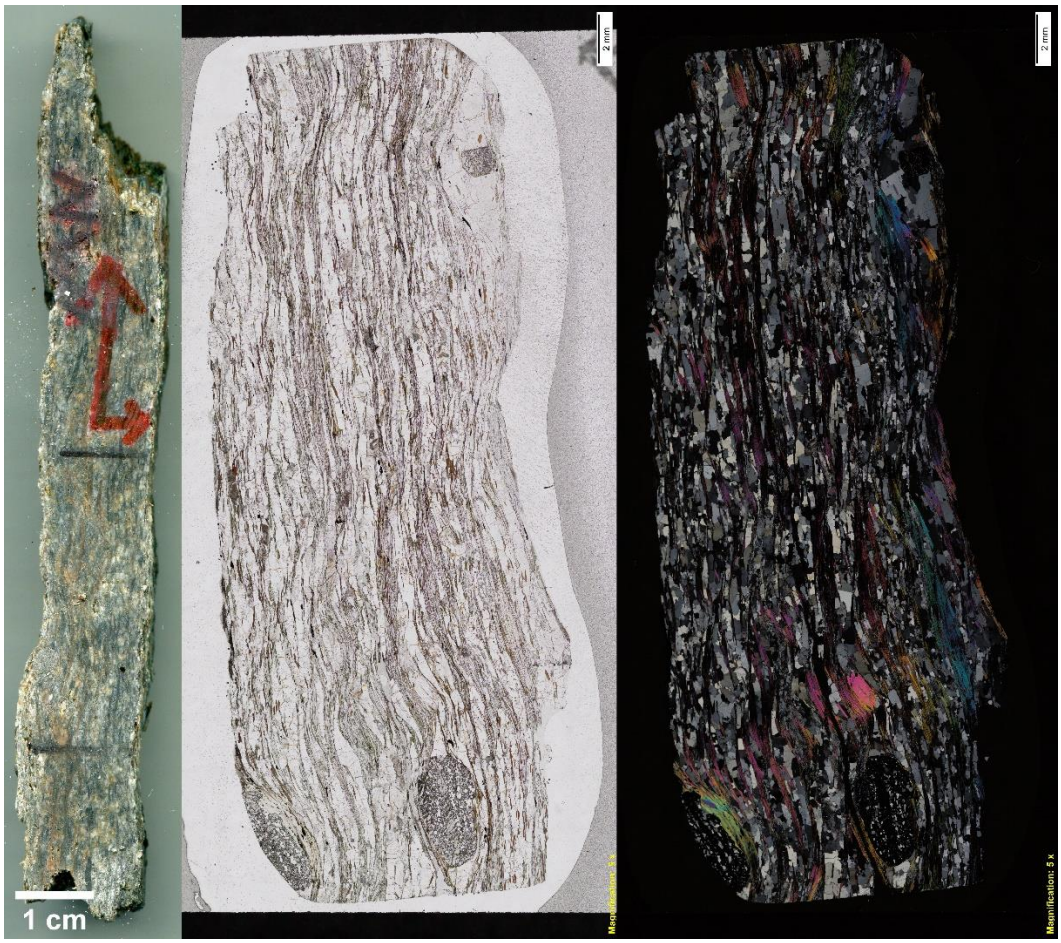


Rock slab, and thin section scans of gmf2020-09. PPL in the middle, XPL to the right.

**gmf2020-10**

**Coordinates**: 66.30725° N, 14.81167° E

**Rock:** Garnet mica schist

**Minerals:**

- Quartz: 40% (fine-grained, 0.11-0.61 mm, average: 0.3 mm, mode: 0.2 mm), anhedral to subhedral, equant to elongated.
- Biotite: 10% (fined-grained, 0.07-0.5 mm, average: 0.27 mm, mode: 0.3 mm), subhedral to euhedral, prismatic.
- Plagioclase: 43% (fine-grained, 0.25-0.98 mm, average: 0.46 mm, mode: 0.5 mm), anhedral to subhedral, tabular.
- Chlorite: 2% (fine-grained, 0.05-0.5 mm, average: 0.22, mode: 0.2 mm), anhedral to euhedral, prismatic to tabular.
- Garnet: 2% (fine to medium-grained, 0.21-3.1 mm, average: 0.67 mm, mode: 0.3 mm)
- Rutile: < 1%
- Muscovite: < 1%
- Apatite: < 1%
- Zircon: < 1%
- Monazite: <1%

**Textures:**

The rock is fine to coarse-grained, porphyroblastic, hypidioblastic showing continuous cleavage. The continuous cleavage is defined by the orientation of fined-grained subhedral to euhedral biotite and chlorite parallel to the folded compositional layering. The microlithons, fined-grained quartz and plagioclase show developed SPO parallel to the compositional layering.

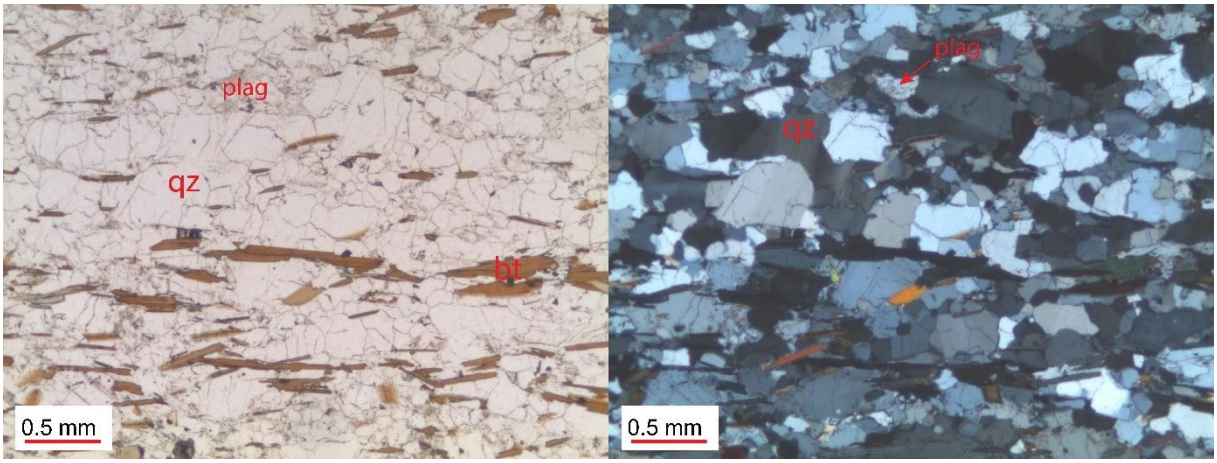


Thin section images of the garnet mica schist (gmf2020-10). PPL left, XPL right.

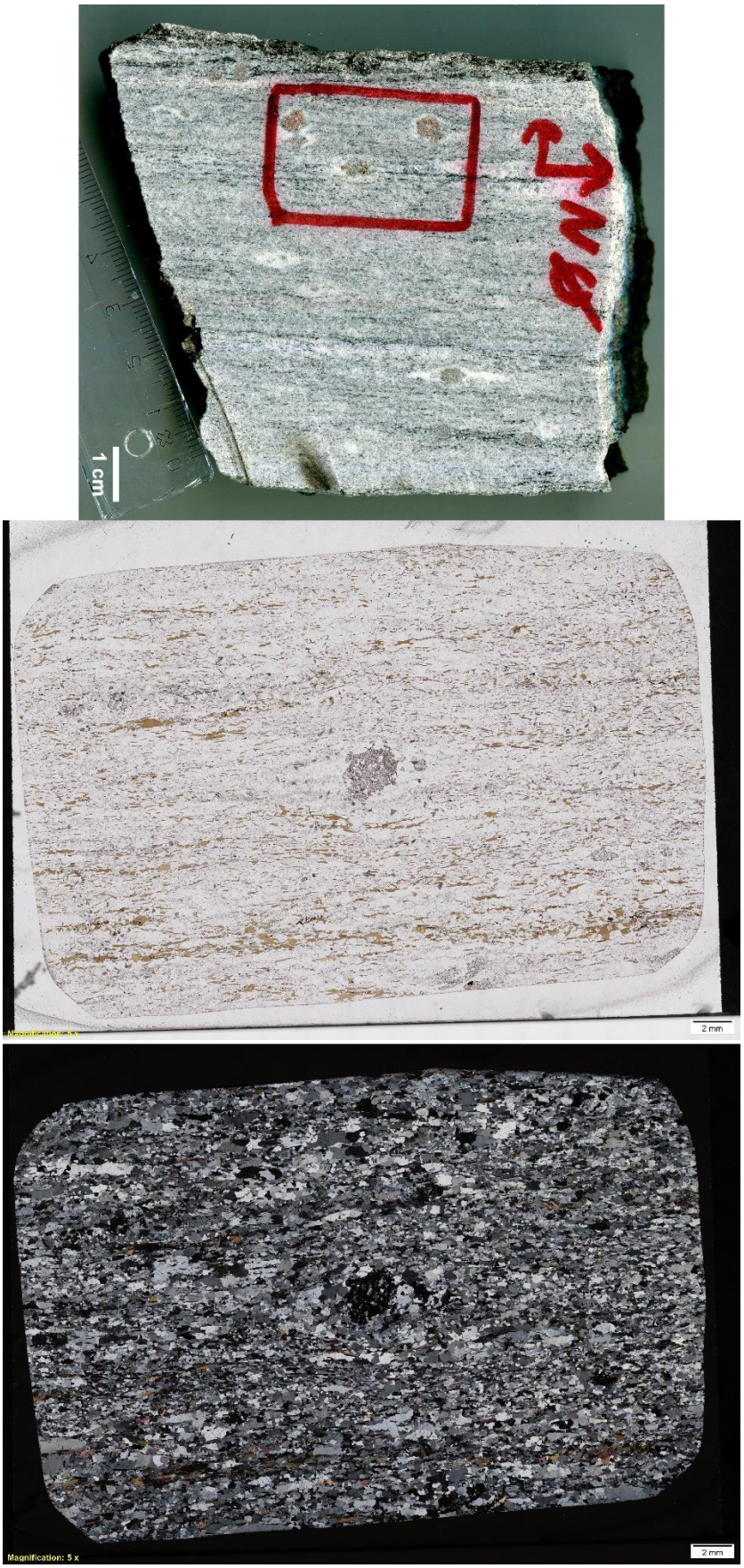


Rock slab, and thin section scans of gmf2020-10. PPL in the middle, XPL, bottom.

**gmf2020-11**

**Coordinates:** 66.18045° N, 14.72946° E

**Rock type:** Garnet mica schist

**Minerals:**

- Biotite: 55% (fined-grained, 0.05-0.36 mm, average: 0.11, mode: 0.1 mm) Anhedral to subhedral, prismatic to tabular
- Quartz: 18% (fined-grained, 0.03-0.25 mm, average: 0.12 mm, mode: 0.1 mm) Anhedral to subhedral,
- Muscovite: 19% (fine-grained, 0.03-0.19 mm, average: 0.08 mm, mode: 0.15 mm) subhedral to euhedral. Acicular, prismatic to tabular.
- Plagioclase: 2% (fine-grained, 0.12-0.46 mm, average: 0.2 mm, mode: 0.2 mm) Subhedral, tabular.
- Garnet: 5% (fine-grained, 0.15-4.5 mm, average: 0.9 mm, mode: 0.7 mm), anhedral, equant to skeletal.
- Monazite < 1%
- Zircon: < 1%
- Apatite: < 1%
- Rutile: < 1%
- Opaque: < 1%

**Textures:**

The rock is porphyroblastic, hypidioblastic, and has continuous cleavage. The rock has garnet porphyroblasts, and the continuous cleavage is defined by oriented biotite, muscovite, quartz, and plagioclase. The quartz and plagioclase show some banding (weak SPO), and polysynthetic twins are visible in the plagioclase. Some muscovite is oriented in a different direction than the foliation, interpreted to be post-tectonic.

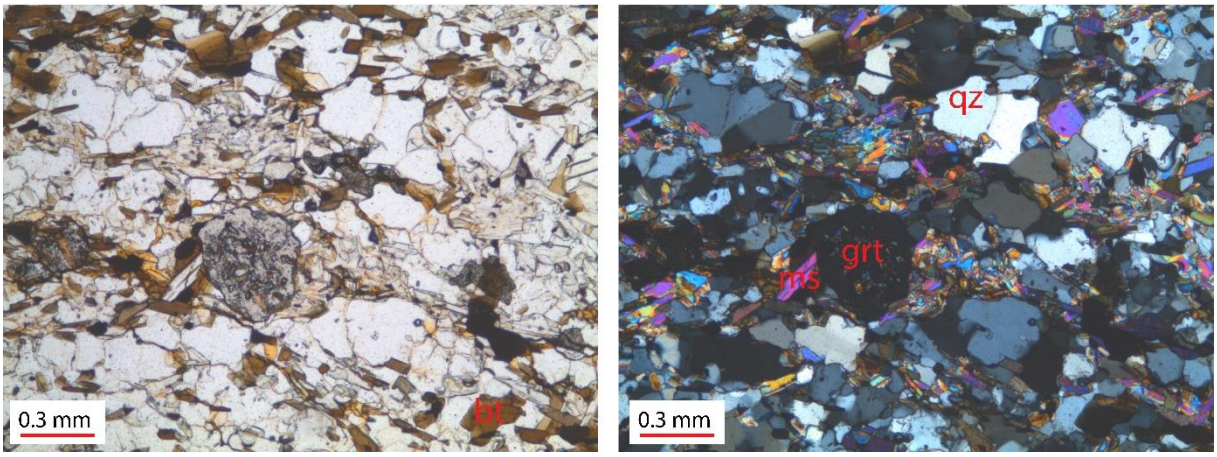


Thin section images of the garnet mica schist (gmf2020-11). PPL left, XPL right.

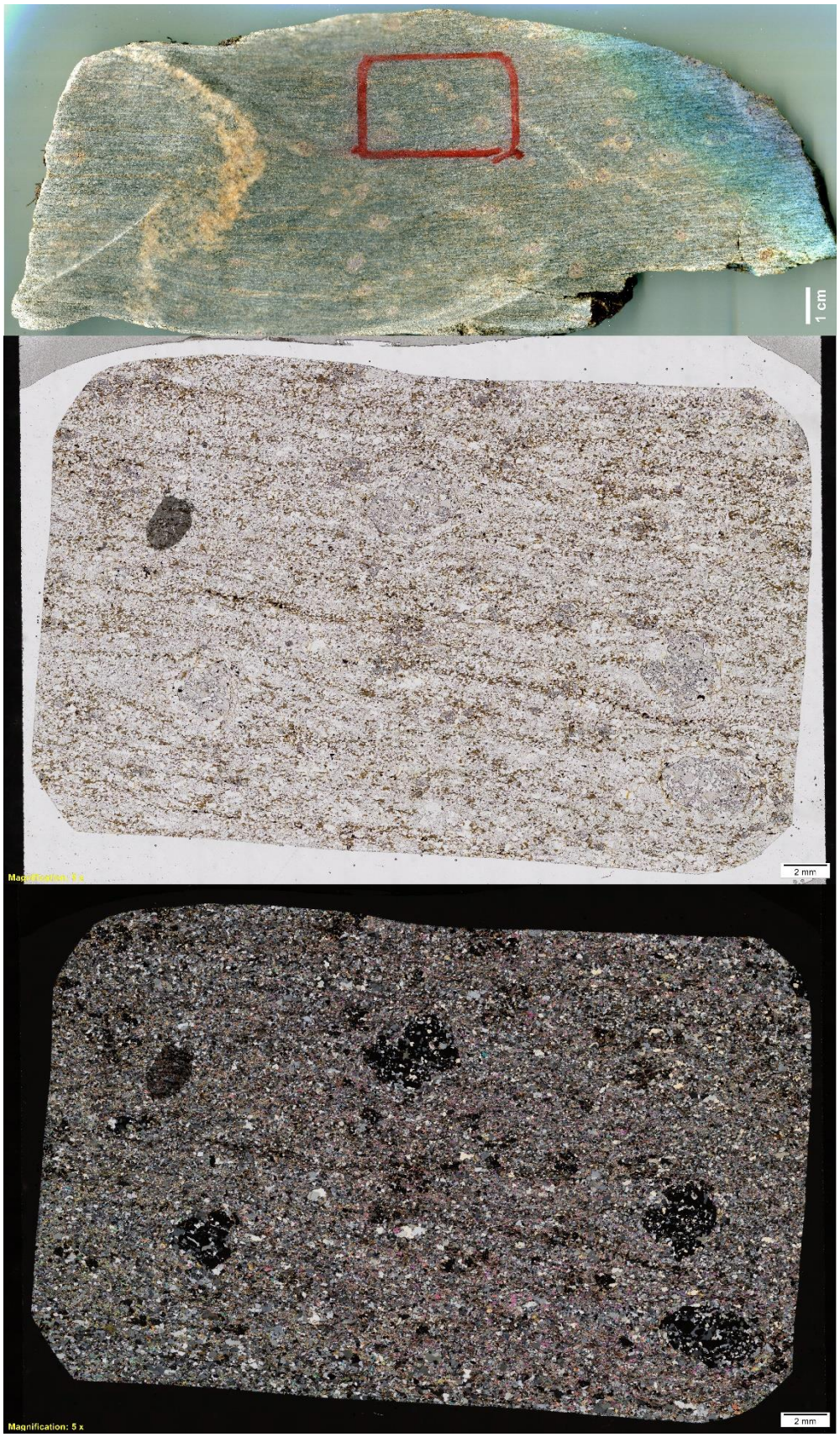


Rock slab, and thin section scans of gmf2020-11. PPL in the middle, XPL at the bottom.

**gmf2020-13**

**Coordinates:** 66.24076° N, 14.78038° E

**Rock type:** Garnet mica schist

**Minerals:**

- Quartz: 28% (fine to medium-grained, 0.09-1.5 mm, average: 0.56 mm, mode: 0.7 and 0.5 mm), anhedral to subhedral, equant to more elongated,
- Plagioclase: 42% (fine to medium-grained, 0.26-1.6 mm, average: 0.73 mm, mode: 0.4, 0.6 and 1 mm) subhedral, tabular.
- Biotite: 10% (fine-grained, 0.04-0.98 mm, average: 0.35 mm, mode: 0.3 mm), subhedral to euhedral, tabular to prismatic.
- Muscovite: 10% (fine to medium-grained, 0.12-2 mm, average: 0.53 mm, mode: 0.5 mm) subhedral to euhedral, prismatic to needle shape.
- Garnet: 5% (0.22-2.39 mm, average: 1.34 mm, mode: 1 and 2 mm), anhedral to subhedral, equant.
- Chlorite: 4% (fine-grained, 0.08-0.35 mm, average: 0.19 mm, mode: 0.2 mm), anhedral, prismatic to acicular.
- Apatite <1%
- Opaque: <1%
- Rutile: <1%

**Textures:**

The rock is fine to medium-grained, hypidioblastic, porphyroblastic, and has a spaced and a crenulation cleavage. The orientation of the mica defines the wriggly, anastomosing spaced cleavage. The crenulation cleavage is defined by the fold axial traces in the folded mica. The mica shows distinct foliation and crenulation cleavage. Seriterization occurs in the plagioclase, and chloritization is associated with mica and garnet. Polysynthetic twins are present in plagioclase. The porphyroblastic texture is defined by the anhedral to subhedral garnet.

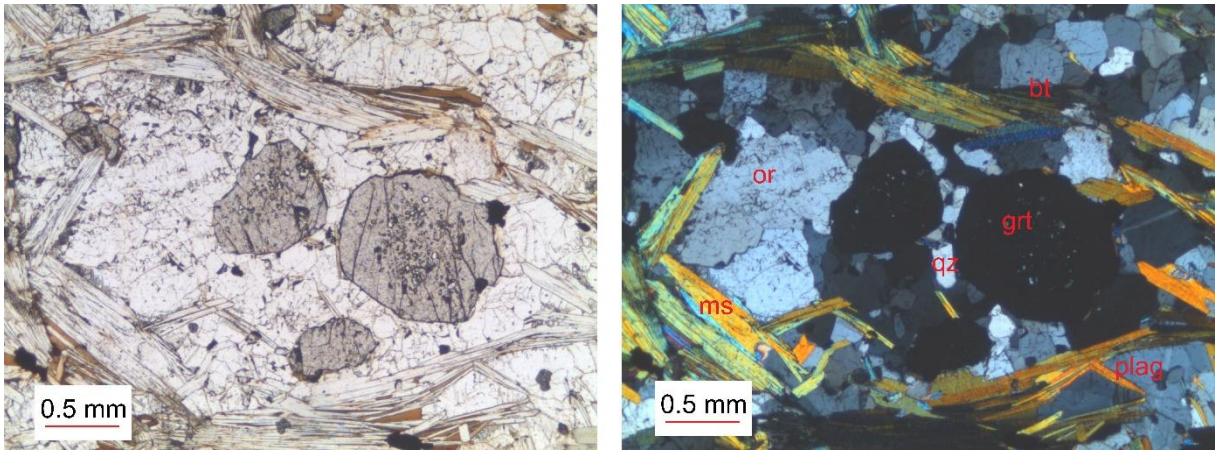

Thin section images of the garnet mica schist (gmf2020-13). PPL left, XPL right.

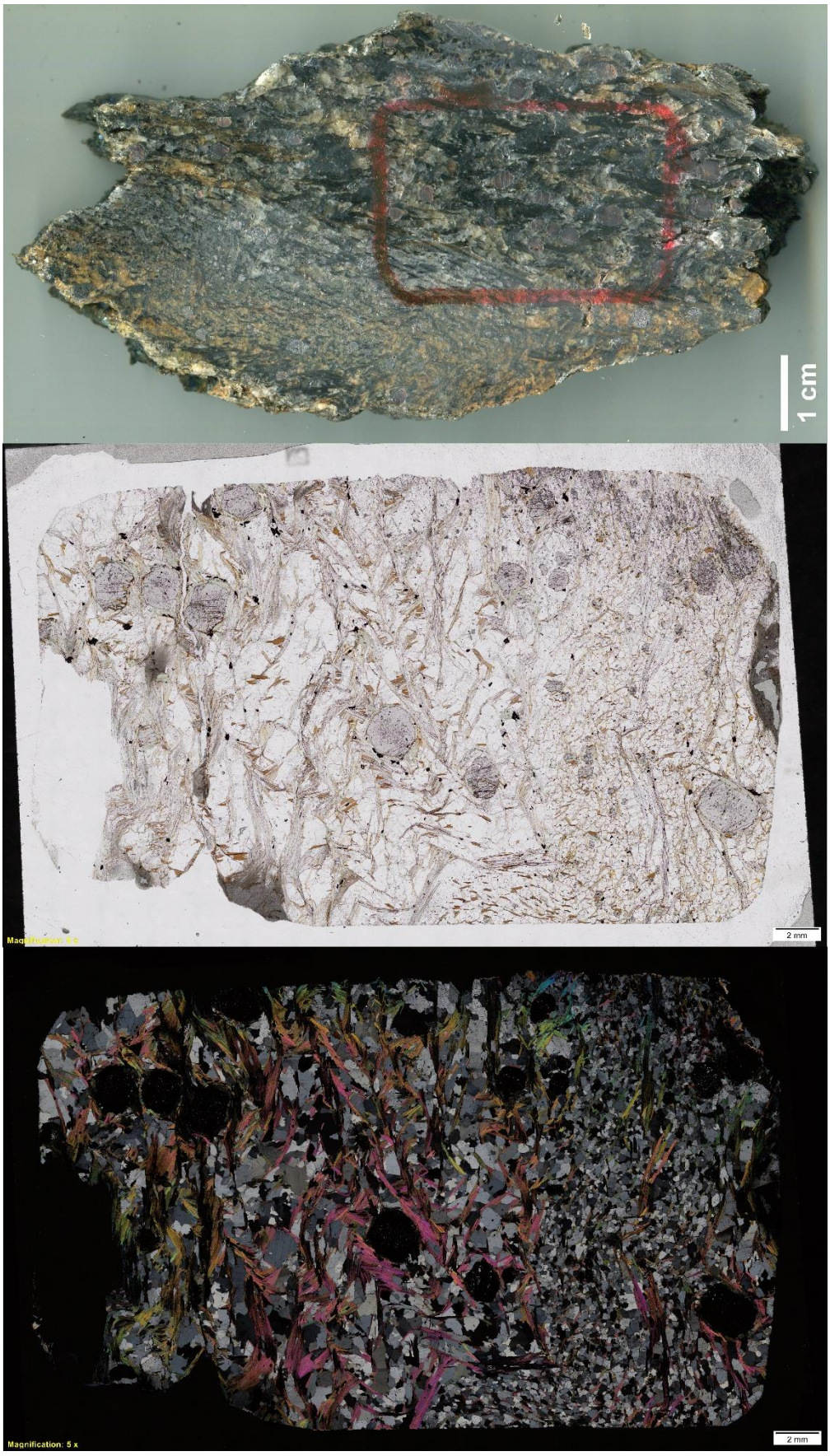


Rock slab, and thin section scans of gmf2020-13. PPL in the middle, XPL at the bottom.

**gmf2020-21**

**Coordinates:** 66.24851° N, 14.98832° E

**Rock:** Felsic vein and reaction rim

Felsic vein

**Minerals**

- Biotite: 5% (Fine to medium-grained, 0.18-1.76 mm, average grain size: 0.6 mm, mode: 0.2 mm), subhedral to euhedral, mostly prismatic, some tabular. Foliated with crenulation cleavage and buckles around the garnet.
- Chlorite: 1% (Fine-grained, 0.07 to 0.75 mm, average: 0.36 mm, mode: 0.2 mm). Subhedral to euhedral, prismatic to equant, mostly prismatic. Associated with biotite and garnet.
- Garnet: 2% (Medium-grained, 1.3 to 2 mm, average 1.5 mm, mode: 1 mm). White to grey in ppl. A lot of inclusions. Anhedral to euhedral. Not all garnets are well developed and have a lot of inclusions. Equant.
- Muscovite: < 1%
- Plagioclase: 32% (Fine to medium-grained, 0.2-1.2 mm, average: 0.66 mm, mode: 0.5 mm). White in ppl. Have polysynthetic twins, tabular, anhedral to subhedral.
- Quartz: 48% (Fine to medium-grained, 0.2-1.7 mm, average grain size: 0.68 mm, mode: 0.4 mm), anhedral, equant. Grain boundary migration texture.
- Apatite: 2-5% (Fine-grained, 0.03-0.2 mm, average: 0.1 mm, mode: 0.1 mm).
- Zircon: < 1%
- Zoisite: < 1%
- Clinozoisite: < 1%
- Rutile: < 1%
- Opaque: < 1%

**Textures:**

The felsic vein is fine to medium-grained, equigranular, hypidioblastic, and has a spaced cleavage parallel to the compositional layering. The parallel wriggly spaced cleavage (5 % cleavage domains) is defined by the oriented subhedral to euhedral biotite. The microlithons, quartz and plagioclase show grain boundary migration.

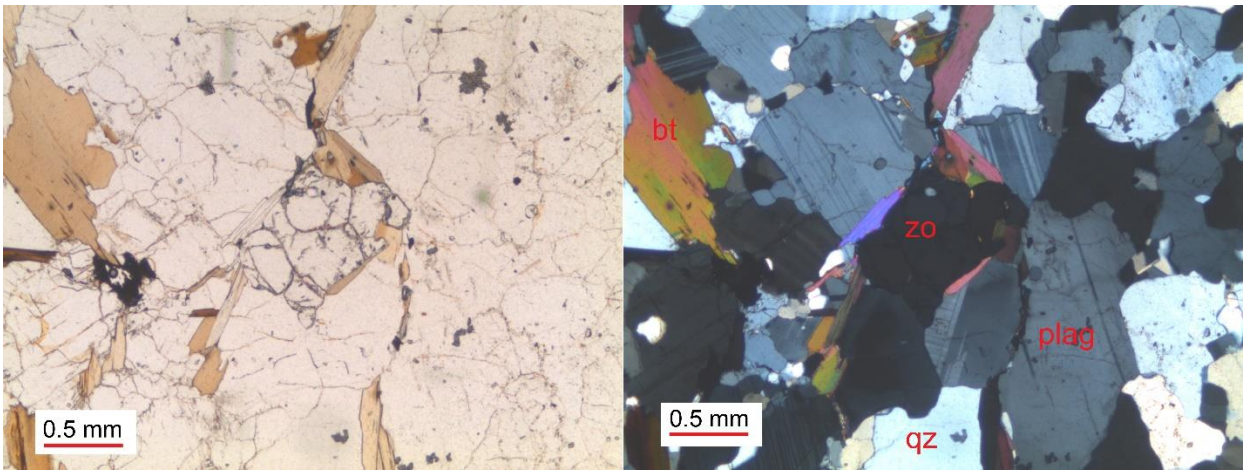

Thin section images of the felsic vein (gmf2020-21). PPL left, XPL right.

Reaction rim:

**Minerals:**

- Biotite: 30% (Fine-grained, 0.06 – 1.4 mm, average: 0.3 mm, mode: 0.2 mm) Subhedral to euhedral, prismatic. Shows distinct crenulation clevage.
- Quartz: 37% (Fine to medium-grained, mostly fine, 0.1-1 mm, average: 0.5 mm, mode: 0.4 mm), subhedral to euhedral, equant, subhedral to anhedral.
- Plagioclase: 20% (Fine to medium-grained, 0.23-1.2 mm, average: 0.47 mm, mode: 0.3 mm), mostly anhedral, some subhedral, equant to more elongated.
- Muscovite: 8% (Fine to medium-grained, 0.16 mm to 1 mm, average: 0.39 mm, 0.2 mm), subhedral to euhedral, prismatic. Buckles around garnet and shows distinct crenulation cleavage.
- Garnet: 5% (Medium grained, 1-2.8 mm, average: 2.1 mm, mode: 2 mm), subhedral to euhedral, equant.
- Apatite: < 1%
- Opaque: < 1%
- Rutile: < 1%
- Chlorite: < 1%
- Clinozoisite: < 1%

**Textures**

The reaction rim is fine to medium-grained, porphyroblastic, hypidioblastic, and has a spaced and crenulation cleavage. The folded parallel to anastomosing spaced cleavage is parallel to the compositional layering and is defined by subhedral to euhedral prismatic biotite and muscovite. The crenulation cleavage is defined by the fold axial traces to the folded spaced cleavage. The microlithons, quartz, and plagioclase show SPO. The porphyroblastic texture is defined by the medium grains subhedral to euhedral equant garnet. Polysynthetic twins are present in the plagioclase.

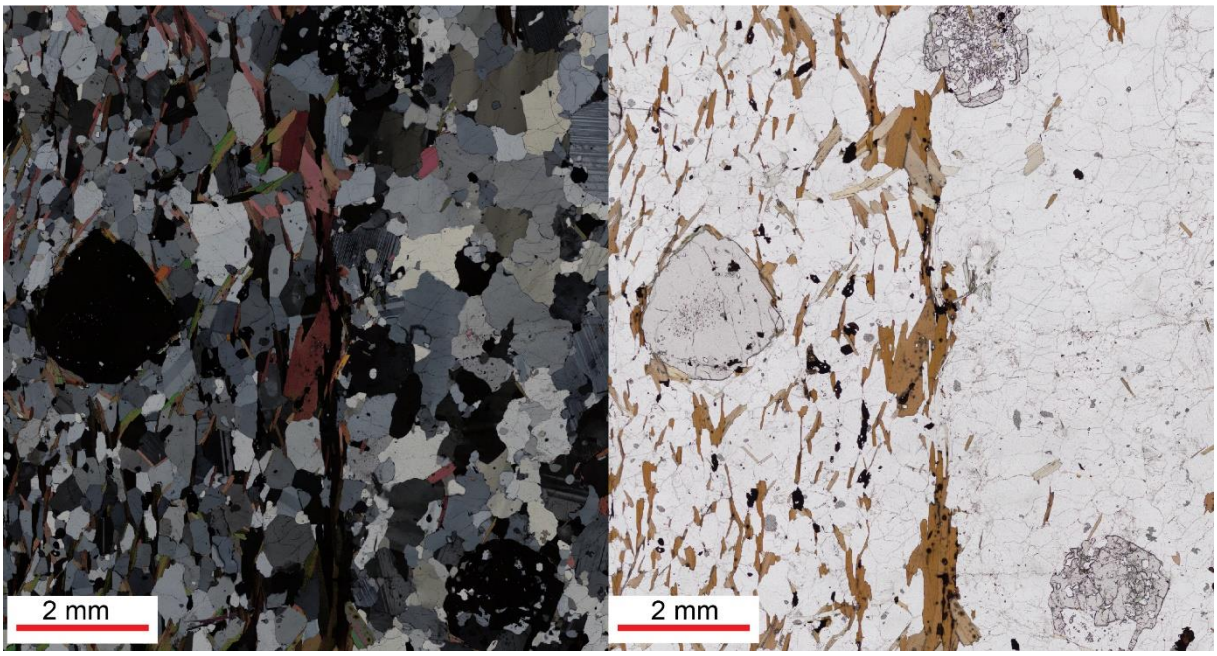


Thin section images of the boundary between the felsic vein and the reaction rim (gmf2020-21), PPL left, XPL right.

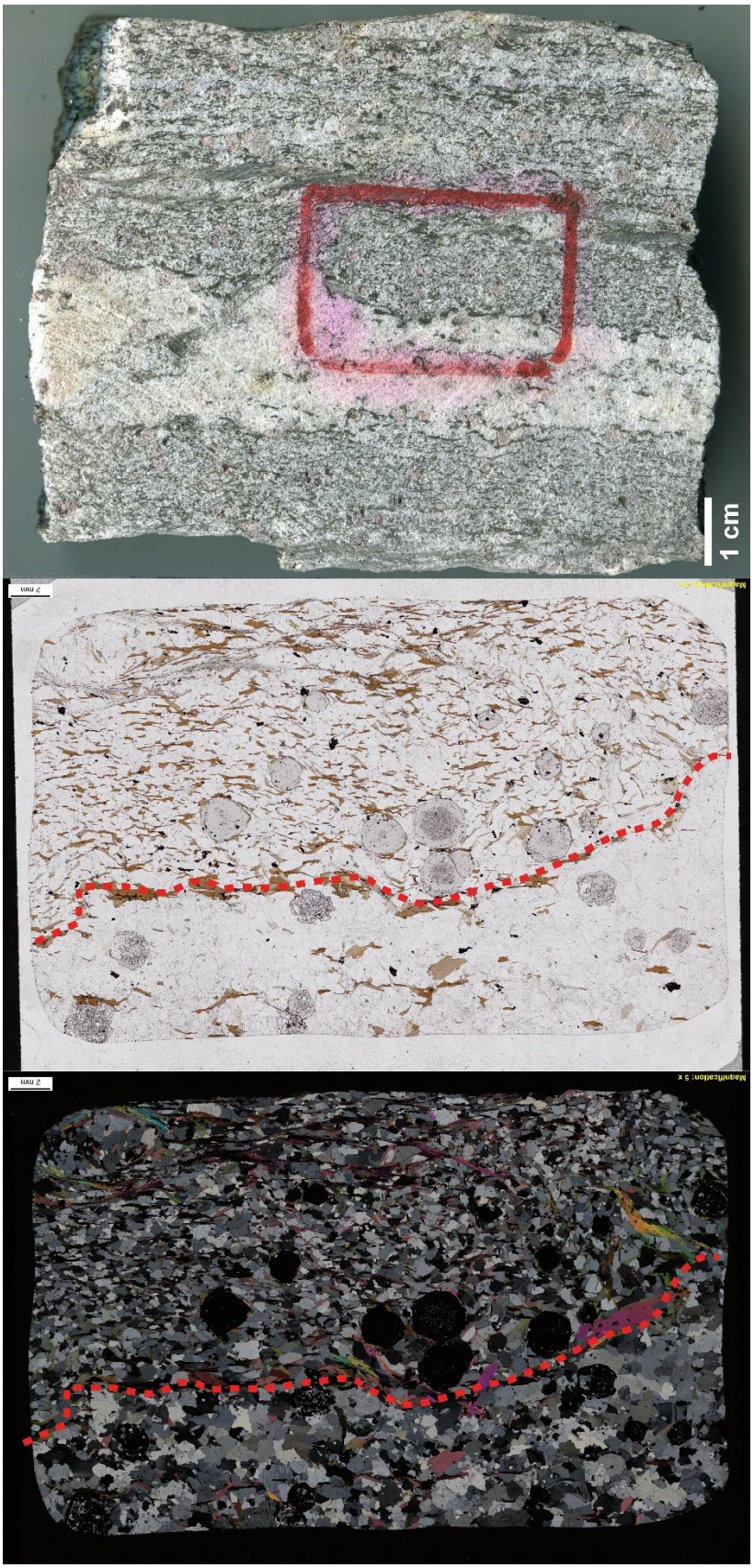


Rock slab, and thin section scans of gmf2020-21. PPL in the middle, XPL, bottom.

**gmf2020-22A**

**Coordinates:** 66.22623° N, 14.77882° E

**Rock type:** Reaction rim

**Minerals:**

- Quartz: 24% (fine to medium-grained, 0.15-1.46, average: 0.76 mm, mode: 0.7 mm), anhedral to subhedral, equant to more elongated
- Biotite: 35% (fine to medium-grained, 0.071-1.66 mm, average: 0.8 mm, mode: 0.65 mm), subhedral, prismatic to tabular.
- Garnet: 20% (fine to medium-grained, 0.26-1.38 mm, average: 0.84 mm, mode: 1 mm), subhedral, equant
- Plagioclase: 10% (fine to medium-grained, 0.26-2.53 mm, average: 0.76 mm, mode: 0.75 mm), subhedral, tabular
- Apatite: < 1%
- Zircon: < 1%
- Rutile: < 1%
- Chlorite: < 1%

**Textures:**

The rock is fine to medium-grained, hypidioblastic, equigranular, and has weak crenulation and spaced cleavage. The crenulation cleavage is defined by the folded spaced cleavage defined by biotite. The spaced parallel to anastomosing cleavage is wriggly to folded and is defined by biotite in the same direction as the compositional layering. The microlithons, quartz, and feldspar have a developed SPO, and the rock show chloriterization and alteration of feldspar. The plagioclase has polysynthetic twins and the quartz has undulating extinction.

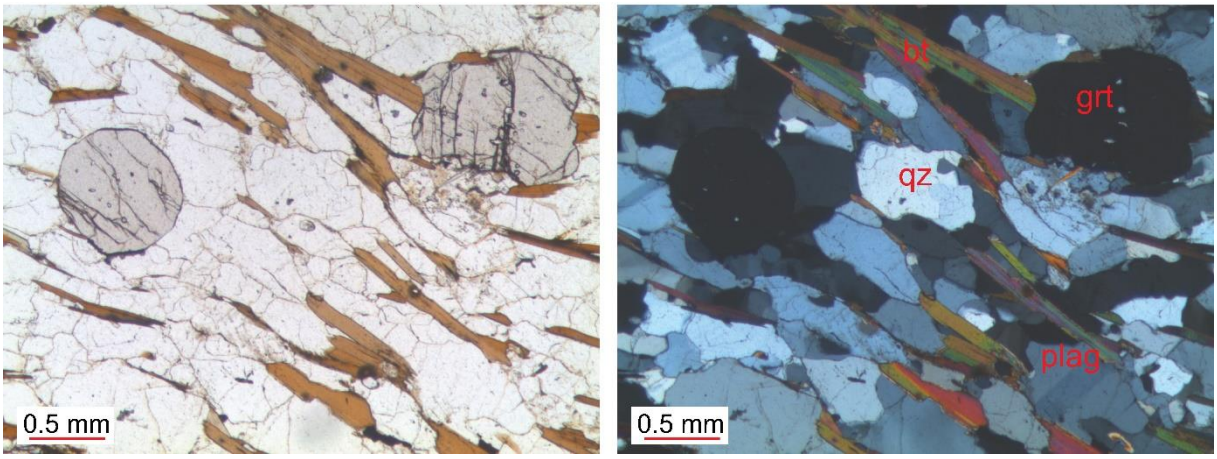


Thin section images of the garnet mica schist (gmf2020-22A). PPL left, XPL right.

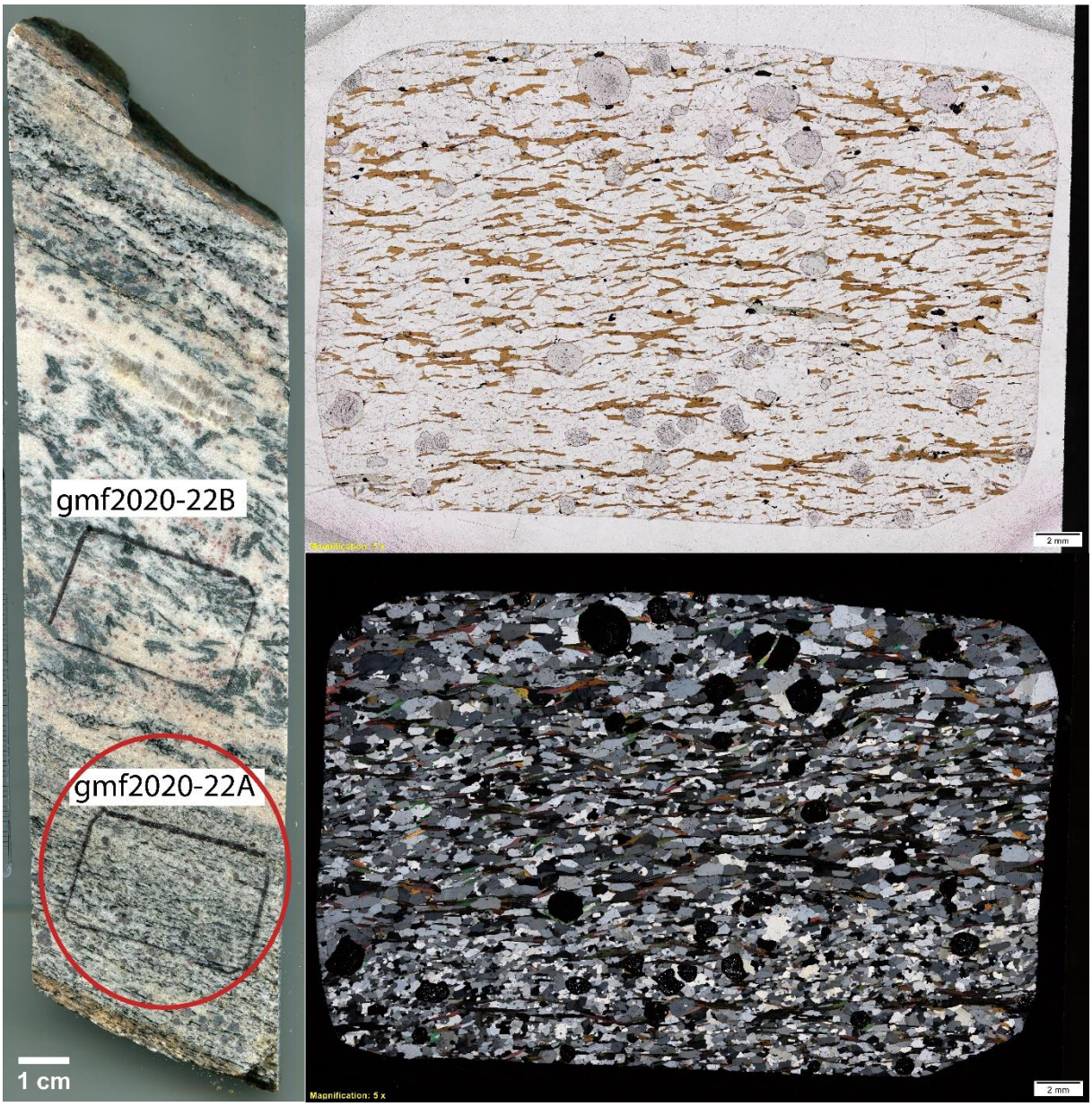


Rock slab, and thin section scans of gmf2020-22A. PPL at top, XPL, bottom.

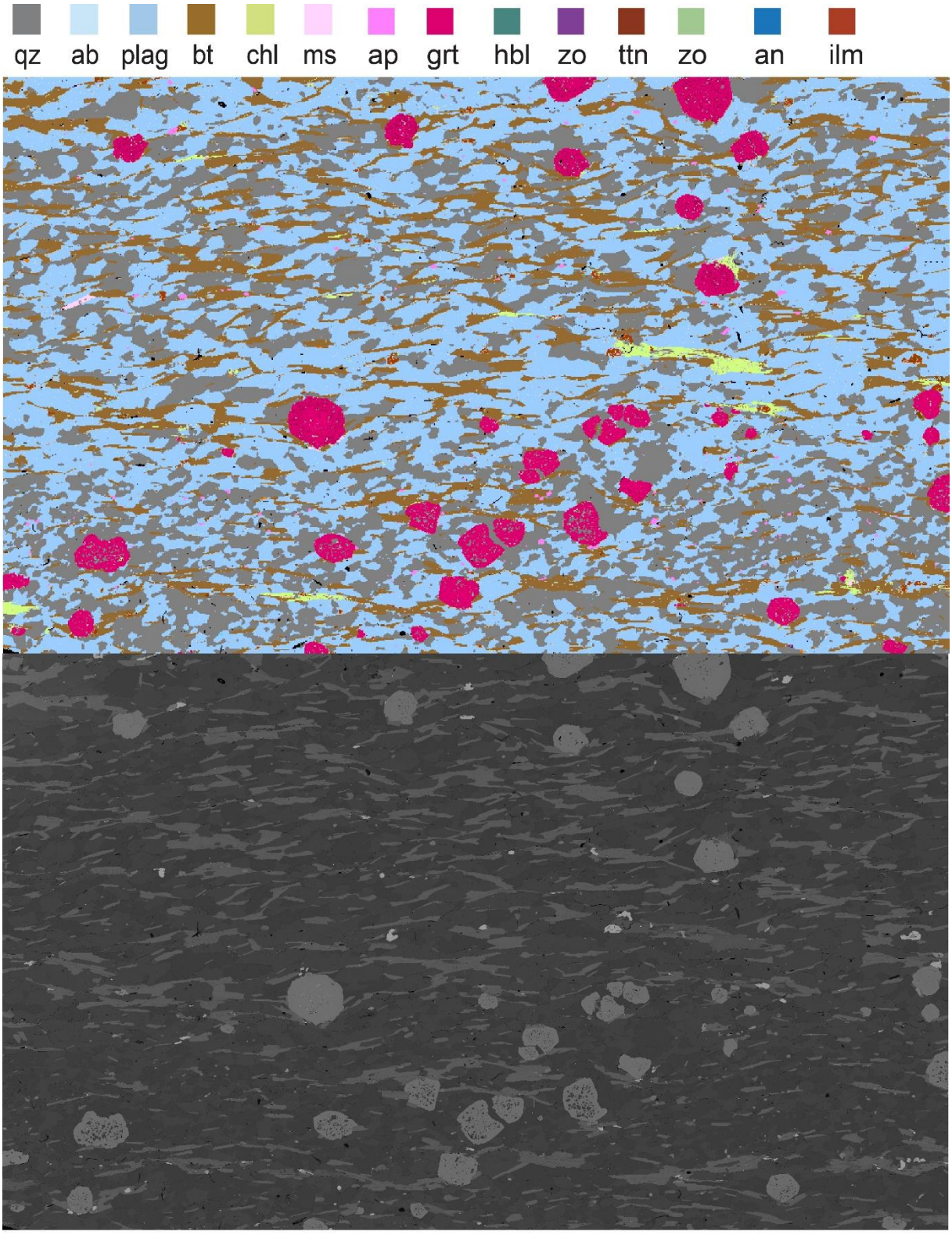


EDS-scan, and BS-image of gmf2020-22A. EDS-scan at top, BS-image, bottom.

**gmf2020-22B**

**Coordinates:** 66.22623° N, 14.77882° E

**Rock type:** Felsic vein

**Minerals:**

- Quartz: 16% (fine to medium-grained, 0.066-3.7 mm, average: 0.82 mm, mode: 0.45 mm), anhedral to subhedral, equant to more elongated.
- Hornblende: 28% (fine to coarse-grained, 0.28-9.32 mm, average: 2.48 mm, mode: 2 mm) subhedral to euhedral, skeletal, tabular to prismatic, inclusion-rich.
- Garnet: 20% (fine-grained, 0.13-0.9 mm, average: 0.58 mm, mode: 0.76 mm), subhedral, equant.
- Zoisite: 20% (fine to medium-grained, 0.13-1.57 mm, average: 0.6 mm, mode: 0.7 mm), subhedral to euhedral, tabular, prismatic to diamond shape.
- Plagioclase: 16% (fine to medium-grained, 0.07-1.2 mm, average: 0.43 mm, mode: 0.4 mm), subhedral, tabular.
- Titanite: 1% (0.049-0.24 mm, average: 0.12 mm, 0.1 mm), subhedral, equant, tabular to diamond shape.
- clinozoisite: < 1%
- Zircon: < 1%

**Textures:**

The rock is porphyroblastic, hypidioblastic, and shows some grain orientation. The porphyroblastic hornblende and zoisite make up the weak foliation. The hornblende seems to have been crystallized after the zoisite. Quartz and plagioclase inclusions are abundant in the hornblende. The quartz and plagioclase seem to have developed an SPO. The quartz shows grain boundary migration texture, and plagioclase has polysynthetic twins.

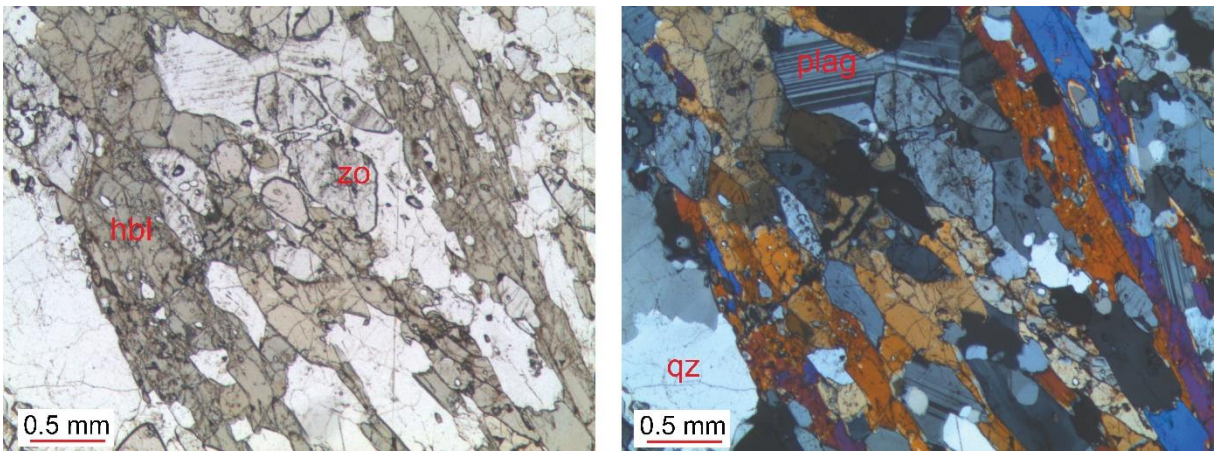


Thin section images of the garnet mica schist (gmf2020-22B). PPL left, XPL right.

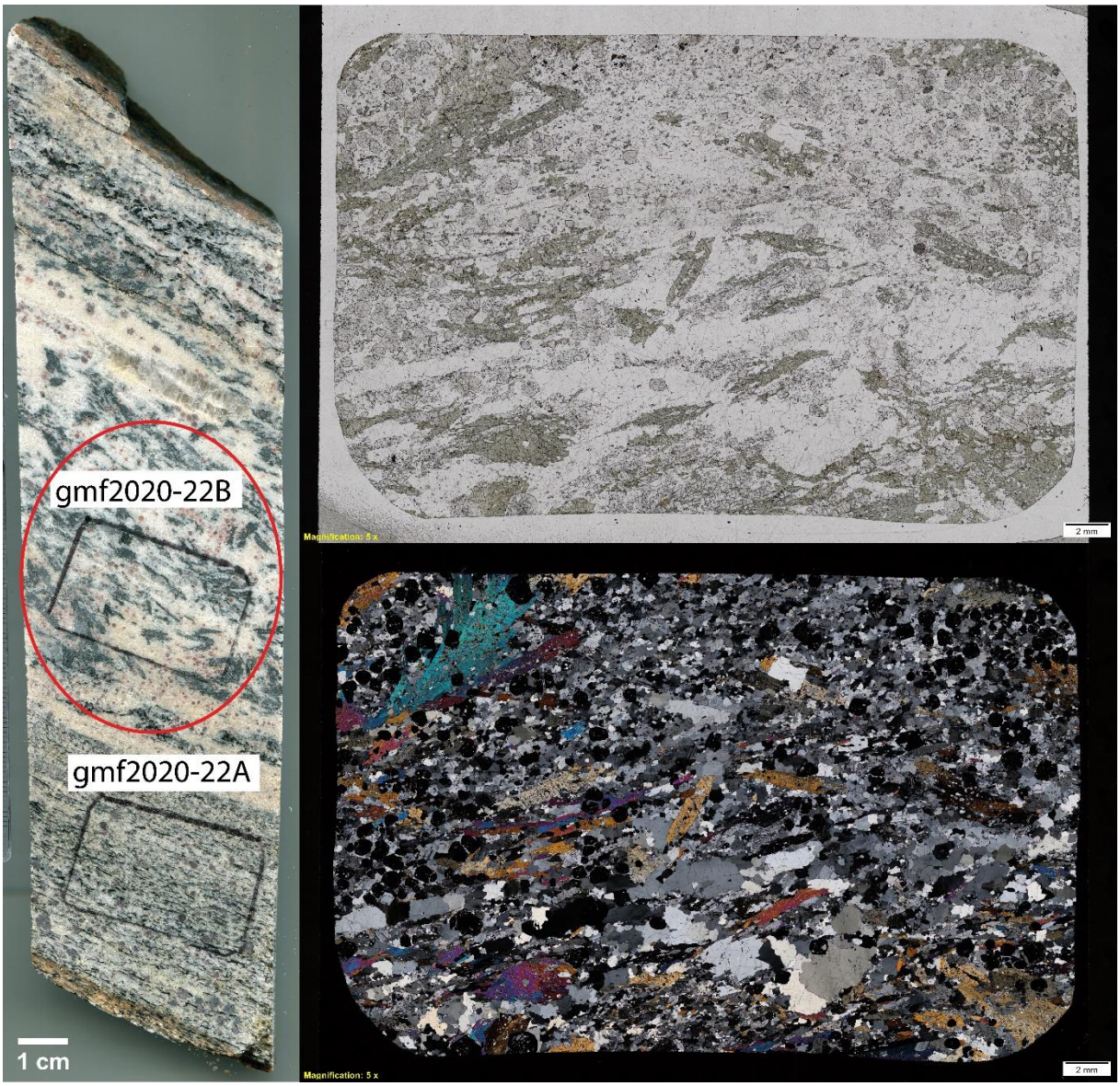


Rock slab, and thin section scans of gmf2020-22B. PPL at top, XPL, bottom.

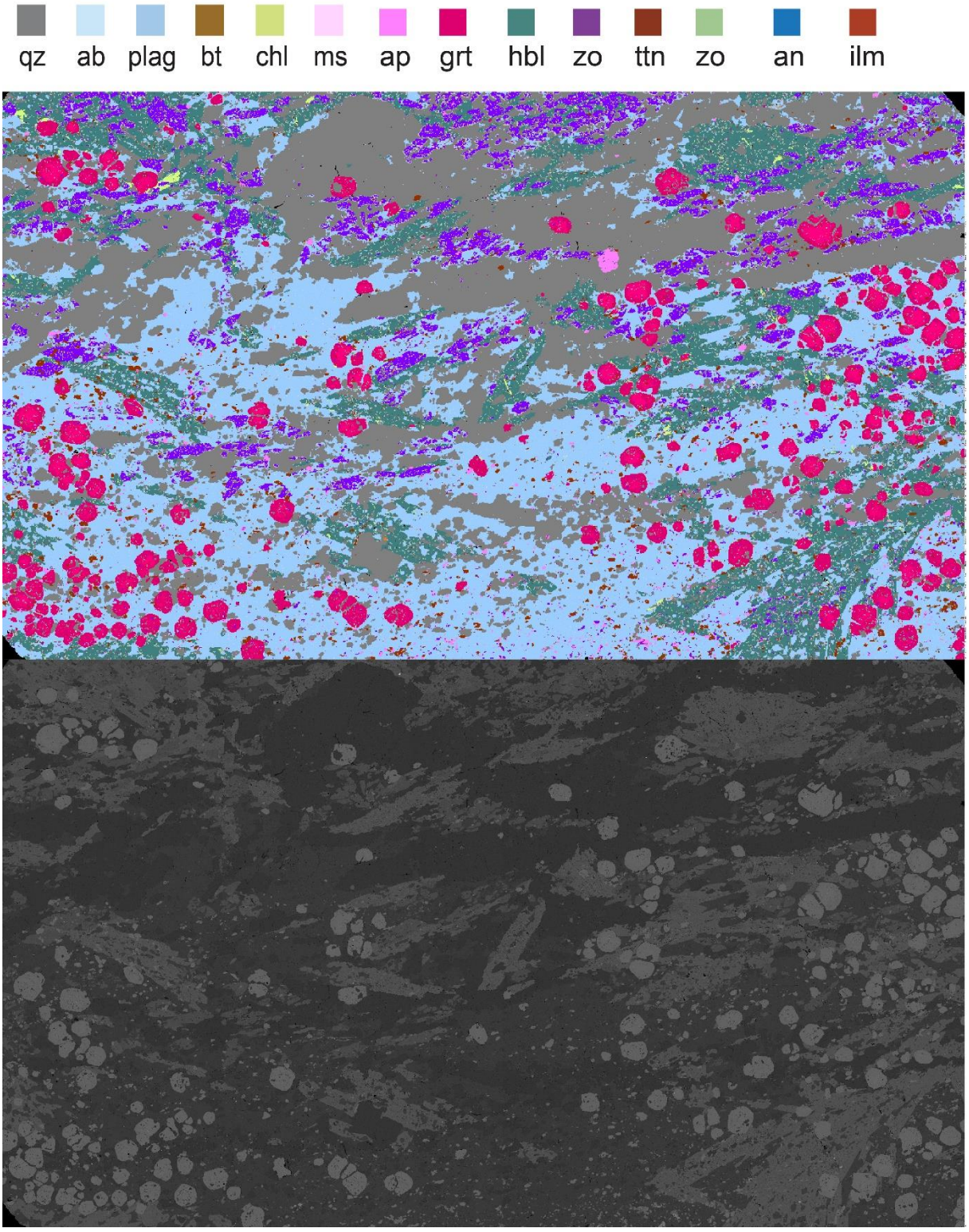


EDS-scan, and BS-image of gmf2020-22B. EDS-scan at top, BS-image, bottom.

**gmf2020-23**

**Coordinates:** 66.23658° N, 14.77882° E

**Rock type:** Garnet amphibolite

**Minerals:**

- Hornblende: 65% (fine to medium-grained, 0.045-1.89 mm, average: 0.7 mm, mode: 0.6 mm), subhedral to euhedral, prismatic to equant/diamond shape.
- Garnet: 10% (fine to medium-grained, 0.6-4.24 mm, average: 2.3 mm, mode: 3 mm), anhedral to subhedral, equant to skeletal.
- Plagioclase: 15% (fine to medium-grained, 0.05-1 mm, average: 0.5 mm, mode: 0.25 mm), subhedral, equant to tabular.
- Biotite: 2% (fine to medium-grained, 0.15-1.25 mm, average: 0.6 mm, mode: 0.6 mm)
- Quartz: 5% (fine to medium-grained, 0.29-3.77 mm, average: 1 mm, mode: 0.5 mm), anhedral to subhedral, equant.
- Titanite: 3% (fine-grained, 0.067-0.5 mm, average: 0.13 mm, mode: 0.1 mm), subhedral to euhedral, tabular to diamond shape.
- Zoisite: 2% (fine-grained, 0.04-0.11 mm, average: 0.066 mm, mode: 0.06 mm), subhedral, equant to tabular.
- Chlorite < 1%
- Zircon < 1%

**Textures:**

The rock is hypidioblastic, porphyroblastic with wavy continuous cleavage parallel to the compositional layering. The rock has garnet porphyroblasts, and the hornblende, quartz, and plagioclase define the continuous cleavage. The garnet amphibolite has a quartz vein with approximately the same orientation as the continuous cleavage. Grain boundary migration texture is present in the quartz, and polysynthetic twins in plagioclase. Saussuritization and chloriterization are present.

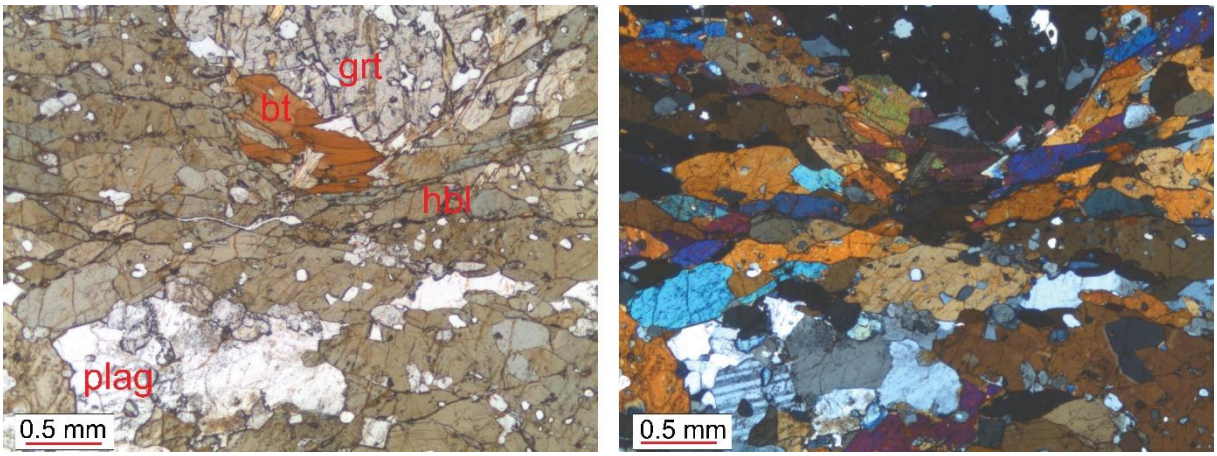


Thin section images of the garnet amphibolite (gmf2020-23). PPL left, XPL right.

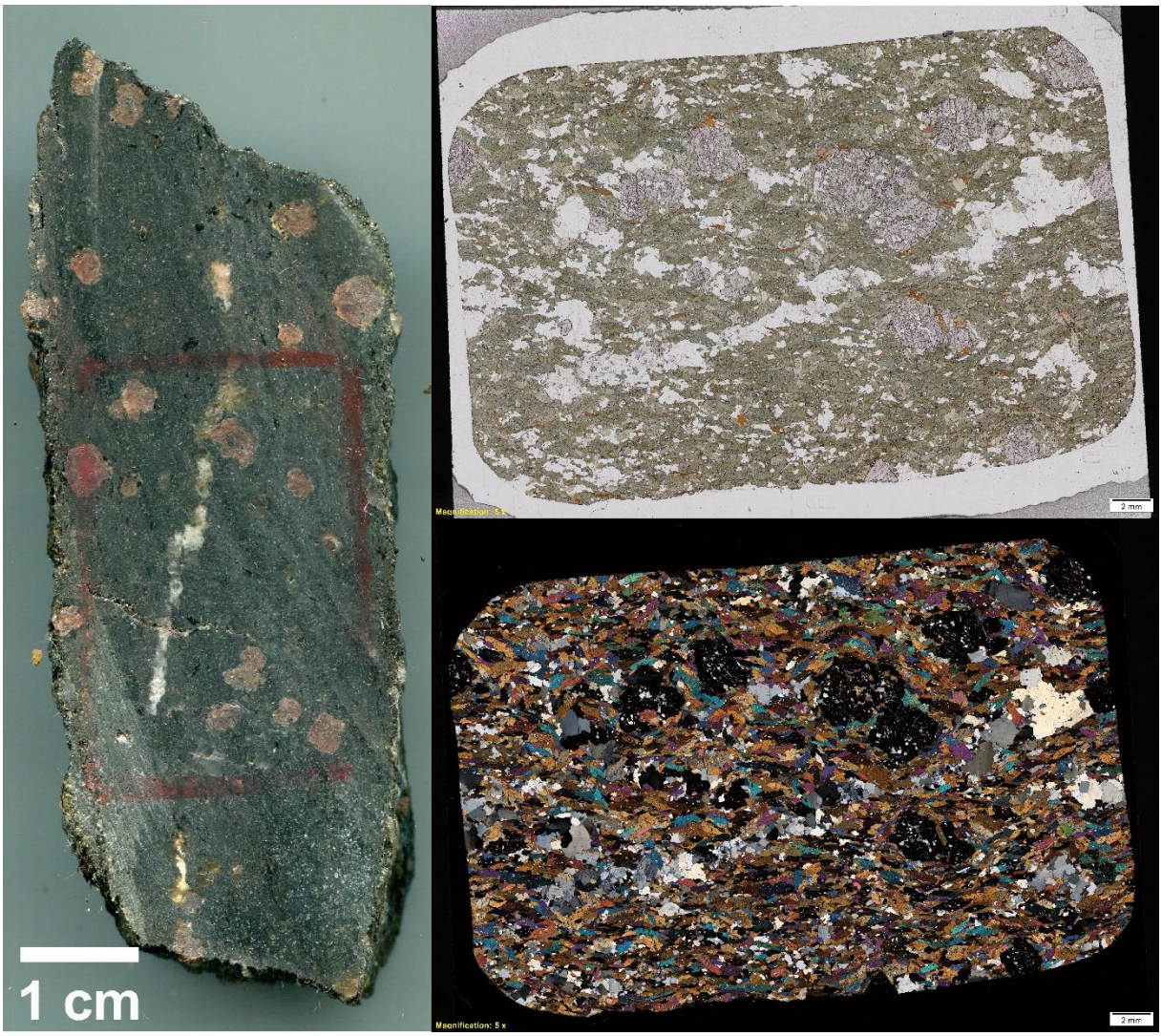


Rock slab, and thin section scans of gmf2020-23. PPL at top, XPL, bottom.

**gmf2020-25**

**Coordinates:** 66.23661° N, 14.77846° E

**Rock type:** Garnet mica schist

**Minerals:**

- Quartz: 20% (fine to medium-grained, 0.19-2.1 mm, average: 0.63 mm, mode: 0.5 mm), anhedral to subhedral, equant to elongated.
- Feldspar: 20% (fine to medium-grained, 0.11-3.2 mm, average: 0.8 mm, mode: 0.2 mm and 1 mm), subhedral to euhedral, equant to tabular.
- Biotite: 35% (fine to medium-grained, 0.07-1.3 mm, average: 0.51 mm, mode: 0.3 and 0.4 mm), subhedral to euhedral, prismatic to tabular.
- Muscovite: 10% (fine to medium-grained, 0.13-1.45 mm, average: 0.62 mm, mode: 0.4 mm, 0.6 and 1 mm), subhedral to euhedral, prismatic to needle, and tabular shaped.
- Garnet: 7% (medium-grained, 1-4.4 mm, average: 2.03 mm, mode: 1 and 2 mm), subhedral, equant.
- Chlorite: 5% (fine-grained, 0.13-0.48 mm, average: 0.22 mm, mode: 0.2 mm), prismatic to needle shape.
- Opaque: 1%
- Zircon: <1%
- Rutile: <1%

**Textures:**

The rock is fine to medium-grained, porphyroblastic, hypidioblastic, and has a spaced and a crenulation cleavage. The subhedral to euhedral biotite, muscovite, and chlorite orientation defines the wavy, anastomosing spaced cleavage. The crenulation cleavage is defined by the fold axial traces belonging to the folded mica. The subhedral equant garnet defines the porphyroblastic texture. Polysynthetic twins in plagioclase and chloritization of garnet and mica are present.

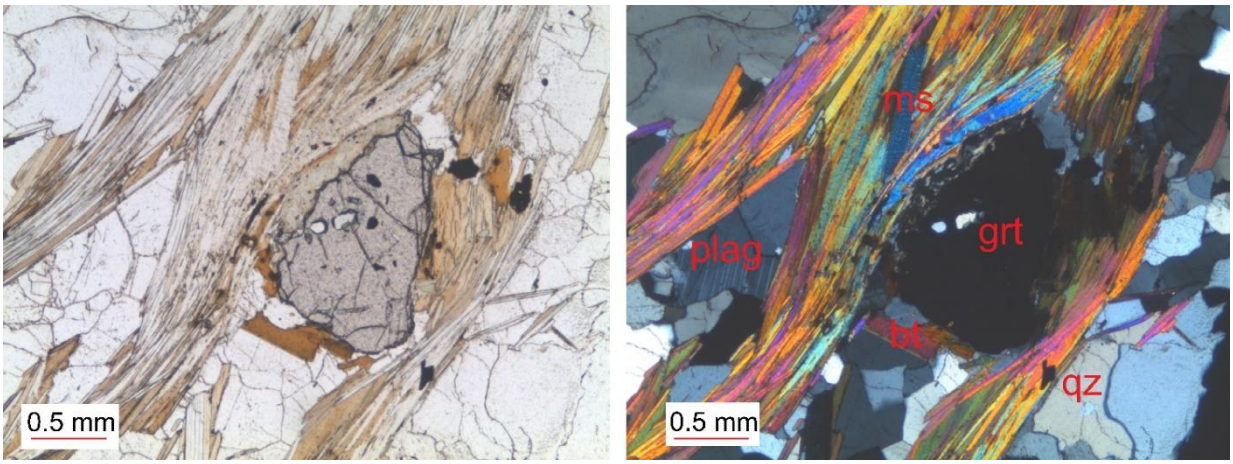


Thin section images of the reaction rim (gmf2020-25). PPL left, XPL right.

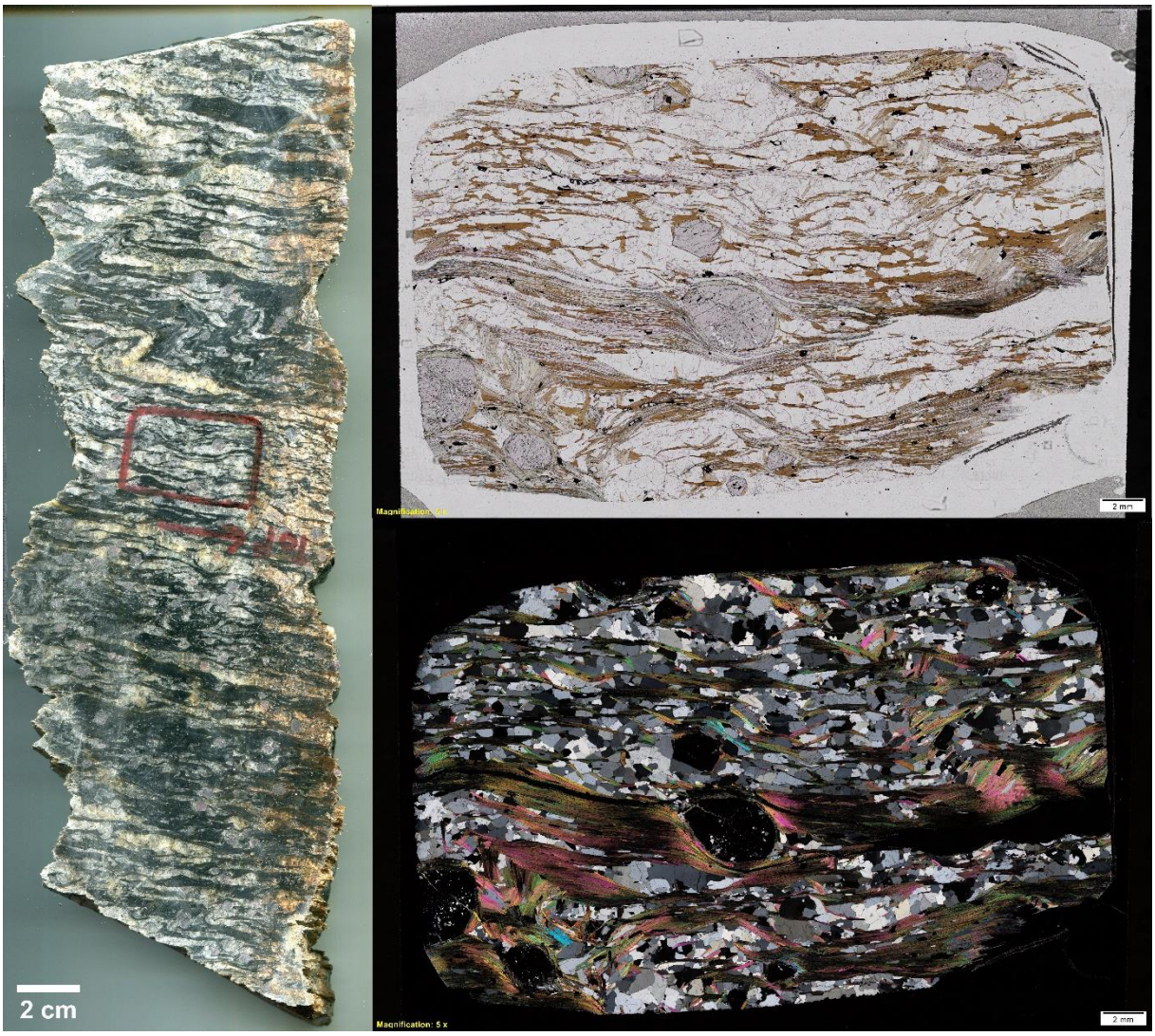


Rock slab, and thin section scans of gmf2020-25. PPL at top, XPL, bottom.

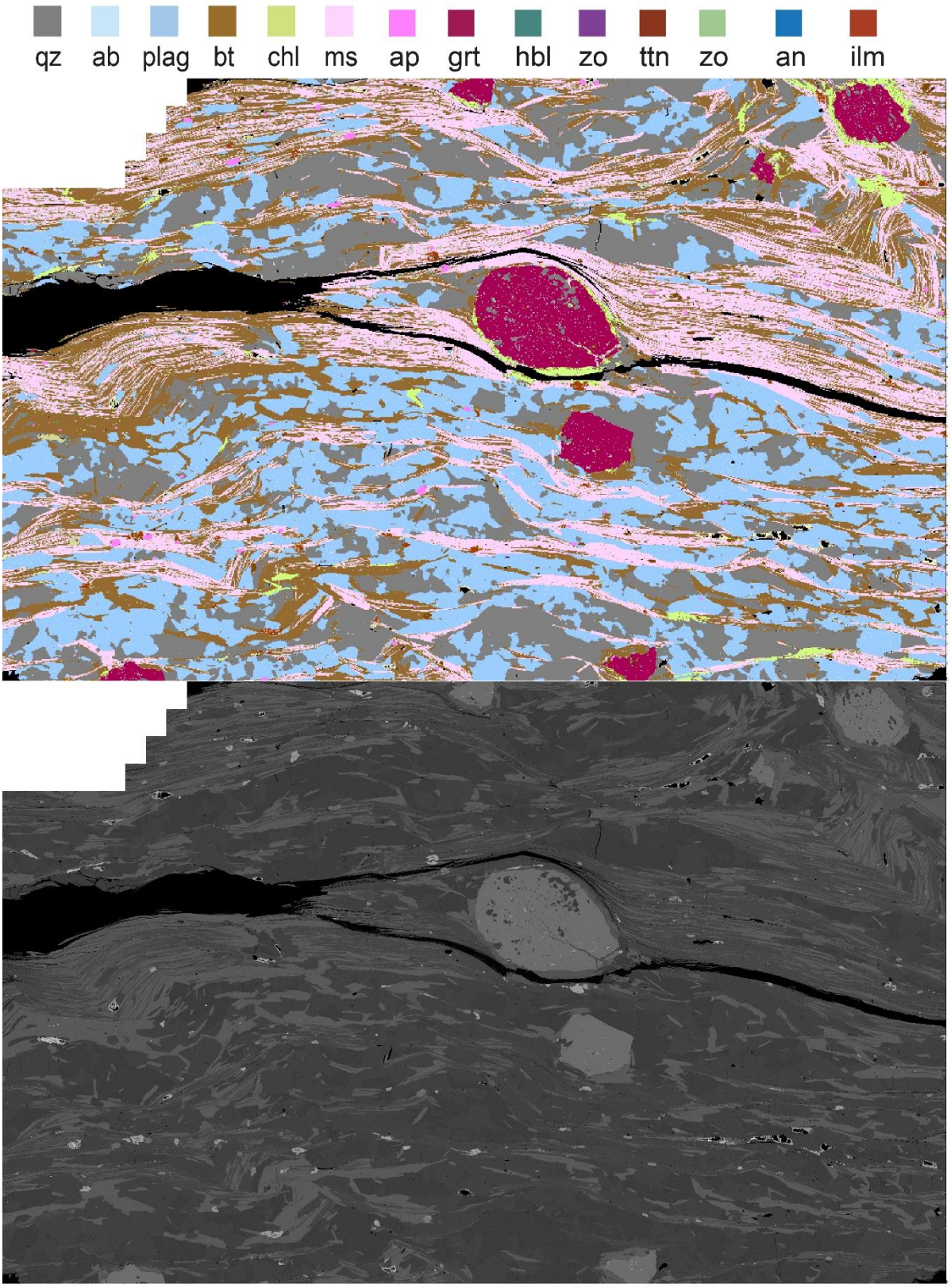


EDS-scan, and BS-image of gmf2020-25. EDS-scan at top, BS-image, bottom.

**gmf2020-26A**

**Coordinates:** 66.23664° N, 14.77851° E

**Rock type**: Reaction rim

**Minerals:**

- Quartz: 37% (fine-grained, 0.99-0.75 mm, average: 0.31 mm, mode: 0.3 mm), subhedral to anhedral, equant to more elongated.
- Plagioclase: 32% (fine grained, 0.18-0.98 mm, average: 0.54 mm, mode: 0.5 and 0.6 mm), subhedral, tabular.
- Biotite: 30% (fine-grained, 0.07 mm-0.89 mm, average: 0.32 mm, mode: 0.3 mm), subhedral to euhedral, prismatic to tabular.
- Chlorite: 1%
- Muscovite: < 1%
- Zircon: < 1%
- Apatite: < 1%
- Rutile: < 1%
- Opaque: < 1%

**Textures:**

The rock is fine-grained, porphyroblastic, hypidioblastic, and has spaced and weak crenulation cleavage. The wriggly to anastomosing spaced cleavage is defined by oriented mica. The fold axial traces to the folded mica define the weak crenulation cleavage. The microlithons, the quartz, and plagioclase show a weak SPO. Chloritization in garnet and biotite and polysynthetic twins in plagioclase is present.

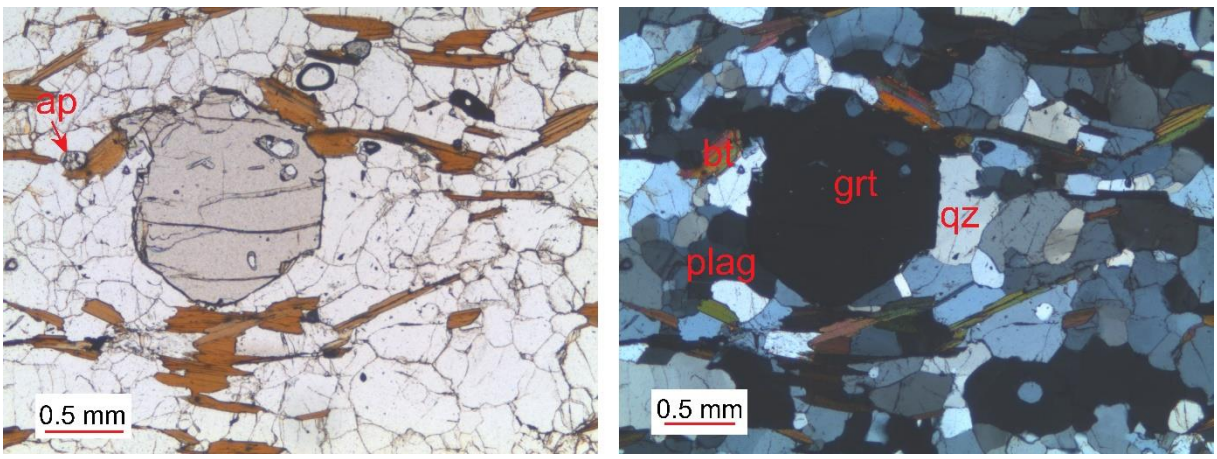

Thin section images of the reaction rim (gmf2020-26A). PPL left, XPL right.

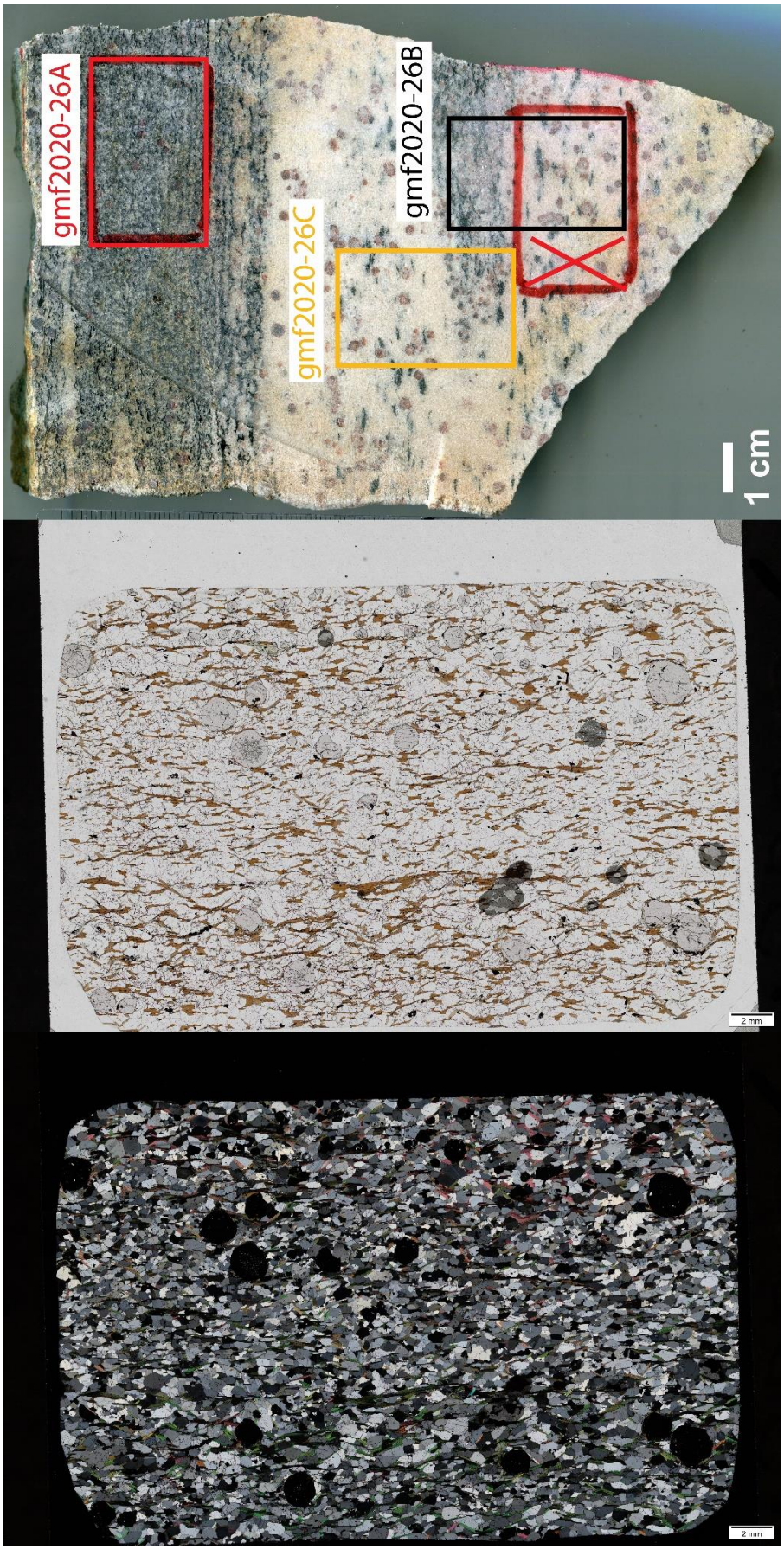


Rock slab, and thin section scans of gmf2020-26A. PPL in the middle, XPL, bottom

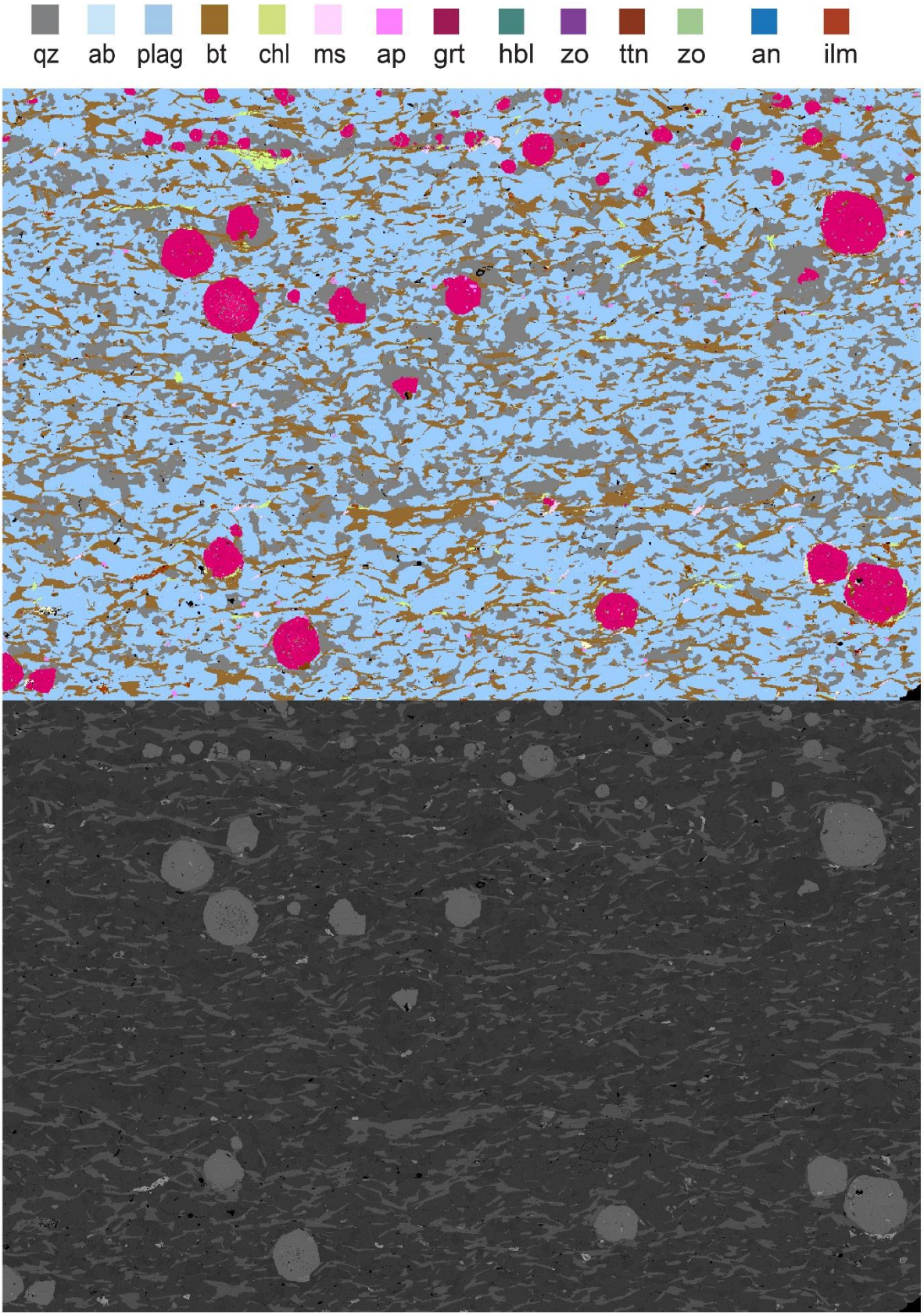


EDS-scan, and BS-image of gmf2020-26A. EDS-scan at top, BS-image, bottom.

**gmf2020-26B (part 1)**

**Coordinates:** 66.23664° N, 14.77851° E

**Rock:** Felsic vein

**Minerals:**

- Quartz: 39% (fine-grained, 0.03-0.82 mm, average: 0.4 mm, mode: 0.3 mm), anhedral to subhedral, equant.
- Plagioclase: 39% (fine-grained, 0.05-0.8 mm, average: 0.43 mm, mode: 0.4 mm and 0.5 mm), subhedral, tabular.
- Garnet: 12% (fine to medium-grained, 0.11-3.3 mm, average: 1.2 mm, mode: 0.2, 0.4 and 0.6 mm), subhedral to euhedral, equant.
- Hornblende: 6% (fine to coarse grained, 0.2-6 mm, average: 1.47 mm, mode: 0.3, 0.4 and 0.5 mm), anhedral to subhedral, prismatic to tabular.
- Zoisite: 3% (fine to medium-grained, 0.16-4.2 mm, average: 1.33 mm, mode: 0.2 mm and 1 mm), subhedral, prismatic to diamond shape.
- Apatite: <1%
- Zircon: <1%
- Titanite: <1%
- Rutile: <1%

**Textures:**

The rock is fine to medium-grained, porphyroblastic, hypidioblastic, and has spaced cleavage. The anhedral to subhedral hornblende and zoisite is oriented and define the rough to parallel spaced cleavage. The garnet and zoisite create the porphyroblastic texture. The garnet has a mantle core texture, with plagioclase representing the core. Quartz and plagioclase, the microlithons show grain boundary migration.

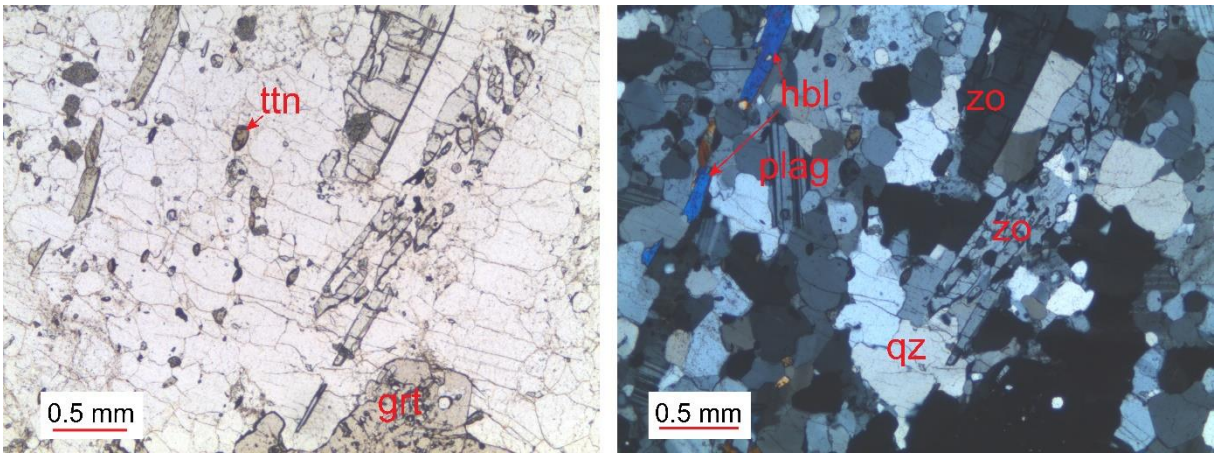

Thin section images of the reaction rim (gmf2020-26B (part 1)). PPL left, XPL right.

**gmf2020-26B (part 2)**

Reaction rim:

**Minerals**

- Quartz: 21% (fine-grained, 0.17-0.55 mm, average: 0.30 mm, mode: 0.3 and 0.5 mm), anhedral to subhedral, equant.
- Plagioclase: 25% (fine-grained, 0.33-0.95 mm, average: 0.5 mm, mode: 0.5 mm), subhedral, tabular.
- Garnet: 34% (fine-grained, 0.1-0.96 mm, average: 0.45 mm, mode: 0.2, 1 and 2 mm), subhedral to euhedral, equant.
- Hornblende: 20% (fine to medium-grained, 0.06-1.8 mm, 0.52 mm, mode: 0.4 and 1 mm), anhedral to subhedral, prismatic to tabular.
- Titanite:< 1%
- Rutile: 1%
- Zoisite: <1%
- Zircon:<1%

**Textures:**

The rock is fine to medium-grained, porphyroblastic, hypidioblastic with spaced cleavage. The wavy, anastomosing spaced cleavage is defined by the preferred orientation of anhedral to subhedral hornblende and is parallel to the compositional layering. The plagioclase and quartz define the microlithons domains and show grain boundary migration.

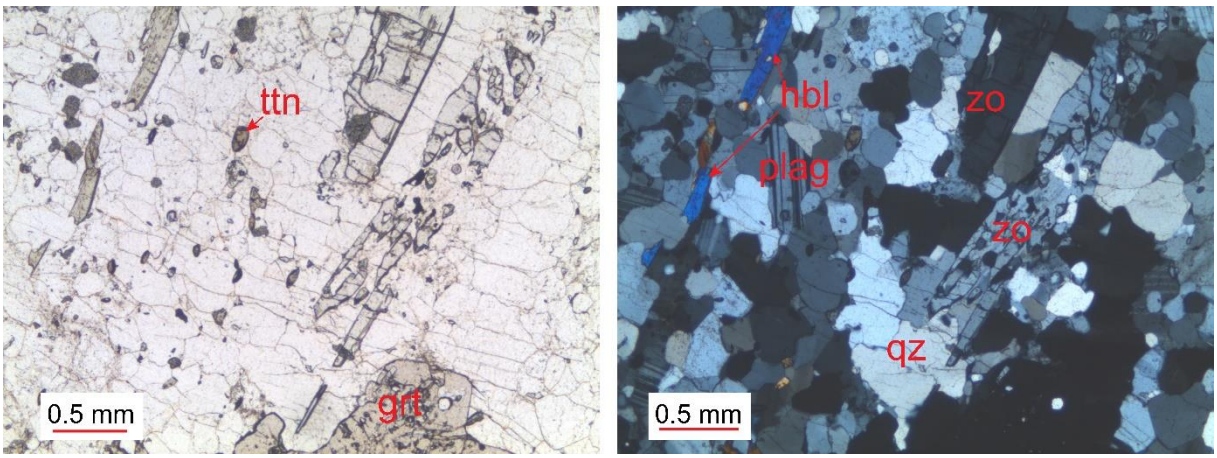


Thin section images of the reaction rim (gmf2020-26B (part 2)). PPL left, XPL right.

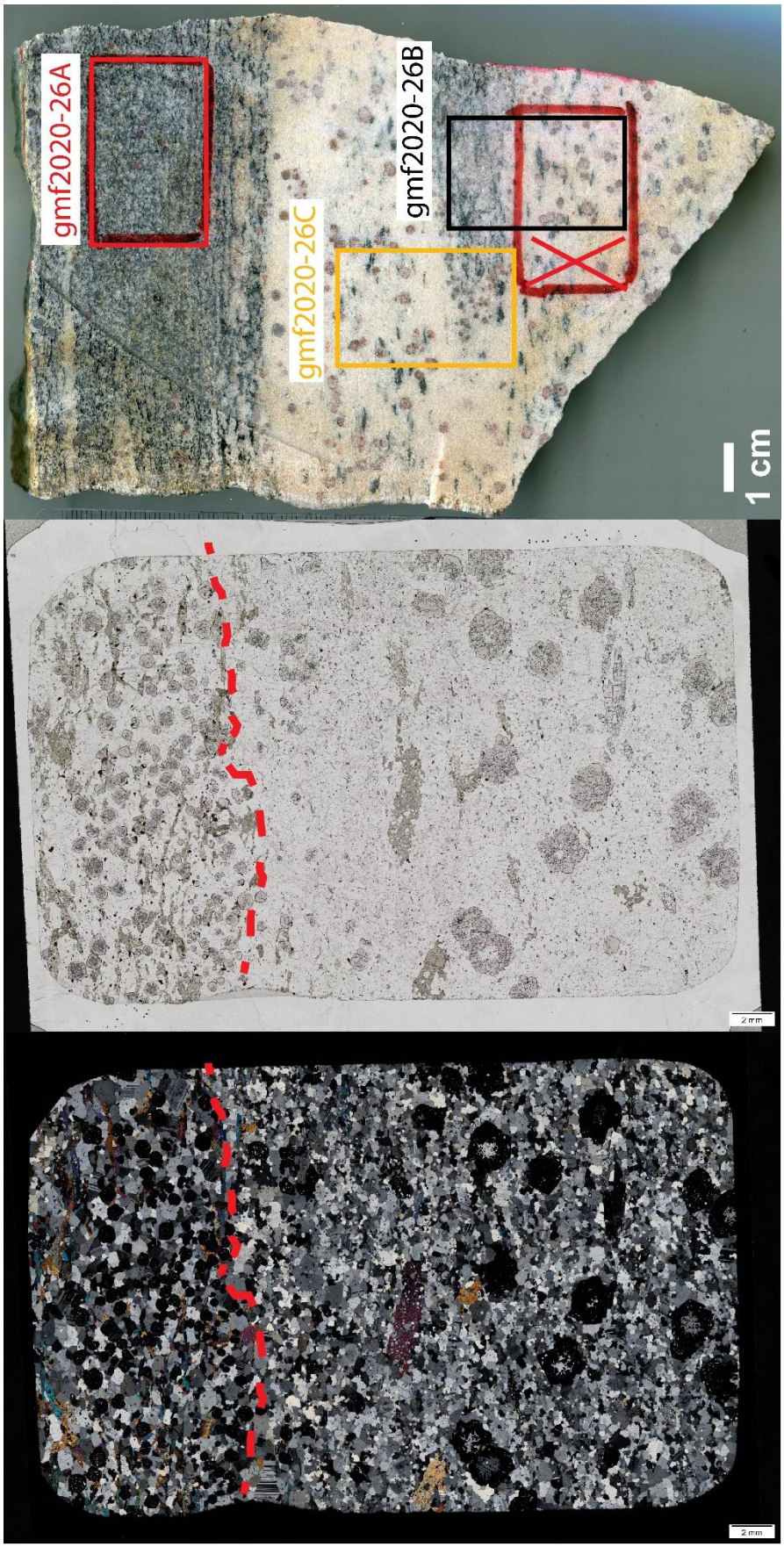


Rock slab, and thin section scans of gmf2020-26B. PPL in the middle, XPL, bottom.

**gmf2020-26C (part 1)**

**Coordinates:** 66.23664° N, 14.77850° E

**Rock type:** Felsic vein

**Minerals:**

- Quartz: 45% (fine to medium-grained, 0.073-2 mm, average: 0.6 mm, mode: 0.4 mm), anhedral to subhedral, equant to more elongated.
- Hornblende: 5 % (fine to medium-grained, 0.1-2.5 mm, average: 1 mm, mode: 1 mm), subhedral to euhedral, skeletal, tabular to prismatic.
- Garnet: 10% (fine to medium-grained, 0.079-2.93 mm, average: 0.9 mm, mode: 0.6 mm) Subhedral, equant.
- Plagioclase: 32% (fine-grained, 0.18-0.89 mm, average: 0.4 mm, mode: 0.4 mm), subhedral, tabular.
- Zoisite: 5% (fine to coarse-grained, 0.28-6.79 mm, average: 1.2 mm, mode: 0.7 mm)
- Titanite: < 1%
- Clinozoisite: < 1%
- Zircon: < 1%

**Textures:**

The rock is hypidioblastic, porphyroblastic, and has spaced cleavage parallel to the compositional layering. The spaced cleavage is parallel, smooth, and defined by the preferred orientation of hornblende and zoisite. Some garnets have a atoll texture with plagioclase as inclusion. The plagioclase has polysynthetic twins, and the quartz has a weakly developed SPO. Some grain boundary migration and undulating extinction are present in the quartz.

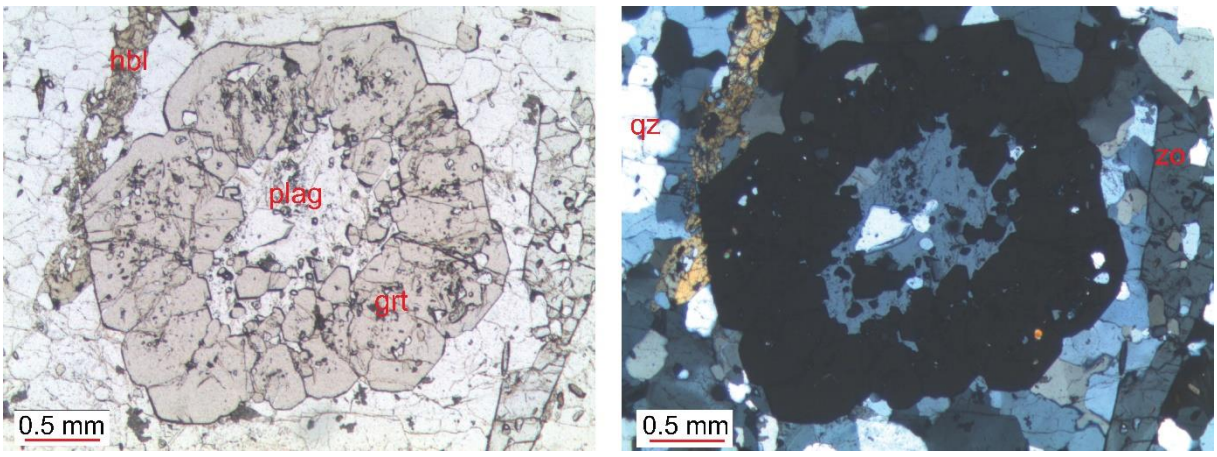


Thin section images of the reaction rim (gmf2020-26C (part 1)). PPL left, XPL right.

**gmf2020-26C (part 2)**

**Rock type:** Reaction rim with some felsic vein

**Minerals:**

- Quartz: 30% ( fine to medium-grained, 0.18-1.1 mm, average: 0.48 mm, mode: 0.5 mm), anhedral to subhedral, equant.
- Hornblende: 10 % (fine to medium-grained, 0.17-3.44 mm, average: 1.2 mm, mode: 0.9 mm), subhedral, prismatic, tabular, diamond shape to skeletal shape.
- Garnet: 40% (0.63-1.78 mm, average: 1.3 mm, mode: 1 mm), subhedral, equant.
- Plagioclase: 20% (0.077-0.85 mm, average: 0.44 mm, mode: 0.5 mm), subhedral, tabular.
- Zoisite: < 1%
- Titanite: < 1%
- Zircon < 1%
- Chlorite < 1%

**Textures:**

The rock is porphyroblastic, hypidioblastic, and has spaced cleavage. The spaced cleavage is parallel, smooth, and is defined by the preferred orientation of hornblende and zoisite. Polysynthetic twins are present in the plagioclase, and undulating extinction and grain boundary migration are visible in the quartz. The garnet is zoned with highly altered cores with inclusions, the rim is more developed and clearer.

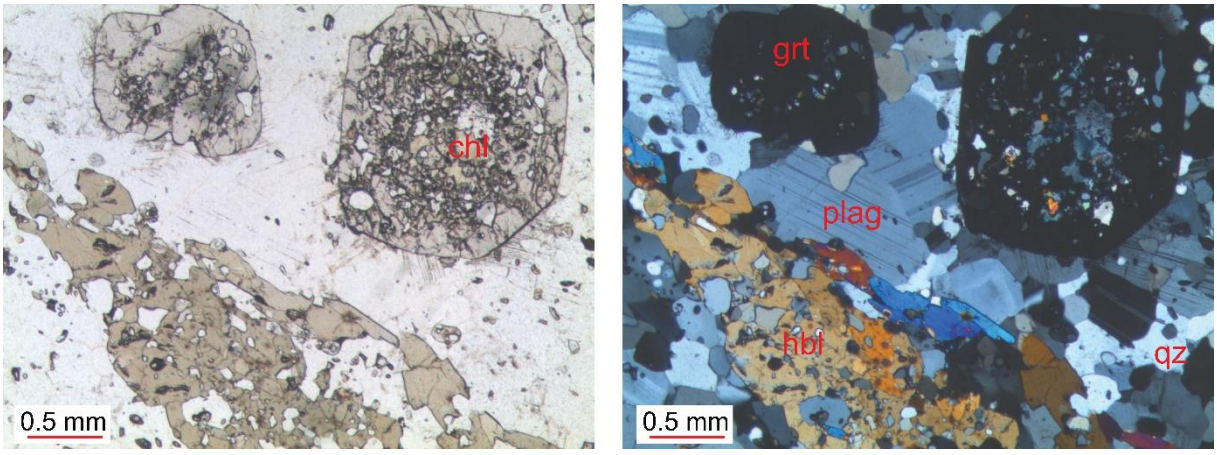


Thin section images of the reaction rim (gmf2020-26C part 2). PPL left, XPL right.

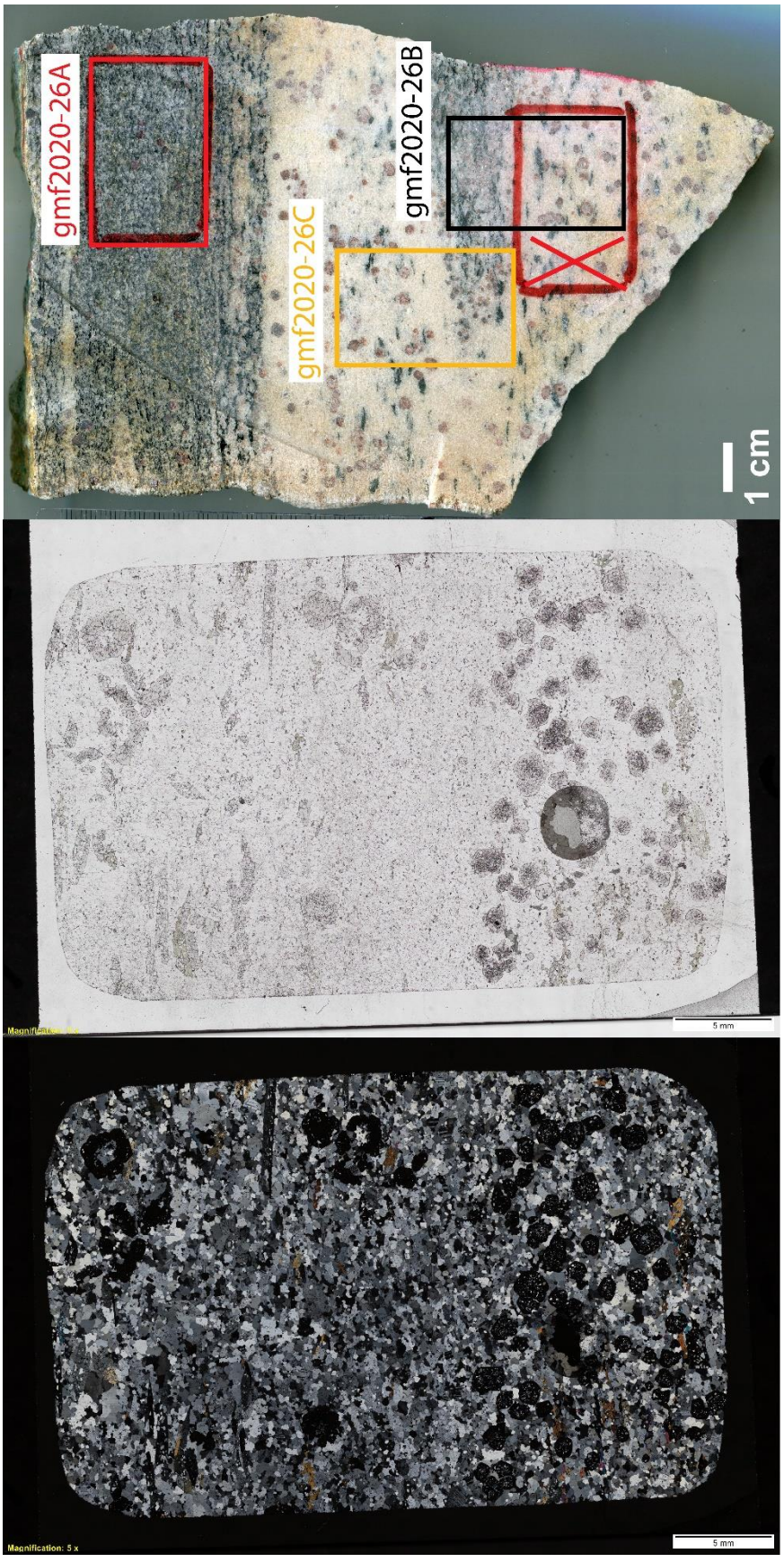


Rock slab, and thin section scans of gmf2020-26C. PPL in the middle, XPL, bottom.

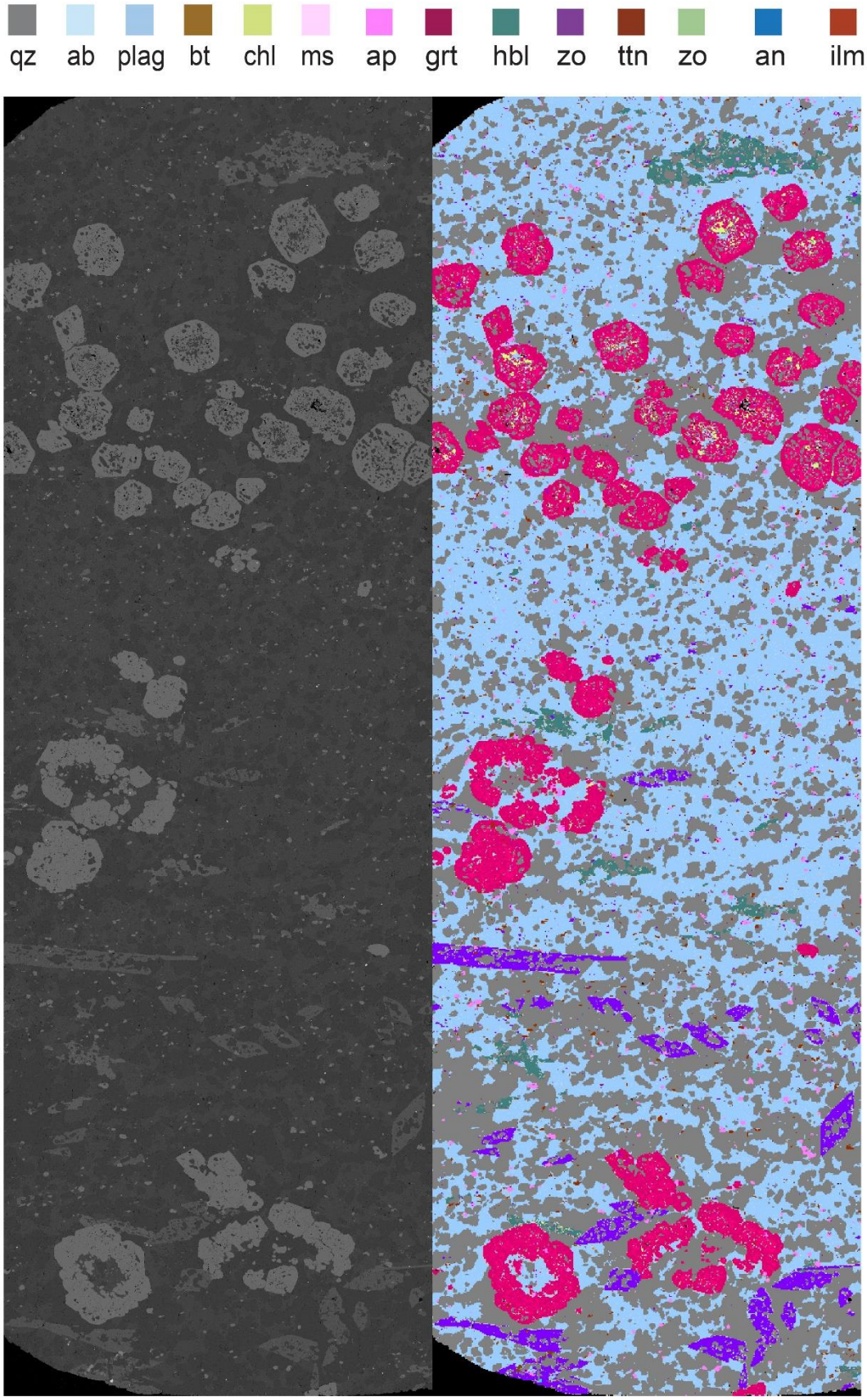


EDS-scan, and BS-image of gmf2020-26C. EDS-scan to the right top, BS-image, left.

**gmf2020-30**

**Coordinates:** 66.16645° N, 14.58547° E

**Rock:** Garnet mica schist

**Minerals:**

- Quartz: 45% (fine-grained, 0.088-0.92 mm, average: 0.37 mm, mode: 0.5), subhedral, equant to elongated.
- Biotite: 30% (fine to medium-grained, 0.087-1.91 mm, average: 0.59 mm, mode: 0.5 mm), subhedral-euhedral, prismatic to tabular.
- Plagioclase: 22% (fine-grained, 0.11-0.93 mm, average: 0.5 mm, mode: 0.5), subhedral, tabular.
- Garnet: 3% (fine to coarse-grained, 3.3-6 mm, average: 4.5 mm, mode: 4.5 mm), anhedral, equant.
- Ilmenite: < 1%
- Rutile: < 1%
- Zoisite: < 1%
- Apatite: < 1%
- Titanite: < 1%
- Zircon: <1%
- Hornblende: < 1%
- Monazite: < 1%

**Textures:**

The rock is fine to coarse-grained, porphyroblastic, hypidioblastic with continuous to crenulation cleavage. The continuous cleavage is defined by the preferred orientation of fined to medium-grained subhedral to euhedral biotite parallel to the compositional layering. The microlithons, fined-grained quartz, and plagioclase show developed SPO in the same direction. The medium to coarse-grained garnet porphyroblasts have foliated inclusions, appear syn-tectonic.

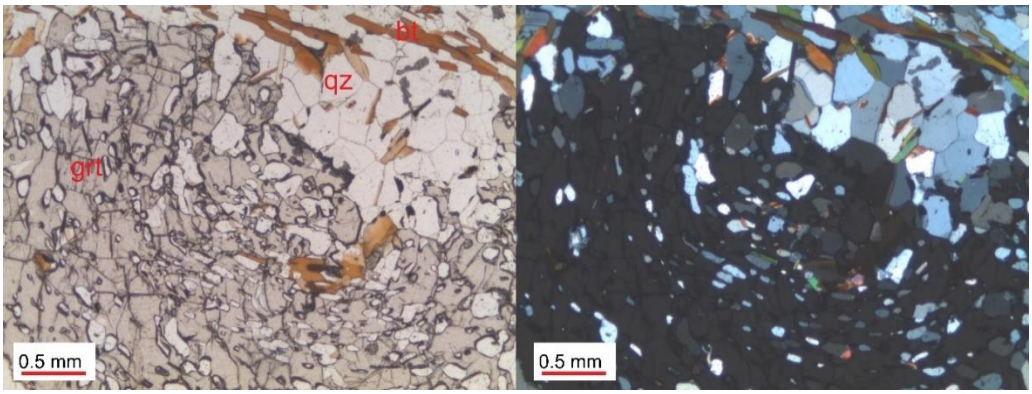


Thin section images of the garnet mica schist (gmf2020-30). PPL left, XPL right. The garnet appears syn-tectonic.


Rock slab, and thin section scans of gmf2020-30. PPL in the middle, XPL, bottom.

**gmf2021-02**

**Coordinates:** 66.23973° N, 14.79466° E

**Rock:** Calc-silicate with three distinct zones.

Overall, the rock is fine-grained and has three distinct zones where the concentrations of quartz, zoisite, and amphibole vary. The rock is fine-grained, porphyroblastic to equigranular, hypidioblastic, and fine-grained.

**Zone 1, hbl-rich**

**Minerals:**

- Zoisite 32% (fine-grained, 0.034-0.25 mm, average: 0.12 mm, mode: 0.1 mm), subhedral, tabular to prismatic.
- Quartz 35% (fine-grained, 0.03-0.8 mm, average: 0.29 mm, mode : 0.3 mm), subhedral to euhedral, equant.
- Hornblende 32% (fine-grained, 0.21-2.86 mm, average: 0.81 mm, mode: 1 mm), subhedral to anhedral, tabular to prismatic.
- Titanite < 1%

**Texture:**

The hornblende-rich zone shows continuous cleavage parallel to the compositional layering defined by oriented subhedral prismatic to tabular hornblende porphyroblasts, with developed SPO in the quartz and zoisite.

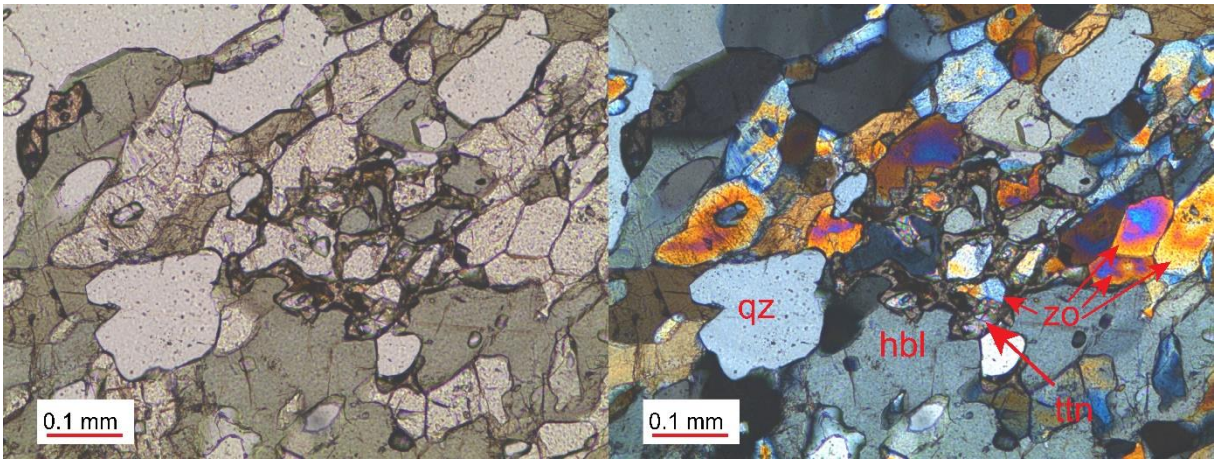


Thin section images of the calc-silicate zone 1 (gmf2021-02). PPL left, XPL right.

**Zone 2, no hbl**

- Quartz: 48% (fine-grained, 0.12-0.42 mm, average: 0.20 mm, mode: 0.2 mm), subhedral-anhedral, equant.
- Zoisite: 52% (fine-grained, 0.03-0.3 mm, average: 0.15 mm, mode: 0.2 mm), subhedral, tabular to prismatic.
- Titanite: < 1%
- Zircon < 1%

**Texture**

The hornblende free area shows grain boundary migration texture in the equigranular quartz and zoisite matrix. Quartz layers parallel to compositional layering are present.

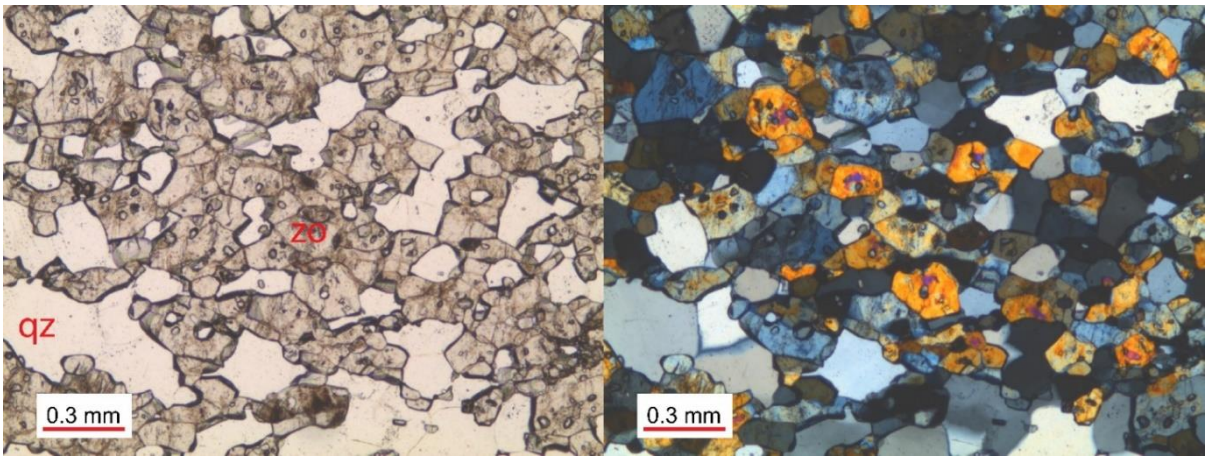


Thin section images of the calc-silicate zone 2 (gmf2021-02). PPL left, XPL right.

**Zone 3, some hbl**

- Quartz: 44% (fine-grained, 0.06-0.6 mm, average : 0.24 mm), subhedral, equant.
- Zoisite: 48% (fine-grained, 0.09-0.22 mm, 0.14 mm), euhedral to subhedral, equant, tabular to prismatic.
- Hornblende: 7% (fine-grained, 0.19-0.43 mm, average: 0.3 mm), anhedral, tabular/prismatic
- Chlorite: 1%

**Texture:**

The last zone is similar to zone 2, but has some oriented anhedral skeletal hornblende porphyroblasts parallel to the compositional layering.

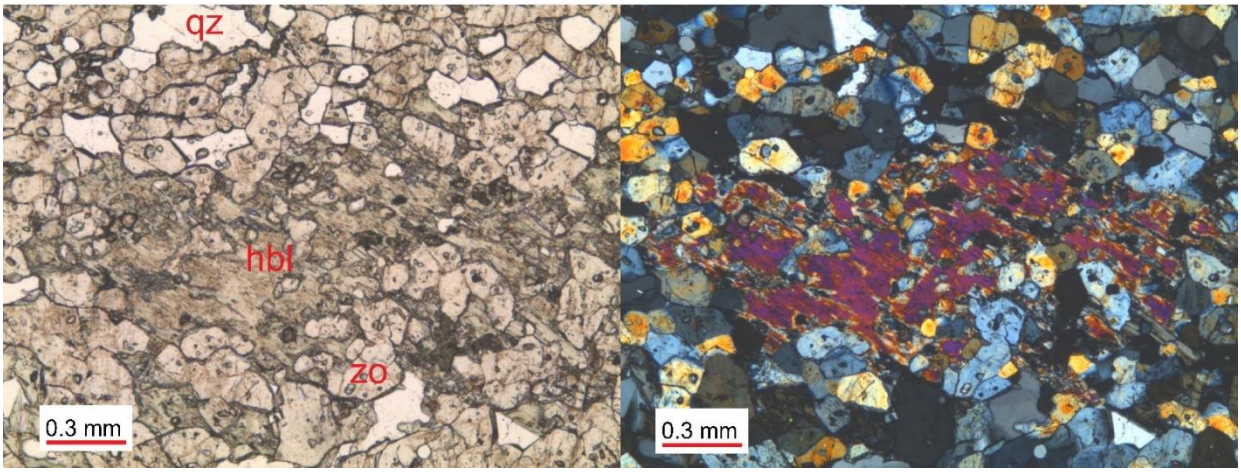


Thin section images of the calc-silicate zone 3 (gmf2021-02). PPL left, XPL right.

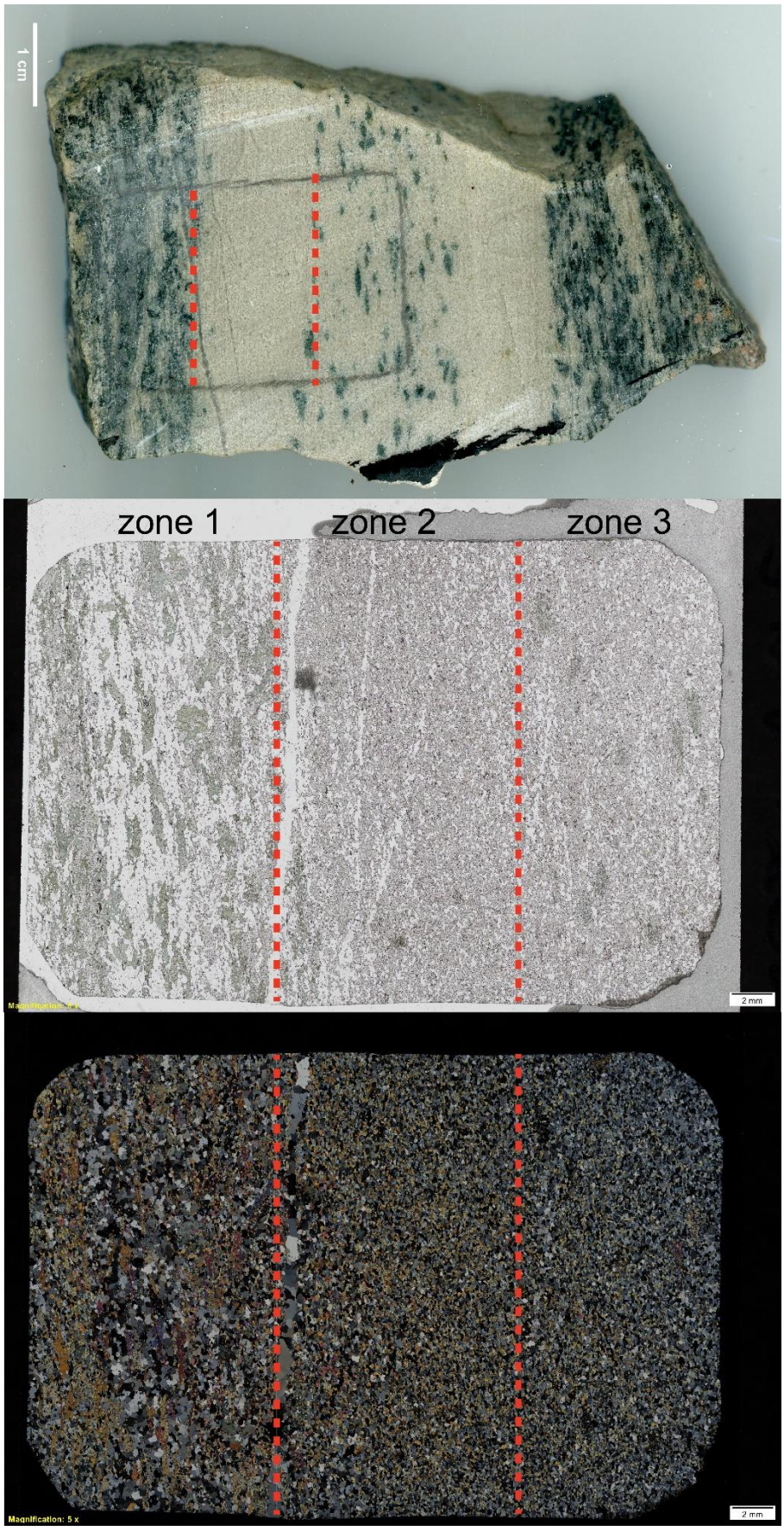


Rock slab, and thin section scans of gmf2021-02. PPL in the middle, XPL, bottom.

**gmf2021-03**

**Coordinates:** 66.23976° N, 14.79715° E

**Rock type**: Garnet amphibolite

**Minerals**:

- Hornblende: 63% (fine-grained, 0.019-0.88 mm, average: 0.38 mm, mode: 0.38 mm), subhedral to euhedral, prismatic to more diamond shape.
- Plagioclase: 22% (fine-grained, 0.058-0.55 mm, average: 0.25 mm, mode: 0.28 mm), anhedral to subhedral, equant, tabular to more elongated.
- Garnet: 10% (fine to medium-grained, 0.43-3.3 mm, average: 1.4 mm, mode: 1.3 mm), anhedral, equant to elongated, skeletal.
- Biotite: 2% (fine-grained, 0.16-0.94, average: 0.39 mm, mode: 0.26 mm), subhedral to euhedral, prismatic to tabular.
- Titanite: 3% (fine-grained, 0.05-0.45 mm, average: 0.14, mode: 0.063)
- Zircon: < 1%.

**Textures**:

The rock is porphyroblastic, xenoblastic, has spaced cleavage parallel to the compositional layering, and weak crenulation cleavage. The rough anastomosing spaced cleavage is defined by subhedral to euhedral hornblende with domains of anhedral to subhedral plagioclase microlithons. The weak crenulation cleavage is defined by the direction of the fold axis to the belonging folded spaced cleavage. The plagioclase shows a weak SPO. The porphyroblastic texture is defined by the anhedral garnet.

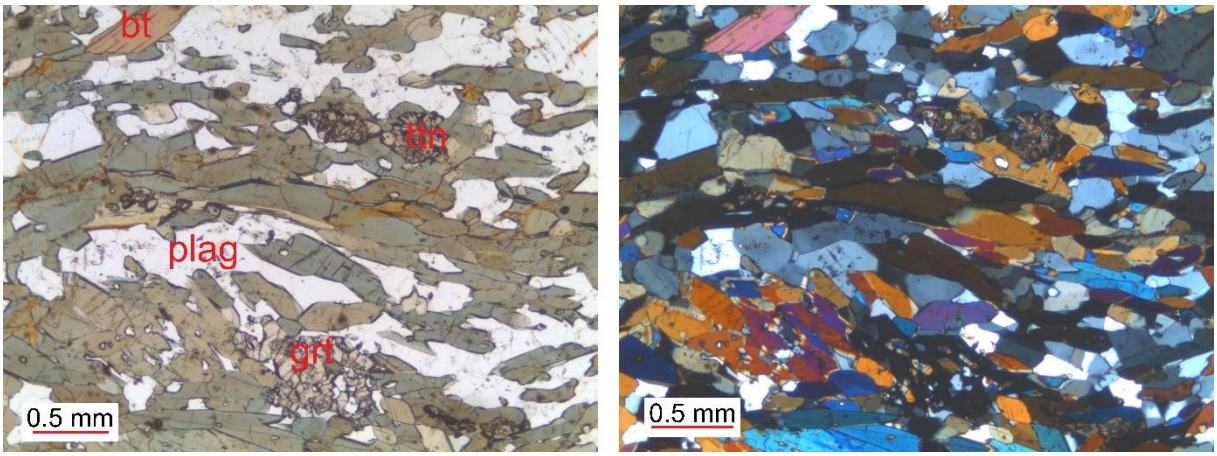


Thin section images of the garnet amphibolite (gmf2021-03). PPL left, XPL right.

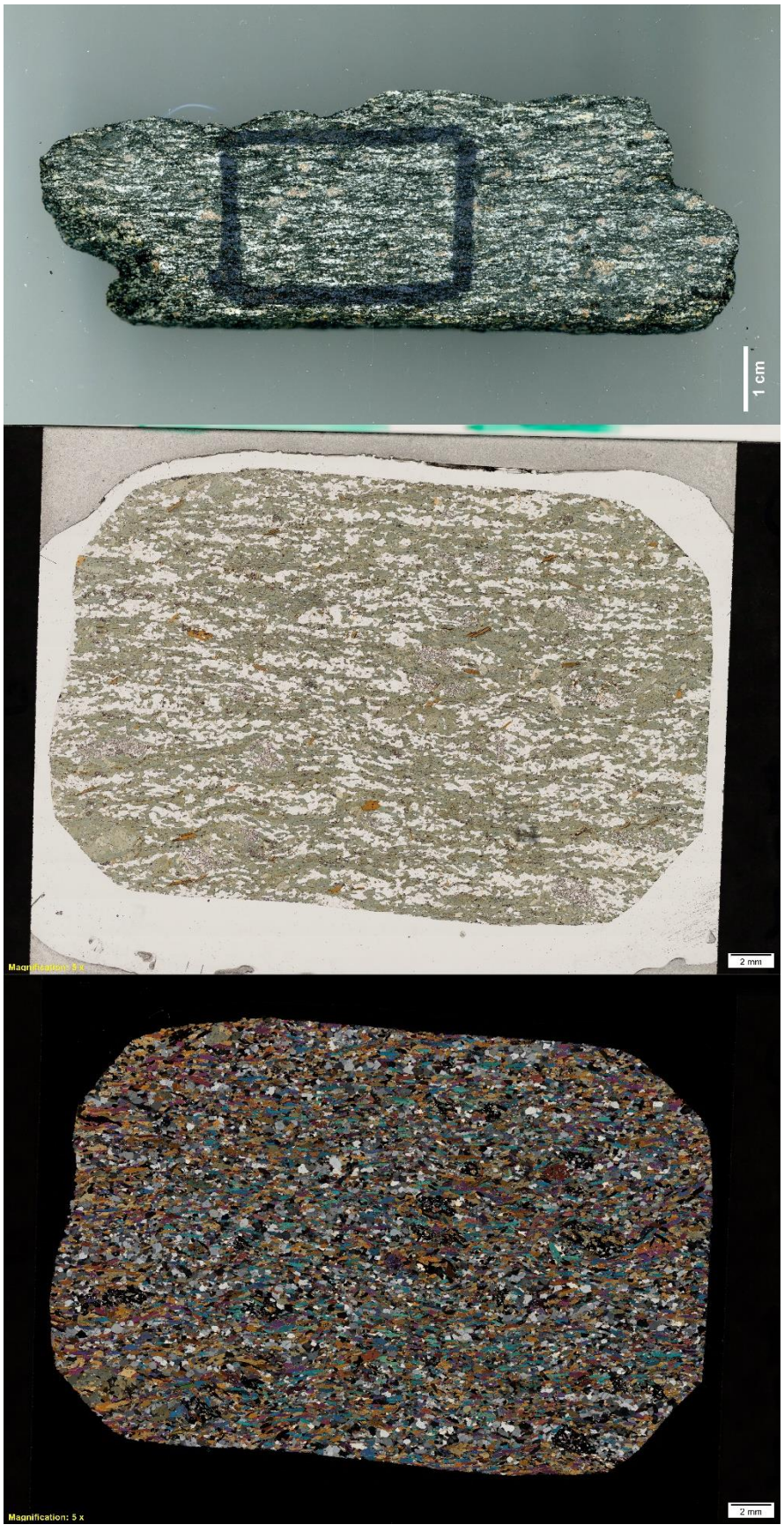


Rock slab, and thin section scans of gmf2021-03. PPL in the middle, XPL, bottom.

**gmf2021-5**

**Coordinates:** 66.23661° N, 14.77872° E

**Rock type:** Felsic vein with reaction rim

Felsic vein:

**Minerals:**

- Plagioclase: 50%, (fine to medium-grained, 0.24-1.4 mm, average: 0.7 mm, mode: 0.6 mm), subhedral to anhedral, equant to prismatic.
- Quartz: 33%. (fine-grained, 0.13-1-7 mm, average: 0.5 mm, mode: 0.4 mm), mostly anhedral, equant.
- Garnet: 5%, (fine-grained, 0.33-0.88 mm, average: 0.6 mm, mode: 0.6 mm), subhedral, equant.
- Biotite: 5%. (fine to medium-grained, 0.15-1 mm, average: 0.57 mm, mode: 0.5 mm), subhedral to euhedral, prismatic.
- Muscovite < 1%
- Zircon: 1%
- Apatite: < 1%
- Clinozoisite: < 1%
- Chlorite: < 1%

Textures:

The felsic vein is fine to medium-grained, hypidioblastic, equigranular, and has a spaced cleavage parallel to the compositional layering (10% cleavage domains). The discontinuous wriggly to anastomosing spaced cleavage is defined by subhedral to euhedral prismatic biotite. The microlithons, quartz, and plagioclase show grain boundary migration. The quartz shows chess pattern, undulating extinction, and the plagioclase shows polysynthetic twinning.

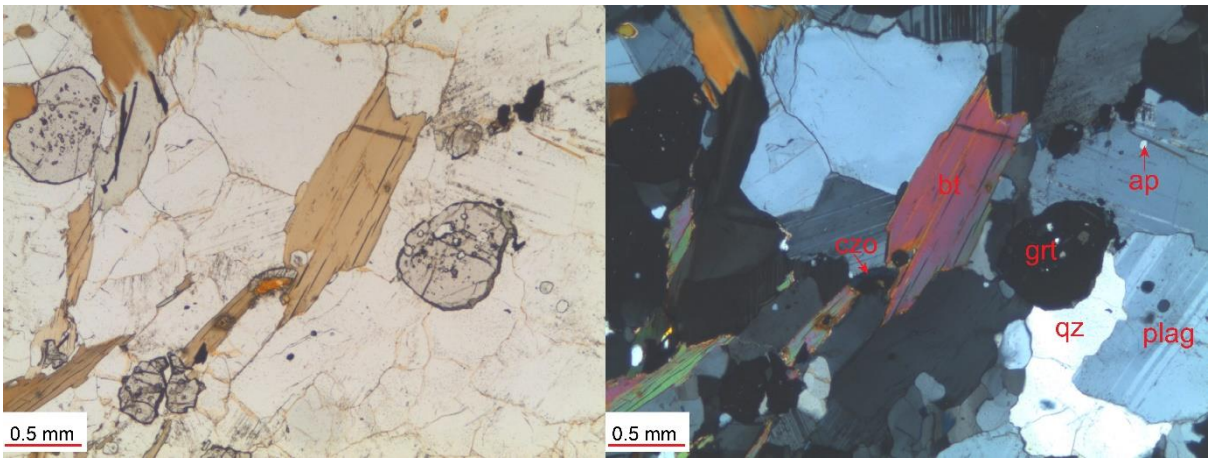


Thin section images of the felsic vein (gmf2021-05). PPL left, XPL right.

Reaction rim:

**Minerals:**

- Quartz: 34%, (fine to medium-grained, 0.1-1 mm, average: 0.5 mm, mode: 0.5 mm), anhedral to subhedral, equant to more elongated.
- Plagioclase: 16% (fine-grained, 0.29-0.75 mm, average: 0.5 mm, mode: 0.5 mm), anhedral to subhedral, equant.
- Garnet: 5% (fine-grained, 0.2 to 0.8 mm, average: 0.4 mm, mode: 0.4 mm), subhedral to euhedral.
- Biotite 20% (medium to fine-grained, 0.07-1 mm, average: 0.43 mm, mode: 0.5 mm), subhedral to euhedral, mostly prismatic, some more tabular.
- Muscovite < 1%
- Apatite < 1%
- Zircon < 1%
- Clinozoisite: < 1%
- Chlorite: < 1%
- Rutile < 1%
- Opaque < 1%

**Textures:**

The reaction rim is fine to medium-grained, hypidioblastic, and has continuous cleavage parallel to the compositional layering. The subhedral to euhedral prismatic to tabular biotite and anhedral to subhedral tabular to more elongated quartz and plagioclase define the continuous cleavage. The quartz and plagioclase show an SPO.

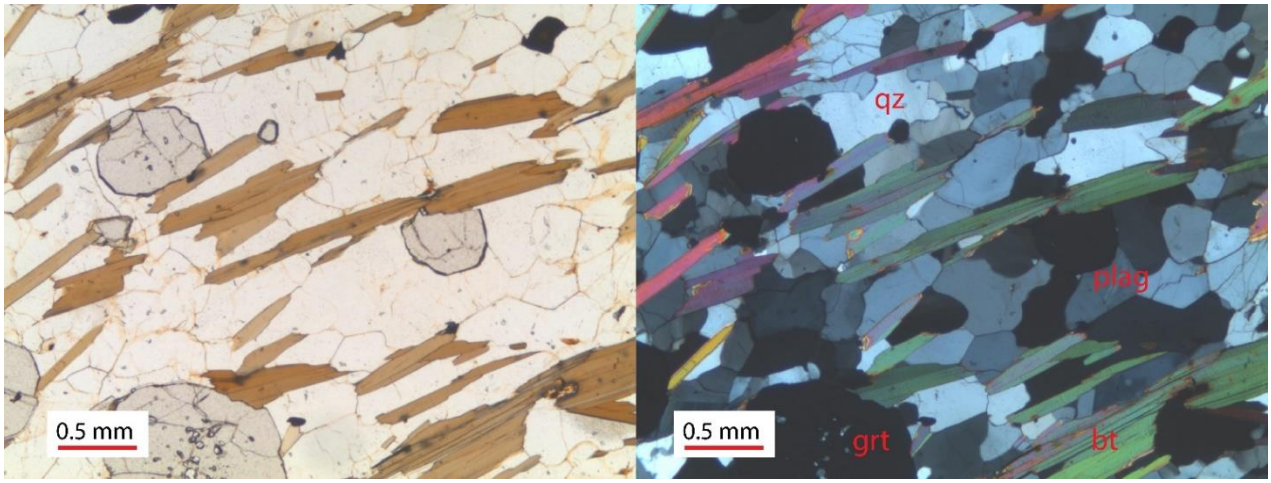


Thin section images of the reaction rim (gmf2021-05). PPL left, XPL right.


Rock slab, and thin section scans of gmf2021-05. PPL in the middle, XPL, bottom.

**gmf2021-06A**

**Coordinates:** 66.23579° N, 14.78038° E

**Rock:** Felsic vein

**Minerals:**

- Quartz: 30% (fine to coarse-grained, 0.09-5.27 mm, average: 1.38 mm, mode: 1 mm), subhedral to anhedral, equant.
- Plagioclase: 45% (fine to medium-grained, 0.16-3.9 mm, average: 1.1 mm, mode: 1 mm), subhedral to anhedral, equant to tabular.
- Garnet: 10% (fine to medium-grained, 0.13-2.37 mm, average: 0.96 mm, mode: 0.8 mm), subhedral to anhedral, mostly anhedral, equant.
- Calcite: < 1%
- Clinozoisite/zoisite: < 1%
- Apatite: < 1%
- Chlorite: < 1%
- Muscovite: < 1%
- Epidote: < 1%
- Biotite < 1%
- Opaque: < 1%

**Textures:**

The rock is hypidioblastic, medium to coarse-grained, and equigranular, with some preferred orientation visible in the rock slab. Chloritization of garnet and sericitization of plagioclase is present. Grain boundary migration occurs in the quartz, polysynthetic twins in feldspar, and calcite deformation twins in calcite. The microphotographs below show myrmekitic texture in a feldspar grain.

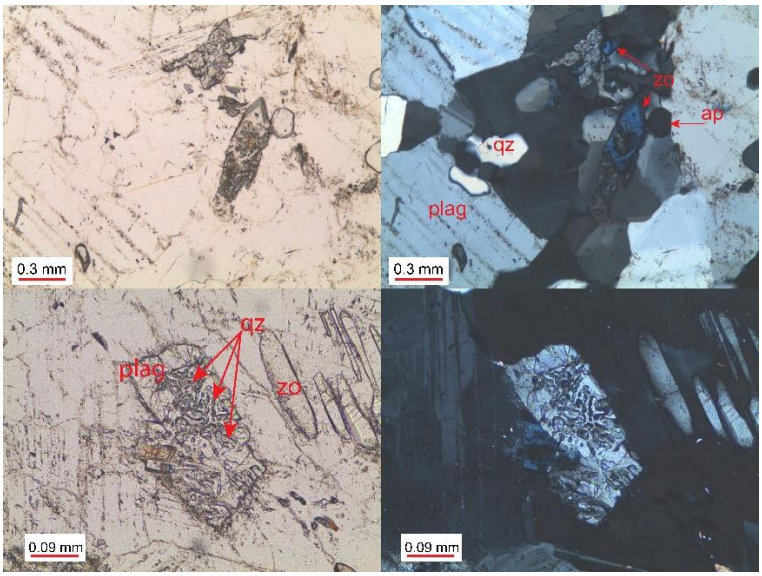


Thin section images of the felsic vein (gmf2021-06A). PPL left, XPL right.

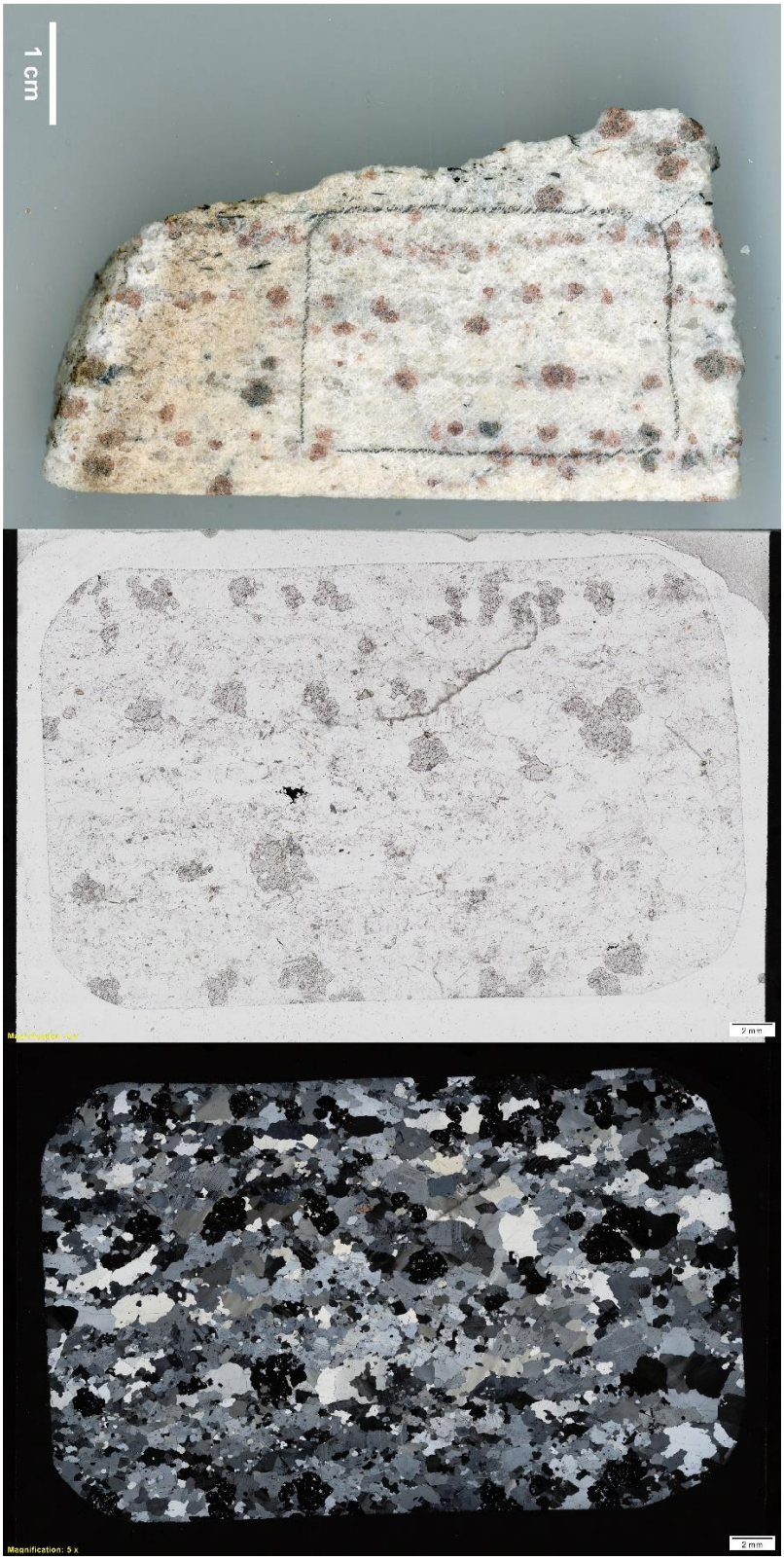


Rock slab, and thin section scans of gmf2021-06A. PPL in the middle, XPL, bottom.

**gmf2021-6B**

**Coordinates:** 66.23579° N, 14.78038° E

**Rock:** Felsic vein with small garnet

**Minerals:**

- Quartz: 30% (fine to medium-grained, 0.12-2.7 mm, average: 0.44 mm, mode: 0.2 mm), anhedral, equant to tabular.
- Plagioclase 45% (fine-grained, 0.12-0.63 mm, average: 0.33 mm, mode: 0.3 mm), anhedral to subhedral, tabular.
- Garnet: 6% (fine-grained, 0.12-0.65 mm, average: 0.40 mm, mode: 0.3 mm), subhedral to euhedral, equant.
- Hornblende: 3% (fine-grained, 0.05-0.93 mm, average: 0.31 mm, mode: 0.3 mm), euhedral to subhedral, prismatic to tabular.
- Zoisite: 4% (fine to medium-grained, 0.08-1.8 mm, average: 0.57 mm, 0.2 mm), subhedral to euhedral, equant to prismatic.
- Biotite: < 1%
- Apatite: < 1%
- Chlorite: < 1%
- Epidote: < 1%
- Zircon < 1%
-

**Textures:**

The rock is fine to medium-grained, equigranular, and hypidioblastic with ca. 3% spaced cleavage domains. The parallel wriggly spaced cleavage parallel to the compositional layering is defined by the orientation of euhedral to subhedral hornblende, subhedral to euhedral zoisite, and biotite. The microlithons consist of quartz and plagioclase.

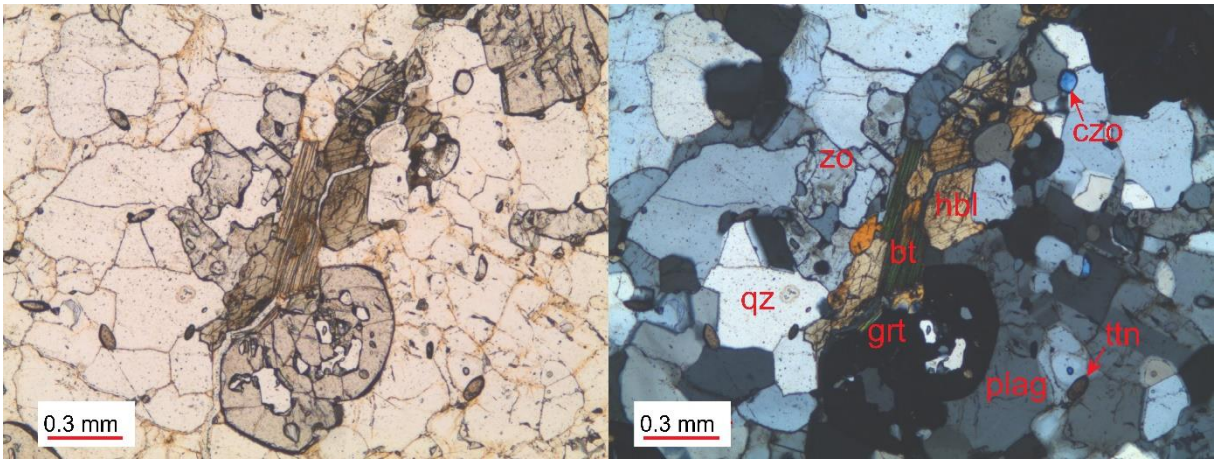


Thin section images of the felsic vein (gmf2021-06B). PPL left, XPL right.

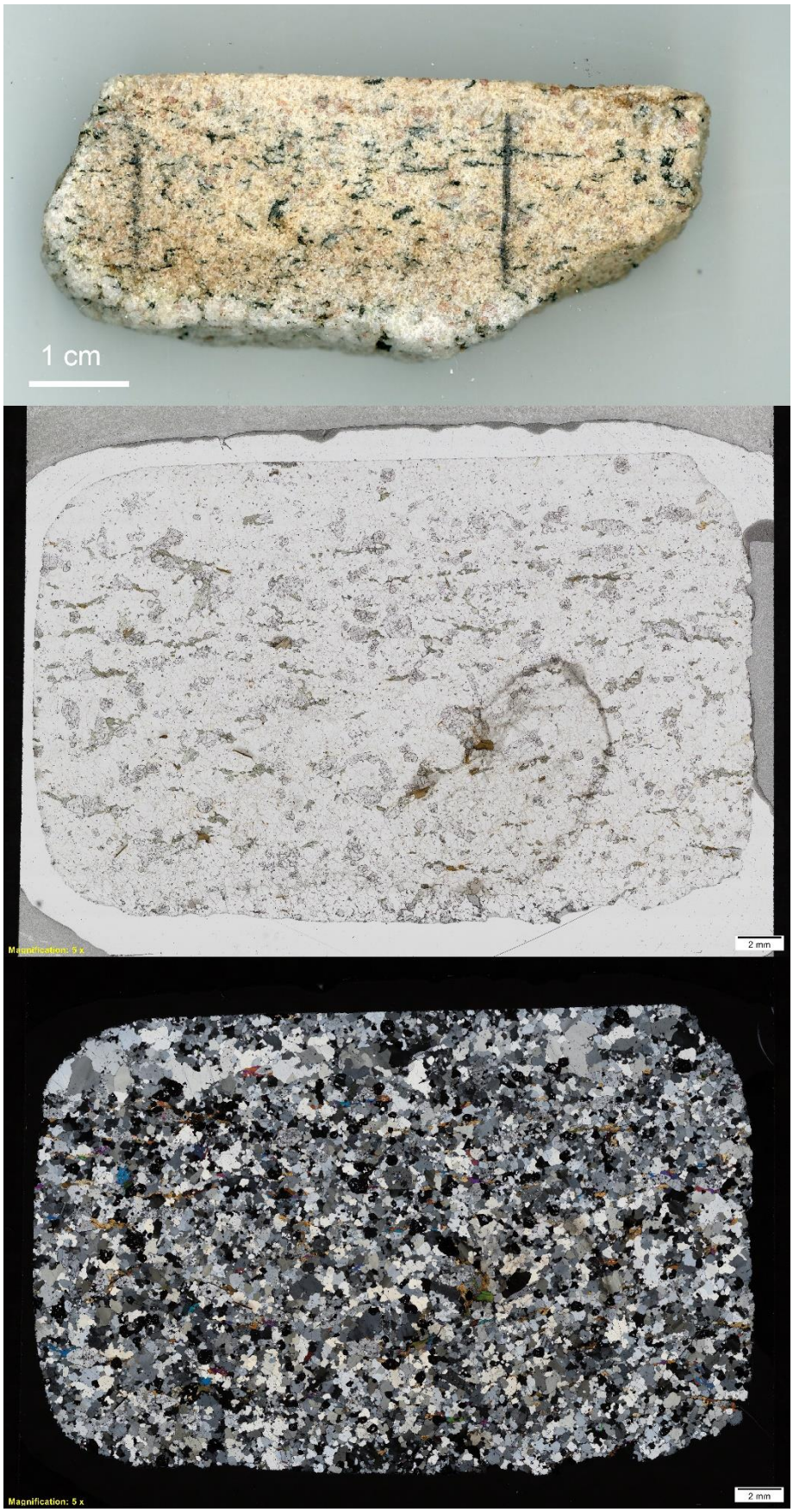


Rock slab, and thin section scans of gmf2021-06B. PPL in the middle, XPL, bottom.

**gmf2021-7A**

**Coordinates:** 66.23534° N, 14.78177° E

**Rock type**: Reaction rim

**Minerals**:

- Quartz: 47% (fine to medium-grained, 0.13-1.1 mm, average: 0.51 mm, mode: 0.4 mm), subhedral to anhedral, equant to more elongated.
- Plagioclase: 22% (fine to medium-grained, 0.4-1.1 mm, average: 0.82 mm, mode: 1 mm), subhedral to anhedral, tabular.
- Biotite: 25%, (fine to medium-grained, 0.08-1.3 mm, average: 0.42 mm, mode: 0.3 mm), euhedral to subhedral, prismatic to tabular.
- Garnet: 5% (fine to medium-grained, 0.26-1 mm, average: 0.63 mm, mode: 0.5 mm), euhedral to subhedral. Equant.
- Muscovite: 1%.
- Chlorite: < 1%
- Apatite: < 1%
- Opaque: < 1%

**Textures:**

The rock is fine to medium-grained, equigranular, hypidiobalstic, and has a continuous cleavage parallel to the compositional layering. The continuous cleavage is visible in PPL by the orientation of the subhedral to euhedral biotite, the quartz is elongated in the same direction. Chloriterization and twinning are present in the plagioclase.

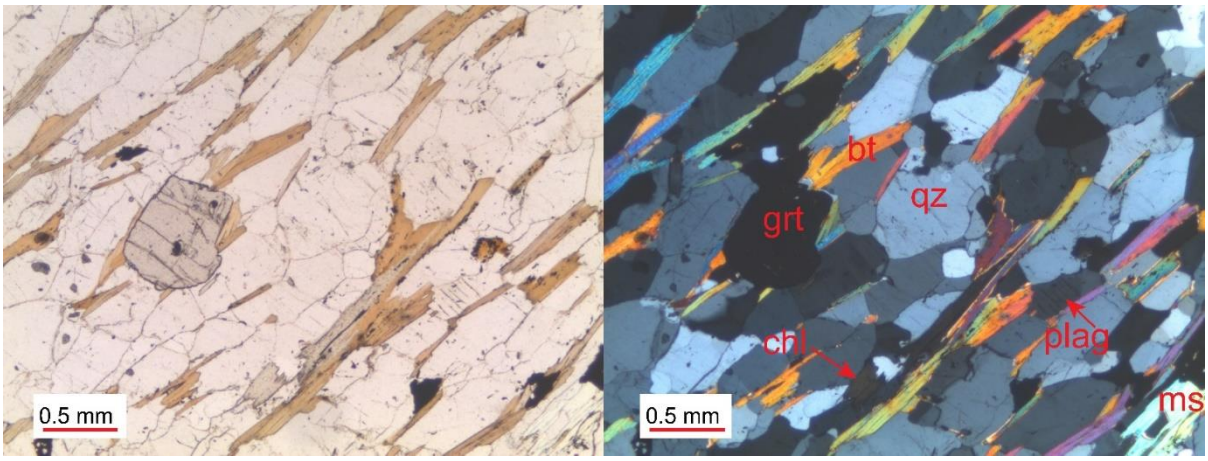


Thin section images of the reaction rim (gmf2021-07A). PPL left, XPL right.


Rock slab, and thin section scans of gmf2021-07A. PPL in the middle, XPL, bottom.

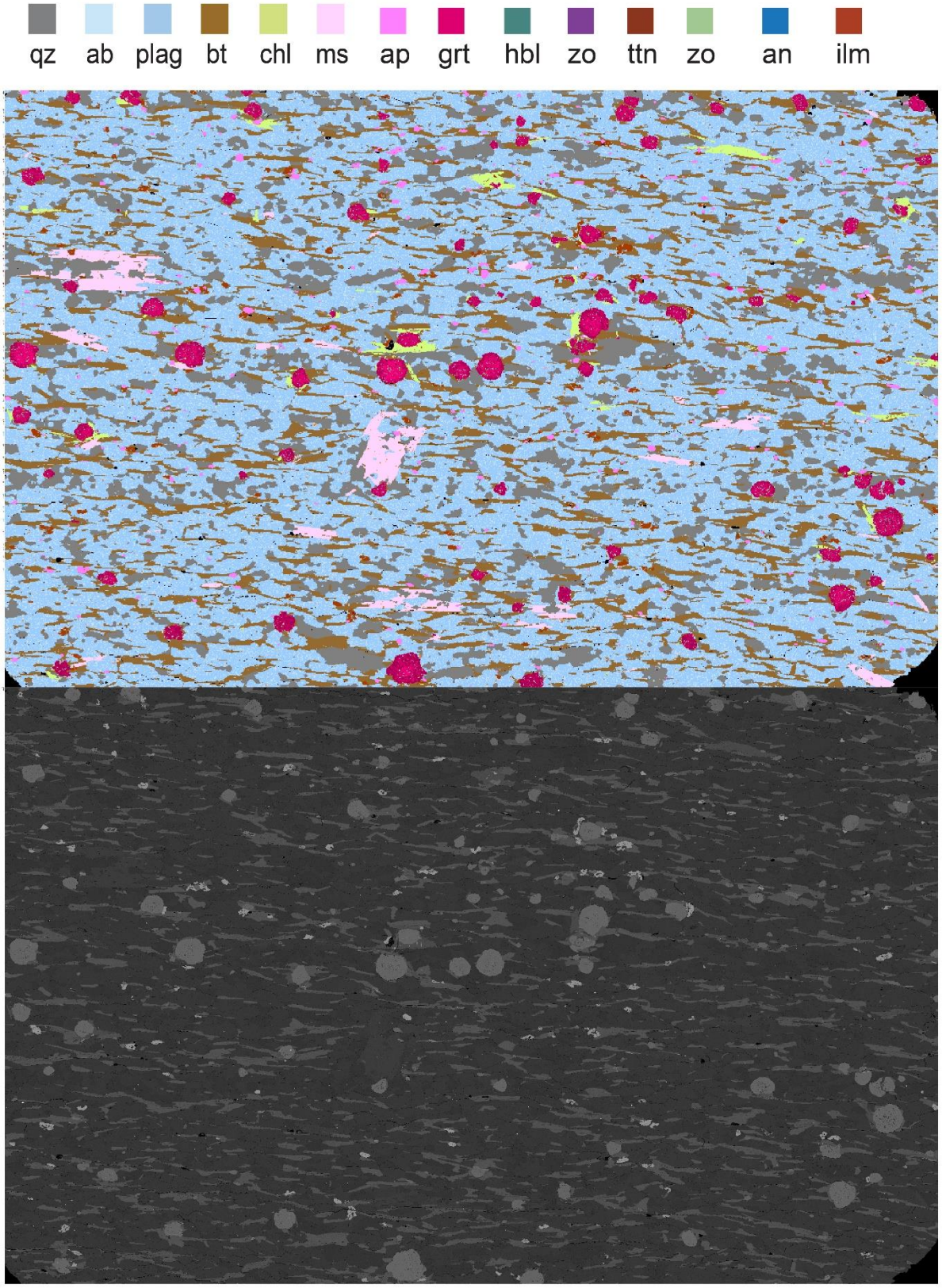


EDS-scan, and BS-image of gmf2021-07A. EDS-scan at top, BS-image, bottom.

**gmf2021-11A**

**Coordinates:** 66.24006° N, 14.78904° E

**Rock:** Zoned felsic vein with reaction rim

**Felsic vein (zone 1)**

**Minerals:**

- Plagioclase: 56% (fine to medium-grained, 0.23-1.77 mm, average: 0.77 mm, mode: 1 mm), subhedral to anhedral, tabular to equant.
- Quartz: 24% (fine-grained, 0.1-0.93 mm, average : 0.37 mm, mode : 0.3 mm), anhedral, equant.
- Biotite: 10% (fine-grained, 0.16-1.2 mm, average: 0.45 mm, mode: 0.4 mm), subhedral to anhedral, prismatic to tabular.
- Garnet: 3% (fine to medium-grained, 0.18-1 mm, average: 0.55 mm, mode: 0.6 mm), mostly anhedral, highly altered, equant.
- Chlorite: 1%
- Apatite: < 1%
- Muscovite < 1%
- Zircon < 1%
- Epidote < 1%
- Opaque < 1%

**Textures:**

The rock is fine to medium-grained, hypidioblastic, porphyroblastic, and has a spaced cleavage. The wriggly spaced cleavage is defined by the orientation of anhedral to subhedral biotite and chlorite. The rock consists of ca. 2% cleavage domains. The microlithons quartz and plagioclase show grain boundary migration. The porphyroblastic texture is defined by anhedral altered garnet.

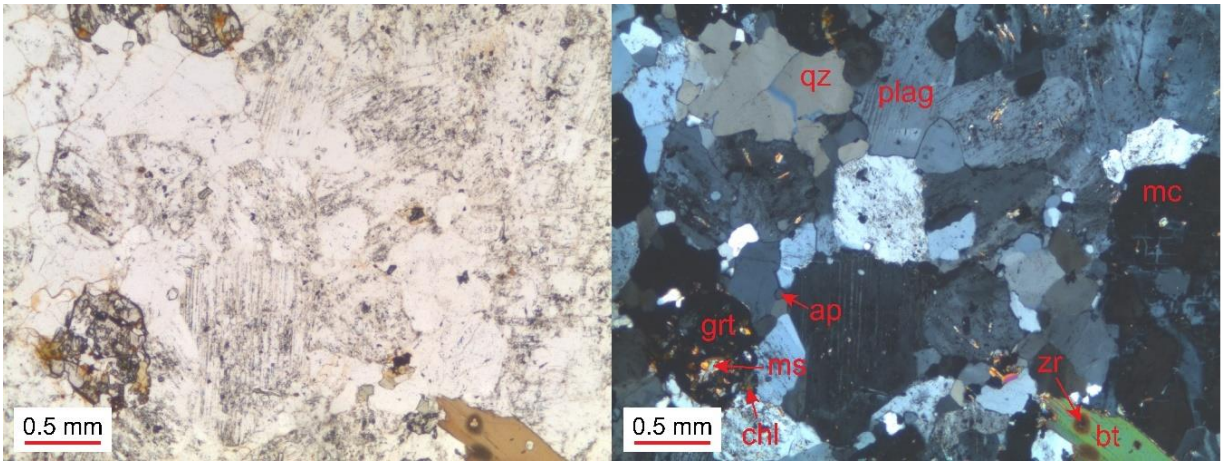


Thin section images of the felsic vein (zone 1) (gmf2021-11A). PPL left, XPL right.

**Felsic vein (zone 2)**

**Minerals:**

- Plagioclase : 36% (fine-grained, 0.07-0.58 mm, average : 0.29 mm, mode: 0.3 mm), subhedral to anhedral, equant to tabular.
- Quartz: 27% (fine-grained, 0.12-0.62 mm, average: 0.33 mm, mode: 0.2 mm), anhedral, equant
- Biotite: 30% (fine to medium-grained, 0.09-1.76 mm, average: 0.42 mm, mode: 0.3 mm), anhedral to euhedral, prismatic to tabular.
- Garnet: 5 % (fine-grained, 0.03-0.34 mm, average: 0.17 mm, mode: 0.2 mm), euhedral to subhedral, equant.
- Muscovite: < 1%
- Zircon < 1%
- Apatite < 1%
- Rutile < 1%
- Opaque < 1%.

**Textures:**

The rock is fine to medium-grained, hypidioblastic, and porphyroblastic with spaced cleavage. The parallel to anastomosing folded spaced cleavage parallel to the compositional layering is defined by oriented anhedral to subhedral biotite and chlorite. The rock consists of ca 40% cleavage domains. The microlithons, quartz, and plagioclase show grain boundary migration texture. The porphyroblastic texture is defined by the prismatic to tabular biotite.

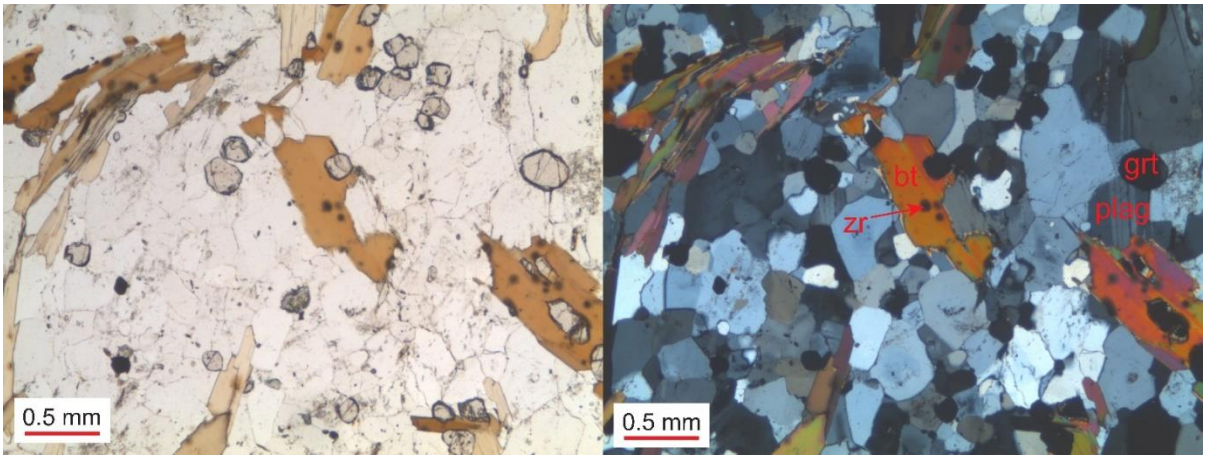


Thin section images of the felsic vein (zone 2) (gmf2021-11A). PPL left, XPL right.

**Reaction rim (zone 3)**

- Quartz: 39% (fine-grained, 0.06-0.72 mm, average: 0.32 mm, mode: 0.3 mm), equant, subhedral to anhedral.
- Plagioclase: 13% (fine-grained, 0.2-0.54 mm, average: 0.39 mm, mode: 0.4 mm), equant, subhedral to anhedral.
- Biotite: 40% (fine-grained, 0.022-0.92 mm, average: 0.32 mm, mode: 0.3 mm), euhedral to subhedral, prismatic to tabular.
- Garnet: 5% (fine to medium-grained, 0.14-1 mm, average: 0.46 mm, mode: 0.4 mm), anhedral to subhedral, equant.
- Chlorite: 3% (fine to medium-grained, 0.15-1.5 mm, average: 0.54 mm, mode: 0.3 mm), subhedral to anhedral, prismatic to tabular.
- Muscovite < 1%
- Apatite < 1%
- Zircon < 1%.
- Opaque: 1%

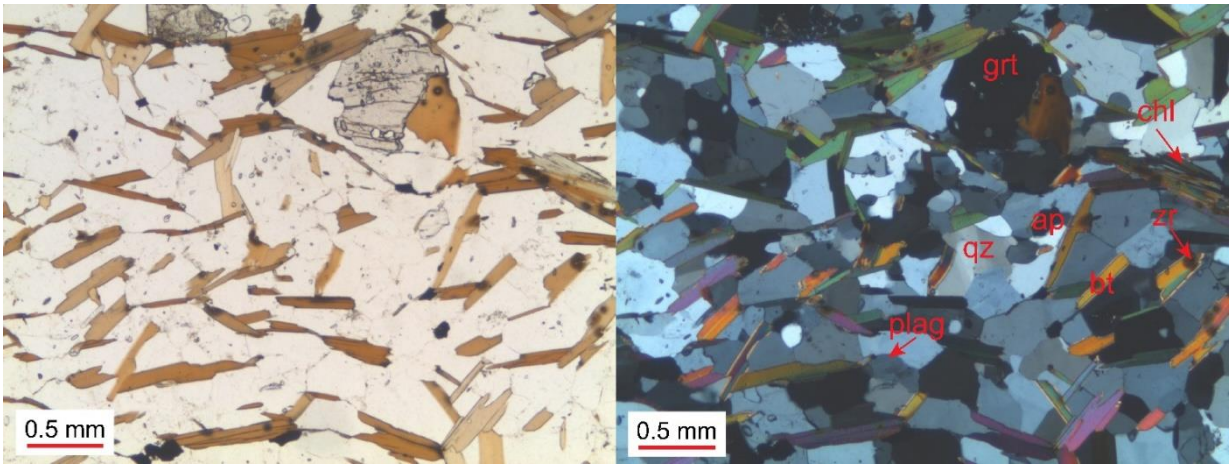


Thin section images of the reaction rim (zone 3) (gmf2021-11A). PPL left, XPL right.

**Textures:**

The rock is fine to medium-grained, hypidioblastic, porphyroblastic with a spaced and crenulation cleavage. The wriggly to folded, parallel to anastomosing spaced cleavage, is defined by the orientation of subhedral to euhedral biotite and anhedral to subhedral chlorite. The spaced cleavage is parallel to the compositional layering, and the crenulation cleavage is defined by the fold axial traces to the folded mica. The porphyroblastic texture is defined by the fine to medium-grained garnet and chlorite. The microlithons, quartz, and plagioclase show an SPO in the same direction as the spaced cleavage.

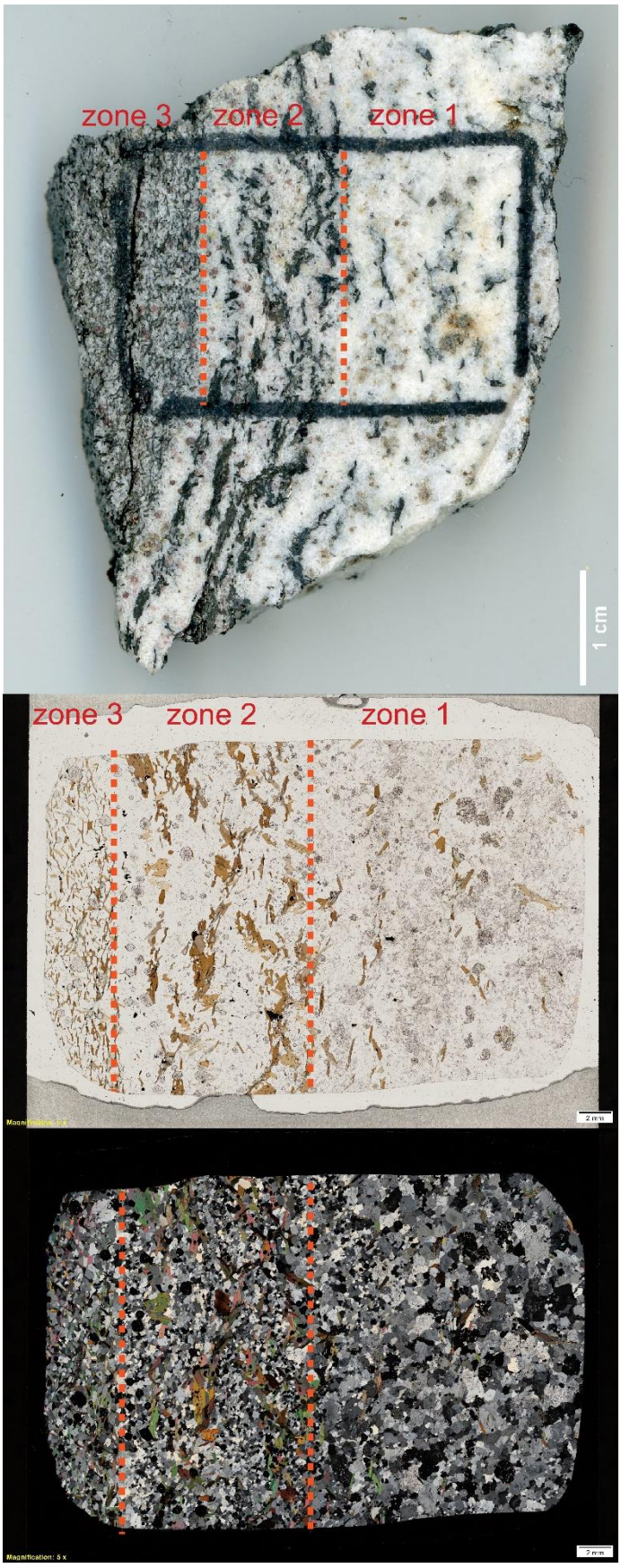


Rock slab, and thin section scans of gmf2021-11A. PPL in the middle, XPL, bottom

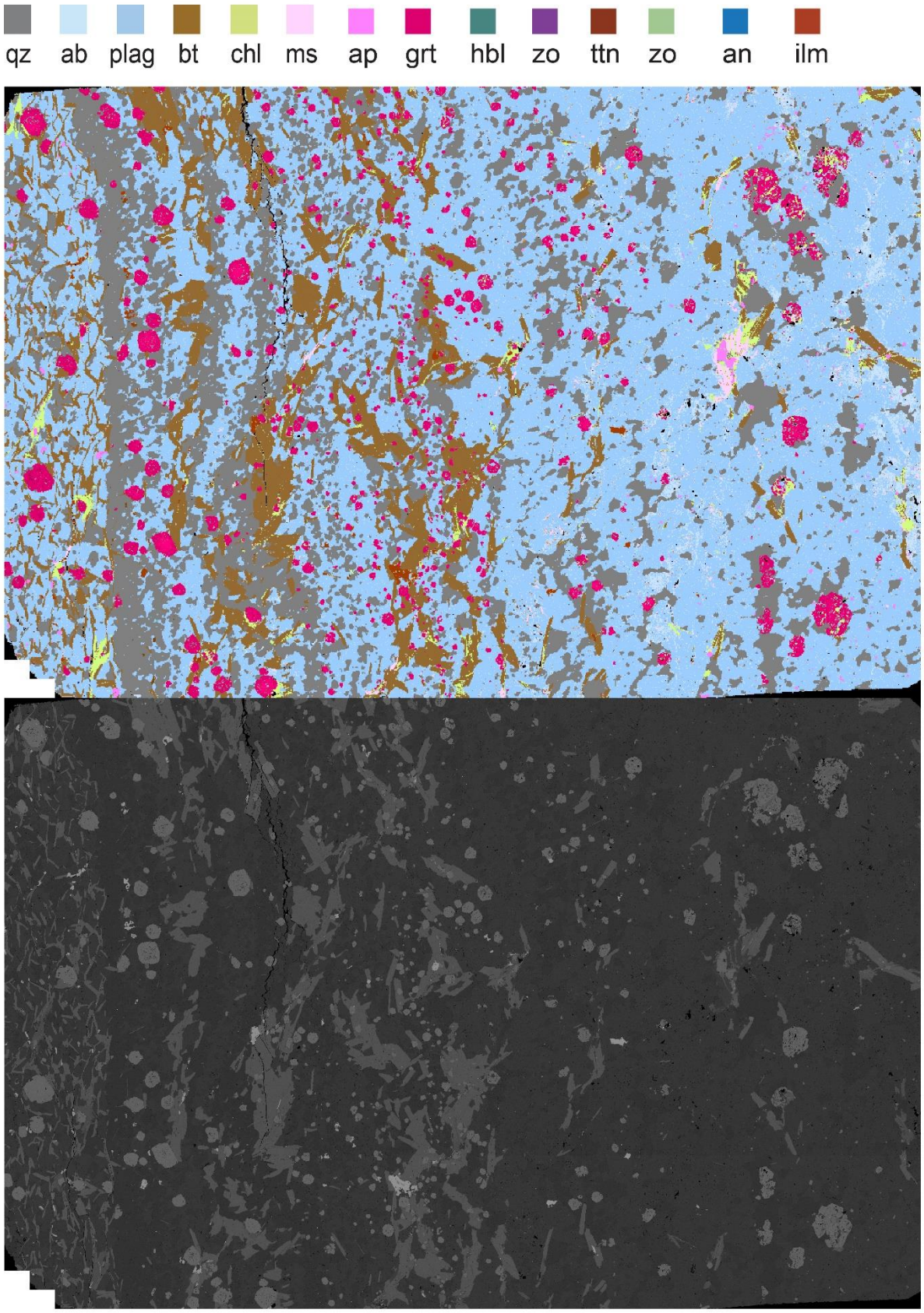


EDS-scan, and BS-image of gmf2021-11A. EDS-scan at top, BS-image, bottom.

**gmf2021-11B**

**Coordinates:** 66.24006° N, 14.78904° E

**Rock:** Reaction rim

**Minerals**

- Plagioclase: 46% (fine-grained, 0.2-0.83 mm, average: 0.47 mm, mode: 0.6 mm), subhedral to anhedral, equant to more elongated.
- Quartz: 25%, (fine to medium-grained, 0.1-1-1 mm, average: 0.4 mm, mode: 0.3 mm), anhedral to subhedral, equant to more elongated.
- Biotite: 20% (fine-grained, 0.09-0.79 mm, average: 0.22, mode: 0.2 mm), mostly subhedral, some euhedral, prismatic to more tabular.
- Garnet: 5% (fine-grained, 0.11-0.94 mm, average: 0.42 mm, mode: 0.3 mm), anhedral to euhedral, equant, some significantly altered by chlorite.
- Chlorite: 1% (fine-grained, 0.05-0.42 mm, average: 0.18 mm, mode: 0.2 mm), anhedral to subhedral, prismatic to tabular.
- Muscovite: < 1%
- Apatite: < 1%
- Zircon: < 1%
- Rutile: < 1%.
- Opaque < 1%

**Textures:**

The rock is hypidioblastic, equigranular, and has a continuous cleavage. The biotite and chlorite show continuous cleavage. The growth of mica in the pressure shadows from the garnet, indicates syn-tectonic growth of chlorite and biotite. Sericitization in feldspar and chloritization of garnet is present.

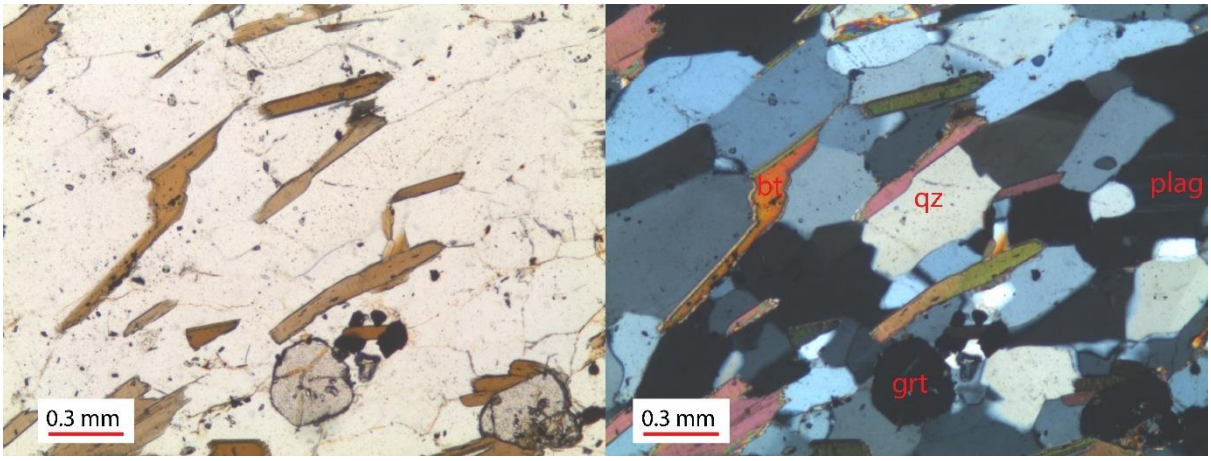


Thin section images of the reaction rim (gmf2021-11B). PPL left, XPL right.

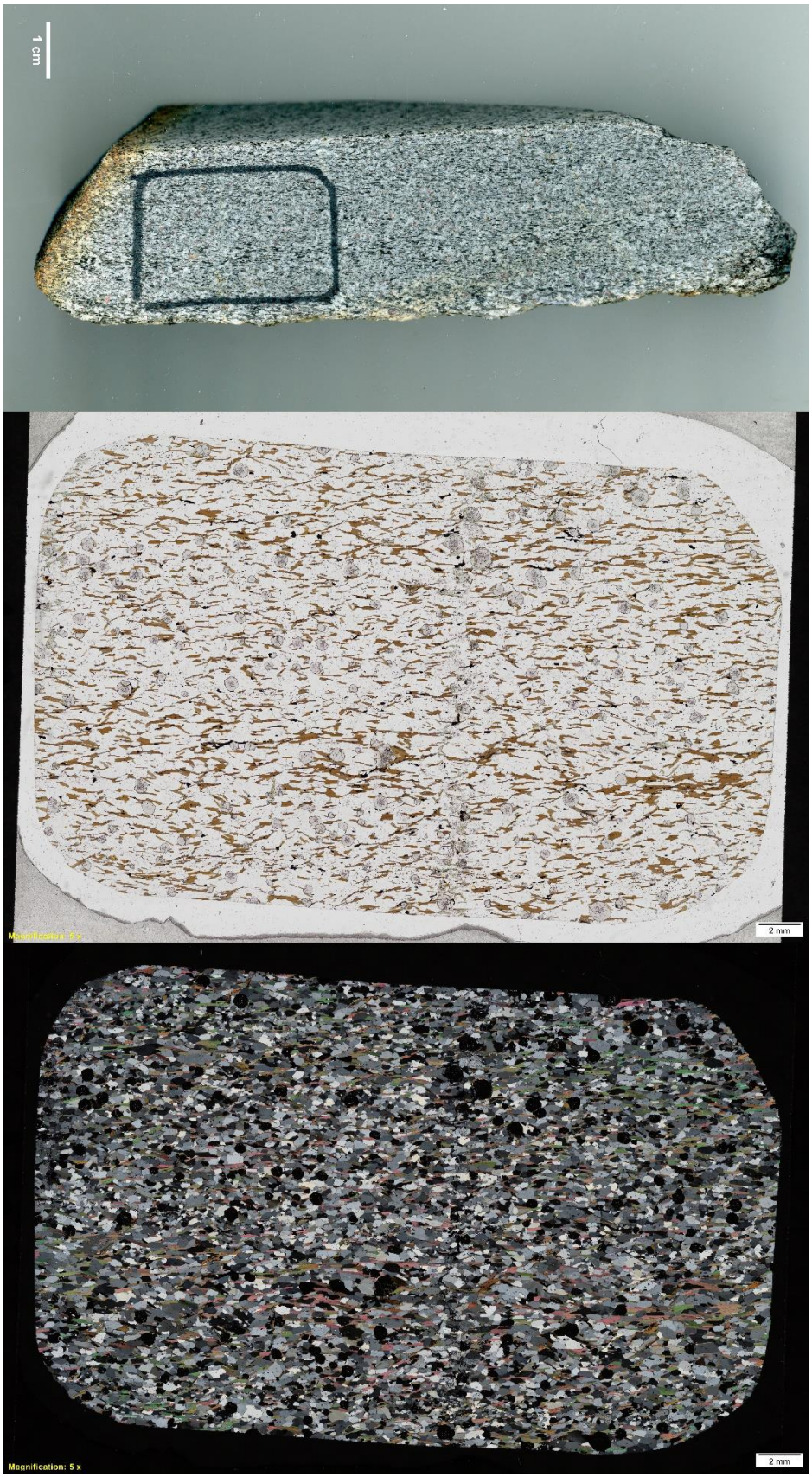


Rock slab, and thin section scans of gmf2021-11B. PPL in the middle, XPL, bottom

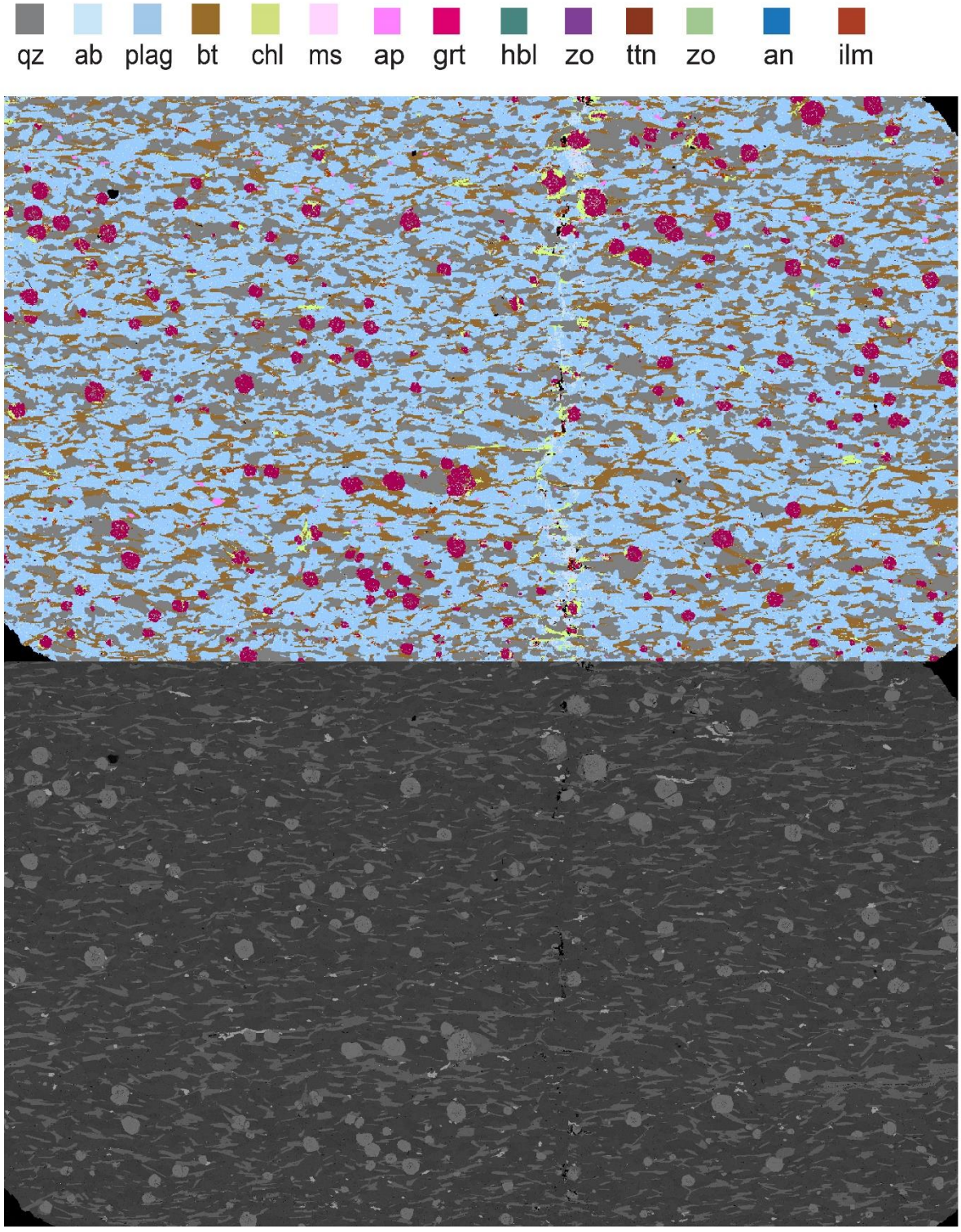
qz
ab
plag
bt
chl
ms
ap
grt
hbl
zo
ttn
zo
an
ilm

**gmf2021-11C**

**Coordinates:** 66.24006° N, 14.78904° E

**Rock:** Garnet mica schist

**Minerals:**

- Quartz: 28% (fine to medium-grained, 0.07-1.4 mm, average: 0.46 mm, mode: 0.45 mm), mostly anhedral, some subhedral, equant to more elongated.
- Biotite: 16% (fine to medium-grained, 0.04-1.26 mm, average: 0.46 mm, mode: 0.5 mm), mostly subhedral, some anhedral and euhedral, prismatic to tabular.
- Muscovite: 23% (medium to fine-grained, 0.09-1.3 mm, average: 0.5 mm, mode: 0.5 mm), mostly subhedral, some anhedral and euhedral, prismatic to tabular.
- Plagioclase: 18% (fine to medium-grained, 0.11-1.4 mm, average: 0.48 mm, mode: 0.3 mm), mostly anhedral, some subhedral, equant to more elongated
- Garnet: 4% (fine to medium-grained, 0.2-1.1 mm, average: 0.53 mm, mode: 0.5 mm), subhedral to euhedral, equant.
- Chlorite: 1%
- Opaque: < 1%
- Apatite: < 1%
- Zircon: < 1%
-

**Textures:**

The rock is fine to medium-grained, hypidioblastic, and equigranular and has a crenulation cleavage. The spaced anastomosing-parallel folded cleavage consists of ca. 40 % volume percentage of cleavage domains with a gradational transition between the cleavage domains and the microlithons. The spaced cleavage is defined by the preferred orientation of mica, such as subhedral-euhedral prismatic biotite and muscovite in the same direction as the compositional layering. The same mica minerals also define the crenulation cleavage. They have a preferred orientation towards the axial planes. Plagioclase and quartz define the microlithons that show SPO for both the spaced- and crenulation cleavage. The rock has undergone both seriterization and chloritization. Polysyntetic twinning is present in the plagioclase.

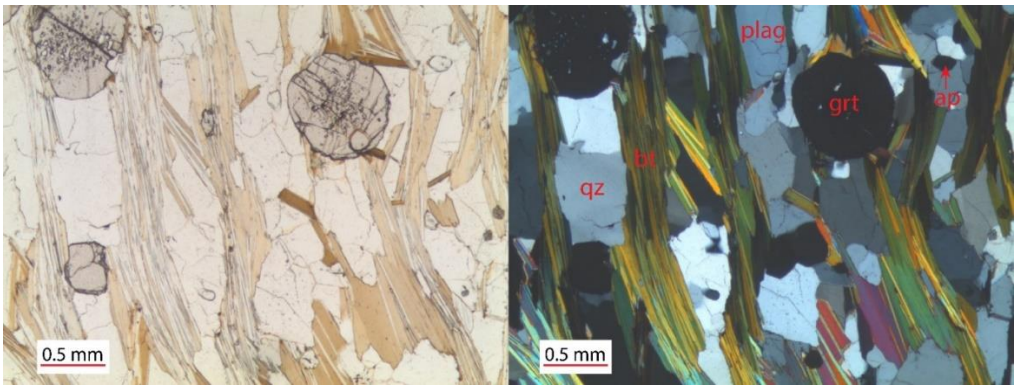


Thin section images of the garnet mica schist (gmf2021-11C). PPL left, XPL right.


Rock slab, and thin section scans of gmf2021-11C. PPL in the middle, XPL, bottom

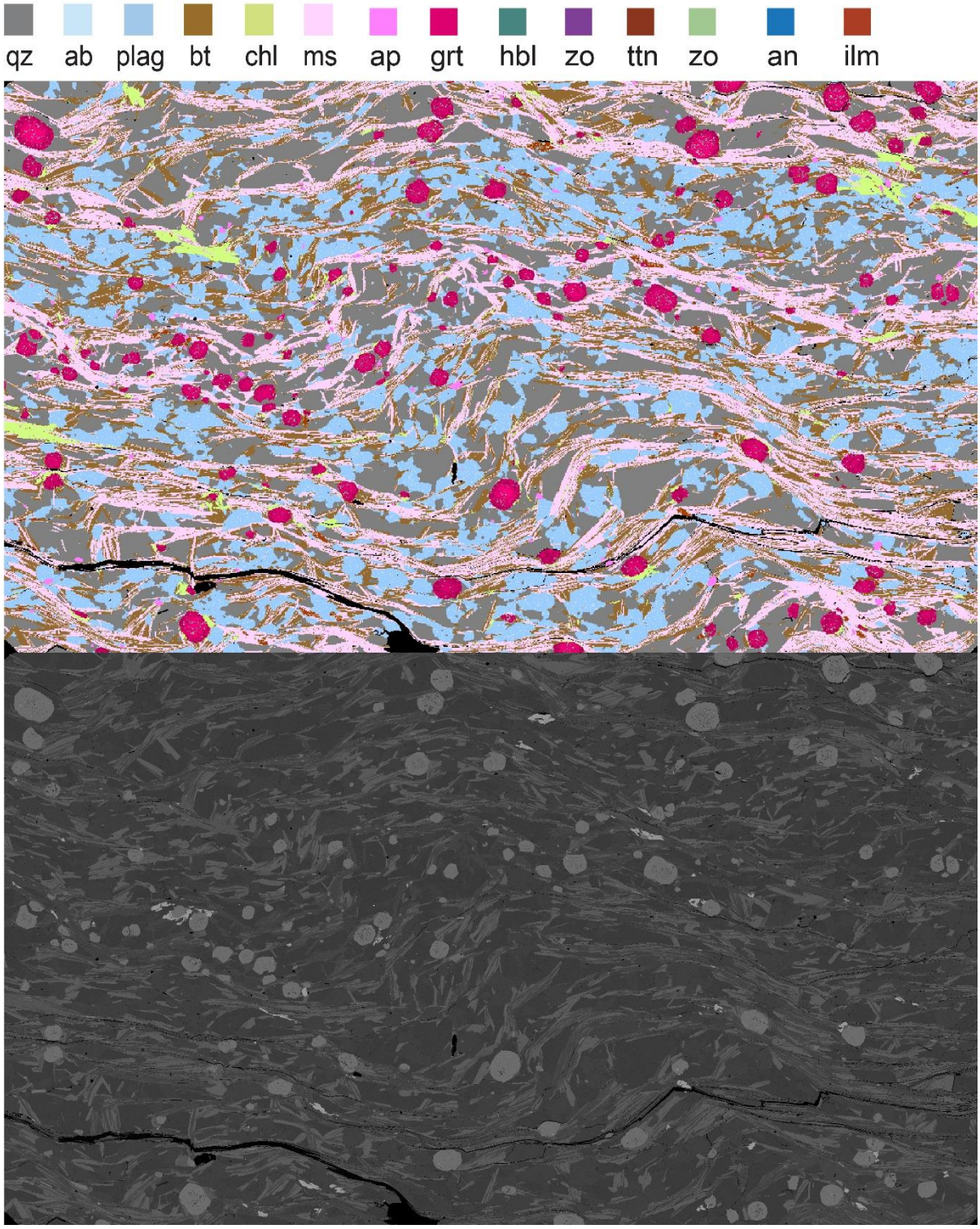


EDS-scan, and BS-image of gmf2021-11C. EDS-scan at top, BS-image, bottom.

**gmf2021-13**

**Coordinates:** 66.24093° N, 14.77668° E

**Rock type:** Garnet mica schist

**Minerals:**

- Quartz: 15% (fine to medium-grained, 0.15-1.1 mm, average: 0.5 mm, mode: 0.5 mm), anhedral to subhedral, equant to more elongated.
- Plagioclase: 35% (0.23-2.85 mm, average: 0.75 mm, mode: 0.4 mm), subhedral, equant to tabular.
- Biotite: 10% (fine-grained, 0.05-0.8 mm, average: 0.24 mm, mode: 0.2 mm), subhedral to euhedral, prismatic to tabular.
- Muscovite: 40% (fine to medium-grained, 0.11-1.6 mm, average: 0.46 mm, mode: 0.5 mm), subhedral to euhedral, prismatic to tabular.
- Garnet: 3% (5 mm), tabular anhedral grain.
- Apatite: <1%
- Opaque: <1%

**Textures:**

The rock is fine to coarse-grained, porphyroblastic, hypidioblastic with a spaced and a crenulation cleavage. The orientation of the mica creates the folded, parallel spaced cleavage parallel to the compositional layering. The crenulation cleavage is defined by the fold axial traces in the folded mica. The coarse anhedral garnet defines the porphyroblastic texture.

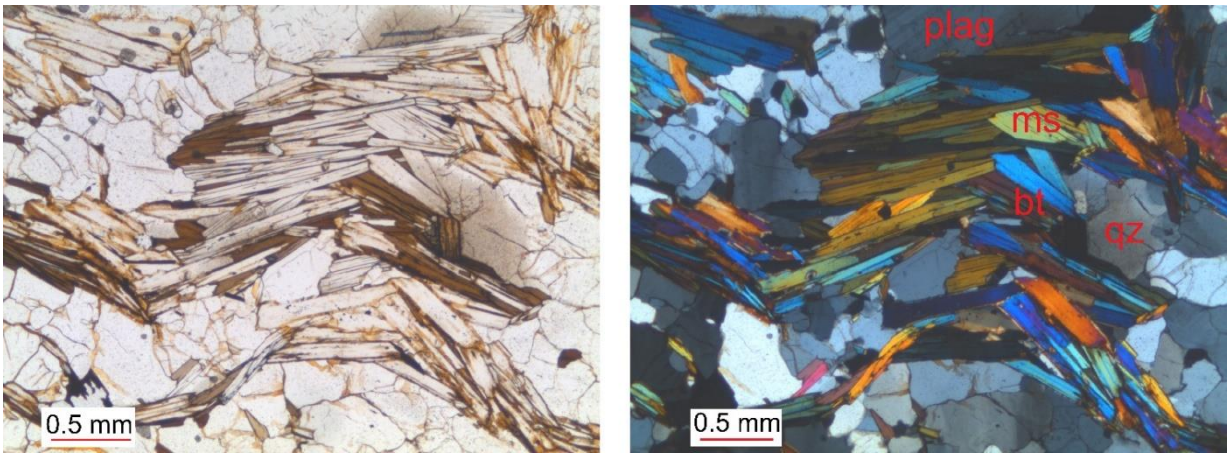


Thin section images of the garnet mica schist (gmf2021-13). PPL left, XPL right.

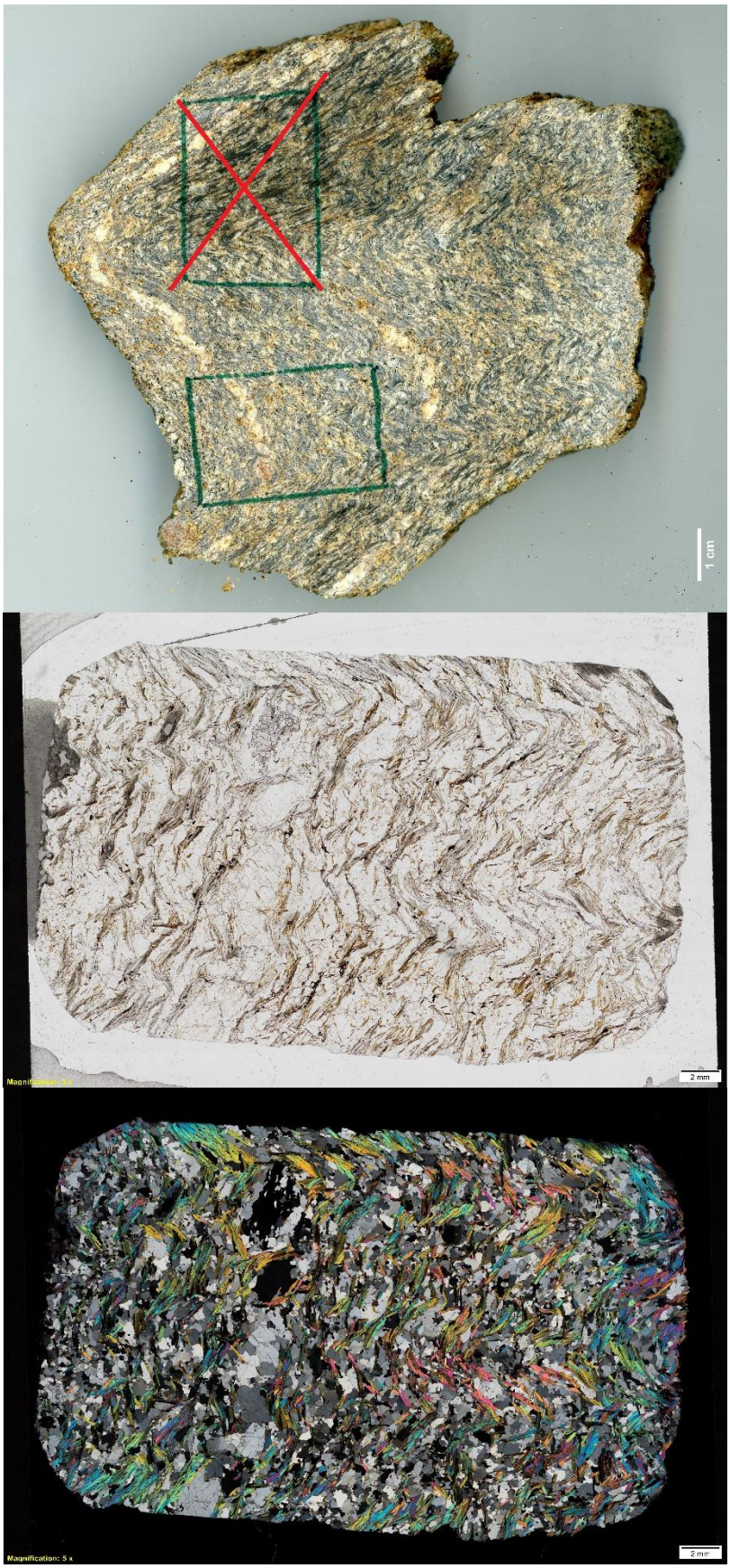


Rock slab, and thin section scans of gmf2021-13. PPL in the middle, XPL, bottom

**gmf2021-14**

**Coordinates:** 66.24005° N, 14.87401° E

**Rock type**: Mica schist

**Minerals**

- Plagioclase: 30% (fine to medium-grained, 0.16-2.26 mm, average: 0.68 mm, mode: 0.6 and 0.4 mm). subhedral to euhedral, tabular.
- Chlorite: 30% (fine to medium-grained, 0.027-1.1 mm, average: 0.35 mm, mode: 0.2 mm), prismatic to tabular, anhedral.
- Quartz: 20% (fine-grained, 0.12-0.75 mm, average: 0.35 mm, mode: 0.2 mm), anhedral to subhedral, equant to more elongated.
- Muscovite: 20% (fine to medium-grained, 0.05-1.4 mm, average: 0.36 mm, mode: 0.5 mm), prismatic to tabular, anhedral to subhedral.
- Zoisite: < 1%
- Apatite: < 1%
- Biotite: < 1%,

**Textures**

The rock is fine to medium-grained, porphyroblastic, hypidioblastic, and highly altered. The pseudo-garnet and plagioclase define the porphyroblastic texture. The orientation of the chlorite and muscovite generates the distinct folded anastomosing spaced cleavage parallel to the compositional layering. The crenulation cleavage is defined by the fold axial traces to the folded spaced cleavage. Chloriterization is abundant in the biotite and the garnet, and sericitization is present in the plagioclase. Polysynthetic twinning is present in the plagioclase.

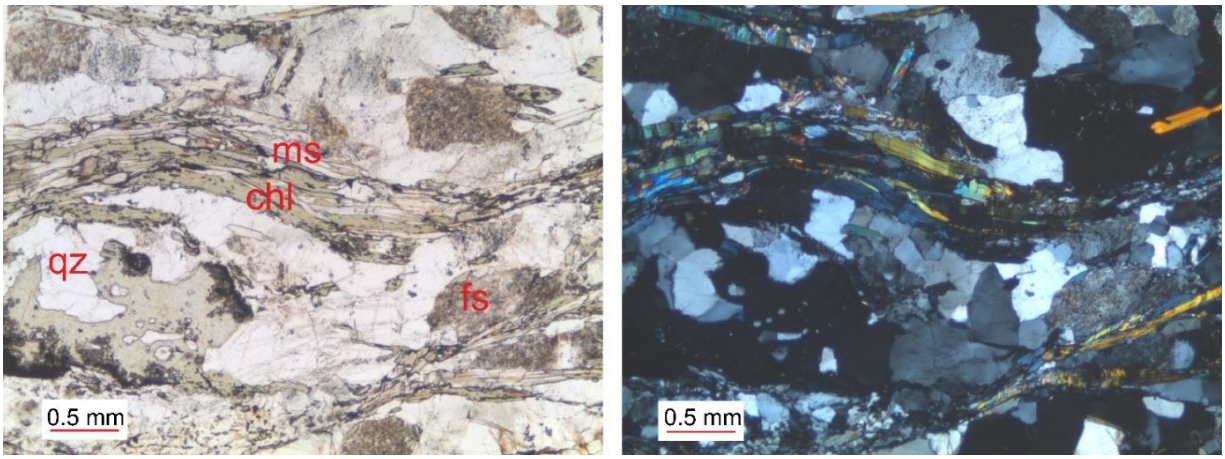


Thin section images of the post mafic felsic vein (gmf2021-14). PPL left, XPL right.

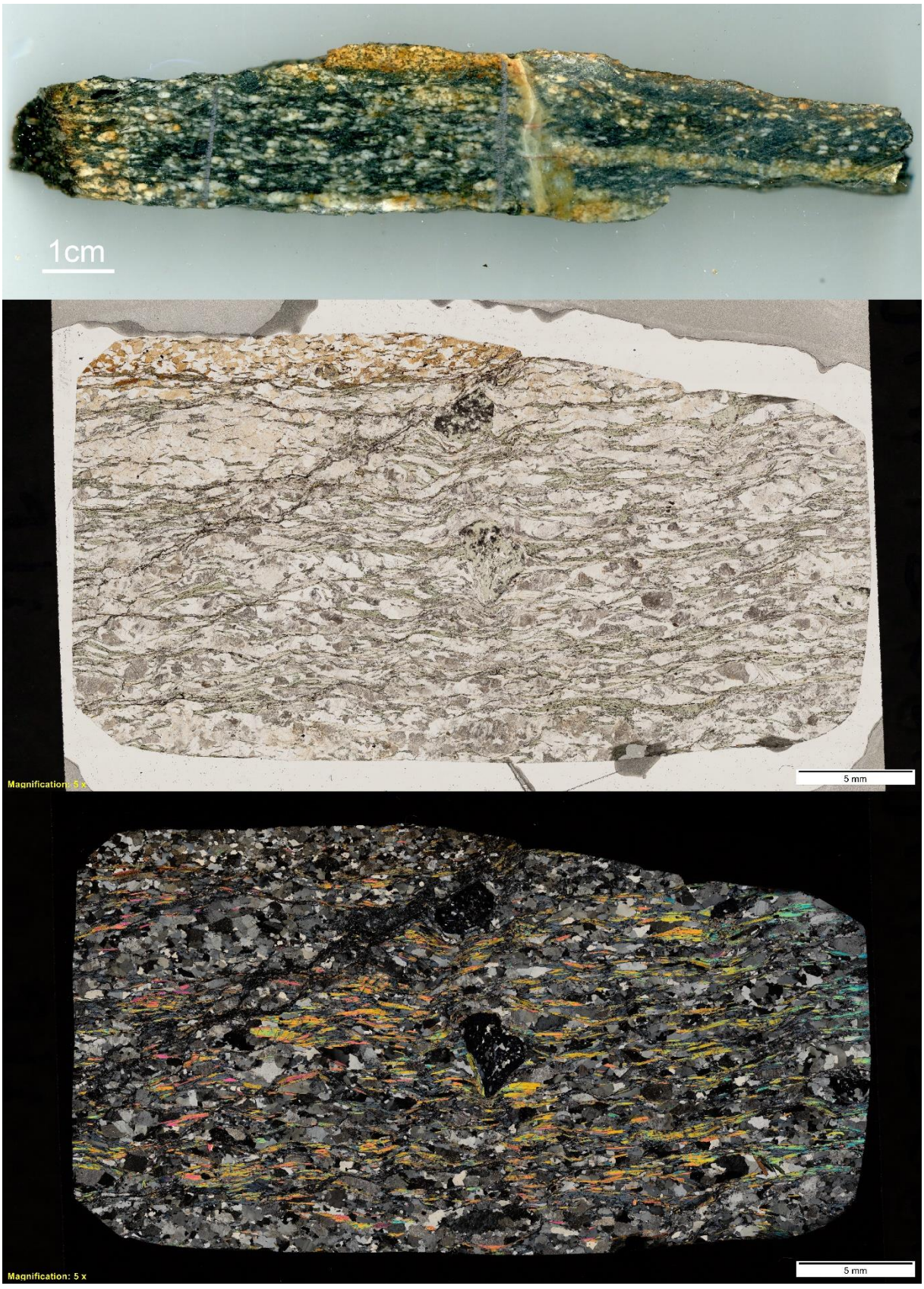


Rock slab, and thin section scans of gmf2021-14. PPL in the middle, XPL, bottom.

**gmf2021-16**

**Coordinates:** 66.24077° N, 14.8705° E

**Rock type**: layered quartz-rich schist

**Minerals:**

- Quartz: 67% (fine to medium-grained, 0.08-1.3 mm, average: 0.42 mm, mode: 0.3 mm) subhedral, equant to elongated.
- Biotite: 18% (fine-grained, 0.04-0.74 mm, average: 0.23 mm, mode: 0.2 mm) subhedral to euhedral, prismatic to tabular.
- Plagioclase: 8% (fine-grained, 0.08-0.56 mm, average: 0.33 mm, mode: 0.4 mm), subhedral, tabular.
- Muscovite: 5% (fine to medium-grained, 0.03-1.2 mm, average: 0.28 mm, mode: 0.2 mm) subhedral to euhedral, prismatic to tabular.
- Titanite: 1%
- Apatite: 1%
- Zoisite:< 1%
- Zircon: < 1%
- Rutile: < 1%
- Opaque: < 1%

**Texture**

The rock is fine to medium-grained, hypidioblastic, equigranular, and has a continuous cleavage parallel to the compositional layering and some parallel layering. The biotite creates the layering, the quartz and feldspar have a weakly developed SPO. Undulating extinction is present in quartz and polysynthetic twins, and sericitization is present in plagioclase.

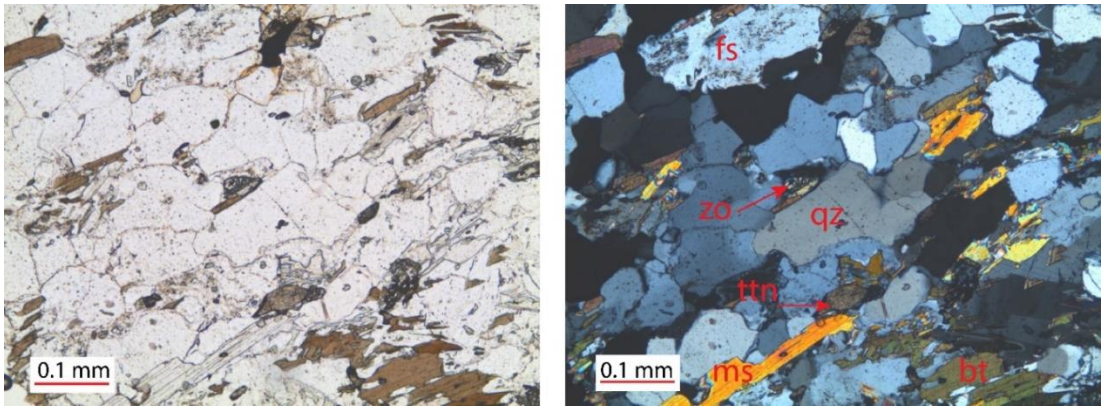


Thin section images of the layered quartz-rich schist (gmf2021-16). PPL left, XPL right.


Rock slab, and thin section scans of gmf2021-16. PPL in the middle, XPL, bottom

**gmf2021-17**

**Coordinates:** 66.24407° N, 14.85232° E

**Rock type**: Felsic vein in mafic layer

**Minerals:**

- Quartz: 38% (fine-grained, 0.07-0.4 mm, average: 0.21 mm, mode: 0.2 mm), subhedral, equant to more elongated,
- Biotite: 28% (fine-grained, 0.056-0.52 mm, average: 0.21 mm, 0.2 mm), , subhedral to euhedral, prismatic to equant.
- Plagioclase: 24% (fine-grained, 0.18-0.6 mm, average: 0.30 mm, mode: 0.3 mm) anhedral to subhedral, equant to tabular,
- Garnet: 5% (fine to medium-grained, 0.6-2.66 mm, average: 1.48 mm, mode: 1 mm), subhedral, equant.
- Titanite: 4% (fine-grained, 0.029-0.49 mm, average: 0.20 mm, mode: 0.2 mm), anhedral, skeletal.
- Apatite: < 1%
- Zircon: < 1%
- Zoisite: < 1%
- Opaue: < 1%

**Textures:**

The rock is fine to medium-grained, porphyroblastic, hypidioblastic with a continuous cleavage. Skeletal titanite and garnet create the porphyroblastic texture, and oriented biotite makes the continuous cleavage apparent in PPL. Polysynthetic twins are present in the plagioclase.

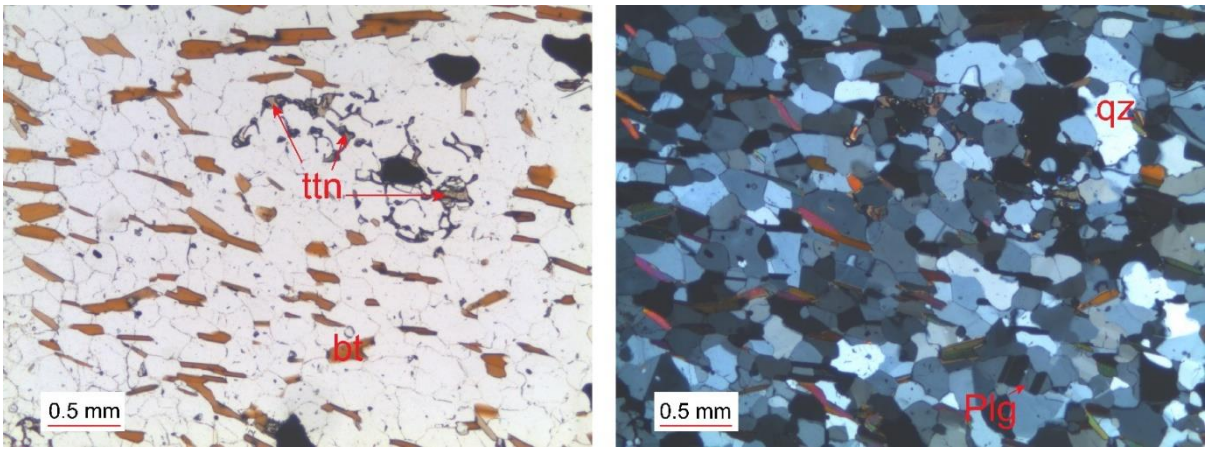


Thin section images of the post mafic felsic vein (gmf2021-17). PPL left, XPL right.

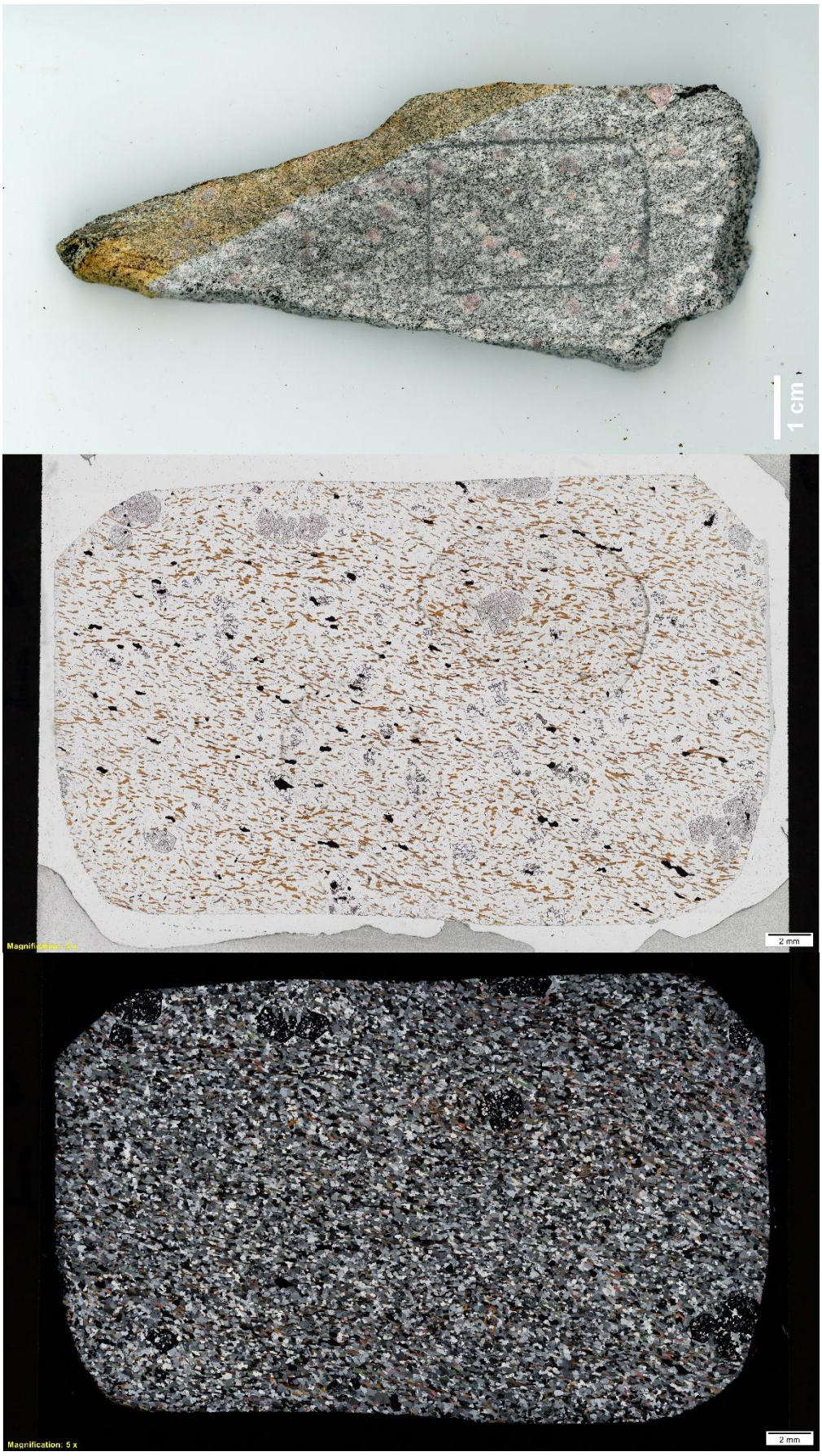


Rock slab, and thin section scans of gmf2021-17. PPL in the middle, XPL, bottom

**gmf2021-21**

**Coordinates:** 66.22967° N, 14.88297° E

**Rock type:** Amphibolite

**Minerals:**

- Hornblende: 78% (fine to medium-grained, 0.05-1.3, average: 0.48 mm, mode: 0.3 mm), subhedral to euhedral, prismatic to equant/diamond shape.
- Plagioclase: 18% (fine-grained, 0.04-0.48 mm, average: 0.24 mm, mode: 0.2 mm), anhedral to subhedral, tabular to more elongated.
- Titanite: 2% (fine-grained, 0.019-0.22 mm, average: 0.098 mm, mode: 0.1 mm), subhedral, diamond shaped.
- Zoisite: 2% (fine-grained, 0.044-0.22 mm, average: 0.13 mm, mode: 0.1 mm)
- Chlorite: < 1%
- Zircon < 1%

**Textures:**

The rock is equigranular, hypidioblastic, and has a continuous cleavage. The subhedral, elongated plagioclase, and the hornblende defines the parallel continuous cleavage. The plagioclase is elongated and shows polysynthetic twins. Garnet was present in the field.

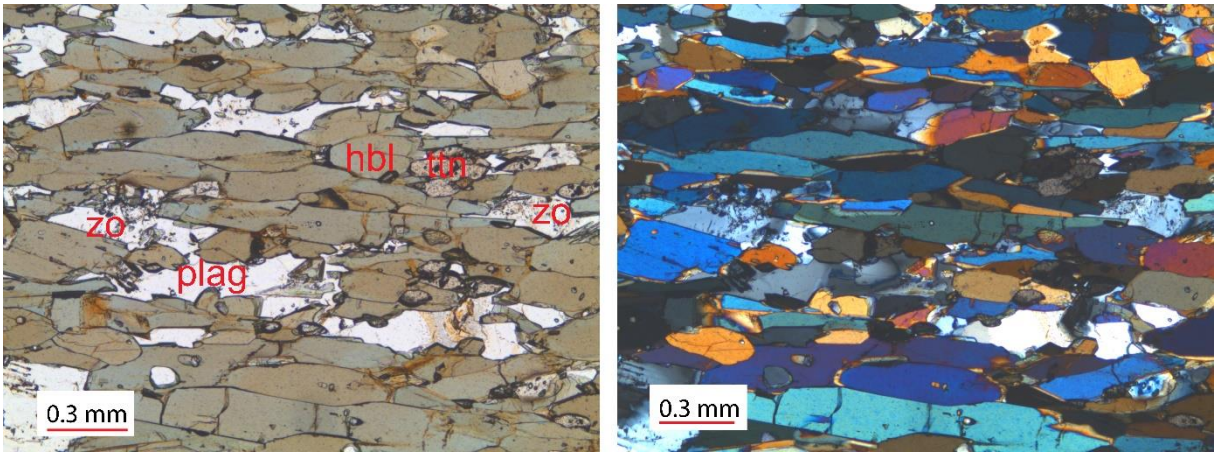


Thin section images of the amphibolite (gmf2021-21). PPL left, XPL right.

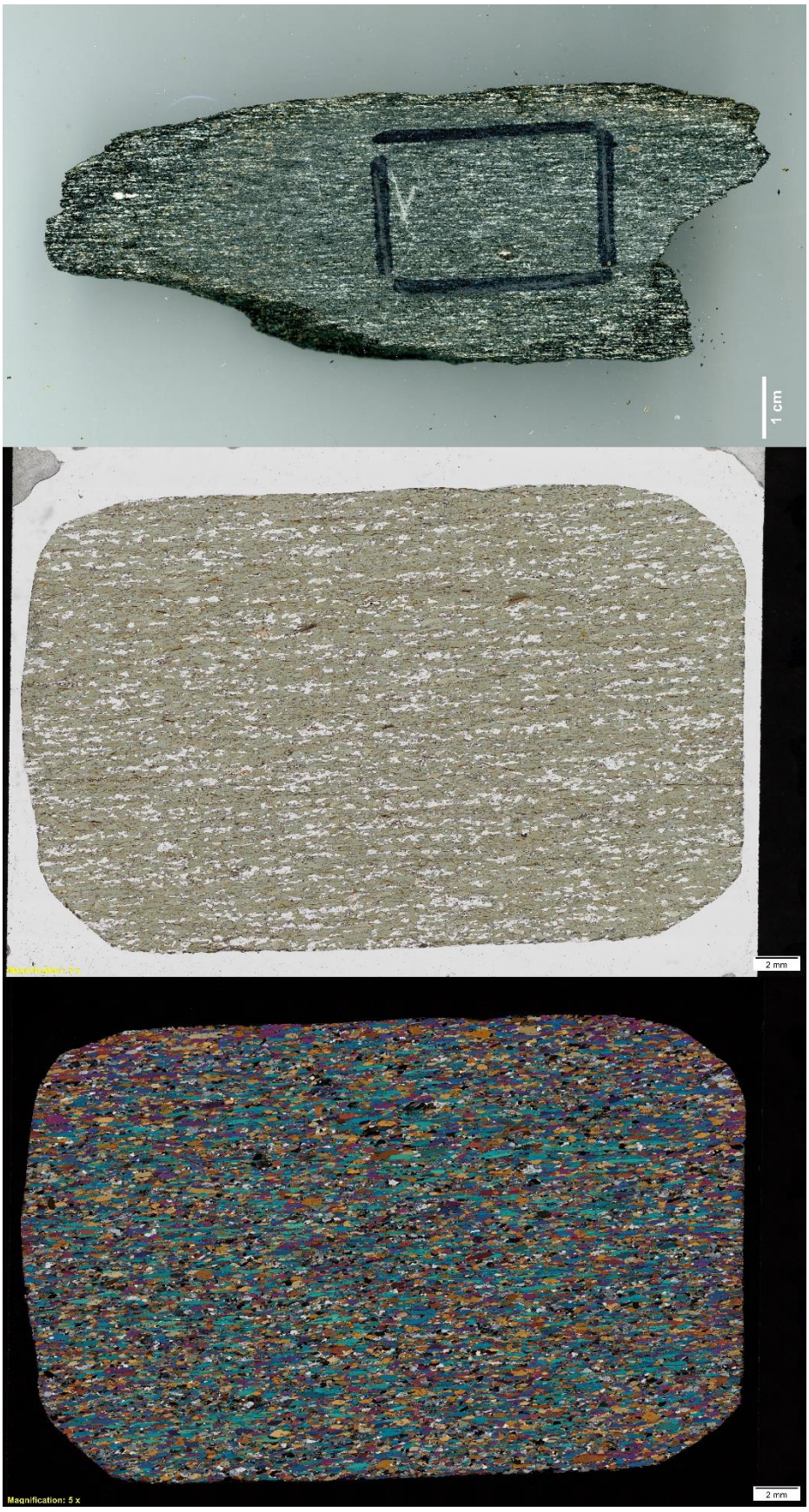


Rock slab, and thin section scans of gmf2021-21. PPL in the middle, XPL, bottom.

# D2: Mineralogic - Area% data

| Sample: | gmf2020-22B | | |
|---|---|---|---|
| | Area % | Average Composition | Assigned Composition |
| Albite | 0,111021319965416 | Si 37,78; O 36,52; Al 16,69; Na 8,57; K 0,3; Ca 0,11; Fe 0,03; Ti 0; | Si 37,78; O 36,52; Al 16,69; Na 8,57; K 0,3; Ca 0,11; Fe 0,03; Ti 0; |
| Amphibole (Fe-actinolite) | 0,000763407868064622 | O 40,32; Si 26,31; Fe 13,21; Ca 10,72; Mg 7,68; Al 1,74; | O 40,32; Si 26,31; Fe 13,21; Ca 10,72; Mg 7,68; Al 1,74; |
| Amphibole (Fe-hornblende) | 14,4016900162258 | O 33,3; Si 20,92; Fe 16,42; Ca 11,88; Al 10,84; Mg 5,85; Na 0,76; Ti 0,01; K 0; Mn 0; | O 33,3; Si 20,92; Fe 16,42; Ca 11,88; Al 10,84; Mg 5,85; Na 0,76; Ti 0,01; K 0; Mn 0; |
| Anorthite | 2,59449625916654 | O 37,11; Si 28,8; Al 18,2; Ca 12,95; Na 2,64; Fe 0,27; K 0,03; | O 37,11; Si 28,8; Al 18,2; Ca 12,95; Na 2,64; Fe 0,27; K 0,03; |
| Apatite | 0,854689666520068 | Ca 49,83; O 34,05; P 15,81; F 0,28; Nd 0,02; Cl 0,01; Ce 0; La 0; | Ca 49,83; O 34,05; P 15,81; F 0,28; Nd 0,02; Cl 0,01; Ce 0; La 0; |
| Biotite | 0,019957663512643 8 | O 36,36; Si 23,01; Fe 15,71; Al 13,32; Mg 6,57; K 5,01; | O 36,36; Si 23,01; Fe 15,71; Al 13,32; Mg 6,57; K 5,01; |
| Biotite (annite) | 0,006979729387 13297 | O 32,33; Fe 25,32; Si 19,17; Al 12,14; Mg 5,95; K 5,06; Ba 0,03; | O 32,33; Fe 25,32; Si 19,17; Al 12,14; Mg 5,95; K 5,06; Ba 0,03; |
| Calcite | 0,000109058628178 88 | O 50,29; Ca 49,71; | O 50,29; Ca 49,71; |
| Cpx (Augite) | 0,045586357258606 | O 46,82; Si 20,89; Al 9,33; Fe 8,34; Ca 6,95; Mg 6,16; Na 1,47; Ti 0,03; | O 46,82; Si 20,89; Al 9,33; Fe 8,34; Ca 6,95; Mg 6,16; Na 1,47; Ti 0,03; |
| Cpx (Diopside) | 0,000109058628178 88 | O 45,44; Si 19,24; Ca 13,27; Fe 9,45; Mg 7,96; Al 4,64; | O 45,44; Si 19,24; Ca 13,27; Fe 9,45; Mg 7,96; Al 4,64; |
| Cpx (Hedenbergite) | 0,000436233051271 55 | O 33,65; Si 24,29; Ca 16,02; Fe 15,16; Mg 8,18; Al 2,7; | O 33,65; Si 24,29; Ca 16,02; Fe 15,16; Mg 8,18; Al 2,7; |
| Epidote | 0,036752637176853 6 | O 32,29; Fe 28,64; Si 16,75; Ca 12,81; Al 9,48; Mg 0,04; | O 32,29; Fe 28,64; Si 16,75; Ca 12,81; Al 9,48; Mg 0,04; |
| Fe-Mg-chlorite | 0,283660566301291 | O 35,74; Fe 28,02; Al 13,67; Si 12,48; Mg 10,09; Ca 0; K 0; | O 35,74; Fe 28,02; Al 13,67; Si 12,48; Mg 10,09; Ca 0; K 0; |
| Fe-Oxide (altered) | 0,005780088382778 58 | O 32,72; Fe 32,51; Si 13,98; Al 9,53; Ca 8,48; Mn 2,4; Mg 0,39; | O 32,72; Fe 32,51; Si 13,98; Al 9,53; Ca 8,48; Mn 2,4; Mg 0,39; |
| Fe-rich clay | 0,005780088411117 98 | O 38,15; Fe 20,87; Si 19,05; Al 15,73; Mg 3,35; Ca 2,76; Na 0,09; | O 38,15; Fe 20,87; Si 19,05; Al 15,73; Mg 3,35; Ca 2,76; Na 0,09; |
| Garnet (alm+Ca) | 6,099301864310 68 | O 30,8; Fe 25,27; Si 18,54; Al 13,94; Ca 9,67; Mg 1,75; Ti 0,02; Mn 0; Zr 0; Cr 0; K 0; | O 30,8; Fe 25,27; Si 18,54; Al 13,94; Ca 9,67; Mg 1,75; Ti 0,02; Mn 0; Zr 0; Cr 0; K 0; |
| Garnet (alm+Mn+Ca) | 1,824981033884 8 | O 29,38; Fe 26,07; Si 17,83; Al 13,58; Ca 8,39; Mn 3,3; Mg 1,42; Ti 0,01; Zr 0; K 0; Cr 0; | O 29,38; Fe 26,07; Si 17,83; Al 13,58; Ca 8,39; Mn 3,3; Mg 1,42; Ti 0,01; Zr 0; K 0; Cr 0 |
| Garnet (almandine) | 0,002399281923690 57 | Fe 37,73; O 30,71; Si 14,83; Al 13,54; Mg 2,83; Mn 0,28; Ca 0,09; | Fe 37,73; O 30,71; Si 14,83; Al 13,54; Mg 2,83; Mn 0,28; Ca 0,09; |
| Garnet (andradite) | 0,001417575299901 7 | O 34,65; Si 22,36; Fe 18,13; Ca 13,56; Mg 7,32; Al 3,65; Ti 0,33; | O 34,65; Si 22,36; Fe 18,13; Ca 13,56; Mg 7,32; Al 3,65; Ti 0,33; |
| Garnet (grossular) | 0,239382903605514 | O 41,99; Ca 19,57; Si 18,43; Al 17,39; Fe 2,45; Mg 0,15; Ti 0,01; Cr 0; Mn 0; | O 41,99; Ca 19,57; Si 18,43; Al 17,39; Fe 2,45; Mg 0,15; Ti 0,01; Cr 0; Mn 0; |
| Illite-smectite | 0,020502954798393 8 | O 36,74; Si 29,19; Al 14,86; K 7,08; Fe 4,95; Ca 4,17; Na 1,63; Mg 1,27; Ti 0,1; | O 36,74; Si 29,19; Al 14,86; K 7,08; Fe 4,95; Ca 4,17; Na 1,63; Mg 1,27; Ti 0,1; |
| Ilmenite | 0,001417575016507 6 | Ti 38,08; Fe 36,71; O 23,58; Mn 0,89; Si 0,51; Al 0,23; | Ti 38,08; Fe 36,71; O 23,58; Mn 0,89; Si 0,51; Al 0,23; |
| Ilmenite_Mn | 0,000327174816793071 | Ti 34,88; O 26,28; Fe 26,2; Mn 9,62; Si 1,39; Ca 1,27; Al 0,35; | Ti 34,88; O 26,28; Fe 26,2; Mn 9,62; Si 1,39; Ca 1,27; Al 0,35; |
| Kaolinite | 0,002290223689212 09 | O 43,95; Si 40,12; Al 15,69; Mg 0,13; Ca 0,11; | O 43,95; Si 40,12; Al 15,69; Mg 0,13; Ca 0,11; |
| Kfsp | 0,008833719968394 69 | O 37,29; Si 34,06; Al 15,44; K 7,14; Na 4,81; Ca 0,73; Fe 0,3; Mg 0,22; | O 37,29; Si 34,06; Al 15,44; K 7,14; Na 4,81; Ca 0,73; Fe 0,3; Mg 0,22; |
| Muscovite | 0,019085197155046 | O 38,37; Si 27,4; Al 22,29; K 10,09; Fe 1,3; Mg 0,54; F 0,01; | O 38,37; Si 27,4; Al 22,29; K 10,09; Fe 1,3; Mg 0,54; F 0,01; |
| Orthoclase | 0,052457027957 83 | O 36,45; Si 35,75; Al 14,67; K 10,78; Na 1,86; Ca 0,4; Fe 0,08; Mg 0,02; | O 36,45; Si 35,75; Al 14,67; K 10,78; Na 1,86; Ca 0,4; Fe 0,08; Mg 0,02; |
| Orthoclase+Ba | 0,000109058291157 296 | O 35,82; Si 34,38; K 14,9; Al 12,62; Ba 2,28; | O 35,82; Si 34,38; K 14,9; Al 12,62; Ba 2,28; |
| Plagioclase | 30,663368735594 1 | O 37,14; Si 32,04; Al 16,93; Na 7,16; Ca 6,72; K 0; | O 37,14; Si 32,04; Al 16,93; Na 7,16; Ca 6,72; K 0; |
| Quartz | 31,130029106135 7 | Si 60,67; O 39,15; Al 0,09; Fe 0,05; Ce 0,02; La 0,02; | Si 60,67; O 39,15; Al 0,09; Fe 0,05; Ce 0,02; La 0,02; |
| Rutile | 0,019194256551440 3 | Ti 67,89; O 30,83; Si 0,59; Fe 0,23; Al 0,23; Ca 0,22; | Ti 67,89; O 30,83; Si 0,59; Fe 0,23; Al 0,23; Ca 0,22; |
| Rutile2 | 0,002726456995538 32 | Ti 99,81; Al 0,12; Si 0,07; | Ti 99,81; Al 0,12; Si 0,07; |
| Titanite | 1,489190693506 3 | O 32,46; Ca 26,05; Ti 25,97; Si 14,05; Al 1,43; Fe 0,03; Nd 0; Ce 0; Sm 0; | O 32,46; Ca 26,05; Ti 25,97; Si 14,05; Al 1,43; Fe 0,03; Nd 0; Ce 0; Sm 0; |
| Ulvospinel | 0,000109058291157 296 | Fe 42,91; O 29,64; Ti 27,45; | Fe 42,91; O 29,64; Ti 27,45; |
| Zircon | 0,014831924905 1484 | Zr 57,52; O 20,93; Si 20,77; Al 0,46; Ca 0,13; Ce 0,1; La 0,05; Nd 0,03; | Zr 57,52; O 20,93; Si 20,77; Al 0,46; Ca 0,13; Ce 0,1; La 0,05; Nd 0,03; |
| Zoisite | 0,708442524292143 | O 35,79; Ca 23,25; Al 20,33; Si 18,54; Fe 2,03; Mg 0,04; Ti 0,02; Cr 0,01; Mn 0; | O 35,79; Ca 23,25; Al 20,33; Si 18,54; Fe 2,03; Mg 0,04; Ti 0,02; Cr 0,01; Mn 0; |
| Zoisite-rim | 5,393694910030 06 | O 35,62; Ca 23,92; Al 21,25; Si 18,6; Fe 0,56; Mg 0,02; Cr 0,02; Ti 0,01; Mn 0; Zr 0; K 0; | O 35,62; Ca 23,92; Al 21,25; Si 18,6; Fe 0,56; Mg 0, |

| Sample: | gmf2020-25 | | |
|---|---|---|---|
| | Area % | Average Composition | Assigned Composition |
| Albite | 0,706663441891758 | Si 37,06; O 36,67; Al 17,11; Na 8,71; K 0,21; Fe 0,18; Ca 0,05; Ti 0; | Si 37,06; O 36,67; Al 17,11; Na 8,71; K 0,21; Fe 0,18; Ca 0,05; Ti 0; |
| Ankerite | 0,000138317363133585 | O 46,44; Ca 28,05; Fe 19,19; Mg 6,31; | O 46,44; Ca 28,05; Fe 19,19; Mg 6,31; |
| Anorthite | 0,214945192804819 | O 40,03; Si 34,72; Al 15,18; Ca 5,83; Na 3,88; K 0,2; Fe 0,17; | O 40,03; Si 34,72; Al 15,18; Ca 5,83; Na 3,88; K 0,2; Fe 0,17; |
| Apatite | 0,237075968533983 | Ca 49,62; O 33,91; P 16,13; F 0,3; Cl 0,03; Nd 0,02; Ce 0; | Ca 49,62; O 33,91; P 16,13; F 0,3; Cl 0,03; Nd 0,02; Ce 0; |
| Biotite | 14,4634323737849 | O 34,52; Si 18,44; Fe 17,49; Al 12,08; K 9,65; Mg 7,81; Ba 0,01; F 0; | O 34,52; Si 18,44; Fe 17,49; Al 12,08; K 9,65; Mg 7,81; Ba 0,01; F 0; |
| Biotite (annite) | 6,82928179721546 | O 32,48; Fe 22,18; Si 17,57; Al 11,19; K 9,45; Mg 7,12; Ba 0,01; F 0; | O 32,48; Fe 22,18; Si 17,57; Al 11,19; K 9,45; Mg 7,12; Ba 0,01; F 0; |
| Calcite | 0,000138317363133585 | Ca 57,37; O 36,05; Fe 6,58; | Ca 57,37; O 36,05; Fe 6,58; |
| Cpx (Hedenbergite) | 0,000138317363133585 | O 38,49; Si 23,23; Ca 21,08; Fe 12,26; Al 3,44; Mg 1,51; | O 38,49; Si 23,23; Ca 21,08; Fe 12,26; Al 3,44; Mg 1,51; |
| Epidote | 0,000414952089400756 | O 36,79; Fe 24,87; Si 15,81; Ca 12,55; Al 9,98; | O 36,79; Fe 24,87; Si 15,81; Ca 12,55; Al 9,98; |
| Fe-Mg-chlorite | 1,2347591551104 | O 37,65; Fe 26,25; Al 13,41; Si 12,15; Mg 10,52; K 0,02; Ca 0; | O 37,65; Fe 26,25; Al 13,41; Si 12,15; Mg 10,52; K 0,02; Ca 0; |
| Fe-Oxide | 0,00594764686634204 | Fe 66,5; O 25,94; S 4,12; Si 2,1; Al 1,23; Mg 0,11; | Fe 66,5; O 25,94; S 4,12; Si 2,1; Al 1,23; Mg 0,11; |
| Fe-Oxide (altered) | 0,025173761492072 | Fe 40,57; O 33,74; Si 11,36; Al 8,51; S 2,38; Ca 1,57; Mg 1,36; Mn 0,33; Ti 0,13; As 0,05; N | Fe 40,57; O 33,74; Si 11,36; Al 8,51; S 2,38; Ca 1,57; Mg 1,36; Mn 0,33; Ti 0,13; As 0,0 |
| Fe-rich clay | 0,0199177009382022 | O 37,67; Fe 24,36; Si 17,91; Al 15,31; Mg 2,8; Ca 1,93; Na 0,02; | O 37,67; Fe 24,36; Si 17,91; Al 15,31; Mg 2,8; Ca 1,93; Na 0,02; |
| Garnet (almandine) | 3,53248727659872 | Fe 34,07; O 30,25; Si 17,72; Al 13,58; Mg 2,15; Ca 1,88; Mn 0,33; Ti 0,01; Zr 0; K 0; Cr 0; | Fe 34,07; O 30,25; Si 17,72; Al 13,58; Mg 2,15; Ca 1,88; Mn 0,33; Ti 0,01; Zr 0; K 0; Cr |
| Garnet (andradite) | 0,00262802989953812 | O 33,43; Si 18,91; Al 16,94; Fe 15,24; Ca 14,88; Mg 0,61; | O 33,43; Si 18,91; Al 16,94; Fe 15,24; Ca 14,88; Mg 0,61; |
| Garnet (grossular) | 0,00041495216128586 | O 34,91; Ca 19,36; Si 18,36; Al 18,06; Fe 8,95; Mg 0,36; | O 34,91; Ca 19,36; Si 18,36; Al 18,06; Fe 8,95; Mg 0,36; |
| Illite-smectite | 2,10588194708794 | O 37,79; Si 21,81; Al 17,04; Fe 9,98; K 9,94; Mg 2,89; S 0,26; Na 0,19; Ti 0,09; Ca 0,01; P 0 | O 37,79; Si 21,81; Al 17,04; Fe 9,98; K 9,94; Mg 2,89; S 0,26; Na 0,19; Ti 0,09; Ca 0,01; |
| Ilmenite | 0,267920738967241 | Ti 38,32; Fe 36,78; O 24,36; Si 0,3; Al 0,18; Mg 0,07; P 0; Mn 0; | Ti 38,32; Fe 36,78; O 24,36; Si 0,3; Al 0,18; Mg 0,07; P 0; Mn 0; |
| Kaolinite | 0,101248313875294 | O 45,12; Si 32,86; Al 18,53; Mg 2,02; Ca 1,46; Na 0,01; | O 45,12; Si 32,86; Al 18,53; Mg 2,02; Ca 1,46; Na 0,01; |
| KFsp | 0,51454061332106 | O 38,58; Si 24,62; Al 20,77; K 11,02; Fe 3,94; Mg 0,64; Na 0,41; Ca 0,02; Ba 0; | O 38,58; Si 24,62; Al 20,77; K 11,02; Fe 3,94; Mg 0,64; Na 0,41; Ca 0,02; Ba 0; |
| Mg-Fe-chlorite | 0,00124485634008737 | O 54,66; Al 13,41; Si 12,23; Mg 12,01; Fe 7,69; | O 54,66; Al 13,41; Si 12,23; Mg 12,01; Fe 7,69; |
| Muscovite | 19,2079946923273 | O 39,92; Si 25,05; Al 22,97; K 10,87; Fe 0,72; Mg 0,45; Ba 0,01; F 0,01; Ca 0; P 0; | O 39,92; Si 25,05; Al 22,97; K 10,87; Fe 0,72; Mg 0,45; Ba 0,01; F 0,01; Ca 0; P 0; |
| Opx | 0,000138317363133585 | Si 39,82; O 38,01; Fe 16,29; Mg 5,88; | Si 39,82; O 38,01; Fe 16,29; Mg 5,88; |
| Opx (ferrosillite) | 0,00138317363133585 | O 39,8; Si 36,58; Fe 20,41; Al 2,01; Mg 1,2; | O 39,8; Si 36,58; Fe 20,41; Al 2,01; Mg 1,2; |
| Orthoclase | 0,151734153467781 | O 38,29; Si 33,68; Al 17,09; K 9,14; Na 0,95; Fe 0,63; Ca 0,14; Mg 0,07; Ba 0; | O 38,29; Si 33,68; Al 17,09; K 9,14; Na 0,95; Fe 0,63; Ca 0,14; Mg 0,07; Ba 0; |
| Orthoclase+Ba | 0,00124485630414482 | O 36,29; Si 29,62; Al 22,2; K 9,26; Ba 2,51; Mg 0,12; | O 36,29; Si 29,62; Al 22,2; K 9,26; Ba 2,51; Mg 0,12; |
| Plagioclase | 26,1501435545397 | O 38,43; Si 32,78; Al 15,93; Na 7,9; Ca 4,94; K 0,02; | O 38,43; Si 32,78; Al 15,93; Na 7,9; Ca 4,94; K 0,02; |
| Pyrite | 0,113420240429291 | Fe 52,48; S 46,38; O 0,93; Si 0,12; Al 0,06; Mg 0,02; Ti 0; Ca 0; | Fe 52,48; S 46,38; O 0,93; Si 0,12; Al 0,06; Mg 0,02; Ti 0; Ca 0; |
| Pyrite (altered) | 0,00788409020181009 | Fe 50,15; O 31,29; S 17,07; Si 1,23; Al 0,25; Mg 0,01; | Fe 50,15; O 31,29; S 17,07; Si 1,23; Al 0,25; Mg 0,01; |
| Pyrrhotite | 0,0455064134413984 | Fe 65,11; S 33,9; O 0,69; Si 0,21; Al 0,07; Mg 0,02; | Fe 65,11; S 33,9; O 0,69; Si 0,21; Al 0,07; Mg 0,02; |
| Quartz | 21,4148483622787 | Si 59,35; O 40,48; Fe 0,07; Al 0,06; Ce 0,03; La 0,02; | Si 59,35; O 40,48; Fe 0,07; Al 0,06; Ce 0,03; La 0,02; |
| Rutile | 0,163214494068731 | Ti 68,09; O 31,04; Si 0,36; Fe 0,25; Al 0,24; Ca 0,02; | Ti 68,09; O 31,04; Si 0,36; Fe 0,25; Al 0,24; Ca 0,02; |
| Ulvospinel | 0,00276634733455681 | Fe 42,7; Ti 29,51; O 27,79; | Fe 42,7; Ti 29,51; O 27,79; |
| Zircon | 0,0297382344395378 | Zr 57,27; O 21,92; Si 20,24; Al 0,41; Ce 0,04; Sm 0,03; Nd 0,03; Hf 0,02; La 0,02; Ca 0,01; | Zr 57,27; O 21,92; Si 20,24; Al 0,41; Ce 0,04; Sm 0,03; Nd 0,03; Hf 0,02; La 0,02; Ca 0,( |
| Zoisite | 0,00248971257234709 | O 35,03; Ca 21,57; Al 18,72; Si 18,19; Fe 6,36; Mg 0,12; | O 35,03; Ca 21,57; Al 18,72; Si 18,19; Fe 6,36; Mg 0,12; |

| Sample | gmf2020-26A | | |
|---|---|---|---|
| | Area % | Average Composition | Assigned Composition |
| Albite | 0,36301511293783 | Si 37,96; O 35,42; Al 17,58; Na 8,59; Fe 0,22; K 0,14; Ca 0,08; Ti 0; | Si 37,96; O 35,42; Al 17,58; Na 8,59; Fe 0,22; K 0,14; Ca 0,08; Ti 0; |
| Amphibole (Fe-actinolite) | 0,000113442230982593 | O 46,8; Si 27,6; Mg 19,4; Fe 3,6; Ca 2,6; | O 46,8; Si 27,6; Mg 19,4; Fe 3,6; Ca 2,6; |
| Amphibole (Fe-hornblende) | 0,00294949782867581 | O 34,83; Fe 24,19; Si 18,43; Al 12,22; Mg 5,56; Ca 4,44; Ti 0,17; Na 0,15; | O 34,83; Fe 24,19; Si 18,43; Al 12,22; Mg 5,56; Ca 4,44; Ti 0,17; Na 0,15; |
| Anorthite | 0,864883505868006 | O 37,61; Si 35,07; Al 16,17; Ca 6,91; Na 4,08; Fe 0,13; K 0,05; | O 37,61; Si 35,07; Al 16,17; Ca 6,91; Na 4,08; Fe 0,13; K 0,05; |
| Apatite | 0,146567354794555 | Ca 50,99; O 32,37; P 16,33; F 0,27; Nd 0,02; Cl 0,01; Ce 0; | Ca 50,99; O 32,37; P 16,33; F 0,27; Nd 0,02; Cl 0,01; Ce 0; |
| Biotite | 11,601963027978 | O 32,77; Si 19,27; Fe 17,36; Al 12,33; K 9,9; Mg 8,36; Ba 0,01; F 0; | O 32,77; Si 19,27; Fe 17,36; Al 12,33; K 9,9; Mg 8,36; Ba 0,01; F 0; |
| Biotite (annite) | 4,61471618642528 | O 30,63; Fe 22,16; Si 18,42; Al 11,43; K 9,77; Mg 7,58; Ba 0,01; F 0; | O 30,63; Fe 22,16; Si 18,42; Al 11,43; K 9,77; Mg 7,58; Ba 0,01; F 0; |
| Epidote | 0,00045376889445177 | O 38,11; Fe 24,26; Ca 15,07; Si 14,06; Al 8,49; | O 38,11; Fe 24,26; Ca 15,07; Si 14,06; Al 8,49; |
| Fe-Mg-chlorite | 0,468176062002015 | O 35,66; Fe 26,47; Al 13,92; Si 12,61; Mg 11,33; Ca 0; K 0; | O 35,66; Fe 26,47; Al 13,92; Si 12,61; Mg 11,33; Ca 0; K 0; |
| Fe-Oxide | 0,00782751379040588 | Fe 69,84; O 21,59; Si 3,45; S 3,12; Al 1,6; Mg 0,34; Mn 0,03; Ca 0,02; | Fe 69,84; O 21,59; Si 3,45; S 3,12; Al 1,6; Mg 0,34; Mn 0,03; Ca 0,02; |
| Fe-Oxide (altered) | 0,0193986203778365 | Fe 44,52; O 30,3; Si 12,25; Al 8,2; Ca 2,85; Mg 1,16; S 0,53; Mn 0,11; Ti 0,07; As 0,02; | Fe 44,52; O 30,3; Si 12,25; Al 8,2; Ca 2,85; Mg 1,16; S 0,53; Mn 0,11; Ti 0,07; As 0,02; |
| Fe-rich clay | 0,0111173377814147 | O 34,78; Fe 22,29; Si 21,23; Al 16,16; Mg 3,22; Ca 2,24; Na 0,05; Ti 0,02; | O 34,78; Fe 22,29; Si 21,23; Al 16,16; Mg 3,22; Ca 2,24; Na 0,05; Ti 0,02; |
| Garnet (alm+Ca) | 4,13043133322549 | Fe 31,84; O 29,04; Si 18,3; Al 13,95; Ca 4,83; Mg 2,02; Ti 0,01; Zr 0; Mn 0; Cr 0; K 0; | Fe 31,84; O 29,04; Si 18,3; Al 13,95; Ca 4,83; Mg 2,02; Ti 0,01; Zr 0; Mn 0; Cr 0; K 0; |
| Garnet (alm+Mn+Ca) | 0,160520741216714 | Fe 31,97; O 27,88; Si 17,91; Al 13,6; Ca 4,42; Mn 2,6; Mg 1,63; | Fe 31,97; O 27,88; Si 17,91; Al 13,6; Ca 4,42; Mn 2,6; Mg 1,63; |
| Garnet (almandine) | 0,184003282528974 | Fe 35,59; O 27,73; Si 19,51; Al 14,89; Mg 2,05; Mn 0,15; Ca 0,07; Ti 0; Cr 0; | Fe 35,59; O 27,73; Si 19,51; Al 14,89; Mg 2,05; Mn 0,15; Ca 0,07; Ti 0; Cr 0; |
| Garnet (grossular) | 0,0108904533194495 | O 39,29; Ca 20,18; Si 18,04; Al 16,43; Fe 5,87; Mg 0,2; | O 39,29; Ca 20,18; Si 18,04; Al 16,43; Fe 5,87; Mg 0,2; |
| Garnet (pyrope) | 0,000113442230982593 | O 53,93; Si 14,21; Al 11,41; Mg 10,76; Fe 9,69; | O 53,93; Si 14,21; Al 11,41; Mg 10,76; Fe 9,69; |
| Illite-smectite | 0,0954049088277548 | O 35,29; Si 30,64; Al 12,26; Fe 10,44; K 6,3; Mg 3,24; Na 1,17; Ca 0,54; Ti 0,1; S 0,01; P 0; | O 35,29; Si 30,64; Al 12,26; Fe 10,44; K 6,3; Mg 3,24; Na 1,17; Ca 0,54; Ti 0,1; S 0,01; P |
| Ilmenite | 0,217241856501659 | Ti 39,36; Fe 36,73; O 23,22; Si 0,43; Al 0,18; Mg 0,07; Ca 0,01; Mn 0; | Ti 39,36; Fe 36,73; O 23,22; Si 0,43; Al 0,18; Mg 0,07; Ca 0,01; Mn 0; |
| Kaolinite | 0,00419736231052713 | O 40,87; Si 38,7; Al 20,3; Ca 0,13; | O 40,87; Si 38,7; Al 20,3; Ca 0,13; |
| KFsp | 0,0124786444942486 | O 35,49; Si 34,14; Al 16,04; K 8,7; Na 3,99; Fe 0,92; Mg 0,44; Ca 0,27; | O 35,49; Si 34,14; Al 16,04; K 8,7; Na 3,99; Fe 0,92; Mg 0,44; Ca 0,27; |
| Mg-Fe-chlorite | 0,000113442201503993 | O 57,3; Al 14,01; Mg 12,43; Si 10,71; Fe 5,55; | O 57,3; Al 14,01; Mg 12,43; Si 10,71; Fe 5,55; |
| Muscovite | 0,191263592563596 | O 37,55; Si 26,27; Al 23,24; K 11,42; Fe 1,02; Mg 0,47; Ba 0,01; F 0,01; | O 37,55; Si 26,27; Al 23,24; K 11,42; Fe 1,02; Mg 0,47; Ba 0,01; F 0,01; |
| Opx (ferrosillite) | 0,00102098004936473 | Si 38,16; O 36,51; Fe 22,84; Al 1,99; Ca 0,35; Mg 0,14; | Si 38,16; O 36,51; Fe 22,84; Al 1,99; Ca 0,35; Mg 0,14; |
| Orthoclase | 0,0622797807119184 | O 35,52; Si 35,26; Al 14,73; K 12,93; Na 1,21; Fe 0,19; Ca 0,13; Mg 0,03; Ba 0,01; | O 35,52; Si 35,26; Al 14,73; K 12,93; Na 1,21; Fe 0,19; Ca 0,13; Mg 0,03; Ba 0,01; |
| Plagioclase | 55,5453961233669 | O 36,45; Si 33,38; Al 16,7; Na 7,65; Ca 5,81; K 0,01; | O 36,45; Si 33,38; Al 16,7; Na 7,65; Ca 5,81; K 0,01; |
| Pyrite | 0,0089619358054458 | Fe 53,13; S 45,6; O 1,02; Si 0,16; Al 0,08; Mg 0; | Fe 53,13; S 45,6; O 1,02; Si 0,16; Al 0,08; Mg 0; |
| Pyrite (altered) | 0,0374359330110881 | Fe 50,77; S 32,14; O 16,38; Si 0,41; Al 0,13; Ca 0,11; Mg 0,03; Ti 0,01; | Fe 50,77; S 32,14; O 16,38; Si 0,41; Al 0,13; Ca 0,11; Mg 0,03; Ti 0,01; |
| Pyrrhotite | 0,00113442225086873 | Fe 63,74; S 34,8; Si 0,69; O 0,49; Al 0,28; | Fe 63,74; S 34,8; Si 0,69; O 0,49; Al 0,28; |
| Quartz | 19,7008301732603 | Si 61,62; O 38,19; Al 0,08; Fe 0,06; Ce 0,02; La 0,02; | Si 61,62; O 38,19; Al 0,08; Fe 0,06; Ce 0,02; La 0,02; |
| Rutile | 0,344297145827974 | Ti 68,9; O 30,15; Si 0,54; Al 0,21; Fe 0,17; Ca 0,03; P 0; | Ti 68,9; O 30,15; Si 0,54; Al 0,21; Fe 0,17; Ca 0,03; P 0; |
| Rutile2 | 0,0368687225047043 | Ti 99,82; Si 0,11; Al 0,04; O 0,03; | Ti 99,82; Si 0,11; Al 0,04; O 0,03; |
| Ulvospinel | 0,00124786436393692 | Fe 42,89; Ti 32,92; O 24,19; | Fe 42,89; Ti 32,92; O 24,19; |
| Zircon | 0,0266589220994928 | Zr 58,2; Si 20,67; O 20,53; Al 0,47; Nd 0,06; Ca 0,03; Sm 0,03; Ce 0,02; La 0,01; | Zr 58,2; Si 20,67; O 20,53; Al 0,47; Nd 0,06; Ca 0,03; Sm 0,03; Ce 0,02; La 0,01; |
| Zoisite | 0,00941570464094037 | O 33,46; Ca 23,08; Al 18,75; Si 18,66; Fe 5,95; Mg 0,09; Mn 0,02; | O 33,46; Ca 23,08; Al 18,75; Si 18,66; Fe 5,95; Mg 0,09; Mn 0,02; |
| Zoisite-rim | 0,00703341790822033 | O 34; Ca 22,85; Si 18,73; Al 18,5; Fe 5,81; Mg 0,1; Cr 0,02; | O 34; Ca 22,85; Si 18,73; Al 18,5; Fe 5,81; Mg 0,1; Cr 0,02; |

| Sample: | gmf2020-26C | | |
|---|---|---|---|
| | Area % | Average Composition | Assigned Composition |
| Albite | 0,10123369619556 | Si 37,76; O 37,7; Al 15,8; Na 8,42; Ca 0,14; K 0,12; Fe 0,05; | Si 37,76; O 37,7; Al 15,8; Na 8,42; Ca 0,14; K 0,12; Fe 0,05; |
| Anorthite | 2,9199148751624 | O 38,68; Si 31,48; Al 16,59; Ca 9,18; Na 3,93; Fe 0,12; K 0,01; | O 38,68; Si 31,48; Al 16,59; Ca 9,18; Na 3,93; Fe 0,12; K 0,01; |
| Apatite | 0,783848232627576 | Ca 49,49; O 34,34; P 15,88; F 0,27; Nd 0,02; Cl 0,01; Ce 0; La 0; | Ca 49,49; O 34,34; P 15,88; F 0,27; Nd 0,02; Cl 0,01; Ce 0; La 0; |
| Biotite | 0,00249519683342947 | O 35,32; Si 22,87; Fe 15,87; Al 12,13; Mg 7,78; K 6,03; | O 35,32; Si 22,87; Fe 15,87; Al 12,13; Mg 7,78; K 6,03; |
| Biotite (annite) | 0,00427748006092711 | O 34,28; Fe 26,1; Si 18,94; Al 13,26; K 4,14; Mg 3,28; | O 34,28; Fe 26,1; Si 18,94; Al 13,26; K 4,14; Mg 3,28; |
| Calcite | 0,000534684996037477 | Ca 52,56; O 47,05; Mg 0,39; | Ca 52,56; O 47,05; Mg 0,39; |
| Cpx (Augite) | 0,00267342511912832 | O 46,86; Si 20,94; Al 9,35; Fe 8,19; Ca 7,13; Mg 6,14; Na 1,39; | O 46,86; Si 20,94; Al 9,35; Fe 8,19; Ca 7,13; Mg 6,14; Na 1,39; |
| Epidote | 0,0659444852992452 | O 32,82; Fe 29,14; Si 16,14; Ca 12,35; Al 9,52; Mg 0,03; | O 32,82; Fe 29,14; Si 16,14; Ca 12,35; Al 9,52; Mg 0,03; |
| Fe-Mg-chlorite | 0,235974321171469 | O 35,55; Fe 34,46; Al 13,53; Si 11,47; Mg 4,96; Ca 0,01; K 0; | O 35,55; Fe 34,46; Al 13,53; Si 11,47; Mg 4,96; Ca 0,01; K 0; |
| Fe-Oxide | 0,000178228332012492 | Fe 65,66; O 25,52; Si 4,14; Al 3,72; Mg 0,97; | Fe 65,66; O 25,52; Si 4,14; Al 3,72; Mg 0,97; |
| Fe-Oxide (altered) | 0,0103372436735473 | Fe 36,53; O 33,19; Si 12,38; Al 9,61; Ca 5,83; Mg 1,54; Mn 0,73; Ti 0,11; As 0,08; | Fe 36,53; O 33,19; Si 12,38; Al 9,61; Ca 5,83; Mg 1,54; Mn 0,73; Ti 0,11; As 0,08; |
| Fe-rich clay | 0,0073073619367077 | O 34,84; Fe 28,02; Si 16,47; Al 15,43; Mg 3,74; Ca 1,49; Na 0,01; | O 34,84; Fe 28,02; Si 16,47; Al 15,43; Mg 3,74; Ca 1,49; Na 0,01; |
| Garnet (alm+Ca) | 8,6859581062644 | O 31,75; Fe 24,4; Si 18,37; Al 13,93; Ca 9,84; Mg 1,68; Ti 0,01; Mn 0; K 0; Cr 0; Zr 0; | O 31,75; Fe 24,4; Si 18,37; Al 13,93; Ca 9,84; Mg 1,68; Ti 0,01; Mn 0; K 0; Cr 0; Zr 0; |
| Garnet (alm+Mn+Ca) | 2,07350849929467 | O 30,37; Fe 24,42; Si 17,71; Al 13,56; Ca 9,47; Mn 2,89; Mg 1,58; Ti 0; Cr 0; | O 30,37; Fe 24,42; Si 17,71; Al 13,56; Ca 9,47; Mn 2,89; Mg 1,58; Ti 0; Cr 0; |
| Garnet (almandine) | 0,028516534001958 | Fe 39,11; O 31,89; Al 12,92; Si 12,89; Mg 2,75; Mn 0,28; Ca 0,16; | Fe 39,11; O 31,89; Al 12,92; Si 12,89; Mg 2,75; Mn 0,28; Ca 0,16; |
| Garnet (grossular) | 0,12600743527157 | O 42,49; Ca 19,11; Si 18,58; Al 17,28; Fe 2,48; Mg 0,04; Ti 0,02; Cr 0,01; Mn 0; | O 42,49; Ca 19,11; Si 18,58; Al 17,28; Fe 2,48; Mg 0,04; Ti 0,02; Cr 0,01; Mn 0; |
| Illite-smectite | 0,00802027531107131 | O 36,6; Si 27,91; Al 15,66; Fe 9,41; K 8,39; Mg 1,05; Ca 0,68; Na 0,23; Ti 0,07; | O 36,6; Si 27,91; Al 15,66; Fe 9,41; K 8,39; Mg 1,05; Ca 0,68; Na 0,23; Ti 0,07; |
| Ilmenite | 0,000534684996037477 | Ti 36,78; Fe 32,17; O 27,86; Mn 1,42; Si 1,13; Al 0,64; | Ti 36,78; Fe 32,17; O 27,86; Mn 1,42; Si 1,13; Al 0,64; |
| Ilmenite_Mn | 0,00071291332804997 | Ti 37,42; Fe 27,6; O 24,4; Mn 8,82; Ca 1,01; Si 0,45; Al 0,29; | Ti 37,42; Fe 27,6; O 24,4; Mn 8,82; Ca 1,01; Si 0,45; Al 0,29; |
| Kaolinite | 0,00463393677126574 | O 42,43; Si 39,04; Al 17,99; Ca 0,54; | O 42,43; Si 39,04; Al 17,99; Ca 0,54; |
| KFsp | 0,00481216514959187 | O 38,78; Si 31,85; Al 15,43; K 7,56; Na 4,64; Ca 1,28; Fe 0,37; Mg 0,07; | O 38,78; Si 31,85; Al 15,43; K 7,56; Na 4,64; Ca 1,28; Fe 0,37; Mg 0,07; |
| Muscovite | 0,0470522822911756 | O 38,34; Si 25,08; Al 21,98; K 11,24; Fe 2,95; Mg 0,36; Ca 0,02; F 0,02; Ba 0,01; | O 38,34; Si 25,08; Al 21,98; K 11,24; Fe 2,95; Mg 0,36; Ca 0,02; F 0,02; Ba 0,01; |
| Opx (ferrosillite) | 0,000178228332012492 | O 40,74; Si 39,86; Fe 16,23; Al 3,17; | O 40,74; Si 39,86; Fe 16,23; Al 3,17; |
| Orthoclase | 0,0406360609956302 | O 37,58; Si 35,72; Al 13,55; K 11,43; Na 1,21; Ca 0,34; Fe 0,16; Mg 0,01; | O 37,58; Si 35,72; Al 13,55; K 11,43; Na 1,21; Ca 0,34; Fe 0,16; Mg 0,01; |
| Plagioclase | 37,9651313247101 | O 38; Si 31,28; Al 16,87; Na 7; Ca 6,86; K 0; | O 38; Si 31,28; Al 16,87; Na 7; Ca 6,86; K 0; |
| Quartz | 40,1890646989772 | Si 59,47; O 40,37; Al 0,08; Fe 0,04; Ce 0,02; La 0,02; | Si 59,47; O 40,37; Al 0,08; Fe 0,04; Ce 0,02; La 0,02; |
| Rutile | 0,0595282640500134 | Ti 67,08; O 31,66; Si 0,99; Al 0,18; Fe 0,05; Ca 0,04; P 0; | Ti 67,08; O 31,66; Si 0,99; Al 0,18; Fe 0,05; Ca 0,04; P 0; |
| Titanite | 0,545022259996414 | O 33,3; Ca 25,62; Ti 25,45; Si 14,13; Al 1,48; Fe 0,02; Nd 0; | O 33,3; Ca 25,62; Ti 25,45; Si 14,13; Al 1,48; Fe 0,02; Nd 0; |
| Zircon | 0,019783345455464 | Zr 58,01; Si 20,76; O 20,51; Al 0,32; Ca 0,21; Ce 0,09; Sm 0,04; Nd 0,04; La 0,01; | Zr 58,01; Si 20,76; O 20,51; Al 0,32; Ca 0,21; Ce 0,09; Sm 0,04; Nd 0,04; La 0,01; |
| Zoisite | 2,19595136172006 | O 36,6; Ca 23,29; Al 20,88; Si 18,5; Fe 0,69; Cr 0,02; Mg 0,01; Mn 0; Ti 0; K 0; | O 36,6; Ca 23,29; Al 20,88; Si 18,5; Fe 0,69; Cr 0,02; Mg 0,01; Mn 0; Ti 0; K 0; |
| Zoisite-rim | 0,48121651472762 | O 37,02; Ca 23,03; Al 20,05; Si 18,4; Fe 1,45; Cr 0,02; Mg 0,01; Mn 0; Ti 0; | O 37,02; Ca 23,03; Al 20,05; Si 18,4; Fe 1,45; Cr 0,02; Mg 0,01; Mn 0; Ti 0; |

| Sample | gmf2021-07A | | |
|---|---|---|---|
| | Area % | Average Composition | Assigned Composition |
| Albite | 11,2194092276764 | Si 37,81; O 35,84; Al 16,56; Na 9,63; Ca 0,09; Fe 0,04; K 0,03; Ti 0; | Si 37,81; O 35,84; Al 16,56; Na 9,63; Ca 0,09; Fe 0,04; K 0,03; Ti 0; |
| Amphibole (Fe-hornblende) | 0,00189719341041592 | O 35,65; Fe 22,59; Si 18,6; Al 11,11; Ca 6,22; Mg 5,83; | O 35,65; Fe 22,59; Si 18,6; Al 11,11; Ca 6,22; Mg 5,83; |
| Ankerite | 0,000118574613185971 | O 40,79; Fe 37,35; Ca 21,87; | O 40,79; Fe 37,35; Ca 21,87; |
| Anorthite | 0,0845436829943398 | O 39,78; Si 37,35; Al 15,3; Ca 4,7; Na 2,71; Fe 0,12; K 0,04; | O 39,78; Si 37,35; Al 15,3; Ca 4,7; Na 2,71; Fe 0,12; K 0,04; |
| Apatite | 0,757573075774185 | Ca 50,45; O 32,77; P 16,43; F 0,3; Cl 0,03; Nd 0,02; Ce 0; La 0; | Ca 50,45; O 32,77; P 16,43; F 0,3; Cl 0,03; Nd 0,02; Ce 0; La 0; |
| Biotite | 9,16403730181222 | O 33,89; Si 18,87; Fe 17,65; Al 12,36; K 9,35; Mg 7,87; Ba 0,01; F 0; | O 33,89; Si 18,87; Fe 17,65; Al 12,36; K 9,35; Mg 7,87; Ba 0,01; F 0; |
| Biotite (annite) | 5,48039904109686 | O 31,78; Fe 22,22; Si 18,1; Al 11,51; K 9,21; Mg 7,17; Ba 0,01; F 0; | O 31,78; Fe 22,22; Si 18,1; Al 11,51; K 9,21; Mg 7,17; Ba 0,01; F 0; |
| Epidote | 0,000118574582373693 | O 38,36; Fe 20,82; Ca 15,9; Si 15,08; Al 9,84; | O 38,36; Fe 20,82; Ca 15,9; Si 15,08; Al 9,84; |
| Fe-Mg-chlorite | 0,704688782086008 | O 36,63; Fe 26,98; Al 13,66; Si 12,2; Mg 10,53; K 0; Ca 0; | O 36,63; Fe 26,98; Al 13,66; Si 12,2; Mg 10,53; K 0; Ca 0; |
| Fe-Oxide (altered) | 0,0058101550293074 | Fe 40,88; O 31,99; Si 13,71; Al 9,33; Ca 1,84; Mn 1,13; Mg 0,85; Ti 0,27; | Fe 40,88; O 31,99; Si 13,71; Al 9,33; Ca 1,84; Mn 1,13; Mg 0,85; Ti 0,27; |
| Fe-rich clay | 0,0368766976756374 | O 34,45; Fe 25,25; Si 20,14; Al 15,41; Mg 3,68; Ca 1,02; Na 0,05; Ti 0,01; | O 34,45; Fe 25,25; Si 20,14; Al 15,41; Mg 3,68; Ca 1,02; Na 0,05; Ti 0,01; |
| Garnet (alm+Ca) | 1,15432364334036 | Fe 32,84; O 30,07; Si 18,22; Al 13,79; Ca 2,78; Mg 2,28; Ti 0,01; Mn 0; Cr 0; K 0; | Fe 32,84; O 30,07; Si 18,22; Al 13,79; Ca 2,78; Mg 2,28; Ti 0,01; Mn 0; Cr 0; K 0; |
| Garnet (alm+Mn+Ca) | 0,224935997152229 | Fe 32,24; O 29,13; Si 17,59; Al 13,4; Ca 2,87; Mn 2,81; Mg 1,94; Ti 0,01; Cr 0; | Fe 32,24; O 29,13; Si 17,59; Al 13,4; Ca 2,87; Mn 2,81; Mg 1,94; Ti 0,01; Cr 0; |
| Garnet (almandine) | 1,37819247424297 | Fe 35; O 29,17; Si 18,55; Al 14,21; Mg 2,34; Mn 0,37; Ca 0,36; K 0; Zr 0; Ti 0; Cr 0; | Fe 35; O 29,17; Si 18,55; Al 14,21; Mg 2,34; Mn 0,37; Ca 0,36; K 0; Zr 0; Ti 0; Cr 0; |
| Garnet (andradite) | 0,000118574582373693 | O 39,47; Ca 21,64; Fe 18,86; Si 14,04; Al 3,51; Mg 2,49; | O 39,47; Ca 21,64; Fe 18,86; Si 14,04; Al 3,51; Mg 2,49; |
| Garnet (grossular) | 0,00379438706733007 | O 40,78; Si 19,79; Ca 18,21; Al 15,71; Fe 5,12; Mg 0,4; | O 40,78; Si 19,79; Ca 18,21; Al 15,71; Fe 5,12; Mg 0,4; |
| Illite-smectite | 0,0955711205416463 | O 36,31; Si 29,58; Al 12,12; Fe 10,64; K 6,75; Mg 3,26; Na 1,2; Ti 0,1; Ca 0,03; P 0; | O 36,31; Si 29,58; Al 12,12; Fe 10,64; K 6,75; Mg 3,26; Na 1,2; Ti 0,1; Ca 0,03; P 0; |
| Ilmenite | 0,571766672133104 | Ti 39,37; Fe 36,93; O 23,05; Si 0,43; Al 0,15; Mg 0,05; Ca 0,02; Mn 0; P 0; | Ti 39,37; Fe 36,93; O 23,05; Si 0,43; Al 0,15; Mg 0,05; Ca 0,02; Mn 0; P 0; |
| Kaolinite | 0,0218177246357488 | Si 41,35; O 40,86; Al 17,72; Mg 0,04; Ca 0,03; Na 0; | Si 41,35; O 40,86; Al 17,72; Mg 0,04; Ca 0,03; Na 0; |
| KFsp | 0,0449397702630415 | O 36,93; Si 34,12; Al 15,05; K 8,12; Na 5,16; Fe 0,36; Mg 0,23; Ca 0,02; | O 36,93; Si 34,12; Al 15,05; K 8,12; Na 5,16; Fe 0,36; Mg 0,23; Ca 0,02; |
| Mg-Fe-chlorite | 0,000355723747121078 | O 52,74; Al 14,65; Si 13,42; Mg 11,59; Fe 7,6; | O 52,74; Al 14,65; Si 13,42; Mg 11,59; Fe 7,6; |
| Monazite_Ce | 0,00225291721916155 | Ce 39,72; O 23,59; P 19,85; Nd 14,52; La 1,22; Ca 1,1; | Ce 39,72; O 23,59; P 19,85; Nd 14,52; La 1,22; Ca 1,1; |
| Monazite_Ce_La_Nd | 0,000118574582373693 | Ce 34,97; La 18,88; P 16,08; O 15,38; Nd 14,69; | Ce 34,97; La 18,88; P 16,08; O 15,38; Nd 14,69; |
| Muscovite | 1,76344130694958 | O 39,14; Si 25,7; Al 23,81; K 10,63; Fe 0,39; Mg 0,31; Ba 0,01; F 0,01; Ca 0; | O 39,14; Si 25,7; Al 23,81; K 10,63; Fe 0,39; Mg 0,31; Ba 0,01; F 0,01; Ca 0; |
| Opx (ferrosillite) | 0,00166004424566853 | O 41,6; Si 34,37; Fe 23,86; Al 0,1; Mg 0,08; | O 41,6; Si 34,37; Fe 23,86; Al 0,1; Mg 0,08; |
| Orthoclase | 0,185687808260492 | O 36,11; Si 35,44; Al 13,67; K 13,38; Na 1,23; Fe 0,14; Mg 0,02; Ca 0,01; Ba 0; | O 36,11; Si 35,44; Al 13,67; K 13,38; Na 1,23; Fe 0,14; Mg 0,02; Ca 0,01; Ba 0; |
| Orthoclase+Ba | 0,000118574582373693 | O 36,67; Si 33,67; Al 16; K 10,67; Ba 3; | O 36,67; Si 33,67; Al 16; K 10,67; Ba 3; |
| Plagioclase | 48,7269238629079 | O 37,7; Si 34,57; Al 15,4; Na 8,73; Ca 3,59; K 0,01; | O 37,7; Si 34,57; Al 15,4; Na 8,73; Ca 3,59; K 0,01; |
| Quartz | 16,9504749847065 | Si 60,44; O 39,38; Al 0,08; Fe 0,05; Ce 0,03; La 0,02; | Si 60,44; O 39,38; Al 0,08; Fe 0,05; Ce 0,03; La 0,02; |
| Rutile | 0,068536112771652 | Ti 67,88; O 30,71; Si 0,67; Fe 0,37; Al 0,34; Ca 0,03; P 0; | Ti 67,88; O 30,71; Si 0,67; Fe 0,37; Al 0,34; Ca 0,03; P 0; |
| Rutile2 | 0,00794449760447069 | Ti 99,84; Al 0,08; Si 0,05; Fe 0,03; | Ti 99,84; Al 0,08; Si 0,05; Fe 0,03; |
| Titanite | 0,000118574613185971 | O 37,78; Ca 23,39; Ti 21,14; Si 14,24; Al 3,45; | O 37,78; Ca 23,39; Ti 21,14; Si 14,24; Al 3,45; |
| Ulvospinel | 0,0028457900077809 | Fe 44; Ti 31,27; O 24,73; | Fe 44; Ti 31,27; O 24,73; |
| Xenotime (Y) | 0,000118574582373693 | Y 44,11; O 26,6; P 23,57; Si 5,72; | Y 44,11; O 26,6; P 23,57; Si 5,72; |
| Zircon | 0,0195648074165872 | Zr 57,28; O 21,2; Si 20,7; Al 0,57; Hf 0,09; La 0,05; Nd 0,04; Sm 0,04; Ce 0,03; | Zr 57,28; O 21,2; Si 20,7; Al 0,57; Hf 0,09; La 0,05; Nd 0,04; Sm 0,04; Ce 0,03; |
| Zoisite | 0,000355723747121078 | O 35,96; Ca 20,16; Si 18,17; Al 17,87; Fe 7,85; | O 35,96; Ca 20,16; Si 18,17; Al 17,87; Fe 7,85; |

| Sample | gmf2021-11A | | |
|---|---|---|---|
| | Area % | Average Composition | Assigned Composition |
| Albite | 4,6214471367455 | Si 38,57; O 34,93; Al 16,54; Na 9,74; Ca 0,12; K 0,06; Fe 0,04; Ti 0; | Si 38,57; O 34,93; Al 16,54; Na 9,74; Ca 0,12; K 0,06; Fe 0,04; Ti 0; |
| Amphibole (Fe-hornblende) | 0,00456225202891733 | O 34,56; Fe 26,82; Si 16,66; Al 11,78; Mg 5,73; Ca 4,1; Ti 0,13; Mn 0,12; Na 0,12; | O 34,56; Fe 26,82; Si 16,66; Al 11,78; Mg 5,73; Ca 4,1; Ti 0,13; Mn 0,12; Na 0,12; |
| Anorthite | 0,327683745449928 | O 38,3; Si 35,34; Al 16,05; Ca 6,49; Na 3,56; Fe 0,15; K 0,11; | O 38,3; Si 35,34; Al 16,05; Ca 6,49; Na 3,56; Fe 0,15; K 0,11; |
| Apatite | 0,298029102386482 | Ca 50,5; O 32,87; P 16,28; F 0,31; Nd 0,02; Cl 0,01; Ce 0; La 0; | Ca 50,5; O 32,87; P 16,28; F 0,31; Nd 0,02; Cl 0,01; Ce 0; La 0; |
| Biotite | 5,58556508647751 | O 32,81; Si 19,08; Fe 17,98; Al 12,52; K 10,08; Mg 7,53; Ba 0,01; F 0; | O 32,81; Si 19,08; Fe 17,98; Al 12,52; K 10,08; Mg 7,53; Ba 0,01; F 0; |
| Biotite (annite) | 5,69232177241879 | O 30,6; Fe 22,51; Si 18,27; Al 11,73; K 10,01; Mg 6,88; Ba 0,01; F 0; | O 30,6; Fe 22,51; Si 18,27; Al 11,73; K 10,01; Mg 6,88; Ba 0,01; F 0; |
| Calcite | 0,000114056305909613 | Ca 51,28; O 44,34; Fe 4,38; | Ca 51,28; O 44,34; Fe 4,38; |
| Epidote | 0,00250923858182063 | O 31,49; Fe 29,75; Si 16,49; Ca 12,5; Al 9,72; Mg 0,04; | O 31,49; Fe 29,75; Si 16,49; Ca 12,5; Al 9,72; Mg 0,04; |
| Fe-Mg-chlorite | 1,07954285446279 | O 34,82; Fe 30,44; Al 13,72; Si 12,24; Mg 8,76; Ca 0,01; K 0,01; | O 34,82; Fe 30,44; Al 13,72; Si 12,24; Mg 8,76; Ca 0,01; K 0,01; |
| Fe-Oxide | 0,00285140744027313 | Fe 69,44; O 24,12; Si 4,57; Al 1,28; S 0,59; | Fe 69,44; O 24,12; Si 4,57; Al 1,28; S 0,59; |
| Fe-Oxide (altered) | 0,0223550344763756 | Fe 40,09; O 30,8; Si 12,98; Al 9,45; Ca 4,45; Mn 1,19; Mg 0,98; Ti 0,04; P 0,01; Ni 0,01; As | Fe 40,09; O 30,8; Si 12,98; Al 9,45; Ca 4,45; Mn 1,19; Mg 0,98; Ti 0,04; P 0,01; Ni 0,01; |
| Fe-rich clay | 0,0136867557310939 | O 35,43; Fe 24,08; Si 19,75; Al 15,59; Mg 3,45; Ca 1,54; Na 0,13; Ti 0,03; | O 35,43; Fe 24,08; Si 19,75; Al 15,59; Mg 3,45; Ca 1,54; Na 0,13; Ti 0,03; |
| Garnet (alm+Ca) | 3,23988320089201 | Fe 30,01; O 29,63; Si 18,64; Al 14,04; Ca 6,22; Mg 1,44; Mn 0,01; Ti 0; K 0; Cr 0; Zr 0; | Fe 30,01; O 29,63; Si 18,64; Al 14,04; Ca 6,22; Mg 1,44; Mn 0,01; Ti 0; K 0; Cr 0; Zr 0; |
| Garnet (alm+Mn+Ca) | 1,21618230947604 | Fe 29,93; O 28,28; Si 17,88; Al 13,51; Ca 6,22; Mn 2,93; Mg 1,25; Ti 0; Zr 0; | Fe 29,93; O 28,28; Si 17,88; Al 13,51; Ca 6,22; Mn 2,93; Mg 1,25; Ti 0; Zr 0; |
| Garnet (almandine) | 0,0810940261514694 | Fe 37,54; O 29,41; Si 16,14; Al 14,09; Mg 2,46; Mn 0,27; Ca 0,07; Ti 0,01; Cr 0; | Fe 37,54; O 29,41; Si 16,14; Al 14,09; Mg 2,46; Mn 0,27; Ca 0,07; Ti 0,01; Cr 0; |
| Garnet (grossular) | 0,013914868668933 | O 37,88; Si 20,47; Ca 17,9; Al 17,28; Fe 6,4; Mg 0,06; | O 37,88; Si 20,47; Ca 17,9; Al 17,28; Fe 6,4; Mg 0,06; |
| Illite-smectite | 0,0926137141153151 | O 36,35; Si 28,17; Al 13,46; Fe 10,73; K 7,2; Mg 2,86; Na 0,9; Ca 0,24; Ti 0,1; | O 36,35; Si 28,17; Al 13,46; Fe 10,73; K 7,2; Mg 2,86; Na 0,9; Ca 0,24; Ti 0,1; |
| Ilmenite | 0,31753273134907 | Ti 39,88; Fe 36,45; O 23,06; Si 0,33; Al 0,14; Mn 0,07; Mg 0,05; Ca 0,01; P 0; | Ti 39,88; Fe 36,45; O 23,06; Si 0,33; Al 0,14; Mn 0,07; Mg 0,05; Ca 0,01; P 0; |
| Ilmenite_Mn | 0,000456225164362111 | Ti 40,32; Fe 25,75; O 23,5; Mn 9,67; Al 0,38; Si 0,38; | Ti 40,32; Fe 25,75; O 23,5; Mn 9,67; Al 0,38; Si 0,38; |
| Kaolinite | 0,00889639117927188 | O 42; Si 38,61; Al 19,23; Ca 0,15; Mg 0,01; | O 42; Si 38,61; Al 19,23; Ca 0,15; Mg 0,01; |
| KFsp | 0,0402618735557634 | O 36,42; Si 33; Al 17,32; K 7,63; Na 4,62; Fe 0,5; Mg 0,26; Ca 0,24; Ba 0,01; | O 36,42; Si 33; Al 17,32; K 7,63; Na 4,62; Fe 0,5; Mg 0,26; Ca 0,24; Ba 0,01; |
| Monazite_Ce | 0,000342168888090668 | Ce 34,45; O 26,85; Ca 20,49; P 9,84; La 8,37; | Ce 34,45; O 26,85; Ca 20,49; P 9,84; La 8,37; |
| Muscovite | 0,61282447442105 | O 37,54; Si 26,12; Al 22,98; K 11,43; Fe 1,49; Mg 0,43; F 0,01; Ba 0; | O 37,54; Si 26,12; Al 22,98; K 11,43; Fe 1,49; Mg 0,43; F 0,01; Ba 0; |
| Opx (ferrosillite) | 0,00171084447009151 | O 39,49; Si 34,78; Fe 24,52; Al 0,95; Mg 0,26; | O 39,49; Si 34,78; Fe 24,52; Al 0,95; Mg 0,26; |
| Orthoclase | 0,123751083198311 | O 36,24; Si 34,6; Al 17,08; K 9,7; Na 2,01; Fe 0,25; Ca 0,08; Mg 0,03; | O 36,24; Si 34,6; Al 17,08; K 9,7; Na 2,01; Fe 0,25; Ca 0,08; Mg 0,03; |
| Orthoclase+Ba | 0,000342168917728839 | O 33,32; Si 33,24; Al 19,81; K 7,79; Ba 2,86; Na 2,58; Mg 0,41; | O 33,32; Si 33,24; Al 19,81; K 7,79; Ba 2,86; Na 2,58; Mg 0,41; |
| Plagioclase | 50,6136229900943 | O 36,64; Si 34,27; Al 16,16; Na 8,22; Ca 4,71; K 0,01; | O 36,64; Si 34,27; Al 16,16; Na 8,22; Ca 4,71; K 0,01; |
| Quartz | 24,4335962717664 | Si 61,54; O 38,25; Al 0,09; Fe 0,06; Ce 0,03; La 0,02; | Si 61,54; O 38,25; Al 0,09; Fe 0,06; Ce 0,03; La 0,02; |
| Rutile | 0,0400337595509502 | Ti 66,92; O 31,07; Si 0,85; Fe 0,75; Al 0,39; Ca 0,03; | Ti 66,92; O 31,07; Si 0,85; Fe 0,75; Al 0,39; Ca 0,03; |
| Rutile2 | 0,00319357620981112 | Ti 99,84; Si 0,12; Al 0,03; | Ti 99,84; Si 0,12; Al 0,03; |
| Titanite | 0,00547470247619423 | O 31,99; Ca 25,84; Ti 25,25; Si 14,64; Al 2,18; Fe 0,1; | O 31,99; Ca 25,84; Ti 25,25; Si 14,64; Al 2,18; Fe 0,1; |
| Ulvospinel | 0,0013686755227245 | Fe 42,65; Ti 31,48; O 25,87; | Fe 42,65; Ti 31,48; O 25,87; |
| Zircon | 0,0124321364550027 | Zr 57,92; Si 21,02; O 20,45; Al 0,41; Sm 0,07; Nd 0,06; Ce 0,04; Ca 0,03; | Zr 57,92; Si 21,02; O 20,45; Al 0,41; Sm 0,07; Nd 0,06; Ce 0,04; Ca 0,03; |
| Zoisite | 0,00216706966409179 | O 35,24; Ca 20,48; Si 18,43; Al 17,92; Fe 7,93; | O 35,24; Ca 20,48; Si 18,43; Al 17,92; Fe 7,93; |
| Zoisite-rim | 0,00125461921681489 | O 34,39; Ca 21,72; Si 18,91; Al 17,88; Fe 7,1; | O 34,39; Ca 21,72; Si 18,91; Al 17,88; Fe 7,1; |

| Sample | gmf2021-11B | | |
|---|---|---|---|
| | Area % | Average Composition | Assigned Composition |
| Albite | 4,01510700083463 | Si 37,51; O 36,4; Al 16,43; Na 9,37; Fe 0,14; Ca 0,09; K 0,06; Ti 0; | Si 37,51; O 36,4; Al 16,43; Na 9,37; Fe 0,14; Ca 0,09; K 0,06; Ti 0; |
| Anorthite | 0,177648430386302 | O 40,02; Si 36,05; Al 15,03; Ca 5,14; Na 3,64; Fe 0,1; K 0,02; | O 40,02; Si 36,05; Al 15,03; Ca 5,14; Na 3,64; Fe 0,1; K 0,02; |
| Apatite | 0,229749455823528 | Ca 49,89; O 33,44; P 16,31; F 0,33; Nd 0,02; Cl 0; Ce 0; | Ca 49,89; O 33,44; P 16,31; F 0,33; Nd 0,02; Cl 0; Ce 0; |
| Biotite | 8,14462970035925 | O 34,08; Si 18,62; Fe 17,93; Al 12,2; K 9,79; Mg 7,37; Ba 0,01; F 0; | O 34,08; Si 18,62; Fe 17,93; Al 12,2; K 9,79; Mg 7,37; Ba 0,01; F 0; |
| Biotite (annite) | 7,3570320397458 | O 31,93; Fe 22,36; Si 17,85; Al 11,38; K 9,8; Mg 6,68; Ba 0,01; F 0; | O 31,93; Fe 22,36; Si 17,85; Al 11,38; K 9,8; Mg 6,68; Ba 0,01; F 0; |
| Cpx (Augite) | 0,000114759963653883 | O 40,66; Si 25,14; Fe 10,63; Ca 10,49; Al 8,33; Mg 4,74; | O 40,66; Si 25,14; Fe 10,63; Ca 10,49; Al 8,33; Mg 4,74; |
| Epidote | 0,000114759993474911 | Fe 34,75; O 30,82; Ca 14,26; Si 11,31; Al 8,85; | Fe 34,75; O 30,82; Ca 14,26; Si 11,31; Al 8,85; |
| Fe-Mg-chlorite | 0,994854158523696 | O 36,54; Fe 29,26; Al 13,2; Si 12,01; Mg 8,97; K 0,02; Ca 0; | O 36,54; Fe 29,26; Al 13,2; Si 12,01; Mg 8,97; K 0,02; Ca 0; |
| Fe-Oxide | 0,00929555747345889 | Fe 67; O 24,45; Si 5,84; Al 2,27; Mg 0,3; S 0,13; Ca 0,02; | Fe 67; O 24,45; Si 5,84; Al 2,27; Mg 0,3; S 0,13; Ca 0,02; |
| Fe-Oxide (altered) | 0,0348870306803999 | Fe 46,35; O 31,09; Si 11,44; Al 7,95; Ca 1,31; Mg 1,29; Mn 0,37; Ti 0,15; As 0,04; P 0,01; | Fe 46,35; O 31,09; Si 11,44; Al 7,95; Ca 1,31; Mg 1,29; Mn 0,37; Ti 0,15; As 0,04; P 0,0 |
| Fe-rich clay | 0,0430349879805415 | O 36,69; Fe 23,54; Si 18,5; Al 15,94; Ca 2,84; Mg 2,4; Na 0,07; Ti 0,03; | O 36,69; Fe 23,54; Si 18,5; Al 15,94; Ca 2,84; Mg 2,4; Na 0,07; Ti 0,03; |
| Garnet (almandine) | 4,17852520482331 | Fe 32,94; O 30,2; Si 18,06; Al 13,7; Ca 2,77; Mg 2,01; Mn 0,29; K 0,01; Ti 0,01; Zr 0,01; Cr | Fe 32,94; O 30,2; Si 18,06; Al 13,7; Ca 2,77; Mg 2,01; Mn 0,29; K 0,01; Ti 0,01; Zr 0,01; |
| Garnet (andradite) | 0,00286899915098913 | O 33,35; Si 18,9; Fe 16,28; Al 16,25; Ca 14,52; Mg 0,69; | O 33,35; Si 18,9; Fe 16,28; Al 16,25; Ca 14,52; Mg 0,69; |
| Garnet (grossular) | 0,000573799848090442 | O 36,12; Si 21,13; Al 17,54; Ca 17,41; Fe 7,8; | O 36,12; Si 21,13; Al 17,54; Ca 17,41; Fe 7,8; |
| Garnet (spessartine) | 0,000229519927307766 | O 32,38; Mn 28,17; Si 20,22; Al 19,23; | O 32,38; Mn 28,17; Si 20,22; Al 19,23; |
| Illite-smectite | 0,31536039252642 | O 37,98; Si 27,13; Fe 11,76; Al 11,5; K 6,71; Mg 3,62; Na 1,16; Ti 0,13; Ca 0,01; S 0; | O 37,98; Si 27,13; Fe 11,76; Al 11,5; K 6,71; Mg 3,62; Na 1,16; Ti 0,13; Ca 0,01; S 0; |
| Ilmenite | 0,443317754952804 | Ti 39,37; Fe 36,05; O 24,12; Si 0,29; Al 0,11; Mg 0,04; Mn 0,01; P 0; | Ti 39,37; Fe 36,05; O 24,12; Si 0,29; Al 0,11; Mg 0,04; Mn 0,01; P 0; |
| Kaolinite | 0,158598275674233 | O 44,57; Si 33,56; Al 17,49; Ca 2,47; Mg 1,89; Na 0,01; | O 44,57; Si 33,56; Al 17,49; Ca 2,47; Mg 1,89; Na 0,01; |
| KFsp | 0,0322475515163606 | O 37,4; Si 29,02; Al 18,46; K 9,46; Na 2,59; Fe 2,44; Mg 0,57; Ca 0,07; | O 37,4; Si 29,02; Al 18,46; K 9,46; Na 2,59; Fe 2,44; Mg 0,57; Ca 0,07; |
| Mg-Fe-chlorite | 0,000114759963653883 | O 55,21; Al 14,25; Si 11,75; Mg 11,31; Fe 7,48; | O 55,21; Al 14,25; Si 11,75; Mg 11,31; Fe 7,48; |
| Muscovite | 0,125547404680684 | O 39,3; Si 26,48; Al 21,92; K 10,71; Fe 1,09; Mg 0,48; F 0,01; | O 39,3; Si 26,48; Al 21,92; K 10,71; Fe 1,09; Mg 0,48; F 0,01; |
| Opx | 0,000114759963653883 | O 39,05; Si 26,44; Mg 19,09; Fe 12,78; Al 2,63; | O 39,05; Si 26,44; Mg 19,09; Fe 12,78; Al 2,63; |
| Opx (ferrosillite) | 0,00539371850047969 | O 40,45; Si 34,83; Fe 23,42; Al 0,87; Mg 0,21; Na 0,16; Ca 0,07; | O 40,45; Si 34,83; Fe 23,42; Al 0,87; Mg 0,21; Na 0,16; Ca 0,07; |
| Orthoclase | 0,0833157368930327 | O 37,31; Si 34,96; Al 15,13; K 11,02; Na 1,25; Fe 0,28; Mg 0,04; Ca 0,02; | O 37,31; Si 34,96; Al 15,13; K 11,02; Na 1,25; Fe 0,28; Mg 0,04; Ca 0,02; |
| Orthoclase+Ba | 0,000344279890961649 | O 38,09; Si 32,38; Al 18,69; K 8,14; Ba 2,69; | O 38,09; Si 32,38; Al 18,69; K 8,14; Ba 2,69; |
| Plagioclase | 46,9040055874814 | O 38,12; Si 33,56; Al 15,71; Na 8,23; Ca 4,35; K 0,03; | O 38,12; Si 33,56; Al 15,71; Na 8,23; Ca 4,35; K 0,03; |
| Pyrrhotite | 0,000114759963653883 | Fe 63,64; S 35,04; Si 1,32; | Fe 63,64; S 35,04; Si 1,32; |
| Quartz | 25,4920907216037 | Si 59,78; O 40; Fe 0,09; Al 0,08; Ce 0,03; La 0,02; | Si 59,78; O 40; Fe 0,09; Al 0,08; Ce 0,03; La 0,02; |
| Rutile | 0,0278866719730612 | Ti 65,96; O 32,27; Si 0,99; Fe 0,41; Al 0,37; | Ti 65,96; O 32,27; Si 0,99; Fe 0,41; Al 0,37; |
| Ulvospinel | 0,00298375923392712 | Fe 41,91; Ti 31,03; O 27,06; | Fe 41,91; Ti 31,03; O 27,06; |
| Xenotime (Y) | 0,00045903988443656 | Y 40,35; O 32,48; P 25,39; Al 1,78; | Y 40,35; O 32,48; P 25,39; Al 1,78; |
| Zircon | 0,0177877952908037 | Zr 56,11; O 22,18; Si 21,01; Al 0,6; La 0,05; Sm 0,02; Ca 0,02; Ce 0,01; Th 0; | Zr 56,11; O 22,18; Si 21,01; Al 0,6; La 0,05; Sm 0,02; Ca 0,02; Ce 0,01; Th 0; |
| Zoisite | 0,000573799818269414 | O 35,11; Ca 20,5; Si 19,06; Al 17,81; Fe 7,25; Mg 0,26; | O 35,11; Ca 20,5; Si 19,06; Al 17,81; Fe 7,25; Mg 0,26; |

| Sample: | gmf2021-11C | | |
|---|---|---|---|
| | Area % | Average Composition | Assigned Composition |
| Albite | 1,56352607893467 | Si 37,44; O 36,17; Al 16,9; Na 9,17; K 0,12; Fe 0,12; Ca 0,06; Ti 0; | Si 37,44; O 36,17; Al 16,9; Na 9,17; K 0,12; Fe 0,12; Ca 0,06; Ti 0; |
| Amphibole (Fe-hornblende) | 0,000983813812824319 | O 37,61; Fe 24,76; Si 13,95; Al 11,31; Mg 6,41; Ca 5,96; | O 37,61; Fe 24,76; Si 13,95; Al 11,31; Mg 6,41; Ca 5,96; |
| Anorthite | 0,070096733276949 | O 40,41; Si 36,13; Al 14,88; Ca 4,99; Na 3,25; K 0,24; Fe 0,09; | O 40,41; Si 36,13; Al 14,88; Ca 4,99; Na 3,25; K 0,24; Fe 0,09; |
| Apatite | 0,476165879399223 | Ca 49,99; O 33,22; P 16,42; F 0,32; Cl 0,02; Nd 0,02; Ce 0; La 0; | Ca 49,99; O 33,22; P 16,42; F 0,32; Cl 0,02; Nd 0,02; Ce 0; La 0; |
| Biotite | 7,84911247904957 | O 34,12; Si 18,53; Fe 18,02; Al 12,38; K 9,81; Mg 7,13; Ba 0,01; F 0; | O 34,12; Si 18,53; Fe 18,02; Al 12,38; K 9,81; Mg 7,13; Ba 0,01; F 0; |
| Biotite (annite) | 8,72679737515598 | O 32,03; Fe 22,48; Si 17,75; Al 11,49; K 9,77; Mg 6,48; Ba 0,01; F 0; | O 32,03; Fe 22,48; Si 17,75; Al 11,49; K 9,77; Mg 6,48; Ba 0,01; F 0; |
| Cpx (Hedenbergite) | 0,000122976698641371 | Si 31,1; Fe 29,84; O 27,67; Ca 8,86; Al 2,53; | Si 31,1; Fe 29,84; O 27,67; Ca 8,86; Al 2,53; |
| Epidote | 0,000491906890434063 | O 36,56; Fe 25,33; Ca 14,8; Si 14,48; Al 8,64; Mg 0,18; | O 36,56; Fe 25,33; Ca 14,8; Si 14,48; Al 8,64; Mg 0,18; |
| Fe-Mg-chlorite | 1,43649113984292 | O 36,88; Fe 28,47; Al 13,37; Si 11,91; Mg 9,36; K 0,02; Ca 0; | O 36,88; Fe 28,47; Al 13,37; Si 11,91; Mg 9,36; K 0,02; Ca 0; |
| Fe-Oxide | 0,0129125563931823 | Fe 70,11; O 24,69; Si 3,38; Al 1,64; Mg 0,17; S 0,01; | Fe 70,11; O 24,69; Si 3,38; Al 1,64; Mg 0,17; S 0,01; |
| Fe-Oxide (altered) | 0,0349253904351537 | Fe 47,64; O 30,71; Si 10,8; Al 7,97; Ca 1,5; Mg 0,89; Mn 0,34; Ti 0,06; P 0,06; As 0,02; Ni ( | Fe 47,64; O 30,71; Si 10,8; Al 7,97; Ca 1,5; Mg 0,89; Mn 0,34; Ti 0,06; P 0,06; As 0,02; |
| Fe-rich clay | 0,0170937648819813 | O 36,86; Fe 24,12; Si 19,55; Al 15,4; Mg 3,04; Ca 0,99; Na 0,04; | O 36,86; Fe 24,12; Si 19,55; Al 15,4; Mg 3,04; Ca 0,99; Na 0,04; |
| Garnet (alm+Ca) | 2,36090720281405 | Fe 32,98; O 30,39; Si 18,06; Al 13,6; Ca 3,15; Mg 1,8; Ti 0,01; Zr 0; Mn 0; Cr 0; K 0; | Fe 32,98; O 30,39; Si 18,06; Al 13,6; Ca 3,15; Mg 1,8; Ti 0,01; Zr 0; Mn 0; Cr 0; K 0; |
| Garnet (alm+Mn+Ca) | 0,299571299501927 | Fe 32,06; O 29,41; Si 17,52; Al 13,2; Ca 3,65; Mn 2,73; Mg 1,42; Zr 0,01; Ti 0,01; | Fe 32,06; O 29,41; Si 17,52; Al 13,2; Ca 3,65; Mn 2,73; Mg 1,42; Zr 0,01; Ti 0,01; |
| Garnet (almandine) | 1,46772723551835 | Fe 35,56; O 29,34; Si 18,4; Al 14,17; Mg 2,01; Ca 0,36; Mn 0,16; Ti 0; Cr 0; K 0; | Fe 35,56; O 29,34; Si 18,4; Al 14,17; Mg 2,01; Ca 0,36; Mn 0,16; Ti 0; Cr 0; K 0; |
| Garnet (grossular) | 0,001475720639346 | O 38,69; Si 18,62; Ca 18,15; Al 16,94; Fe 7,6; | O 38,69; Si 18,62; Ca 18,15; Al 16,94; Fe 7,6; |
| Illite-smectite | 1,79865758435412 | O 36,98; Si 22,22; Al 16,35; Fe 11,15; K 9,89; Mg 3,1; Na 0,21; Ti 0,09; Ca 0; P 0; S 0; | O 36,98; Si 22,22; Al 16,35; Fe 11,15; K 9,89; Mg 3,1; Na 0,21; Ti 0,09; Ca 0; P 0; S 0; |
| Ilmenite | 0,285797912481667 | Ti 39,07; Fe 36,31; O 24,26; Si 0,2; Al 0,12; Mg 0,04; Mn 0; Ca 0; P 0; | Ti 39,07; Fe 36,31; O 24,26; Si 0,2; Al 0,12; Mg 0,04; Mn 0; Ca 0; P 0; |
| Kaolinite | 0,00430418550700236 | O 40,47; Si 39,14; Al 20,25; Ca 0,14; | O 40,47; Si 39,14; Al 20,25; Ca 0,14; |
| KFsp | 0,110187146205465 | O 40,53; Si 27,27; Al 18,31; K 11,83; Na 0,87; Fe 0,75; Mg 0,37; Ca 0,07; | O 40,53; Si 27,27; Al 18,31; K 11,83; Na 0,87; Fe 0,75; Mg 0,37; Ca 0,07; |
| Monazite_Ce | 0,000245953461195128 | Ce 44,2; O 32,01; P 23,79; | Ce 44,2; O 32,01; P 23,79; |
| Muscovite | 23,6778156502439 | O 39,17; Si 25,2; Al 22,72; K 11,21; Fe 1,19; Mg 0,49; Ba 0,01; F 0,01; Ca 0; P 0; | O 39,17; Si 25,2; Al 22,72; K 11,21; Fe 1,19; Mg 0,49; Ba 0,01; F 0,01; Ca 0; P 0; |
| Opx (ferrosillite) | 0,00356632515537316 | O 39,53; Si 35,82; Fe 23,35; Al 1,02; Na 0,29; | O 39,53; Si 35,82; Fe 23,35; Al 1,02; Na 0,29; |
| Orthoclase | 0,303014649844072 | O 37,91; Si 34,84; Al 17,33; K 8,69; Na 0,62; Fe 0,51; Mg 0,07; Ca 0,03; Ba 0; | O 37,91; Si 34,84; Al 17,33; K 8,69; Na 0,62; Fe 0,51; Mg 0,07; Ca 0,03; Ba 0; |
| Orthoclase+Ba | 0,0033203714065723 | O 35,91; Si 29,62; Al 21,37; K 9,32; Ba 2,92; Na 0,28; Mg 0,28; Fe 0,15; Ca 0,15; | O 35,91; Si 29,62; Al 21,37; K 9,32; Ba 2,92; Na 0,28; Mg 0,28; Fe 0,15; Ca 0,15; |
| Plagioclase | 18,6570448952724 | O 38,09; Si 33,67; Al 15,67; Na 8,29; Ca 4,26; K 0,02; | O 38,09; Si 33,67; Al 15,67; Na 8,29; Ca 4,26; K 0,02; |
| Quartz | 28,1711394302907 | Si 59,81; O 39,99; Fe 0,09; Al 0,07; Ce 0,02; La 0,02; | Si 59,81; O 39,99; Fe 0,09; Al 0,07; Ce 0,02; La 0,02; |
| Rutile | 0,00233655765766036 | Ti 64,75; O 32,25; Si 1,65; Al 0,7; Fe 0,65; | Ti 64,75; O 32,25; Si 1,65; Al 0,7; Fe 0,65; |
| Ulvospinel | 0,00442716210977515 | Fe 43,25; Ti 29,96; O 26,8; | Fe 43,25; Ti 29,96; O 26,8; |
| Zircon | 0,014880183699269 | Zr 57,27; O 21,55; Si 20,37; Al 0,73; La 0,07; Ce 0,01; | Zr 57,27; O 21,55; Si 20,37; Al 0,73; La 0,07; Ce 0,01; |
| Zoisite | 0,000983813780868126 | O 37,3; Ca 19,47; Si 17,44; Al 17,38; Fe 8,41; | O 37,3; Ca 19,47; Si 17,44; Al 17,38; Fe 8,41; |
| Zoisite-rim | 0,000860837050270562 | O 36,06; Ca 19,24; Al 18,88; Si 18,87; Fe 6,95; | O 36,06; Ca 19,24; Al 18,88; Si 18,87; Fe 6,95; |

# Appendix E – U-Pb Geochronology

E1: BS-images and zircon on tape (Kallvatnet)

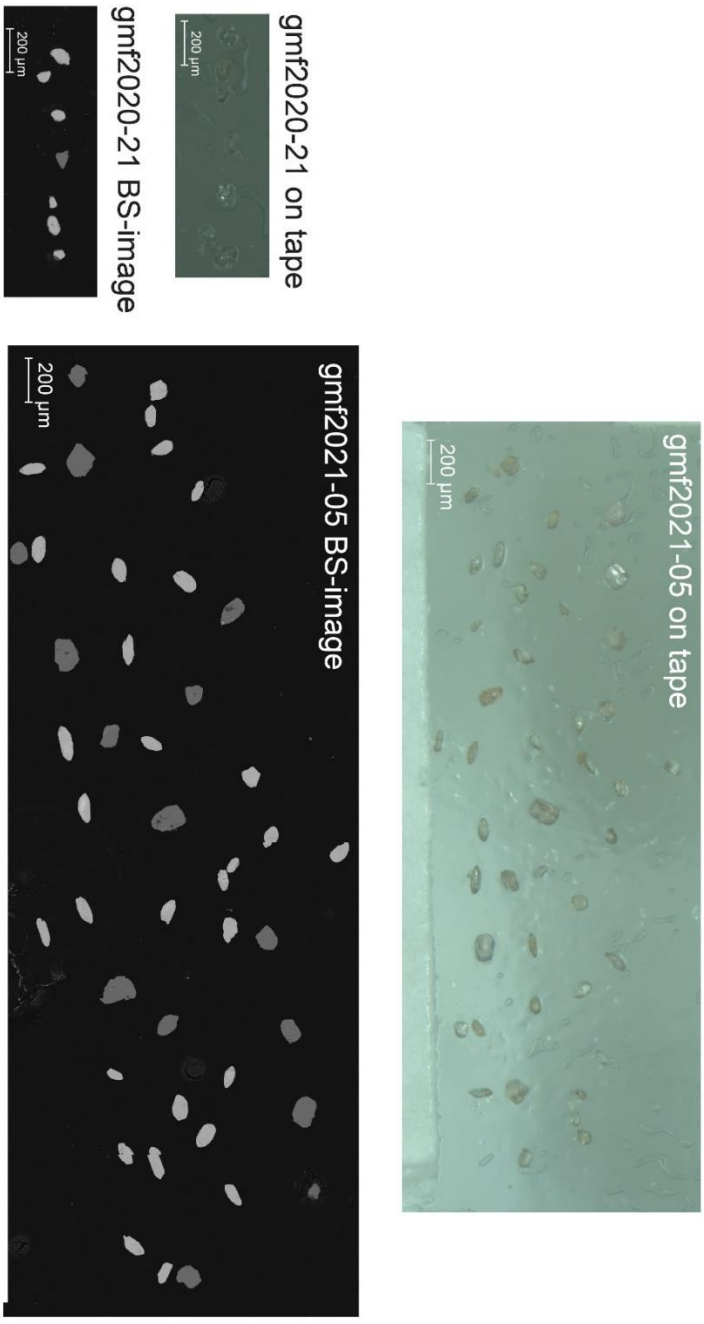

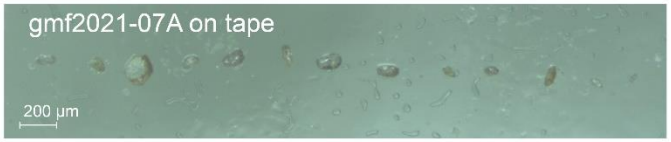
gmf2021-07A on tape
200 µm

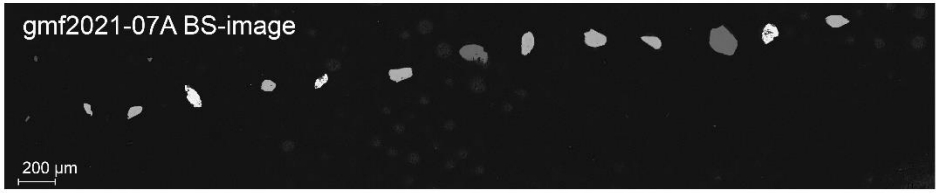
gmf2021-07A BS-image
200 µm

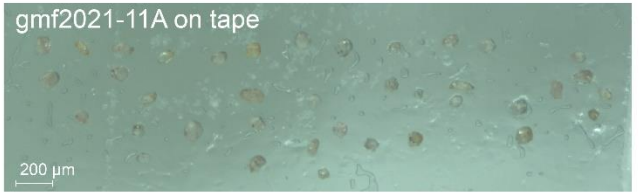
gmf2021-11A on tape
200 µm

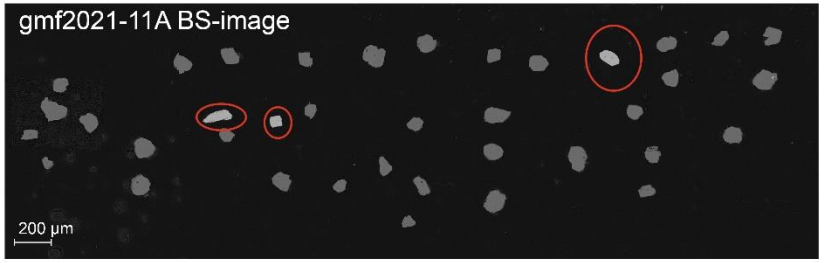
gmf2021-11A BS-image
200 µm


gmf2021-11C on tape
200 µm
gmf2021-11C BS-image
200 µm

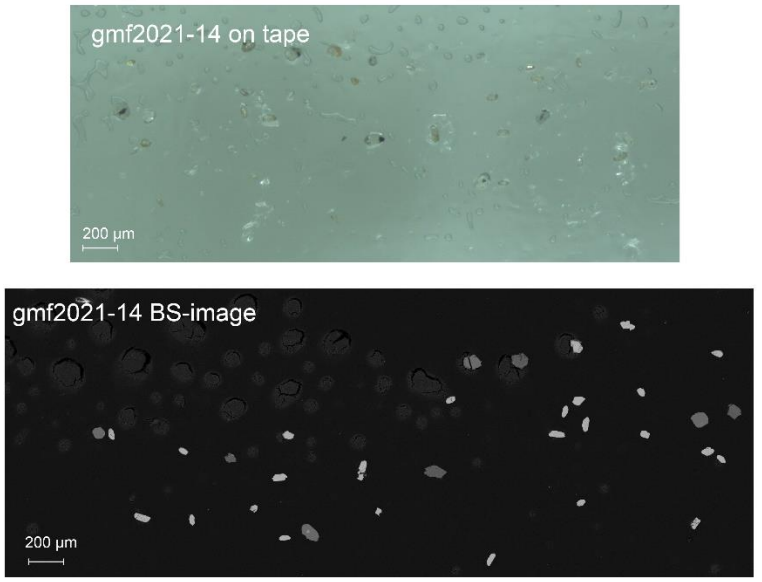
gmf2021-14 on tape
200 µm
gmf2021-14 BS-image
200 µm

E2: CL-images with laser traces (Kallvatnet)

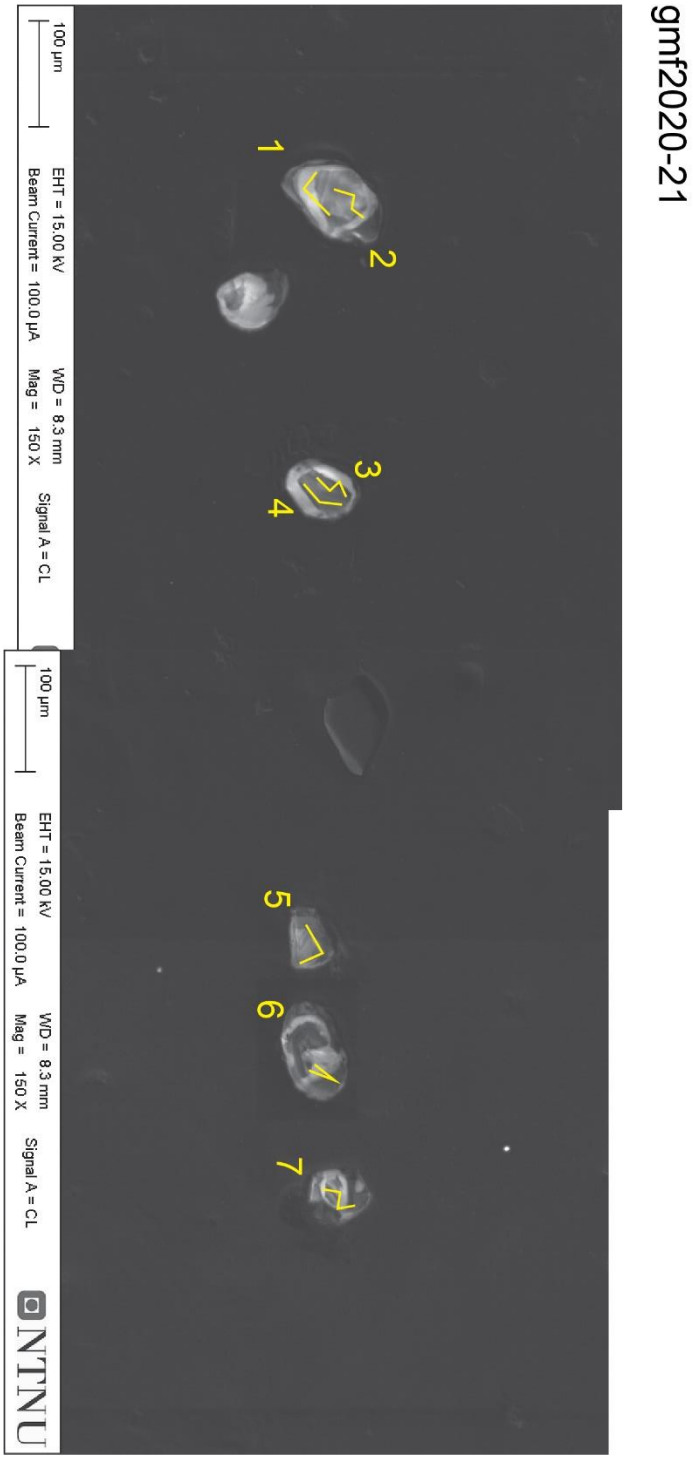

# gmf2021-05: Line analyses 1-19

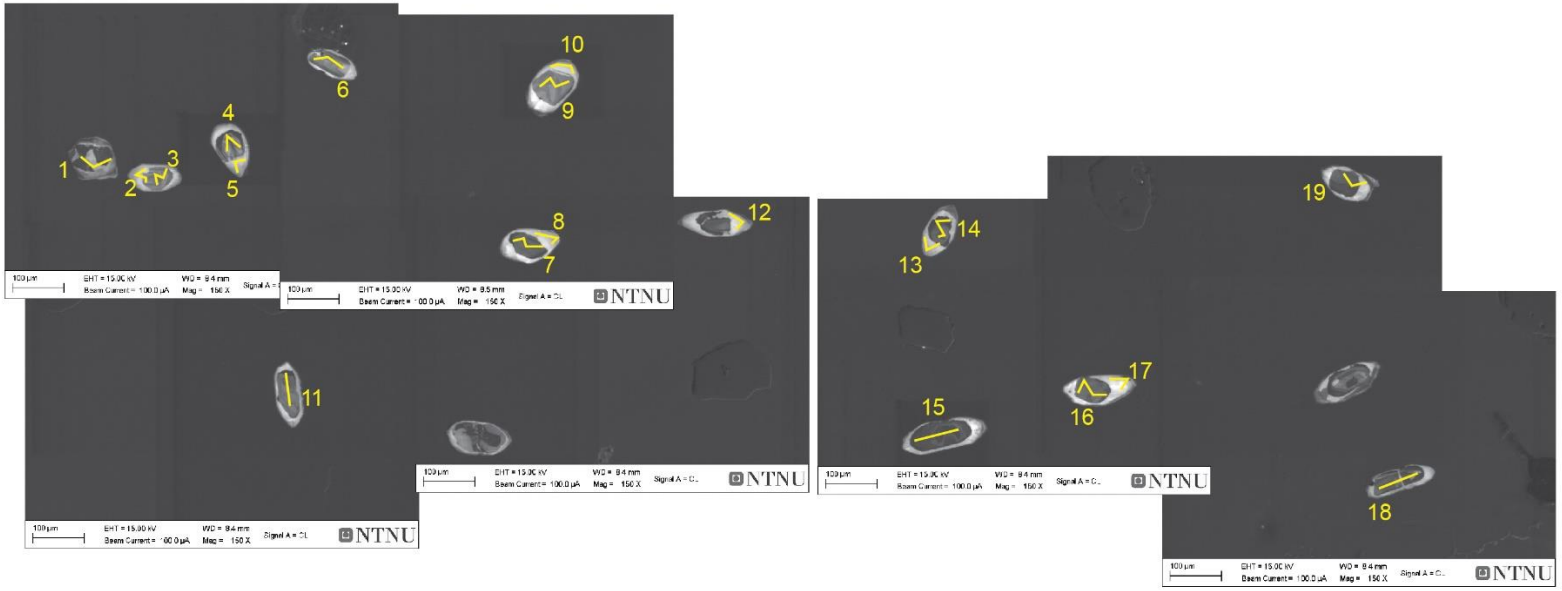


gmf2021-05: Line analyses 20-32

# gmf2021-07A

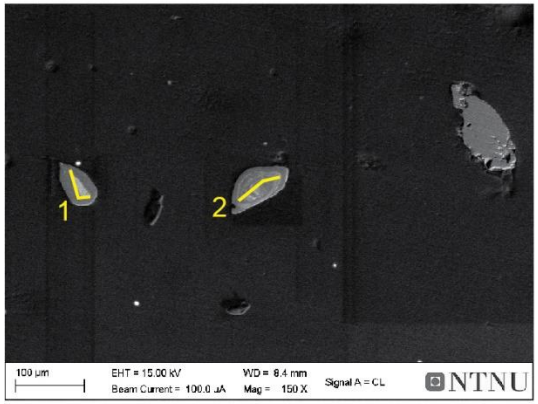
1
2
100 µm
EHT = 15.00 kV
Beam Current = 100.0 µA
WD = 8.4 mm
Mag = 150 X
Signal A = CL
NTNU

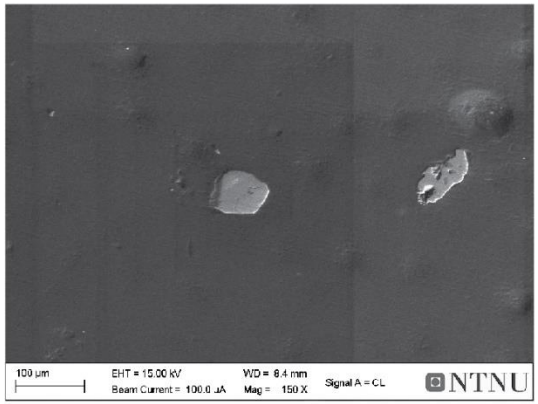
100 µm
EHT = 15.00 kV
Beam Current = 100.0 µA
WD = 8.4 mm
Mag = 150 X
Signal A = CL
NTNU

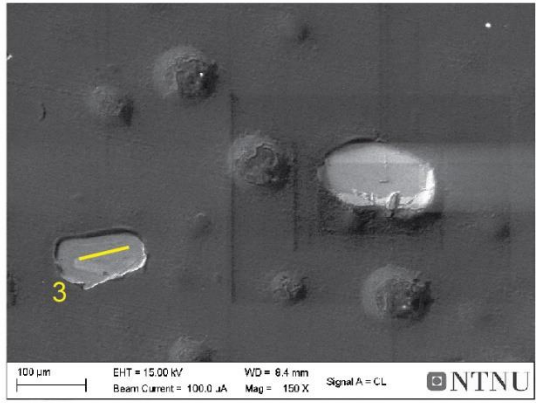
3
100 µm
EHT = 15.00 kV
Beam Current = 100.0 µA
WD = 8.4 mm
Mag = 150 X
Signal A = CL
NTNU

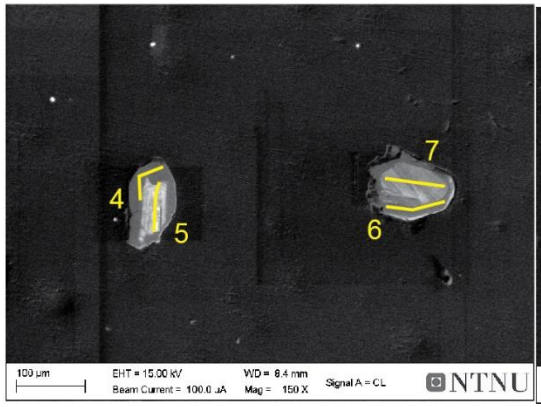
4
5
6
7
100 µm
EHT = 15.00 kV
Beam Current = 100.0 µA
WD = 8.4 mm
Mag = 150 X
Signal A = CL
NTNU

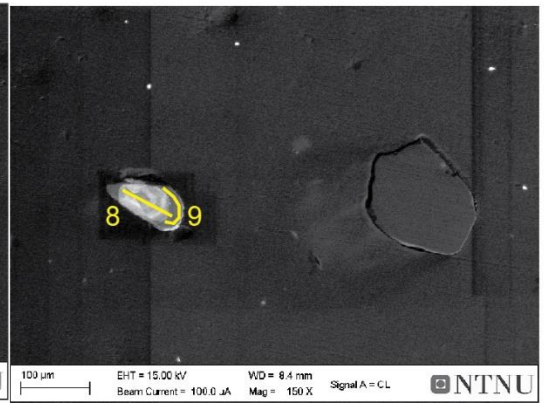
8
9
100 µm
EHT = 15.00 kV
Beam Current = 100.0 µA
WD = 8.4 mm
Mag = 150 X
Signal A = CL
NTNU

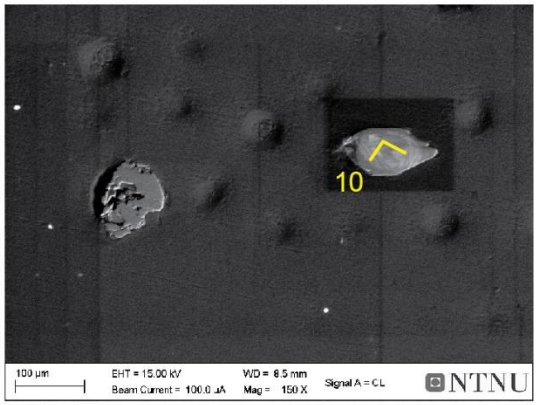
10
100 µm
EHT = 15.00 kV
Beam Current = 100.0 µA
WD = 8.5 mm
Mag = 150 X
Signal A = CL
NTNU

gmf2021-11A

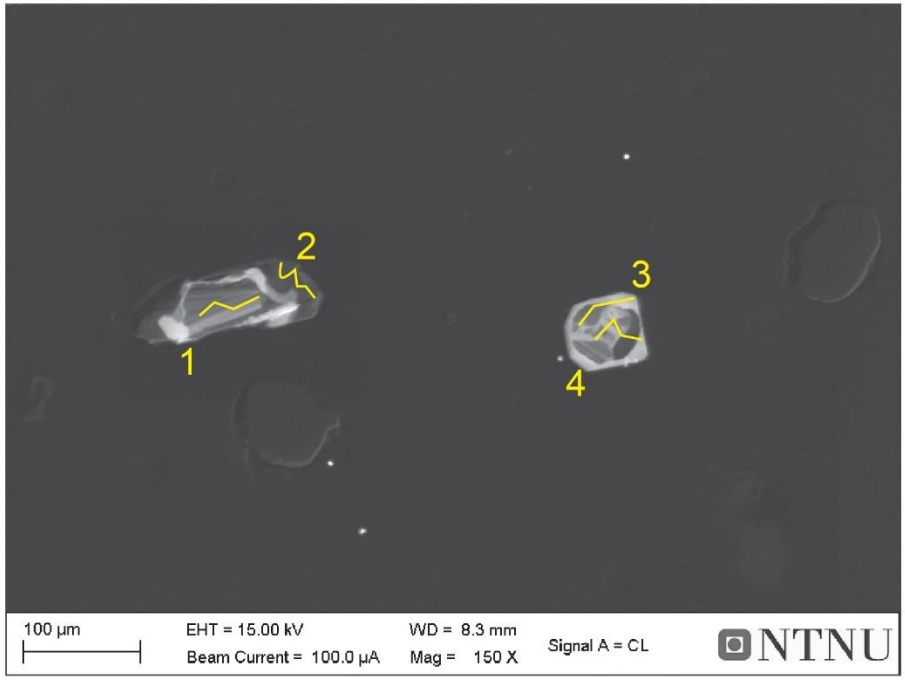
1
2
3
4
100 µm
EHT = 15.00 kV
Beam Current = 100.0 µA
WD = 8.3 mm
Mag = 150 X
Signal A = CL
NTNU

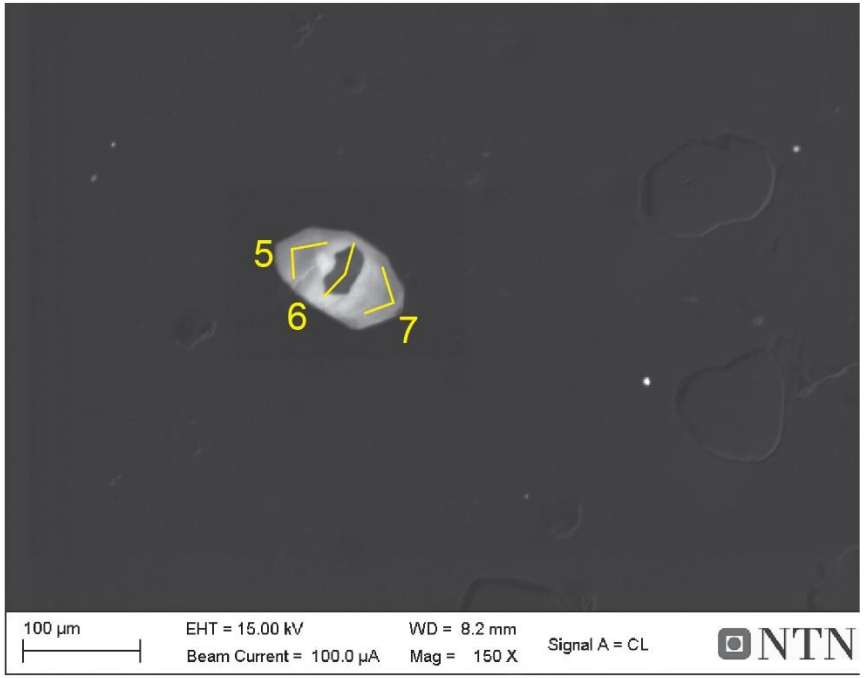
5
6
7
100 µm
EHT = 15.00 kV
Beam Current = 100.0 µA
WD = 8.2 mm
Mag = 150 X
Signal A = CL
NTN

# gmf2021-11C line analyses 1-10

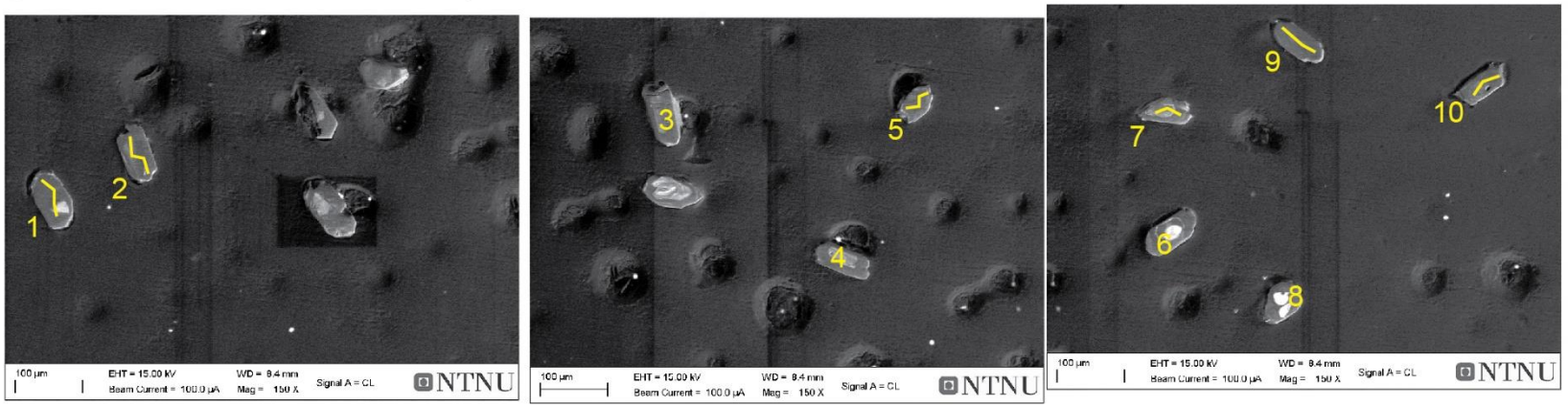

# gmf2021-11C line analyses 11-23

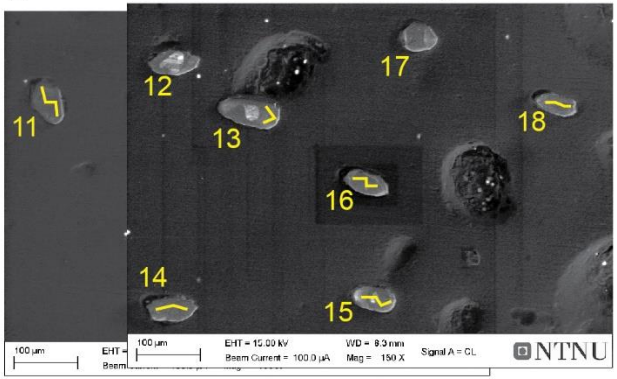


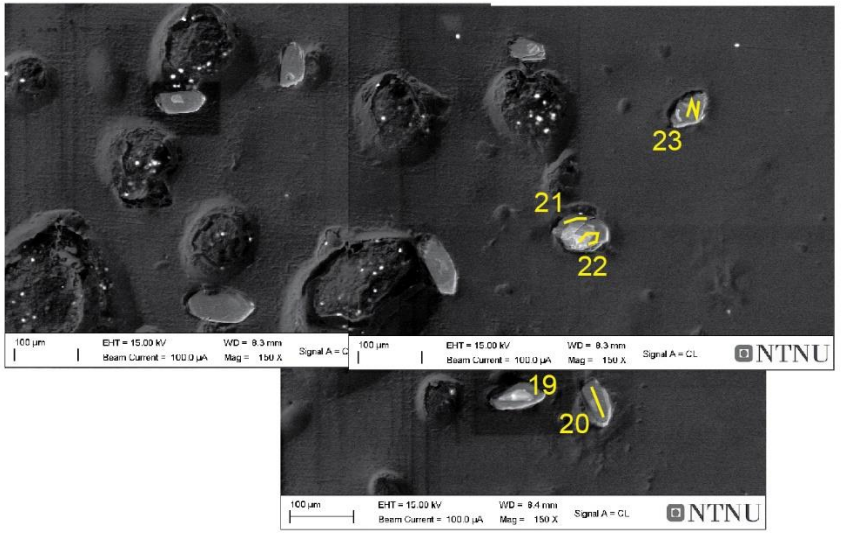

# gmf2021-14 line analyses 1-7

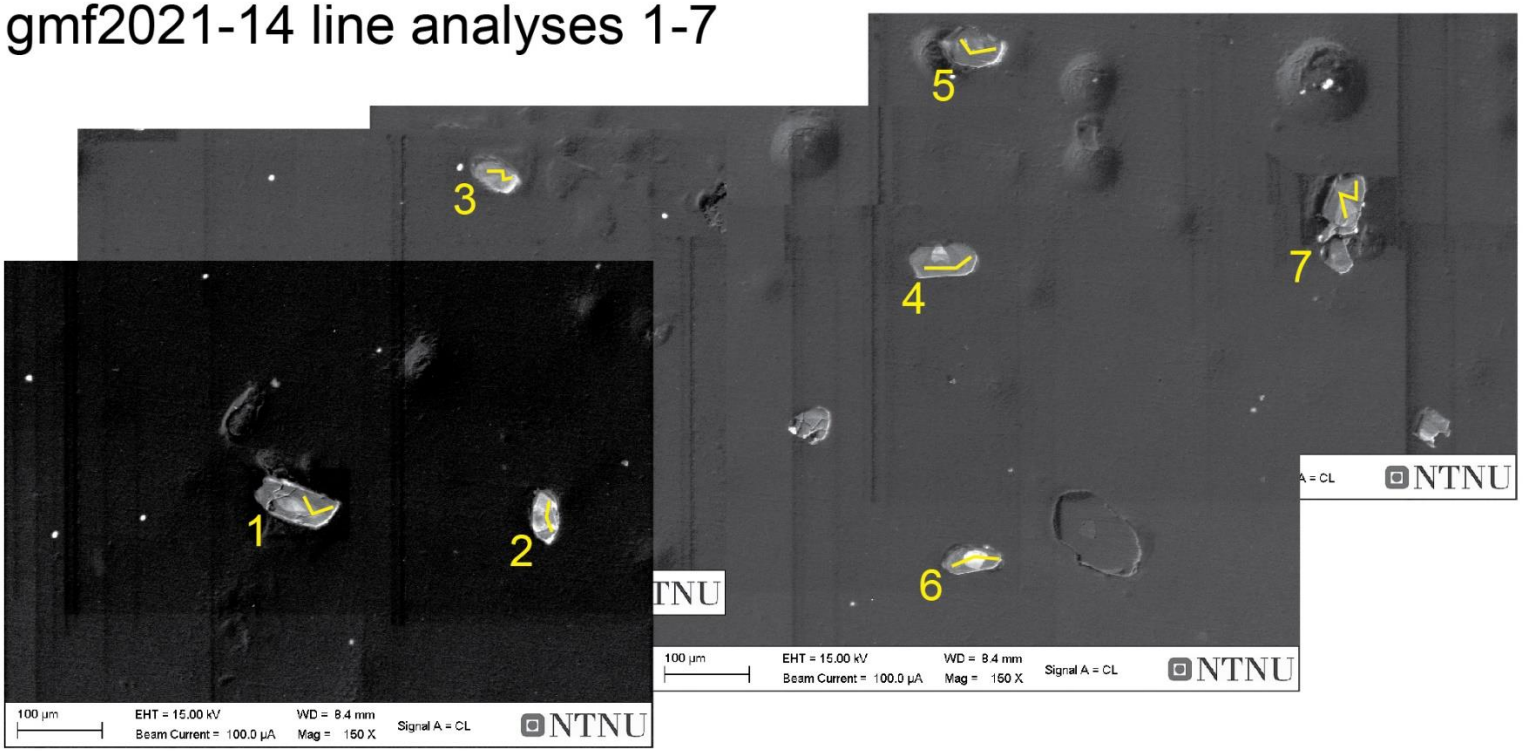

gmf2021-14 line analyses 8-18

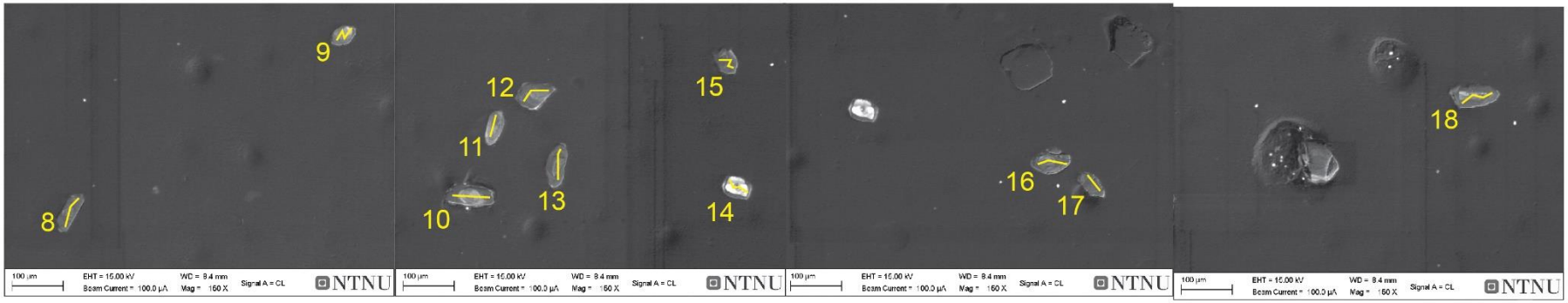

E3: CL-images with laser traces (Umbukta)

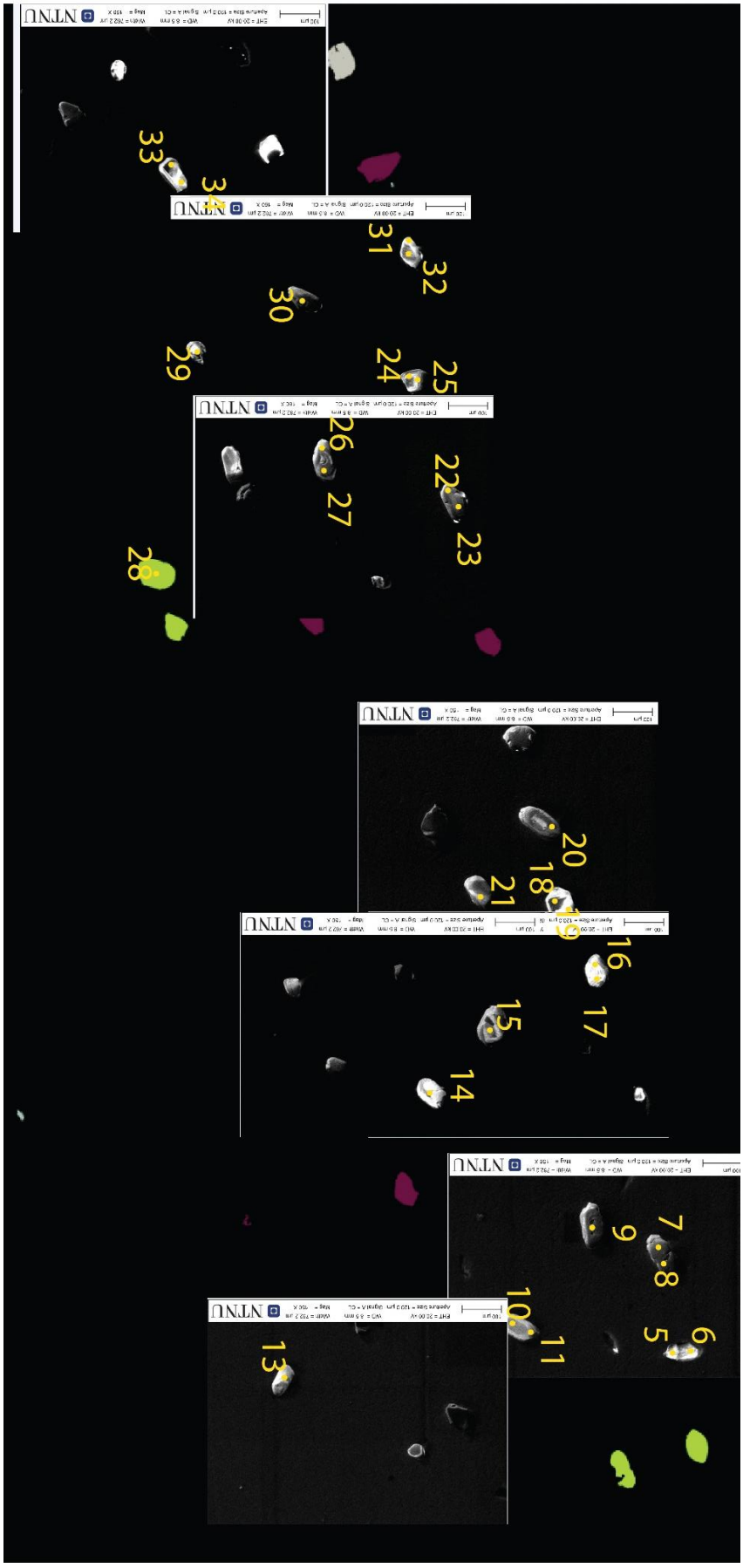

E4: Metamorphic zircon U-Pb data (Kallvatnet)

| | | Concordia output | | | | Tera-Wesserburg output | | | Age estimates | | | | | | Concentrations | | | | | |
|---|---|---|---|---|---|---|---|---|---|---|---|---|---|---|---|---|---|---|---|---|
| **gmf2020-21** | | | | | | | | | | | | | | | | | | | | |
| Grain | Line analysis | 206Pb/238U | 1s% | 206Pb/238U | 1s% | rho | 238/206 | 1s% | 207/206 | 1s% | 206Pb/207Pb | 1s | 206Pb/238U | 1s | conc | Th/U | U* | Th* | Pbtot* | Pb com. >LLD (%) | Comment |
| 1 | 1 | 0.6845 | 6.25 | 0.07815 | 1.87 | 0.07 | 12.79591 | 1.868202 | 0.06352 | 6.391688 | 726 | 130 | 530 | 26 | 485 | 9 | 66.9 | 0.00 | 23 | 0 | 2 | - | Rim (CL and Th/U --> metamorphic) |
| 1 | 2 | 3.6844 | 1.32 | 0.27463 | 1.07 | 0.41 | 3.64126 | 1.070531 | 0.0973 | 1.315519 | 1573 | 24 | 1568 | 11 | 1564 | 15 | 99.4 | 0.56 | 88 | 50 | 31 | 4.6 | Core (CL and Th/U --> detrital) |
| 2 | 3 | 3.3107 | 1.12 | 0.25663 | 1.04 | 0.49 | 3.89666 | 1.036512 | 0.09356 | 1.090209 | 1499 | 21 | 1484 | 9 | 1473 | 14 | 98.2 | 0.35 | 247 | 87 | 76 | 1.2 | Core (CL and Th/U --> detrital) |
| 2 | 4 | 3.3012 | 1.19 | 0.25791 | 1.05 | 0.46 | 3.87732 | 1.050754 | 0.09283 | 1.174189 | 1484 | 22 | 1481 | 9 | 1479 | 14 | 99.6 | 0.35 | 168 | 59 | 52 | 1.7 | Rim (CL --> metamorphic) |
| 3 | 5 | 2.9976 | 1.35 | 0.23858 | 1.07 | 0.41 | 4.19147 | 1.073015 | 0.09112 | 1.338894 | 1449 | 25 | 1407 | 10 | 1379 | 13 | 95.2 | 1.00 | 80 | 79 | 27 | 4.2 | Core (CL and Th/U --> detrital) |
| 4 | 6 | 0.5387 | 1.93 | 0.06961 | 1.11 | 0.28 | 14.36575 | 1.106163 | 0.05612 | 1.942267 | 457 | 43 | 438 | 7 | 434 | 5 | 95.0 | 0.00 | 272 | 1 | 20 | 3.6 | Rim (CL and Th/U --> metamorphic) |
| 5 | 7 | 0.6178 | 2.95 | 0.07266 | 1.25 | 0.17 | 13.76273 | 1.252408 | 0.06167 | 2.999838 | 663 | 63 | 489 | 11 | 452 | 5 | 68.2 | 0.00 | 182 | 1 | 14 | 6.2 | xed core and rim (Th/U --> metamorphic rir |
| **gmf2021-05** | | | | | | | | | | | | | | | | | | | | | | | |
| | | Concordia output | | | | Tera-Wesserburg output | | | Age estimates | | | | | | Concentrations | | | | | |
| Grain | Line analysis | 206Pb/238U | 1s% | 206Pb/238U | 1s% | rho | 238/206 | 1s% | 207/206 | 1s% | 206Pb/207Pb | 1s | 206Pb/238U | 1s | conc | Th/U | U* | Th* | Pbtot* | Pb com. >LLD (%) | Comment |
| 1 | 1 | 3.70337 | 1.09 | 0.27 | 1.03 | 0.48 | 3.68732 | 1.03 | 0.09903 | 1.08 | 1606 | 20 | 1572 | 9 | 1547 | 14 | 96.3 | 0.99 | 278 | 275 | 101 | 0.7 | Rim (CL --> metamorphic) |
| 2 | 2 | 3.31004 | 1.83 | 0.27 | 1.15 | 0.30 | 3.74827 | 1.15 | 0.08997 | 1.85 | 1425 | 35 | 1483 | 14 | 1525 | 16 | 107.0 | 0.40 | 85 | 34 | 27 | 3.6 | Rim (CLL--> metamorphic) |
| 2 | 3 | 3.34650 | 1.19 | 0.26 | 1.04 | 0.44 | 3.81971 | 1.04 | 0.09270 | 1.19 | 1482 | 22 | 1492 | 9 | 1499 | 14 | 101.2 | 0.52 | 112 | 59 | 36 | - | Core (CL and Th/U --> detrital) |
| 3 | 4 | 4.05149 | 1.54 | 0.29 | 1.11 | 0.35 | 3.41006 | 1.11 | 0.10019 | 1.55 | 1628 | 28 | 1645 | 13 | 1658 | 16 | 101.8 | 1.13 | 74 | 84 | 30 | 3.2 | Core (CL and Th/U --> detrital) |
| 3 | 5 | 4.01116 | 2.01 | 0.29 | 1.21 | 0.28 | 3.49004 | 1.21 | 0.10152 | 2.04 | 1652 | 37 | 1637 | 16 | 1624 | 17 | 98.3 | 0.76 | 33 | 25 | 12 | 4.1 | Rim (CL --> metamorphic) |
| 4 | 6 | 2.11288 | 1.45 | 0.20 | 1.07 | 0.36 | 5.05331 | 1.07 | 0.07743 | 1.46 | 1132 | 29 | 1153 | 10 | 1164 | 11 | 102.8 | 0.38 | 75 | 28 | 18 | 2.7 | Core (CL and Th/U --> detrital) |
| 5 | 7 | 2.86319 | 1.20 | 0.24 | 1.04 | 0.44 | 4.19569 | 1.04 | 0.08712 | 1.19 | 1363 | 23 | 1372 | 9 | 1378 | 13 | 101.1 | 0.34 | 120 | 41 | 34 | - | Core (CL and Th/U --> detrital) |
| 5 | 8 | 0.48630 | 4.61 | 0.06 | 1.50 | 0.09 | 16.28399 | 1.50 | 0.05743 | 4.72 | 508 | 101 | 402 | 15 | 384 | 6 | 75.7 | 0.16 | 59 | 9 | 4 | - | Rim (CL --> metamorphic) |
| 6 | 9 | 3.30399 | 1.17 | 0.26 | 1.04 | 0.45 | 3.86324 | 1.04 | 0.09257 | 1.16 | 1479 | 22 | 1482 | 9 | 1484 | 14 | 100.3 | 0.38 | 117 | 45 | 37 | 2.7 | Core (CL and Th/U --> detrital) |
| 6 | 10 | 2.32341 | 2.32 | 0.20 | 1.23 | 0.24 | 4.88234 | 1.23 | 0.08226 | 2.35 | 1252 | 45 | 1220 | 16 | 1201 | 13 | 96.0 | 0.10 | 47 | 5 | 11 | 10.0 | Rim (CL and Th/U --> metamorphic) |
| 7 | 11 | 3.50436 | 1.17 | 0.26 | 1.04 | 0.45 | 3.86175 | 1.04 | 0.09814 | 1.16 | 1589 | 22 | 1528 | 9 | 1484 | 14 | 93.4 | 0.73 | 175 | 128 | 59 | 1.0 | Core (CL and Th/U --> detrital) |
| 8 | 12 | 3.66271 | 3.96 | 0.28 | 1.75 | 0.18 | 3.58333 | 1.75 | 0.09518 | 4.03 | 1532 | 74 | 1563 | 32 | 1587 | 25 | 103.6 | 1.28 | 31 | 39 | 11 | 29.4 | Rim (CL --> metamorphic) |
| 9 | 13 | 2.63779 | 1.26 | 0.23 | 1.05 | 0.42 | 4.42028 | 1.05 | 0.08456 | 1.25 | 1305 | 24 | 1311 | 9 | 1315 | 12 | 100.7 | 0.29 | 211 | 62 | 56 | 1.6 | Rim (CL --> metamorphic) |
| 9 | 14 | 2.81256 | 1.14 | 0.24 | 1.03 | 0.46 | 4.19445 | 1.03 | 0.08555 | 1.13 | 1328 | 22 | 1359 | 9 | 1378 | 13 | 103.8 | 0.38 | 159 | 61 | 45 | 1.1 | Core (CL and Th/U --> detrital) |
| 10 | 15 | 2.41515 | 1.09 | 0.21 | 1.02 | 0.49 | 4.85037 | 1.02 | 0.08495 | 1.07 | 1314 | 21 | 1247 | 8 | 1208 | 11 | 91.9 | 0.52 | 483 | 252 | 124 | 0.6 | Core (CL and Th/U --> detrital) |
| 11 | 16 | 3.30093 | 1.12 | 0.26 | 1.03 | 0.47 | 3.89226 | 1.03 | 0.09317 | 1.11 | 1491 | 21 | 1481 | 9 | 1474 | 14 | 98.8 | 0.49 | 179 | 87 | 57 | 1.6 | Core (CL and Th/U --> detrital) |
| 11 | 17 | 0.54419 | 6.61 | 0.07 | 1.93 | 0.07 | 14.47807 | 1.93 | 0.05713 | 6.76 | 496 | 143 | 441 | 24 | 431 | 8 | 86.8 | 0.00 | 47 | 0 | 3 | 34.3 | Rim (CL and Th/U --> metamorphic) |
| 12 | 18 | 3.62447 | 1.13 | 0.27 | 1.03 | 0.47 | 3.75559 | 1.03 | 0.09871 | 1.11 | 1600 | 21 | 1555 | 9 | 1522 | 14 | 95.1 | 0.49 | 146 | 72 | 48 | 1.3 | Core (CL and Th/U --> detrital) |
| 13 | 19 | 3.80185 | 1.13 | 0.28 | 1.03 | 0.47 | 3.58950 | 1.03 | 0.09897 | 1.12 | 1605 | 21 | 1593 | 9 | 1584 | 14 | 98.7 | 0.37 | 182 | 67 | 61 | 1.1 | Core (CL and Th/U --> detrital) |
| 14 | 20 | 0.59854 | 2.28 | 0.07 | 1.14 | 0.22 | 14.10636 | 1.14 | 0.06123 | 2.32 | 647 | 49 | 476 | 9 | 442 | 5 | 68.2 | 0.38 | 44 | 17 | 3 | 16.1 | Rim (CL --> metamorphic) |
| 15 | 21 | 1.76806 | 5.37 | 0.17 | 1.92 | 0.12 | 5.82581 | 1.92 | 0.07470 | 5.49 | 1060 | 107 | 1034 | 35 | 1021 | 18 | 96.3 | 0.50 | 28 | 14 | 6 | - | Rim (CL --> metamorphic) |
| 16 | 22 | 3.24956 | 1.24 | 0.25 | 1.05 | 0.42 | 4.07548 | 1.05 | 0.09604 | 1.24 | 1549 | 23 | 1469 | 10 | 1415 | 13 | 91.3 | 0.70 | 68 | 48 | 22 | 2.4 | Rim (CL --> metamorphic) |
| 16 | 23 | 3.14287 | 1.27 | 0.25 | 1.05 | 0.42 | 4.08047 | 1.05 | 0.09300 | 1.27 | 1488 | 24 | 1443 | 10 | 1413 | 13 | 95.0 | 0.54 | 64 | 34 | 20 | 2.0 | Core (CL and Th/U --> detrital) |
| 17 | 24 | 3.71819 | 1.27 | 0.26 | 1.06 | 0.41 | 3.80981 | 1.06 | 0.10273 | 1.28 | 1674 | 23 | 1575 | 10 | 1503 | 14 | 89.8 | 0.44 | 152 | 66 | 49 | 1.1 | Core (CL and Th/U --> detrital) |
| 18 | 25 | 2.41510 | 1.25 | 0.21 | 1.05 | 0.42 | 4.81881 | 1.05 | 0.08440 | 1.26 | 1302 | 24 | 1247 | 9 | 1216 | 12 | 93.4 | 0.34 | 100 | 34 | 25 | 2.5 | Rim (CL --> metamorphic) |
| 18 | 26 | 2.74561 | 1.20 | 0.23 | 1.04 | 0.44 | 4.33426 | 1.04 | 0.08630 | 1.19 | 1345 | 23 | 1341 | 9 | 1338 | 13 | 99.5 | 0.30 | 91 | 27 | 25 | 2.6 | Core (CL and Th/U --> detrital) |
| 19 | 27 | 2.22957 | 1.23 | 0.20 | 1.04 | 0.43 | 4.95221 | 1.04 | 0.08007 | 1.22 | 1199 | 24 | 1190 | 9 | 1186 | 11 | 98.9 | 0.28 | 112 | 32 | 26 | 2.6 | Core (CL and Th/U --> detrital) |
| 19 | 28 | 0.55242 | 3.10 | 0.07 | 1.26 | 0.15 | 14.30820 | 1.26 | 0.05732 | 3.16 | 503 | 69 | 447 | 11 | 436 | 5 | 86.5 | 0.02 | 76 | 2 | 6 | 8.6 | Rim (CL and Th/U --> metamorphic) |
| 20 | 29 | 2.65732 | 1.42 | 0.22 | 1.07 | 0.37 | 4.62364 | 1.07 | 0.08910 | 1.43 | 1406 | 27 | 1317 | 10 | 1262 | 12 | 89.8 | 1.09 | 41 | 44 | 12 | 3.8 | Core (CL and Th/U --> detrital) |
| 21 | 30 | 3.02256 | 1.10 | 0.23 | 1.02 | 0.48 | 4.27040 | 1.02 | 0.09361 | 1.09 | 1500 | 20 | 1413 | 8 | 1356 | 13 | 90.4 | 0.18 | 412 | 73 | 110 | 1.0 | Core (CL and Th/U --> detrital) |
| 22 | 31 | 3.88291 | 1.10 | 0.28 | 1.03 | 0.48 | 3.52386 | 1.03 | 0.09923 | 1.09 | 1610 | 20 | 1610 | 9 | 1610 | 15 | 100.0 | 1.16 | 258 | 299 | 103 | 0.6 | Core (CL and Th/U --> detrital) |
| 23 | 32 | 3.75486 | 1.19 | 0.27 | 1.04 | 0.44 | 3.64285 | 1.04 | 0.09920 | 1.19 | 1609 | 22 | 1583 | 10 | 1564 | 14 | 97.2 | 0.53 | 88 | 46 | 30 | - | Core (CL and Th/U --> detrital) |

**gmf2021-07A**

| | | Concordia output | | | | | Tera-Wesserburg output | | | | Age estimates | | | | | | | Concentrations | | | | | |
|---|---|---|---|---|---|---|---|---|---|---|---|---|---|---|---|---|---|---|---|---|---|---|---|
| Grain | Line analysis | Pb207/U235 | 1s% | Pb206/U238 | 1s% | roh | 238/206 | 1s% | 207/206 | 1s% | Pb207/Pb206 | 1s | Pb207/U235 | 1s | Pb206/U238 | 1s | conc | Th/U | U* | Th* | Pbtot* | Pb com. >LLD (%) | Comment |
| 1 | 1 | 0.82759 | 1.44 | 0.08831 | 1.06 | 0.37 | 11.32375 | 1.06 | 0.06796 | 1.44 | 867 | 30 | 612 | 7 | 546 | 6 | 62.9 | 0.11 | 751 | 82 | 74 | 1.0 | Mantle (CL --> metamorphic) |
| 2 | 2 | 3.50678 | 1.07 | 0.25903 | 1.03 | 0.50 | 3.86056 | 1.03 | 0.09818 | 1.05 | 1590 | 19 | 1529 | 8 | 1485 | 14 | 93.4 | 0.21 | 538 | 111 | 162 | - | detrital (CL and Th/U) |
| 3 | 3 | 2.66775 | 1.06 | 0.22327 | 1.03 | 0.51 | 4.47888 | 1.03 | 0.08665 | 1.04 | 1353 | 20 | 1320 | 8 | 1299 | 12 | 96.0 | 0.46 | 933 | 431 | 256 | 0.4 | detrital (CL and Th/U) |
| 4 | 4 | 0.56579 | 1.22 | 0.07272 | 1.05 | 0.44 | 13.75138 | 1.05 | 0.05642 | 1.21 | 468 | 27 | 455 | 4 | 453 | 5 | 96.6 | 0.01 | 988 | 7 | 76 | - | Rim (CL and Th/U --> metamorphic) |
| 4 | 5 | 2.56958 | 1.21 | 0.20697 | 1.05 | 0.45 | 4.83162 | 1.05 | 0.09004 | 1.20 | 1426 | 23 | 1292 | 9 | 1213 | 12 | 85.0 | 0.84 | 92 | 77 | 24 | 5.5 | Core (CL and Th/U --> detrital) |
| 5 | 6 | 1.96338 | 1.14 | 0.16092 | 1.04 | 0.47 | 6.21427 | 1.04 | 0.08848 | 1.12 | 1393 | 21 | 1103 | 8 | 962 | 9 | 69.1 | 0.32 | 500 | 158 | 98 | 1.1 | Rim (CL --> metamorphic) |
| 5 | 7 | 3.6549 | 1.09 | 0.26621 | 1.03 | 0.49 | 3.75643 | 1.03 | 0.09957 | 1.07 | 1616 | 20 | 1562 | 9 | 1522 | 14 | 94.2 | 0.34 | 180 | 61 | 57 | - | Core (CL and Th/U --> detrital) |
| 6 | 8 | 3.75154 | 1.12 | 0.27551 | 1.04 | 0.49 | 3.62963 | 1.04 | 0.09875 | 1.09 | 1601 | 20 | 1582 | 9 | 1569 | 14 | 98.0 | 0.44 | 146 | 64 | 49 | - | Core (CL and Th/U --> detrital) |
| 6 | 9 | 0.54953 | 1.17 | 0.07153 | 1.03 | 0.46 | 13.98015 | 1.03 | 0.05571 | 1.15 | 441 | 25 | 445 | 4 | 445 | 4 | 101.1 | 0.01 | 740 | 6 | 56 | - | Rim (CL and Th/U --> metamorphic) |
| 7 | 10 | 2.30074 | 1.13 | 0.20632 | 1.04 | 0.47 | 4.84684 | 1.04 | 0.08087 | 1.11 | 1218 | 22 | 1213 | 8 | 1209 | 11 | 99.3 | 0.11 | 180 | 19 | 41 | - | Core (CL and Th/U --> detrital) |

**gmf2021-11A**

| | | Concordia output | | | | | Tera-Wesserburg output | | | | Age estimates | | | | | | | Concentrations | | | | | |
|---|---|---|---|---|---|---|---|---|---|---|---|---|---|---|---|---|---|---|---|---|---|---|---|
| Grain | Line analysis | Pb207/U235 | 1s% | Pb206/U238 | 1s% | roh | 238/206 | 1s% | 207/206 | 1s% | Pb207/Pb206 | 1s | Pb207/U235 | 1s | Pb206/U238 | 1s | conc | Th/U | U* | Th* | Pbtot* | Pb com. >LLD (%) | Comment |
| 1 | 1 | 3.27491 | 1.19 | 0.25387 | 1.05 | 0.46 | 3.93902 | 1.05 | 0.09355 | 1.17 | 1499 | 22 | 1475 | 9 | 1458 | 14 | 97.3 | 0.39 | 116 | 45 | 35 | 2.3 | Core (CL and Th/U --> detrital) |
| 1 | 2 | 0.51897 | 1.59 | 0.06644 | 1.07 | 0.33 | 15.05117 | 1.07 | 0.05665 | 1.59 | 477 | 35 | 425 | 6 | 415 | 4 | 86.9 | 0.00 | 449 | 1 | 32 | - | Rim (CL and Th/U --> metamorphic) |
| 2 | 3 | 3.58417 | 1.22 | 0.26171 | 1.05 | 0.44 | 3.82102 | 1.05 | 0.09932 | 1.21 | 1611 | 22 | 1546 | 10 | 1499 | 14 | 93.0 | 0.34 | 74 | 25 | 23 | 3.3 | ixed rim & coree (Th/U --> detrital dominan |
| 2 | 4 | 3.4552 | 1.08 | 0.25495 | 1.03 | 0.50 | 3.92234 | 1.03 | 0.09829 | 1.06 | 1592 | 20 | 1517 | 9 | 1464 | 14 | 92.0 | 0.17 | 318 | 53 | 93 | 1.0 | Core (CL and Th/U --> detrital) |
| 3 | 5 | 1.85417 | 6.41 | 0.07648 | 2.77 | 0.08 | 13.07531 | 2.77 | 0.17582 | 6.79 | 2614 | 109 | 1065 | 42 | 475 | 13 | 18.2 | 0.37 | 17 | 6 | 2 | 135.2 | Rim (CL --> metamorphic) |
| 3 | 6 | 3.40038 | 1.11 | 0.2556 | 1.04 | 0.49 | 3.91236 | 1.04 | 0.09648 | 1.09 | 1557 | 20 | 1505 | 9 | 1467 | 14 | 94.2 | 0.42 | 225 | 95 | 71 | 1.4 | Core (CL and Th/U --> detrital) |
| 3 | 7 | 1.08478 | 5.74 | 0.0903 | 1.89 | 0.08 | 11.07420 | 1.89 | 0.08712 | 5.89 | 1363 | 109 | 746 | 30 | 557 | 10 | 40.9 | 0.01 | 18 | 0 | 2 | 206.3 | Rim (CL and Th/U --> metamorphic) |

**gmf2021-11C**

| Grain | Line analysis | Concordia output | | | | | Tera-Wesserburg output | | | | Age estimates | | | | | | conc | Concentrations | | | | Pb com. >LLD (%) | Comment |
|---|---|---|---|---|---|---|---|---|---|---|---|---|---|---|---|---|---|---|---|---|---|---|---|
| | | Pb207/U235 | 1s% | Pb206/U238 | 1s% | roh | 238/206 | 1s% | 207/206 | 1s% | Pb207/Pb206 | 1s | Pb207/U235 | 1s | Pb206/U238 | 1s | | Th/U | U* | Th* | Pbtot* | | |
| 1 | 1 | 0.556 | 1.201 | 0.07247 | 1.035 | 0.445 | 13.79881 | 1.035 | 0.05564 | 1.186 | 438 | 26 | 449 | 4 | 451 | 5 | 103.1 | 0.00 | 797 | 3 | 61 | - | Mantle (CL and Th/U --> metamorphic) |
| 2 | 2 | 2.51672 | 1.060 | 0.21327 | 1.027 | 0.504 | 4.68889 | 1.027 | 0.08558 | 1.040 | 1329 | 20 | 1277 | 8 | 1246 | 12 | 93.8 | 0.20 | 1389 | 284 | 341 | - | Core (CL and Th/U --> detrital) |
| 3 | 3 | 5.18478 | 1.081 | 0.33079 | 1.031 | 0.501 | 3.02307 | 1.031 | 0.11367 | 1.056 | 1859 | 19 | 1850 | 9 | 1842 | 17 | 99.1 | 0.38 | 422 | 159 | 171 | - | Grain (CL and Th/U --> detrital |
| 4 | 4 | 0.55211 | 1.518 | 0.07102 | 1.056 | 0.341 | 14.08054 | 1.056 | 0.05638 | 1.525 | 467 | 34 | 446 | 5 | 442 | 5 | 94.8 | 0.01 | 917 | 11 | 69 | - | Mixed core & rim (Th/U --> metamorphic) |
| 5 | 5 | 0.58476 | 1.628 | 0.07407 | 1.067 | 0.314 | 13.50074 | 1.067 | 0.05725 | 1.642 | 501 | 36 | 468 | 6 | 461 | 5 | 92.0 | 0.00 | 833 | 3 | 65 | 2.2 | Grain (CL and Th/U --> metamorphic) |
| 6 | 6 | 0.56321 | 1.179 | 0.07127 | 1.038 | 0.450 | 14.03115 | 1.038 | 0.05731 | 1.169 | 503 | 26 | 454 | 4 | 444 | 4 | 88.2 | 0.01 | 895 | 7 | 68 | - | Mantle (CL and Th/U --> metamorphic) |
| 7 | 7 | 0.59789 | 1.492 | 0.07142 | 1.064 | 0.350 | 14.00168 | 1.064 | 0.06071 | 1.499 | 629 | 32 | 476 | 6 | 445 | 5 | 70.7 | 0.02 | 697 | 15 | 54 | 0.7 | Mixed core & rim (Th/U --> metamorphic) |
| 8 | 8 | 0.55567 | 1.449 | 0.07224 | 1.052 | 0.360 | 13.84275 | 1.052 | 0.05579 | 1.452 | 444 | 32 | 449 | 5 | 450 | 5 | 101.4 | 0.02 | 752 | 17 | 58 | 1.0 | Mantle (CL and Th/U --> metamorphic) |
| 9 | 9 | 0.55499 | 1.623 | 0.07174 | 1.073 | 0.315 | 13.93922 | 1.073 | 0.05611 | 1.640 | 456 | 36 | 448 | 6 | 447 | 5 | 97.9 | 0.01 | 645 | 7 | 49 | 0.8 | Grain (CL and Th/U --> metamorphic) |
| 10 | 10 | 0.545 | 1.297 | 0.07038 | 1.037 | 0.414 | 14.20858 | 1.037 | 0.05616 | 1.282 | 458 | 28 | 442 | 5 | 438 | 4 | 95.6 | 0.01 | 653 | 7 | 49 | - | Grain (CL and Th/U --> metamorphic) |
| 11 | 11 | 3.37927 | 1.100 | 0.25767 | 1.032 | 0.486 | 3.88093 | 1.032 | 0.09511 | 1.083 | 1530 | 20 | 1500 | 9 | 1478 | 14 | 96.6 | 0.07 | 740 | 54 | 212 | 0.7 | Grain (Th/U --> metamorphic) |
| 12 | 12 | 0.56072 | 1.721 | 0.07105 | 1.084 | 0.307 | 14.07460 | 1.084 | 0.05723 | 1.730 | 500 | 38 | 452 | 6 | 443 | 5 | 88.5 | 0.01 | 407 | 6 | 31 | 4.5 | Mixed core & rim (Th/U --> metamorphic) |
| 13 | 13 | 0.53771 | 1.207 | 0.06913 | 1.042 | 0.450 | 14.46550 | 1.042 | 0.05641 | 1.188 | 468 | 26 | 437 | 4 | 431 | 4 | 92.1 | 0.00 | 419 | 2 | 31 | - | Mantle (CL and Th/U --> metamorphic) |
| 14 | 14 | 0.60981 | 1.666 | 0.07462 | 1.072 | 0.318 | 13.40123 | 1.072 | 0.05926 | 1.671 | 577 | 36 | 483 | 6 | 464 | 5 | 80.5 | 0.01 | 580 | 9 | 46 | 0.9 | Grain (CL and Th/U --> metamorphic) |
| 15 | 15 | 0.55238 | 1.414 | 0.0708 | 1.045 | 0.370 | 14.12429 | 1.045 | 0.05658 | 1.414 | 475 | 31 | 447 | 5 | 441 | 4 | 92.9 | 0.02 | 683 | 13 | 52 | 1.8 | Mixed core & rim (Th/U --> metamorphic) |
| 16 | 16 | 0.57893 | 1.328 | 0.07496 | 1.041 | 0.399 | 13.34045 | 1.041 | 0.05601 | 1.321 | 452 | 29 | 464 | 5 | 466 | 5 | 103.0 | 0.01 | 714 | 10 | 57 | 2.0 | Grain (Th/U --> metamorphic) |
| 17 | 17 | 1.66836 | 1.151 | 0.15705 | 1.038 | 0.459 | 6.36740 | 1.038 | 0.07704 | 1.142 | 1122 | 23 | 997 | 7 | 940 | 9 | 83.8 | 0.19 | 538 | 101 | 97 | - | Grain (CL and Th/U --> detrital |
| 18 | 18 | 0.54012 | 2.083 | 0.06934 | 1.125 | 0.249 | 14.42169 | 1.125 | 0.05649 | 2.107 | 471 | 46 | 439 | 7 | 432 | 5 | 91.7 | 0.05 | 345 | 17 | 25 | - | Grain (CL and Th/U --> metamorphic) |
| 19 | 19 | 0.65203 | 1.140 | 0.07731 | 1.035 | 0.465 | 12.93494 | 1.035 | 0.06117 | 1.128 | 645 | 24 | 510 | 5 | 480 | 5 | 74.4 | 0.05 | 932 | 50 | 79 | - | Rim (CL and Th/U --> metamorphic) |
| 20 | 20 | 0.57987 | 1.416 | 0.07307 | 1.054 | 0.364 | 13.68551 | 1.054 | 0.05755 | 1.425 | 512 | 31 | 464 | 5 | 455 | 5 | 88.7 | 0.01 | 1308 | 13 | 101 | 0.7 | Grain (CL and Th/U --> metamorphic) |
| 21 | 21 | 1.78311 | 1.118 | 0.13941 | 1.033 | 0.480 | 7.17309 | 1.033 | 0.09276 | 1.100 | 1483 | 21 | 1039 | 7 | 841 | 8 | 56.7 | 0.09 | 854 | 74 | 137 | 0.4 | Rim (CL and Th/U --> metamorphic) |
| 21 | 22 | 0.70546 | 1.334 | 0.07871 | 1.042 | 0.386 | 12.70487 | 1.042 | 0.065 | 1.338 | 774 | 28 | 542 | 6 | 488 | 5 | 63.1 | 0.03 | 925 | 29 | 79 | 1.1 | Mixed core & rim (Th/U --> metamorphic) |
| 22 | 23 | 0.67379 | 1.259 | 0.07466 | 1.045 | 0.420 | 13.39405 | 1.045 | 0.06545 | 1.253 | 789 | 26 | 523 | 5 | 464 | 5 | 58.8 | 0.03 | 619 | 22 | 50 | 1.9 | Grain (CL and Th/U --> metamorphic) |

**gmf2021-14**

| | | Concordia output | | | | | Tera-Wesserburg output | | | | Age estimates | | | | | | | Concentartions | | | | | |
|---|---|---|---|---|---|---|---|---|---|---|---|---|---|---|---|---|---|---|---|---|---|---|---|
| Grain | Line analysis | Pb207/U235 | 1s% | Pb206/U238 | 1s% | roh | 238/206 | 1s% | 207/206 | 1s% | Pb207/Pb206 | 1s | Pb207/U235 | 1s | Pb206/U238 | 1s | conc | Th/U | U* | Th* | Pbtot* | Pb com. >LLD (%) | Comment |
| 1 | 1 | 1.01117 | 1.474 | 0.11168 | 1.066 | 0.358 | 8.95415 | 1.066 | 0.06566 | 1.477 | 796 | 31 | 710 | 8 | 683 | 7 | 85.8 | 0.08 | 361 | 29 | 44 | 2.0 | Mantle (CL and Th/U --> metamorphic) |
| 2 | 2 | 2.17863 | 1.278 | 0.20083 | 1.051 | 0.417 | 4.97934 | 1.051 | 0.07867 | 1.271 | 1164 | 25 | 1174 | 9 | 1180 | 11 | 101.4 | 0.42 | 121 | 51 | 29 | 1.4 | Grain (CL and Th/U --> detrital) |
| 3 | 3 | 1.67063 | 1.198 | 0.15789 | 1.039 | 0.445 | 6.33352 | 1.039 | 0.07673 | 1.186 | 1114 | 24 | 997 | 8 | 945 | 9 | 84.8 | 0.18 | 542 | 96 | 99 | - | Grain (CL and Th/U --> detrital) |
| 4 | 4 | 0.56553 | 1.843 | 0.07162 | 1.089 | 0.271 | 13.96258 | 1.089 | 0.05726 | 1.869 | 501 | 40 | 455 | 7 | 446 | 5 | 89.0 | 0.00 | 359 | 1 | 27 | 2.3 | Mantle (CL and Th/U --> metamorphic) |
| 5 | 5 | 2.95911 | 1.083 | 0.23904 | 1.025 | 0.486 | 4.18340 | 1.025 | 0.08977 | 1.069 | 1421 | 20 | 1397 | 8 | 1382 | 13 | 97.3 | 0.28 | 789 | 217 | 222 | 0.2 | Grain (CL and Th/U --> detrital) |
| 6 | 6 | 4.51474 | 1.592 | 0.30769 | 1.128 | 0.349 | 3.25002 | 1.128 | 0.10641 | 1.598 | 1739 | 29 | 1734 | 13 | 1729 | 17 | 99.5 | 1.02 | 49 | 50 | 21 | - | Core (CL and Th/U --> detrital) |
| 7 | 7 | 0.56514 | 1.524 | 0.07314 | 1.066 | 0.339 | 13.67241 | 1.066 | 0.05603 | 1.535 | 453 | 33 | 455 | 6 | 455 | 5 | 100.4 | 0.00 | 827 | 3 | 64 | 1.1 | Rim (CL and Th/U --> metamorphic) |
| 8 | 8 | 0.57601 | 1.899 | 0.07144 | 1.106 | 0.276 | 13.99776 | 1.106 | 0.05847 | 1.916 | 547 | 41 | 462 | 7 | 445 | 5 | 81.3 | 0.00 | 388 | 1 | 29 | 4.1 | Grain (Th/U --> metamorphic) |
| 9 | 9 | 4.53381 | 1.138 | 0.30893 | 1.036 | 0.465 | 3.23698 | 1.036 | 0.10643 | 1.128 | 1739 | 20 | 1737 | 9 | 1735 | 16 | 99.8 | 0.56 | 135 | 76 | 53 | 1.9 | Core (CL and Th/U --> detrital) |
| 10 | 10 | 3.33032 | 1.322 | 0.26244 | 1.063 | 0.409 | 3.81039 | 1.063 | 0.09203 | 1.315 | 1468 | 25 | 1488 | 10 | 1502 | 14 | 102.4 | 0.38 | 64 | 24 | 20 | - | Core (CL and Th/U --> detrital) |
| 11 | 11 | 3.54203 | 1.233 | 0.27351 | 1.049 | 0.434 | 3.65617 | 1.049 | 0.09392 | 1.224 | 1506 | 23 | 1537 | 10 | 1559 | 15 | 103.5 | 0.34 | 93 | 32 | 30 | - | Grain (CL and Th/U --> detrital) |
| 12 | 12 | 1.88014 | 1.241 | 0.17743 | 1.043 | 0.425 | 5.63603 | 1.043 | 0.07684 | 1.236 | 1117 | 24 | 1074 | 8 | 1053 | 10 | 94.3 | 0.02 | 178 | 3 | 34 | - | Grain (low Th/U, but CL indicate detrital) |
| 13 | 13 | 3.17523 | 1.354 | 0.24629 | 1.068 | 0.400 | 4.06025 | 1.068 | 0.09349 | 1.348 | 1498 | 25 | 1451 | 10 | 1419 | 14 | 94.8 | 0.38 | 211 | 79 | 63 | 1.1 | Core (CL amd Th/U --> detrital) |
| 14 | 14 | 1.5461 | 1.514 | 0.11321 | 1.086 | 0.340 | 8.83314 | 1.086 | 0.09904 | 1.535 | 1606 | 28 | 949 | 9 | 691 | 7 | 43.0 | 0.63 | 91 | 57 | 13 | 12.0 | Core (CL and Th/U --> detriatl) |
| 15 | 15 | 0.55924 | 1.874 | 0.07235 | 1.092 | 0.276 | 13.82170 | 1.092 | 0.05605 | 1.891 | 454 | 41 | 451 | 7 | 450 | 5 | 99.1 | 0.01 | 567 | 6 | 43 | - | Grain (Th/U --> metamorphic) |
| 16 | 16 | 0.58586 | 1.369 | 0.06521 | 1.043 | 0.384 | 15.33507 | 1.043 | 0.06515 | 1.366 | 779 | 29 | 468 | 5 | 407 | 4 | 52.3 | 0.08 | 813 | 63 | 59 | 1.5 | Grain (Th/U) --> metamorphic |
| 17 | 17 | 1.69179 | 1.225 | 0.16539 | 1.040 | 0.436 | 6.04631 | 1.040 | 0.07418 | 1.213 | 1047 | 24 | 1005 | 8 | 987 | 10 | 94.3 | 0.15 | 523 | 77 | 97 | 0.5 | Grain (Th/U --> metamorphic) |
| 18 | 18 | 2.20557 | 1.455 | 0.20453 | 1.071 | 0.365 | 4.88926 | 1.071 | 0.0782 | 1.458 | 1152 | 29 | 1183 | 10 | 1200 | 12 | 104.1 | 0.49 | 128 | 62 | 30 | 2.4 | ore and rim (Th/U --> magmatic, detrital do |

E5: Zircon U-Pb data (Sample from Storruste (2017)) (Umbukta)

| | | Isotope ratios Tera-Wasserburg output | | | | Age estimates (ma) | | | | | Concentrations | | |
|---|---|---|---|---|---|---|---|---|---|---|---|---|---|
| Analysis_# | Comments | 238/206 | 2SE | 207/206 | 2SE | Pb207 Pb206 | 2SE | Pb206 U238 | 2SE | conc | Th/U | U* | Th* | Pbtot* |
| **BKS132409** | | | | | | | | | | | | | | |
| BKS132409-05 | | 5.71121 | 0.03767 | 0.07539 | 0.00039 | 1077 | 10 | 1041 | 6 | 96.7 | 0.79 | 109 | 86.35049 | 400.9089 |
| BKS132409-06 | | 7.03804 | 0.18314 | 0.07415 | 0.00081 | 1039 | 22 | 875 | 22 | 84.2 | 0.64 | 108 | 69.08842 | 300.6799 |
| BKS132409-07 | | 5.55358 | 0.03474 | 0.07458 | 0.00015 | 1056 | 4 | 1068 | 6 | 101.1 | 0.23 | 759 | 174.5617 | 748.7476 |
| BKS132409-08 | | 6.83611 | 0.04206 | 0.07326 | 0.00019 | 1020 | 5 | 881 | 5 | 86.3 | 0.10 | ### | 273.9354 | 597.4627 |
| BKS132409-09 | | 6.32547 | 0.15841 | 0.07893 | 0.00044 | 1169 | 11 | 954 | 23 | 81.6 | 0.15 | 718 | 105.7345 | 550.8678 |
| BKS132409-10 | | 3.29685 | 0.03582 | 0.10314 | 0.00051 | 1680 | 9 | 1710 | 16 | 101.8 | 0.94 | 146 | 138.0617 | 967.0219 |
| BKS132409-11 | | 3.30521 | 0.03296 | 0.10371 | 0.00058 | 1690 | 10 | 1707 | 15 | 101.0 | 0.95 | 113 | 107.1792 | 720.3075 |
| BKS132409-13 | | 4.44076 | 0.02629 | 0.08630 | 0.00041 | 1344 | 9 | 1310 | 7 | 97.5 | 0.47 | 175 | 82.68897 | 427.0235 |
| BKS132409-14 | | 4.31018 | 0.07771 | 0.09016 | 0.00058 | 1426 | 12 | 1354 | 23 | 94.9 | 0.41 | 67 | 27.4453 | 181.7677 |
| BKS132409-15 | | 3.08936 | 0.02675 | 0.11058 | 0.00044 | 1808 | 7 | 1809 | 14 | 100.1 | 0.43 | 244 | 104.3206 | 755.5327 |
| BKS132409-16 | | 3.23070 | 0.02174 | 0.10792 | 0.00048 | 1764 | 8 | 1740 | 10 | 98.6 | 1.15 | 78 | 90.14385 | 656.1426 |
| BKS132409-17 | | 3.08312 | 0.03543 | 0.10778 | 0.00059 | 1761 | 10 | 1815 | 18 | 103.1 | 1.55 | 58 | 89.99604 | 664.3682 |
| BKS132409-18 | | 5.66958 | 0.05464 | 0.07356 | 0.00053 | 1026 | 15 | 1050 | 9 | 102.3 | 1.98 | 155 | 306.7371 | 1334.696 |
| BKS132409-19 | | 5.55639 | 0.10437 | 0.07296 | 0.00085 | 1014 | 25 | 1072 | 18 | 105.7 | 0.50 | 64 | 31.87124 | 155.5332 |
| ~~BKS132409-20~~ | ~~no signal~~ | ~~########~~ | ~~######~~ | ~~0.62837~~ | ~~1.22397~~ | ~~2803~~ | ~~464~~ | ~~1~~ | ~~54~~ | ~~0.0~~ | ~~0.70~~ | ~~0.1~~ | ~~0.0745~~ | ~~0.49601~~ |
| BKS132409-21 | | 4.07375 | 0.02861 | 0.08785 | 0.00042 | 1377 | 9 | 1417 | 9 | 102.9 | 0.57 | 121 | 69.6545 | 402.4019 |
| BKS132409-22 | | 3.92050 | 0.02970 | 0.09096 | 0.00032 | 1444 | 7 | 1467 | 10 | 101.5 | 0.23 | 266 | 60.06344 | 393.9992 |
| BKS132409-23 | | 4.03600 | 0.02787 | 0.08966 | 0.00030 | 1417 | 6 | 1429 | 9 | 100.8 | 0.25 | 265 | 66.68717 | 394.1618 |
| BKS132409-24 | | 5.85668 | 0.03499 | 0.07338 | 0.00033 | 1023 | 9 | 1017 | 6 | 99.4 | 0.93 | 153 | 141.6229 | 586.8605 |
| BKS132409-25 | | 5.25857 | 0.07730 | 0.07343 | 0.00113 | 1021 | 31 | 1125 | 15 | 110.1 | 0.61 | 53 | 31.89361 | 149.1845 |
| BKS132409-26 | | 3.71358 | 0.02770 | 0.09362 | 0.00029 | 1499 | 6 | 1538 | 10 | 102.6 | 0.48 | 356 | 170.8461 | 971.2973 |
| BKS132409-27 | | 3.90886 | 0.02236 | 0.09246 | 0.00023 | 1476 | 5 | 1470 | 8 | 99.6 | 0.56 | 412 | 230.1585 | 1315.343 |
| BKS132409-28 | | 5.31161 | 0.13283 | 0.07783 | 0.00102 | 1142 | 27 | 1132 | 27 | 99.1 | 0.63 | 16 | 10.33062 | 47.22916 |
| BKS132409-29 | | 3.92768 | 0.02286 | 0.09967 | 0.00025 | 1617 | 5 | 1462 | 7 | 90.4 | 0.16 | 382 | 59.5107 | 389.1535 |
| BKS132409-30 | | 3.30777 | 0.02640 | 0.10177 | 0.00026 | 1656 | 5 | 1704 | 12 | 102.9 | 0.45 | 978 | 439.3833 | 3026.209 |
| BKS132409-31 | | 3.89780 | 0.03005 | 0.09323 | 0.00033 | 1491 | 7 | 1474 | 10 | 98.9 | 0.90 | 137 | 122.5893 | 762.9297 |
| BKS132409-32 | | 3.85728 | 0.02654 | 0.09280 | 0.00039 | 1482 | 8 | 1488 | 9 | 100.4 | 0.56 | 128 | 71.29979 | 442.1451 |
| BKS132409-33 | | 3.33920 | 0.04225 | 0.10049 | 0.00056 | 1631 | 10 | 1690 | 18 | 103.6 | 0.75 | 166 | 124.0826 | 857.9768 |
| BKS132409-34 | | 3.33889 | 0.03551 | 0.10029 | 0.00057 | 1627 | 11 | 1691 | 16 | 103.9 | 0.63 | 81 | 50.83246 | 358.5917 |

E6: Igneous zircon U-Pb data (Tonalite from Trond Slagstad (unpublished))

| | Isotope ratios | | | | | | | | | | Age estimates (ma) | | | | | | Concentrations | | | | |
|---|---|---|---|---|---|---|---|---|---|---|---|---|---|---|---|---|---|---|---|---|---|
| | Concordia output | | | | | Tera-Wasserburg output | | | | | | | | | | | | | | | |
| | Pb207/U235 | 1s% | Pb206/U238 | 1s% | roh | 238/206 | 1s% | 207/206 | 1s% | Pb207/Pb206 | 1s | Pb207/U235 | 1s | Pb206/U238 | 1s | conc | Th/U | U* | Th* | Pbtot* | Pb com. >LLD (%) |
| **Analysis_#** | | | | | | | | | | | | | | | | | | | | | |
| **Tonalite** | | | | | | | | | | | | | | | | | | | | | |
| MO_028781_21 | 0.5608 | 1.18 | 0.0717 | 1.05 | 0.46 | 13.95673 | 1.05 | 0.05676 | 1.16 | 481.7 | 25.63 | 452.1 | 4.32 | 446.1 | 4.52 | 92.6 | 0.08 | 475 | 37 | 37 | - |
| MO_028781_14 | 0.5667 | 1.47 | 0.0718 | 1.07 | 0.37 | 13.92176 | 1.07 | 0.05721 | 1.47 | 499 | 32.04 | 455.8 | 5.41 | 447.2 | 4.63 | 89.6 | 0.17 | 230 | 40 | 18 | 7 |
| MO_028781_11 | 0.5784 | 1.20 | 0.072 | 1.06 | 0.46 | 13.89661 | 1.06 | 0.05829 | 1.18 | 539.9 | 26.24 | 463.4 | 4.48 | 447.9 | 4.54 | 83.0 | 0.17 | 354 | 59 | 28 | 4 |
| MO_028781_20 | 0.5701 | 1.59 | 0.0722 | 1.08 | 0.34 | 13.85809 | 1.08 | 0.05730 | 1.59 | 502.5 | 34.36 | 458.1 | 5.85 | 449.1 | 4.70 | 89.4 | 0.40 | 228 | 91 | 19 | 7 |
| MO_028781_01 | 0.566 | 1.32 | 0.0728 | 1.06 | 0.41 | 13.74570 | 1.06 | 0.05642 | 1.31 | 468.2 | 28.82 | 455.4 | 4.84 | 452.7 | 4.62 | 96.7 | 0.21 | 364 | 78 | 30 | 4 |
| MO_028781_07 | 0.5752 | 1.57 | 0.0732 | 1.08 | 0.35 | 13.65747 | 1.08 | 0.05697 | 1.56 | 489.6 | 34.54 | 461.3 | 5.81 | 455.5 | 4.74 | 93.0 | 0.19 | 169 | 33 | 14 | 15 |
| MO_028781_13 | 0.5792 | 1.29 | 0.0735 | 1.06 | 0.44 | 13.60915 | 1.06 | 0.05716 | 1.26 | 497.3 | 27.93 | 464 | 4.79 | 457.1 | 4.66 | 91.9 | 0.13 | 923 | 116 | 75 | 2 |
| MO_028781_12 | 0.5837 | 1.22 | 0.074 | 1.05 | 0.45 | 13.50621 | 1.05 | 0.05718 | 1.21 | 497.8 | 26.54 | 466.8 | 4.58 | 460.4 | 4.67 | 92.5 | 0.24 | 416 | 100 | 35 | 6 |
| MO_028781_16 | 0.5756 | 1.42 | 0.0742 | 1.06 | 0.39 | 13.46983 | 1.06 | 0.05622 | 1.41 | 460.3 | 31.2 | 461.6 | 5.28 | 461.7 | 4.75 | 100.3 | 0.09 | 487 | 43 | 39 | - |
| MO_028781_09 | 0.5853 | 1.32 | 0.0746 | 1.06 | 0.42 | 13.40842 | 1.06 | 0.05691 | 1.30 | 487.4 | 28.84 | 467.8 | 4.95 | 463.7 | 4.73 | 95.1 | 0.08 | 244 | 19 | 20 | 12 |
| MO_028781_24 | 0.588 | 1.30 | 0.0746 | 1.06 | 0.43 | 13.40123 | 1.06 | 0.05715 | 1.28 | 496.8 | 28.33 | 469.6 | 4.90 | 463.9 | 4.74 | 93.4 | 0.21 | 209 | 44 | 18 | - |
| MO_028781_17 | 0.5925 | 1.41 | 0.0749 | 1.07 | 0.39 | 13.35827 | 1.07 | 0.05740 | 1.39 | 506.3 | 30.23 | 472.4 | 5.31 | 465.4 | 4.79 | 91.9 | 0.39 | 318 | 124 | 28 | 4 |
| MO_028781_19 | 0.5793 | 1.40 | 0.0749 | 1.07 | 0.39 | 13.35292 | 1.07 | 0.05609 | 1.39 | 455.7 | 30.21 | 464 | 5.22 | 465.6 | 4.79 | 102.2 | 0.08 | 264 | 22 | 21 | - |
| MO_028781_02 | 0.5967 | 1.29 | 0.0751 | 1.05 | 0.43 | 13.31735 | 1.05 | 0.05763 | 1.27 | 515.3 | 27.92 | 475.1 | 4.88 | 466.8 | 4.75 | 90.6 | 0.13 | 364 | 47 | 30 | 5 |
| MO_028781_22 | 0.5803 | 1.23 | 0.0752 | 1.05 | 0.46 | 13.30672 | 1.05 | 0.05600 | 1.20 | 451.9 | 26.07 | 464.6 | 4.57 | 467.1 | 4.74 | 103.4 | 0.26 | 337 | 88 | 29 | 5 |
| MO_028781_06 | 0.5836 | 1.52 | 0.0753 | 1.08 | 0.36 | 13.27492 | 1.08 | 0.05618 | 1.51 | 458.8 | 33.45 | 466.8 | 5.69 | 468.2 | 4.85 | 102.0 | 0.18 | 317 | 58 | 27 | 6 |
| MO_028781_08 | 0.5789 | 1.51 | 0.0754 | 1.07 | 0.36 | 13.26260 | 1.07 | 0.05568 | 1.51 | 439.4 | 32.68 | 463.8 | 5.62 | 468.6 | 4.85 | 106.6 | 0.45 | 254 | 113 | 23 | - |
| MO_028781_23 | 0.5868 | 1.47 | 0.0754 | 1.07 | 0.38 | 13.26084 | 1.07 | 0.05643 | 1.45 | 468.6 | 32.14 | 468.8 | 5.50 | 468.7 | 4.84 | 100.0 | 0.18 | 288 | 52 | 24 | 6 |
| MO_028781_10 | 0.5889 | 1.32 | 0.0754 | 1.06 | 0.42 | 13.25732 | 1.06 | 0.05661 | 1.31 | 475.8 | 28.88 | 470.1 | 4.98 | 468.8 | 4.79 | 98.5 | 0.24 | 186 | 44 | 16 | 10 |
| MO_028781_03 | 0.5869 | 1.19 | 0.0756 | 1.05 | 0.46 | 13.23276 | 1.05 | 0.05632 | 1.17 | 464.4 | 25.73 | 468.9 | 4.46 | 469.6 | 4.74 | 101.1 | 0.36 | 338 | 123 | 30 | 4 |
| MO_028781_05 | 0.592 | 1.16 | 0.076 | 1.04 | 0.47 | 13.16309 | 1.04 | 0.05651 | 1.13 | 471.6 | 25.01 | 472.1 | 4.37 | 472 | 4.76 | 100.1 | 0.48 | 511 | 246 | 47 | - |
| MO_028781_18 | 0.5955 | 1.24 | 0.076 | 1.05 | 0.45 | 13.15963 | 1.05 | 0.05684 | 1.21 | 484.5 | 26.86 | 474.4 | 4.69 | 472.1 | 4.79 | 97.4 | 0.40 | 237 | 96 | 21 | - |
| MO_028781_15 | 0.5908 | 1.45 | 0.0761 | 1.07 | 0.38 | 13.14924 | 1.07 | 0.05634 | 1.44 | 464.9 | 31.83 | 471.4 | 5.47 | 472.5 | 4.87 | 101.6 | 0.29 | 369 | 108 | 32 | - |
| MO_028781_04 | 0.5903 | 1.26 | 0.0766 | 1.06 | 0.43 | 13.06336 | 1.06 | 0.05592 | 1.25 | 448.9 | 27.03 | 471.1 | 4.76 | 475.5 | 4.83 | 105.9 | 0.50 | 258 | 129 | 24 | - |

E7: Igneous zircon U-Pb data (Umbukta from Trond Slagstad (unpublished))

| | Isotope ratios | | | | | | | | | Age estimates (ma) | | | | | | | Concentrations | | | | |
|---|---|---|---|---|---|---|---|---|---|---|---|---|---|---|---|---|---|---|---|---|---|
| | Concordia output | | | | | Tera-Wasserburg output | | | | | | | | | | | | | | | Pb com. |
| Analysis_# | Pb207 U235 | 1s% | Pb206 U238 | 1s% | roh | 238/206 | 1s% | 207/206 | 1s% | Pb207 Pb206 | 1s | Pb207 U235 | 1s | Pb206 U238 | 1s | conc | Th/U | U* | Th* | Pbtot* | >LLD (%) |
| **Umbukta** | | | | | | | | | | | | | | | | | | | | | |
| 200037_01 | 0.8167 | 1.11 | 0.0976 | 1.06 | 0.52 | 10.248 | 1.06 | 0.0607 | 1.05 | 628.7 | 22.66 | 606.2 | 5.05 | 600.2 | 6.05 | 95.5 | 0.34 | 789 | 272 | 90 | - |
| 200037_02 | 0.8572 | 1.10 | 0.1032 | 1.06 | 0.53 | 9.68711 | 1.06 | 0.0602 | 1.05 | 611.6 | 22.61 | 628.6 | 5.16 | 633.3 | 6.37 | 103.5 | 0.41 | 1318 | 543 | 162 | 1 |
| 200037_03 | 0.8148 | 1.10 | 0.0981 | 1.06 | 0.52 | 10.1968 | 1.06 | 0.0603 | 1.06 | 612.8 | 22.66 | 605.1 | 5.03 | 603.1 | 6.08 | 98.4 | 0.47 | 1339 | 629 | 158 | - |
| 200037_04 | 0.8222 | 1.13 | 0.0993 | 1.06 | 0.51 | 10.0715 | 1.06 | 0.0601 | 1.08 | 605.6 | 23.28 | 609.3 | 5.17 | 610.3 | 6.16 | 100.8 | 0.56 | 842 | 468 | 105 | 1 |
| 200037_05 | 0.8666 | 1.15 | 0.0964 | 1.06 | 0.50 | 10.3778 | 1.06 | 0.0652 | 1.10 | 781.4 | 22.99 | 633.7 | 5.40 | 593.1 | 6.00 | 75.9 | 0.38 | 826 | 317 | 94 | 2 |
| 200037_06 | 0.8513 | 1.19 | 0.1025 | 1.06 | 0.47 | 9.75515 | 1.06 | 0.0602 | 1.16 | 611.7 | 24.75 | 625.4 | 5.57 | 629.1 | 6.37 | 102.8 | 0.34 | 493 | 168 | 59 | 1 |
| 200037_07 | 0.8435 | 1.16 | 0.102 | 1.06 | 0.50 | 9.80681 | 1.06 | 0.06 | 1.12 | 603.4 | 24.1 | 621.1 | 5.41 | 625.9 | 6.33 | 103.7 | 0.57 | 1509 | 864 | 190 | - |
| 200037_08 | 0.8201 | 1.11 | 0.0996 | 1.05 | 0.53 | 10.0452 | 1.05 | 0.0597 | 1.05 | 594.2 | 22.92 | 608.1 | 5.07 | 611.8 | 6.17 | 103.0 | 0.35 | 1080 | 373 | 125 | - |
| 200037_09 | 0.8255 | 1.10 | 0.0998 | 1.05 | 0.52 | 10.02 | 1.05 | 0.06 | 1.05 | 603.2 | 22.58 | 611.1 | 5.05 | 613.2 | 6.18 | 101.7 | 0.62 | 1186 | 735 | 148 | - |
| 200037_10 | 0.8477 | 1.14 | 0.1008 | 1.06 | 0.50 | 9.91768 | 1.06 | 0.061 | 1.10 | 638.2 | 23.38 | 623.4 | 5.31 | 619.3 | 6.25 | 97.0 | 0.38 | 480 | 184 | 57 | - |
| 200037_11 | 0.8053 | 1.36 | 0.0972 | 1.08 | 0.42 | 10.2891 | 1.08 | 0.0601 | 1.33 | 606.8 | 28.52 | 599.8 | 6.15 | 597.9 | 6.15 | 98.5 | 0.44 | 133 | 58 | 15 | - |
| 200037_12 | 0.8142 | 1.10 | 0.0989 | 1.05 | 0.52 | 10.1112 | 1.05 | 0.0597 | 1.06 | 593.2 | 22.23 | 604.8 | 5.01 | 608 | 6.13 | 102.5 | 0.74 | 1031 | 765 | 132 | - |
| 200037_13 | 0.8238 | 1.11 | 0.098 | 1.06 | 0.52 | 10.2093 | 1.06 | 0.061 | 1.07 | 639 | 22.66 | 610.2 | 5.09 | 602.4 | 6.08 | 94.3 | 0.35 | 866 | 300 | 99 | - |
| 200037_14 | 0.7972 | 1.28 | 0.098 | 1.07 | 0.44 | 10.2041 | 1.07 | 0.059 | 1.25 | 566.9 | 27.02 | 595.2 | 5.78 | 602.7 | 6.16 | 106.3 | 0.28 | 187 | 53 | 21 | - |
| 200037_15 | 0.778 | 1.14 | 0.0938 | 1.06 | 0.50 | 10.6621 | 1.06 | 0.0602 | 1.10 | 609.4 | 23.48 | 584.4 | 5.06 | 577.9 | 5.86 | 94.8 | 0.56 | 807 | 455 | 93 | - |
| 200037_16 | 0.783 | 1.15 | 0.0955 | 1.06 | 0.50 | 10.4712 | 1.06 | 0.0595 | 1.11 | 583.9 | 23.8 | 587.2 | 5.12 | 588 | 5.96 | 100.7 | 0.34 | 875 | 296 | 98 | - |
| 200037_17 | 0.7852 | 1.12 | 0.0948 | 1.05 | 0.51 | 10.5463 | 1.05 | 0.0601 | 1.08 | 605.7 | 23.15 | 588.5 | 5.02 | 584 | 5.91 | 96.4 | 0.48 | 648 | 311 | 74 | 1 |
| 200037_18 | 0.8209 | 1.11 | 0.0978 | 1.05 | 0.51 | 10.227 | 1.05 | 0.0609 | 1.07 | 635.3 | 22.65 | 608.5 | 5.07 | 601.4 | 6.07 | 94.7 | 0.31 | 853 | 265 | 97 | 1 |
| 200037_19 | 0.8364 | 1.15 | 0.0999 | 1.06 | 0.50 | 10.011 | 1.06 | 0.0607 | 1.10 | 629.7 | 23.6 | 617.2 | 5.31 | 613.7 | 6.21 | 97.5 | 0.37 | 1240 | 461 | 146 | - |
| 200037_20 | 0.832 | 1.11 | 0.0982 | 1.06 | 0.53 | 10.1843 | 1.06 | 0.0615 | 1.06 | 655.1 | 22.62 | 614.7 | 5.12 | 603.8 | 6.10 | 92.2 | 0.42 | 1037 | 439 | 122 | 1 |
| 200037_21 | 0.8104 | 1.11 | 0.0966 | 1.06 | 0.52 | 10.3509 | 1.06 | 0.0608 | 1.07 | 633.3 | 22.77 | 602.7 | 5.06 | 594.5 | 6.01 | 93.9 | 0.43 | 878 | 381 | 101 | - |
| 200037_22 | 0.7894 | 1.17 | 0.095 | 1.06 | 0.49 | 10.5219 | 1.06 | 0.0602 | 1.13 | 612.1 | 24.06 | 590.8 | 5.22 | 585.3 | 5.94 | 95.6 | 0.35 | 353 | 124 | 39 | - |
| 200037_23 | 0.8183 | 1.31 | 0.0986 | 1.07 | 0.44 | 10.1399 | 1.07 | 0.0602 | 1.28 | 609.9 | 27.43 | 607.1 | 5.99 | 606.3 | 6.22 | 99.4 | 0.27 | 212 | 57 | 24 | - |
| 200037_24 | 0.7992 | 1.15 | 0.0974 | 1.06 | 0.50 | 10.2712 | 1.06 | 0.0595 | 1.11 | 586.5 | 23.71 | 596.4 | 5.17 | 598.9 | 6.07 | 102.1 | 0.34 | 648 | 218 | 73 | - |

| | Isotope ratios | | | | | | | | | | Age estimates (ma) | | | | | | | Concentrations | | | | |
|---|---|---|---|---|---|---|---|---|---|---|---|---|---|---|---|---|---|---|---|---|---|---|
| | Concordia output | | | | | Tera-Wasserburg output | | | | | | | | | | | | | | | | Pb com. |
| Analysis_# | Pb207 U235 | 1s% | Pb206 U238 | 1s% | roh | 238/206 | 1s% | 207/206 | 1s% | | Pb207 Pb206 | 1s | Pb207 U235 | 1s | Pb206 U238 | 1s | conc | Th/U | U* | Th* | Pbtot* | >LLD (%) |
| Umbukta | | | | | | | | | | | | | | | | | | | | | | |
| 200038_01 | 0.7949 | 1.39 | 0.0956 | 1.08 | 0.40 | 10.4657 | 1.08 | 0.0603 | 1.38 | | 615.5 | 29.27 | 594 | 6.27 | 588.3 | 6.08 | 95.6 | 0.67 | 175 | 117 | 21 | 5 |
| 200038_02 | 0.7998 | 1.35 | 0.098 | 1.08 | 0.43 | 10.2062 | 1.08 | 0.0592 | 1.32 | | 574.6 | 28.56 | 596.7 | 6.11 | 602.6 | 6.20 | 104.9 | 0.64 | 203 | 129 | 25 | - |
| 200038_03 | 0.7878 | 1.57 | 0.0966 | 1.10 | 0.36 | 10.3563 | 1.10 | 0.0592 | 1.55 | | 573.3 | 33.35 | 589.9 | 7.00 | 594.2 | 6.23 | 103.6 | 0.53 | 159 | 85 | 19 | - |
| 200038_04 | 0.7688 | 1.38 | 0.0928 | 1.08 | 0.42 | 10.7805 | 1.08 | 0.0601 | 1.35 | | 607.5 | 28.95 | 579.1 | 6.08 | 571.8 | 5.91 | 94.1 | 0.46 | 128 | 59 | 14 | - |
| 200038_05 | 0.822 | 1.45 | 0.0983 | 1.09 | 0.39 | 10.176 | 1.09 | 0.0607 | 1.43 | | 627.2 | 30.52 | 609.1 | 6.65 | 604.3 | 6.27 | 96.3 | 0.49 | 134 | 66 | 16 | - |
| 200038_06 | 0.8035 | 1.26 | 0.0964 | 1.07 | 0.46 | 10.3788 | 1.07 | 0.0605 | 1.22 | | 620.8 | 26.29 | 598.8 | 5.72 | 593 | 6.07 | 95.5 | 0.56 | 176 | 98 | 21 | 6 |
| 200038_07 | 0.7999 | 1.32 | 0.0977 | 1.08 | 0.43 | 10.2407 | 1.08 | 0.0594 | 1.30 | | 581.9 | 27.81 | 596.7 | 5.97 | 600.6 | 6.17 | 103.2 | 0.45 | 135 | 60 | 16 | - |
| 200038_08 | 0.8037 | 1.41 | 0.0968 | 1.08 | 0.41 | 10.3295 | 1.08 | 0.0602 | 1.38 | | 611 | 29.66 | 598.9 | 6.38 | 595.7 | 6.16 | 97.5 | 0.36 | 103 | 37 | 12 | - |
| 200038_09 | 0.7677 | 1.16 | 0.0936 | 1.06 | 0.50 | 10.6883 | 1.06 | 0.0595 | 1.11 | | 585.6 | 24 | 578.4 | 5.11 | 576.6 | 5.86 | 98.5 | 1.10 | 746 | 824 | 98 | - |
| 200038_10 | 0.7683 | 1.56 | 0.094 | 1.10 | 0.37 | 10.6338 | 1.10 | 0.0593 | 1.54 | | 576.3 | 33.1 | 578.8 | 6.86 | 579.4 | 6.07 | 100.5 | 0.32 | 77 | 24 | 8 | - |
| 200038_11 | 0.7957 | 1.22 | 0.0966 | 1.07 | 0.48 | 10.3563 | 1.07 | 0.0598 | 1.17 | | 594.6 | 25.55 | 594.4 | 5.47 | 594.2 | 6.06 | 99.9 | 0.67 | 267 | 179 | 33 | - |
| 200038_12 | 0.7786 | 1.16 | 0.0947 | 1.07 | 0.50 | 10.5552 | 1.07 | 0.0596 | 1.12 | | 589 | 24.12 | 584.7 | 5.18 | 583.5 | 5.93 | 99.1 | 0.66 | 357 | 236 | 43 | - |
| 200038_13 | 0.7815 | 1.27 | 0.0969 | 1.07 | 0.46 | 10.3178 | 1.07 | 0.0585 | 1.23 | | 547.8 | 26.83 | 586.4 | 5.68 | 596.4 | 6.10 | 108.9 | 0.61 | 189 | 115 | 23 | - |
| 200038_14 | 0.7736 | 1.28 | 0.095 | 1.07 | 0.45 | 10.5307 | 1.07 | 0.0591 | 1.25 | | 570.3 | 26.97 | 581.8 | 5.69 | 584.8 | 5.99 | 102.5 | 0.58 | 159 | 91 | 19 | - |
| 200038_15 | 0.8027 | 1.29 | 0.0969 | 1.07 | 0.45 | 10.321 | 1.07 | 0.0601 | 1.25 | | 606.4 | 26.85 | 598.3 | 5.82 | 596.2 | 6.11 | 98.3 | 0.54 | 159 | 87 | 19 | - |
| 200038_16 | 0.8134 | 1.41 | 0.0982 | 1.08 | 0.41 | 10.1792 | 1.08 | 0.0601 | 1.38 | | 605.5 | 29.73 | 604.4 | 6.44 | 604.1 | 6.25 | 99.8 | 0.45 | 114 | 51 | 13 | - |
| 200038_17 | 0.7965 | 1.30 | 0.0957 | 1.08 | 0.45 | 10.4482 | 1.08 | 0.0604 | 1.26 | | 616.4 | 27.07 | 594.9 | 5.85 | 589.2 | 6.05 | 95.6 | 0.59 | 179 | 106 | 22 | 5 |
| 200038_18 | 0.8046 | 1.29 | 0.0963 | 1.07 | 0.45 | 10.3842 | 1.07 | 0.0606 | 1.25 | | 624.9 | 26.94 | 599.4 | 5.86 | 592.7 | 6.08 | 94.8 | 0.46 | 155 | 71 | 18 | - |
| 200038_19 | 0.8019 | 1.28 | 0.0977 | 1.07 | 0.45 | 10.2312 | 1.07 | 0.0595 | 1.24 | | 585.5 | 26.77 | 597.9 | 5.78 | 601.1 | 6.16 | 102.7 | 0.62 | 166 | 102 | 20 | - |
| 200038_20 | 0.7778 | 1.16 | 0.0942 | 1.06 | 0.51 | 10.6135 | 1.06 | 0.0599 | 1.10 | | 598.8 | 23.86 | 584.2 | 5.14 | 580.4 | 5.90 | 96.9 | 0.84 | 474 | 400 | 59 | - |
| 200038_21 | 0.8102 | 1.72 | 0.0981 | 1.11 | 0.32 | 10.1958 | 1.11 | 0.0599 | 1.72 | | 600.4 | 36.66 | 602.6 | 7.82 | 603.1 | 6.42 | 100.4 | 0.32 | 69 | 22 | 8 | - |
| 200038_22 | 0.8023 | 1.17 | 0.0965 | 1.07 | 0.49 | 10.3638 | 1.07 | 0.0603 | 1.13 | | 614.6 | 24.01 | 598.1 | 5.27 | 593.8 | 6.03 | 96.6 | 0.76 | 375 | 284 | 47 | - |
| 200038_23 | 0.8092 | 1.38 | 0.0982 | 1.08 | 0.42 | 10.1864 | 1.08 | 0.0598 | 1.35 | | 595.1 | 29.63 | 602 | 6.28 | 603.7 | 6.23 | 101.4 | 0.41 | 127 | 52 | 15 | - |
| 200038_24 | 0.8032 | 1.34 | 0.0983 | 1.08 | 0.43 | 10.1771 | 1.08 | 0.0593 | 1.32 | | 577.4 | 28.21 | 598.6 | 6.07 | 604.2 | 6.22 | 104.6 | 0.50 | 147 | 73 | 17 | - |

E8: Monazite U-Pb data (Kallvatnet)

| | | | | Isotope ratios | | | | | | | | | | Age estimates (ma) | | | | |
|---|---|---|---|---|---|---|---|---|---|---|---|---|---|---|---|---|---|---|
| | | | | Concordia output | | | | | Tera-Wasserburg output | | | | | | | | | |
| Analysis_# | Comments | analysis nr. | | Pb207/U235 | 1s% | Pb206/U238 | 1s% | roh | 238/206 | 1s% | 207/206 | 1s% | Pb207/Pb206 | 1s | Pb207/U235 | 1s | Pb206/U238 | 1s | conc |
| monazite_001 | **gmf2020-02** omr 6 #1 | 1 | matrix | 0.647 | 1.51 | 0.07647 | 1.01 | 0.28 | 13.07702 | 1.01 | 0.06128 | 1.57 | 649.1 | 4.6 | 506.8 | 5.09 | 475 | 6.04 | 73.2 |
| monazite_002 | gmf2020-02 omr 1 #1 | 2 | garnet | 0.571 | 1.15 | 0.07373 | 0.96 | 0.37 | 13.56300 | 0.96 | 0.05605 | 1.20 | 454.1 | 4.29 | 458.6 | 4.80 | 458.6 | 4.25 | 101.0 |
| monazite_003 | gmf2020-02 omr 1 #2 | 3 | garnet | 0.811 | 1.11 | 0.09585 | 0.97 | 0.39 | 10.43297 | 0.97 | 0.06126 | 1.16 | 648.5 | 5.45 | 603.1 | 6.58 | 590.1 | 5.04 | 91.0 |
| ~~monazite_004~~ | ~~gmf2020-02 omr 1 #3~~ | 4 | garnet, exclu | ~~101.3~~ | ~~8.98~~ | ~~0.50778~~ | ~~9.72~~ | ~~0.60~~ | ~~1.96936~~ | ~~9.72~~ | ~~1.44386~~ | ~~8.36~~ | ~~5748.5~~ | ~~211.1~~ | ~~4699~~ | ~~13.48~~ | ~~2647~~ | ~~90.26~~ | ~~46.1~~ |
| monazite_005 | gmf2020-02 omr 1 #4 | 5 | garnet | 0.744 | 1.28 | 0.09141 | 0.98 | 0.34 | 10.93972 | 0.98 | 0.05894 | 1.32 | 564.9 | 5.3 | 564.9 | 5.82 | 563.9 | 5.52 | 99.8 |
| monazite_006 | gmf2020-02 omr 1 #5 | 6 | garnet | 0.626 | 1.31 | 0.07788 | 0.99 | 0.32 | 12.84027 | 0.99 | 0.05816 | 1.36 | 535.3 | 4.59 | 493.4 | 5.40 | 483.5 | 5.11 | 90.3 |
| monazite_007 | gmf2020-02 omr 2 #1 | 7 | matrix | 0.615 | 1.12 | 0.07784 | 0.96 | 0.39 | 12.84687 | 0.96 | 0.05721 | 1.15 | 499.2 | 4.51 | 486.8 | 5.03 | 483.2 | 4.32 | 96.8 |
| monazite_008 | gmf2020-02 omr 3 #1 | 8 | garnet | 0.709 | 1.14 | 0.08404 | 0.98 | 0.39 | 11.89910 | 0.98 | 0.06105 | 1.18 | 641.1 | 4.86 | 544 | 5.60 | 520.2 | 4.79 | 81.1 |
| monazite_011 | **gmf2020-10** omr 2 #1 | 1 | matrix | 14.17 | 4.03 | 0.20046 | 3.45 | 0.25 | 4.98853 | 3.45 | 0.51171 | 4.61 | 4275.3 | 37.14 | 2761 | 1544.64 | 1178 | 38.27 | 27.5 |
| monazite_012 | gmf2020-10 omr 3 #1 | 2 | garnet? | 0.608 | 5.21 | 0.05841 | 1.78 | 0.08 | 17.12036 | 1.78 | 0.07533 | 5.36 | 1077.3 | 6.31 | 482.3 | 23.70 | 366 | 19.99 | 34.0 |
| monazite_013 | gmf2020-10 omr 4 #1 | 3 | matrix | 7.405 | 1.07 | 0.09417 | 1.01 | 0.41 | 10.61909 | 1.01 | 0.5692 | 1.13 | 4431.3 | 5.6 | 2162 | 1.78 | 580.1 | 9.57 | 13.1 |
| monazite_014 | gmf2020-10 omr 1 #1 | 4 | matrix | 0.557 | 1.60 | 0.06611 | 1.01 | 0.27 | 15.12630 | 1.01 | 0.06094 | 1.64 | 637.1 | 4.08 | 449.3 | 13.15 | 412.7 | 5.80 | 64.8 |
| monazite_025 | **gmf2020-11** omr 6 #1 | 1 | matrix | 0.702 | 1.42 | 0.08992 | 1.01 | 0.32 | 11.12100 | 1.01 | 0.05649 | 1.45 | 471.1 | 5.36 | 540 | 5.98 | 555.1 | 5.94 | 117.8 |
| monazite_026 | gmf2020-11 omr 17 #1 | 2 | matrix | 1.062 | 1.28 | 0.09394 | 1.00 | 0.35 | 10.64509 | 1.00 | 0.0818 | 1.32 | 1240.7 | 5.56 | 734.8 | 6.33 | 578.8 | 6.69 | 46.7 |
| monazite_027 | gmf2020-11 omr 18 #1 | 3 | matrix | 1.336 | 1.11 | 0.10077 | 0.98 | 0.41 | 9.92359 | 0.98 | 0.09591 | 1.15 | 1546 | 5.82 | 861.3 | 6.33 | 618.9 | 6.46 | 40.0 |
| monazite_028 | gmf2020-11 omr 19 #1 | 4 | matrix | 2.046 | 1.25 | 0.10755 | 1.02 | 0.37 | 9.29800 | 1.02 | 0.13766 | 1.29 | 2197.9 | 6.38 | 1131 | 6.53 | 658.5 | 8.52 | 30.0 |
| monazite_029 | gmf2020-11 omr 20 #1 | 5 | matrix | 1.194 | 1.14 | 0.0968 | 0.99 | 0.41 | 10.33058 | 0.99 | 0.08927 | 1.17 | 1409.9 | 5.63 | 797.9 | 6.45 | 595.6 | 6.28 | 42.2 |
| monazite_030 | gmf2020-11 omr 30 #1 | 6 | matrix | 1.732 | 2.63 | 0.10328 | 1.36 | 0.18 | 9.68242 | 1.36 | 0.12132 | 2.74 | 1975.7 | 8.16 | 1020 | 9.86 | 633.6 | 16.96 | 32.1 |

Gaute Moe Fløan

# Caledonian structural, metamorphic and magmatic evolution of the Rödingsfjället Nappe Complex

NTNU
Norwegian University of
Science and Technology